USAFSAM-TR-85-73

RADIOFREQUENCY RADIATION DOSIMETRY HANDBOOK

(Fourth Edition)

Carl H. Durney, Ph.D.
Habib Massoudi, Ph.D.
Magdy F. Iskander, Ph.D.

Electrical Engineering Department
The University of Utah
Salt Lake City, UT 84112

October 1986

Final Report for Period 1 July 1984 – 31 December 1985

Approved for public release; distribution is unlimited.

Prepared for

USAF SCHOOL OF AEROSPACE MEDICINE
Aerospace Medical Division (AFSC)
Brooks Air Force Base, TX 78235-5301

DISCLAIMER NOTICE

THIS DOCUMENT IS BEST QUALITY
PRACTICABLE. THE COPY FURNISHED
TO DTIC CONTAINED A SIGNIFICANT
NUMBER OF PAGES WHICH DO NOT
REPRODUCE LEGIBLY.

NOTICES

This final report was submitted by the University of Utah, Salt Lake City, Utah, under contract F33615-82-C-0601, job order 7757-01-95, with the USAF School of Aerospace Medicine, Aerospace Medical Division, AFSC, Brooks Air Force Base, Texas. Mr. William Hurt (USAFSAM/RZP) was the Laboratory Project Scientist-in-Charge.

When Government drawings, specifications, or other data are used for any purpose other than in connection with a definitely Government-related procurement, the United States Government incurs no responsibility nor any obligation whatsoever. The fact that the Government may have formulated or in any way supplied the said drawings, specifications, or other data, is not to be regarded by implication, or otherwise in any manner construed, as licensing the holder or any other person or corporation; or as conveying any rights or permission to manufacture, use, or sell any patented invention that may in any way be related thereto.

The Office of Public Affairs has reviewed this report, and it is releasable to the National Technical Information Service where it will be available to the general public, including foreign nationals.

This report has been reviewed and is approved for publication.

WILLIAM D. HURT, M.S.
Project Scientist

JOHN C. MITCHELL, B.S.
Supervisor

JEFFREY G. DAVIS, Colonel, USAF, MC
Commander

REPORT DOCUMENTATION PAGE

1a. REPORT SECURITY CLASSIFICATION UNCLASSIFIED		1b. RESTRICTIVE MARKINGS		
2a. SECURITY CLASSIFICATION AUTHORITY		3. DISTRIBUTION / AVAILABILITY OF REPORT Approved for public release; distribution is unlimited.		
2b. DECLASSIFICATION / DOWNGRADING SCHEDULE				
4. PERFORMING ORGANIZATION REPORT NUMBER(S)		5. MONITORING ORGANIZATION REPORT NUMBER(S) USAFSAM-TR-85-73		
6a. NAME OF PERFORMING ORGANIZATION Electrical Engineering Dept. University of Utah	6b. OFFICE SYMBOL (If applicable)	7a. NAME OF MONITORING ORGANIZATION USAF School of Aerospace Medicine (RZP)		
6c. ADDRESS (City, State, and ZIP Code) 4504 Merrill Engineering Building Salt Lake City, UT 84112		7b. ADDRESS (City, State, and ZIP Code) Aerospace Medical Division (AFSC) Brooks Air Force Base, TX 78235-5301		
8a. NAME OF FUNDING / SPONSORING ORGANIZATION	8b. OFFICE SYMBOL (If applicable)	9. PROCUREMENT INSTRUMENT IDENTIFICATION NUMBER F33615-82-C-0601		
8c. ADDRESS (City, State, and ZIP Code)		10. SOURCE OF FUNDING NUMBERS		

		PROGRAM ELEMENT NO. 62202F	PROJECT NO. 7757	TASK NO. 01	WORK UNIT ACCESSION NO. 95

11. TITLE (Include Security Classification)

Radiofrequency Radiation Dosimetry Handbook (Fourth Edition)

12. PERSONAL AUTHOR(S)
Durney, Carl H.; Massoudi, Habib; and Iskander, Magdy F.

13a. TYPE OF REPORT Final	13b. TIME COVERED FROM 1 Jul 84 TO 31 Dec 85	14. DATE OF REPORT (Year, Month, Day) 1986, October	15. PAGE COUNT 510

16. SUPPLEMENTARY NOTATION
Supersedes first three editions of the handbook:
USAFSAM-TRs 76-35, 78-22, and 80-32

17.	COSATI CODES		18. SUBJECT TERMS (Continue on reverse if necessary and identify by block number)
FIELD	GROUP	SUB-GROUP	Radiation biology (dosimetry, health physics) Thermodynamics
06	18		
20	13		

19. ABSTRACT (Continue on reverse if necessary and identify by block number)

The purpose of this fourth edition is to provide a convenient compilation of information contained in the previous editions, including updated tables of published data, and to add new information. Chapter 2 contains information about how to use this handbook. Chapter 3 contains a discussion of the basics of electromagnetics for readers who are not physicists or engineers. Chapter 4 gives information about permittivities and contains an updated compilation of the summaries of published data from previous editions. Theoretical dosimetry is discussed in Chapter 5, including a brief discussion of methods used for dosimetric calculations, data for models of biological systems, and a tabulated summary of published work in theoretical dosimetry. The calculated dosimetric data in Chapter 6 contains, in addition to material from previous editions, some new calculated average-SAR data for spheroidal models at frequencies well beyond resonance. These calculations were made by a new technique called the iterative extended boundary condition method (IEBCM),

(continued)

20. DISTRIBUTION / AVAILABILITY OF ABSTRACT ☒ UNCLASSIFIED/UNLIMITED ☐ SAME AS RPT. ☐ DTIC USERS	21. ABSTRACT SECURITY CLASSIFICATION Unclassified	
22a. NAME OF RESPONSIBLE INDIVIDUAL William D. Hurt	22b. TELEPHONE (Include Area Code) (512) 536-2209	22c. OFFICE SYMBOL USAFSAM/RZP

DD FORM 1473, 84 MAR

83 APR edition may be used until exhausted.
All other editions are obsolete.

19. ABSTRACT (continued).

which was developed at the University of Utah after the third edition was published. Chapter 6 also contains some new calculated average-SAR data for spheroidal models irradiated by near fields. Chapter 7 contains information about experimental dosimetry, including a history of experimental dosimetry and a discussion of experimental techniques. Chapter 8 contains updated experimental dosimetric data. Information on very low frequency radiation dosimetry, which is not found in any previous edition, is given in Chapter 9. The information on heat-response calculations in Chapter 10 is compiled and updated from previous editions. Chapter 11 contains a discussion of current RFR safety standards.

PREFACE

The first edition of the Radiofrequency Radiation Dosimetry Handbook, SAM-TR-76-35 (September 1976), was published with the objective of providing the best information then available about electromagnetic energy absorption. In that edition the dosimetric data were limited mostly to the lower part of the electromagnetic spectrum, principally in the 10 kHz-1.5 GHz range, and also to homogeneous spheroidal and ellipsoidal models of humans and other animals. The data clearly demonstrated the importance of frequency, geometric configuration, and orientation in the assessment of biological effects induced by radiofrequency (RF) radiation.

The second edition of the handbook, SAM-TR-78-22 (May 1978), provided expanded dosimetric data. The frequency range was broadened to the 10 MHz-100 GHz band. The data included absorption of models irradiated by planewaves in free space, absorption of models on or near ground planes, heat-response calculations, and some scattering data. Empirical relations for calculating the rate of energy absorption; some rules of thumb for electromagnetic absorption; and data from the literature for metabolic rates, dielectric constants, and conductivities were also included as well as tables summarizing the experimental data and theoretical techniques found in the literature.

The third edition of the handbook, SAM-TR-80-32 (August 1980), was published mainly to provide new data on near-field absorption, which up until that time was scarce because near-field calculations are so difficult to make. The data consisted of specific absorption rates (SARs) for spheroids and cylinders irradiated by short dipoles and small loops, and a block model of man irradiated by simple aperture fields. Also included were absorption data for spheroidal models irradiated by circularly polarized planewaves, multilayered cylindrical models irradiated by planewaves, and spheroidal models irradiated in K polarization by planewaves for frequency ranges in which calculations had not been possible for the second edition. Tables in the second edition that summarized experimental data and theoretical techniques found in the literature were updated; although generally speaking, material contained in the first and second editions was not included in the third edition.

- iii -

The third edition also had a section on dosimetric techniques, which included a history of electromagnetic dosimetry and a section on qualitative near-field dosimetry. The material on qualitative explanations of near-field SARs is especially important because near-field SARs cannot be normalized to incident-power density, as planewave SARs can be. Since near-field radiation fields vary so much from one radiation source to another, near-field dosimetric data for specific sources could not be given; only near-field SAR data for simple illustrative radiation fields were presented.

The purpose of this fourth edition is to provide a convenient compilation of information contained in the previous editions, including updated tables of published data, and to add new information.

ACKNOWLEDGMENTS

Collaborators and Contributors

Eleanor R. Adair, Ph.D.
John B. Pierce Foundation Laboratory
Yale University, New Haven, Connecticut

Stewart J. Allen, B.S.
National Center for Devices and Radiological Health
Rockville, Maryland

Peter W. Barber, Ph.D.
Clarkson College, Potsdam, New York

Arthur W. Guy, Ph.D.
University of Washington, Seattle, Washington

William D. Hurt, M.S.
U.S. Air Force School of Aerospace Medicine
Brooks Air Force Base, Texas

Curtis C. Johnson (deceased)

James L. Lords, Ph.D.
University of Utah, Salt Lake City, Utah

Luis Lozano (deceased)

John C. Mitchell, B.S.
U.S. Air Force School of Aerospace Medicine
Brooks Air Force Base, Texas

David K. Ryser, B.S.
Rochester, Minnesota

Herman P. Schwan, Ph.D.
University of Pennsylvania, Philadelphia, Pennsylvania

Reviewers

Stewart J. Allen, B.S.
National Center for Devices and Radiological Health
Rockville, Maryland

Kenneth R. Foster, Ph.D.
University of Pennsylvania, Philadelphia, Pennsylvania

Donald I. McRee, Ph.D.
    National Institute of Environmental Health Sciences
    Research Triangle Park, North Carolina

Richard G. Olsen, Ph.D.
    Naval Aerospace Medical Research Laboratory
    Pensacola, Florida

Herman P. Schwan, Ph.D.
    University of Pennsylvania, Philadelphia, Pennsylvania

Thomas S. Tenforde, Ph.D.
    University of California, Berkeley, California

CONTENTS

LIST OF ILLUSTRATIONS

LIST OF TABLES

RADIOFREQUENCY RADIATION DOSIMETRY HANDBOOK
(Fourth Edition)

CHAPTER 1. INTRODUCTION

The radiofrequency portion of the electromagnetic spectrum extends over a wide range of frequencies, from about 10 kHz to 300 GHz. In the last two or three decades, the use of devices that emit radiofrequency radiation (RFR) has increased dramatically. Radiofrequency devices include, for example, radio and television transmitters, military and civilian radar systems, extensive communications systems (including satellite communications systems and a wide assortment of mobile radios), microwave ovens, industrial RF heat sealers, and various medical devices.

The proliferation of RF devices has been accompanied by increased concern about ensuring the safety of their use. Throughout the world many organizations, both government and nongovernment, have established RFR safety standards or guidelines for exposure. Because of different criteria, the USSR and some of the Eastern European countries have more stringent safety standards than most Western countries. The Soviet standards are based on central-nervous-system and behavioral responses attributed to RFR exposure in animals. In Western countries the standards are based primarily on the calculated thermal burden that would be produced in people exposed to RFR. In each case, better methods are needed to properly extrapolate or relate effects observed in animals to similar effects expected to be found in people. (The development of new RFR safety guidelines is discussed in Chapter 11.) Safety standards will be revised as more knowledge is obtained about RFR effects on the human body.

An essential element of the research in biological effects of RFR is dosimetry--the determination of energy absorbed by an object exposed to the electromagnetic (EM) fields composing RFR. Since the energy absorbed is directly related to the internal EM fields (that is, the EM fields inside the object, not the EM fields incident upon the object), dosimetry is also interpreted to mean the determination of internal EM fields. The internal and incident EM fields can be quite different, depending on the size and shape of

the object, its electrical properties, its orientation with respect to the incident EM fields, and the frequency of the incident fields. Because any biological effects will be related directly to the internal fields, any cause-and-effect relationship must be formulated in terms of these fields, not the incident fields. However, direct measurement of the incident fields is easier and more practical than of the internal fields, especially in people, so we use dosimetry to relate the internal fields (which cause the effect) to the incident fields (which are more easily measured). As used here, the term "internal fields" is to be broadly interpreted as fields that interact directly with the biological system and include, for example, the fields that, in perception of 60-Hz EM fields, move hair on the skin as well as fields that act on nerves well inside the body. In general, the presence of the body causes the internal fields to be different from the incident fields (the fields without the body present).

Dosimetry is important in experiments designed to discover biological effects produced by RFR and in relating those effects to RFR exposure of people. First, we need dosimetry to determine which internal fields in animals cause a given biological effect. Then we need dosimetry to determine which incident fields would produce similar internal fields in people, and therefore a similar biological effect. Dosimetry is needed whether the effects are produced by low-level internal fields or the higher level fields that cause body temperature to rise.

In small-animal experiments dosimetry is especially important because size greatly affects energy absorption. For example, at 2450 MHz the average absorption per unit mass in a medium rat could be about 10 times that in an average man for the same incident fields. Thus at 2450 MHz at the same average energy absorption per unit mass, a hypothetical biological effect that occurred in the rat should not be expected to occur in man unless the incident fields for the man were much higher than those irradiating the rat. Similarly, an effect observed in one animal in some given incident fields may not be observed in a different-size animal in the same incident fields, only because the internal fields could be quite different in the two animals. Another possibility is that the physiological response to the internal fields

of the two species could be quite different. For example, different species often respond differently to the added heat burden of applied EM fields.

The dosimetric data are presented here in terms of the specific absorption rate (SAR) in watts per kilogram. Adoption of the term "SAR" was suggested by the National Council on Radiation Protection and Measurement and has been generally accepted by the engineering and scientific community. The terms "dose rate" and "density of absorbed power" (often called absorbed-power density), which commonly appear in the engineering literature, are equivalent to SAR. Each of these terms refers to the amount of energy absorbed per unit time per unit volume, or per unit time per unit mass. In this document we give the SAR in watts per kilogram by assuming that the average tissue density is 1 g/cm^3. The total power absorbed in comparison with the body surface is also of interest. In many animals heat is dissipated through the surface by evaporation or radiative heat transfer; thus power density in watts per square meter of body surface area may indicate the animal's ability to dissipate electromagnetic power. This is not a rigorous indicator of hazard for animals, however, as many other heat-dissipation mechanisms specific to species are also important, as well as environmental temperature and humidity effects.

The rigorous analysis of a realistically shaped inhomogeneous model for humans or experimental animals would be an enormous theoretical task. Because of the difficulty of solving Maxwell's equations, which form the basis of analysis, a variety of special models and techniques have been used, each valid only in a limited range of frequency or other parameter. Early analyses were based on plane-layered, cylindrical, and spherical models. The calculated dosimetric data presented in this handbook are based primarily on a combination of cylindrical, ellipsoidal, spheroidal, and block models of people and experimental animals. Although these models are relatively crude representations of the size and shape of the human body, experimental results show that calculations of the average SAR agree reasonably well with measured values. Calculations of the local distribution of the SAR, however, are much more difficult and are still in early stages of development.

CHAPTER 2. HOW TO USE DOSIMETRIC DATA IN THIS HANDBOOK

The material in this section is intended to help the reader interpret and use the qua. itative dosimetric information contained in this handbook. Readers not familiar with some of the concepts or terms used in this chapter may wish to read Chapter 3 (background and qualitative information about dosimetry) in conjunction with this material.

Although the dosimetry data are given in terms of SAR, the internal E-field can be obtained directly from the SAR by solving for the internal E-field from Equation 3.49 (Section 3.3.6):

$$E_{in} = \sqrt{\frac{\rho_m \text{ SAR}}{\omega \epsilon_o \epsilon''}} \qquad (2.1)$$

For a given frequency, the internal fields in irradiated objects are a strong function of the size of the object (see Chapters 6 and 8). In extrapolating results obtained from an experimental animal of one size to an animal of another size or from an experimental animal to a man, it is often important to determine what incident fields would produce the same (or approximately the same) internal fields in these different-size animals. For example, a person studying biological effects in rats irradiated at 2450 MHz may want to relate those to effects expected to occur in humans exposed to the same radiation. Since the rat and man are very different in size, exposing them to the same incident fields would result in quite different internal fields. Therefore, if their internal fields are to be similar, the incident fields irradiating each must be different. We have two general ways to adjust the incident fields to get similar internal fields:

1. Change the power density of the incident radiation.
2. Change the frequency of the incident radiation.

The first might be called power extrapolation; the second, frequency extrapolation. Under either condition, the internal-field patterns in the two cases would differ even if the average SARs were the same. The internal distributions can be made similar in a very approximate sense, however, by relating the wavelength of the incident radiation to the length of the object.

When biological effects are due to heat generated by the radiation, combined power and frequency extrapolation is probably the better course; it makes the average SARs nearly the same and results in a similar distribution of internal fields, which depends strongly on the relationship of absorber size to wavelength. For studying effects that might be strongly frequency dependent, such as a molecular resonance of some kind, frequency extrapolation would not be appropriate.

The following examples will illustrate both kinds of extrapolation and generally how the dosimetric data in this handbook might be used.

EXAMPLE 1

Suppose that in a study of RF-induced biological effects a 320-g rat is being exposed to E-polarized RF radiation at 2450 MHz with an incident-power density of 20 mW/cm^2. The researcher desires to know what exposure conditions would cause approximately the same average SAR and internal-field distribution in an average man that the 20 mW/cm^2 at 2450 MHz produces in the rat. Since the physiological characteristics of rats differ significantly in many respects from those of people, any interpretation of the rat's biological responses in terms of possible human responses must be made with great care. By this example we are not implying that any such interpretation would be at all meaningful; that must be left to the judgment of the researcher for a particular experiment. On the other hand, knowing exposure conditions that would produce similar average SARs and internal-field distributions in rats and people is desirable for many experiments. The following information is provided for such cases.

First, because the rat is much smaller than a man, at 2450 MHz their internal field patterns will differ considerably. One indication of this difference can be obtained from Equation 3.46 (Section 3.3.4). The skin depth (δ) at 2450 MHz is about 2 cm. From Tables 5.2 and 5.4, the values of the semiminor axis (b) for prolate spheroidal models of an average man and a 320-g rat are 13.8 and 2.76 cm respectively; thus the ratio δ/b for an average man is 0.14; for the rat, 0.72. These ratios indicate that any RF heating would be like surface heating for the man but more like whole-body heating for

the rat. Consequently, comparing RF effects in humans and smaller animals may not be meaningful at 2450 MHz. Comparison might be more meaningful at a lower frequency, where the internal field patterns in the man and the rat would be more similar. A simple way to choose an approximate frequency for human exposure is to make $\lambda/2a$, the ratio of the free-space wavelength to length, the same for both the man and the rat. This approximation neglects the change in permittivity with frequency, which is acceptable for these approximate calculations. (More precise methods that include the dependence of permittivity are described in Section 7.2.6.) Since $\lambda = c/f$ (Equation 3.29, Section 3.2.8), requiring $2af$ to be the same for the rat and the man would be equivalent. Thus, we can calculate the frequency for the human exposure to be:

$$2a_h f_h = 2a_r f_r \qquad (2.2)$$

$$f_h = \frac{2a_r}{2a_h} f_r = \frac{20 \text{ cm}}{175 \text{ cm}} \; 2450 \text{ MHz} = 280 \text{ MHz} \qquad (2.3)$$

where subscripts h and r stand for human and rat respectively. This result shows that we should choose a frequency in the range 200-400 MHz for human exposure to compare with the rat exposure at 2450 MHz. Permittivity changes with frequency, so the $\lambda/2a$ ratio does not correspond to the δ/b ratio; however, since both ratios are approximations and the $\lambda/2a$ ratio is easier to calculate, it seems just as well to use it. Another point regarding frequency extrapolation is that meaningful comparisons can probably be made when the frequency for both absorbers is below resonance; but if the frequency for one absorber is far above resonance and the frequency for the other absorber is below resonance, comparisons of SAR will not be meaningful.

Now that we have completed the frequency extrapolation, we can calculate the incident-power density required at 280 MHz to provide the same average SAR in an average man that is produced in a 320-g rat at 2450 MHz with 20-mW/cm^2 incident-power density. The average SAR in the rat for 1-mW/cm^2 incident-power density is 0.22 W/kg (Figure 6.16); thus the average SAR in the rat for 20-mW/cm^2 incident-power density is 4.4 W/kg. The average SAR in the average man at 280 MHz is 0.041 W/kg for 1 mW/cm^2 (Figure 6.3); thus to produce an

average SAR of 4.4 W/kg in the average man would require an incident-power density of $(4.4/0.041)(1 \text{ mW/cm}^2)$, or 107 mW/cm^2.

Our frequency extrapolation resulted in similar relative positions with respect to resonance on the SAR curves for the rat and the man. Yet because the SAR curve for the rat is generally higher than that for man, equivalent exposure of man requires considerably higher incident-power density. The generally higher level of the SAR curve in the rat is due to the combination of size and variation of permittivity with frequency.

EXAMPLE 2

An average man is exposed to an electromagnetic planewave with a power density of 10 mW/cm^2 at 70 MHz with E polarization. What radiation frequency would produce the same average SAR in a small rat as was produced in the man?

Here, as in the previous example, comparing SARs may be meaningful only at frequencies for which the $\lambda/2a$ ratios are similar. From the relation developed in the last example, we find that

$$f_r = \frac{2a_h}{2a_r} f_h = \frac{175 \text{ cm}}{14 \text{ cm}} \, 70 \text{ MHz} = 875 \text{ MHz} \qquad (2.4)$$

Since 70 MHz is approximately the resonant frequency for man (Figure 6.3) and 875 MHz is close to the resonant frequency (900 MHz) for the small rat (Figure 6.15), let's use 900 MHz for the rat. At 70 MHz the average SAR for the average man exposed to 10 mW/cm^2 is 2.4 W/kg (Figure 6.3). For the small rat, the average SAR for 1 mW/cm^2 at 900 mHz is 1.1 W/kg. Hence at 900 MHz, the incident power density for the rat should be $(2.4/1.1)(1 \text{ mW/cm}^2)$, or 2.18 mW/cm^2.

EXAMPLE 3

A 420-g rat (22.5 cm long) is irradiated with an incident planewave power density of 25 mW/cm^2 at a frequency of 400 MHz with E polarization. What incident planewave power density and frequency would be expected to produce a similar internal-field distribution and average SAR in an average man?

Again, frequency extrapolation should be used because 400 MHz is above resonance for the man and below resonance for the rat. The approximate equivalent exposure frequency for man is

$$f_h = \frac{22.5 \text{ cm}}{175 \text{ cm}} \, 400 \text{ MHz} = 51 \text{ MHz} \tag{2.5}$$

Since a curve for a 420-g rat is not included in the dosimetric data, we will calculate the average SAR for the rat by using the empirical formula given in Equation 5.1. The first step is to calculate b for the rat. Since $2a = 22.5$ cm and the volume of the rat is 420 cm^3 (assuming a density of 1 g/cm^3), we can solve for b from the relation for the volume of a prolate spheroid:

$$V = \frac{4}{3} \pi a b^2 \tag{2.6}$$

$$b = \sqrt{\frac{3V}{4\pi a}} = \sqrt{\frac{3 \, (420) \text{ cm}^3}{4\pi \, 11.25 \text{ cm}}} = 2.99 \text{ cm} = 0.0299 \text{ m} \tag{2.7}$$

Now, substituting $a = 0.1125$ m and $b = 0.0299$ m into Equations 5.2 through 5.6 gives us

$$f_o = 567 \text{ MHz}$$

$$f_{o1} \doteq 860 \text{ MHz}$$

$$f_{o2} = 1579 \text{ MHz}$$

$$A_1 = 717$$

$$A_2 = 1226$$

Since f_{o1} and f_{o2} are both larger than 400 MHz, we need not calculate A_3, A_4, and A_5 because $u(f - f_{o1}) = u(f - f_{o2}) = 0$. Substituting into Equation 5.1 results in SAR = 0.44 W/kg for the rat exposed to 1 mW/cm^2 at 400 MHz. The average SAR for the rat exposed to 25 mW/cm^2 at 400 MHz is 11.0 W/kg. For the

average man at 51 MHz for 1-mW/cm^2 incident-power density, the average SAR is 0.11 W/kg (Figure 6.3); hence, to produce 11 W/kg in the man would require 11/0.11 mW/cm^2, or 100 mW/cm^2.

EXAMPLE 4

With E polarization, what incident-power density at resonance would produce in a small rat an average SAR equal to twice the resting metabolic rate? Compare this with the incident-power density at resonance that would produce in an average man an average SAR equal to twice the resting metabolic rate.

For a small rat the resting metabolic rate is 8.51 W/kg (Table 10.4), and the average SAR at resonance is 1.1 W/kg for 1-mW/cm^2 incident-power density (Figure 6.15). The incident-power density to produce an average SAR of 2 × 8.51 W/kg is therefore 17.02/1.1 mW per cm^2, or 15.5 mW/cm^2. For an average man the resting metabolic rate is 1.26 W/kg (Table 10.2), and the average SAR at resonance is 0.24 W/kg for 1-mW/cm^2 incident-power density (Figure 6.3). The incident-power density required to produce an average SAR equal to twice the resting metabolic rate is therefore 2.52/0.24 mW per cm^2, or 10.5 mW/cm^2. Even though the resting metabolic rate for the rat is nearly 7 times larger than that for the man, the incident-power density required for the rat is only 1.5 times that required for the man because the average SAR for the rat is higher than for the man. In general, since smaller animals have higher metabolic rates and also higher values of average SAR at resonance, the ratio of resting metabolic rate to average SAR at resonance probably does not vary by more than an order of magnitude for most animal sizes.

EXAMPLE 5

Suppose that experiments were conducted in which a 200-g rat (16 cm long) was irradiated with an incident planewave power density of 10 μW/cm^2 at a frequency of 2375 MHz, with experimental conditions similar to those of Shandala et al. (1977). Since the incident E- and H-field vectors were parallel to a horizontal plane in which the rat was free to move, the rat was

CHAPTER 3. SOME BASICS OF ELECTROMAGNETICS

A number of concepts are important to understanding any work that involves electromagnetic (EM) fields. The purpose of this chapter is to summarize the most important of these concepts as background for the specific applications described in this handbook. So that they can be understood by readers without an extensive background in electrical engineering or physics, the concepts are explained without complicated mathematical expressions where practical. This material is intended not to encompass all of EM theory but to provide a convenient summary.

3.1. TERMS AND UNITS

3.1.1. Glossary

The following terms are used in this section and throughout this handbook. The list is more an explanation of terms than precise definitions. Boldface symbols indicate vector quantities (see Section 3.1.3 for an explanation of vectors and vector notation).

antenna: A structure that is designed to radiate or pick up electromagnetic fields efficiently. Individual antennas are often used in combinations called antenna arrays.

dielectric constant: Another name for relative permittivity.

electric dipole: Two equal charges of opposite sign separated by an infinitesimally small distance.

electric field: A term often used to mean the same as E-field intensity, or strength.

electric-field intensity: Another term for E-field strength.

electric-field strength: A vector-force field used to represent the forces between electric charges. E-field strength is defined as the vector force per unit charge on an infinitesimal charge at a given place in space.

electric-flux density (displacement): The electric flux passing through a surface, divided by the area of the surface. The total electric flux

passing through a closed surface is equal to the total charge enclosed inside the surface, also equal to the E-field intensity times the permittivity.

electric polarization: Separation of charges in a material to form electric dipoles or alignment of existing electric dipoles in a material when an E-field is applied. Usually designated P, the units of polarization are dipole moments per cubic meter.

energy density: Electromagnetic energy in a given volume of space divided by the volume. The units are joules per cubic meter (J/m^3).

far fields: Electromagnetic fields far enough away from the source producing them that the fields are approximately planewave in nature.

field: A correspondence between a set of points and a set of values. That is, a value is assigned to each of the points. If the value is a scalar, the field is a scalar field; if the value is a vector, the field is a vector field. The temperature at all points in a room is an example of a scalar field. The velocity of the air at all points in a room is an example of a vector field.

field point: A point at which the electric or magnetic field is being evaluated.

frequency: The time rate at which a quantity, such as electric field, oscillates. Frequency is equal to the number of cycles through which the quantity changes per second.

impedance, wave: The ratio of the electric field to magnetic field in a wave. For a planewave in free space, the wave impedance is 377 ohms. For a planewave in a material, the wave impedance is equal to 377 times the square root of the permeability divided by the square root of the permittivity.

magnetic field: A term often used to mean the same as magnetic-flux density, also commonly used to mean the same as magnetic-field intensity. The term has no clear definition or pattern of usage.

magnetic-field intensity: A vector field equal to the magnetic-flux density divided by the permeability. H is a useful designation because it is independent of the magnetization current in materials.

magnetic-flux density: A vector-force field used to describe the force on a moving charged particle, and perpendicular to the velocity of the particle. Magnetic-flux density is defined as the force per unit charge on an infinitesimal charge at a given point in space: $F/q = v \times B$, where F is the vector force acting on the particle, q is the particle's charge, v is its velocity, and B is the magnetic-flux density.

near fields: Electromagnetic fields close enough to a source that the fields are not planewave in nature. Near fields usually vary more rapidly with space than far fields do.

nodes: Positions at which the amplitude is always zero in a standing wave.

permeability: A property of material that indicates how much magnetization occurs when a magnetic field is applied.

permittivity: A property of material that indicates how much polarization occurs when an electric field is applied. Complex permittivity is a property that describes both polarization and absorption of energy. The real part is related to polarization; the imaginary part, to energy absorption.

planewave: A wave in which the wave fronts are planar. The E and H vectors are uniform in the planes of the wave fronts; and E, H, and the direction of propagation (**k**) are all mutually perpendicular.

polarization: Orientation of the incident E- and H-field vectors with respect to the absorbing object.

Poynting vector: A vector equal to the cross product of E and H. The Poynting vector represents the instantaneous power transmitted through a surface per unit surface area. It is usually designated as S, is also known as energy-flux (power) density, and has units of watts per square meter (W/m^2).

propagation constant: A quantity that describes the propagation of a wave. Usually designated **k**, it is equal to the radian frequency divided by the phase velocity, and has units of per meter $\left(m^{-1}\right)$. A complex propagation constant describes both propagation and attenuation. The real part describes attenuation; the imaginary part, propagation.

radian frequency: Number of radians per second at which a quantity is oscillating. The radian frequency is equal to $2\pi f$, where f is the frequency.

radiation: Electromagnetic fields emitted by a source.

reflection coefficient: Ratio of reflected-wave magnitude to incident-wave magnitude.

relative permittivity: Permittivity of a material divided by the permittivity of free space.

scalar field: See field.

specific absorption rate (SAR): Time rate of energy absorbed in an incremental mass, divided by that mass. Average SAR in a body is the time rate of the total energy absorbed divided by the total mass of the body. The units are watts per kilogram (W/kg).

spherical wave: A wave in which the wave fronts are spheres. An idealized point source radiates spherical waves.

standing wave: The wave pattern that results from two waves of the same frequency and amplitude propagating in opposite directions. Destructive interference produces nodes at regularly spaced positions.

standing-wave ratio: Ratio of E_{max} to E_{min} where E_{max} is the maximum value, and E_{min} the minimum, of the magnitude of the E-field intensity anywhere along the path of the wave. A similar definition holds for other quantities that have wave properties.

vector: A quantity having both a magnitude and a direction. Velocity is an example of a vector: Direction of motion is the direction of the velocity vector, and speed is its magnitude.

vector field: See field.

velocity of propagation: Velocity at which a wave propagates. Units are meters per second (m/s). It is equal to how far one point on the wave, such as the crest or trough, travels in 1 s.

wave impedance: (See impedance, wave).

wavelength: The distance between two crests of the wave (or between two troughs or other corresponding points). Units are meters (m).

3.1.2. Measurement Units

The SI system of units was adopted by the Eleventh General Conference on Weights and Measures, held in Paris in 1970. SI is an internationally agreed-upon abbreviation for Système International d'Unitès (International System of Units). Some units we use are listed in Tables 3.1 and 3.2.

TABLE 3.1. THE SI BASIC UNITS

Quantity	Unit	Symbol
Length	meter	m
Mass	kilogram	kg
Time	second	s
Electric current	ampere	A
Temperature	Kelvin	K
Luminous intensity	candela	cd

TABLE 3.2.   SOME DERIVED SI UNITS

Quantity		Measurement Term			
Name	Common Symbol	Name of Unit	Symbol for Unit	Expression in Terms of Other Units	Expression in Terms of SI Base Units
capacitance	C	farad	F	C/V	$m^{-2} \cdot kg^{-1} \cdot s^4 \cdot A^2$
charge	q	coulomb	C	A·s	s·A
conductance	G	siemens	S	Ω^{-1} or A/V	$m^{-2} \cdot kg^{-1} \cdot s^3 \cdot A^2$
conductivity	σ	siemens per meter	S/m	$\Omega^{-1} \cdot m^{-1}$	$m^{-3} \cdot kg^{-1} \cdot s^3 \cdot A^2$
current density	J	ampere per square meter	A/m^2		$m^{-2} \cdot A$
electric-field intensity	E	volts per meter	V/m		$m \cdot kg \cdot s^{-3} \cdot A^{-1}$
electric-flux density (displacement)	D	coulomb per square meter	C/m^2		$m^{-2} \cdot s \cdot A$
energy	W	joule	J	N·m	$m^2 \cdot kg \cdot s^{-2}$
energy-flux density (power density)	S	watt per square meter	W/m^2	$J \cdot s^{-1} \cdot m^{-2}$	$kg \cdot s^{-3}$
frequency	f	hertz	Hz		s^{-1}
impedance	Z	ohm	Ω	V/A	$m^2 \cdot kg \cdot s^{-3} \cdot A^{-2}$
inductance	L	henry	H	Wb/A	$m^2 \cdot kg \cdot s^{-2} \cdot A^{-2}$
magnetic-field intensity	H	ampere per meter	A/m		$m^{-1} \cdot A$
magnetic-flux density	B	tesla	T	Wb/m^2	$kg \cdot s^{-2} \cdot A^{-1}$
permeability	μ	henry per meter	H/m		$m \cdot kg \cdot s^{-2} \cdot A^{-2}$
permittivity	ε	farad per meter	F/m		$m^{-3} \cdot kg^{-1} \cdot s^4 \cdot A^2$
power	P	watt	W	J/s	$m^2 \cdot kg \cdot s^{-3}$
reactance	X	ohm	Ω	V/A	$m^2 \cdot kg \cdot s^{-3} \cdot A^{-2}$
resistance	R	ohm	Ω	V/A	$m^2 \cdot kg \cdot s^{-3} \cdot A^{-2}$
resistivity	ρ	ohm meters	Ωm		$m^3 \cdot kg \cdot s^{-3} \cdot A^{-2}$
voltage (potential difference)	V	volt	V	W/A	$m^2 \cdot kg \cdot s^{-3} \cdot A^{-1}$

3.1.3. Vectors and Fields

Vector Algebra--Vectors are used extensively in descriptions of electric and magnetic fields, so in this section we briefly explain vectors and vector notation. A scalar is a quantity that has only a magnitude; in contrast, a vector is a quantity that has a direction and a magnitude. A familiar example of a vector quantity is velocity of a particle. The direction of movement of the particle is the vector's direction, and the speed of the particle is the vector's magnitude. Vectors are represented graphically by directed line segments, as illustrated in Figure 3.1. The length of the line represents the vector's magnitude, and the direction of the line represents its direction.
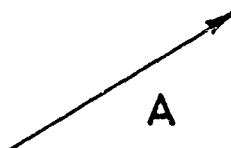
Figure 3.1. A vector quantity represented by a directed line segment.

In this handbook, vectors are represented by boldface type; e.g., **A**. The magnitude of a vector is represented by the same symbol in plain type; thus A is the magnitude of vector **A**.

A summary of vector calculus, or even vector algebra, is beyond the scope of this handbook, but we will describe the basic vector addition and multiplication operations because they are important in understanding electro-magnetic-field characteristics described later. Because vectors have the two properties, magnitude and direction, algebraic vector operations are more complicated than algebraic scalar operations.

Addition of any two vectors A and B is defined as

$$\mathbf{A} + \mathbf{B} = \mathbf{C} \qquad (3.1)$$

where **C** is the vector along the parallelogram shown in Figure 3.2. The negative of a vector **A** is defined as a vector having the same magnitude as **A** but opposite direction. Subtraction of any two vectors **A** and **B** is defined as

$$A - B = A + (-B) \qquad (3.2)$$

where −**B** is the negative of **B**.
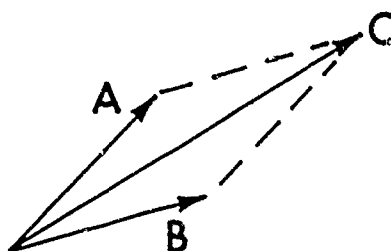
Figure 3.2. Vector addition.

There are two kinds of vector multiplication. One is called the vector dot product. If **A** and **B** are any two vectors, their vector dot product is defined as

$$A \cdot B = A B \cos \theta \qquad (3.3)$$

where θ is the angle between **A** and **B**, as shown in Figure 3.3. The dot product of two vectors is a scalar. As indicated in Figure 3.3, **A** · **B** is also equal to the projection of **A** on **B**, times B. This interpretation is often very useful. When two vectors are perpendicular, their dot product is zero because the cosine of 90° is zero (the projection of one along the other is zero).
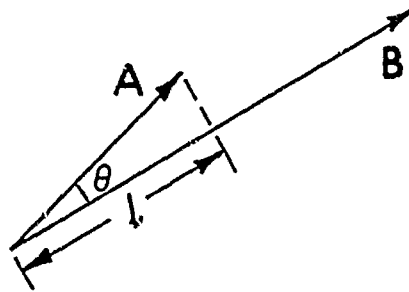
Figure 3.3. Vector dot product $\mathbf{A} \cdot \mathbf{B}$.

The other kind of vector multiplication is called the <u>vector cross product</u> and is defined as

$$\mathbf{A} \times \mathbf{B} = \mathbf{C} \tag{3.4}$$

where C is a vector whose direction is perpendicular to both A and B and whose magnitude is given by

$$C = A \, B \, \sin \theta \tag{3.5}$$

As shown in Figure 3.4, the direction of C is the direction a right-handed screw would travel if turned in the direction of A turned into B. The cross product of two parallel vectors is always zero because the sine of zero is zero.
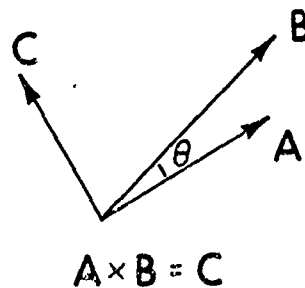
Figure 3.4. Vector cross product $\mathbf{A} \times \mathbf{B}$.

Fields--Two kinds of fields are used extensively in electromagnetic-field theory, scalar fields and vector fields. A field is a correspondence between a set of points and a set of values; that is, in a set of points a value is assigned to each point. When the value assigned is a scalar, the field is called a scalar field. Temperature at all points in a room is an example of a scalar field. When the value assigned to each point is a vector, the field is called a vector field. Air velocity at all points in a room is an example of a vector field. Electric potential is a scalar field. Electric and magnetic fields are vector fields.

Scalar fields are usually represented graphically by connecting points of equal value by lines, as illustrated in Figure 3.5. In a temperature field, these lines are called isotherms. In a potential field, the lines are called equipotential lines. In the general three-dimensional field, points of equal potential form equipotential surfaces.
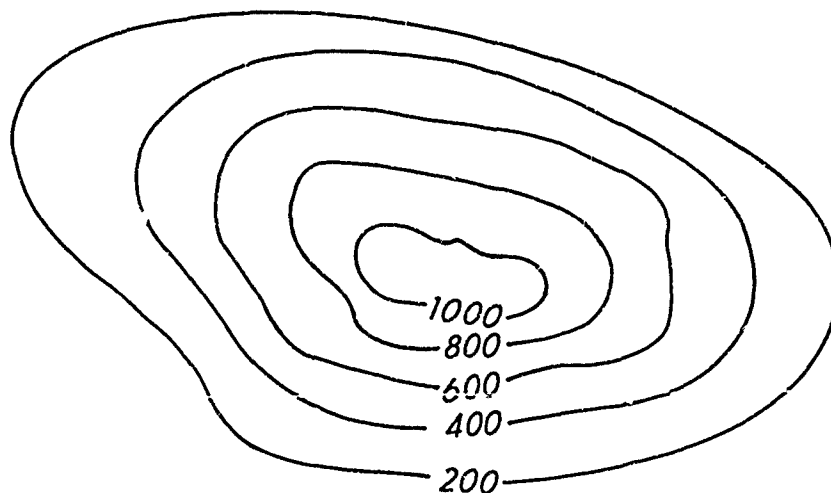
Figure 3.5. Graphical representation of a scalar field, such as temperature. Each line represents all points of equal value.

Vector fields are more difficult to represent graphically because both the magnitude and direction of the vector values must be represented. This is

done by drawing lines tangent to the direction of the vector field at each point, with arrowheads showing the direction of the vector. The magnitude of the field is represented by the spacing between the lines. When the lines are far apart, the magnitude is small. An example of air velocity for air flowing between two plates is shown in Figure 3.6. Since many vector fields represent a physical flow of particles, such as fluid velocity, the field lines often represent a flux density. Hence, the field lines have come to be called <u>flux lines</u>, even for fields like electric and magnetic fields that do not represent a flow of particles, and fields are said to be a <u>flux density</u>. In electromagnetic-field theory, the flux passing through a surface is often calculated by finding the component of the flux density normal to the surface and integrating (summing) it over the surface.
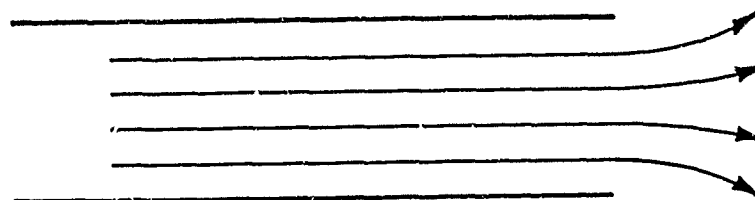
Figure 3.6. Graphical representation of a vector field, such as air velocity between two plates.

3.2. FIELD CHARACTERISTICS

3.2.1. Electric Fields

All of electromagnetics is based on the phenomenon of the forces that electric charges exert on each other. The mathematical statement of the force on one charge, q, due to the presence of another charge, Q, is called Couloumb's law:

$$F = qQ\hat{R}/4\pi\epsilon_o R^2 \tag{3.6}$$

where $\hat{R}$ is a unit vector along a straight line from Q to q and pointing toward q, and R is the distance between the two charges, as shown in Figure 3.7. In the SI system of units, ε_o is a constant called the __permittivity of free space__. The units of charge are coulombs, and the units of permittivity are farads per meter (see Section 3.1). When both q and Q have the same sign, the force in Equation 3.5 is repulsive. When the charges have opposite signs, the force is attractive. When more than one charge is present, the force on one charge is the summation of all forces acting on it due to each of the other individual charges. Keeping track of all the charges in a complicated electrical system is not always convenient, so we use a quantity called __electric-field strength vector__ (E-field) to account for the forces exerted on charges by each other.
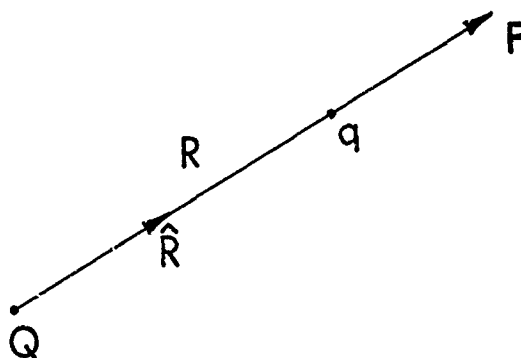
Figure 3.7. Force on a charge, q, due to the presence of another charge, Q.

The E-field is defined in terms of a very simple and idealized model experiment. A point test body charged to a very small net positive charge, q, is brought into a region of space where an E-field exists. According to Coulomb's law, the force, F, on the test charge is proportional to q. The E-field strength vector is defined as

$$E = F/q \qquad (3.7)$$

where it is understood that q is infinitesimally small, so it does not affect the measurement. The units of E are volts per meter. Thus we could, in principle, determine whether an E-field existed at a given point in space by placing a small charge at that point and measuring the force on it. If no force, the E-field would be zero at that point. If a force were on it, the force's direction would be the direction of the E-field at that point, and the magnitude of the E-field would be equal to the force's magnitude divided by the charge. Although not a practical way to detect or measure E-field intensity, this idealized "thought" experiment is valuable for understanding the basic nature of E-fields.

From the definition of electric field, it follows that the force on a charge, q, placed in an E-field is given by

$$F = q\,E \tag{3.8}$$

Thus if E is known, the force on any charge placed in E can easily be found.

3.2.2. Magnetic Fields

When electric charges are moving, a force in addition to that described by Coulomb's law (Equation 3.6) is exerted on them. To account for this additional force, we defined another force field, analogous to the E-field definition in the previous section. This second force field is called the magnetic-flux-density (B-field) vector, B. It is defined in terms of the force exerted on a small test charge, q. The magnitude of B is defined as

$$B = F_m/qv \tag{3.9}$$

where F_m is the maximum force on q in any direction, and v is the velocity of q. The units of B are webers per square meter. The B-field is more complicated than the E-field in that the direction of force exerted on q by the B-field is always perpendicular to both the velocity of the particle and to the B-field. This force is given by

- 3.13 -

$$F = q(\mathbf{v} \times \mathbf{B}) \qquad\qquad (3.10)$$

(which is analogous to Equation 3.7). The quantity in parentheses is called a vector cross product. The direction of the vector cross product is perpendicular to both $\mathbf{v}$ and $\mathbf{B}$ and is in the direction that a right-handed screw would travel if $\mathbf{v}$ were turned into $\mathbf{B}$ (see Section 3.1.3). When a moving charge, q, is placed in a space where both an E-field and a B-field exist, the total force exerted on the charge is given by the sum of Equations 3.8 and 3.10:

$$F = q(\mathbf{E} + \mathbf{v} \times \mathbf{B}) \qquad\qquad (3.11)$$

Equation 3.11 is called the Lorentz force equation.

3.2.3. Static Fields

The basic concepts of E- and B-fields are easier to understand in terms of static fields than time-varying fields for two main reasons:

1. Time variation complicates the description of the fields.
2. Static E- and B-fields are independent of each other and can be treated separately, but time-varying E- and B-fields are coupled together and must be analyzed by simultaneous solution of equations.

Static Electric Fields--Perhaps the simplest example of an E-field is that of one static point charge, Q, in space. Let q be a small test charge used to determine the field produced by Q. Then using the definition of E in Equation 3.7 and the force on q from Equation 3.6, we see that the E-field due to Q is

$$E = Q\hat{R}/4\pi\varepsilon_o R^2 \qquad\qquad (3.12)$$

A graphical representation of this vector E-field is shown in Figure 3.8(a). The direction of the arrows shows the direction of the E-field, and the spacing between the field lines shows the intensity of the field. The field is most intense when the spacing of the field lines is the closest.

(See Section 3.1.3 for a discussion of vector-field representations.) Thus near the charge, where the field lines are close together, the field is strong; and it dies away as the reciprocal of the distance squared from the charge, as indicated by Equation 3.12. The E-field produced by an infinitely long, uniform line of positive charge is shown in Figure 3.8(b). In this case the field dies away as the reciprocal of the distance from the line charge. Note that, in every case, the direction of the E-field line is the direction of the force that would be exerted on a small positive test charge, q, placed at that point in the field. For a negative point charge, the E-field lines would point toward the charge, since a positive test charge would be attracted toward the negative charge producing the field.
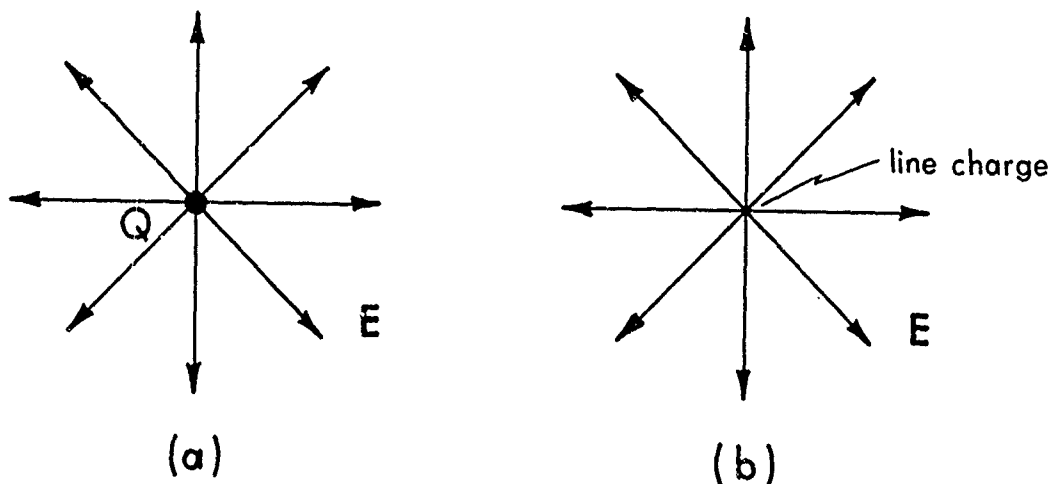
Figure 3.8. (a) E-field produced by one point charge, Q, in space.
            (b) E-field produced by a uniform line of charge
                (looking down at the top of the line charge).

The sources of static E-fields are charges. For example, E-fields can be produced by charges picked up by a person walking across a deep pile rug. This kind of E-field sometimes produces an unpleasant shock when the person touches a grounded object, such as a water faucet. The charge configurations that produce E-fields are often mechanical devices (such as electric genera-tors) or electrochemical devices (such as automobile batteries).

Figure 3.9 depicts E-field lines between a pair of parallel infinite plates. This field could be produced by connecting a voltage source across the plates, which would charge one plate with positive charge and the other plate with negative charge.
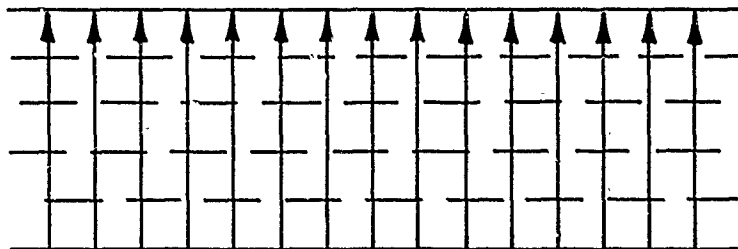

Figure 3.9. Field lines between infinite parallel conducting plates. Solid lines are E-field lines. Dashed lines are equipotential surfaces.

An important characteristic of E-fields is illustrated in Figure 3.10(a); a small metallic object is placed in the field between the parallel plates of Figure 3.9. The sharp corners of the object concentrate the E-field, as indicated by the crowding of the field lines around the corners. Figure 3.10(b) shows how the edges of finite plates also concentrate the field lines. Generally, any sharp object will tend to concentrate the E-field lines. This explains why arcs often occur at corners or sharp points in high-voltage devices. Rounding sharp edges and corners will often prevent such arcs. Another important principle is that static E-field lines must always be perpendicular to surfaces with high ohmic conductivity. An approximate sketch of E-field lines can often be made on the basis of this principle. For example, consider the field plot in Figure 3.10(a). This sketch can be made by noting that the originally evenly spaced field lines of Figure 3.9 must be modified so that they will be normal to the surface of the metallic object placed between the plates, and they must also be normal to the plates. This concept is often sufficient to understand qualitatively the E-field behavior for a given configuration.

- 3.16 -

(a)

(b)
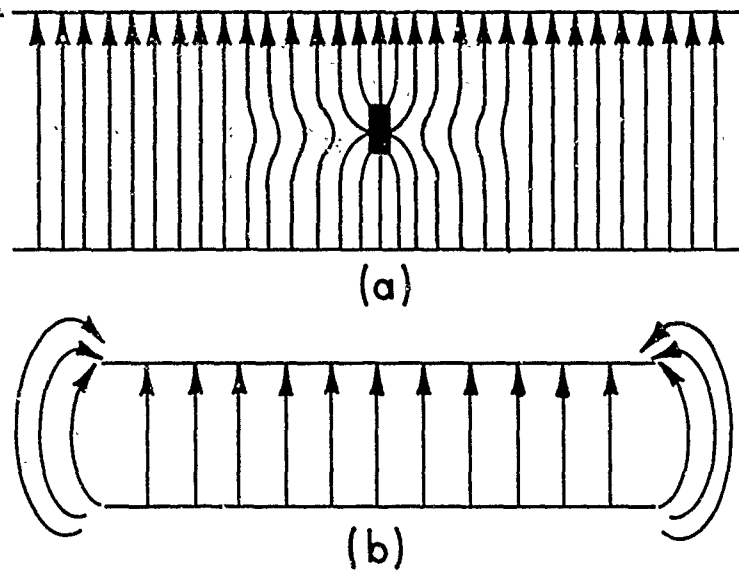
Figure 3.10. (a) E-field lines when a small metallic object is placed between the plates.
(b) E-field lines between parallel conducting plates of finite size.

Static Magnetic Fields--Perhaps the simplest example of a static B-field is that produced by an infinitely long, straight dc element, as shown in Figure 3.11. The field lines circle around the current, and the field dies away as the reciprocal of the distance from the current.
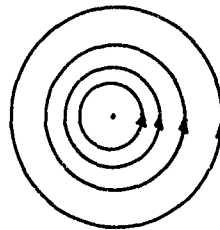

Figure 3.11. B-field produced by an infinitely long, straight dc element out of the paper.

Figure 3.12 shows another example, the B-field produced by a simple circular loop of current. A simple qualitative rule for sketching static B-field lines is that the field line circle around the current element and are strongest near the current. The direction of the field lines with respect to the direction of the current is obtained from the <u>right-hand rule</u>: Put the thumb in the direction of the positive current and the fingers will circle in the direction of the field lines.

current loop

looking at the edge of the current loop
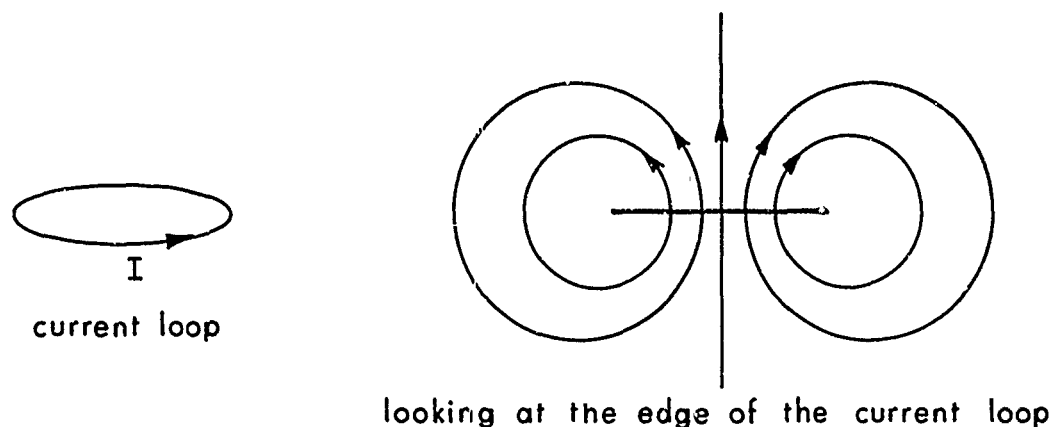
Figure 3.12. B-field produced by a circular current loop.

3.2.4. Quasi-Static Fields

An important class of electromagnetic fields is quasi-static fields. These fields have the same spatial patterns as static fields but vary with time. For example, if the charges that produce the E-fields in Figures 3.8–3.10 were to vary slowly with time, the field patterns would vary correspondingly with time but at any one instant would be similar to the static-field patterns shown in the figures. Similar statements could be made for the static B-fields shown in Figures 3.11 and 3.12. Thus when the frequency of the source charges or currents is low enough, the fields produced by the sources can be considered quasi-static fields; the field patterns will be the same as the static-field patterns but will change with time. Analysis of quasi-static fields is thus much easier than analysis of fields that change more rapidly with time, as explained in Section 3.2.7.

3.2.5. Electric Potential

Because of the force exerted by an electric field on a charge placed in that field, the charge possesses potential energy. If a charge were placed in an E-field and released, its potential energy would be changed to kinetic energy as the force exerted by the E-field on the charge caused it to move. Moving a charge from one point to another in an E-field requires work by whatever moves the charge. This work is equivalent to the change in potential energy of the charge. The potential energy of a charge divided by the magnitude of the charge is called electric-field potential. E-field potential is a scalar field (see Section 3.1.3). This potential scalar field is illustrated in Figure 3.13 for two cases:

  a.   Fields produced by a point charge

  b.   Fields between two infinite parallel conducting plates

The equipotential surfaces for (a) are spheres; those for (b) are planes. The static E-field lines are always perpendicular to the equipotential surfaces.

For static and quasi-static fields, the difference in E-field potential is the familiar potential difference (commonly called voltage) between two points, which is used extensively in electric-circuit theory. The difference of potential between two points in an E-field is illustrated in Figure 3.13.

(a)   (b)
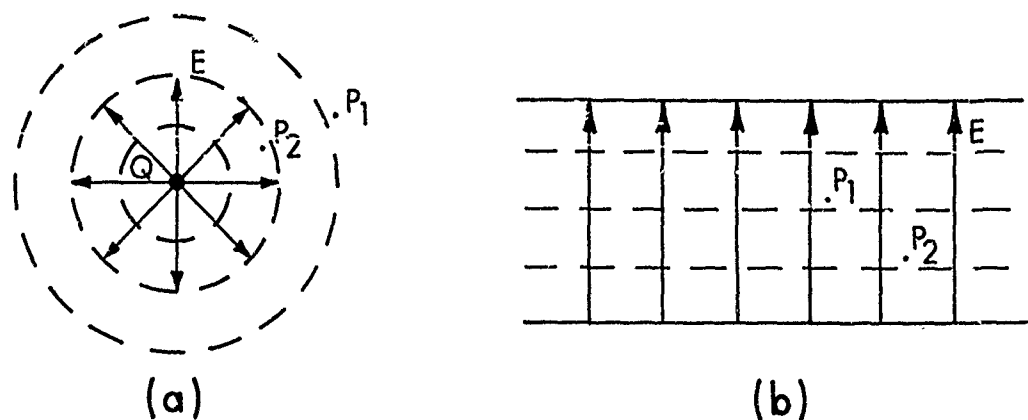
Figure 3.13.   Potential scalar fields (a) for a point charge
and (b) between infinite parallel conducting
plates. Solid lines are E-field lines;
dashed lines are equipotential surfaces.

In each case the potential difference of point P_2 with respect to point P_1 is positive: Work must be done against the E-field to move a test charge from P_1 to P_2 because the force exerted on a positive charge by the E-field would be in the general direction from P_2 to P_1. In Figure 3.13(b) the E-field between the plates could be produced by charge on the plates transferred by a dc source, such as a battery connected between the plates. In this case the difference in potential of one plate with respect to the other would be the same as the voltage of the battery. This potential difference would be equal to the work required to move a unit charge from one plate to the other.

The concepts of potential difference (voltage) and current are very useful at the lower frequencies, but at higher frequencies (for example, microwave frequencies) these concepts are not useful and electromagnetic-field theory must be used. More is said about this in Section 3.2.7.

3.2.6. Interaction of Fields with Materials

Electric and magnetic fields interact with materials in two ways. First, The E- and B-fields exert forces on the charged particles in the materials, thus altering the charge patterns that originally existed. Second, the altered charge patterns in the materials produce additional E- and B-fields (in addition to the fields that were originally applied). Materials are usually classified as being either magnetic or nonmagnetic. Magnetic materials have magnetic dipoles that are strongly affected by applied fields; nonmagnetic materials do not.

Nonmagnetic Materials--In nonmagnetic materials, mainly the applied E-field has an effect on the charges in the material. This occurs in three primary ways:

1. Polarization of bound charges
2. Orientation of permanent dipoles
3. Drift of conduction charges (both electronic and ionic)

Materials primarily affected by the first two kinds are called dielectrics; materials primarily affected by the third kind, conductors.

The _polarization_ of _bound_ _charges_ is illustrated in Figure 3.14(a).
Bound charges are so tightly bound by restoring forces in a material that they
can move only very slightly. Without an applied E-field, positive and nega-
tive bound charges in an atom or molecule are essentially superimposed upon
each other and effectively cancel out; but when an E-field is applied, the
forces on the positive and negative charges are in opposite directions and the
charges separate, resulting in an _induced_ _electric_ _dipole_. A dipole consists
of a combination of a positive and a negative charge separated by a small
distance. In this case the dipole is said to be induced because it is caused
by the applied E-field; when the field is removed, the dipole disappears.
When the charges are separated by the applied E-field, the charges no longer
cancel; in effect a new charge is created, called _polarization_ _charge_, which
creates new fields that did not exist previously.

The _orientation_ _of_ _permanent_ _dipoles_ is illustrated in Figure 3.14(b).
The arrangement of charges in some molecules produces permanent dipoles that
exist whether or not an E-field is applied to the material. With no E-field
applied, the permanent dipoles are randomly oriented because of thermal exci-
tation. With an E-field applied, the resulting forces on the permanent
dipoles tend to align the dipole with the applied E-field (Figure 3.14(b)).
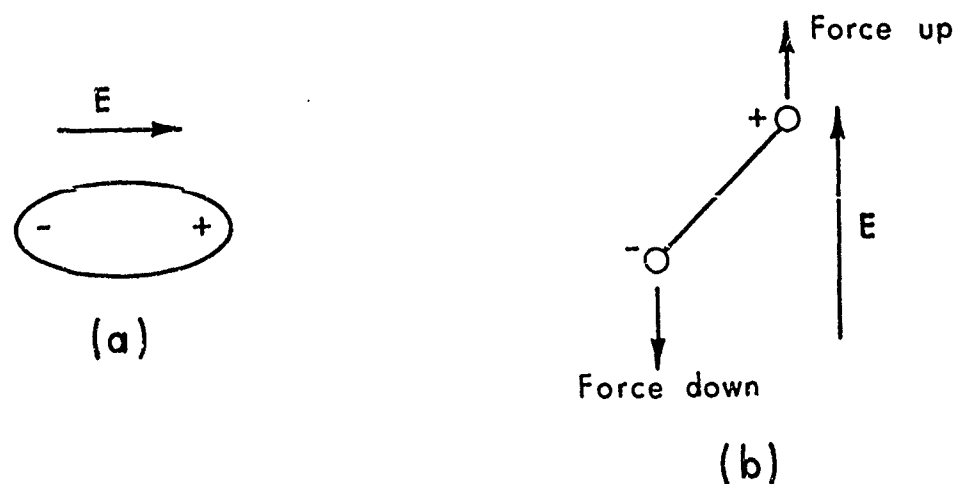
Figure 3.14.   (a) Polarization of bound charges.
                (b) Orientation of permanent dipoles.

- 3.21 -

The orientation of each dipole is slight because the thermal excitation is relatively strong, but on the average there is a net alignment of dipoles over the randomness that existed without an applied E-field. Like induced dipoles, this net alignment of permanent dipoles produces new fields.

The drift of conduction charges in an applied E-field occurs because these charges are free enough to move significant distances in response to forces of the applied fields. Both electrons and ions can be conduction charges. Movement of the conduction charges is called drift because thermal excitation causes random motion of the conduction charges, and the forces due to the applied fields superimpose only a slight movement in the direction of the forces on this random movement. The drift of conduction charges amounts to a current, and this current produces new fields that did not exist before E-fields were applied.

Permittivity--The two effects--creation of new charges by an applied field and creation of new fields by these new charges--are both taken into account for induced dipoles and orientation of permanent dipoles by a quantity called permittivity. Permittivity is a measure of how easily the polarization in a material occurs. If an applied E-field results in many induced dipoles per unit volume or a high net alignment of permanent dipoles per unit volume, the permittivity is high. The drift of conduction charges is accounted for by a quantity called conductivity. Conductivity is a measure of how much drift occurs for a given applied E-field. A large drift means a high conductivity. For sinusoidal steady-state applied fields, complex permittivity is defined to account for both dipole charges and conduction-charge drift. Complex permittivity is usually designated as

$$\varepsilon^* = \varepsilon_o(\varepsilon' - j\varepsilon'') \qquad \text{F/m} \qquad (3.13)$$

where ε_o is the permittivity of free space; $\varepsilon' - j\varepsilon''$, the complex relative permittivity; ε', the real part of the complex relative permittivity (ε' is also called the dielectric constant); and ε'', the imaginary part of the complex relative permittivity. This notation is used when the time variation of the electromagnetic fields is described by $e^{j\omega t}$, where $j = \sqrt{-1}$ and ω is the

radian frequency. Another common practice is to describe the time variation of the fields by $e^{-i\omega t}$, where $i = \sqrt{-1}$. For this case complex permittivity is defined by $\varepsilon^* = \varepsilon_0(\varepsilon' + i\varepsilon'')$. ε'' is related to the <u>effective conductivity</u> by

$$\varepsilon'' = \sigma/\omega\varepsilon_0 \qquad (3.14)$$

where σ is the effective conductivity, ε_0 is the permittivity of free space, and

$$\omega = 2\pi f \text{ radians/s} \qquad (3.15)$$

is the radian frequency of the applied fields. The ε' of a material is primarily a measure of the relative amount of polarization that occurs for a given applied E-field, and the ε'' is a measure of both the friction associated with changing polarization and the drift of conduction charges.

Generally ε is used to designate permittivity; ε^* is usually used only for sinusoidal steady-state fields.

Energy Absorption--Energy transferred from applied E-fields to materials is in the form of kinetic energy of the charged particles in the material. The rate of change of the energy transferred to the material is the <u>power</u> transferred to the material. This power is often called <u>absorbed power</u>, but the bioelectromagnetics community has accepted specific absorption rate (SAR) as a preferred term (see Section 3.3.6).

A typical manifestation of average (with respect to time) absorbed power is heat. The average absorbed power results from the friction associated with movement of induced dipoles, the permanent dipoles, and the drifting conduction charges. If there were no friction in the material, the average power absorbed would be zero.

A material that absorbs a significant amount of power for a given applied field is said to be a <u>lossy</u> material because of the loss of energy from the applied fields. A measure of the lossiness of a material is ε'': The larger the ε'', the more lossy the material. In some tables a quantity called

the loss tangent is listed instead of ε''. The loss tangent, often designated as tan δ, is defined as

$$\tan \delta = \varepsilon''/\varepsilon' \qquad (3.16)$$

The loss tangent usually varies with frequency. For example, the loss tangent of distilled water is about 0.040 at 1 MHz and 0.2650 at 25 GHz. Sometimes the loss factor is called the dissipation factor. Generally speaking, the wetter a material is, the more lossy it is; and the drier it is, the less lossy it is. For example, in a microwave oven a wet piece of paper will get hot as long as it is wet; but when the paper dries out, it will no longer be heated by the oven's electromagnetic fields.

For steady-state sinusoidal fields, the time-averaged power absorbed per unit volume at a point inside an absorber is given by

$$P = \sigma \left| E \right|^2 = \omega \varepsilon_o \varepsilon'' \left| E \right|^2 \qquad (3.17)$$

where $\left| E \right|$ is the root-mean-square (rms) magnitude of the E-field vector at that point inside the material. If the peak value of the E-field vector is used, a factor of 1/2 must be included on the right-hand side of Equation 3.17.' The rms and peak values are explained in Section 3.2.8. Unless otherwise noted, rms values are usually given. To find the total power absorbed by an object, the power density given by Equation 3.17 must be calculated at each point inside the body and summed (integrated) over the entire volume of the body. This is usually a very complicated calculation.

Electric-Flux Density--A quantity called electric-flux density or displacement-flux density is defined as

$$D = \varepsilon E \qquad (3.18)$$

An important property of D is that its integral over any closed surface (that is, the total flux passing through the closed surface) is equal to the total free charge (not including polarization or conduction charge in materials)

inside the closed surface. This relationship is called Gauss's law. Figure 3.15 shows an example of this. The total flux passing out through the closed mathematical surface, S, is equal to the total charge, Q, inside S, regardless of what the permittivity of the spherical shell is. Electric-flux density is a convenient quantity because it is independent of the charges in materials.

spherical shell

integral of D over S = Q

Q

E

mathematical closed surface S
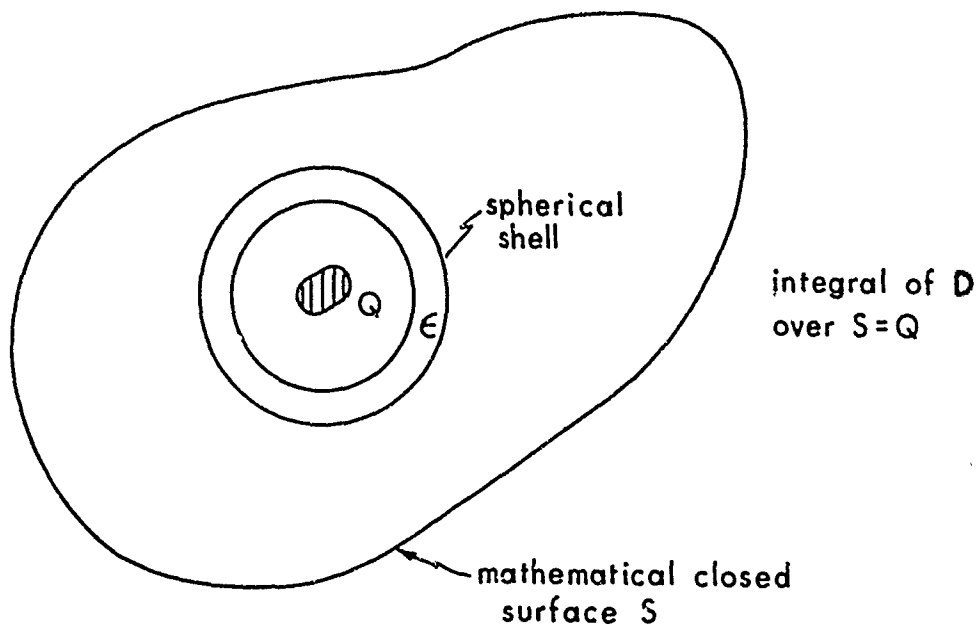
Figure 3.15. Charge Q inside a dielectric spherical shell. S is a closed mathematical surface.

Magnetic Materials--Magnetic materials have magnetic dipoles that tend to be oriented by applied magnetic fields. The resulting motion of the magnetic dipoles produces a current that creates new E- and B-fields. Both the effect of the applied fields on the material and the creation of new fields by the moving magnetic dipoles in the material are accounted for by a property of the material called permeability.

For sinusoidal steady-state fields, the complex permeability is usually designated as

$$\mu^* = \mu_o(\mu' - j\mu'') \qquad (3.19)$$

where $\mu' - j\mu''$ is the <u>complex relative permeability</u> and μ_o is the permeability of free space. For the general case, permeability is usually designated by μ.

Another field quantity, H, or <u>magnetic-field intensity</u>, is defined by

$$H = B/\mu \qquad (3.20)$$

The magnetic-field intensity is a useful quantity because it is independent of magnetic currents in materials. The term "magnetic field" is often applied to both B and H. Whether to use B or H in a given situation is not always clear, but since they are related by Equation 3.20, either could usually be specified.

Since biological materials are mostly nonmagnetic, permeability is usually not an important factor in bioelectromagnetic interactions.

3.2.7. Maxwell's Equations

Four equations, along with some auxiliary relations, form the theoretical foundation for all classical electromagnetic-field theory. These are called Maxwell's equations, named for James Clerk Maxwell, the famous Scotsman who added a missing link to the electromagnetic-field laws known at that time and formulated them in a unified form. These equations are very powerful, but they are also complicated and difficult to solve. Although mathematical treatment of these equations is beyond the stated scope of this document, for background information we will list the equations and describe them qualitatively. Maxwell's equations for fields are

$$\nabla \times E = -\partial B/\partial t \qquad (3.21)$$

$$\nabla \times H = J + \partial D/\partial t \qquad (3.22)$$

$$\nabla \cdot \mathbf{D} = \rho \qquad\qquad (3.23)$$

$$\nabla \cdot \mathbf{B} = 0 \qquad\qquad (3.24)$$

where

   $\mathbf{B} = \mu \mathbf{H}$

   $\mathbf{D} = \epsilon \mathbf{E}$

   $\mathbf{J}$ is free-current density in A/m^2

   ρ is free-charge density in C/m^3

   $\nabla \times$ stands for a mathematical operation involving partial derivatives, called the <u>curl</u>

   $\nabla \cdot$ stands for another mathematical operation involving partial derivatives, called the <u>divergence</u>

   $\partial \mathbf{B}/\partial t$ and $\partial \mathbf{D}/\partial t$ are the time rate of change of $\mathbf{B}$ and $\mathbf{D}$ respectively.
The other quantities have been defined previously.

Any vector field can be completely defined by specifying both the curl and the divergence of the field. Thus the quantities equal to the curl and the divergence of a field are called <u>sources</u> of the field. The terms on the right-hand side of Equations 3.21 and 3.22 are sources related to the curl of the fields on the left-hand side, and the terms on the right-hand side of Equations 3.23 and 3.24 are sources related to the divergence of the fields on the left-hand side.

Equation 3.21 thus means that a time-varying B-field produces an E-field, and the relationship is such that the E-field lines so produced tend to encircle the B-field lines. Equation 3.21 is called <u>Faraday's law</u>.

Equation 3.22 states that both current density and a time-varying E-field produce a B-field. The B-field lines so produced tend to encircle the current density and the E-field lines. Since a time-varying E-field acts like current density in producing a B-field, the last term on the right in Equation 3.22 is called <u>displacement current density</u>.

Equation 3.23 states that charge density produces an E-field, and the E-field lines produced by the charges begin and end on those charges.

Equation 3.24 states that no sources are related to the divergence of the B-field. This means that the B-field lines always exist in closed loops; there is nothing analogous to electric charge for the B-field lines either to begin or end on.

Equations 3.21 and 3.22 show that the E- and B-fields are coupled together in the time-varying case because a changing B is a source of E in Equation 3.21 and a changing D is a source of H in Equation 3.22. For static fields, however, $\partial B/\partial t = 0$ and $\partial D/\partial t = 0$ and the E- and B-fields are not coupled together; thus the static equations are easier to solve.

Since Maxwell's equations are generally difficult to solve, special techniques have been developed to solve them within certain ranges of parameters. One class of solutions, electromagnetic waves, is discussed next. Techniques useful for specific frequency ranges are discussed in Section 3.2.9.

3.2.8. Wave Solutions to Maxwell's Equations

One class of solutions to Maxwell's equations results in wave descriptions of the electric and magnetic fields. When the frequency of the source charges or currents is high enough, the E- and B-fields produced by these sources will radiate out from them. A convenient and commonly used description of this radiation is wave propagation. Although a wave description of electromagnetic fields is not necessary, it has many advantages. The basic ideas of wave propagation are illustrated in Figures 3.16 and 3.17. Electromagnetic wave propagation is analogous to water waves rolling in on a beach. As shown in Figure 3.16, the distance from one crest to the next (in meters or some other appropriate unit of length) is defined as the wavelength, which is usually designated as λ. The velocity of propagation is the velocity at which the wave is traveling and (from Figure 3.16) is equal to the distance traveled divided by the time it took to travel:

$$v = \Delta z/(t_2 - t_1) \tag{3.25}$$
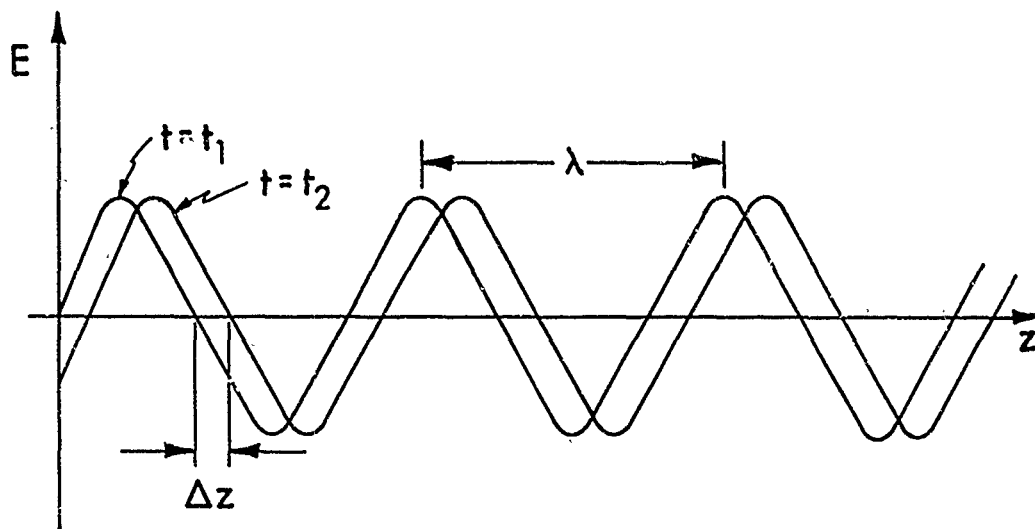
Figure 3.16. Snapshots of a traveling wave at two instants of time, t_1 and t_2.
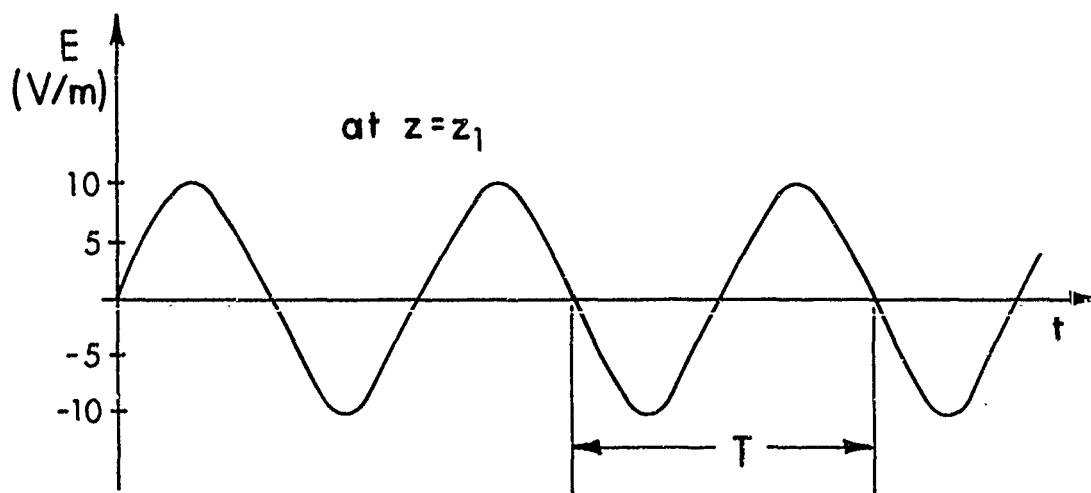
Figure 3.17. The variation of E at one point in space as a function of time.

A detector at one point in space would observe a function that oscillated with time as the wave passed by. This is like someone standing on the beach and watching the wave go by. The height of the water above some reference plane would change with time, as in Figure 3.17. The peak value of the crest is called the wave's _amplitude_; in Figure 3.17, the peak value (amplitude) is 10 V/m.

Another important value is that of the _period_, T, of the oscillation, which is defined as the time between corresponding points on the function (see Figure 3.17). The _frequency_, f, is defined as

$$f = 1/T \qquad\qquad (3.26)$$

The units of T are seconds; those of f are hertz (equivalent to cycles per second). The frequency of a water wave could be obtained by standing in one place and counting the number of crests (or troughs) that passed by in 1 s.

For convenience in power relationships (as explained in Section 3.2.6), the rms value of a function is defined. For a given periodic function, f(t), the rms value, F, is

$$F = \left[\frac{1}{T} \int_{t_o}^{t_o+T} f^2(t)dt \right]^{1/2} \qquad\qquad (3.27)$$

where T is the period of the function and t_o is any value of t. Equation 3.27 shows that the rms value is obtained by squaring the function, integrating the square of the function over any period, dividing by the period, and taking the square root. Integrating over a period is equivalent to calculating the area between the function, f^2, and the t axis. Dividing this area by T is equivalent to calculating the average, or mean, of f^2 over one period. For example, the rms value of the f(t) shown in Figure 3.18 is calculated as follows: The area between the $f^2(t)$ curve and the t axis between t_o and $t_o + T$ is (25 × 30) + (4 × 10) = 790; hence the rms value of f is

$$F = \sqrt{\frac{1}{40}\left[(25 \times 30) + (4 \times 10) \right]} = \sqrt{\frac{790}{40}} = 4.44$$
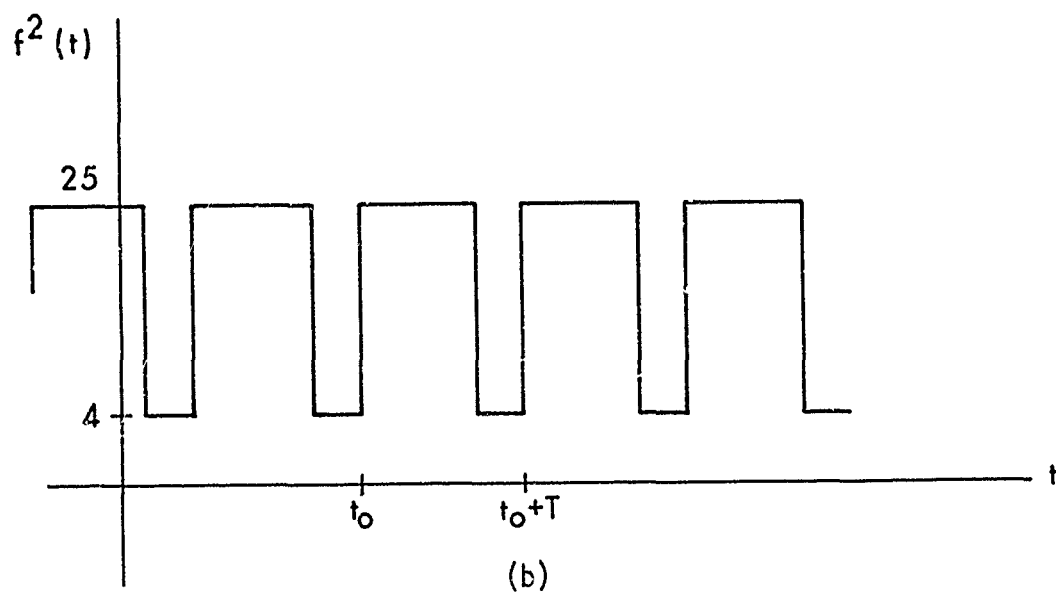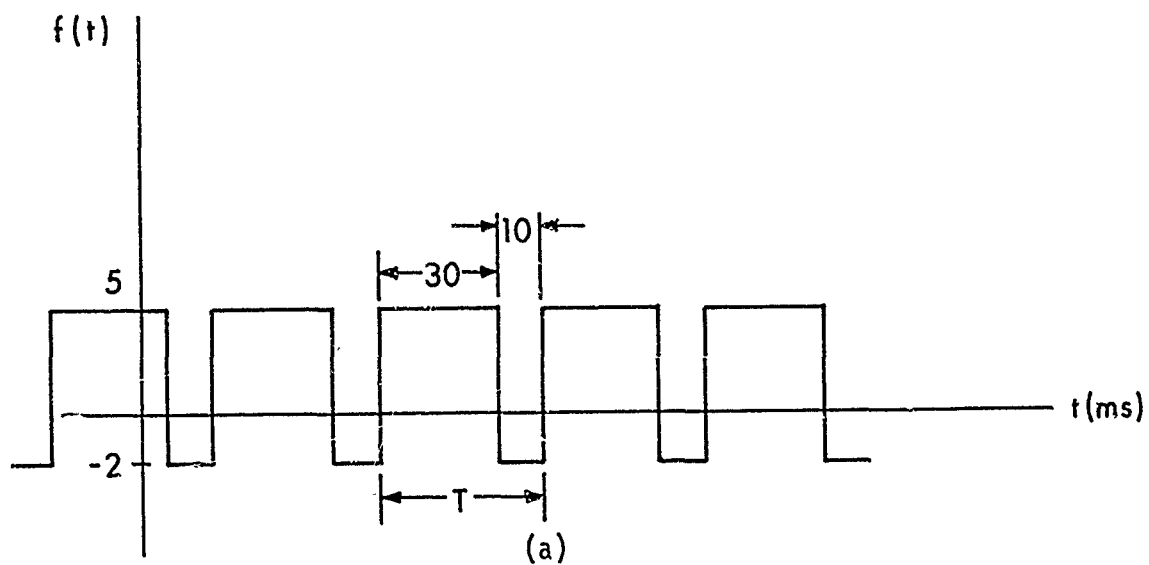
Figure 3.18. (a) A given periodic function [f(t)] versus time (t).

(b) The square of the function $[f^2(t)]$ versus time.

The rms value of a sinusoid is given by

$$G = g_p/\sqrt{2} \qquad (3.28)$$

where g_p is the peak value of the sinusoid.

The quantities defined above are related by the following equation:

$$\lambda = v/f \qquad (3.29)$$

In free space, v is equivalent to the speed of light (c). In a dielectric material the velocity of the wave is slower than that of free space.

Two idealizations of wave propagation are commonly used: spherical waves and planewaves.

Spherical Waves--A spherical wave is a model that represents approximately some electromagnetic waves that occur physically, although no true spherical wave exists. In a spherical wave, wave fronts are spherical surfaces, as illustrated in Figure 3.19. Each crest and each trough is a spherical surface. On every spherical surface, the E- and H-fields have constant values everywhere on the surface. The wave fronts propagate radially outward from the source. (A true spherical wave would have a point source.) E and H are both tangential to the spherical surfaces.
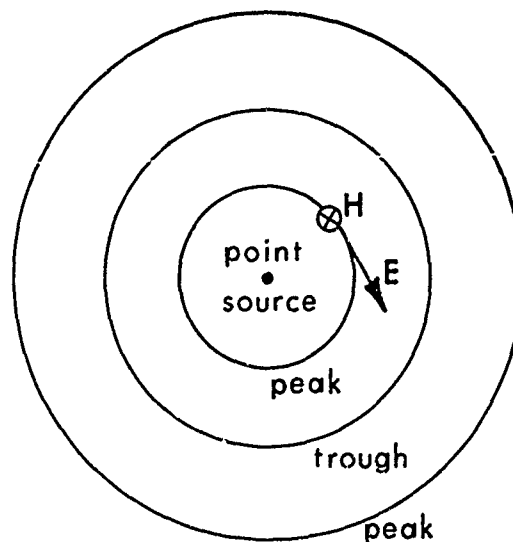
Figure 3.19. A spherical wave. The wave fronts are spherical surfaces. The wave propagates radially outward in all directions.

Spherical waves have several characteristic properties:

1. The wave fronts are spheres.

2. E, H, and the direction of propagation (k) are all mutually perpendicular.

3. $E/H = \sqrt{\mu/\varepsilon}$ (called the wave impedance). For free space, $E/H = 377$ ohms. For the sinusoidal steady-state fields, the wave impedance, $\sqrt{\mu*/\varepsilon*}$, is a complex number that includes losses in the medium in which the wave is traveling.

4. Both E and H vary as $1/r$, where r is the distance from the source.

5. Velocity of propagation is given by $v = 1/\sqrt{\mu\varepsilon}$. The velocity is less and the wavelength is shorter for a wave propagating in matter than for one propagating in free space. For sinusoidal steady-state fields, the phase velocity is the real part of the complex number $1/\sqrt{\mu*\varepsilon*}$. The imaginary part describes attenuation of the wave caused by losses in the medium.

Planewaves--A planewave is another model that approximately represents some electromagnetic waves, but true planewaves do not exist. Planewaves have characteristics similar to spherical waves:

1. The wave fronts are planes.

2. E, H, and the direction of propagation (k) are all mutually perpendicular.

3. $E/H = \sqrt{\mu/\varepsilon}$ (called the wave impedance). For free space, $E/H = 377$ ohms. For the sinusoidal steady-state fields, the wave impedance, $\sqrt{\mu*/\varepsilon*}$, is a complex number that includes losses in the medium in which the wave is traveling.

4. E and H are constant in any plane perpendicular to k.

5. Velocity of propagation is given by $v = 1/\sqrt{\mu\varepsilon}$. The velocity is less and the wavelength is shorter for a wave propagating in matter than for one propagating in free space. For sinusoidal steady-state fields, the phase velocity is the real part of the complex number $1/\sqrt{\mu*\varepsilon*}$. The imaginary part describes attenuation of the wave caused by losses in the medium.

Figure 3.20 shows a planewave. E and H could have any directions in the plane as long as they are perpendicular to each other. Far away from its source, a spherical wave can be considered to be approximately a planewave in a limited region of space, because the curvature of the spherical wavefronts is so small that they appear to be almost planar. The source for a true planewave would be a planar source, infinite in extent.
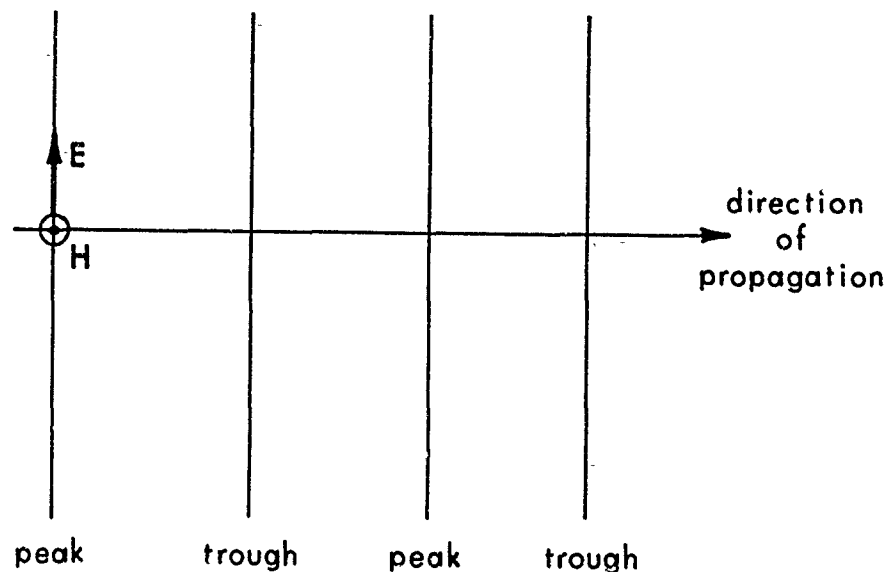
Figure 3.20. A planewave.

3.2.9. Solutions of Maxwell's Equations Related to Wavelength

Maxwell's equations apply over the entire electromagnetic frequency spectrum. They apply from zero frequency (static fields) through the low frequencies, the RF frequencies, the microwave region of the spectrum, the infrared and visible portions of the spectrum, the ultraviolet frequencies, and even through the x-ray portion of the spectrum. Because they apply over this tremendously wide range of frequencies, Maxwell's equations are powerful but are generally very difficult to solve except for special cases. Consequently, special techniques have been developed for several ranges of the

frequency spectrum. The special techniques are each valid in a particular frequency range defined by the relationship between wavelength and the nominal size of the system or objects to which Maxwell's equations are being applied. Let the nominal size of the system (some general approximate measure of the size of the system) be L. For example, if the system included a power transmission line 500 km long, then L would be 500 km; if the system were an electric circuit that would fit on a 1- x 2-m table, then L would be the diagonal of the table, $\sqrt{1^2 + 2^2}$ m = $\sqrt{5}$ m.

Three main special techniques are used for solving Maxwell's equations-- according to the relationship between λ (the wavelength of the electromagnetic fields involved) and L:

$\lambda \gg L$ electric circuit theory (Kirchhoff's laws)

$\lambda \approx L$ microwave theory or electromagnetic-field theory

$\lambda \ll L$ optics or ray theory

When $\lambda \gg L$, Maxwell's equations may be approximated by circuit-theory equations, principally Kirchhoff's laws, which are much easier to solve than Maxwell's equations. Since the free-space wavelength at 1 MHz is 300 m, any system that will fit in an ordinary room can usually be treated by circuit theory at frequencies of 1 MHz and below. Historically, circuit theory did not evolve as an approximation to Maxwell's equations--the laws of circuit theory were formulated independently--but it is indeed an approximation to the more general Maxwell's equations. Fortunately we do have circuit theory; in comparison, having to solve Maxwell's equations for such applications would be very difficult and cumbersome.

When the nominal size of the system and the wavelength are of the same order of magnitude, microwave theory must be used. This essentially amounts to solving Maxwell's equations directly, with a minimum of approximations. From frequencies of 300 MHz to 300 GHz, the corresponding wavelengths range from 1 m to 1 mm. Hence in this part of the electromagnetic spectrum, most systems must be treated by microwave theory.

When $\lambda \ll L$--such as above frequencies of 3000 GHz, where the wavelength is smaller than 100 μm--the theory of optics can be used for most systems. The equations of optics also approximate Maxwell's equations, but optical theory did not historically evolve as such approximations; it was formulated

independently from physical observations. In the frequency ranges beyond the visible and ultraviolet light regions, ray theory and particle theory are usually used.

Wavelength boundaries that define the regions where these techniques are valid are not sharply defined; as the wavelength changes in the transitional regions, the technique becomes a poorer and poorer approximation until it finally becomes useless and another technique must be used. Combinations of those techniques are often used in the transitional regions between circuit theory and microwave theory; and in the transitional regions between microwave theory and optics, hybrid techniques are frequently used.

Important qualitative understanding can often be obtained by considering the size of an object compared to the wavelength of the electromagnetic fields. For example, if a particle small compared to a wavelength is irradiated by an electromagnetic wave, the particle will have little effect on the wave; that is, it will not produce much scattering of the wave and will probably absorb relatively little energy. On the other hand, a particle of approximately the same size as a wavelength will usually produce significant scattering and will absorb relatively larger amounts of energy. Likewise, a metallic screen with a mesh size small compared to a wavelength will reflect a wave almost as well as a solid metallic plate; only small amounts of energy will be transmitted through the holes in the screen. If the mesh size is large compared to a wavelength, though, the screen will appear semitransparent, as ordinary window screen does to visible light.

3.2.10. Near Fields

In regions close to sources, the fields are called near fields. In the near fields the E- and H-fields are not necessarily perpendicular; in fact, they are not always conveniently characterized by waves. They are often more nonpropagating in nature and are therefore called <u>fringing fields</u> or <u>induction fields</u>. The near fields often vary rapidly with space. The mathematical expressions for near fields generally contain the terms $1/r$, $1/r^2$, $1/r^3$, ..., where r is the distance from the source to the field point (point at which the field is being determined). Objects placed near sources may strongly affect

the nature of the near fields. For example, placing a probe near a source to measure the fields may change the nature of the fields considerably.

3.2.11. Far Fields

At larger distances from the source, the $1/r^2$, $1/r^3$, and higher-order terms are negligible compared with the $1/r$ term in the field variation; and the fields are called far fields. These fields are approximately spherical waves that can in turn be approximated in a limited region of space by plane-waves. Making measurements is usually easier in far fields than in near fields, and calculations for far-field absorption are much easier than for near-field absorption.

The boundary between the near-field and far-field regions is often taken to be

$$d = 2L^2/\lambda \tag{3.30}$$

where

    d is the distance from the source

    L is the largest dimension of the source antenna

    λ is the wavelength of the fields

The boundary between the near-field and far-field regions is not sharp because the near fields gradually become less important as the distance from the source increases.

3.2.12. Guided Waves

Electromagnetic energy often must be transmitted from one location to another and can be transmitted through space without any transmission lines whatsoever. Communication systems of many kinds are based on signals transmitted through space. At frequencies below the GHz range, however, electromagnetic energy cannot be focused into narrow beams. Beaming electromagnetic energy through space, therefore, is very inefficient in terms of the amount of energy received at a location compared to the amount of energy transmitted. The transmitted energy simply spreads out too much as it travels. This is not a serious problem in communication systems, such as broadcast radio, where the main objective is transmission of information, not energy. For many

applications, though, transmitting electromagnetic energy through space without a transmission line is not practical because of either poor efficiency, poor reliability, or poor signal-to-noise ratios. For these applications, guiding structures (transmission lines) are used.

At very low frequencies, like the 60 Hz used in many power systems, transmission lines can be simply two or more wires. At these frequencies quasi-static-field theory and voltage and current relationships can be used to analyze and design the systems. At higher frequencies, however, transmission along a guiding structure is best described in terms of wave propagation. In the MHz range two-conductor lines such as twin-lead or coaxial cables are commonly used for transmission. In the GHz range the loss in two-conductor transmission lines is often too high, and waveguides are usually used as guiding structures.

Two-Conductor Transmission Lines—Twin-lead line (often used for connecting antennas to television sets) and coaxial cables are the two most commonly used two-conductor transmission lines. The E- and H-fields' configuration that exists on most two-conductor transmission lines is called the TEM (transverse electromagnetic) mode. It means that no component of the E- or H-field is in the direction of wave propagation on the transmission line. Examples of the field patterns in the TEM mode are shown in Figure 3.21.

Coaxial cable   Twin lead
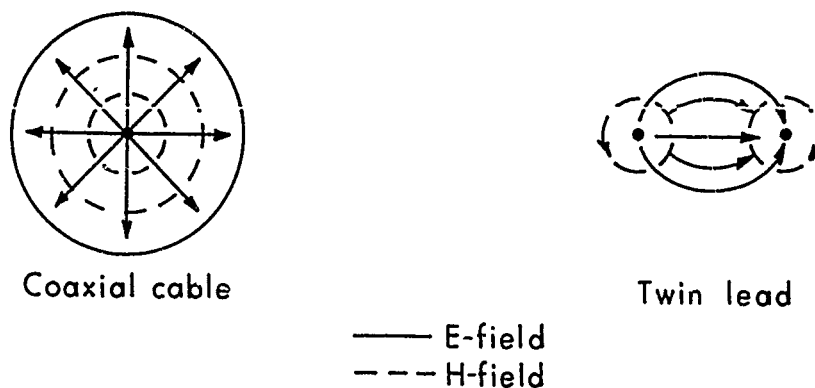
——— E-field
— — — H-field

Figure 3.21. Cross-sectional views of the electric- and magnetic-field lines in the TEM mode for coaxial cable and twin lead.

Voltage and current concepts are valid for the TEM mode, even at the higher frequencies. The potential difference between the two conductors and the current in each conductor both form wave patterns that propagate along the transmission line. These traveling waves of voltage and current have the same form as the traveling wave shown in Figure 3.16. An infinitely long two-conductor transmission line excited by a generator with an impedance Z_g is shown in Figure 3.22(a). On an infinitely long line, the voltage will be a wave propagating only to the right. The current also will consist of a wave propagating only to the right. The ratio of the voltage to the current when all waves propagate in only one direction is called the <u>characteristic imped</u><u>ance</u> of the transmission line. The characteristic impedance, usually desig-nated Z_0, is an important parameter of the transmission line. Coaxial cables are manufactured with a variety of characteristic impedances, but the most common are 50 Ω and 75 Ω.
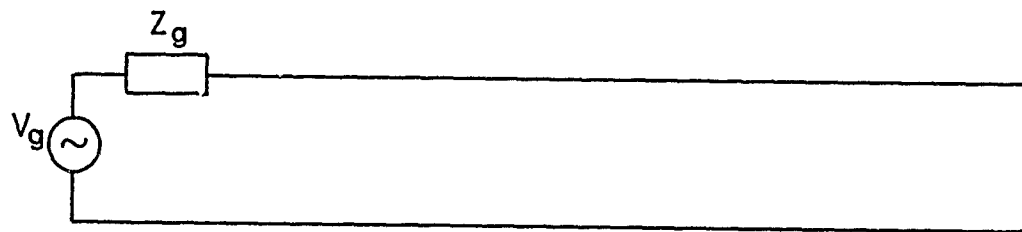
(a) Infinitely long transmission line
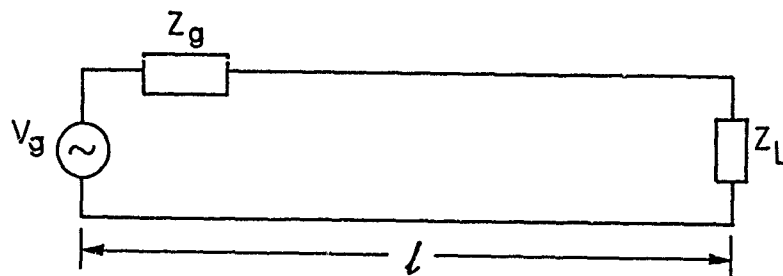
(b) Transmission line of length l and load impedance Z_L

Figure 3.22. Schematic diagrams of two-conductor transmission lines.

A transmission line of finite length with a load impedance at the end is shown in Figure 3.22(b). If the load impedance is not exactly equal to the characteristic impedance of the transmission line, reflected waves of voltage and current will occur so that at the end of the line the ratio of the total voltage in both waves to the total current in both waves will be equal to the load impedance, as it must be. In other words, the total voltage and current must satisfy the boundary conditions at the load impedance. Since the voltage-to-current ratio in one wave is the characteristic impedance, one wave alone could not satisfy the boundary condition unless the load impedance were exactly equal to the characteristic impedance. In the special case where they are exactly equal, there is no reflected wave, the transmission line is said to be <u>terminated</u>, and the load is said to be <u>matched</u> to the transmission line. For best transmission of energy from a generator to a load, having the load matched to the line is usually desirable; also, having the generator impedance matched to the line--that is, $Z_g = Z_0$--is usually best.

Standing Waves--When the load impedance is either zero (a perfect short circuit) or infinite (a perfect open circuit), the reflected and incident waves are equal in magnitude and their combination forms a special pattern called a standing wave. A graph of total voltage, V, and current, I, on a transmission line with a perfect short at the end is shown in Figure 3.23. The total voltage as a function of position for two times $\left(t_1 \text{ and } t_2\right)$ is shown in Figure 3.23(a). At any instant of time, the variation of the field with position is sinusoidal; and at any position, the variation of the voltage with time is sinusoidal. Figure 3.23(b) shows the envelope of voltage variation with position through a full cycle in time. At certain positions the voltage is zero for all values of time; these positions are called <u>nodes.</u> The voltage is zero at the shorted end, and the nodes for the voltage occur at multiples of one-half wavelength from the shorted end. The current is not zero at the shorted end, but the nodes for current are still spaced a half-wavelength apart (Figure 3.23(c)).

A standing wave is always produced by the combination of a wave traveling to the right (incident wave) and a wave of equal magnitude traveling to the left (reflected wave). When the load impedance is not zero or infinite

- 3.40 -
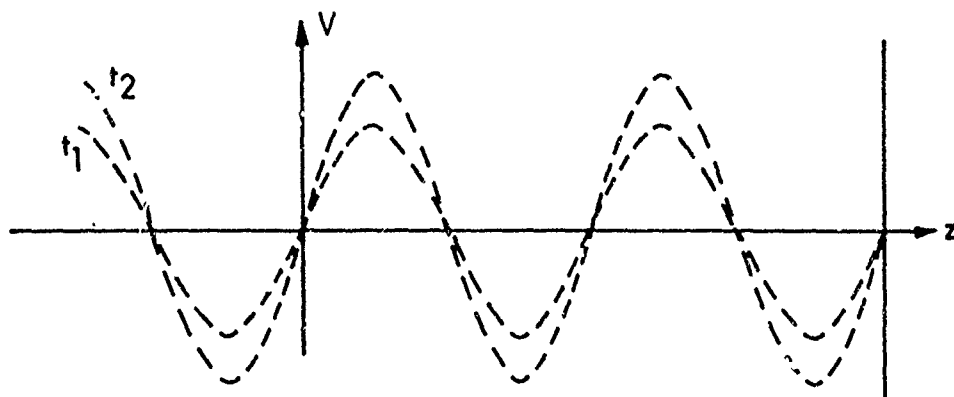
(a) Total voltage as a function of position at two different times, t_1 and t_2.
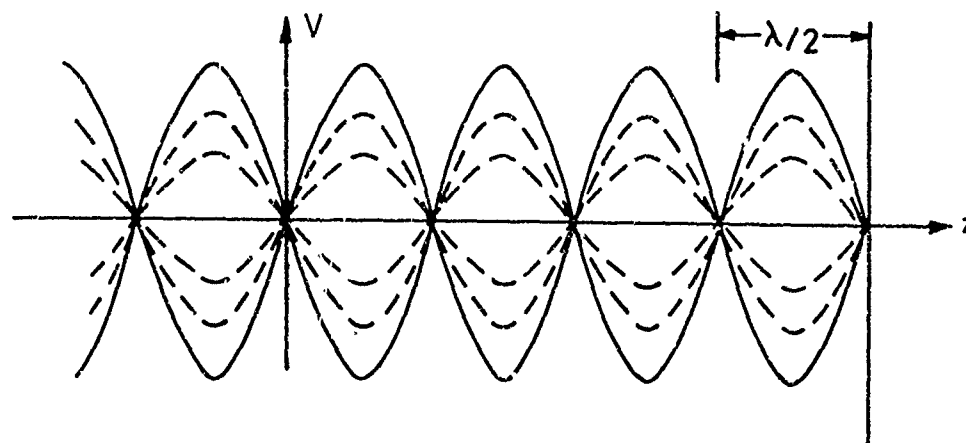
(b) Total voltage as a function of position for various times through a full cycle, and the envelope of the standing wave.
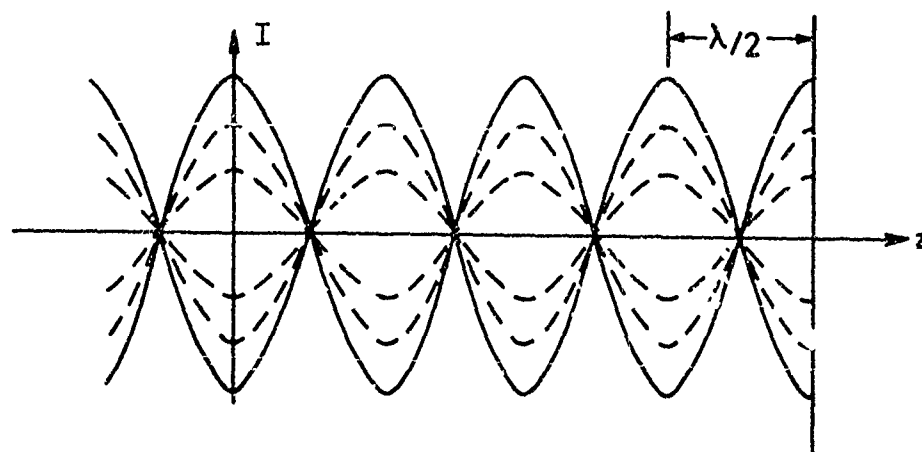
(c) Total current as a function of position at various times through a full cycle, and the envelope of the standing wave.

Figure 3.23. Total waves, incident plus reflected.

and is not equal to the characteristic impedance, the magnitude of the reflected wave is not equal to the incident wave. The pattern formed is similar to a standing wave pattern except the waves do not add to form nodes, but rather minima. Figure 3.24 shows the top half of the envelope of the voltage pattern produced by the sum of an incident wave and a wave reflected by the load impedance. The voltage at each position is a sinusoidal function of time. The graph shows only the magnitude of the sinusoid at each position. Since the magnitude of the reflected wave is smaller than that of the incident wave, there are no nodes; however, maximum and minimum values of the sinusoid occur at specific positions along the line. The maximum values are spaced one-half wavelength apart, and the minimum values are spaced likewise. A suitable voltage probe that measures the magnitude of the voltage could be used to obtain a graph like the one shown in Figure 3.24.
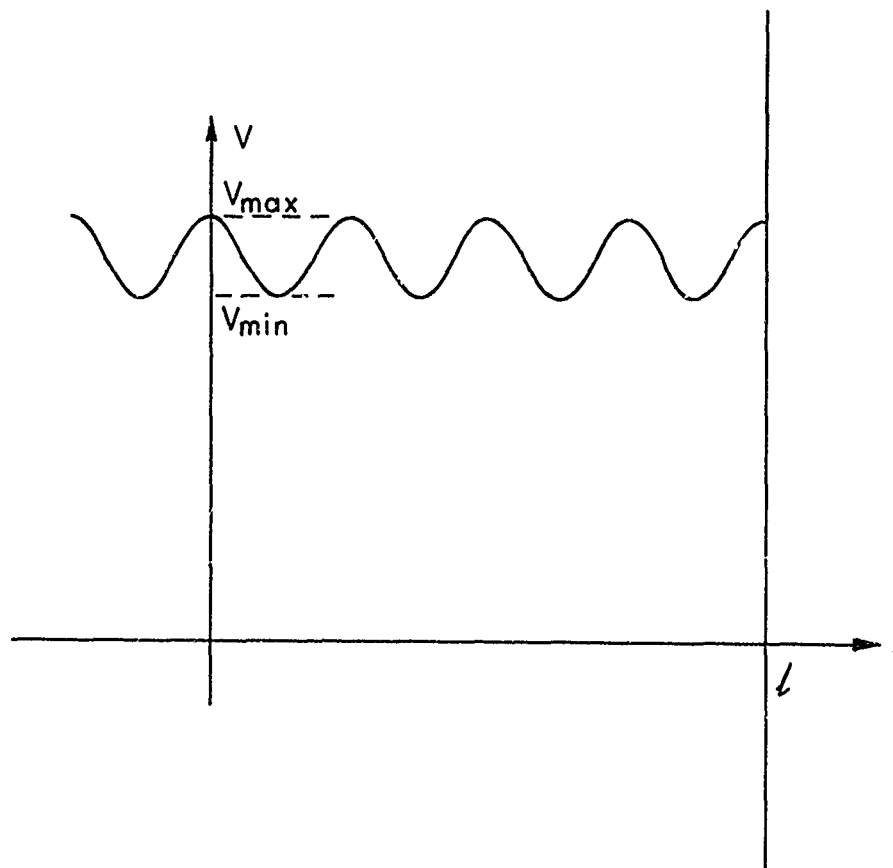
Figure 3.24. Top half of the envelope resulting from an incident and reflected voltage wave.

- 3.42 -

For any wave pattern the standing-wave ratio (often designated by S) is defined as the ratio of the maximum value of the sinusoid at any position to its minimum value at any position. For the wave pattern shown in Figure 3.24, the definition of the standing-wave ratio is

$$S = V_{max}/V_{min} \tag{3.31}$$

The values of S range from unity to infinity. For the standing wave shown in Figure 3.23(b), $S = \infty$. A wave pattern is called a standing wave only when nodes exist, so the minimum value of the sinusoid is zero.

The standing-wave ratio is a measure of reflection. With no reflection, $S = 1$; with total reflection, $S = \infty$. In terms of the reflection coefficient, S is given by

$$S = (1 + \rho)/(1 - \rho) \tag{3.32}$$

where ρ is the magnitude of the reflection coefficient--the ratio of the reflected wave's magnitude to the incident wave's magnitude. For a terminated transmission line (the load impedance is equal to the characteristic impedance), the reflection coefficient is zero and the standing-wave ratio is unity.

Waveguides--Two-conductor transmission lines are not usually used in the GHz frequency range because they are too lossy at higher frequencies. Instead, hollow conducting structures called waveguides are used. Electromagnetic waves propagate inside hollow conductors much like water flows in pipes. Although hollow conductors of any shape will guide electromagnetic waves, the two most commonly used waveguides are rectangular and circular.

Electromagnetic fields that propagate in waveguides are described as the sum of a series of characteristic field patterns called modes. Waveguides have two kinds of modes, TE and TM. TE stands for transverse electric, which means that no E-field component is in the direction of propagation. TM stands for transverse magnetic, which means that there is no H-field component along the direction of propagation.

Each TE and TM mode is labeled with two subscripts (TE_{mn}, TM_{mn}) that indicate the variation of the E- and H-field across the waveguide. Subscript m tells how many half-cycle variations of the fields are in the x direction, and subscript n tells the same thing for the y direction. The field variation of the TE_{10} mode is illustrated in Figure 3.25. The E-field goes to zero on the side walls and is maximum in the center. The H-field is maximum on the walls and circles around the E-field. The pattern reverses direction every half-wavelength down the waveguide and propagates down the waveguide like the wave on a two-conductor transmission line. Thus in the TE_{10} mode, the E-field has one one-half-cycle variation in the x direction and no variation in the y direction. This means that the E-field is maximum in the center of the wave-guide and goes to zero at each of the side walls. In the TE_{20} mode, the E-field would have two half-cycle variations in the x direction and none in the y direction, which means that the E-field is zero at both side walls and in the center of the waveguide.
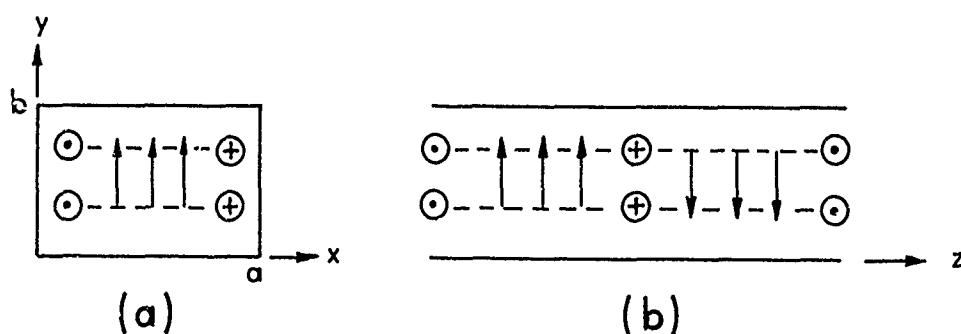
Figure 3.25. Field variation of the TE_{10} mode in a rectangular waveguide (a) as would be seen looking down the waveguide and (b) as seen looking at the side of the waveguide. The solid lines are electric field and the dotted lines are magnetic field.

In general, the electromagnetic fields inside a waveguide will consist of the sum of an infinite number of both TE and TM modes. Depending on the frequency and dimensions of the waveguide, however, some modes will propagate with low attenuation and some will attenuate very rapidly as they travel down

the guide. The modes that attenuate very rapidly are said to be _evanescent_ or _cutoff_ modes. For each mode in a waveguide of given dimensions, the mode will cut off below some particular frequency (the _cutoff frequency_). The cutoff frequency is related to the dimensions of the waveguide by

$$f_{co\ mn} = (c/2) \sqrt{(m/a)^2 + (n/b)^2} \qquad (3.33)$$

where

c = 3×10^8 m/s (the velocity of propagation of a planewave in free space)

a and b are the inside dimensions of the waveguide in meters, as shown in Figure 3.25

The cutoff frequency for the TE_{10} mode is given by $f_{co} = c/2a$. Using the relation between frequency and wavelength given in Equation 3.29, this cutoff frequency is the frequency at which one-half wavelength just fits across the waveguide, i.e., $\lambda/2 = a$.

For b = a/2, which is a typical case, the cutoff frequency is given by

$$f_{co\ mn} = (c/2a) \sqrt{m^2 + 4n^2} \qquad (3.34)$$

The relative cutoff frequencies for a few modes are shown in Figure 3.26. Both m and n cannot be zero for any mode, because that would require _all_ the fields to be zero. For the same reason, neither m nor n can be zero for the
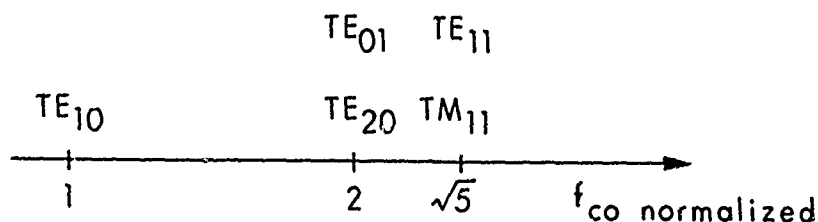
Figure 3.26. Some relative cutoff frequencies for a waveguide with b = a/2, normalized to that of the TE_{10} mode.

TM modes. As indicated in the diagram, the TE_{10} mode has the lowest cutoff frequency. Since having only one mode propagating in a waveguide is usually desirable, the waveguide dimensions and the frequency are often adjusted so that only the TE_{10} mode will be propagating and the higher-order modes will be cut off. This requires that the bandwidth be limited to the separation between the cutoff frequency for the TE_{10} mode and that of the TE_{01} and TE_{20} modes. This separation is a maximum for waveguides with $b = a/2$.

Each mode in a waveguide has its own characteristic impedance, which is the ratio of the E- and H-field components in a cross section of the waveguide for a wave propagating in only one direction. Any discontinuity in a waveguide (such as an object placed in it or a change in its dimensions) which does not have an impedance equivalent to the characteristic impedance of the incident wave, will, when the incident wave strikes it, cause a reflected wave to be generated. If all modes are cut off except one, the discontinuity will also generate all the cutoff modes. Since these cutoff modes will attenuate very rapidly away from the discontinuity, they will exist only in a small region around it. They must be present, however, to satisfy the boundary conditions at the discontinuity. In single-mode waveguides, the incident and reflected waves of the mode will produce wave patterns in the waveguide exactly like those on a two-conductor transmission line. The reflection coefficient and the standing-wave ratio are defined just as they are for TEM modes in two-conductor transmission lines. Concepts of voltage and current are not useful for waveguides in the same sense that they are for two-conductor transmission lines. In waveguides, the E and the H form the wave patterns. These patterns are usually measured by putting E- or H-field probes through narrow slots in the waveguide walls.

A highly conducting wall across the opening of the waveguide will produce a "short" in it. This causes a standing-wave pattern, just as a short does in a TEM-mode transmission line. A lossy tapered material in the waveguide will terminate it. The lossy material absorbs the energy in the incident wave, and an appropriate taper causes essentially no reflection.

3.3. ABSORPTION CHARACTERISTICS

The previous section describes primarily the characteristics of the electromagnetic fields themselves. This section describes how energy is absorbed by objects irradiated by electromagnetic fields.

3.3.1. Poynting's Theorem (Energy Conservation Theorem)

Poynting's theorem is a powerful statement of energy conservation. It can be used to relate power absorption in an object to incident fields but is often misunderstood and misinterpreted. Avoiding complicated mathematical expressions (as stated in the beginning) is still a goal of this chapter, but Poynting's theorem requires a mathematical statement for a satisfactory description. We will explain enough to allow understanding with only a minimum knowledge of mathematics. According to Poynting's theorem, if S is any closed mathematical surface and V is the volume inside S, then

$$\frac{\partial}{\partial t} \int_V (\mathcal{W}_c + \varepsilon E \cdot E + \mu H \cdot H)dV + \oint_S E \times B \cdot dS = 0 \qquad (3.35)$$

where

$\mathcal{W}_c$ is the energy possessed by charged particles at a given point in V

$\varepsilon E \cdot E$ is the energy stored in the E-field at a given point in V

$\mu H \cdot H$ is the energy stored in the H-field at a given point in V.

A closed surface is any surface that completely encloses a volume. The integral over the volume V corresponds to a sum of the terms in the integrand over all points inside V. Thus the integral over V corresponds to the total energy inside V possessed by all charged particles and that stored in the E- and H-fields. The term on the left, then, is the time rate of change of the total energy inside V, which is total power. The term on the right is an integral over the closed mathematical surface enclosing V. For convenience, let

$$\mathcal{P} = E \times H \qquad (3.36)$$

- 3.47 -

P, which is called the Poynting vector, has units of watts per square meter and is interpreted as a power density. As explained in Section 3.1.3, the direction of the cross product of E and H is perpendicular to both E and H, and the vector dot product of E × H and dS selects the component of E × H that is parallel to dS (see Figure 3.27). $P \cdot$ dS is the power passing out through the differential surface element (dS), and the surface integral is the sum of the power passing through the dS elements over the entire surface (S), which is equal to the total power passing out through S. Thus Poynting's theorem is a statement of the conservation of energy: the time rate of change of the total energy inside V is equal to the total power passing out through S.

The Poynting vector E × H is very useful in understanding energy absorption, but Poynting's theorem applies only to a closed surface and the volume enclosed by that surface. Misapplying Poynting's theorem to field relations at a given point, or to only part of a closed surface instead of to an entire closed surface, can lead to serious misunderstanding of energy absorption characteristics. We will illustrate this after considering Poynting's theorem for time-averaged fields.

$$A = P \cdot dS$$
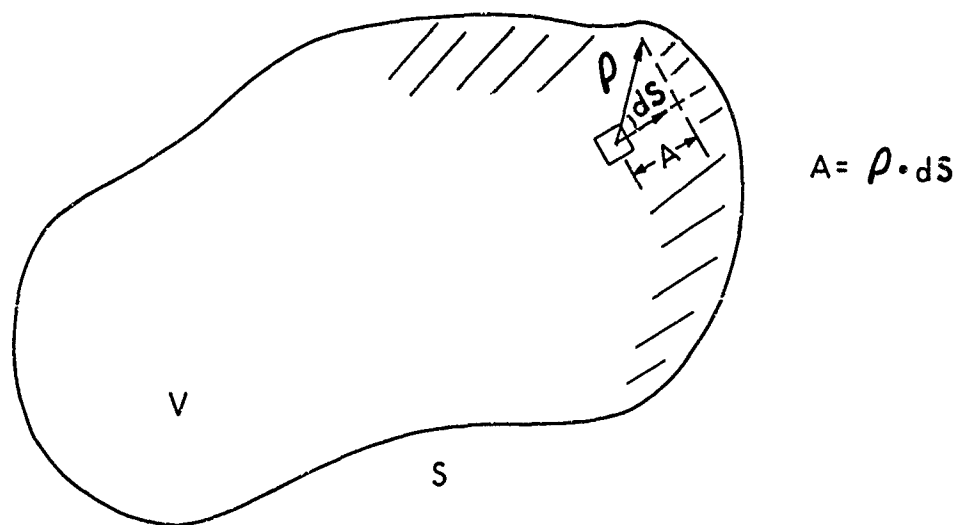
Figure 3.27. A volume (V) bounded by a closed surface (S). dS is the differential surface vector. $P \cdot$ dS is the projection of P on dS, which corresponds to power passing out through dS.

- 3.48 -

Poynting's theorem for time-averaged power and energy of steady-state sinusoidal E- and H-fields is of special interest. Equation 3.35 is valid at any instant of time for fields of general time variation. For sinusoidal fields, however, the time average of the energy stored in the E- and H-fields is zero; this is analogous to storing energy in a frictionless spring. Over one part of the cycle the spring is compressed so that it stores energy, but over the next part of the cycle the spring extends and gives back the energy, so the average energy stored is zero. The time average of energy possessed by charged particles is also zero if no friction (such as due to collisions) is involved in the particles' motion. Friction, however, results in energy loss (usually transformed to heat) that cannot be returned, which corresponds to a nonzero time-average change in energy.

In terms of average power, Poynting's theorem is

$$\int_V \langle \mathcal{P}_c \rangle dV + \oint_S \langle P \rangle \cdot dS = 0 \qquad (3.37)$$

where the brackets designate the time average of the quantity inside. Equation 3.37 states that the sum of the average power possessed by charged particles in V and the total average power passing out through S is always equal to zero. Equation 3.38 shows this relationship in another way:

$$-\oint \langle P \rangle \cdot dS = \int_V \langle \mathcal{P}_c \rangle dV \qquad (3.38)$$

The term on the left is the total average power passing <u>in through S</u>, which is equal to the total average power transferred to the charged particles in V. Thus, <u>if interpreted properly with respect to a closed surface</u>, the Poynting vector E × H can be a useful parameter in describing radiation fields, but it must be used with considerable caution. Some examples will help clarify this point.

Consider the case of a planewave incident on an absorbing object, as illustrated in Figure 3.28. Using the impedance relationship for planewaves, $E/H = 377$ (see Section 3.2.8), the magnitude of the Poynting vector for a planewave in free space is the familiar expression

$$\mathcal{P} = E^2/377 \tag{3.39}$$

When the incident fields impinge on the absorber, E- and H-fields are scattered by the absorber. Poynting's theorem applied to this situation gives

$$-\oint \langle E_i + E_s \rangle \times \langle H_i + H_s \rangle \cdot dS = \int_V \langle \mathcal{P}_c \rangle dV \tag{3.40}$$

Since

$$\left(E_i + E_s\right) \times \left(H_i + H_s\right) = \left(E_i \times H_i\right) + \left(E_i \times H_s\right) + \left(E_s \times H_i\right) + \left(E_s \times H_s\right) \tag{3.41}$$

integrating $E_i \times H_i$, the Poynting vector for the incident wave, over S would not give the total power transferred from the incident wave to the absorber. Finding this total power from integration of the Poynting vector over S would require knowing the scattered fields and including them in the calculation according to Equation 3.40. Calculating the scattered fields is generally very difficult. It is true that the power transferred to the absorber would be proportional to the Poynting vector of the incident planewave. For a given absorber and a given planewave, for example, the power transferred to the absorber would be twice as much if the incident-power density (Poynting vector of the incident wave) were 2 mW/cm^2 as it would if that density were 1 mW/cm^2. The actual amount of power transferred to the absorber in each case, however, would depend on the characteristics of the absorber. Thus although the incident-power density of planewaves is commonly used to indicate their ability to cause power absorption in objects they irradiate, this is only a relative indication, not an absolute one.

E_i

H_i ⊙ ⌇⌇⌇⌇→

planewave incident from
the left on an absorber

absorber

scattered fields
E_s, H_s

S
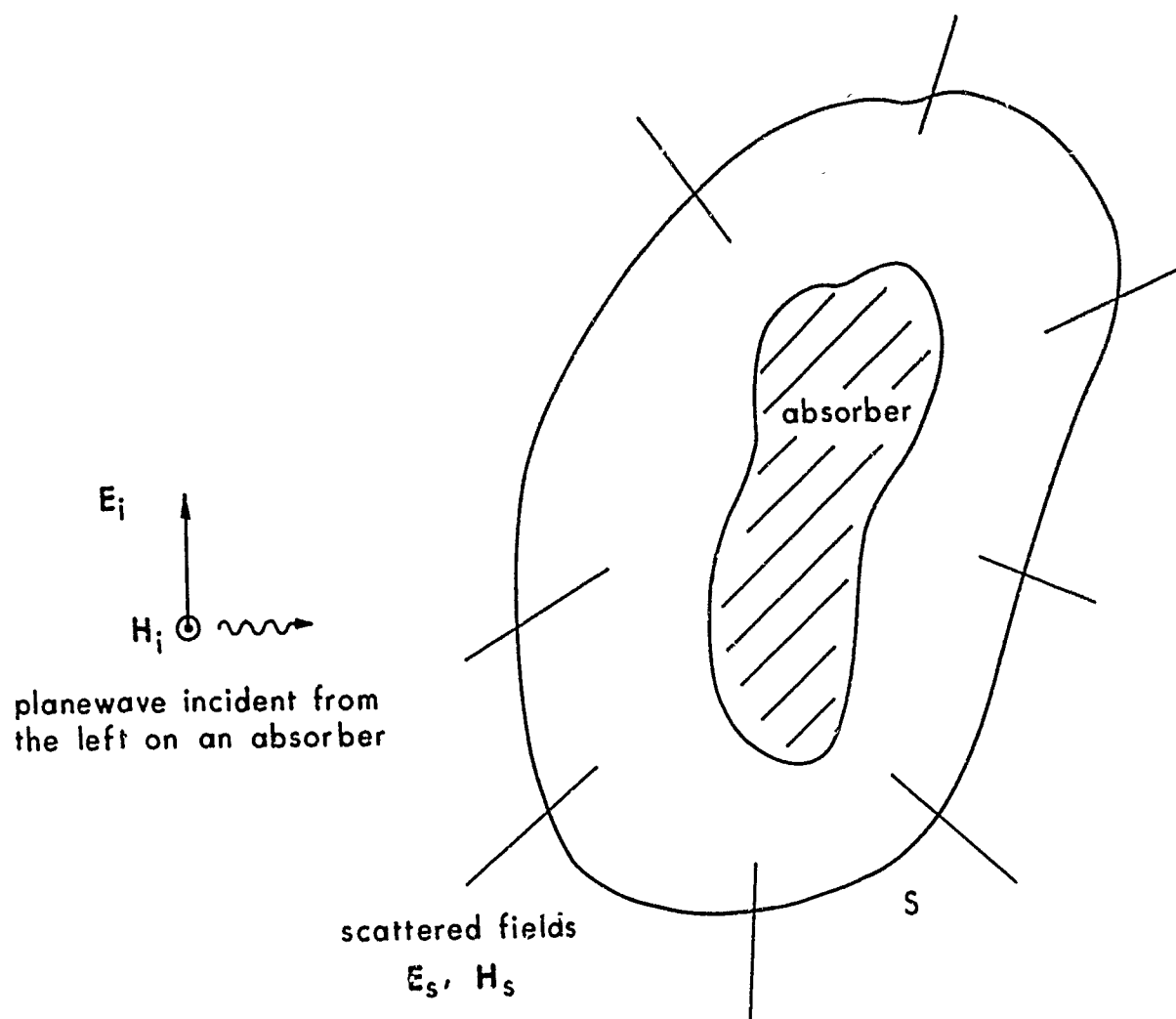
Figure 3.28. A planewave irradiating an absorber. S is a closed surface
used with Poynting's theorem. Scattered fields are pro-
duced by the incidence of the planewave on the absorber.

The situation shown in Figure 3.29 further illustrates difficulties sometimes encountered in applying Poynting's theorem. Suppose a planewave is incident on a perfectly conducting plane, thus causing a reflected wave that combines with the incident wave to produce a standing wave (see Sections 3.2.12, 3.3.2). Then suppose that an absorber is placed in front of the conducting plane at a position where the incident and reflected E-fields add to produce a field of twice the magnitude as that of the incident wave. How would the power transferred to the absorber with the reflector compare to the power transferred to the absorber without the reflector? The first important point is that the Poynting vectors of the incident and reflected wave cannot be added, as indicated by Equation 3.41. So it is not correct to say that the power density incident on the absorber with the reflector would be twice that without it. The principle of superposition can be used with the incident E and H but not with P. The second point is that we cannot draw conclusions from the Poynting vector about power transmitted to the absorber without considering the scattered fields and integrating over a closed surface. For example, suppose that we were to use superposition to add the E-fields and add the H-fields of the incident and reflected waves, and then calculate the Poynting vector from these total fields. Considering what the P would be at a distance of $\lambda/2$ from the reflector shows the incorrectness of this procedure. As explained later (Section 3.3.2 and Figure 3.32), the total H at that distance is zero. A calculation of P based on the total E and H at that distance would therefore give a value of zero for P, which does not make sense.

In summary, the Poynting vector should not be used to draw conclusions about energy absorption unless an integration over a closed surface is carried out. Furthermore, the principle of superposition applies to E- and H-fields but not to P.
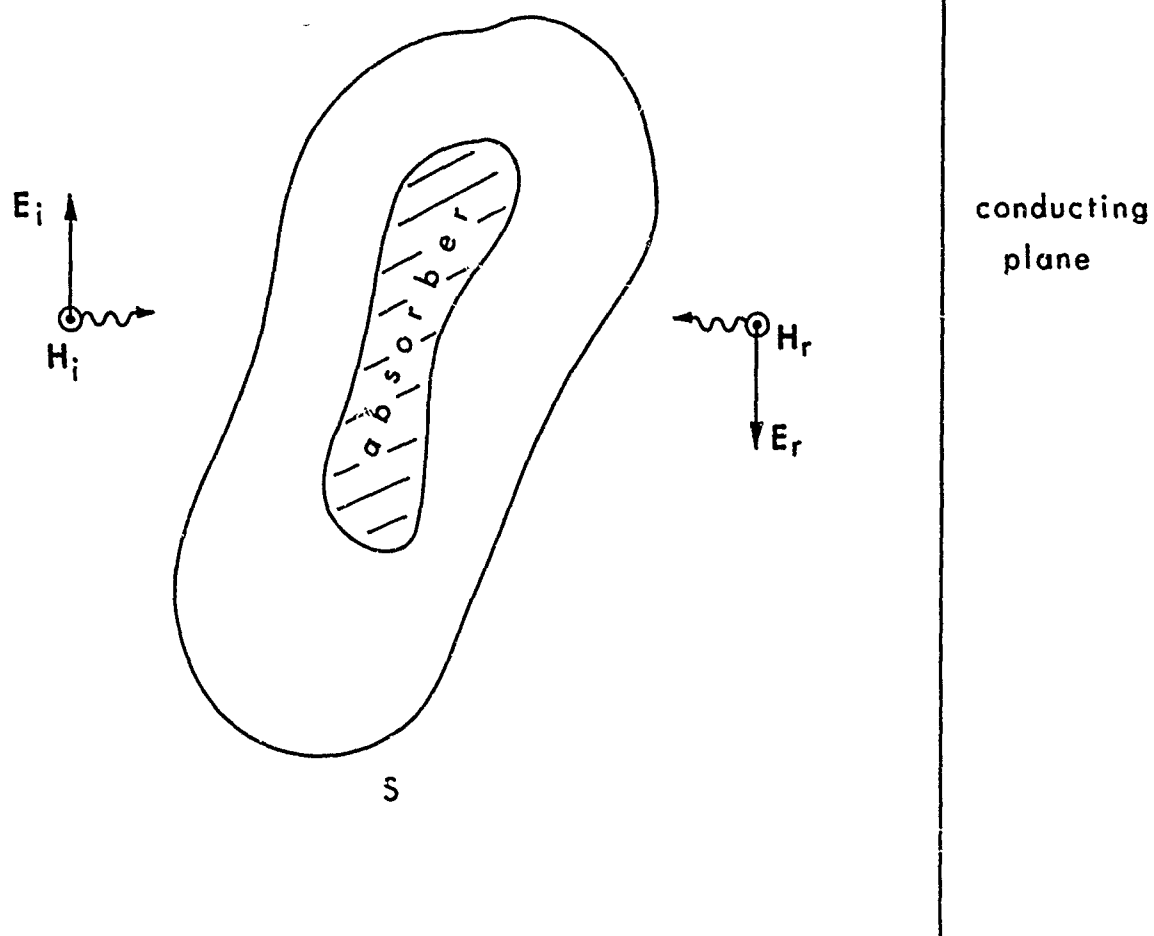
Figure 3.29. Absorber placed between an incident planewave and a conducting plane.

- 3.53 -

3.3.2. Interaction of Fields with Objects

Boundary Conditions--At any boundary between different materials, the E- and H-fields must satisfy certain conditions. These boundary conditions, which can often be used to help explain qualitatively the interaction of fields with objects, are

$$\epsilon_1 E_{1n} = \epsilon_2 E_{2n} \tag{3.42}$$

$$E_{1p} = E_{2p} \tag{3.43}$$

$$\mu_1 H_{1n} = \mu_2 H_{2n} \tag{3.44}$$

$$H_{1p} = H_{2p} \tag{3.45}$$

where subscript n stands for the component of E or H normal (perpendicular) to the boundary, and subscript p stands for the component parallel to the boundary. Subscripts 1 and 2 stand for the two different materials, as indicated in Figure 3.30 for two dielectrics. In each case the field is the total field in the material, which may consist of the fields in both an incident and a reflected wave. These relations hold only at the boundary; with distance away from it, the fields may vary rapidly.
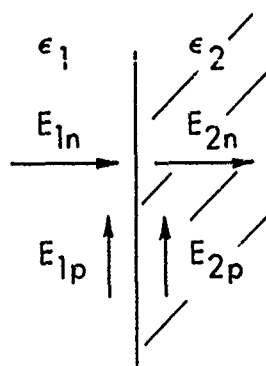
Figure 3.30. Electric-field components at a boundary between two materials.

The relationships contained in Equations 3.42-3.45 can sometimes be used to understand field behavior qualitatively. For example, if a high-permittivity dielectric object were placed in a low-frequency uniform E-field with the E-field essentially normal to the dielectric object, Equation 3.42 would require that the field inside the object be smaller than the field outside by the ratio of the permittivities of the two materials, the object and its surrounding. This would be true only at the boundary, but it would give a general idea of the field pattern. On the other hand, if the object were placed parallel to the field, Equation 3.43 would require that the field inside the object be equal to the field outside the object at the boundary.

At low frequencies the boundary conditions at the surface of a perfect conductor are that the parallel component of the E-field must be zero. This was explained in Section 3.2.1.

Planar Conductors--When a propagating wave strikes an object, part of the wave is reflected or scattered by the object and part penetrates into the object. The total E- and H-fields at any point outside the object consist of the incident and the scattered fields. The simplest example of scattering is a planewave incident on a planar object. Figure 3.31 shows a planewave normally incident on a planar conductor. When the incident wave enters the conductor, it produces currents that are sources of additional E- and H-fields, called <u>scattered fields</u> (or reflected fields). If the conductor has infinite conductivity (perfect conductor), the sum of the incident and the scattered fields is zero everywhere inside the conductor. A graph of the total E- and H-fields (sum of the incident and scattered fields) to the left of the perfect conductor is shown in Figure 3.32: (a) shows the total E-field as a function of position for times t_1 and t_2. At any instant of time, the variation of the field with position is sinusoidal; and at any position, the variation of the field with time is sinusoidal. As the field varies through a full cycle in time, the envelope of the field varies with position (Figures 3.32(b) and (c)). These wave patterns are identical to those for voltage and current on a two-conductor transmission line with a short at the end (Figure 3.23), and the same definitions are made for nodes, standing wave, etc. The nodes for the E-field occur at multiples of half a wavelength from the conductor, and the E-field is zero at the surface of the conductor. The H-field is

not zero at the surface of the conductor, but the nodes for H are still spaced a half wavelength apart. Remember that E and H are constant everywhere in a plane perpendicular to the direction of propagation. The patterns shown in Figure 3.32 thus represent the magnitudes of E and H in planes parallel to the conductor. At the nodes, the E and H are zero everywhere in that plane.
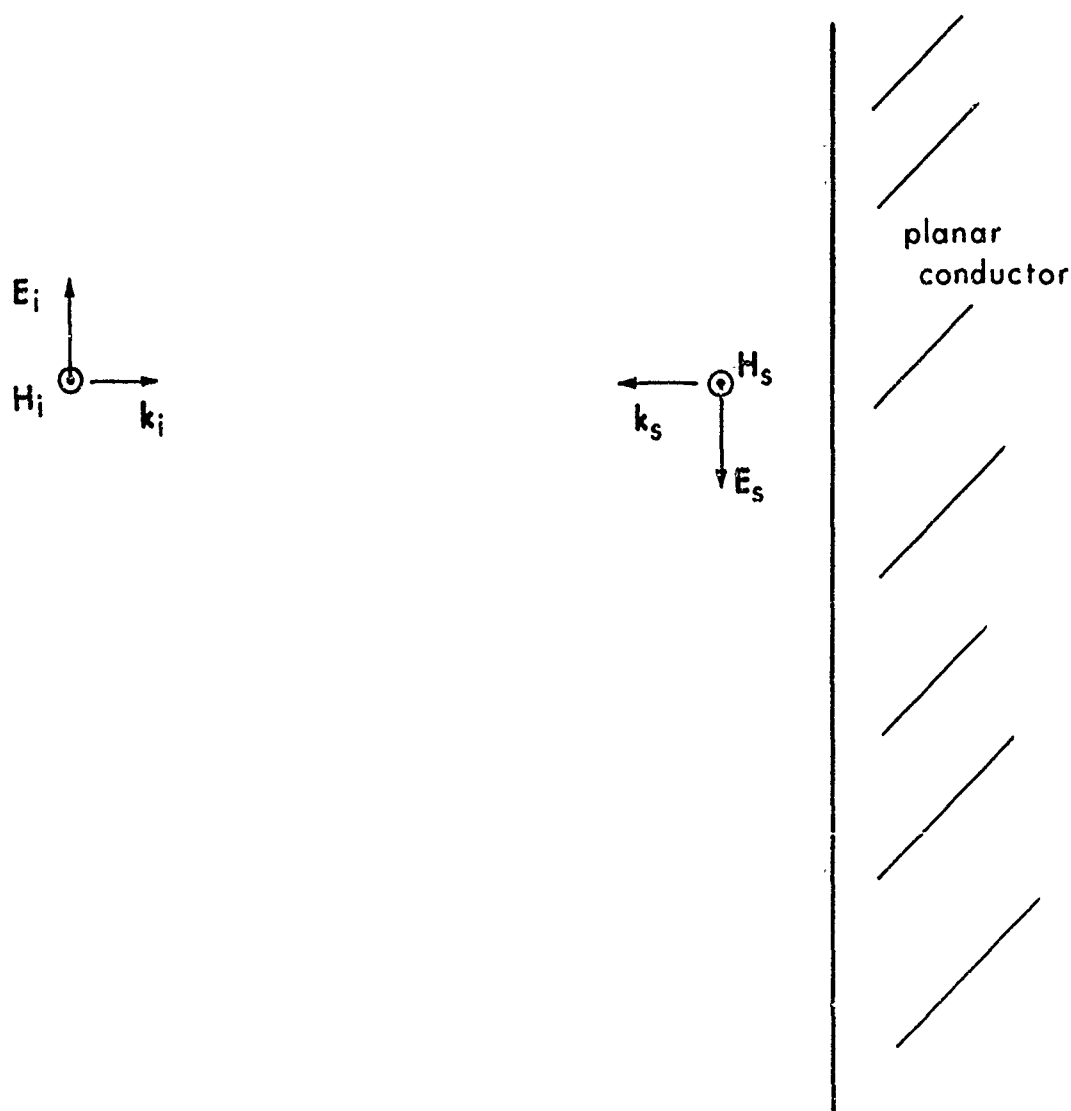
Figure 3.31. Planewave incident on a planar conductor.
The conductor produces a scattered wave.
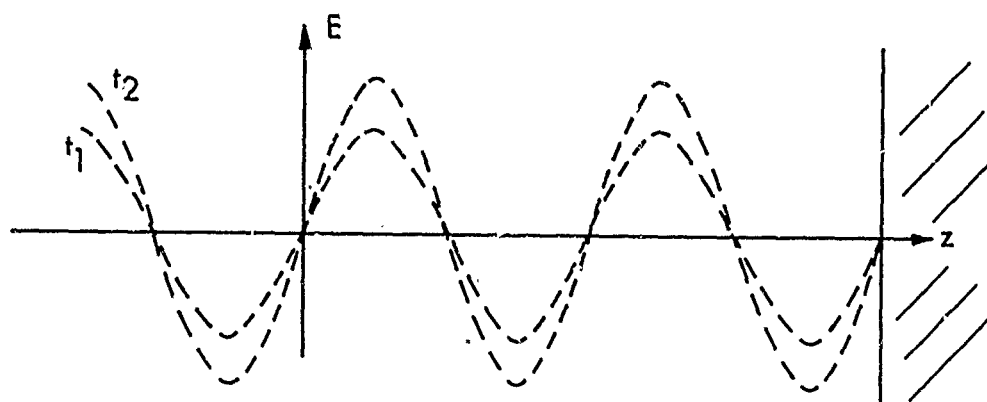
(a) Total E-field as a function of position at two times, t_1 and t_2.
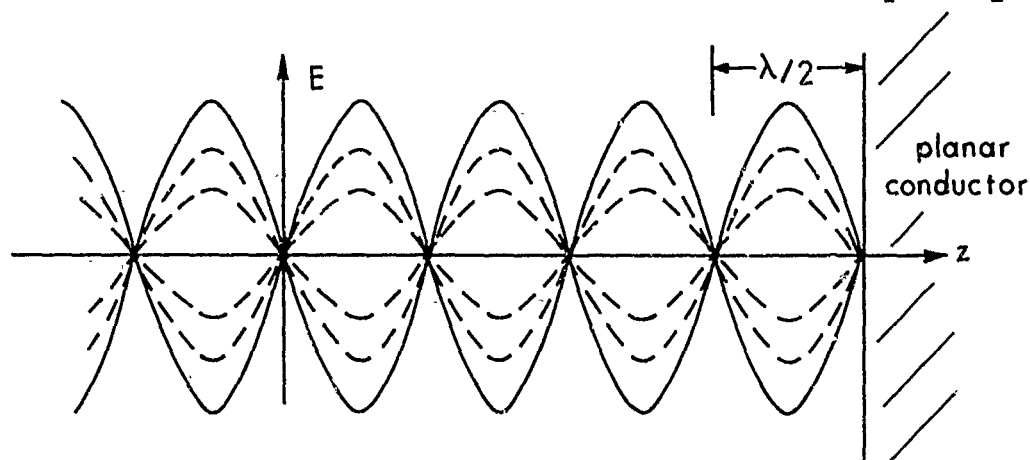
(b) Total E-field as a function of position at various times through a full cycle, and the envelope of the standing wave.
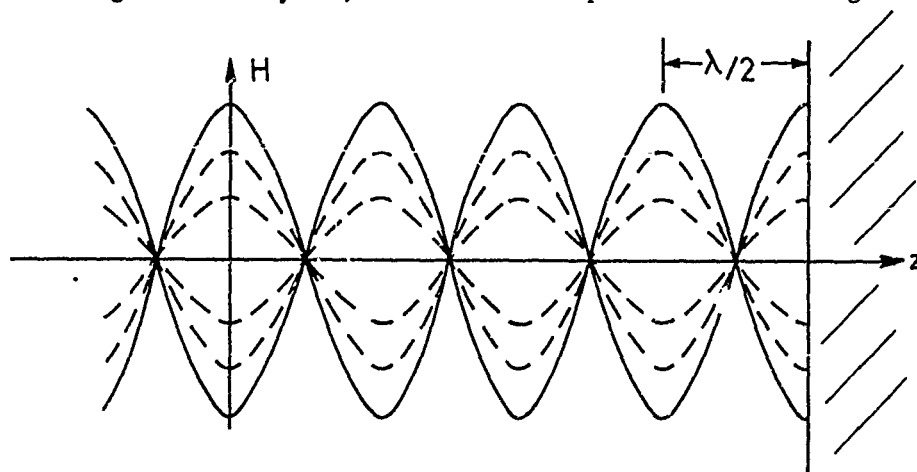
(c) Total H-field as a function of position at various times through a full cycle, and the envelope of the standing wave.

Figure 3.32. Total fields, incident plus scattered.

- 3.57 -

Figure 3.33 is a diagram of a planewave obliquely incident on a perfect planar conductor. In this case the angle of reflection is equal to the angle of incidence. The angles are defined as the angles between the direction of propagation and the normal to the planar conductor. The sum of the incident and scattered waves for oblique incidence is also a standing wave, but in this case the nodes do not occur at half-wavelength spacing. Their spacing depends on the angle of incidence. For large angles of incidence, the spacing between nodes is much smaller than half a wavelength.
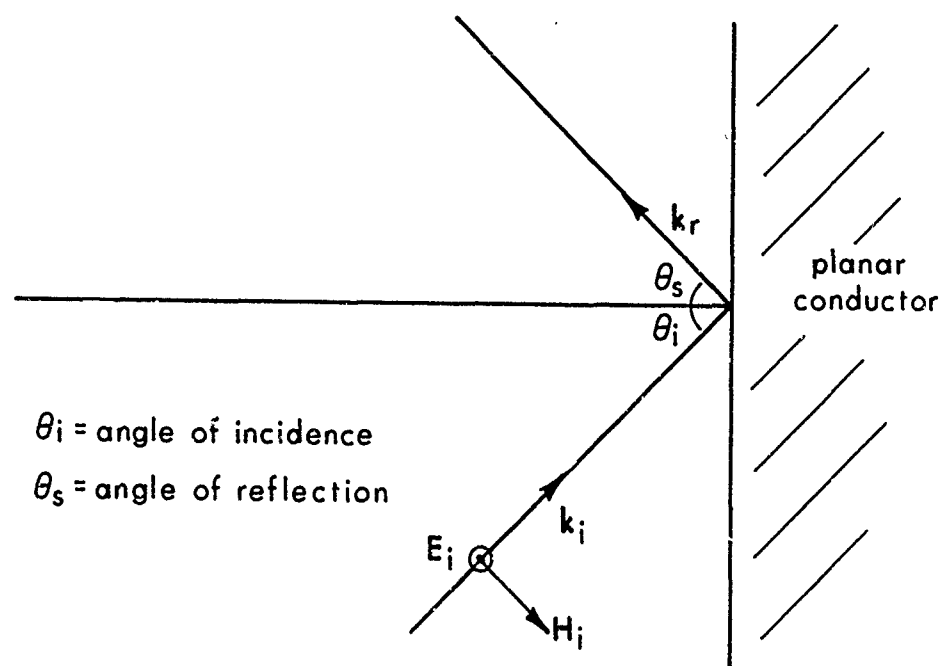
Figure 3.33. Planewave obliquely incident on a planar conductor.

Planar Dielectrics--When a planewave is incident on a planar dielectric, the incident wave produces currents in the dielectric which produce additional fields, just as a conductor does. Unlike the fields inside a conductor, however, the fields inside a dielectric do not necessarily add to zero. A planewave incident on a planar dielectric produces scattered fields outside the dielectric and a wave inside the dielectric called the transmitted (refracted) wave, as shown diagramatically in Figure 3.34 for oblique

incidence. With a lossy dielectric (see Section 3.2.6), the transmitted wave is attenuated as it travels into the dielectric, becoming essentially zero at some depth related to the ε" of the dielectric. For large ε", the transmitted wave does not penetrate very far into the dielectric.
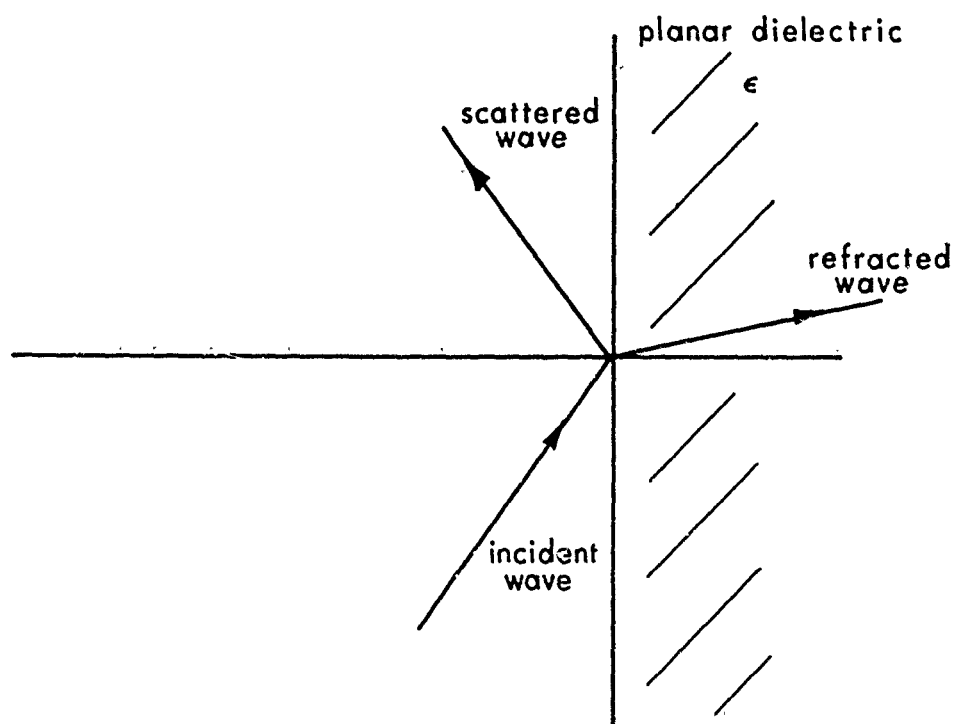
Figure 3.34. Planewave obliquely incident on a planar dielectric.

Nonplanar Objects--The scattering of E- and H-fields by nonplanar objects is more complicated than that by planar objects. The scattering depends on the size, shape, and material properties of the object and the frequency of the incident fields. If the object is very small compared to a wavelength of the incident fields or if the object's relative permittivity is very close to unity, not much scattering occurs. When the object's size is comparable to or larger than a wavelength, significant scattering generally occurs. More specific information about scattering and absorption by biological tissue is given next.

3.3.3. Electrical Properties of Biological Tissue

The permeability of biological tissue is essentially equal to that of free space; in other words, biological tissue is essentially nonmagnetic. The permittivity of biological tissue is a strong function of frequency. Figure 3.35 shows the average ϵ' and ϵ'' for the human body as a function of frequency. Calculations have shown that the average ϵ' and ϵ'' for the whole human body are equal to approximately two-thirds that of muscle tissue. At frequencies below about 1 MHz, body tissue is anisotropic; i.e., conductivity in one direction is significantly different from the conductivity in another direction.

Permittivity generally decreases with frequency. This manifests the inability of the charges in the tissue to respond to the higher frequencies of the applied fields, thus resulting in lower permittivity values.

In tissue the ϵ'' represents mostly ionic conductivity and absorption due to relaxational processes, including friction associated with the alignment of electric dipoles and with vibrational and rotational motion in molecules.

3.3.4. Planewave Absorption Versus Frequency

The absorption of energy by an object irradiated by electromagnetic fields is a strong function of frequency. Many calculations of absorbed energy, although generally very difficult, have been made; and significant data, both calculated and measured, are available. Absorption characteristics are explained below, first for planar models, which are the simplest but least representative of humans, and then for more realistic models.

Planar Models--Although planar models do not represent humans well, analyses of these models have provided important qualitative understanding of energy-absorption characteristics. When a planewave is incident on a planar dielectric object, the wave transmitted into the dielectric attenuates as it travels and transfers energy to the dielectric (as explained in Section 3.3.2). For very lossy dielectrics, the wave attenuates rapidly. This characteristic is described by <u>skin depth</u>--the depth at which the E- and H-fields
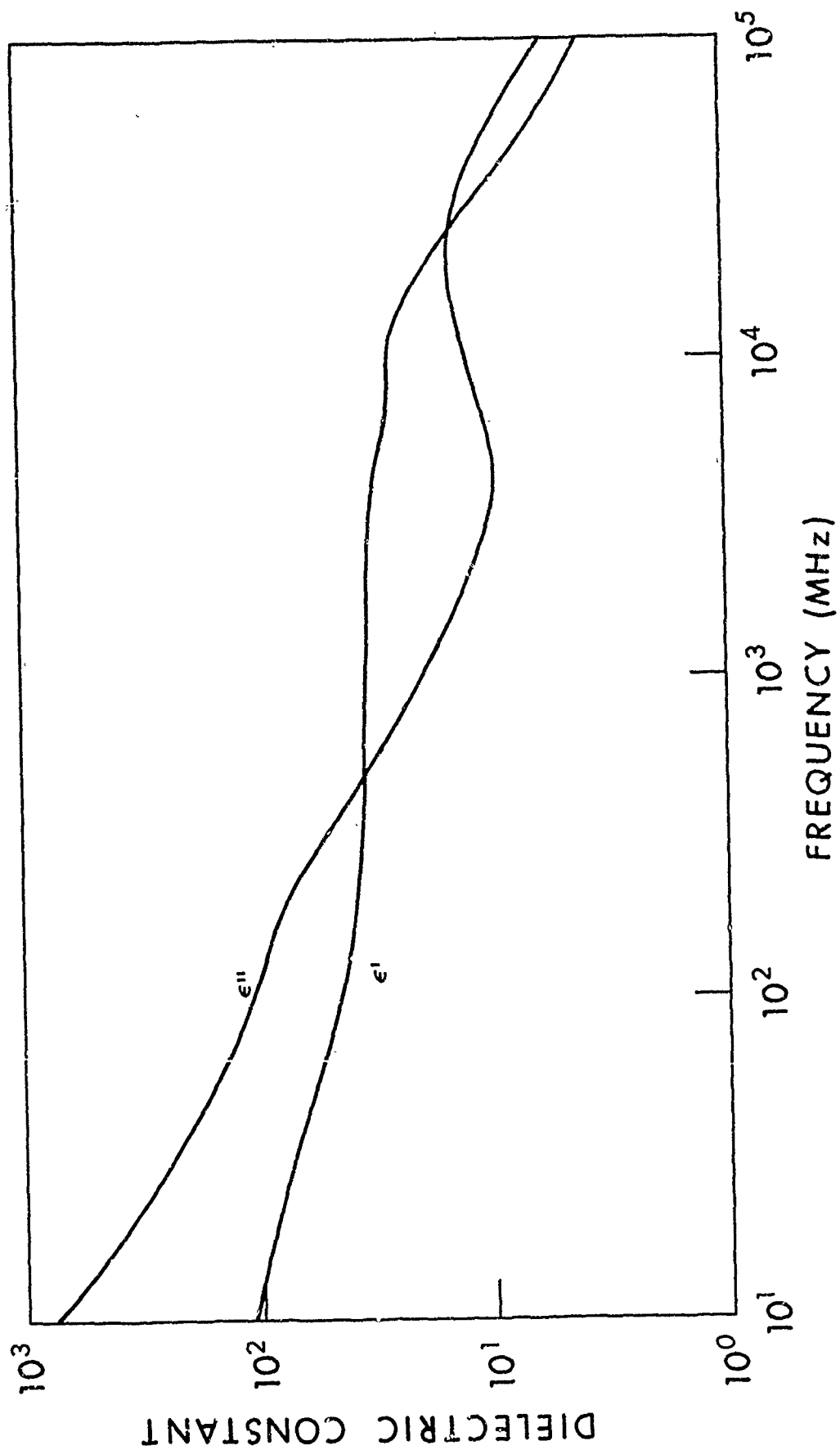
Figure 3.35. Average permittivity of the human body (equivalent to two-thirds that of muscle tissue) as a function of frequency.

have decayed to e^{-1} $\left(e^{-1} = 0.368\right)$ of their value at the surface of the dielectric. Skin depth is also the depth at which the Poynting vector has decayed to e^{-2} $\left(e^{-2} = 0.135\right)$ of its value at the surface. For a planewave incident on a planar dielectric, skin depth is given by

$$\delta = (67.52/f)\left[\sqrt{(\varepsilon')^2 + (\varepsilon'')^2} - \varepsilon'\right]^{-1/2} \qquad m \qquad (3.46)$$

where f is the frequency in MHz. Figure 3.36 shows skin depth as a function of frequency for a planar dielectric with a permittivity equal to two-thirds that of muscle tissue (see Figure 3.35). At higher frequencies, the skin depth is very small; thus most of the energy from the fields is absorbed near the surface. For example, at 2450 MHz the skin depth is about 2 cm; at 10 GHz, about 0.4 cm.
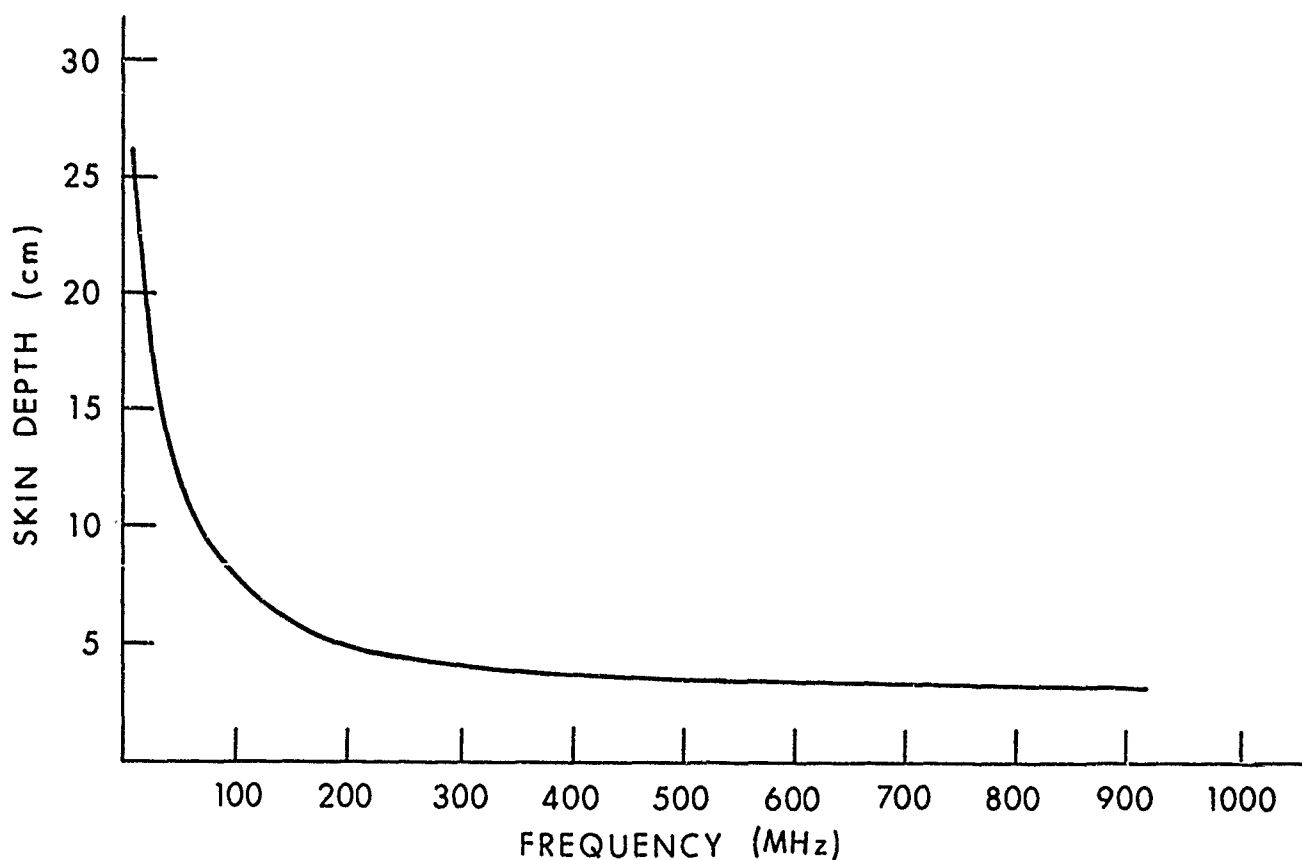
Figure 3.36. Skin depth versus frequency for a dielectric half-space with permittivity equal to two-thirds that of muscle.

The results for planar models have a characteristic generally true for other objects as well: At low frequencies the fields penetrate much deeper than at high frequencies. At very high frequencies any lossy-material heating due to planewave irradiation will be primarily surface heating.

Other Models—Other models—spheres, cylinders, prolate spheroids, block models (cubical mathematical cells arranged in a shape like a human body)— have been used to represent the human body in calculating and measuring energy absorbed during planewave irradiation. The internal E and H are a function of the incident fields, the frequency, and the permittivity and size and shape of the object. Some typical absorption results and characteristics are given in the following sections. Especially important for nonplanar objects are the effects of polarization of the incident fields.

3.3.5. Polarization

Orientation of incident E- and H-fields with respect to the irradiated object has a very strong effect on the strength of fields inside the object. This orientation is defined in terms of polarization of the incident fields.

Polarization for objects of revolution (circular symmetry about the long axis) is defined by the incidenc-field vector—E, H, or k—parallel to the long axis of the body. The polarization is called E polarization if E is parallel to the long axis, H if H is parallel, and K if k is parallel. This definition is illustrated in terms of prolate spheroids in Figure 3.37.
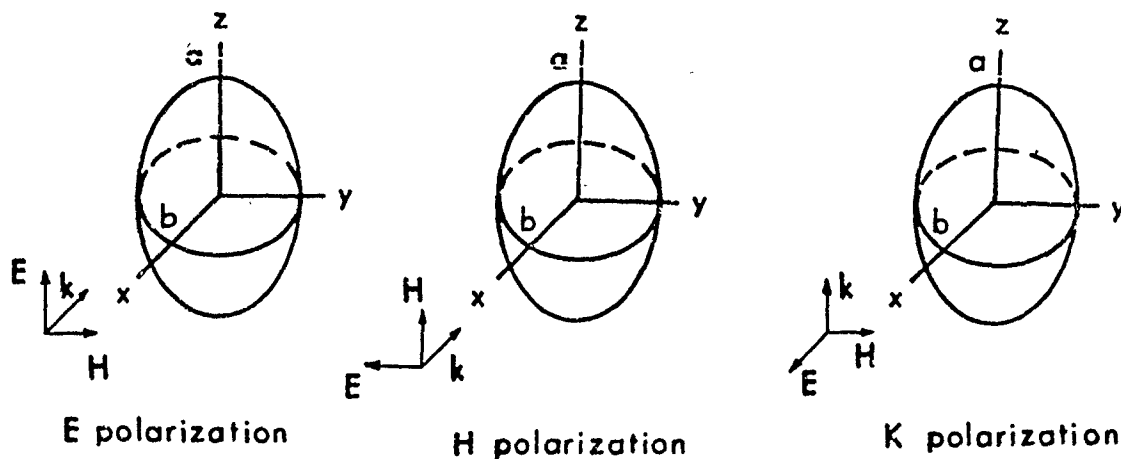
Figure 3.37. Polarization of the incident field with respect to an irradiated object.

For objects (like the human body) that are not objects of revolution, six polarizations are defined, as illustrated in Figure 3.38 for ellipsoids. The ellipsoid has three semiaxes with lengths a, b, and c, where a > b > c. The polarization is defined by which vector (E, H, or k) is parallel to which axis. For example, EHK polarization is the orientation where E lies along a, H lies along b, and k lies along c.

EHK polarization   HEK polarization   EKH polarization

KEH polarization   KHE polarization   HKE polarization
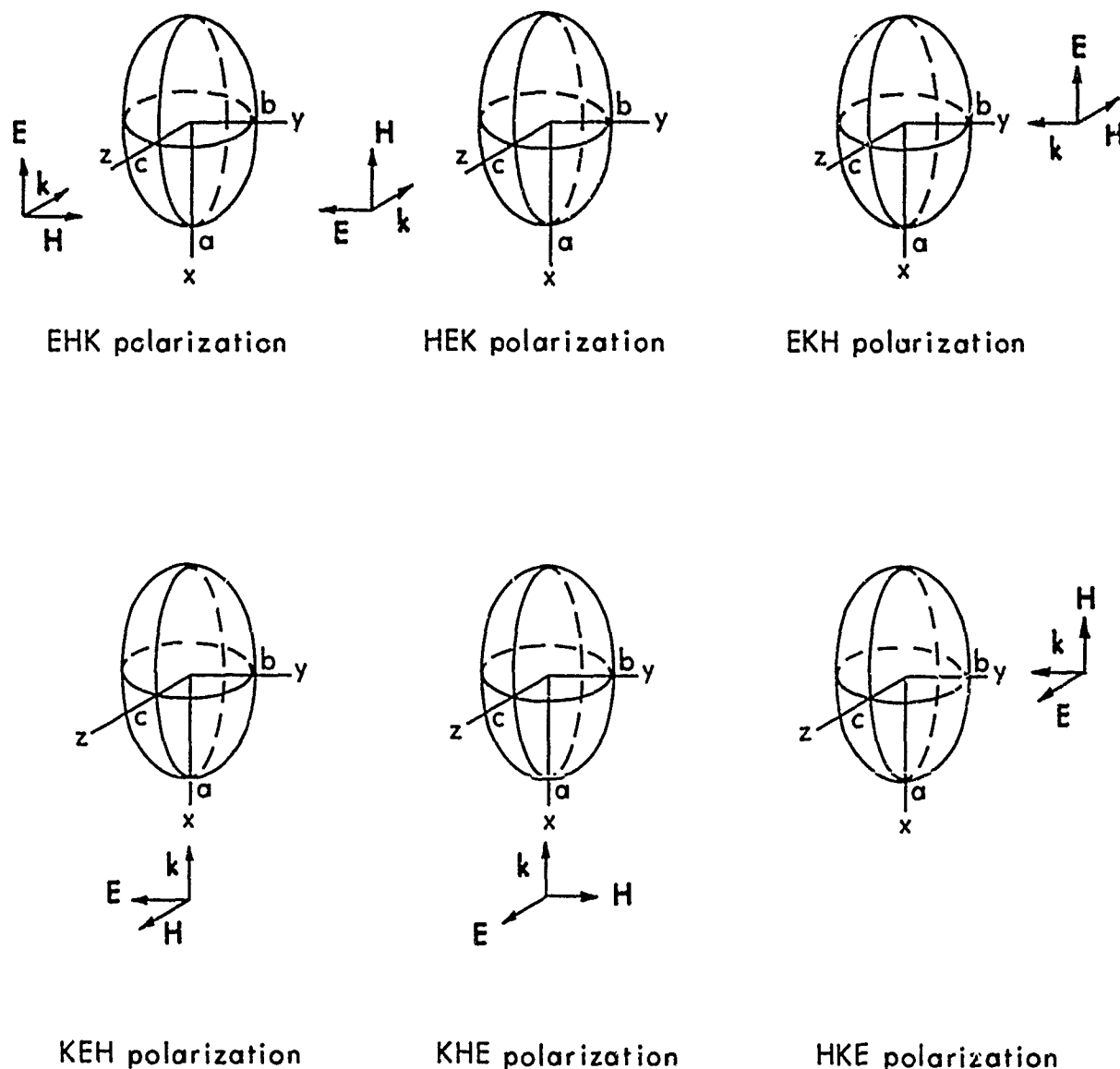
Figure 3.38. Polarization for objects that do not have circular symmetry about the long axis.

- 3.64 -

3.3.6. Specific Absorption Rate

Definition—In dosimetry, the transfer of energy from electric and magnetic fields to charged particles in an absorber is described in terms of the specific absorption rate (SAR). "Specific" refers to the normalization to mass; "absorption," the absorption of energy; and "rate," the time rate of change of the energy absorption. SAR is defined, at a point in the absorber, as the time rate of change of energy transferred to charged particles in an infinitesimal volume at that point, divided by the mass of the infinitesimal volume. From Equation 3.35,

$$\text{SAR} = \left(\partial W_c/\partial t\right)/\rho_m \tag{3.47}$$

where ρ_m is the mass density of the object at that point. For sinusoidal fields, the time-average SAR at a point is given by the term $\langle P_c \rangle/\rho_m$ in Equation 3.38. This is also called the local SAR or SAR distribution to distinguish it from the whole-body average SAR. The whole-body average SAR is defined as the time rate of change of the total energy transferred to the absorber, divided by the total mass of the body. From Poynting's theorem for the time-average sinusoidal steady-state case (see Equation 3.38), the whole-body average SAR is given by

$$\text{Average SAR} = \int_V \langle P_c \rangle dV/M \tag{3.48}$$

where M is the total mass of the absorber. In practice, the term "whole-body average SAR" is often shortened to just "average SAR."

The local SAR is related to the internal E-field through Equation 3.17:

$$\text{SAR} = P/\rho_m = \sigma\left|E\right|^2/\rho_m = \omega\varepsilon_o\varepsilon''\left|E\right|^2/\rho_m \tag{3.49}$$

Thus if the E-field and the conductivity are known at a point inside the object, the SAR at that point can easily be found; conversely, if the SAR and conductivity at a point in the object are known, the E-field at that point can easily be found. Traditionally P has been called absorbed-power density, and

the relation in Equation 3.49 illustrates why SAR is also called absorbed-power density. The bioelectromagnetics community, however, has generally accepted SAR as the preferred term.

SAR Versus Frequency--SAR is an important quantity in dosimetry both because it gives a measure of the energy absorption that can be manifest as heat and because it gives a measure of the internal fields which could affect the biological system in ways other than through ordinary heat. The internal fields, and hence the SAR, are a strong function of the incident fields, the frequency, and the properties of the absorber. Since any biological effects would be caused by internal fields, not incident fields, being able to determine internal fields or SARs in people and experimental animals for given radiation conditions is important. Without such determination in both the animal and the person, we could not meaningfully extrapolate observed biological effects in irradiated animals to similar effects that might occur in irradiated people.

The general dependence of average SAR on frequency is illustrated by Figures 3.39 and 3.40 for models of an average-sized man and a medium-sized rat for the three standard polarizations. For E polarization a resonance occurs at about 80 MHz for the man; at about 600 MHz for the rat. From these two graphs the resonance frequency appears to be related to the length of the body, and indeed it is. In general, resonance occurs for long thin metallic objects at a frequency for which the object is approximately one-half of a free-space wavelength long. For biological bodies, resonance occurs at a frequency for which the length of the body is about equal to four-tenths of a wavelength. A more accurate formula for the resonant frequency is given in Section 3.5. Below resonance the SAR varies approximately as f^2; and just beyond resonance, as $1/f$.
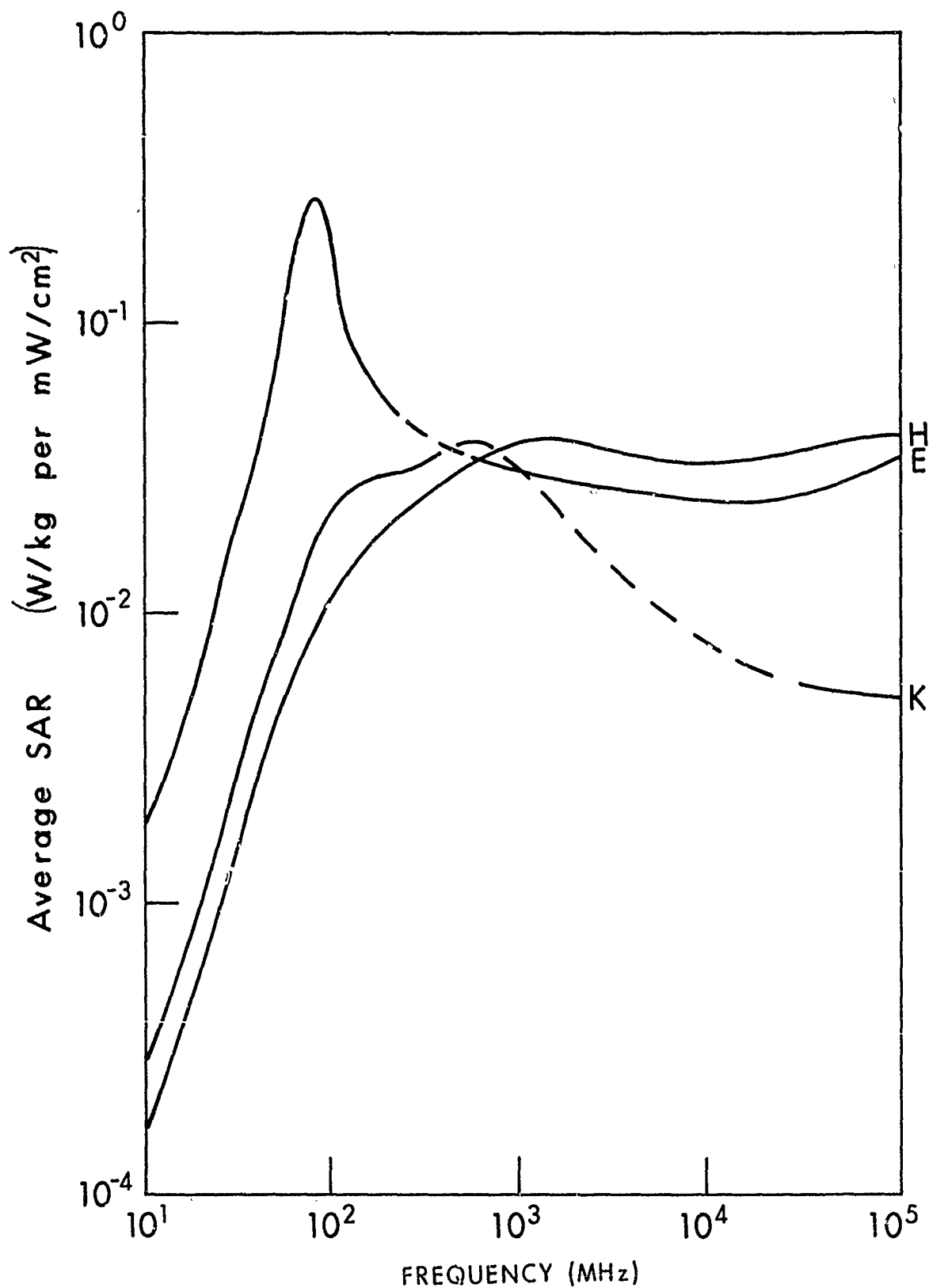
Figure 3.39. Calculated whole-body average SAR versus frequency for models of an average man for three standard polarizations. The incident-power density is 1 mW/cm^2.

- 3.67 -
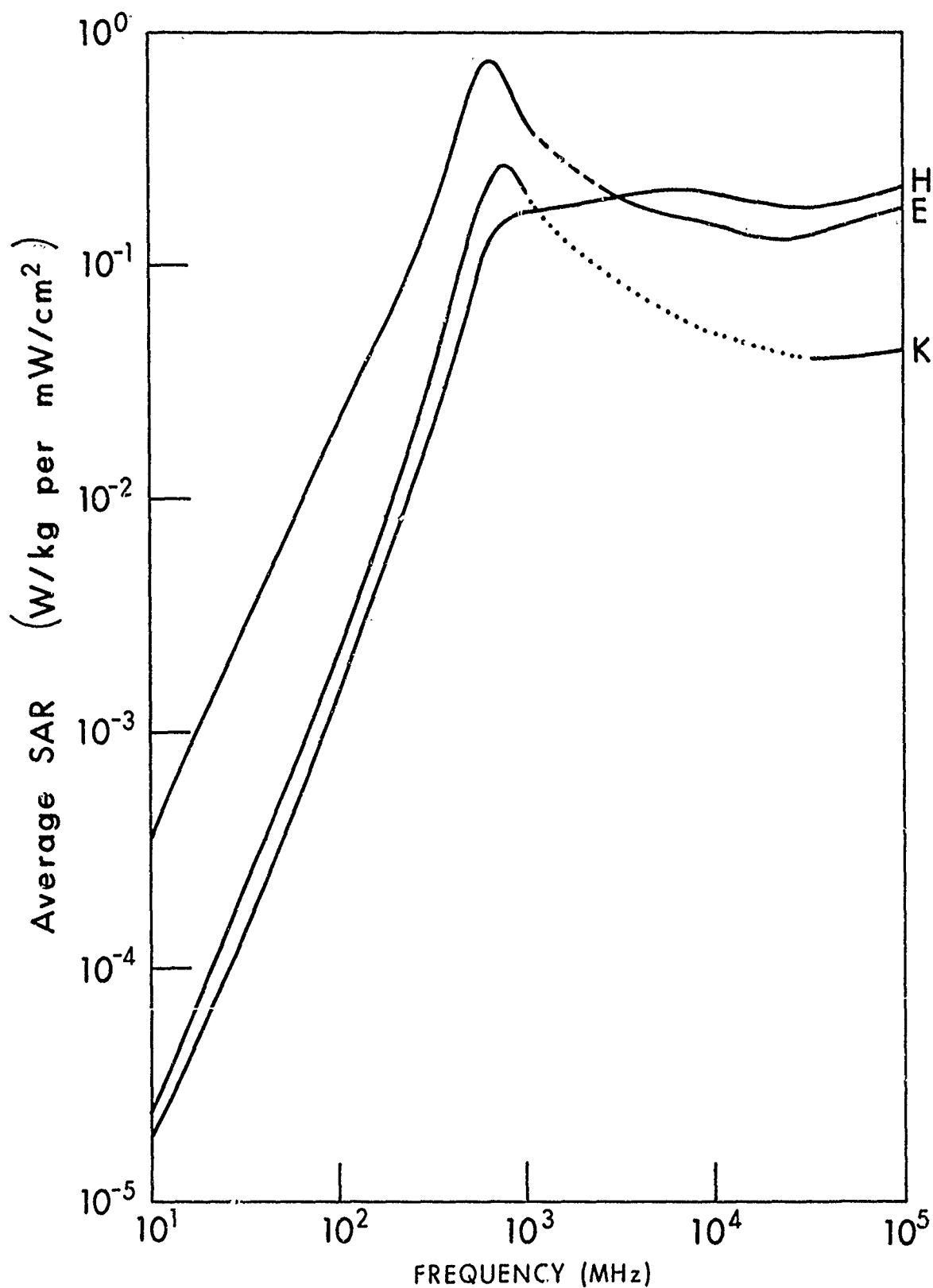
Figure 3.40. Calculated whole-body average SAR versus frequency for models of a medium-sized rat for three standard polarizations. The incident-power density is 1 mW/cm^2.

Figures 3.39 and 3.40 also indicate that below resonance the SAR is generally higher for E polarization, intermediate for K, and lower for H. Again, this is generally true. These characteristics can be explained by two qualitative principles:

1. The SAR is higher when the incident E-field is more parallel to the body than perpendicular.

2. The SAR is higher when the cross section of the body perpendicular to the incident H-field is larger than when it is smaller.

The average SAR is higher for E polarization because the incident E-field is more parallel to the body than perpendicular to it, and the cross section of the body perpendicular to the incident H-field is relatively larger (see Figure 3.37). For H polarization, however, the incident E-field is more perpendicular to the body than parallel to it, and the cross section of the body perpendicular to the incident H-field is relatively smaller; both conditions contribute to a lower average SAR. The average SAR for K polarization is intermediate between the other two because the incident E-field is more perpendicular to the body, contributing to a lower SAR; but the cross section perpendicular to the incident H-field is large, contributing to a larger SAR.

When a man is standing on a perfectly conducting ground plane, for E polarization the ground plane has the effect of making the man appear electrically to be about twice as tall, which lowers the resonant frequency to, approximately half of that in free space. For a man on a ground plane, the graph of SAR versus frequency for E polarization would therefore be almost like the one in Figure 3.39 but shifted to the left by approximately 40 MHz. This is generally true for objects on ground planes for E polarization.

Another important qualitative characteristic is that when the incident E-field is mostly parallel to the body, the average SAR goes up if the body is made longer and thinner. Some of these "rules of thumb" are summarized in Section 3.5. More detailed information about SAR characteristics is given in Section 5.1.

3.4. CONCEPTS OF MEASUREMENTS

Three kinds of electromagnetic measurement techniques are of primary interest: the electric field, the magnetic field, and the SAR. The basic concepts underlying these measurement techniques are discussed in this section. More detailed information is given in Chapter 7.

3.4.1. Electric-Field Measurements

Devices for measuring an E-field usually consist of two main components: a small antenna or other pickup device that is sensitive to the presence of an E-field, and a detector that converts the signal to a form that can be registered on a readout device such as a meter. The pickup is typically a short dipole. The dipole can be two short pieces of thin wire (Figure 3.41(a)) or two short strips of thin metal as on a printed circuit (Figure 3.41(b)). Sometimes the dipole is flared out to look like a bow tie (Figure 3.41(c)) to improve the bandwidth of the dipole.

(a)   (b)   (c)
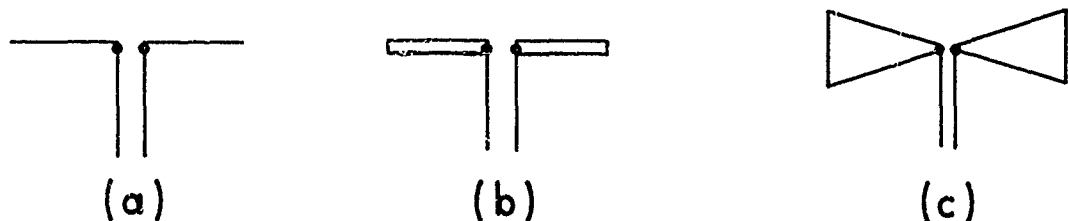
Figure 3.41. Short dipole used to sense the presence of an electric field.

The detector is usually a diode or a thermal sensor. A diode rectifies the signal so that it can register on a dc meter. A thermal sensor responds to heat produced in some lossy material that absorbs energy from the E-field. The heat produces a voltage or current that can be registered on a meter. An example of a thermal sensor is a thermocouple, which consists of two junctions of dissimilar metals. The two junctions produce a voltage proportional to the temperature difference between them.

Leads are required to transmit the voltage or current from the detector to the meter or other readout devices, as illustrated in Figure 3.42. The leads often cause problems because they themselves can be sensitive to the presence of an E-field and may produce erroneous readings through unwanted E-field pickup. To overcome this problem, high-resistance leads are often used in E-field probes. The sensitivity of the pickup element is roughly proportional to its length compared to a wavelength of the E-field to be measured. At low frequencies, where the wavelength is very long, short elements are sometimes not sensitive enough; however, if the element is too long it may perturb the field to be measured. To avoid field perturbation, the element should be short compared to a wavelength; thus the tradeoff between sensitivity and perturbation is difficult.
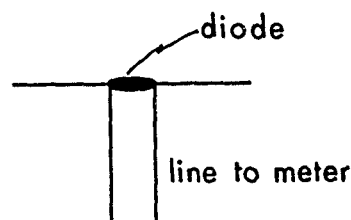
Figure 3.42. Simple electric-field probe with a diode detector.

The dipole element is sensitive only to the E-field component parallel to the dipole; an E-field perpendicular to the dipole will not be sensed. This can be understood in terms of the force that the E-field exerts on the charges in the dipole, for that is the basic mechanism by which the dipole senses the E-field. An E-field parallel to the dipole produces forces on charges that tend to make them move along the dipole from end to end, which amounts to a current in the dipole. An E-field perpendicular to the dipole, however, tries to force the charges out through the walls of the dipole, which produces essentially no current useful for sensing the E-field. In practice, three orthogonal dipoles are often used, one to sense the E-field component in each direction. By electronic circuitry, each component is then squared and the results are added to get the magnitude of the E-field vector.

Although commercial instruments for measuring E-field are based on the simple concepts described here, they are very sophisticated in their design and fabrication. Some of them are described in Chapter 7.

3.4.2. Magnetic-Field Measurements

Devices for measuring B-field also consist of two basic components, the pickup and the detector. For the B-field the pickup is usually some kind of loop, as shown in Figure 3.43. The loop is sensitive only to the B-field component perpendicular to the plane of the loop, as indicated. A time-varying B-field produces a voltage in the loop that is proportional to the loop's area and the rapidity (frequency) of the B-field's time variation. Thus at low frequencies the loop must be large to be sensitive to weak fields. As with the E-field probe, making the probe large to improve the sensitivity yet small enough to minimize the perturbation of the field being measured requires a tradeoff.
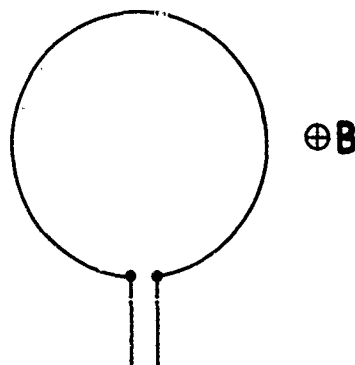
Figure 3.43. Loop antenna used as a pickup for measuring magnetic field.

Diode detectors are commonly used with B-field probes, although some thermal sensors have been used. Leads can also cause unwanted pickup of fields in B-field measurements. Another problem with the loop sensors is that they may be sensitive to E- as well as B-field. Special techniques have been used to minimize the E-field pickup in loops used with commercial B-field

probes. Some of the available commercial B-field probes are described in Chapter 7.

3.4.3. SAR Measurements

Usually only research laboratories make SAR measurements because they are relatively difficult and require specialized equipment and conditions (see Chapter 7). Three basic techniques are used for measuring SARs. One is to measure the E-field inside the body, using implantable E-field probes, and then to calculate the SAR from Equation 3.49; this requires knowing the conductivity of the material. This technique is suitable for measuring the SAR only at specific points in an experimental animal. Even in models using tissue-equivalent synthetic material, measuring the internal E-field at more than a few points is often not practical.

A second basic technique for measuring SAR is to measure the temperature change due to the heat produced by the radiation, and then to calculate the SAR from that. Probes inserted into experimental animals or models can measure local temperatures, and then the SAR at a given point can be calculated from the temperature rise. Such calculation is easy if the temperature rise is linear with time; that is, the irradiating fields are intense enough so that heat transfer within and out of the body has but negligible influence on the temperature rise. Generating fields intense enough is sometimes difficult. If the temperature rise is not linear with time, calculation of the SAR from temperature rise must include heat transfer and is thus much more difficult. Another problem is that the temperature probe sometimes perturbs the internal E-field patterns, thus producing artifacts in the measurements. This problem has led to the development of temperature probes using optical fibers or high-resistance leads instead of ordinary wire leads.

A third technique is to calculate absorbed power as the difference between incident power and scattered power in a radiation chamber. This is called the differential power method (see Section 7.2.5).

Whole-body (average) SAR in small animals and small models can be calculated from the total heat absorbed, as measured with whole-body calorimeters. Whole-body SARs have also been determined in saline-filled

- 3.73 -

models by shaking them after irradiation to distribute the heat and then measuring the average temperature rise of the saline.

3.5. RULES OF THUMB AND FREQUENTLY USED RELATIONSHIPS

This section contains a summary of some of the "rules of thumb" (Table 3.3) discussed in previous sections as well as a summary of some of the more frequently used relationships of electromagnetics (Table 3.4).

TABLE 3.3.   SOME RULES OF THUMB

1. Wetter materials (muscle, high-water content tissues) are generally more lossy than drier materials (fat, bone) and hence absorb more energy from electromagnetic fields.

2. The SAR is higher when the incident E-field is more parallel to the body than perpendicular to it.

3. The SAR is higher when the cross section of the body perpendicular to the incident H-field is larger than when the section is smaller.

4. Sharp corners, points, and edges concentrate E-fields. When placed perpendicular to E-fields, conducting wires and plates cause minimum perturbation to the fields; when placed parallel to them, maximum perturbation.

5. A uniform incident field does not generally produce a uniform internal field.

6. Depth of penetration decreases as conductivity increases, also as frequency increases.

7. Objects small compared to a wavelength cause little perturbation and/or scattering of electromagnetic fields.

8. Below resonance, the SAR varies approximately as f^2.

9. For E polarization, SAR increases faster than f^2 just below resonance; just beyond resonance, SAR decreases approximately as $1/f$ and then levels off. Variation of SAR with frequency is most rapid near resonance.

10. Near resonance and below, SAR is greatest for E polarization, least for H polarization, and intermediate for K polarization.

11. For E polarization, the SAR increases as an object becomes longer and thinner, and decreases as an object gets shorter and fatter.

TABLE 3.4. SOME FREQUENTLY USED RELATIONSHIPS

$\sigma = \omega \epsilon_o \epsilon''$

σ is conductivity in siemens/meter
$\epsilon_o = 8.85 \times 10^{-12}$ F/m: permittivity of free space
ϵ'' is the imaginary part of complex relative permittivity

$\omega = 2\pi f$

ω is radian frequency in radians/second
f is frequency in hertz

$\tan \delta = \epsilon''/\epsilon'$

$\tan \delta$ is the loss tangent

$P = \sigma |E|^2$

P is density of absorbed power at a point in watts/cubic meter
σ is conductivity in siemens/meter at the point
$|E|$ is rms electric-field intensity in rms volts/meter

$D = \epsilon E$

D is electric-flux density in coulombs/square meter
ϵ is permittivity in farads/meter
E is electric-field intensity in volts/meter

$B = \mu H$

B is magnetic-flux density in tesla
μ is permeability in henry/meter
H is magnetic-field intensity in amperes/meter

$\epsilon_o = 8.85 \times 10^{-12}$ F/m

ϵ_o is the permittivity of free space

$\mu_o = 4\pi \times 10^{-7}$ H/m

μ_o is the permeability of free space

$f = 1/T$

f is frequency in hertz
T is period in seconds

$\lambda = v/f$

λ is wavelength in meters
v is velocity of propagation in meters/second
f is frequency in hertz

TABLE 3.4. (continued)

$E/H = \sqrt{\mu/\epsilon}$

E/H = 377 ohms in free space

E/H is the wave impedance in ohms

E is the magnitude of the electric-field intensity in volts/meter

H is the magnitude of the magnetic-field intensity in amperes/meter

$v = 1/\sqrt{\mu\epsilon}$

$v = 3 \times 10^8$ m/s in free space

v is the velocity of propagation in meters/second

μ is the permeability in henry/meter

ϵ is the permittivity in farad/meter

$\langle P \rangle = \langle E \times H \rangle$

$\langle P \rangle$ is the time-averaged Poynting's vector in watts/ square meter

E is the electric-field intensity in rms volts/meter

H is the magnetic-field intensity in rms amperes/ meter

$P = E^2/377$

P is the magnitude of the time-averaged Poynting vector for a planewave in free space

E is the magnitude of the electric-field intensity in rms volts/meter

377 is the wave impedance of free space in ohms

$S = E_{max}/E_{min}$

S is the standing-wave ratio (unitless)

E_{max} is the maximum value of the magnitude of the electric-field intensity anywhere along the wave

E_{min} is the minimum value of the magnitude of the electric-field intensity anywhere along the wave

$S = (1 + \rho)/(1 - \rho)$

S is the standing-wave ratio (unitless)

ρ is the magnitude of the reflection coefficient (ratio of reflected E-field to incident E-field)

$$\delta = \frac{67.52}{f} \times \left[\sqrt{(\epsilon')^2 + (\epsilon'')^2} - \epsilon' \right]^{-1/2}$$

δ is the skin depth in meters

ϵ' is the real part of the permittivity

ϵ'' is the imaginary part of the permittivity

f is the frequency in MHz

TABLE 3.4. (continued)

$$SAR = \sigma |E|^2 / \rho_m$$

SAR is the local specific absorption rate in watts/kilogram
σ is the conductivity in siemens/meter
$|E|$ is the electric-field strength in rms volts/meter
ρ_m is the mass density in kilograms/cubic meter

$$f_o = 2.75 \times 10^8 \times \left[2\ell^2 + \frac{\pi^2}{4} \left(\ell^2 + d^2 \right) \right]^{-1/2}$$

f_o is the resonant frequency in hertz of the SAR for E polarization
ℓ is the average length of the absorbing object
d is the average diameter of the absorbing object

$$F = \left[\frac{1}{T} \int_0^T f^2(t) dt \right]^{1/2}$$

F is the rms value of the periodic function $f(t)$
T is the period of the function

$$G = g_p / \sqrt{2}$$

G is the rms value of a sinusoid
g_p is the peak value of the sinusoid

$$d = 2L^2 / \lambda$$

d is the approximate distance from an antenna at which the near fields become negligible and the fields are approximately far fields
L is the largest dimension of the antenna
λ is the wavelength

- 3.77 -

CHAPTER 4. DIELECTRIC PROPERTIES

Information about the dielectric properties of biological systems is essential to RF dosimetry. This information is important in both experiments and calculations that include the interaction of electromagnetic fields with biological systems. This chapter describes the basic dielectric properties of biological substances and summarizes methods used to measure these properties; it includes a tabulated summary of the measured values.

4.1. CHARACTERISTICS OF BIOLOGICAL TISSUE

The material in this section was written by H. P. Schwan, Ph.D., Department of Bioengineering, University of Pennsylvania. It was published in a paper titled "Dielectric Properties of Biological Tissue and Physical Mechanisms of Electromagnetic Field Interaction" in Biological Effects of Nonionizing Radiation, ACS Symposium Series 157, Karl H. Illinger, Editor, published by the American Chemical Society, Washington, DC, 1981. It is presented here with minor changes by permission of the author and the publisher.

4.1.1. Electrical Properties

We will summarize the two electrical properties that define the electrical characteristics, namely, the dielectric constant relative to free space (ε) and conductivity (σ). Both properties change with temperature and, strongly, with frequency. As a matter of fact, as the frequency increases from a few hertz to gigahertz, the dielectric constant decreases from several million to only a few units; concurrently, the conductivity increases from a few millimhos per centimeter to nearly a thousand.

Figure 4.1 indicates the dielectric behavior of practically all tissues. Two remarkable features are apparent: exceedingly high dielectric constants at low frequencies and three clearly separated relaxation regions—α, β, and γ—of the dielectric constant at low, medium, and very high frequencies. In its simplest form each of these relaxation regions is characterized by equations of the Debye type as follows,

$3 \cdot 10^6$ Muscle

ϵ

10^6

10^2

α

β

γ

10^2 10^6

GROSS STRUCTURE
α Exc. Membrane?
   Intracell Struct ?
β Tissue Struct. (Max-Wag)
γ Water

FINE STRUCTURE
α_1 Charge Transfer (Ion Rel.)
β_1 (Subcell. Components
        Biol. Macromol.)
δ BD. H_2O, Side Chain Rot.,
      Amino Acid
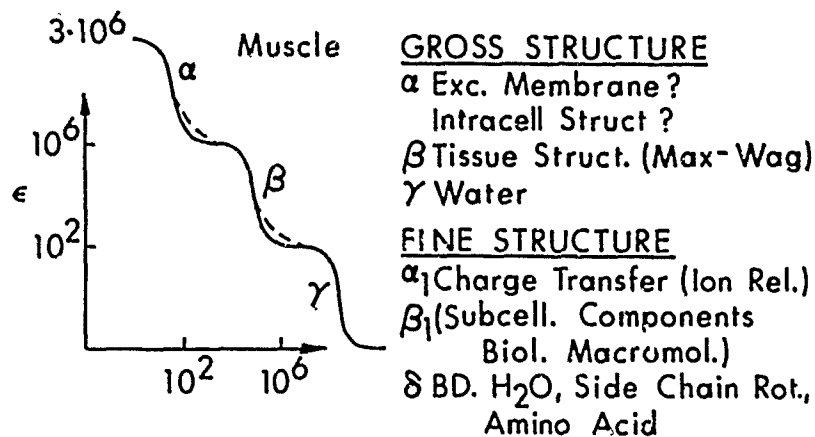
Figure 4.1. Frequency dependence of the dielectric
constant of muscle tissue (Schwan, 1975).

Dominant contributions are responsible for the α, β,
and γ dispersions.   They include for the α-effect,
apparent membrane property changes as described in the
text; for the β-effect, tissue structure (Maxwell-
Wagner effect); and for the γ-effect, polarity of the
water molecule (Debye effect).   Fine structural
effects are responsible for deviations as indicated by
the dashed lines.   These include contributions from
subcellular organelles, proteins, and counterion
relaxation effects.

$$\epsilon = \epsilon_\infty + \frac{\epsilon_s - \epsilon_\infty}{1 + x^2} \quad ; \quad \sigma = \sigma_s + \left(\sigma_\infty - \sigma_s\right)\frac{x^2}{1 + x^2} \qquad (4.1)$$

where x is a multiple of the frequency and the constants are determined by the
values at the beginning and end of the dispersion change. However, biological
variability may cause the actual data to change with frequency somewhat more
smoothly than indicated by the equations.

The separation of the relaxation regions greatly aids in identifying the
underlying mechanism.   The mechanisms responsible for these three relaxation
regions are indicated in Table 4.1.   Inhomogeneous structure is responsible
for the β-dispersion--the polarization resulting from the charging of inter-
faces, i.e., membranes through intra- and extracellular fluids (Maxwell-Wagner
effect).   A typical example is presented in Figure 4.2 in the form of an
impedance locus. The dielectric properties of muscle tissue are seen to

- 4.2 -

TABLE 4.1. ELECTRICAL RELAXATION MECHANISM (Schwan, 1975)

Three categories of relaxation effects are listed as
they contribute to gross and fine structure relaxa-
tional effects. They include induced-dipole effects
(Maxwell-Wagner and counterion) and permanent-dipole
effects (Debye).

Inhomogeneous structure   β
    (Maxwell-Wagner)

Permanent-dipole rotation   γ, β tail
    (Debye)

Subcellular organelles   α
    (Maxwell-Wagner)

Counterion relaxation   α
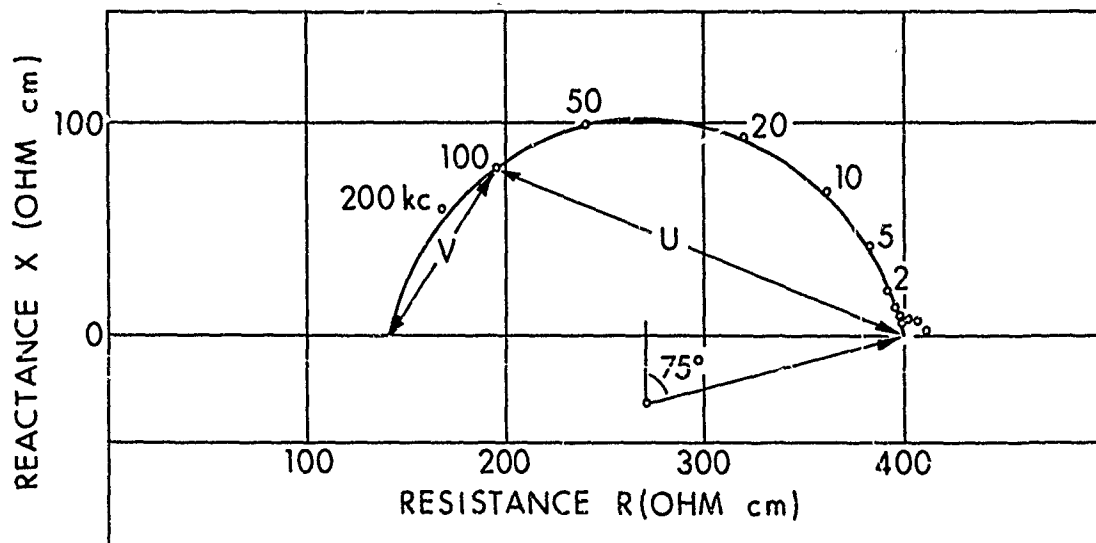
Figure 4.2. Dielectric properties of muscle in the impedance plane,
             with reactance X plotted against resistance R and the
             impedance Z = R + jX (Schwan, 1957). The large circle
             results from the β-dispersion and the small one from the
             α-dispersion. The plot does not include the γ-dispersion.

- 4.3 -

closely conform to a suppressed circle, i.e., to a Cole-Cole distribution function of relaxation times. A small second circle at low frequencies represents the α-dispersion effect. Rotation of molecules having a permanent dipole moment, such as water and proteins, is responsible for the γ-dispersion (water) and a small addition to the tail of the β-dispersion resulting from a corresponding β_1-dispersion of proteins. The tissue proteins only slightly elevate the high-frequency tail of the tissue's β-dispersion because the addition of the β_1-effect caused by tissue proteins is small compared to the Maxwell-Wagner effect and occurs at somewhat higher frequencies. Another contribution to the β-dispersion is caused by smaller subcellular structures, such as mitochondria, cell nuclei, and other subcellular organelles. Since these structures are smaller in size than the surrounding cell, their relaxation frequency is higher but their total dielectric increment smaller. They therefore contribute another addition to the tail of the β-dispersion $\left(\beta_1\right)$.

The γ-dispersion is due solely to water and its relaxational behavior near about 20 GHz. A minor additional relaxation (δ) between β and γ-dispersion is caused in part by rotation of amino acids, partial rotation of charged side groups of proteins, and relaxation of protein-bound water which occurs somewhere between 300 and 2000 MHz.

The α-dispersion is presently the least clarified. Intracellular structures, such as the tubular apparatus in muscle cells, that connect with the outer cell membranes could be responsible in tissues that contain such cell structures. Relaxation of counterions about the charged cellular surface is another mechanism we suggest. Last but not least, relaxational behavior of membranes per se, such as reported for the giant squid axon membrane, can account for the α-dispersion (Takashima and Schwan, 1974). The relative contribution of the various mechanisms varies, no doubt, from one case to another and needs further elaboration.

No attempt is made to summarize conductivity data. Conductivity increases similarly in several major steps symmetrical to the changes of the dielectric constant. These changes are in accord with the theoretical demand that the ratio of capacitance and conductance changes for each relaxation mechanism is given by its time constant, or in the case of distributions of

time constants, by an appropriate average time constant and the Kramers-Kronig relations.

Table 4.2 indicates the variability of the characteristic frequency for the various mechanisms--α, β, γ, and δ from one biological object to another. For example, blood cells display a weak α-dispersion centered at about 2 kHz, while muscle displays a very strong one near 0.1 kHz. The β-dispersion of blood is near 3 MHz, that of muscle tissue near 0.1 MHz. The considerable variation depends on cellular size and other factors. The variation may not be as strong in the δ-case as in the α- and β-dispersion frequencies. The γ-dispersion, however, is always sharply defined at the same frequency range.

TABLE 4.2. RANGE OF CHARACTERISTIC FREQUENCIES OBSERVED WITH BIOLOG-
ICAL MATERIAL FOR α-, β-, δ-, and γ-DISPERSION EFFECTS

Dispersion	Frequency Range (Hz)
α	$1 - 10^4$
β	$10^4 - 10^8$
δ	$10^8 - 10^9$
γ	$2 \cdot 10^{10}$

Table 4.3 indicates at what level of biological complexity the various mechanisms occur. Electrolytes display only the γ-dispersion characteristic of water. To the water's γ-dispersion, biological macromolecules add a δ-dispersion. It is caused by bound water and rotating side groups in the case of proteins, and by rotation of the total molecule in the case of the amino acids; in particular, proteins and nucleic acids add further dispersions in the β- and α-range as indicated. Suspensions of cells free of protein would display a Maxwell-Wagner β-dispersion and the γ-dispersion of water. If the cells contain protein an additional, comparatively weak β-dispersion due to the polarity of protein is added, and a δ-dispersion. If the cells carry a net charge, an α-mechanism due to counterion relaxation is added; and if their

TABLE 4.3. BIOLOGICAL COMPONENTS AND RELAXATION
MECHANISMS THEY DISPLAY (Schwan, 1975)

Electrolytes	γ
Biological macromolecules	
Amino acids	$\delta + \gamma$
Proteins	$\beta + \delta + \gamma$
Nucleic acids	$\alpha + \beta + \delta + \gamma$
Cells, free of protein	$\beta + \gamma$
Charged	$\alpha + \beta + \gamma$
With excitable membranes	$\alpha + \beta + \gamma$

membranes relax on their own as some excitable membranes do, an additional α-mechanism may appear.

Evidence in support for the mechanism outlined above may be summarized as follows.

Water and Tissue Water--The dielectric properties of pure water have been well established from dc up to microwave frequencies approaching the infrared (Afsar and Hasted, 1977). For all practical purposes, these properties are characterized by a single relaxation process centered near 20 GHz at room temperature. Static and infinite frequency permittivity values are close to 78 and 5, respectively, at room temperature. Hence, the microwave conductivity increase predicted by Equation 4.1 is close to 0.8 mho/cm above 20 GHz, much larger than typical low-frequency conductivities of biological fluids which are about 0.01 mho/cm. The dielectric properties of water are independent of field strength up to fields of the order 100 kV/cm.

The dielectric properties of electrolytes are almost identical to those of water with the addition of a σ_S term in Equation 4.1 due to the ionic conductance of the dissolved ion species. The static dielectric permittivity of electrolytes of usual physiological strength (0.15 N) is about two units lower than that of pure water (Hasted, 1963), a negligible change.

Three dielectric parameters are characteristic of the electrical and viscous properties of tissue water:

a. The conductance of ions in water

b. The relaxation frequency, f_c

c. The static dielectric permittivity, ε_s, observed at
$f \ll f_c = 20$ GHz

A detailed study of the internal conductivity of erythrocytes revealed the intracellular ionic mobility to be identical with that of ions in dilute electrolyte solutions if appropriate allowance is made for internal friction with suspended macromolecules (Pauly and Schwan, 1966). Tissue conductivities near 100 or 200 MHz, sufficiently high that cell membranes do not affect tissue electrical properties, are comparable to the conductivity of blood and to somewhat similar protein suspensions in electrolytes of physiological strength. Hence the mobility of ions in the tissue fluids apparently does not differ noticeably from their mobility in water.

Characteristic frequencies may be found from dielectric permittivity data or, even better, from conductivity data. The earlier data by Herrick et al. (1950) suggest that there is no apparent difference between the relaxation frequency of tissue water and that of the pure liquid (Schwan and Foster, 1977). However, these data extend only to 8.5 GHz, one-third the relaxation frequency of pure water at 37°C (25 GHz), so small discrepancies might not have been uncovered. We have made measurements on muscle at 37°C and 1°C (where the pure-water relaxation frequency is 9 GHz), up to 17 GHz. The dielectric properties of the tissue above 1 GHz show a Debye relaxation at the expected frequency of 9 GHz (Foster et al., 1980) (Figure 4.3). The static dielectric constant of tissue water as determined at 100 MHz compares with that of free water if allowance is made for the fraction occupied by biological macromolecules and their small amount of bound water (Schwan, 1957; Schwan and Foster, 1980). Thus from all points considered, tissue water appears to be identical with normal water.
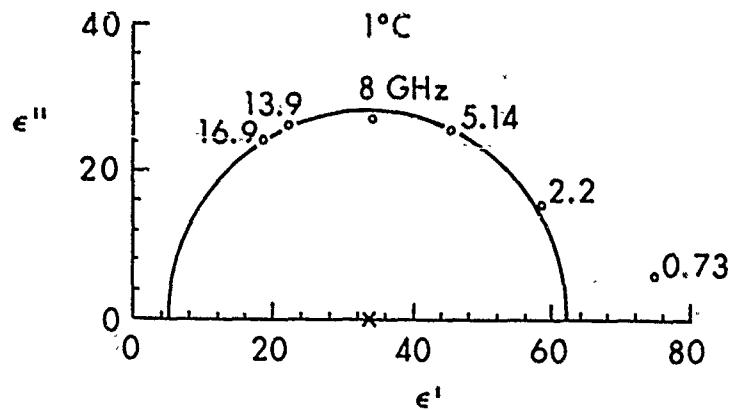
Figure 4.3. Dielectric properties of barnacle muscle in the microwave frequency range are presented in the complex dielectric constant plane (Foster et al., 1980).

ϵ' and $\epsilon'' = \sigma/\omega\epsilon_o$ are the components of the complex dielectric constant $\epsilon_r^* = \epsilon' - j\epsilon''$. The frequency at the peak of the circle is the characteristic frequency of the dispersion and identical with that of normal water, demonstrating the identity of tissue water in normal water from a dielectric point of view.

Protein Solutions--The dielectric properties of proteins and nucleic acids have been extensively reviewed (Takashima, 1969; Takashima and Minikata, 1975). Protein solutions exhibit three major dispersion ranges. One occurs at RF's and is believed to arise from molecular rotation in the applied electric field. Typical characteristic frequencies range from about 1 to 10 MHz, depending on the protein size. Dipole moments are of the order of 200-500 Debyes, and low-frequency increments of dielectric permittivity vary between 1 and 10 units/g protein per 100 ml of solution. The high-frequency dielectric permittivity of this dispersion is lower than that of water because of the low dielectric permittivity of the protein, leading to a high-frequency decrement of the order of 1 unit/g protein per 100 ml. This RF dispersion is quite noticeable in pure protein solutions, but it contributes only slightly to the large β-dispersion found in tissues and cell suspensions.

At microwave frequencies the dielectric properties of tissues are dominated by the water relaxation centered near 20 GHz. The magnitude of this water dispersion in tissues is typically diminished by some 20 dielectric units, due to the proteins which displace a corresponding volume of water.

Between these two readily noticeable dispersions is a small one, termed the δ-dispersion by Grant. It was first noted for hemoglobin (Schwan, 1965b) and then carefully examined for hemoglobin (Pennock and Schwan, 1969) and albumin (Grant et al., 1968). This dispersion is characterized by a fairly broad spectrum of characteristic frequencies extending from some hundred to some thousand megahertz. Its magnitude is considerably smaller than that of the other two dispersions, and it is thought to be caused by a corresponding dispersion of protein-bound water and/or partial rotation of polar subgroups.

Grant (1979) and Schwan (1977b) pointed out that the conductivity of protein-bound water is higher than that of water and electrolytes in the frequency range from ~500 to ~2000 MHz. Grant has suggested that this might establish a local interaction mechanism of some biological significance.

Dielectric saturation for proteins can be predicted from the Langevin equation and occurs in the range of 10 to 100 kV/cm. Indeed, onset of saturation has been experimentally observed in PBLG (poly-γ-benzyl-L-glutamate) at 50 kV/cm (Jones et al., 1969), which is in good agreement with the Langevin estimate. Any irreversible changes in protein structure that accompany its rotational responses to an electrical field are unlikely to occur at field levels smaller than required for complete orientation, i.e., dielectric saturation. The thermal energy kT (where k is the Boltzmann constant, and T the absolute temperature) is in this case greater than the product μE (where μ is the dipole moment, and E the field strength), representing the change in potential energy that occurs with rotation. Thus changes in protein structure caused by nonsaturating electric fields would probably occur spontaneously in the absence of any exciting field at normal temperatures.

Illinger (1977) has discussed the possibilities of vibrational and torsional substructural effects at microwave or millimeter-wave frequencies. A calculation of internal vibrations in an alanine dipeptide in water, using a molecular dynamics approach, has been presented by Rossky and Karplus (1979). In this model the lowest frequency internal oscillations that occur

(dihedral angle torsions at 1500 GHz) are strongly damped; large proteins might exhibit lower frequency internal vibrations. We would expect any macromolecular vibration that displaces surrounding water to be overdamped by the water medium, which is quite lossy at frequencies below 100 GHz; however, a detailed analysis of the response of such a resonator surrounded by a lossy medium has not yet been applied to this case. Illinger has not discussed the field strengths required to saturate submolecular vibrational transitions, but the Langevin equation predicts that saturation for smaller polar units requires higher field-strength values (Froehlich, 1949). Thus we would expect that biologically critical field strengths are, for the various modes suggested by Illinger, probably well above the levels required by the Langevin equation for the complete rotational orientation of the total molecules.

In summary, the dielectric properties of proteins and biopolymers have been investigated extensively. For the rotational process, the field saturation levels are rather high; perhaps even higher for internal vibrational and torsional responses. For nonlinear RF responses due to counterion movement and chemical relaxation, the levels are unknown but probably also high. In all these processes, reversible polarizations occur in competition with large thermal energies, and irreversible changes are not expected at field-strength levels of the order of a few volts per centimeter.

Membranes--Membranes are responsible for the dielectric properties of tissues and cell suspensions at RF's, as demonstrated by studies involving cell suspensions. Yeast, blood, bacteria, pleuropneumonia-like organisms, vesicles, and cellular organelles have been extensively investigated by many investigators, including Fricke (1923), Cole (1972), and Schwan (1957). This work has led to a detailed understanding of the role of cell membranes in the polarization processes of biological media in the RF range. (The relatively simple geometrical shapes of cells in suspensions facilitated this understanding.) The principal mechanism for dielectric polarization at RF's and below is the accumulation of charges at membranes from extra- and intracellular fluids. For spherical particles, the following expressions were derived (Schwan, 1957):

$$\epsilon_s - \epsilon_\infty = \frac{9}{4\epsilon_r} \frac{\rho R C_m}{\left[1 + R G_m \left(\rho_i + \frac{1}{2}\rho_a\right)\right]^2} \rightarrow \frac{9}{4\epsilon_r} \rho R C_m \qquad (4.2)$$

$$\sigma_s = \sigma_a \left[1 - 1.5\,\rho\, \frac{1 + R G_m\left(\rho_i - \rho_a\right)}{1 + R G_m\left(\rho_i + \frac{1}{2}\rho_a\right)}\right] \rightarrow \sigma_a(1 - 1.5\,\rho) \qquad (4.3)$$

$$\sigma_\infty \approx \sigma_a \left[1 + 3\,\rho\, \frac{\sigma_i - \sigma_a}{\sigma_i + 2\sigma_a}\right] \qquad (4.4)$$

for the limit values of the simple dispersion that characterizes the frequency dependence. The time constant is

$$\tau = \frac{R C_m}{2\,\dfrac{\sigma_a \sigma_i}{\sigma_i + 2\sigma_a} + R G_m} \rightarrow R C_m\left(\rho_i + 0.5\,\rho_a\right) \qquad (4.5)$$

In these equations, C_m and G_m are capacitance and conductance per square centimeter of the cell membrane; R is the cell radius; ρ is the cellular volume fraction, and $\sigma_i = 1/\rho_i$ and $\sigma_a = 1/\rho_a$ are the conductivities of the cell interior and suspending medium. The equations apply for small-volume fractions, ρ, and assume that the radius of the cell is very large compared with the membrane thickness. More elaborate closed-form expressions have been developed for cases when these assumptions are no longer valid (Schwan and Morowitz, 1962; Schwan et al., 1970), and an exact representation of the suspension dielectric properties as a sum of two dispersions is available (Pauly and Schwan, 1959). If, as is usually the case, the membrane conductance is sufficiently low, Equations 4.2-4.5 reduce to the simple forms to the right of the arrows.

$$\sigma_{\infty} - \sigma_s = \rho_i + \tfrac{1}{2}\rho_a$$

$$\epsilon_s - \epsilon_{\infty} = RC_m$$

$$\frac{\sigma - \sigma_s}{\omega\epsilon_0}$$

ϵ'' Increasing Frequency

ϵ'

ϵ_{∞} ϵ_s
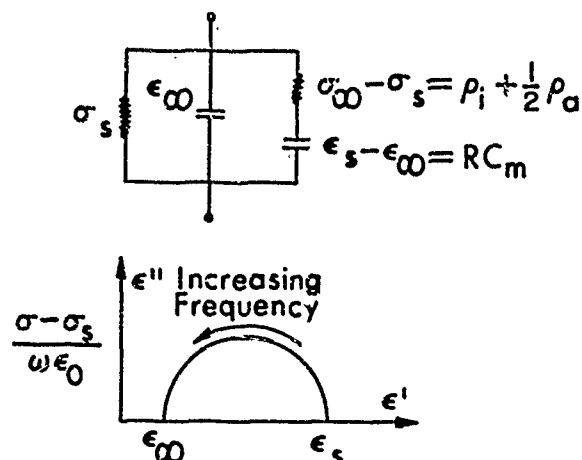
Figure 4.4. Equivalent circuit for the β-dispersion of a cell suspension and corresponding plot in the complex dielectric constant plane (Schwan and Foster, 1980).

A physical insight into Equations 4.2-4.5 is gained by considering the equivalent circuit shown in Figure 4.4, which displays the same frequency response defined in these equations. The membrane capacitance per unit area, C_m, appears in series with the access impedance, $\rho_i + \rho_a/2$, while the term σ_a (1-1.5 ρ) provides for the conductance of the shunting extracellular fluid. Hence, the time constant, τ, which determines the frequency where the impedances $1/\omega C_m R$ and $\left(\rho_i + \rho_a/2\right)$ are equal is given by Equation 4.5. Using typical values of σ_i, $\sigma_a \sim 0.01$ mho/cm, $C_m = 1$ μF/cm^2, R = 10 μm, and ρ = 0.5, with Equations 4.2-4.5 we see that the dispersion must occur at RF's and that its magnitude, $\epsilon_s - \epsilon_{\infty}$, is exceptionally high.

From experimental dispersion curves and hence values of the four quantities σ_s, σ_{∞}, $\left(\epsilon_s - \epsilon_{\infty}\right)$, and τ, the three quantities C_m, σ_i, and σ_a can be determined with an additional equation available to check for internal consistency. Values for extracellular and intracellular resistivities thus obtained agree well with independent measurements. Dispersions disappear as expected after destroying the cell membranes, and their characteristic frequencies are readily shifted to higher or lower frequencies as intracellular or extracellular ionic strengths are experimentally changed. This gives confidence in the model, whose validity is now generally accepted.

This work led to the important conclusion that the capacitance of all biological membranes, including cellular membranes and those of subcellular organelles such as mitochondria, is of the order of 1 $\mu F/cm^2$. This value is apparently independent of frequency in the total RF range; at low audio frequencies, capacitance values increase with decreasing frequencies due to additional relaxation mechanisms in or near the membranes. These mechanisms will not be discussed here and have been summarized elsewhere (Schwan, 1957; Schwan, 1965a).

From the membrane capacitance, we can estimate values for the transmembrane potentials induced by microwave fields. At frequencies well above the characteristic frequency (a few MHz), the membrane-capacitance impedance becomes very small by comparison with the cell-access impedance $\left(\rho_i + \rho_a/2\right)$, and the membrane behaves electrically like a short circuit. Since intracellular and extracellular conductivities are comparable, the average current density through the tissue is comparable to that in the membrane. For an in situ field of 1 V/cm (induced by an external microwave-field flux of about 10 mW/cm^2), the current density, i, through the membrane is about 10 mA/cm^2 since typical resistivities of tissues are of the order of 100 Ω-cm at microwave frequencies. Thus the evoked membrane potential, $\Delta V = i/j\omega C_m$, is about 0.5 μV at 3 GHz and diminishes with increasing frequency. This value is 1000 times lower than potentials recognized as being biologically significant. Action potentials can be triggered by potentials of about 10 mV across the membrane, but (dc) transmembrane potentials somewhat below 1 mV have been recognized as being important (Schmitt et al., 1976).

If $f \ll f_c$, the total potential difference applied across the cell is developed across the membrane capacitance. In this limit, the induced membrane potential, ΔV, across a spherical cell is $\Delta V = 1.5$ ER, where E represents the applied external field. Thus the cell samples the external-field strength over its dimensions and delivers this integrated voltage to the membranes, which is a few millivolts at these low frequencies for cells larger than 10 μm and external fields of about 1 V/cm. These transmembrane potentials can be biologically significant.

4.1.2. Membrane Interactions

Table 4.4 summarizes information relevant to electrical fields and their effects on biological membranes. Low-frequency alternating fields of the order of some hundred millivolts across the membrane can destroy it, as later described. The propagation of action potentials along nerves is initiated or interfered with by pulses or low-frequency potentials of roughly 10 mV across the membrane. Corresponding current densities and field-strength values in tissues and the medium external to the affected cell are of the order of 1 mA/cm^2 and 1 V/cm (Schwan, 1972; National Academy of Sciences, 1977; Schwan, 1971).

TABLE 4.4. ELECTRICAL-FIELD EFFECTS ON MEMBRANES

Summary of various field effects on membranes (some established, some proposed). ΔV_M is the field-induced membrane potential; E, corresponding field strength in situ. E and ΔV_M are interrelated by ΔV_M = 1.5 ER (for spherical cells).

	ΔV_m	E, in situ
Membrane destruction	100–300 mV	
Action potential (excitation)	10 mV	1 V/cm
Subtle effects	0.1–1 mV	
Extraordinary sensitivities		
A. Related to membranes	0.1 μV	0.01 μV/cm
B. Possibly not related to membranes	< 1 nV	0.1 μV/cm
Microwave sensitivities (1 GHz)	1 μV[*]	1 V/cm

---

[*] From ΔV_M = 1.5 ER

In recent years, some extraordinary sensitivities have been reported. Electrosensitive species, such as rays and sharks, detect fields of intensities as low as 0.1 µV/cm. To achieve these sensitivities, they sample the field over considerable distances with the aid of special organs, the Ampullae Lorenzini, and operate over a small frequency range extending from dc to only a few hertz (National Academy of Sciences, 1977; Kalmijn, 196<). Some reports also indicate effects, due to ELF fields of the order of volts per centimeter in air, on timing responses and calcium efflux (Bawin and Adey, 1976; Gavalas-Medici and Day-Magdaleno, 1976). Corresponding in situ fields would be of the order of 0.1 µV/cm, as listed in Table 4.4, and corresponding fields across membranes below 1 nV. It is, however, not yet obvious if the reported effects are caused by membrane processes; hence the reduction of external fields to in situ fields and then membrane potentials is not necessarily sensible. A more detailed discussion of this topic is given by Schwan (1971) and Bawin and Adey (1976) and the detailed report of the National Academy of Sciences-National Research Council on the biological effects of electric and magnetic fields (1977).

Microwave sensitivities of the order of 1 V/cm in situ have been frequently reported and correspond to external flux values of the order of 1 to 10 mW/cm^2. (See, for example, the recent text by Baranski and Czerski, (1976).) Some suspect that these sensitivities correspond to direct interactions with the central nervous system. However, it is straightforward to translate in situ field levels to corresponding membrane potentials; and these are at levels of the order of 1 µV or less, depending on microwave frequency, as discussed by Schwan (1971). The implications of these calculations have been challenged (Baranski and Czerski, 1976; Frey, 1971) by the argument that we do not yet know how the brain processes information. But Schwan finds it difficult to see how this rather general and no doubt valid statement pertains to his calculation of microwave-induced membrane potentials. At microwave frequencies, field-strength levels in membranes and in situ field levels are comparable within 1 order of magnitude. This must be so because in situ currents readily pass the membranes and enter the cell interior as well as the interior of subcellular organisms; moreover, dielectric constants of membranes (about 10) and cellular fluids (about 60 or less, depending on frequency) are

similar in magnitude (Schwan, 1957). The membrane potential is, therefore, simply the product of in situ field strength and membrane thickness of about 10^{-6} cm. This simple argument does not depend on any particular model.

Although the microwave-induced membrane potential of about 1 µV is comparable to and even higher than the perception level across the end-epithelium of the Ampullae of Lorenzini, the high sensitivity of this end-organ is achieved only over a narrow bandpath range of some hertz. If microwave sensitivities existed over such narrow bandpath ranges, they would be hardly noticeable experimentally.

Also, the sensitivities of excitable cells to electric fields decrease rapidly as the electric stimulus is applied for time periods decreasingly short in comparison to the refractory period of the order of 1 ms. Hence quotation of reported low-frequency membrane sensitivities, as done by Frey (1971), carries no implication with regard to sensitivities claimed at microwave frequencies that correspond to time periods of the order of 1 ns, which is a million times smaller than the refractory period. More recently, Bawin and Adey (1977) have postulated that microwave fields may well be perceived if they are modulated with frequencies below 10 or 20 Hz. This would be possible in principle if induced in situ fields and if currents could be rectified with some degree of efficiency so that microwave fields would generate detectable low-frequency currents. No evidence for such a mechanism has been demonstrated so far at the membrane level.

In Table 4.5 available evidence on the threshold of biological excitation phenomena is summarized for various fields. In cardiology extended experience exists with pacemakers, and threshold values range about 0.1-10 mA/cm^2, depending on electrode size and other parameters (Roy et al., 1976). In electrohypnosis, electrosleep, and electrical anesthesia, total currents applied are about 10-100 mA. Corresponding current densities in the brain may be estimated based on the work by Driscoll (1970). For a total 1-mA current applied to the head, internal brain current densities are of the order of 10 $\mu A/cm^2$ (Driscoll, 1970). Hence 10-100 mA of total current correspond to brain-tissue current densities of 0.1-1 mA/cm^2. Very extended work has been carried out on electrical hazards caused by low-frequency potentials applied

TABLE 4.5. BIOLOGICAL THRESHOLDS

Current density thresholds noticed in various disciplines.

Cardiology	$0.03\text{-}10 \text{ mA/cm}^2$
Electrosleep and electrical anesthesia	$10\text{-}100 \text{ mA}$
Electrohazards:	
Sensation	1 mA
"Let Go"	10 mA
Fibrillation	100 mA
Biophysics and axonology	1 mA/cm^2
$\Delta V_M = 1.5 \text{ ER}$	$(10 \ \mu m, \ 1 \text{ mV})$
$\Delta V_M = R \cdot J \ \left(\text{mA/cm}^2\right)$	

to the human body (Schwan, 1972). The values quoted in Table 4.5 as thresholds for sensation, "let go," and fibrillation are all consistent with a current density of about 1 mA/cm^2. Thus membrane potentials in the millivolt range are consistent with the experience gained with pacenakers, effects on brain tissue, and electrical hazards.

4.1.3. Field-Generated Force Effects

Electric fields can directly interact with matter and create forces that can act on molecules as well as on cellular and larger structures. Most of these interactions are reversible and do not necessarily have demonstrable biological effects. An example is the movement of ions in an ac field, which is inconsequential if the field is weak enough to prevent undue heating from molecular collisions (e.g., below about 1 V/cm, corresponding to 1 mA/cm^2 in a physiological medium). Another example is the orientation of polar macromolecules. For field-strength values of interest here, only a very partial, preferential orientation with the field results. Complete orientation and consequent dielectric saturation requires field strengths of thousands of

volts per centimeter. (Changes of this magnitude do occur in membranes on depolarization, hence field-induced orientation and changes in orientation of membrane molecules appear possible. Corresponding tissue current densities would be in milliamperes per square centimeter.)

Electric fields can interact just as well with nonpolar cells and organelles in the absence of any net charge. These "ponderomotive" forces are well known and understood. Any system exposed to an electric field will tend to minimize its electric potential energy by appropriate rearrangement. This statement is equally true for dc and ac fields because the potential energy is a function of the square of the field strength. Inasmuch as the induced-dipole moment of a cell or large particle depends on both the square of field strength and the volume, it is not surprising that the threshold field to overcome thermal agitation is proportional to $R^{-1.5}$, where R is the effective radius of the particle. Experimental evidence confirms the principle: threshold-field values for responses of 10-μm cells are about 10 V/cm; but for 10-nm macromolecules, the fields are about 10 kV/cm--comparable with the fields needed for complete orientation--due to the existence of a typical dipole moment of about 10 or 100 Debyes.

Table 4.6 summarizes observed manifestations of field-generated forces. The field effects may manifest themselves as an orientation of particles in the direction of the field or perpendicular to it, or "pearl chain" formation (i.e., the alignment of particles in the field direction) may occur. This has long been considered a mysterious demonstration of microwave-induced biological effects. Cells can be deformed or destroyed with fields. In inhomogeneous electrical fields, the movement of cells can be affected.

TABLE 4.6. MECHANISMS CAUSED BY FIELD-GENERATED FORCES

Orientation

"Pearl chain" formation

Deformation

Movement

Destruction

- 4.18 -

Zimmerman et al. (1974) have observed the destruction of red cells and ghost formation. Neumann and Rosenheck (1972) studied the effects of fields on chromaffin vesicles. Friend et al. (1974) as well as Goodman et al. (1975, 1976) studied the effects of fields on fairly large cellular organisms. Orientation effects have been observed by Teixeirra-Pinto et al. (1960), Sher (1963), and Novak and Bentrup (1973). Pohl (1973) developed "dielectrophoresis" as a tool of separating cells in inhomogeneous fields, and Elul (1967) observed cell-destruction phenomena and cell-shape changes. No attempt is made here to summarize the total literature on this topic, and additional discussions have been presented elsewhere (Bawin and Adey, 1977; Schwan, 1977a). Some of these field-generated force effects can be very startling and dramatic, especially near the tip of small electrodes. Of a similar nature is the movement of magnetotactic bacteria, reported by Blakemore (1975), in magnetic fields of fairly low intensity. Apparently these bacteria are equipped with magnetic properties and are therefore significantly oriented by the magnetic field and motivated to move in the field direction.

Experimental and theoretical evidence indicates that pulsed fields cannot have greater effects than continuous fields of the same average power (Sher et al., 1970). Modulation is therefore not expected to have special effects.

Field forces due to the induced-dipole moment of the field have been listed as evidence of nonthermal action of electric fields on biologic systems. The effects, however, require fairly large field strengths, frequently above those that give rise to heating or stimulation of excitable tissues. The field forces also depend on the electric properties of the particle considered and its environment.

Sher (1968) has given a more detailed derivation of the dielectrophoretic force in lossy dielectric media, based in turn on a derivation of the potential electric energy of a lossy dielectric body given by Schwarz (1963).

All sorts of biological particles of different effective complex dielectric constants behave similarly in an electrolyte medium. Figure 4.5 illustrates this fact. Neumann and Rosenheck's (1972) results on chromaffin vesicles are combined with Sher's data (1963) on E. coli, erythrocytes, and silicon particles (full circles). The total material fits convincingly the solid

line of slope -1.5 which is demanded by the theoretical requirement that particle volume must be inversely related to the square of the threshold-field strength mentioned here and discussed in greater detail elsewhere (Schwan and Sher, 1969).
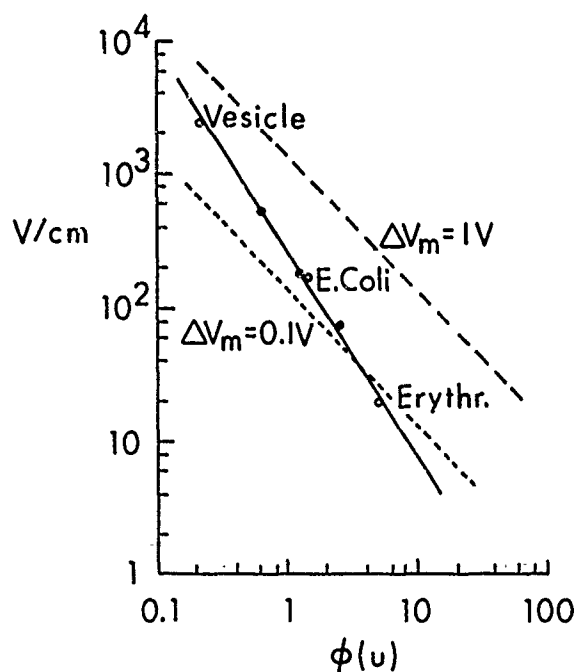
Figure 4.5. Threshold field-strength values as a
function of particle size (Schwan, 1977a).

(————) Field-generated force effects; (————) damage resulting from membrane breakdown at the quoted membrane potentials of 0.1 and 1 V; (O) results obtained with biological cells; and (●) data with silicone particles. The data fit the theoretical demand indicated by (————) and appear to be insensitive to the dielectric properties of the particles.

The dashed curves in Figure 4.5 pertain to another model. The threshold of a cellular response or destruction is assumed to be reached when the induced membrane potential reaches the dielectric breakthrough level. This level may be in the range of 0.1 to 1 V across the membrane, corresponding to

- 4.20 -

membrane field-strength levels from 100 kV/cm to 1,000,000 V/cm. The inverse relationship of the threshold-field level in the medium with the particle diameter follows from the equation $\Delta V_M = 1.5$ ER (Table 4.4). The dashed curves in Figure 4.5 establish threshold particle relationships somewhat similar to those resulting from a consideration of field-generated forces. Hence separating biological effects due to field-generated forces from those due to induced high membrane potentials may at times be difficult.

In general, available evidence and present understanding indicate that significant effects with field-evoked forces require field-strength values above 1 V/cm in the medium unless cellular dimensions are well above 100 μm.

4.1.4. Possibility of Weak Nonthermal Interactions

The considerations presented above do not suggest any weak nonthermal mechanism by which biological systems could react to low-intensity microwave fields. Fields of the order of a few kilovolts per centimeter are needed to orient long biopolymers, and probably still higher fields to excite internal vibrations or produce submolecular orientation. External fields acting on biopolymers must further overcome strong local fields, which are 1.5 kV/cm at a distance of 100 angstroms from a monovalent ion and 1.8 kV/cm at the same distance from a hemoglobin molecule. Microwave frequencies are well above those corresponding to significant rotational diffusion times, excluding orientational effects. Transmembrane potentials induced by typical nonthermal microwave fields are vanishingly small relative to potentials required for stimulation and compared with membrane noise. Field-induced force effects are unlikely to be significant on a single molecular or cellular level because the threshold field strengths necessary to overcome thermal disturbances are too high (Schwan, 1977a).

Some principles emerge, however, regarding possible mechanisms of weak microwave interaction, if such a concept exists. Field-force effects become more probable as the volume of the exposed particle increases (Schwan, 1977a). Transmembrane potentials become larger for a given in situ field strength as the cell size is increased. Finally, molecules can become signif- icantly reoriented by the field if $\mu E \gtrsim kT$ (where μ is the dipole moment, E is

the field strength, k is the Boltzman constant, and T is the absolute temperature); thus larger physical dimensions or larger permanent- or induced-dipole moments are more likely to respond to weak fields.

The large dimensions necessary for biological responses to weak microwave fields might be achieved by a cooperative reaction of a number of cells or macromolecules to the microwave stimulus, which increases the effective size of the structure and correspondingly reduces the threshold required for an effect. Bawin and Adey (1976) suggested that such cooperation might be induced in the counterions loosely bound near membrane surfaces which contain a loose framework of charged polysaccharides.

Froehlich (1973, 1975) suggested that giant dipole moments may be formed during enzyme substrate reactions and that the corresponding dielectric absorption processes might be highly resonant and nonlinear, and likely to channel energy into lower frequency modes of vibration. He also considered the membrane as a likely site of resonant electromagnetic (EM) interactions; and from the velocity of sound and the membrane thickness, he derived an estimate of the resonant frequencies to be of the order of 100 GHz. Acceleration and deceleration of a variety of biological reponses that suggest resonances in the millimeter frequency range have been reported by Webb and Booth (1971), by Devyatkov (1974), and more recently by Grundler et al. (1977). But some of these studies have been criticized on technical grounds, and the Russian work (only summarized in 1974) has not yet been published in detail. Gandhi et al. (1979) conducted continuous dielectric spectroscopy measurements at millimeter-wave frequencies with no indication of any resonance processes. Also, on a variety of cellular processes they found no effects of millimeter-wave radiation that were not attributable to sample heating. But the resonance phenomena reported by Grundler et al. and postulated by Froehlich may only involve a minor fraction of the total cellular entity and thus not demonstrate itself strongly enough to be observed in the bulk dielectric data.

4.2. MEASUREMENT TECHNIQUES

4.2.1. Introduction

Measurement of tissue dielectric properties is important because it provides information necessary for calculating RF power absorption by biological models and for constructing tissue-equivalent models. Experiments with tissue-equivalent models are useful in evaluating biological hazards as well as the EM heating patterns of devices used to produce hyperthermia. Also, many biophysical interaction mechanisms of EM fields with biological systems can be inferred from the characteristic behavior of tissue permittivity as a function of frequency.

For complete characterization of the dielectric properties of biological substances and to identify and characterize the various relaxation processes, the complex permittivity should be measured over a broad frequency band. The two principal broad-band measurement systems are frequency domain and time domain. In frequency-domain measurements, sweeping the frequency over the band of interest provides broad-band information; in time-domain measurements, broad-band information can be obtained from a single measurement of the pulse response of the material under test. Both methods require biological sample holders specially designed for evaluating the effect of parameters such as temperature and physiological factors on the measurements. Several measurement techniques are commonly used, each valid only in a specific frequency band. For example, at frequencies below 1 MHz--where all sample lengths, electrical paths, and connecting leads are short compared to a wavelength--a lumped-circuit approach is usually used. Typically a sample of the material under test is contained in a parallel plate or a coaxial capacitor.

Commercially available impedance-measuring bridges and vector voltmeters are used to determine the input impedance of the sample holder. This method can, in theory, be extended down to zero frequency; however, practical measurements on conductive biological solutions are difficult below 1 kHz because of electrode polarization effects. At frequencies above 10 MHz, on the other hand, measurements are less straightforward and the results are subject to greater error. In this frequency range, a distributed-circuit

approach rather than a lumped-circuit approach is required because the sample size is usually a considerable fraction of a wavelength. The sample is often placed in or at the end of a section of coaxial transmission line or waveguide or in a microwave cavity. Coaxial-cable methods are usually used in the frequency range from 50 MHz to 10 GHz. Between 10 GHz and 100 GHz, waveguides are often used; above 40 GHz, free-space quasi-optical techniques are usually used.

Instrumentation problems initially limited time-domain techniques to the lower frequency range. With the advent of sampling oscilloscopes and step-function generators with very short rise times, however, time-domain methods now provide valuable measurements in the frequency range from 10 MHz to 10 GHz. The 10-GHz limit is due to the rise time of the step-voltage excitation of typical time-domain reflectometers (TDRs).

The various time-domain and frequency-domain techniques are reviewed below and some typical examples of broad-band methods are given. Also, in vitro and in vivo results are compared.

4.2.2. Low-Frequency Techniques

Impedance bridges and series or parallel resonant circuits are usually used to measure dielectric properties below 100 MHz. The sample holder is usually either a parallel-plate or coaxial capacitor, with the test material forming the dielectric between its plates. Since biological materials are conductive (lossy), the input impedance of the capacitor is complex and is usually represented by an equivalent circuit consisting of a parallel connection of a resistance and a capacitance. A typical bridge circuit with the equivalent circuit of the sample holder is shown in Figure 4.6 (Von Hippel, 1954). The bridge is like a Wheatstone bridge, but impedances are measured instead of resistance. Balancing the bridge requires adjusting one or more of the impedances $(Z_1, Z_2, \text{ and } Z_3)$. If the complex permittivity of the material under test is given by

$$\varepsilon^* = \varepsilon_o(\varepsilon' - j\varepsilon'') \qquad (4.6)$$

- 4.24 -
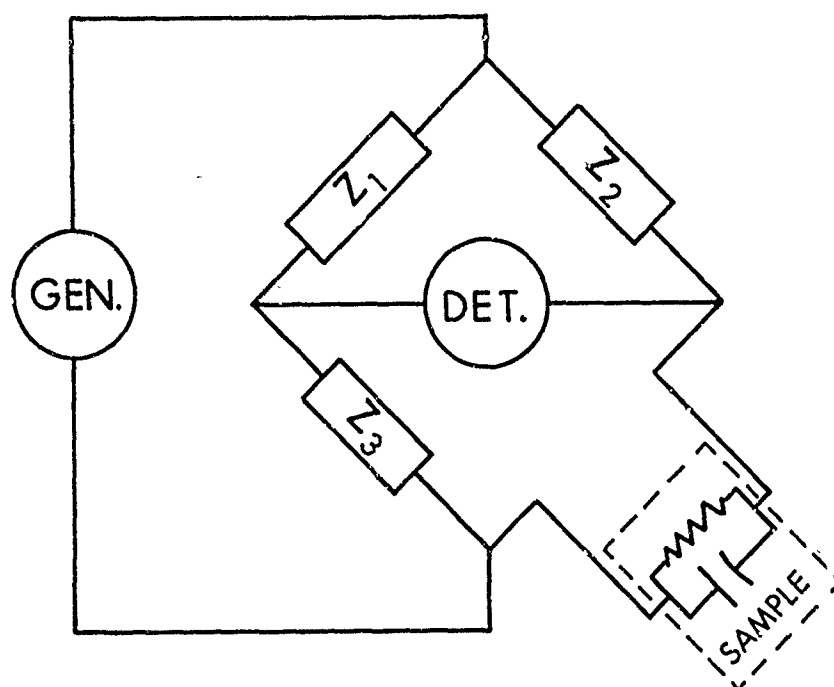
Figure 4.6. Bridge circuit for measuring dielectric proper-
ties of materials at frequencies below 100 MHz.

where ε_o is the permittivity of free space, the admittance Y of the capacitor
is given by $Y = j\omega C$. For a lossy capacitor filled with the dielectric mate-
rial under test,

$$Y = j\omega K\varepsilon_o (\varepsilon' - j\varepsilon'') \qquad (4.7)$$

where K is a constant dependent on the geometry of the sample holder. For
example, $K = A/d$ for an ideal parallel-plate capacitor, where A is the area
of the plates and d is the separation between the plates. The imaginary and
real parts of the admittance are hence given by

$$B = \omega K\varepsilon_o \varepsilon' \qquad (4.8)$$

$$G = \omega K\varepsilon_o \varepsilon'' \qquad (4.9)$$

The real part of the permittivity can thus be found from the imaginary part of the measured admittance, and the imaginary part of the permittivity can be found from the real part of the measured admittance. Although the capacitor sample holder seems easy to use, accuracy of measurements may be limited by a number of factors such as effects of the lead impedance (particularly at higher frequencies), effects of fringing fields at the edges of the electrodes, and electrode polarization effects.

Accuracy of bridge methods at frequencies above a few MHz is often limited by the self-inductance of the cell and its associated leads. Careful cell design and calibration to account for fringing capacitance and self-inductance are required to overcome this problem (Grant et al., 1978).

At lower frequencies, measurements are limited by electrode polarization, which is caused by the piling up of ions at the electrode-sample interfaces when direct or low-frequency current is passed through the measuring system. Measurement of dielectric properties of conductive materials is particularly restricted by electrode polarization, as is any measurement at frequencies where the signal period is long enough to permit ions to migrate over appreciable distances and accumulate at the electrode-dielectric interface. Large electrode separation would minimize this polarization but is undesirable because it increases the error due to stray fields.

Electrochemists have overcome electrode polarization problems by using four electrodes, two for applying the RF signal and two for picking up the potential difference within the material under test (Collett, 1959). Electrode-solution combinations that are nonpolarizing or only slightly polarizing are also used to minimize electrode polarization effects (Chang and Kaffe, 1952). These electrode-solution combinations are known as reversible electrode systems. An example of such a system is electrodes containing a layer of platinum black (Schwan, 1963b). The reversible electrodes reduce the polarization errors by providing a large effective area of electrode surface. This large area allows the migrating ions to spread out very thinly over the electrode surface so that the capacitance of the double layer, which is in series with the sample capacitance, is very large. This reduces measurement errors. Sandblasted platinum-black electrodes also minimize electrode polarization problems in biological applications. There is no known way

to completely eliminate polarization problems, however, and some analytical procedures to calibrate for electrode polarization effects should always be incorporated into low-frequency measurement techniques (Grant et al., 1978).

4.2.3. High-Frequency Techniques

A distributed-circuit instead of a lumped-circuit approach must be used at frequencies above 100 MHz because the sample size nears a considerable fraction of a wavelength for these frequencies. In distributed-circuit techniques, the sample is typically placed in or at the end of a section of transmission line or waveguide or in a microwave cavity. Since these transmission-line methods are broad-band, they are often preferred over the narrow-band cavity techniques.

In the transmission-line methods the complex reflection and/or transmission coefficients are measured instead of the sample impedance. In reflection methods, the sample holder is treated as a one-port network terminating a 50-ohm coaxial line. When transmission coefficients are measured, the sample typically fills the space between inner and outer conductors of a coaxial line with two low-dielectric beads confining the sample to the desired length. In the latest techniques, the scattering parameters (S-parameters) of the sample are measured with an automatic computer-based network analyzer such as the one shown in Figure 4.7 (Burdette et al., 1980; Iskander and DuBow, 1983). The key elements of the network analyzer system are a stable synthesizer, broad-band and high-ratio directional couplers, and a computer-controlled processor capable of making corrections in real-time measurements and calculating changes in permittivity from measured changes in reflection and/or transmission coefficients. The coaxial sample holder is connected to the S-parameter device, which has two outputs. One output is proportional to the incident signal and is connected to the reference channel of the network analyzer. The other output provides a signal either reflected by the sample or transmitted through the sample. This output is connected to the test channel of the network analyzer. The analyzer, using a calibrated superhetrodyne receiver, provides a measurement of the reflection and transmission coefficients by comparing the amplitudes and phases of the reflected and transmitted waves,
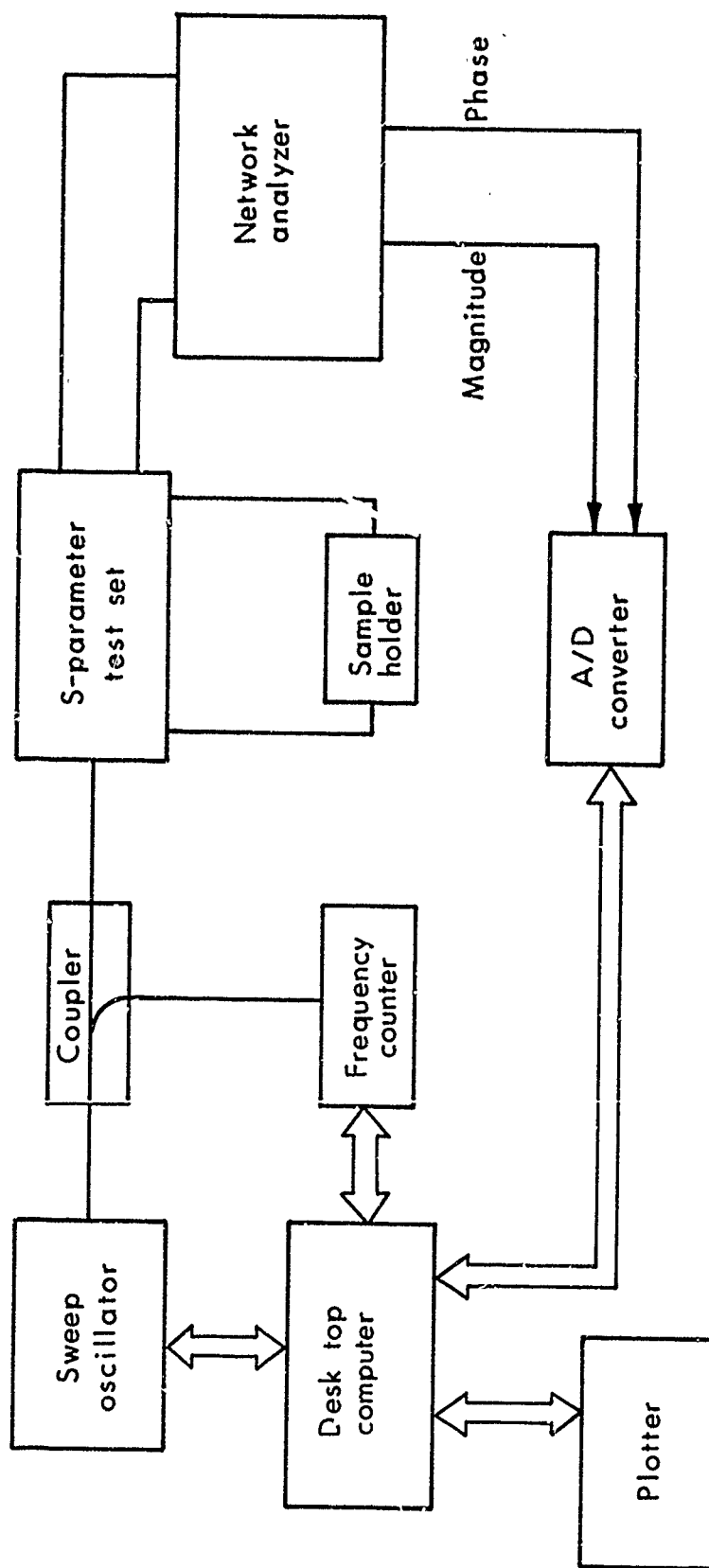
Figure 4.7. Experimental setup for measuring S-parameters, using an automatic network analyzer.

respectively, with those of the incident wave. With the reflection (S_{11}) and transmission (S_{12}) parameters measured, the real and imaginary parts of the complex permittivity $\varepsilon^* = \varepsilon_o(\varepsilon' - j\varepsilon'')$ can be determined from

$$\varepsilon' = \frac{1}{\omega\varepsilon_o} \ \text{Im} \left(\frac{1 - \hat{\Gamma}}{1 + \hat{\Gamma}}\right) \frac{1}{L} \ \ln \frac{1}{P} \qquad (4.10)$$

$$\varepsilon'' = \frac{1}{\omega\varepsilon_o} \ \text{Re} \left(\frac{1 - \hat{\Gamma}}{1 + \hat{\Gamma}}\right) \frac{1}{L} \ \ln \frac{1}{P} \qquad (4.11)$$

where Im means imaginary part; Re, real part; $\hat{\Gamma}$, the complex reflection coefficient assuming the sample to be of infinite length; and P, the propagation factor. $\hat{\Gamma}$ and P are given in terms of the S-parameters by

$$\hat{\Gamma} = x \pm \sqrt{x^2 - 1} \qquad (4.12)$$

where

$$x = \frac{S_{11}^2 - S_{12}^2 + 1}{2S_{11}} \qquad (4.13)$$

and

$$P = e^{\gamma L} = \frac{S_{11} + S_{12} - \hat{\Gamma}}{1 - (S_{12} + S_{11})\hat{\Gamma}} \qquad (4.14)$$

where γ is the propagation constant and L is the length of the sample under test. This measurement procedure provides enough information to obtain the complex permeability of the sample as well as the complex permittivity. To avoid resonance effects in these measurements, the sample length should be limited to less than a quarter of a wavelength at the highest frequency of operation. Typical sample holders suitable for these measurements at microwave frequencies are shown in Figure 4.8. For the lumped-capacitor holder in

Figure 4.8b, only measurement of the reflection coefficient is required; and the calculations are made as described in the following section.
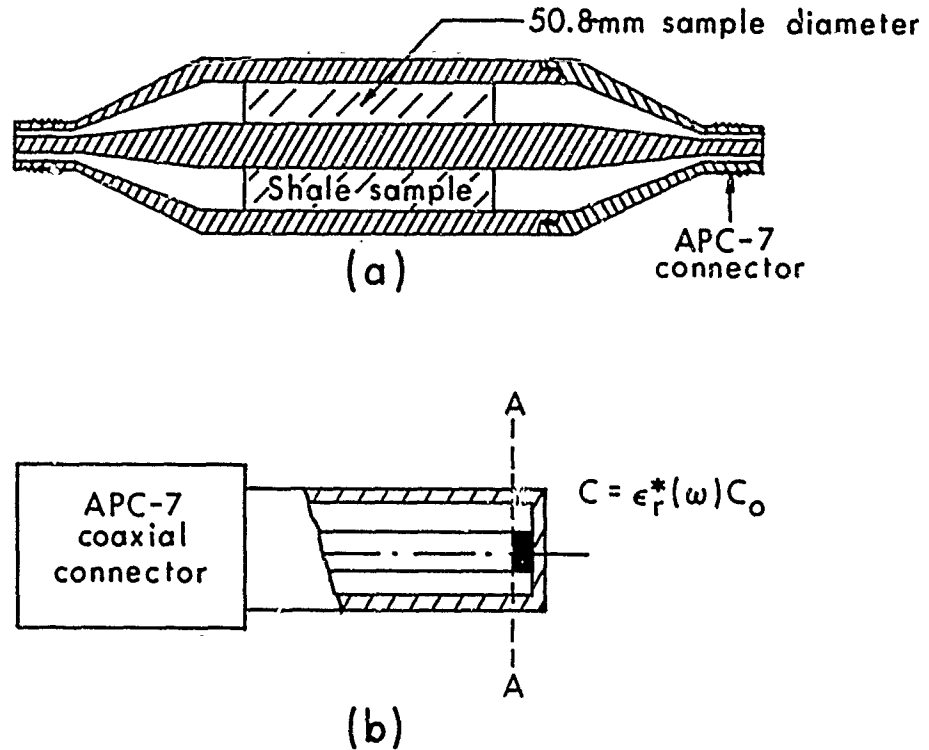
Figure 4.8. Typical sample holders for measuring the dielectric properties of biological substances at microwave frequencies. (a) Coaxial sample holder. (b) Lumped capacitor terminating a section of a coaxial transmission line.

4.2.4. Time-Domain Measurements

Measurements over the broad frequency range necessary to characterize dielectric properties can be very time consuming and tedious unless automated frequency-domain techniques are available, but such techniques are generally not practical because a single RF oscillator will not work over a sufficiently wide frequency range. Several RF oscillators are usually required, one for each range of frequencies. A single technique capable of covering the frequency band from 100 kHz to the higher microwave frequencies with acceptable

accuracy is therefore desirable. Time-domain techniques can provide such capabilities. Since their introduction in the late sixties, they have been widely used to measure dielectric properties of materials over broad frequency ranges. These techniques are also conceptually simple and experimentally straightforward, particularly when used in conjunction with modern data-acquisition systems. They are also less expensive than conventional frequency-domain microwave dielectric spectroscopic systems. Below 10 GHz, time-domain measurements can be made with about the same accuracy as swept-frequency measurements, which is generally less than that obtainable with single-frequency measurements. The strong decrease above 10 GHz in the spectral intensity of the exciting step-voltage generator in commercially available time-domain reflectometers limits their use to frequencies below 10 GHz.

In time-domain methods, the Fourier transform of the measured response of the dielectric sample to short-rise-time pulses is calculated. The dielectric properties over a wide frequency range can be obtained from this Fourier transform because the frequency spectrum of the short-rise-time pulses is very wide. The four essential parts of a time-domain system are a subnanosecond step-function generator, a broad-band sampling oscilloscope, a temperature-controlled sample holder, and a microcomputer for data processing. A typical time-domain reflectometer (TDR) system is shown in Figure 4.9 (Iskander and DuBow, 1983).

With this brief discussion of the relative merits of the frequency-domain and time-domain techniques as background, a specific example of a time-domain method used in our laboratory, called the lumped-element time-domain method (Iskander and Stuchly, 1977), is described next. Information about a system analogous to the automated microwave network-analyzer technique described in Section 4.2.3 is available in the literature (Nicholson and Ross, 1970). In the lumped-element time-domain method used in our laboratory, the sample holder is a small shunt capacitor terminating a section of coaxial transmission line. This sample bridges the gap between the low-frequency measurements, where lumped capacitors are often used, and the high-frequency measurements, where distributed elements such as a section of transmission line are used. The capacitor sample-holder consists of a cap screwed on the outer conductor of the coaxial line. The center conductor is made slightly
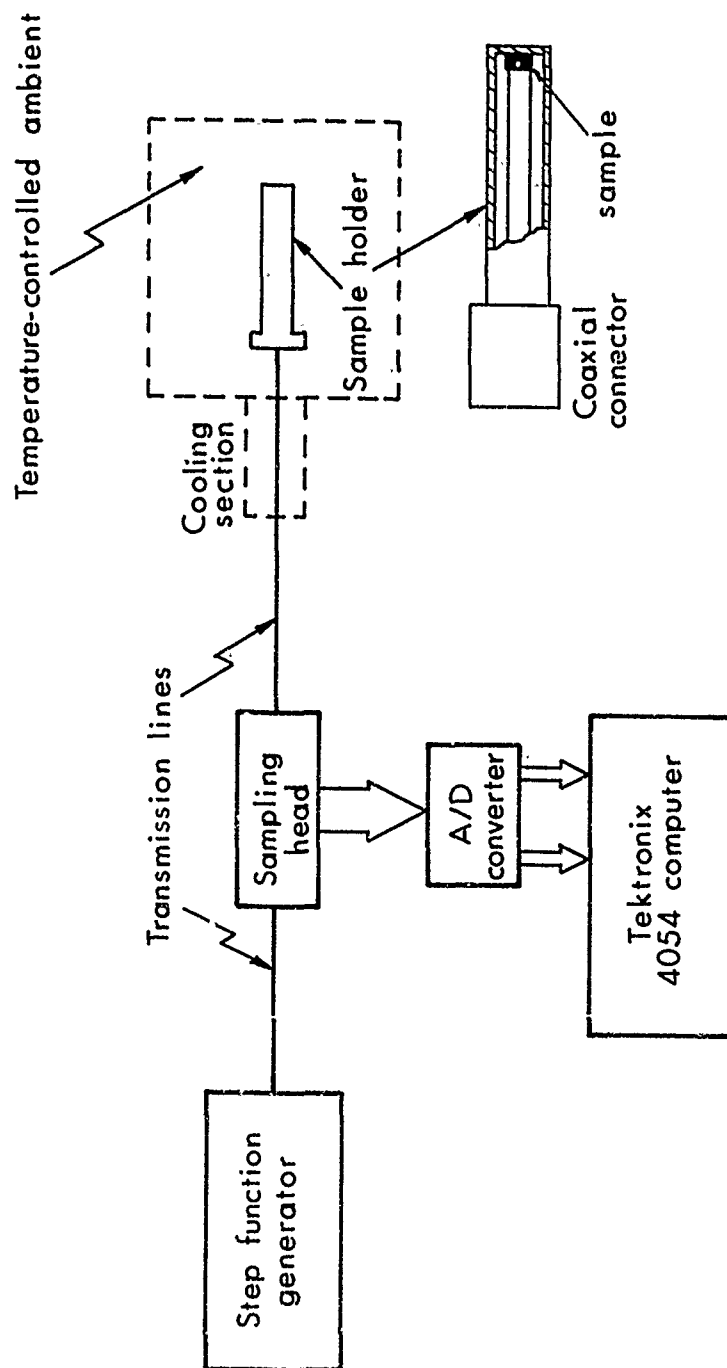
Figure 4.9. Typical experimental setup for time-domain measurement of complex permittivities.

shorter than the outer conductor to form a gap between the center conductor and the cap, which is the capacitor at the end of the transmission line. A schematic diagram of the sample holder is shown in Figure 4.8b.

The measurement procedure is to first replace the sample holder by a short circuit and obtain a reference signal, then to replace the sample holder and record the reflected signal at the sample interface. Both signals are digitized and their Fourier transforms calculated. The frequency dependence of the reflection coefficient is given by

$$\hat{\Gamma}(\omega) = \left|\hat{\Gamma}(\omega)\right| e^{j\theta(\omega)} = \frac{\mathcal{F}[V_r(t - t_o)]}{\mathcal{F}[V_{in}(t - t_o)]} = \frac{[V_o(t) - V_{in}(t - 2t_o)]}{- [V_{sc}(t - t_o)]} \quad (4.15)$$

where $\mathcal{F}$ represents the Fourier transform; V_{in} and V_r, the incident and reflected voltages respectively; V_{sc}, the reflected voltage when the sample holder is replaced by a short circuit; V_o, the total voltage signal recorded on the TDR screen; and t_o, the propagation time between the sampling probe and the sample holder. The real and imaginary parts of the relative permittivity are calculated from the complex reflection coefficient in Equation 4.15 using the following relations:

$$\varepsilon' = \frac{2\varepsilon_o \left|\hat{\Gamma}(\omega)\right| \sin \theta(\omega)}{\omega C_o Z_o [\left|\hat{\Gamma}(\omega)\right|^2 + 2\left|\hat{\Gamma}(\omega)\right| \cos \theta(\omega) + 1]} \quad (4.16)$$

$$\varepsilon'' = \frac{\varepsilon_o [1 - \left|\Gamma(\omega)\right|^2]}{\omega C_o Z_o [\left|\hat{\Gamma}(\omega)\right|^2 + 2\left|\hat{\Gamma}(\omega)\right| \cos \theta(\omega) + 1]} \quad (4.17)$$

where $\left|\hat{\Gamma}(\omega)\right|$ and $\theta(\omega)$ are, respectively, the magnitude and phase of the frequency-domain reflection coefficient, and C_o is the capacitance of the air-filled capacitor terminating the transmission line of characteristic impedance Z_o.

4.2.5. Measurement of In Vivo Dielectric Properties

Most measurements of the dielectric properties of tissue have been made on excised samples. Making measurements in vivo, though, would be better for two main reasons. First, preparing samples that fit the sample holder properly is difficult; and second, the condition of the tissue deteriorates rapidly after it is removed from the body. How dielectric properties of excised tissue compare with those of tissue in a living body is difficult to determine.

Two procedures for measuring the dielectric properties of tissue in vivo are described in this section. Both use an open-ended coaxial transmission line placed in or on the tissue. The first technique is simpler but works only for higher permittivity tissues. The second technique is more complicated but can be used to measure the dielectric properties of the lower permittivity tissue like fat and bone.

Measurement of High-Permittivity Tissues--Two probes are available for measuring the dielectric properties of tissue in vivo. Both consist of a section of coaxial transmission line (see Figure 4.10): one with the center conductor extended (Burdette et al., 1980), and one without (Athey et al., 1982). During the measurement, the center conductor is pressed against the material being tested.

The primary theoretical basis for the concept of the in vivo probe measurement is found in an antenna modeling theorem (Burdette et al., 1980) that applies to a short monopole antenna (antenna length much less than 0.1 wavelength). This theorem relates the impedance of a short antenna operating at frequency ω and radiating in the material under test, to the impedance at frequency $n\omega$ and radiating into free space. For nonmagnetic materials, the theorem states

$$\frac{Z\left(\omega, \varepsilon^*\right)}{n} = \frac{Z\left(n\omega, \varepsilon_o\right)}{n_o} \tag{4.18}$$

where

Z = antenna impedance

ϵ^* = complex permittivity of the material being measured

$\eta = \sqrt{\mu_o/\epsilon^*}$ = intrinsic impedance of the material being measured

$\eta_o = \sqrt{\mu_o/\epsilon_o}$ = intrinsic impedance of free space

$n = \sqrt{\epsilon^*/\epsilon_o}$ = index of refraction of the material being measured relative to free space

COAXIAL LINE TERMINATED WITH SAMPLE
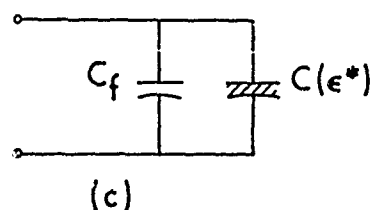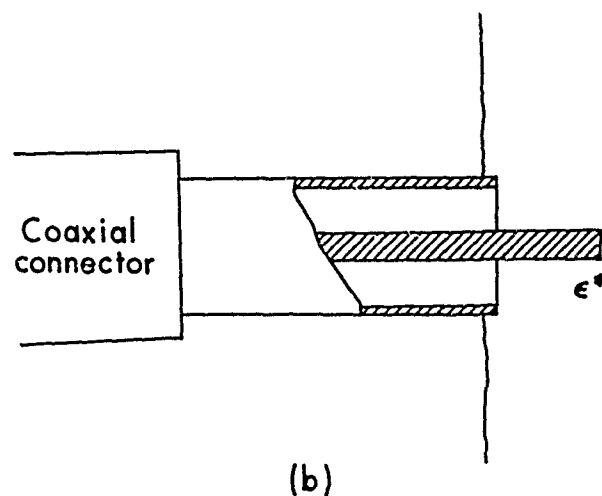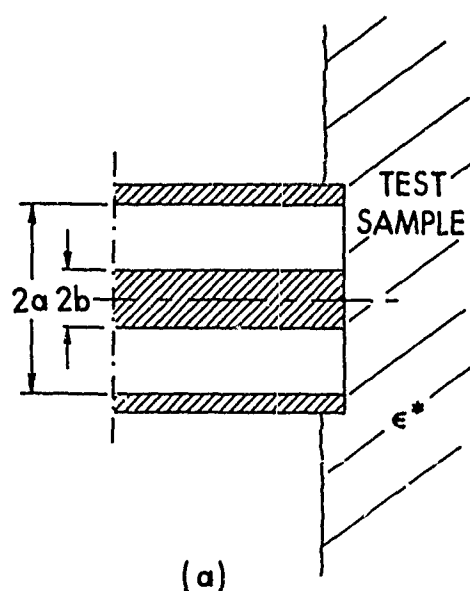
Figure 4.10. In vivo dielectric probes for measuring dielectric properties of biological substances. (a) Open-ended section of coaxial transmission line. (b) A short electric monopole immersed in the material under test. (c) The low-frequency (neglecting radiation resistance) equivalent circuits.

When a short monopole antenna is used as the probe, the probe impedance is given by

$$Z(n\omega, \epsilon_o) = A\omega^2 + \frac{1}{j\omega C} \qquad (4.19)$$

where A and C are constants determined by the probe's dimensions. This expression is valid when the probe length is less than 10% of the wavelength in the material being measured. Combining this expression with Equation 4.18 gives the following expressions for the resistance and reactance of the complex impedance $Z(\omega, \epsilon*) = R + jX$:

$$R = \frac{\sin 2\delta}{2\epsilon'\omega C} + A\sqrt{\epsilon'}\ \omega^2 \sqrt{\frac{\sec \delta + 1}{2}} \qquad (4.20)$$

$$X = \frac{\cos^2 \delta}{\epsilon'\omega C} + A\sqrt{\epsilon'}\ \omega^2 \sqrt{\frac{\sec \delta - 1}{2}} \qquad (4.21)$$

where tan δ is the loss tangent. In the above pair of equations all parameters except ϵ' and δ are known or can be determined from experimental measurements. Because simultaneous solution of these equations is difficult, an iterative method of solution is usually used. The second terms in Equations 4.20 and 4.21 are small at low frequencies. When these terms are neglected, the following equations result:

$$R = \frac{\sin 2\delta}{2\epsilon'\omega C} \qquad (4.22)$$

$$X = \frac{\cos^2 \delta}{\epsilon'\omega C} \qquad (4.23)$$

Solutions to these equations are obtained by dividing Equation 4.22 by 4.23 to get tan δ = R/X; therefore, by measuring the input impedance of a short monopole antenna inserted into a material, we can calculate both the relative dielectric constant, ϵ', and the conductivity, σ.

The other probe used for in vivo measurements of dielectric properties is a special type of the monopole antenna just described. An open coaxial line, placed in contact with a test sample, serves as a sensor. The equivalent circuit of the sensor consists of two elements (Figure 4.10): a lossy capacitor, $C(\varepsilon^*)$, and a capacitor, C_F, that accounts for the fringing field in the Teflon. $C(\varepsilon^*) = C_o\varepsilon^*$, where C_o is the capacitance when the line is in air. This equivalent circuit is valid only at frequencies for which the dimensions of the line are small compared to a wavelength, so the open end of the line does not radiate. At higher frequencies, increased evanescent TM modes excited at the junction discontinuity cause C_o to increase with frequency. When the evanescent modes are taken into account, C_o should be replaced by $C_o + Af^2$, where A is a constant dependent on the line dimensions.

Measurement of Low-Permittivity Tissues--The probes just described work well for measuring the permittivity when it is high but not when it is low, such as in fatty tissue. For low-permittivity tissues better accuracy is obtained by extending the length of the center conductor of the coaxial transmission-line probe further into the tissue (Olson and Iskander, 1986). The analysis described for high-permittivity measurement is not valid here. A procedure for this case was developed with the following new features:

a. A rigorous expression developed by Wu (1963) is used for the input impedance of the in vivo probe immersed in the material under test. The method of analysis, therefore, accounts for the radiation resistance of the probe for larger values of h/λ, where h is the length of the center-conductor extension, and λ is the wavelength.

b. Because the mathematical expressions for this case are very complex, the dielectric parameters of the sample under test are determined by comparing the measured and calculated values of the input impedance, using an iterative two-dimensional (error surface) complex zero-finding routine. This procedure is illustrated graphically in Figure 4.11 (Olson and Iskander, 1986).
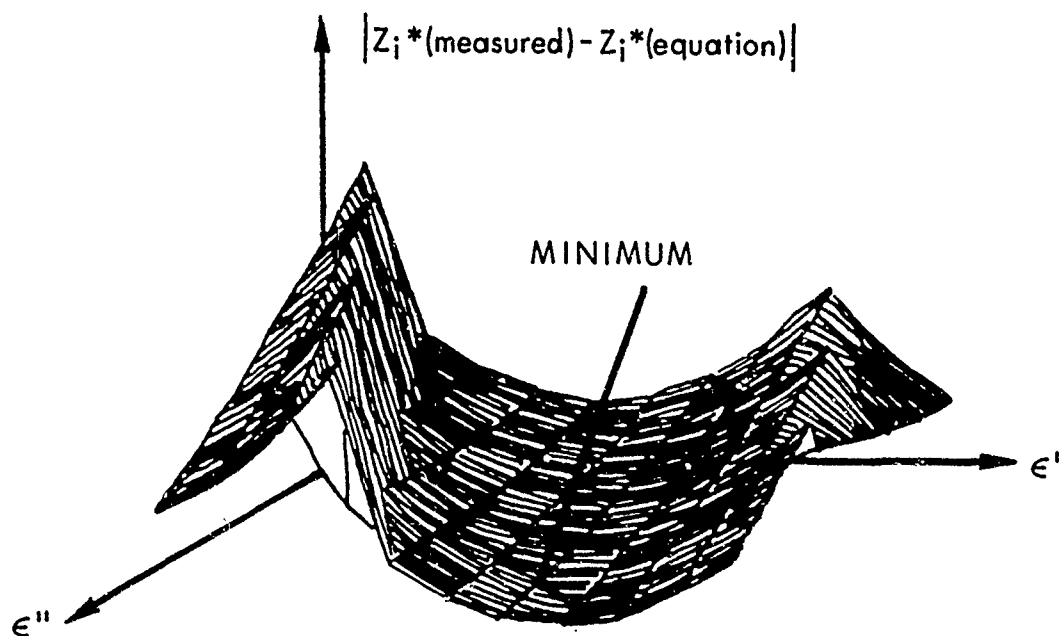
Figure 4.11. Graphical illustration of the iterative procedure for cal-
culating complex permittivity parameters by minimizing the
difference between measured and calculated values of the
input impedance of the in vivo dielectric probe. The
minimum on the error surface $|Z_{measured} - Z_{calculated}|$
indicates the most appropriate values of ϵ' and ϵ'' that
satisfy the measured value of the input impedance.

Except for these new features, the measurement procedure is like that
described in Section 4.2.3. As with all other in vivo probes, special effort
should be made to maintain good contact between the dielectric probe and the
material under test. For low permittivities, a ground plane of approximately
12-cm radius is needed to fine tune the measured values of the input imped-
ance. We evaluated the accuracy of the in vivo probe measurements for low-
permittivity materials by measuring the complex permittivity of known lossy
(octyl alcohol) and lossless (heptane) materials. The measured results were
all within less than ±5% of the measured values given in the literature.

4.2.6. Summary

At frequencies below 100 MHz, methods based on impedance bridges are satisfactory for measuring the permittivity of tissue samples. Above 250 MHz distributed-circuit methods must be used; with these, the sample holder is typically a section of transmission line or waveguide. The use of impedance-bridge techniques is bounded on the low-frequency end by electrode polarization; on the high-frequency end by the self-inductance of the cell and its leads.

Modern transmission-line techniques based on automatic network analyzers are remarkably accurate and relatively easy to use, for both in vitro and in vivo measurements. In all cases, however, the sensitivity of the measured permittivity to the experimental errors in the measured parameters should be analyzed to determine the advantages and limitations of a given method in a specified frequency band. Examples of such analyses are those developed for the time-domain measurements using the lumped capacitance method (Iskander and Stuchly, 1972). These calculations were later used with frequency-domain measurements using in vitro (Stuchly et al., 1974) and in vivo probes (Athey et al., 1982; Stuchly et al., 1982). Such uncertainty analyses lead not only to bounding the measurement errors but also to optimizing the parameters of the measuring cell, such as the value of the capacitance in the lumped-capacitance method (Iskander and DuBow, 1983). Uncertainty analyses should, therefore, be included in all measurement techniques, even when complicated expressions relating the measured parameters to the dielectric properties of the material under test are involved (Olson and Iskander, 1986).

4.3. TABULATED SUMMARY OF MEASURED VALUES

This section contains a summary of the measured values of dielectric properties of biological substances as a function of frequency and temperature, as reported in primary sources in the literature. Further information can be found in the listed references.

Tables 4.7 and 4.8 give the dielectric constant and conductivity values of different animal tissues, at indicated temperatures and frequencies. The temperature coefficient of the dielectric constant and conductivity of various body tissues are shown in Tables 4.9 and 4.10.

TABLE 4.7. REAL PART OF THE COMPLEX-DIELECTRIC CONSTANT (RELATIVE
PERMITTIVITY) OF VARIOUS BODY TISSUES
(Letters designate footnotes found at end of table)

Frequency (MHz)	Muscle	Heart Muscle	Liver	Lung*	Spleen
10^{-5}	2.5×10^6[s] $< 1 \times 10^7$[a]	$<7 \times 10^6$[a]	$<1.6 \times 10^7$[a]	$<8 \times 10^6$[a]	----
10^{-4}	8×10^5[a][s] 10^6	$(8-8.2) \times 10^5$[a]	$(8.5-9) \times 10^5$[a]	4.5×10^5[a]	----
10^{-3}	1.3×10^5[a][s] 1.7×10^5[f] 1.0×10^5	$(3-3.2) \times 10^5$[a]	1.5×10^4[a]	9×10^4[a]	----
10^{-2}	$(5-6) \times 10^4$[a][s] 9×10^4[f] 5×10^4	1×10^5[a]	$(5-6) \times 10^4$[a]	3×10^4[a]	----
10^{-1}	3×10^4[s] 2×10^4[f]	---	$7 \times 10^3 - 1.2 \times 10^4$[g]	---	----
1	2×10^3[f]	---	$1.2 \times 10^3 - 2 \times 10^3$[g]	---	----
10	179[ee]	---	320[ee]	---	----
25	103–115[t]	---	136–138[t]	---	>200[t]
50	85–97[t]	---	88–93[t]	---	135–140[t]
1×10^2	69–73[c] 71–76[m]	--- ---	65–75[k] 72–74[c] 76–79[m]	--- ---	88–90[c] 100–101[m]
2×10^2	56[t]	59–63[t]	50–56[t]	35[t]	---
3×10^2	55–57[y]	55–62[y]	48–56[y]	36[y]	---
4×10^2	52–54[t] 54–56[y]	52–56[t] 54–58[y]	44–51[t] 46–53[y]	35[t] 36[y]	---
6×10^2	55–56[y]	54–58[y]	46–53[y]	36[y]	---
7×10^2	52–53[t] 55–56[y]	50–55[t] 53–58[y]	42–51[t] 46–54[y]	34[t] 35[y]	---

Kidney	Brain	Fatty Tissue	Bone	Bone Marrow	Whole Blood	Skin
---	---	---	---	---	---	---
---	---	1.5×10^{5a}	---	---	---	---
---	---	5×10^{4a}	---	---	2.9×10^{3d}	---
---	---	2×10^{4a}	---	---	2.81×10^{3d}	---
1.2×10^{4ee}	3×10^{3ee}	---	---	---	2.74×10^{3d}	---
2.5×10^{3ee}	870^{ee}	---	---	---	2.04×10^{3d}	---
465^{ee}	240^{ee}	---	---	---	200^{d}	---
$>200^{t}$	$>160^{t}$	---	---	---	---	---
$119\text{-}132^{t}$	$110\text{-}114^{t}$	$11\text{-}13^{t}$	---	$6.8\text{-}7.7^{t}$	---	---
$83\text{-}84^{c}$ $87\text{-}92^{m}$	$70\text{-}75^{c}$ $81\text{-}83^{m}$	$8\text{-}13^{k}$ $11\text{-}13^{m}$	---	$6.8\text{-}7.7^{v}$	$72\text{-}74^{c}$ $73\text{-}76^{m}$	---
62^{t}	---	$4.5\text{-}7.5^{t}$	---	---	---	---
$57\text{-}60^{y}$	---	---	---	---	63^{y}	---
$53\text{-}55^{t}$ $55\text{-}57^{y}$	---	$4\text{-}7^{t}$	---	---	64^{y}	---
$54\text{-}56^{y}$	---	---	---	---	62^{y}	---
$50\text{-}53^{t}$ $53\text{-}56^{y}$	---	---	---	---	62^{y}	---

TABLE 4.7.   (continued)

Frequency (MHz)	Muscle	Heart Muscle	Liver	Lung*	Spleen
9×10^2	$53\text{--}55^y$	$53\text{--}57^y$	$44\text{--}52^y$	35^y	---
1×10^3	$49\text{--}52^n$ $53\text{--}55^o$ 61^p	$53\text{--}57^o$	$46\text{--}47^n$ $44\text{--}52^o$ 50^p	35°	---
1.77×10^3	---	---	---	---	---
1.78×10^3	51^x	---	---	---	---
2.98×10^3	51^x	---	---	---	---
2.99×10^3	---	---	---	---	---
3×10^3	$45\text{--}48^t$	---	$42\text{--}43^t$	---	---
3.59×10^3	48.25^x	---	---	---	---
4.63×10^3	47.33^x	---	---	---	---
8.5×10^3	$40\text{--}42^t$	---	$34\text{--}38^t$	---	---
9.39×10^3	---	---	---	---	---
9.43×10^3	---	---	---	---	---
1×10^4	$40\text{--}42^n$ 29^q 45^{cc}	---	$34\text{--}38^n$	---	---
2.362×10^4	---	---	---	---	---
2.377×10^4	---	---	---	---	---

Kidney	Brain	Fatty Tissue	Bone	Bone Marrow	Whole Blood	Skin
$53\text{-}56^y$	----	$3.2\text{-}6^y$	----	----	63^y	----
$53\text{-}56^o$	----	$4.3\text{-}7.5^n$ $3.2\text{-}6^o$ 9.5^p	8^n	$4.3\text{-}7.8^n$	$58\text{-}62^n$ 63°	----
----	----	----	----	----	59.2^z 56.8^{aa} 56.2^{bb}	----
----	----	9.7^x	8.4^x	----	----	45.6^x
----	----	8.43^x	8.35^x	----	----	44.5^x
----	----	----	----	----	59.9^z 57.7^{aa} 56.0^{bb}	----
----	32^{dd}	$3.9\text{-}7.2^t$	----	$4.2\text{-}5.8^t$	----	----
----	----	7.90^x	8.3^x	----	----	44.25^x
----	----	6.56^x	7.83^x	----	----	41.53^x
----	----	$3.5\text{-}4.5^t$	----	$4.4\text{-}5.4^t$	----	----
----	----	----	----	----	42.4^z 45.5^{aa} 47.8^{bb}	----
----	----	4.5^w	7.6^w	----	45^w	35.5^w
----	----	$3.5\text{-}3.9^n$ 3.6^q	8.0^n 6.6^q 5.7^{cc}	$4.4\text{-}6.6^n$ 5.8^q	$50\text{-}52^n$ 45^q 48^r	----
----	----	3.4^w	6.3^w	----	32^w	23^w
----	----	----	----	----	25.0^{aa} 30.2^{bb}	----

FOOTNOTES FOR TABLES 4.7 AND 4.8

* Partially or totally deflated, except material described in Footnote a (Schwan, 1956b).

[a] Dog, material in situ at body temperature (Schwan, 1956b, 1957, 1963a).

[b] Sheep, material at 18°C (Schwan, 1956b, 1963a).

[c] Beef and pork, excised material at 20°C (Schwan, 1956b, 1963a).

[d] Rabbit, at room temperature (Schwan, 1956b, 1963a).

[e] Rabbit, excised material at 37°C (Schwan, 1956b, 1963a).

[f] Rabbit, excised piece at room temperature (Schwan, 1956b, 1963a).

[g] Man and various animals, excised pieces and minced material at 23°C (Schwan, 1956b, 1963a).

[h] Sheep, 18°C (Schwan, 1956b, 1963a).

[i] Man, minced material at 23°C (Schwan, 1956b, 1963a).

[j] Rabbit, minced material at 23°C (Schwan, 1956b, 1963a).

[k] Man, minced material at 37°C (Schwan, 1956b, 1963a).

[l] Sheep, at 20°C (Schwan, 1956b, 1963a).

[m] Beef and pork, excised material at 37°C (Schwan, 1956b, 1957, 1963a).

[n] Dog and horse, blood and excised tissues measured at 38°C, except bone and bone marrow at 25°C (Schwan, 1956b, 1957, 1963a; Schwan and Piersol, 1954).

TABLE 4.8. CONDUCTIVITY (S/m) OF VARIOUS BODY TISSUES
(Letters designate footnotes for Tables 4.7 and 4.8)

Frequency (MHz)	Muscle	Heart Muscle	Liver	Lung*	Spleen
10^{-5}	0.104[a]	0.104[a]	0.082-0.119[a]	0.09[a]	---
10^{-4}	0.114[a]	0.108[a]	0.094-0.125[a]	0.091[a]	---
10^{-3}	0.121-0.125[a] 0.102[f]	0.118-0.133[a] 0.111-0.12[e]	0.103-0.13[a] 0.063-0.1[e] 0.077-0.143[g]	0.1-0.25[a] 0.053-0.071[e]	0.233-0.385[g] ---
10^{-2}	0.132[a] 0.114[f]	0.167[a]	0.118-0.146[a]	0.105[a]	---
10^{-1}	0.4-0.588[i] 0.192[f]	0.417-0.526[i]	0.217[a] 0.182-0.455[i] 0.125-0.182[g] 0.238[j]	0.5-0.606[i]	0.2-0.4[i]
1	0.476-0.625[i] 0.4[f]	0.435-0.556[i]	0.238-0.476[i] 0.182-0.25[g] 0.25[j]	0.357-0.667[i]	0.263-0.435[i]

- 4.44 -

o Man, excised piece at 27°C (Schwan, 1956b, 1963a).

P Beef, minced material at 22°C (Schwan, 1956b, 1963a).

q Man, excised piece at 37°C (Schwan, 1956b, 1963a).

r Man, excised material at 35°C (Schwan, 1956b, 1963a).

s Frog, excised piece at 25°C (Schwan, 1956b, 1963a).

t Various body tissues at 37°C (Schwan, 1957; Schwan and Piersol, 1954; Schwan and Li, 1953).

u Human tissues at 37°C (Rajewski, 1938).

v Animal tissues at 37°C (Rajewski, 1938).

w Human tissues, taken from surgical operations, at 37°C (England, 1950).

x Human tissues at 37°C (Cook, 1952).

y Human autopsy, material of normal composition at 27°C (Schwan and Li, 1953).

z Human blood containing average cells in concentration 4.9×10^6 per mm^3, at 15°C (Cook, 1951).

aa Human blood containing average cells in concentration 4.9×10^6 per mm^3, at 25°C (Cook, 1951).

bb Human blood containing average cells in concentration 4.9×10^6 per mm^3, at 35°C (Cook, 1951).

cc Biological material (Swicord et al., 1976).

dd Human brain at 37°C (Schwan, 1957).

ee Animal tissues at 37°C (Stoy et al., 1982).

Kidney	Brain	Fatty Tissue	Bone	Bone Marrow	Whole Blood	Skin
---	---	---	---	---	---	---
---	---	---	---	---	---	---
---	0.125-0.2[e] 0.182-0.222[g]	0.02-0.067[a]	---	---	0.602[b] 0.680[d] 0.741-0.833[e] 0.556-0.769[h]	---
---	---	---	---	---	0.680[d]	---
0.37-0.667[i]	0.118-0.217[i]	---	---	---	0.680[d]	---
0.4-0.714[i]	0.143-0.233[i]	---	---	---	0.714[d]	---

TABLE 4.8. (continued)

Frequency (MHz)	Muscle	Heart Muscle	Liver	Lung*	Spleen
10	$0.588-0.667^i$	$0.556-0.714^i$	$0.385-0.556^i$ 0.40^j	$0.667-0.909^i$	$0.588-0.667^i$
25	$0.47-0.99^{ee}$	---	$0.476-0.541^t$	---	0.93^{ee}
50	$0.68-0.885^t$	---	$0.513-0.578^t$	$0.222-0.385^t$	$0.662-0.781^t$
10^2	$0.769-1.0^k$ $0.625-0.833^i$ $0.5-0.714^c$ $0.667-0.833^m$ $0.85-1.04^u$ $0.68-0.85^v$	$0.588-0.769^i$ $0.78-0.92^u$	$0.69-0.833^k$ $0.5-0.667^i$ $0.476-0.556^c$ $0.556-0.667^m$ $0.63-0.87^u$ $0.56-0.65^v$	$0.769-1.053^k$ $0.714-1.0^i$ $0.7 \ldots 15^u$	$0.952-1.176^k$ $0.667-0.909^i$ 0.667^c 0.833^m $0.96-1.16^u$ $0.83-0.84^v$
2×10^2	$0.952-1.053^t$ $0.833-0.909^y$	$0.87-1.053^t$ $0.769-0.909^y$	$0.667-0.909^t$ $0.588-0.80^y$	0.625^t 0.526^y	---
3×10^2	$0.909-0.952^y$	$0.833-0.952^y$	$0.645-0.833^y$	0.613^y	---
4×10^2	$0.91-1.176^t$ $0.952-1.0^y$	$1-1.176^t$ $0.87-1.0^y$	$0.769-0.952^t$ $0.667-0.833^y$	0.714^t 0.613^y	--- ---
6×10^2	$1-1.064^y$	$0.87-1.053^y$	$0.714-0.909^y$	0.641^y	---
7×10^2	$1.266-1.37^t$ $1.075-1.49^y$	$1.053-1.282^t$ $0.909-1.082^y$	$0.87-1.176^t$ $0.769-1.0^y$	0.769^t 0.658^y	--- ---
9×10^2	$1.19-1.235^y$	$1-1.205^y$	$0.833-1.087^y$	0.73^y	---
10^3	$1.266-1.333^n$ $1.19-1.235^o$ 1.299^p	$1-1.205^o$	$0.943-1.02^n$ $1-1.087^o$ 1.0^p	0.730^o	---
1.77×10^3	---	---	---	---	---
1.78×10^3	2.245^x	---	---	---	---
2.98×10^3	2.984^x	---	---	---	---
2.99×10^3	---	---	---	---	---

	Kidney	Brain	Fatty Tissue	Bone	Bone Marrow	Whole Blood	Skin
	0.588-0.833[i]	0.222-0.333[i]	---	---	---	1.111[d]	---
	0.83[ee]	0.455[t]	---	---	---	---	---
	0.69-1.111[t]	0.476-0.526[t]	0.04-0.059[t]	---	0.02-0.036[t]	---	---
	0.833-1[k] 0.667-1.0[i] 0.625-0.769[c] 0.714-1.111[m] 0.85-1.0[u] 0.69-1.1[v]	0.435-0.625[k] 0.333-0.5[i] 0.385-0.455[c] 0.5-0.556[m] 0.45-0.625[u] 0.41-0.59[v]	0.08-0.085[k] 0.067[i] 0.023-0.045[c] 0.04-0.059[m] 0.083[u] 0.04-0.058[v]	---	0.019-0.024[c] 0.02-0.033[m] 0.02-0.035[v]	1.220[l] 0.667-0.833[c] 1-1.25[m] 1-1.25[v]	0.21-0.625[u]
	0.69[t] 0.962[y]	---	0.029-0.095[t] 0.02-0.067[y]	---	---	1.042[y]	---
	1.02[y]	---	---	---	---	1.11[y]	---
	1.176[t] 1.02[y]	---	0.036-0.111[t] 0.075-0.77[y]	---	---	1.099[y]	---
	1.064-1.11[y]	---	---	---	---	1.087[y]	---
	1.299-1.316[t] 1.11-1.12[y]	---	---	---	---	1.176[y]	---
	1.22-1.235[y]	---	0.029-0.091[y]	---	---	1.25[y]	---
	1.22-1.235[o]	---	0.071-0.143[n] 0.29-0.91[o] 0.04[p]	0.05[n]	0.043-0.1[n]	1.389-1.563[n] 1.250[o]	---
	---	---	---	---	---	1.753[z] 1.753[aa] 1.782[bb]	---
	---	---	0.270[x]	0.149[x]	---	---	1.926[x]
	---	---	0.341[x]	0.219[x]	---	---	2.244[x]
	---	---	---	---	---	3.310[z] 2.844[aa] 2.645[bb]	---

TABLE 4.8. (continued)

Frequency (MHz)	Muscle	Heart Muscle	Liver	Lung*	Spleen
3.0×10^3	2.174-2.336[t]	---	2.0-2.041[t]	---	---
3.59×10^3	3.186[x]	---	---	---	---
4.63×10^3	4.808[x]	---	---	---	---
8.5×10^3	8.333[t]	---	5.882-6.667[t]	---	---
9.39×10^3	---	---	---	---	---
9.43×10^3	---	---	---	---	---
1×10^4	8.333[n] 7.692[q] 8.0[cc]	---	5.882-6.667[n]	---	---
2.362×10^4	---	---	---	---	---
2.377×10^4	---	---	---	---	---

Kidney	Brain	Fatty Tissue	Bone	Bone Marrow	Whole Blood	Skin
---	3.0[dd]	0.111–0.227[t] 0.267[w]	---	0.116–C.225[t]	2.503[w]	2.754[w]
---	---	0.309[x]	0.258[x]	---	---	2.557[x]
---	---	0.381[x]	0.335[x]	---	---	3.606[x]
---	---	0.27–0.417[t]	---	0.167–0.476[t]	---	---
---	---	---	---	---	13.95[z] 12.02[aa] 10.29[bb]	---
---	---	0.498[w]	0.761[w]	---	12.066[w]	8.394[w]
---	---	0.27–0.417[n] 0.476[q] 0.57[cc]	0.667[n] 0.769[q]	0.5–1.667[n] 1.0[q]	9.091[n] 10.526[q] 10.753[r]	---
---	---	1.445[w]	1.445[w]	---	26.28[w]	17.082[w]
---	---	---	---	---	32.79[aa] 34.38[bb]	---

TABLE 4.9.   TEMPERATURE COEFFICIENT OF DIELECTRIC CONSTANT OF
VARIOUS BODY TISSUES $(100 \ (\Delta\varepsilon/\varepsilon)/°C)$ (Schwan, 1954)

Type of Tissue	Frequency (MHz)			
	50	200	400	900
Muscle	0.3	---	-0.2	-0.2
Liver	0.3	0.2	-0.2	-0.4
Spleen	1.0	---	---	---
Kidney	0.5	0.2	-0.2	-0.4
Brain	1.1	---	---	---
Blood	0.3	---	---	---
Serum and 0.9% saline	-0.4	-0.4	-0.4	-0.4
Fat	---	1.3	---	1.1

TABLE 4.10.   TEMPERATURE COEFFICIENT OF CONDUCTIVITY OF VARIOUS
BODY TISSUES $(100 \ (\Delta\sigma/\sigma)/°C)$ (Schwan, 1954)

Type of Tissue	Frequency (MHz)			
	50	200	400	900
Muscle	2.5	1.5	1.3	1.0
Liver	2.0	1.8	1.8	1.4
Spleen	2.3	---	---	---
Kidney	1.6	2.0	2.0	1.3
Brain	1.4	---	---	---
Blood	2.7	---	---	---
Serum and 0.9% saline	2.0	1.7	1.6	1.3
Fat	1.7-4.3	4.9	---	4.2

The complex permittivity is generally frequency dependent and at a frequency $f = \omega/2\pi$, can be described by the Debye equation, similar to Equation 4.1 (Schwan and Foster, 1980; Foster et al., 1980):

$$\varepsilon^* = \varepsilon' - j\varepsilon'' = \varepsilon_\infty - \frac{j\sigma_s}{\omega\varepsilon_o} + \sum_{i=1}^{n} \frac{\Delta i}{1 + j(\omega/\omega_i)} \qquad (4.24)$$

where

$$\varepsilon'' = \sigma/\omega\varepsilon_o$$

$$\varepsilon_\infty = \lim_{\omega \to \infty} \varepsilon'$$

$$\sigma_S = \lim_{\omega \to 0} \sigma$$

Δi = relative-permittivity change due to dispersion associated with ω_i

From Equation 4.24, we get

$$\varepsilon' = \varepsilon_\infty + \sum_{i=1}^{n} \frac{\Delta i}{1 + (\omega/\omega_i)^2} \qquad (4.25)$$

and

$$\sigma = \sigma + \omega^2 \varepsilon_o \sum_{i=1}^{n} \frac{\Delta i/\omega_i}{1 + (\omega/\omega_i)^2} \qquad (4.26)$$

Hurt (1985) has written a Fortran program that performs a least-squares fit of Equations 4.25 and 4.26 to permittivity data. Figures 4.12 and 4.13 are the curves for relative dielectric permittivity and conductivity, respectively, that result from fitting a 5-term Debye relation to muscle data (Tables 4.7 and 4.8). For muscle, ε_∞ is set equal to 4.3 (Grant et al., 1978; Hill, 1963).

The complex dielectric data in Tables 4.7-4.10 are from in vitro measurements of permittivity on excised human or animal tissues. Interest in reexamining tissue-permittivity values based on in vivo measurements has been increasing (Toler and Seals, 1977). With the in vivo procedure, a short monopole antenna is inserted into living tissue, and changes in the terminal impedance of the antenna are measured (Burdette et al., 1980). These impedance values can then be related to the complex permittivity of tissue.

$$\epsilon' = \frac{2340000}{1+(f/78)^2} + \frac{62100}{1+(f/76\times10^3)^2} + \frac{1970}{1+(f/2.6\times10^6)^2}$$

$$+ \frac{30.8}{1+(f/340\times10^6)^2} + \frac{41.3}{1+(f/23\times10^9)^2} + 4.3$$
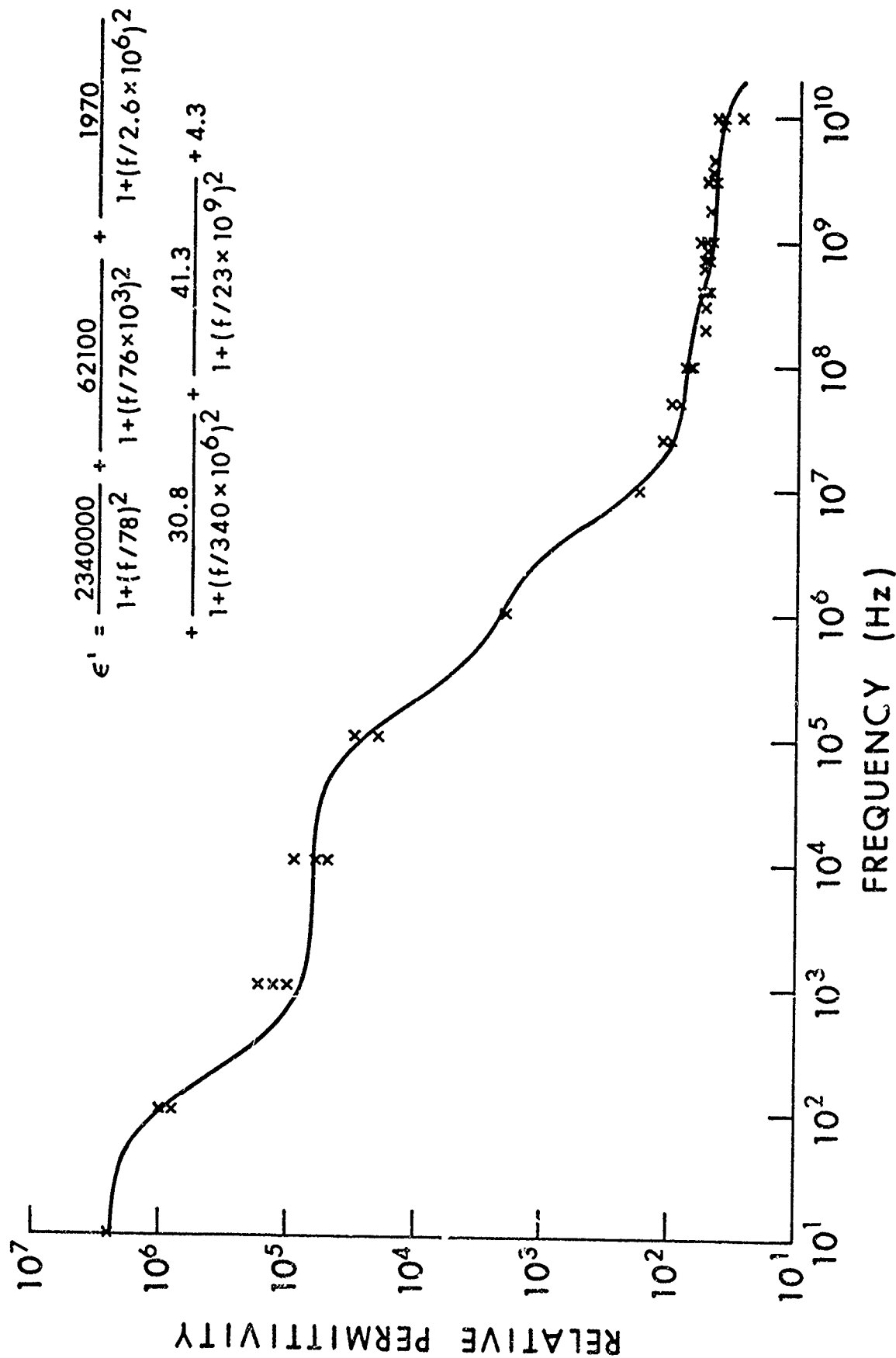
Figure 4.12. Relative dielectric permittivity for muscle (W. D. Hurt, private communication, USAF School of Aerospace Medicine, 1985).
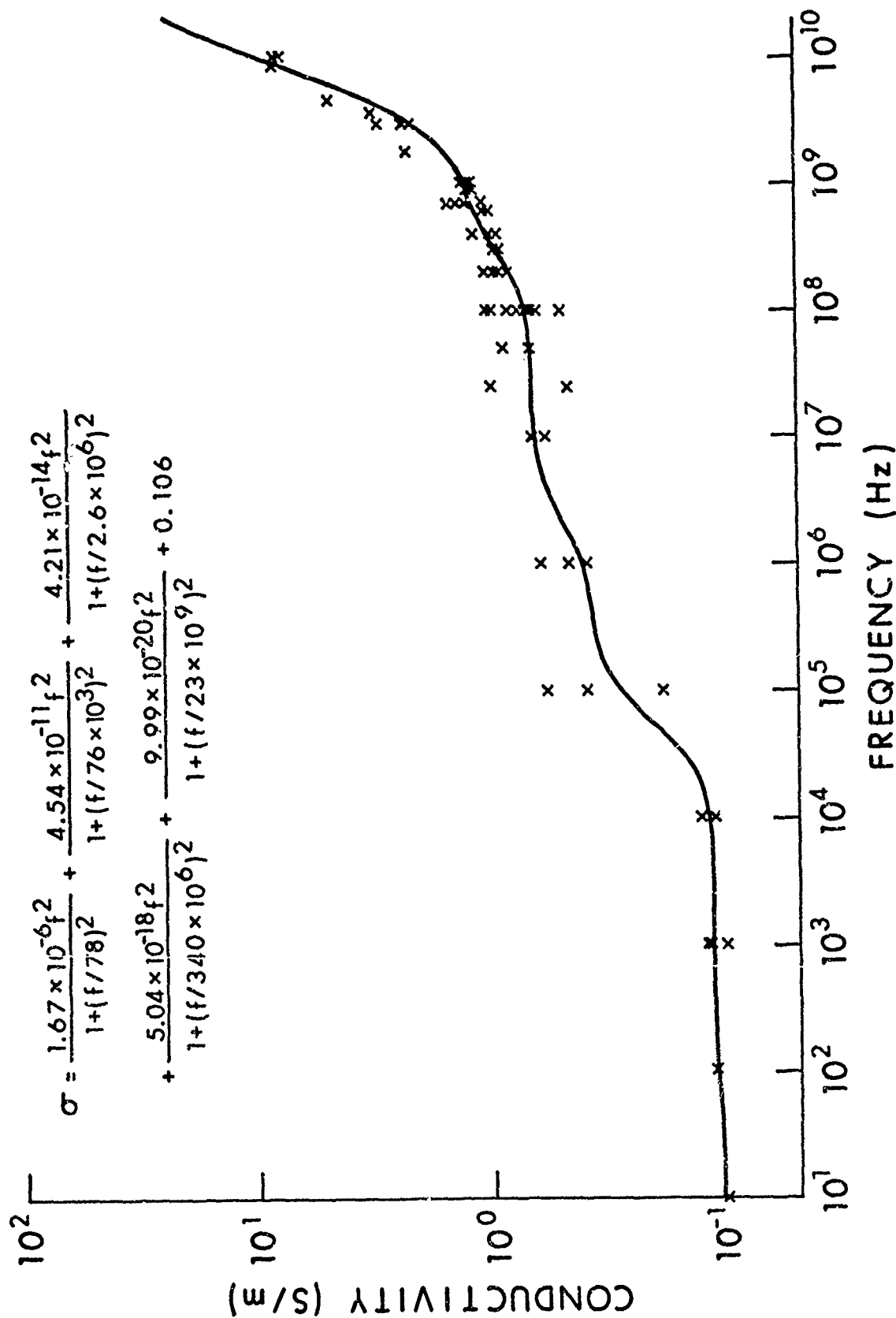
Figure 4.13. Conductivity for muscle (W. D. Hurt, private communication, USAF School of Aerospace Medicine, 1985).

The figure contains the equation:

$$\sigma = \frac{1.67 \times 10^{-6} f^2}{1+(f/78)^2} + \frac{4.54 \times 10^{-11} f^2}{1+(f/76 \times 10^3)^2} + \frac{4.21 \times 10^{-14} f^2}{1+(f/2.6 \times 10^6)^2}$$

$$+ \frac{5.04 \times 10^{-18} f^2}{1+(f/340 \times 10^6)^2} + \frac{9.99 \times 10^{-20} f^2}{1+(f/23 \times 10^9)^2} + 0.106$$

Figures 4.14-4.16 compare in vivo data for dielectric constants and conductivity with in vitro data; Figures 4.17-4.19 give additional in vivo data. These figures show only slight differences between the in vivo and in vitro values, except in the case of canine fat tissue (Figure 4.17) where the in vivo dielectric constant values are a factor of approximately 1.5-2 times the reported in vitro results above 100 MHz. These differences in the dielectric constant are attributed primarily to possible differences in water content between the in vivo and in vitro measurement conditions (Burdette et al., 1980). Conductivity values are also generally higher than in vitro values found in the literature (Schwan, 1957).
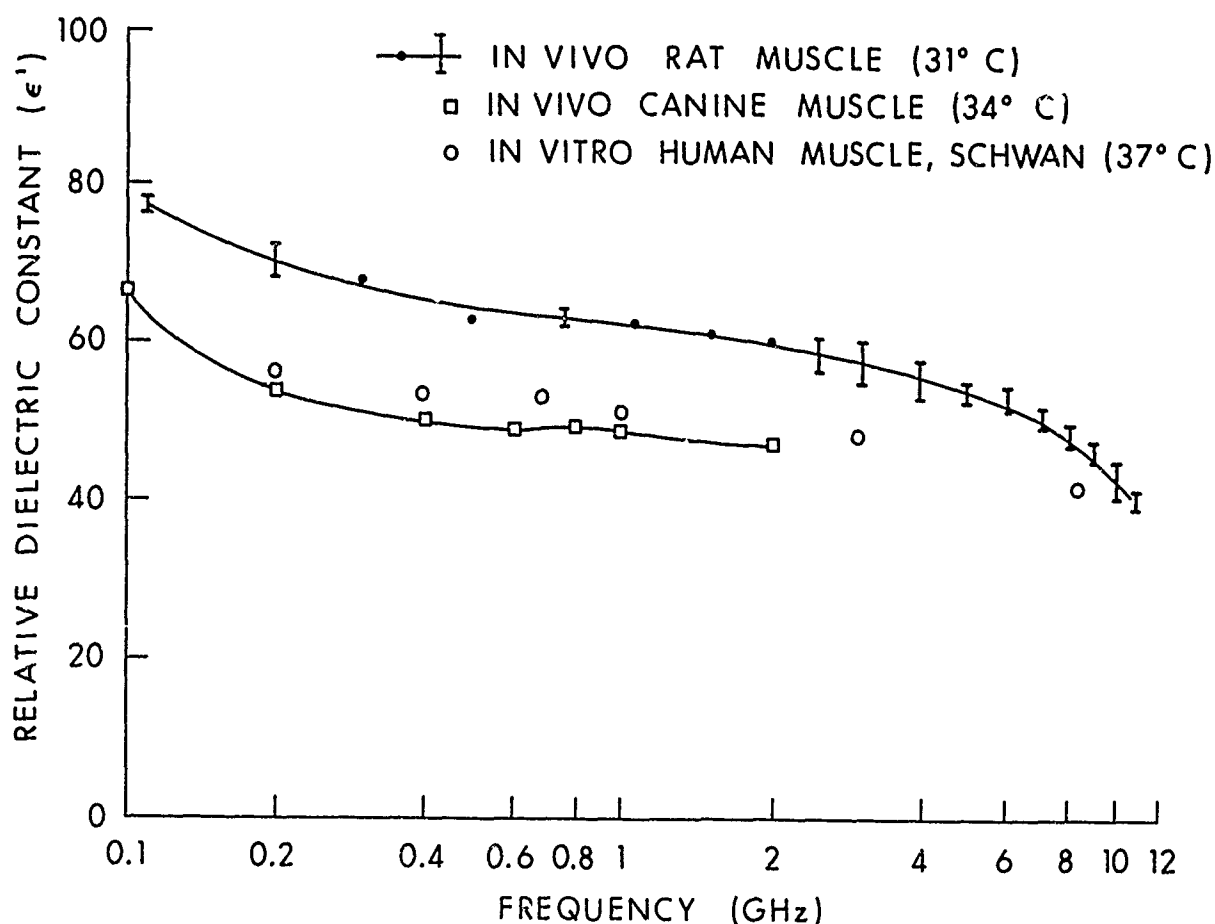
Figure 4.14. Measured values of relative dielectric constant of in vivo rat muscle and canine muscle (Burdette et al., 1980) compared to reference data (Schwan, 1975).
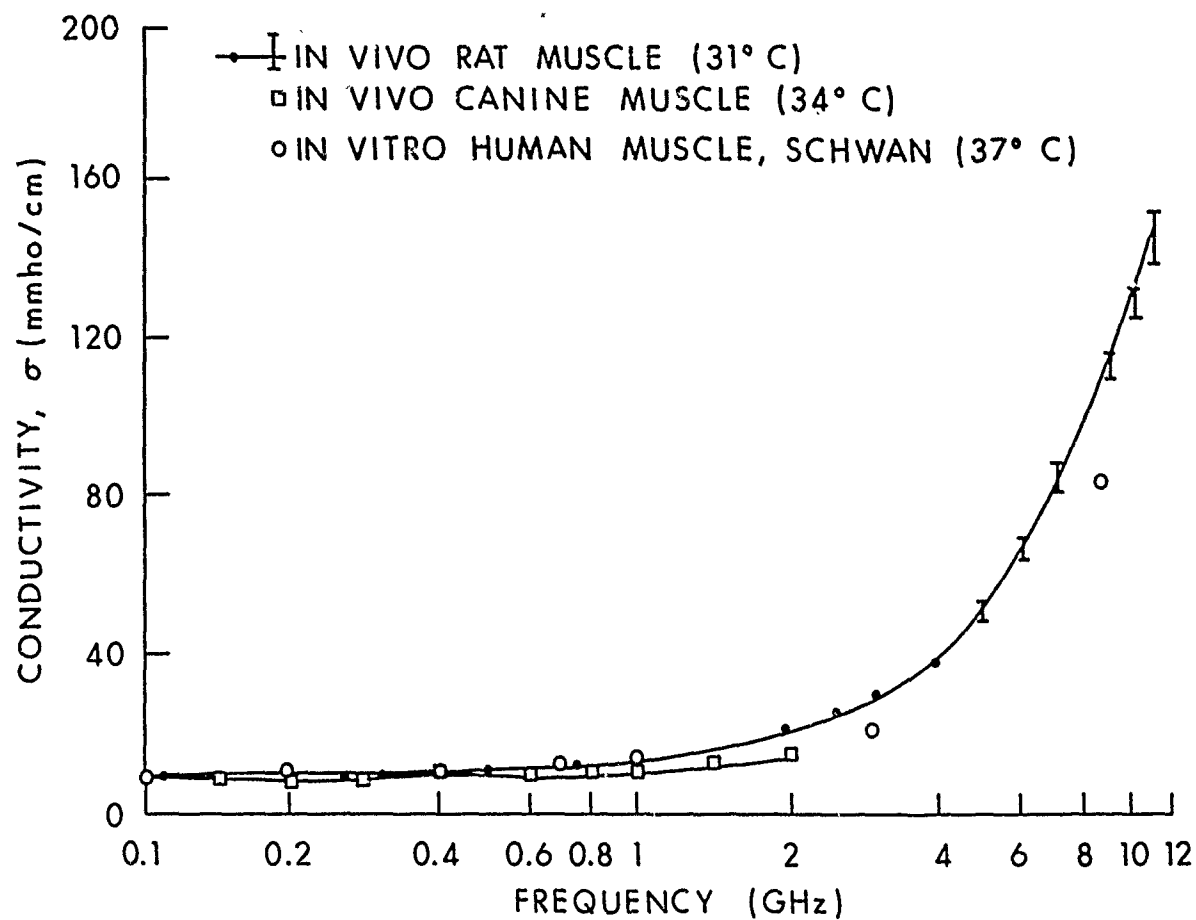
Figure 4.15. Measured values of conductivity of in vivo rat muscle and canine muscle (Burdette et al., 1980) compared to reference data (Schwan, 1957).
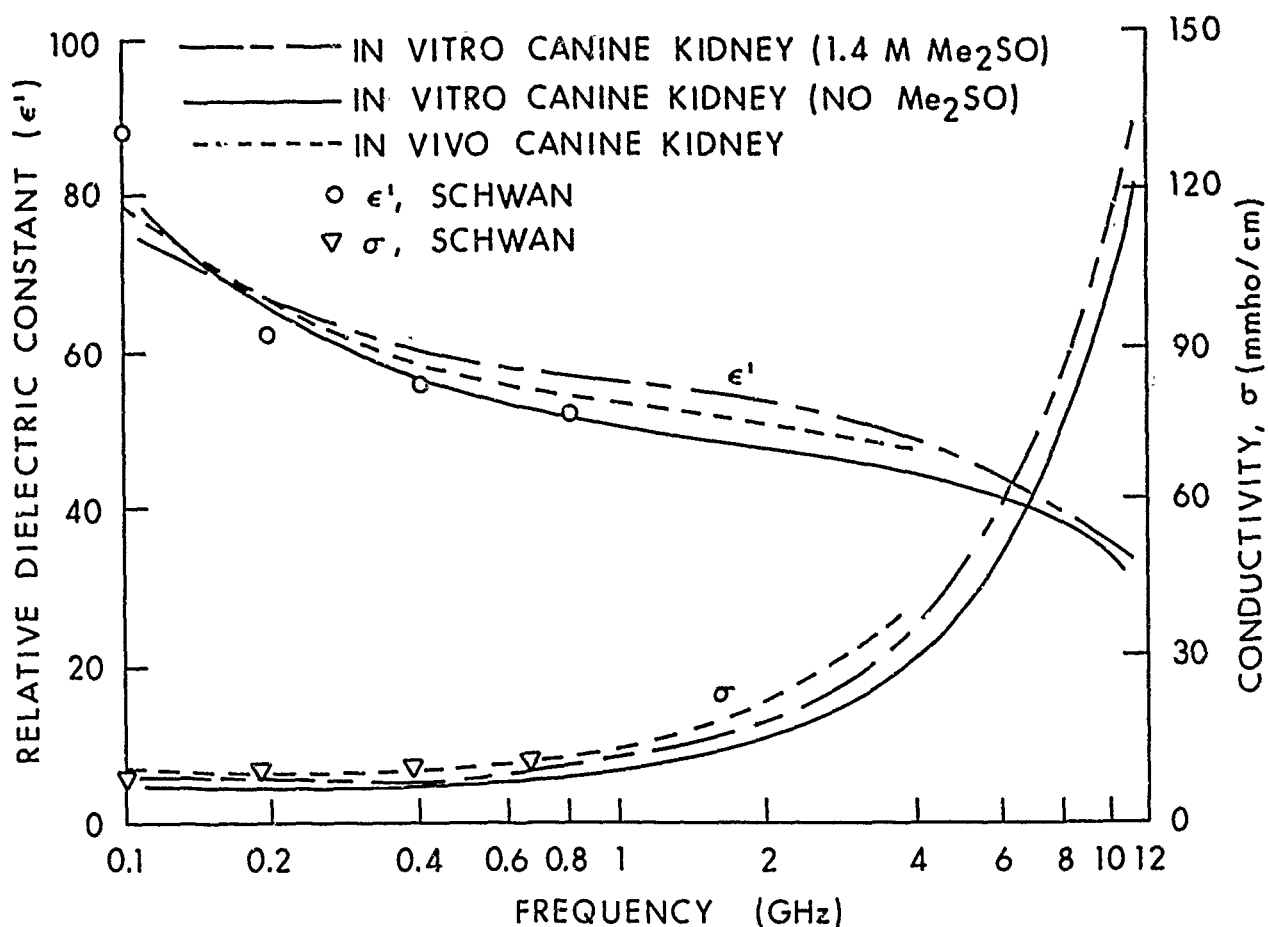
Figure 4.16. Measured values of relative dielectric constant and conductivity of in vivo and in vitro canine kidney cortex (Burdette et al., 1980) compared to reference data (Schwan, '957).
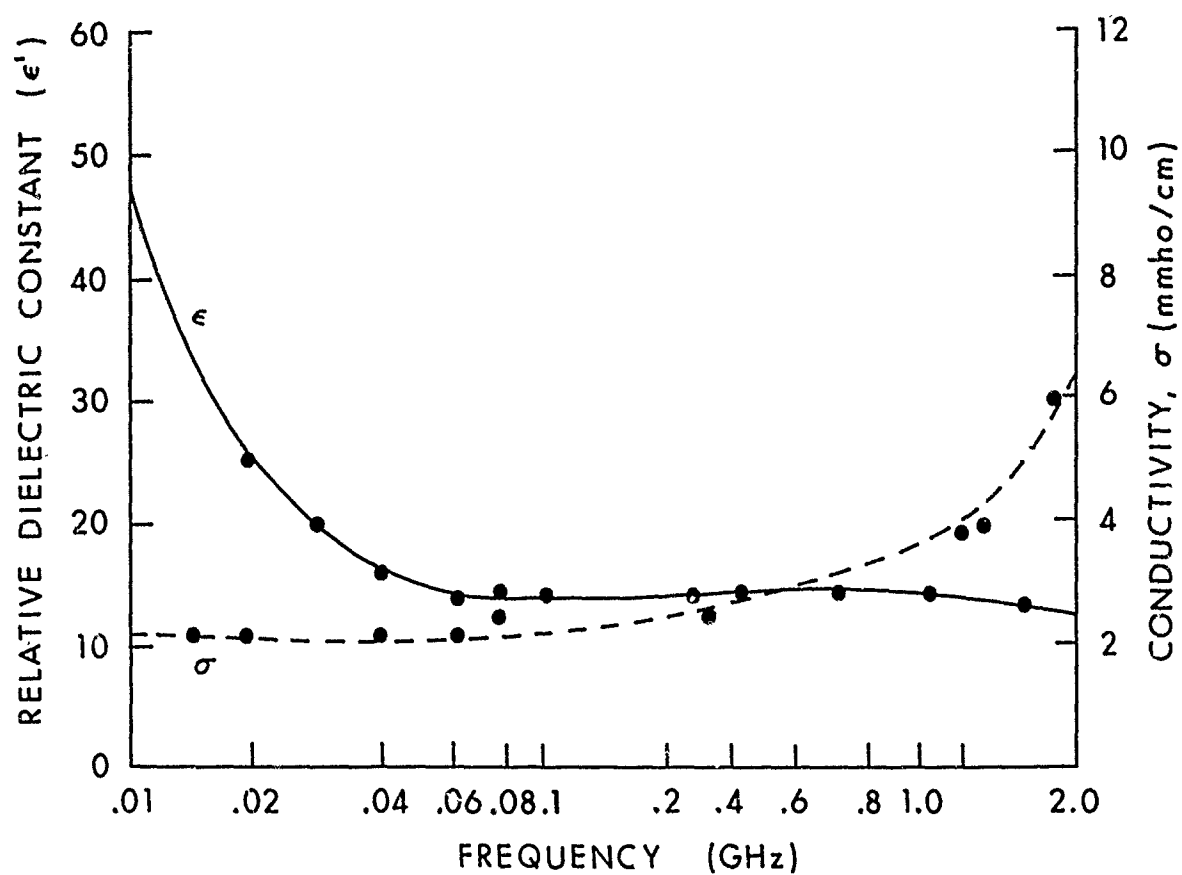
Figure 4.17.   Measured values of relative dielectric constant and conductivity of in vivo canine fat tissue at 37°C (Burdette et al., 1980).
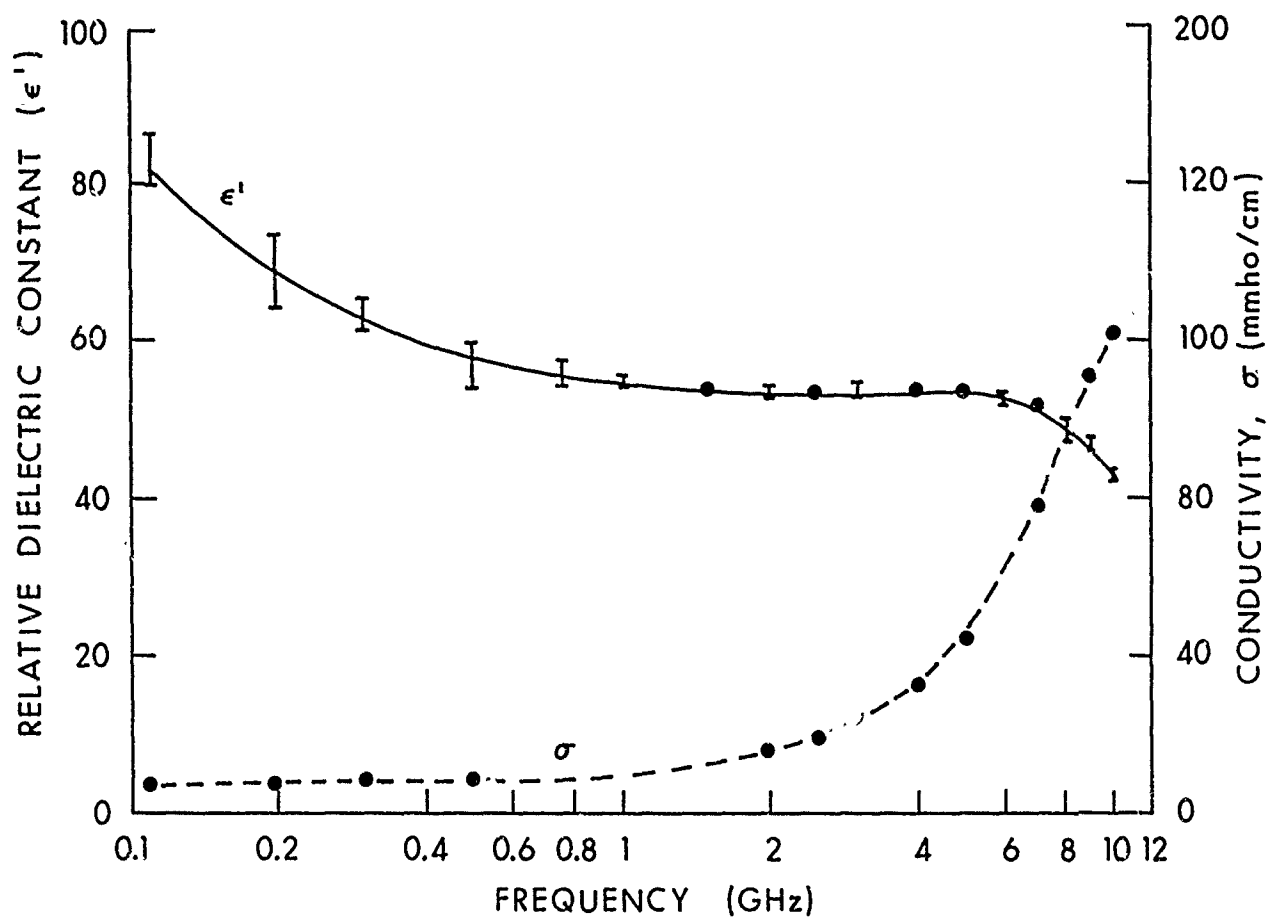
Figure 4.18.   Measured values of relative dielectric constant
and conductivity of in vivo rat brain   at 32°C.
Maximum SEM for ε' is indicated by error bars
and SEM for ε" = ± 0.9 (Burdette et al., 1980).
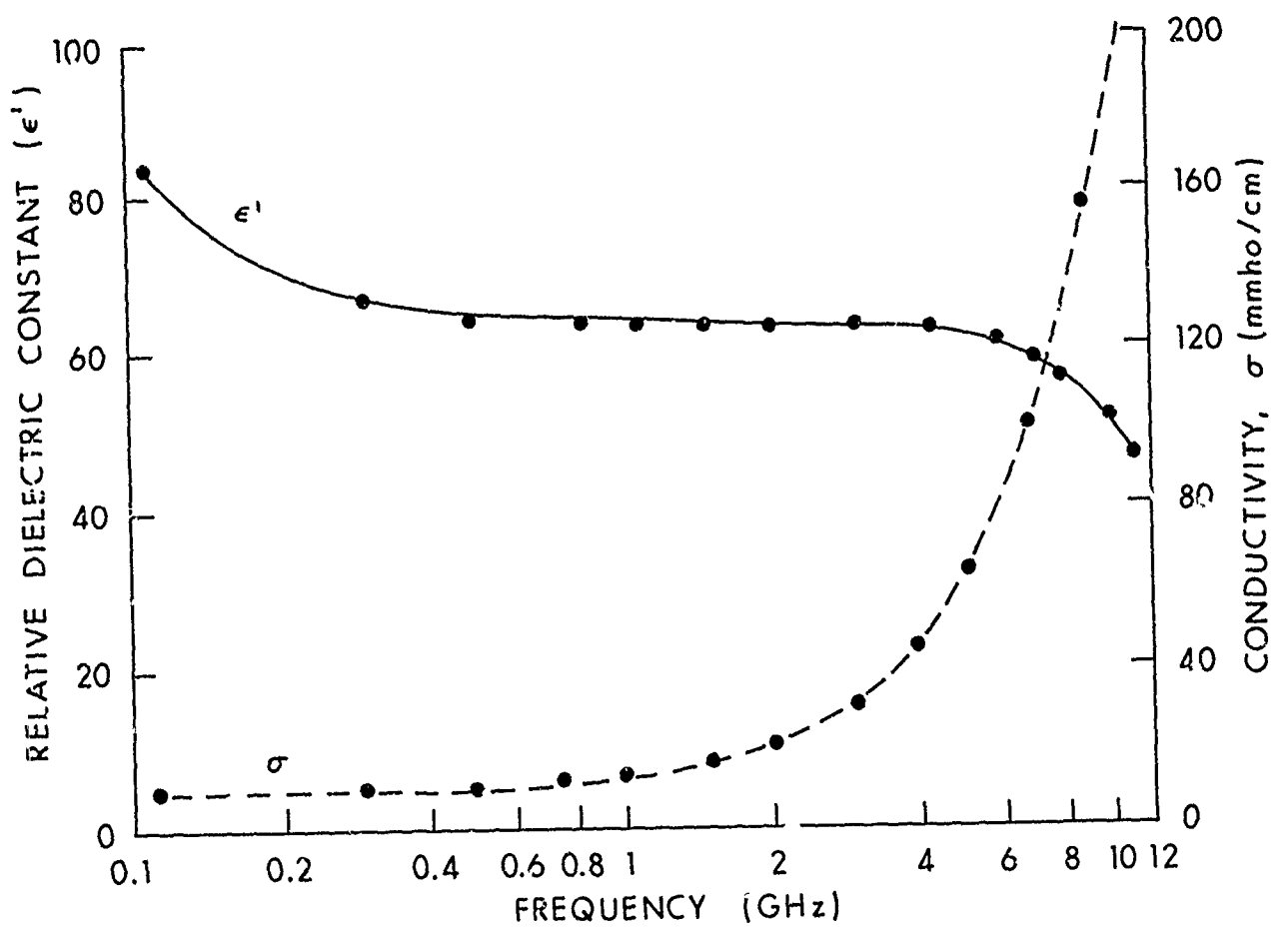
Figure 4.19. Measured values of relative dielectric constant and conductivity of rat blood at 23°C (Burdette et al., 1980).

Figures 4.20-4.24 show recently obtained in vivo data for several feline tissues at frequencies between 10 MHz and 1 GHz (Stuchly et al., 1981). These figures show significant differences in the properties of different types of the same tissue (e.g., skeletal and smooth muscle).
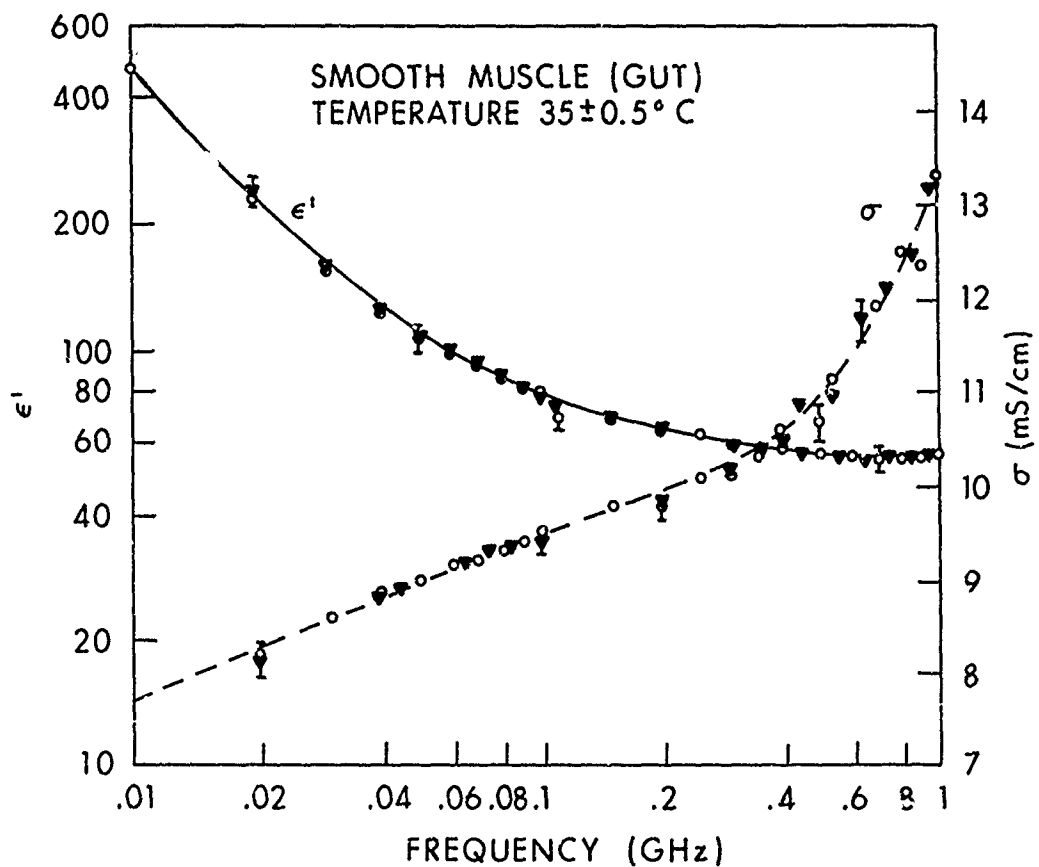
Figure 4.20. Relative permittivity of cat smooth muscle in vivo: ▼ and O show results obtained for two locations in the tissue. The vertical bars show the uncertainty due to the estimated measurement errors (SD) (Stuchly et al., 1981).
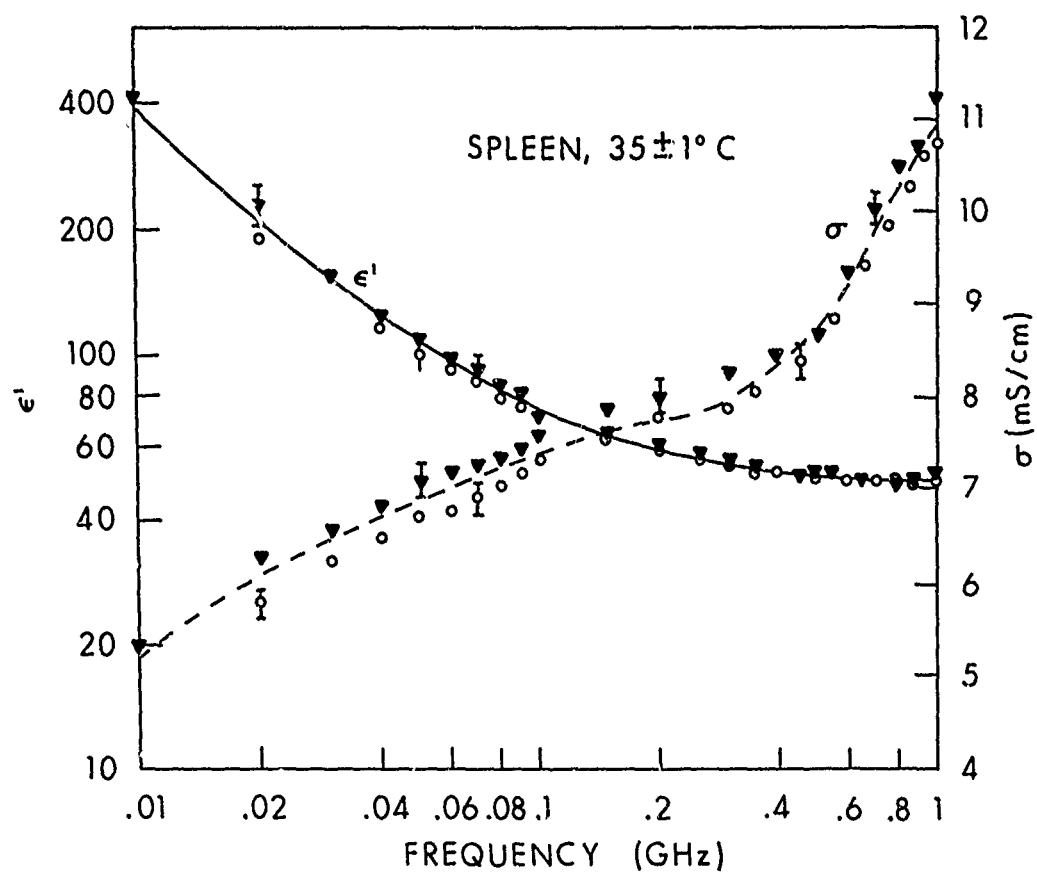
Figure 4.21. Relative permittivity of cat spleen in vivo: ▼ and O
show results obtained for two locations; the vertical
bars show the uncertainty due to estimated measure-
ment errors (SD) (Stuchly et al., 1981).
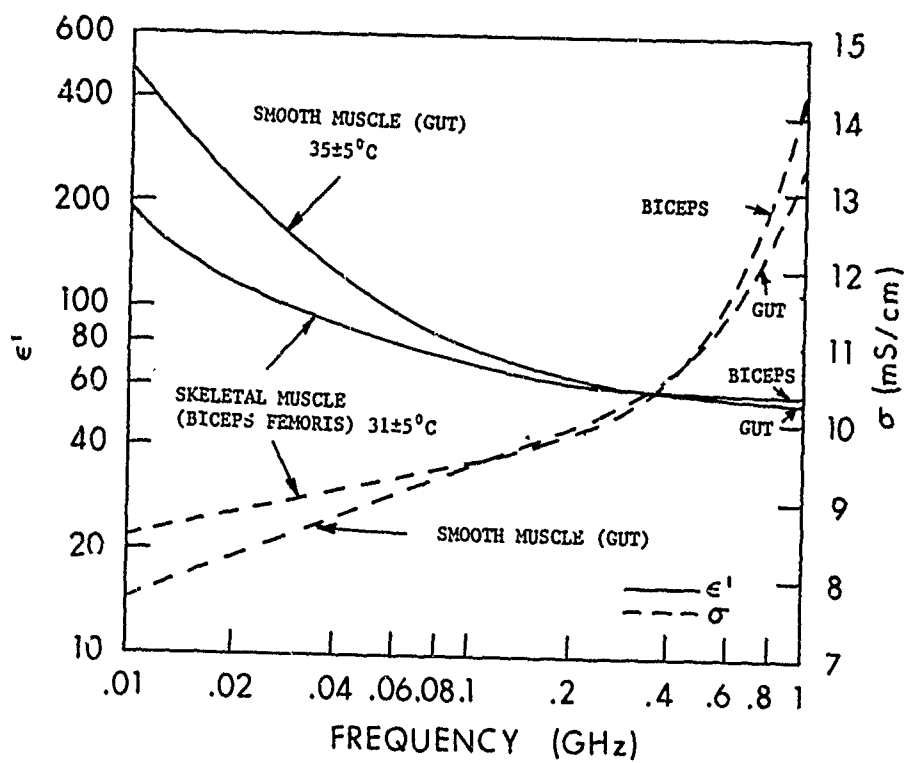
Figure 4.22. Average relative permittivity of two types of cat muscle in vivo (five samples for each point) (Stuchly et al., 1981).
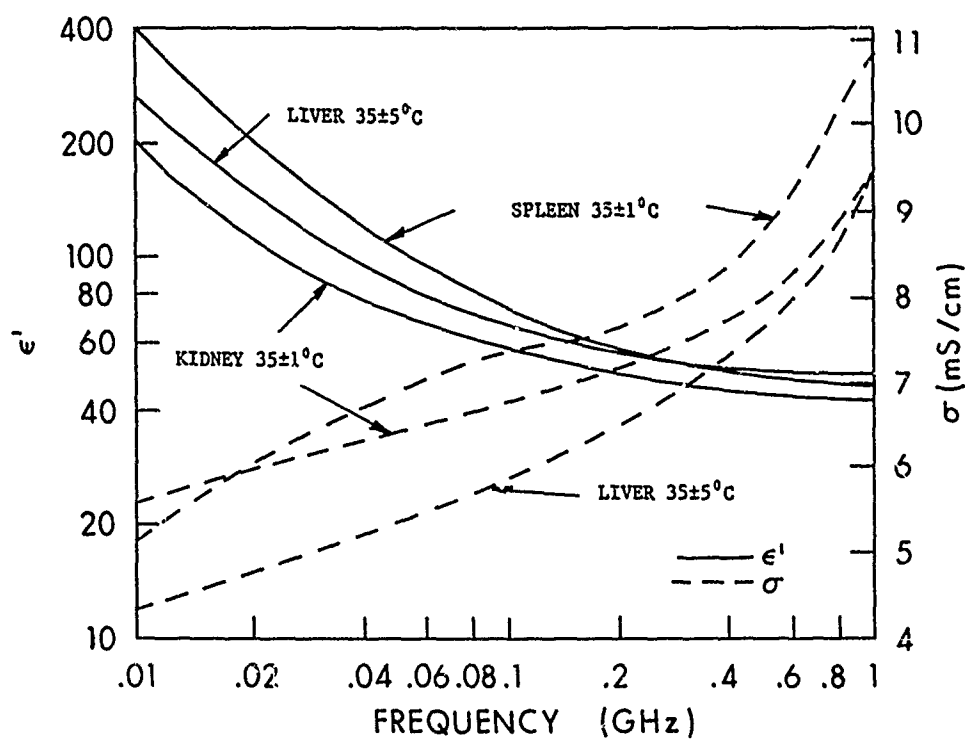
Figure 4.23. Average relative permittivity of cat internal organs in vivo
(three to five samples for each point) (Stuchly et al., 1981).
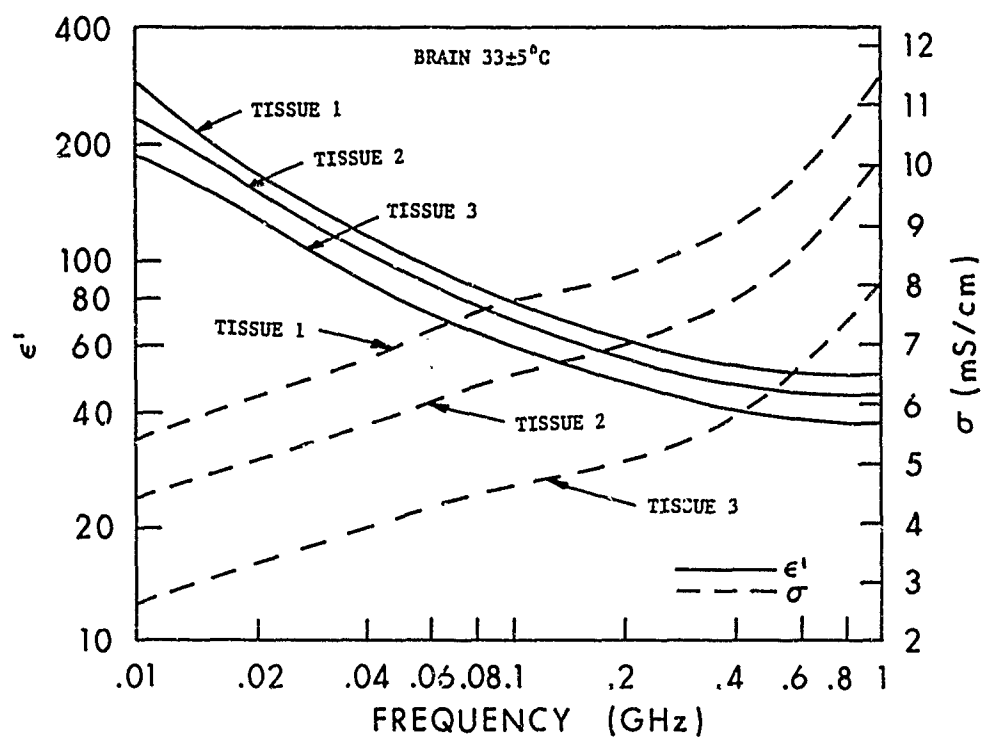
Figure 4.24.   Relative permittivity of cat brain: tissue 1 — gray mat-
ter; tissue 2 — gray matter, 3 mm thick over white mat-
ter; tissue 3 — white matter (Stuchly et al., 1981).

At frequencies below 100 kHz, a strong conductance anisotropy exists in muscle tissue (Rush et al., 1963). Data for anisotropic permittivity at low frequencies can be found in the works of Rush et al. (1963), Schwan (1957), and Johnson et al. (1975). Figure 4.25 shows the real part of the dielectric constant and conductivity of muscle tissue as a function of frequency for the parallel and perpendicular orientations (Epstein and Foster, 1983).

(a)

(b)
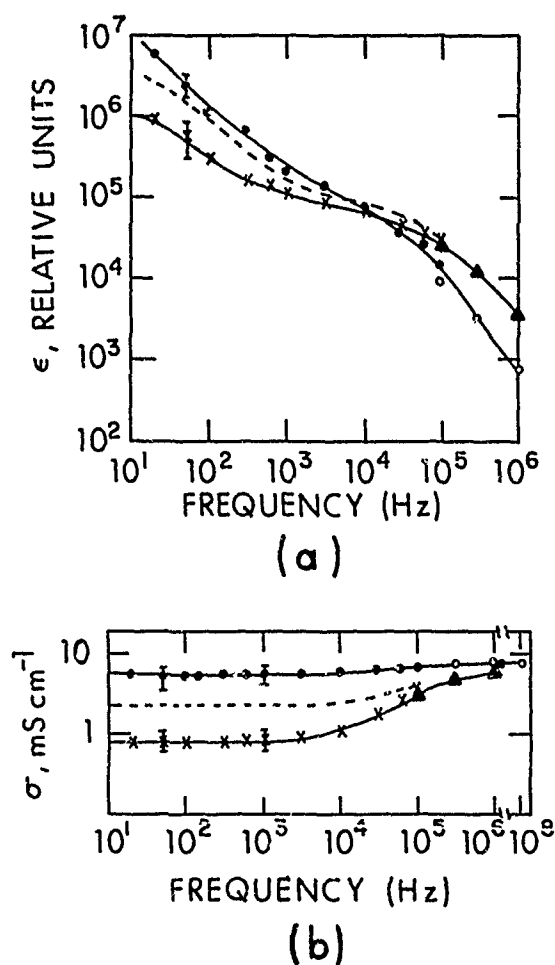
Figure 4.25. The real part of the dielectric constant (a) and the conductivity (b) of the canine skeletal muscle tissue at 37°C as a function of frequency, in parallel orientation (open and closed circles) and perpendicular orientation (crosses and triangles), averaged over five measurements on different samples. The dotted lines are the data for nonoriented muscle tissue (Epstein and Foster, 1983).

Figures 4.26-4.28 show the real and imaginary parts of the dielectric constant and the conductivity of ocular tissue at 37°C as a function of frequency (Gabriel et al., 1983). Figures 4.29 and 4.30 compare the dielectric constant and conductivity of the normal and tumor mouse tissue as a function of frequency (Rogers et al., 1983).
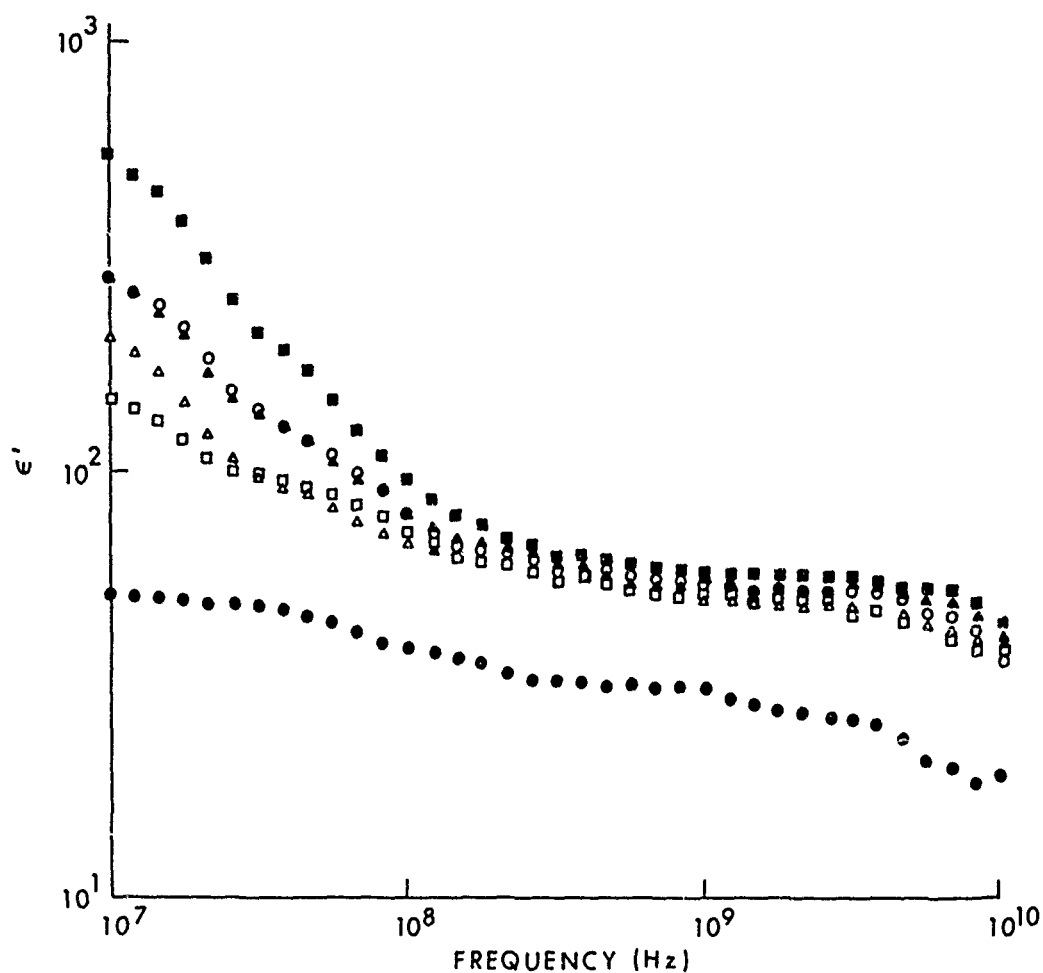
Figure 4.26. The real part of the dielectric constant, ε', of ocular tissues at 37°C (Gabriel et al., 1983). Key: ■ retina, ○ iris, ▲ choroid, □ cornea, △ lens cortex, and ● lens nucleus.
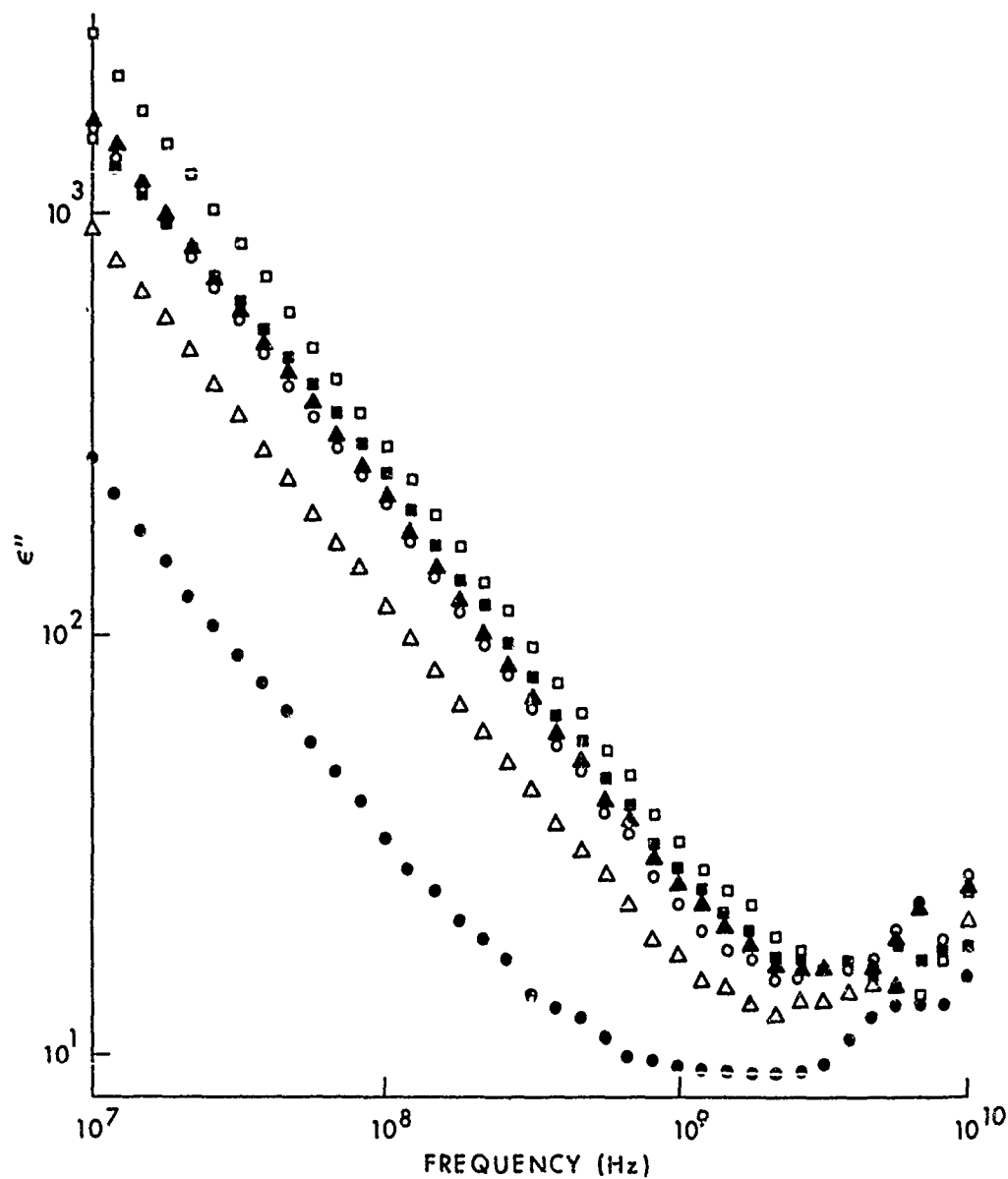
Figure 4.27. The imaginary part of the dielectric constant, ε",
of ocular tissues at 37°C (Gabriel et al., 1983).
Key: ■ retina, ○ iris, ▲ choroid, □ cornea,
△ lens cortex, and ● lens nucleus.
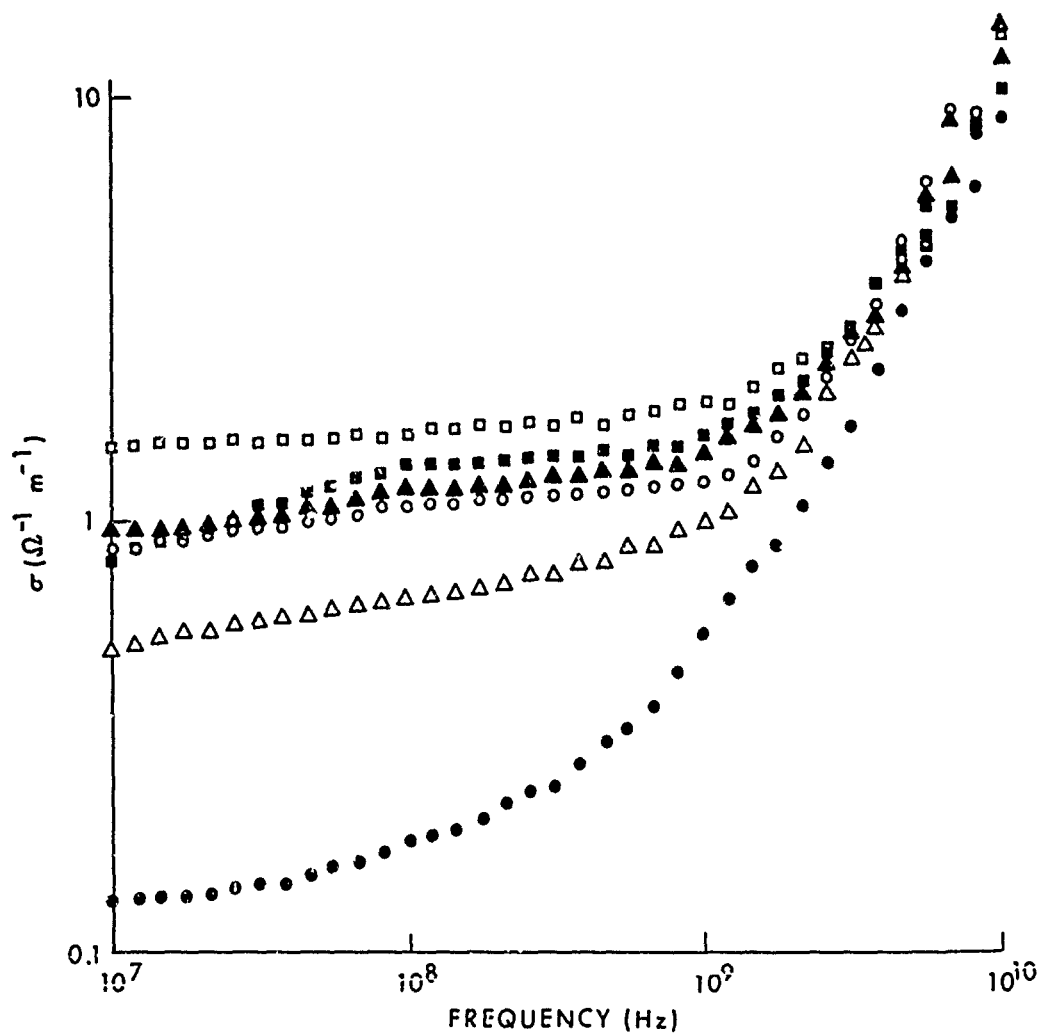
Figure 4.28.   The conductivity of ocular tissues at 37°C
               (Gabriel et al., 1983).
               Key: ■ retina, O iris, ▲ choroid, □ cornea,
                     △ lens cortex, and ● lens nucleus.
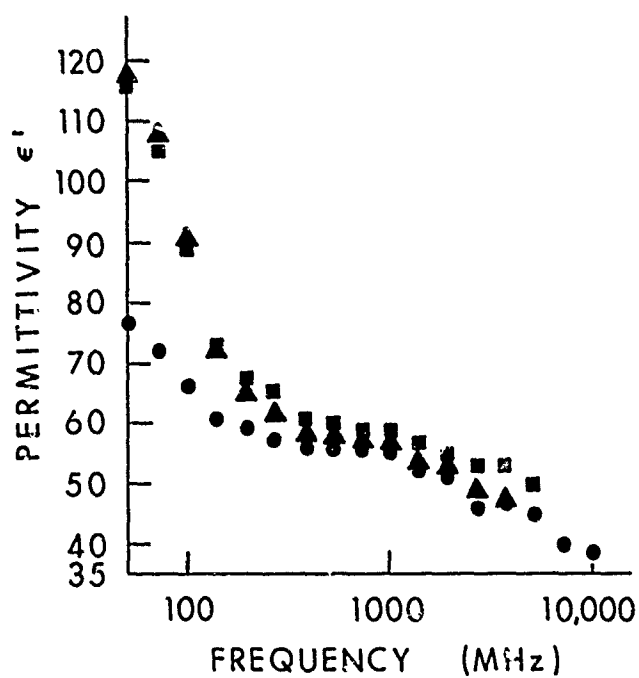
Figure 4.29. Real part of the dielectric constant, ε', of normal and tumor mouse tissue as a function of frequency (Rogers et al., 1983). ● mouse muscle, ▣ KHT fibrosarcoma tumor, ▲ RIF/1 fibrosarcoma tumor.
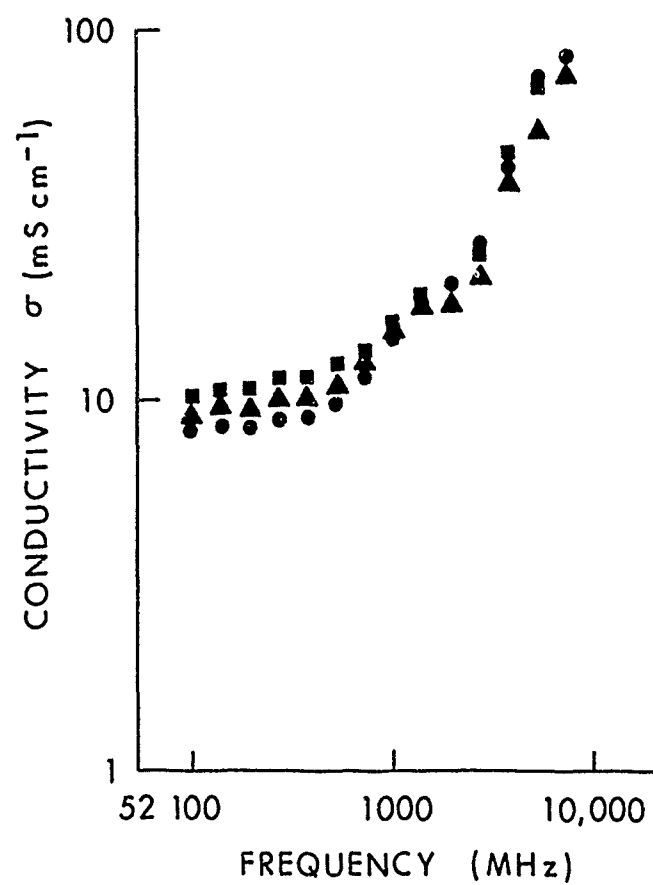
Figure 4.30. Conductivity of normal and tumor mouse tissue as a function of frequency (Rogers et al., 1983). ● mouse muscle, ▉ KHT fibrosarcoma tumor, ▲ RIF/1 fibrosarcoma tumor.

CHAPTER 5. THEORETICAL DOSIMETRY

5.1. METHODS OF CALCULATION

5.1.1. Plan... ive Dosimetry

In principle, the internal fields in any object irradiated by electro-
magnetic fields can be calculated by solving Maxwell's equations. In prac-
tice, this is very difficult and can be done only for a few special cases.
Because of the mathematical complexities involved in calculating SARs, a
combination of techniques has been used to obtain SARs as a function of fre-
quency for various models (Durney, 1980). Each technique gives information
over a limited range of parameters. The combined information gives a reason-
ably good description of SAR versus frequency over a wide range of frequencies
and for a number of useful models. Figure 5.1 summarizes the combination of
techniques used in the various frequency ranges to obtain the average SAR
versus frequency for a model of an average man.

With spheroidal models we used a method called the long-wavelength
approximation up to frequencies of about 30 MHz; the extended-boundary-
condition method (EBCM) up to approximately rec nance (80 MHz); and the itera-
tive extended-boundary-condition method (IEBCM), an extension of the EBCM, up
to 400 MHz. With cylindrical models we used the classical solution of
Maxwell's equations to obtain useful average SAR data for E polarization from
about 500 to 7,000 MHz, and for H polarization from about 100 to 7,000 MHz;
above approximately 7,000 MHz, we used an approximation based on geometrical
optics. Up to about 400 MHz we used the moment-method solution of a Green's-
function integral equation for the electric field; for K polarization we used
the surface-integral-equation (SIE) tec .ique with a model consisting of a
truncated cylinder capped on each end by hemispheres. An empirical relation
developed for E polarization gives a good approximation for the average SAR
over the entire frequency spectrum up to 10 GHz. For K polarization we used
estimated values based on experimental results for the range between 400 and
7,000 MHz because calculations are not yet possible in this frequency range.
Each of these techniques will be briefly described.
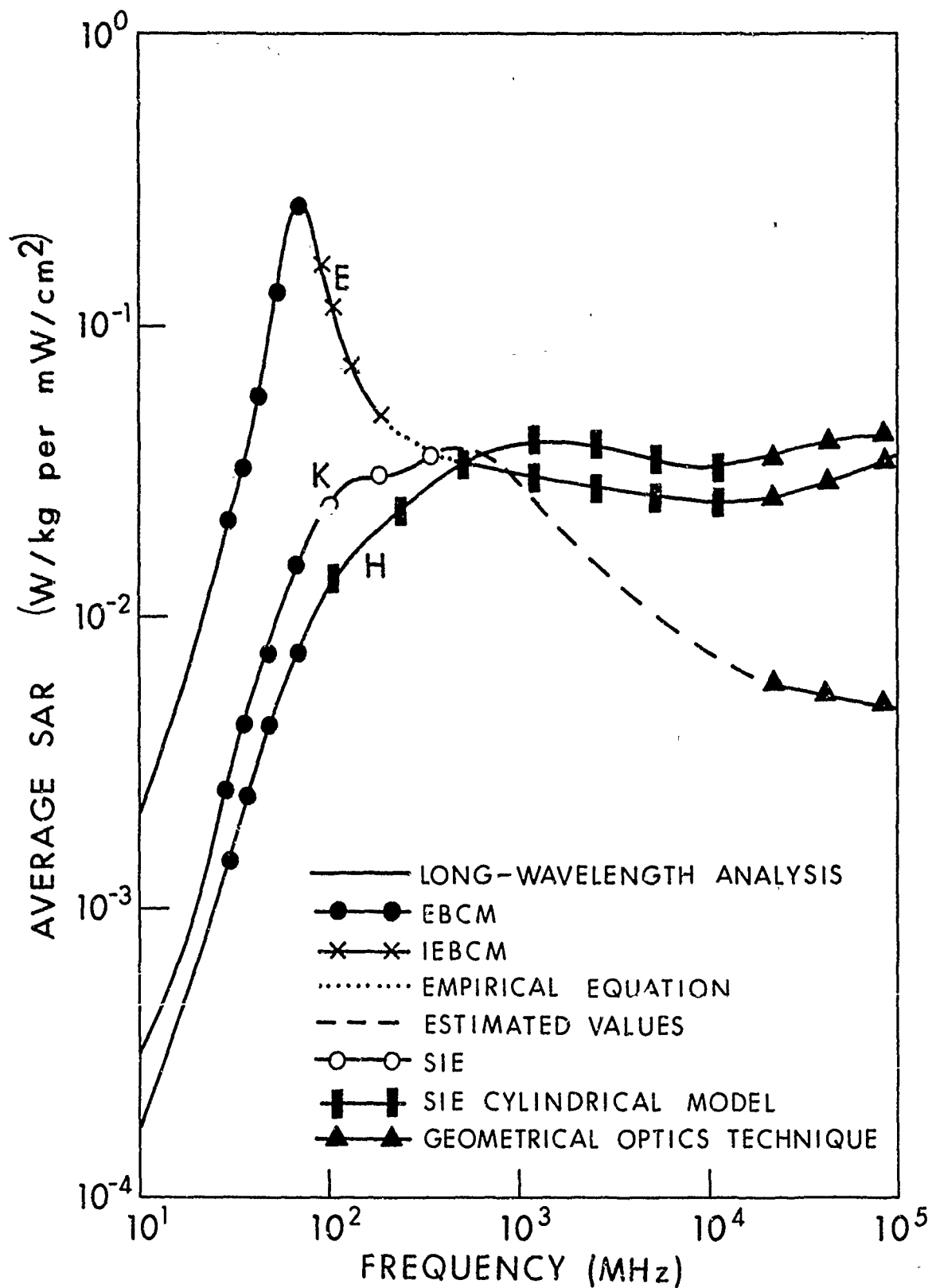
Figure 5.1. Illustration of different techniques, with their frequency limits, used for calculating SAR data for models of an average man.

<u>Long-Wavelength Approximation</u>--In the frequency range where the length of the irradiated object is approximately two-tenths or less of a free-space wavelength, we have approximated the SAR calculations, based on the first-order term of a power series expansion in k of the electric and magnetic fields, where k is the free-space propagation constant (Durney et al., 1975). This is called a perturbation method because the resulting fields are only a small change from the static fields. Equations for SAR have been derived for homogeneous spheroidal and ellipsoidal models of humans and animals (Johnson et al., 1975; Massoudi et al., 1977a, 1977b, 1977c). Detailed relations (given in the referenced articles) have been used here to calculate the SAR in the low-frequency range.

<u>Extended-Boundary-Condition Method</u>--The EBCM is a matrix formulation based on an integral equation and expansion of the EM fields in spherical harmonics. This method was developed by Waterman (1971) and has been used to calculate the SAR in prolate spheroidal models of humans and animals (Barber, 1977a, 1977b). The EBCM is exact within the limits of numerical computation capabilities; but for prolate spheroidal models of humans, numerical problems limit the method to frequencies below about 80 MHz. In SAR calculations for these models, the long-wavelength approximation and the EBCM give identical results up to about 30 MHz, where the long-wavelength approximation begins to be inaccurate.

<u>Iterative-Extended-Boundary-Condition Method</u>--The EBCM has been extended (Lakhtakia et al., 1983b) to a technique (the IEBCM) that is capable of SAR calculations up to at least 400 MHz in prolate spheroidal models of man. The IEBCM differs from the EBCM in two main respects. By using more than one spherical harmonic expansion, the IEBCM allows better convergence for elongated bodies and at higher frequencies; and it uses iteration, beginning with an approximate solution, to converge to the solution. These two features have significantly extended the calculation range of the IEBCM over that of the EBCM.

<u>The Cylindrical Approximation</u>--In the frequency range where the wavelength is very short compared to the length of the spheroid, the SAR calculated

for an appropriately long section of an infinitely long cylinder is a good approximation to the SAR of spheroids. The lowest frequency at which the approximation is useful depends both on the length of the spheroid and on the ratio of the major axis to the minor axis. For man-sized spheroids, the lower frequency limit occurs for E polarization when the wavelength is about four-tenths the length of the spheroid (Massoudi et al., 1979a).

Moment-Method Solution--A moment-method solution of a Green's-function integral equation for the E-field has been used to calculate the internal E-field in block models, so-called because the mathematical cells of which the model is composed are cubes (Chen and Guru, 1977a, 1977b, 1977c; Hagmann et al., 1979a, 1979b). Whole-body average SARs calculated by this method are very close to those calculated for spheroidal models. Although the block model--with simulated arms, legs, and head--has the advantage of resembling the human body better than a spheroid, the calculations of the spatial distribution of the internal fields have been unreliable (Massoudi et al., 1984). One problem with this technique is that the E-field in each mathematical cell is approximated by a constant (called a pulse function), and this approximate field cannot satisfy the boundary conditions between cells well enough. Another problem is that the discontinuities at the sharp corners of the cells make the calculated fields at the corners between cells of different permittivities vary rapidly with position, which causes problems in numerical calculations.

Surface-Integral-Equation Technique--The SIE method, based on a formulation of the EM-field equations in terms of integrals over induced currents on the surface of an object (Wu, 1979; Harrington and Mautz, 1972), has been used to calculate average SARs, principally for K polarization and mostly for models consisting of a truncated cylinder capped on each end by hemispheres. Average SARs for this model are close to those for a spheroid, depending on how the dimensions of the cylinder-hemispheres model are chosen relative to the spheroid.

Empirical Relations for Free-Space Irradiation--Techniques for calculating SARs (especially over a wide frequency range) are complex and expensive,

so a simplified method for calculating approximate average SAR over a broad range of frequencies could be very useful, even if it gave results within 10% or 15% of those calculated by more sophisticated methods. Kucia (1972) and Gandhi and Hagmann (1977a) made some approximate calculations based on antenna theory. Gandhi and Hagmann found from experimental data that the resonant frequency for E polarization occurs when the length of the object is equal to approximately 0.4 λ, where λ is the free-space wavelength. They also noticed that the SAR decreases approximately as $1/f$ (f is frequency) in the postresonance region. Using a combination of antenna theory, circuit theory, and curve fitting, we have developed empirical relations for calculating the average SAR over the whole frequency range of interest for a prolate spheroidal model of any human or animal (Durney et al., 1979). We have also developed semiempirical methods for calculating the average SAR of an irradiated object near or on a ground plane or connected to a ground plane by a resistive connection. These relations are described below.

Based on available calculated and experimental data, we formulated the following expression of average SAR for an incident-power density of 1 mW/cm^2 and E polarization for a spheroid with semimajor axis, a, and semiminor axis, b, in meters:

$$
\text{SAR (W/kg)} = \frac{A_1 f^2/f_o^2 \left[1 + A_3(f/f_o)u(f - f_{o1}) + A_4 A_5(f^2/f_o^2)u(f - f_{o2}) \right]}{10^3 f^2/f_o^2 + A_2(f^2/f_o^2 - 1)^2} \quad (5.1)
$$

where (as given by Equations 5.5-5.9) A_1, A_2, A_3, and A_4 are functions of a and b, and A_5 is a function of ϵ. Unit step function $u(f - f_{o1})$ is defined by

$$
u(f - f_{o1}) = \begin{cases} 0 & \text{if } f < f_{o1} \\ \\ 1 & \text{if } f > f_{o1} \end{cases}
$$

and $u(f - f_{o2})$ is similarly defined. Also, $f_o < f_{o1} < f_{o2}$. The resonant frequency, f_o, is given by the following empirical relation:

$$f_o(\text{Hz}) = 2.75 \times 10^8 \left[8a^2 + \pi^2\left(a^2 + b^2\right)\right]^{-1/2} \qquad (5.2)$$

We obtained Equation 5.2 by constructing a function of a and b with adjustable parameters and using a least-squares-error procedure to fit the function to calculated values of f_o. The function was constructed from the observation that resonance is a combination of the length being near a half wavelength and the circumference being near a wavelength. Values calculated from Equation 5.2 are within 5% of all resonant frequency values calculated by more accurate methods.

The empirically derived quantities f_{o1} and f_{o2} are defined by

$$\frac{f_{o1}}{f_o} = -0.421\,a + 1.239\,a/b + 1.090\,a^2 - 0.295\,(a/b)^2 + 0.020\,(a/b)^3 \qquad (5.3)$$

$$\frac{f_{o2}}{f_o} = 21.800\,a + 0.502\,a/b - 50.810\,a^2 - 0.068\,(a/b)^2 + 34.120\,a^3 \qquad (5.4)$$

By requiring Equation 5.1 to provide a best least-squares fit to all the data available, we obtained the following expressions:

$$A_1 = -0.994 - 10.690\,a + 0.172\,a/b + 0.739\,a^{-1} + 5.660\,a/b^2 \qquad (5.5)$$

$$A_2 = -0.914 + 41.400\,a + 399.170\,a/b - 1.190\,a^{-1} - 2.141\,a/b^2 \qquad (5.6)$$

$$A_3 = 4.822\,a - 0.084\,a/b - 8.733\,a^2 + 0.0016\,(a/b)^2 + 5.369\,a^3 \qquad (5.7)$$

$$A_4 = 0.335\,a + 0.075\,a/b - 0.804\,a^2 - 0.0075\,(a/b)^2 + 0.640\,a^3 \qquad (5.8)$$

$$A_5 = \left|\varepsilon/\varepsilon_{20}\right|^{-1/4} \qquad (5.9)$$

where ε_{20} is the complex permittivity at 20 GHz.

A_5 is a function of ε, the complex permittivity of muscle, and is used to describe the SAR in the geometrical optics region.

Equation 5.1 is a powerful relation because it allows using a hand calculator to get good approximate values of SAR for _any_ prolate spheroidal model between rat size and man size, whereas the SAR data in this handbook and its previous editions require sophisticated and expensive calculation methods and are plotted only for specific cases. Numerical results from Equation 5.1 are shown in Figure 5.2 as data points on the E polarization curve.

This empirical formula (Equation 5.1) is included, however, to complement but not substitute for the SAR data given in the handbook. In its present form, Equation 5.1 is useful for calculating the SAR for models of intermediate sizes between humans and rats. Although the coefficients A_1, A_2, ..., A_5 were derived by fitting available SAR data for 18 models, the accuracy is rather limited in the transition regions at $f = f_{o1}$ and $f = f_{o2}$, where step functions begin to be effective. Because of the abrupt nature of the step function, SAR values in close proximity to f_{o1} and f_{o2} are usually inaccurate. Also, since the frequency-dependent permittivity is not explicitly included in Equation 5.1, SAR-value fluctuations caused by the variation of ε with frequency are not always accurately represented.

William D. Hurt and Luis Lozano (USAFSAM) modified Equation 5.1 to eliminate the step functions. Their equation is

$$
SAR = \frac{A_1 f^2/f_o^2 \left[1 + A_4 A_5 \left(f/f_o - 1 \right)^2 \left(f/f_o \right)^B \right]}{1000 \ f^2/f_o^2 + A_2 \left(f^2/f_o^2 - 1 \right)^2}
\tag{5.10}
$$

where

$$
B = u^{f_o/f} - 1
\tag{5.11}
$$

$$
u = -0.16 + 1.128 \ (\log m)^2 - 0.0438 \ (\log m)^4 + 51.4 \ b
\tag{5.12}
$$

$$
- 271 \ b^2 - 8.902 \ a + 9 \ a^2
$$

$$
m = \frac{4}{3} \ \pi ab^2
$$

and a, b, A_1, A_2, A_4, A_5, and f_o are as defined previously.
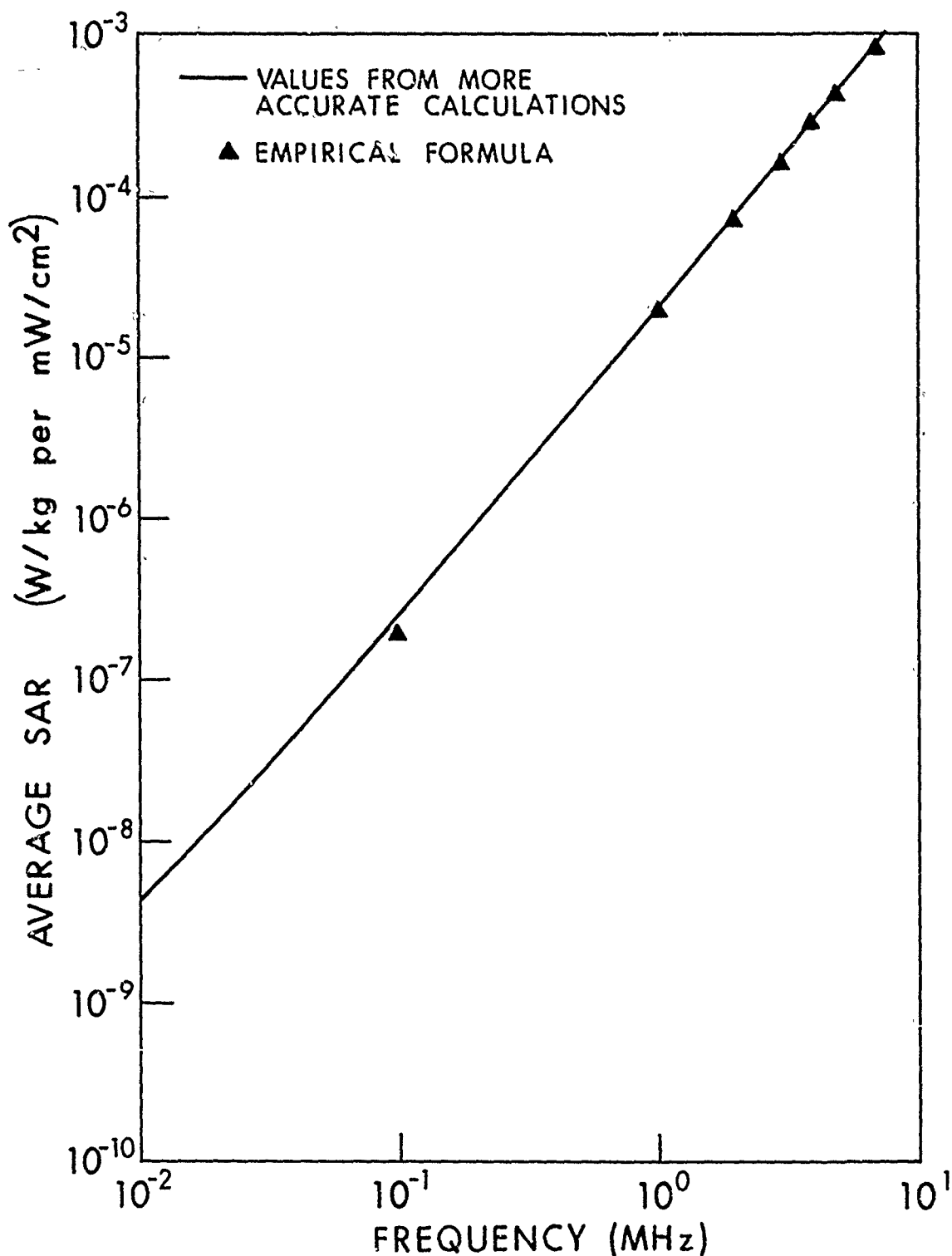
Figure 5.2. Average SAR calculated by the empirical formula compared with the curve obtained by other calculations for a 70-kg man in E polarization. For the prolate spheroidal model, a = 0.875 m and b = 0.138 m; for the cylindrical model, the radius of the cylinder is 0.1128 m and the length is 1.75 m.
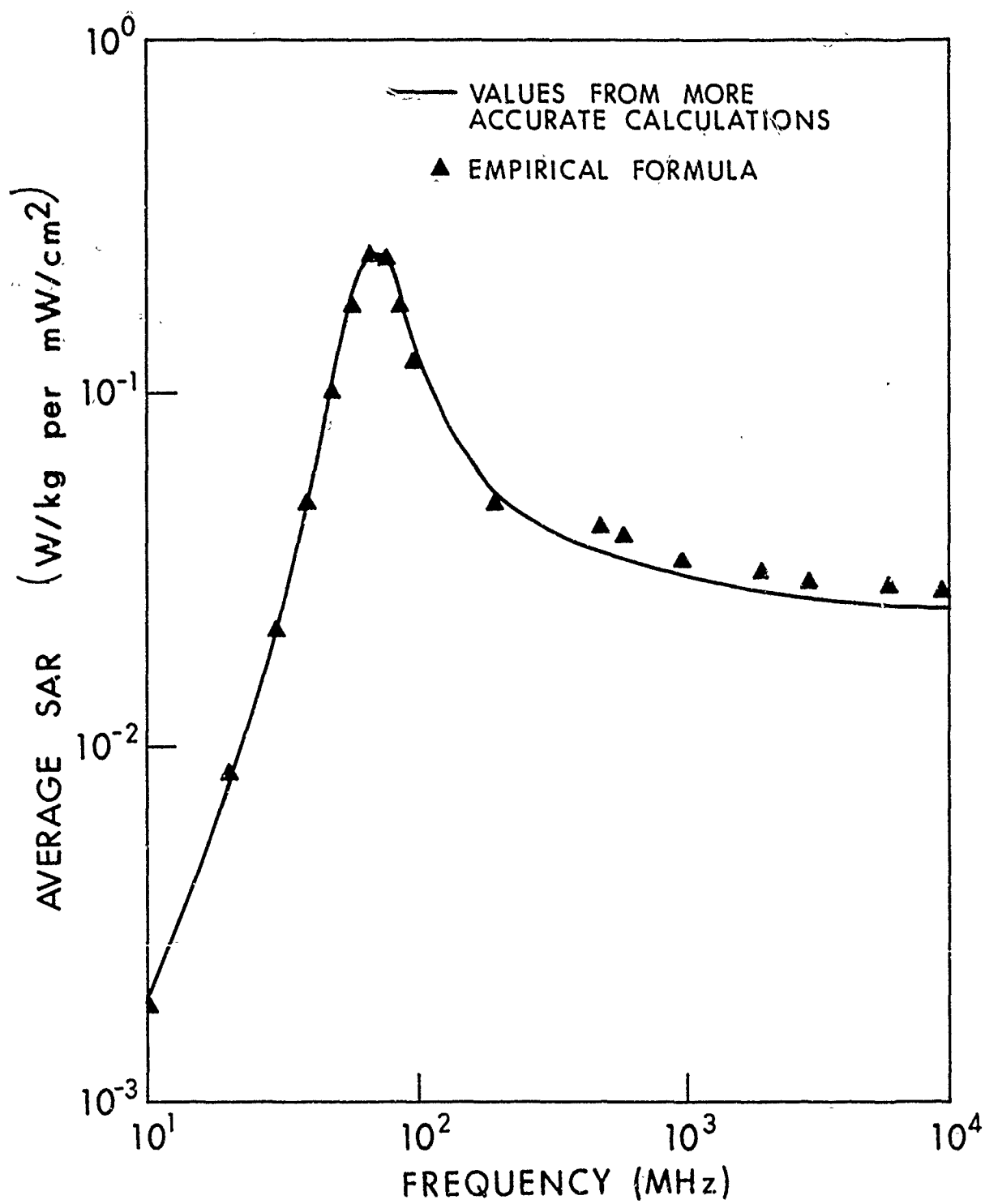
Figure 5.2 (continued).

Equation 5.10 has the advantage of being continuous because it contains no step functions. It is identical to Equation 5.1 for low, resonance, and high frequencies but differs somewhat in the immediate postresonance frequency range, where it gave values within 30% of those calculated for specific models (data in Chapter 6) except for the average endomorphic man, for which it gave results that were 40% below the handbook values.

William D. Hurt (USAFSAM) developed another empirical relation that incorporates in one continuous expression both the long-wavelength approximation for prolate spheroids on the low end of the frequency spectrum and the geometrical optics approximation on the high end. This empirical equation is

$$ SAR = \frac{A_1 f^2/f_o^2 \left(1 + \left(1 - e^{-\lambda/f_o}\right)\left[A_3(f/f_o - 1) + A_5 B_2(f/f_o)(f/f_o - 1)\right]\right)}{1000\, f^2/f_o^2 + B_1\left(f^2/f_o^2 - 1\right)^2} \quad (5.13) $$

where A_1, A_3, and A_5 are defined in Equations 5.5, 5.7, and 5.9, and

$$ B_1 = \frac{605A_1}{f_o^2 \sigma \left[\left(B_e/377\sigma\right)^2 + a^2 b^2/5\left(a^2 + b^2\right)\right]} \quad (5.14) $$

$$ B_2 = 0.0035 B_1/bA_1 \quad (5.15) $$

$$ f_o = 275/\left[8a^2 + \pi^2(a^2 + b^2)\right]^{1/2} \text{ MHz} \quad (5.16) $$

$$ B_e = \left(U^2 - 1\right)^{-1}\left((U/2)\ln[(U + 1)/(U - 1)] - 1\right)^{-1} \quad (5.17) $$

$$ U = a/\left(a^2 - b^2\right)^{1/2} \quad (5.18) $$

Also, σ is the conductivity of the spheroid in siemens per meter.

The SARs calculated from Equation 5.13 were within about 25% of the values for specific models as given in Chapter 6 except for the small rat, for which the values differed by about 40% at 5 GHz.

Semiempirical Relations for Irradiation Near a Ground Plane--Knowing how shoes and soles affect the SAR in man on a ground plane is desirable. Such an

effect, however, is very difficult to estimate even by using complicated numerical techniques (Hagmann and Gandhi, 1979). In this section we present a simple semiempirical formula for calculating the SAR of a half-spheroid placed over, but at a distance from, an infinitely large ground plane.

To derive this formula, we first put Equation 5.1 in the form of the power absorbed in a series RLC circuit. Hence

$$SAR = \frac{(1/2)(V^2/R)f^2/f_o^2}{f^2/f_o^2 + Q_o^2(f^2/f_o^2 - 1)^2} \tag{5.19}$$

where

$$Q_o = \omega_o L/R$$
$$f_o = 1/2\pi\sqrt{LC}$$
$$V = {}^\gamma aE_o \quad \left(E_o \text{ is the incident E-field intensity}\right)$$

Comparing Equations 5.1 (up to resonance) and 5.19--and keeping in mind that input voltage aE_o is applied across the input impedance and the radiation impedance of a monopole rather than a dipole antenna--the parameters R, L, and C of Equation 5.19 can be expressed in terms of A_1, A_2, and f_o. Therefore, we first compute the parameters A_1, A_2, and f_o so that the power calculated from Equation 5.1 will fit (with least-squares error) the numerical results of the SAR in a man model on a ground plane (Hagmann and Gandhi, 1979). The corresponding R, L, and C parameters will hence be valid for a half-spheroid in direct contact with a perfectly conducting ground plane. Introducing a small separation distance between the half-spheroid and the ground plane, in the form of an air gap or a resistive gap representing shoes, will correspond to adding the following R_g and X_g parameters in series with the previously derived resonance circuit:

$$R_g = \frac{R_1}{1 + \omega^2 C_1^2 R_1^2} \quad \text{and} \quad X_g = \frac{\omega C_1 R_1^2}{1 + \omega^2 C_1^2 R_1^2} \tag{5.20}$$

where R_1 and C_1 are the parallel combination describing the gap impedance. R_g and X_g are frequency dependent and will result in changes in both the SAR values and the resonance frequency at which maximum absorption occurs.

At frequencies higher than 1 Mhz and at separation distances more than 1 cm from a relatively dry earth, R_g can be shown to be negligible with respect to the resistance of the equivalent circuit in Equation 5.19. For this case the effect of only X_g is shown in Figure 5.3. As the gap distance increases, the SAR curve continues to shift to the right toward the limiting case of a man in free space. The SAR curve reaches this limiting case for a separation distance of about 7.5 cm. Since the introduction of C_g will not account for any changes in the SAR value at resonance, the peak value in the figure remains the same.

For wet earth and particularly for spheroids at small separation distances, the effect of gap resistance R_g should be taken into account (Spiegel, 1977). Figure 5.4 illustrates such an effect where small reductions in the SAR values are generally observed.

Although the presence of the ground plane shifts the resonant frequency in each case, it does not significantly affect the maximum value of the average SAR. At a given frequency well below resonance (e.g., 10 MHz), however, the presence of the ground plane increases the average SAR by an order of magnitude over the free-space value.

Penetration as a Function of Frequency--The concept of skin depth discussed in Section 3.3.4 shows that for the special case of a planewave incident on a lossy dielectric half-space, the penetration of the planewave becomes shallower and shallower as the frequency increases. For example, from Equation 3.46 the skin depth in a dielectric half-space having a permittivity equal to two-thirds that of muscle tissue is only 0.41 cm at 10 GHz. Although the concept of skin depth in a dielectric half space can give a qualitative indication of how penetration changes with frequency in nonplanar objects, it must be used with caution.
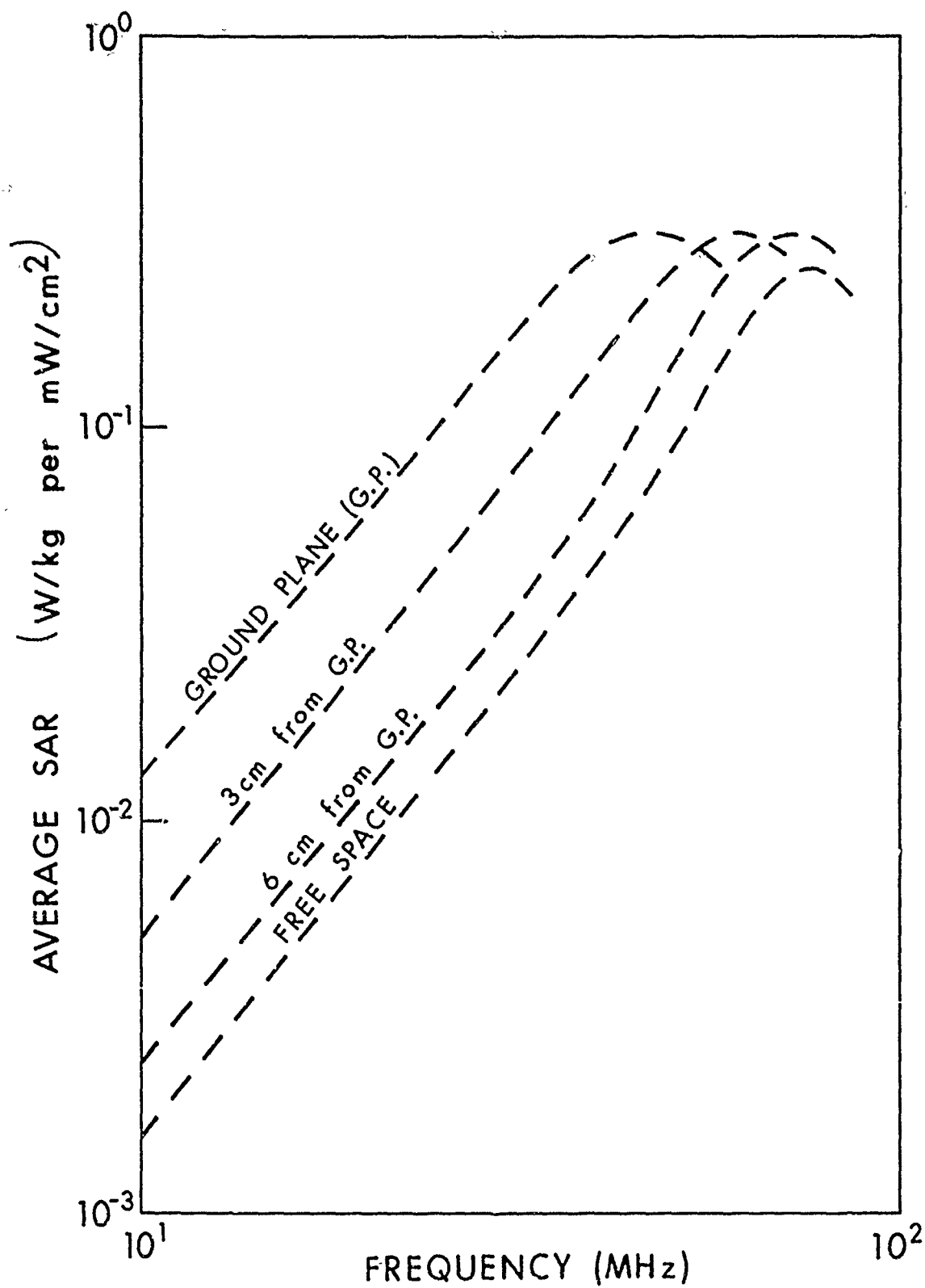
Figure 5.3. Calculated effect of a capacitive gap, between
man model and ground plane, on average SAR.
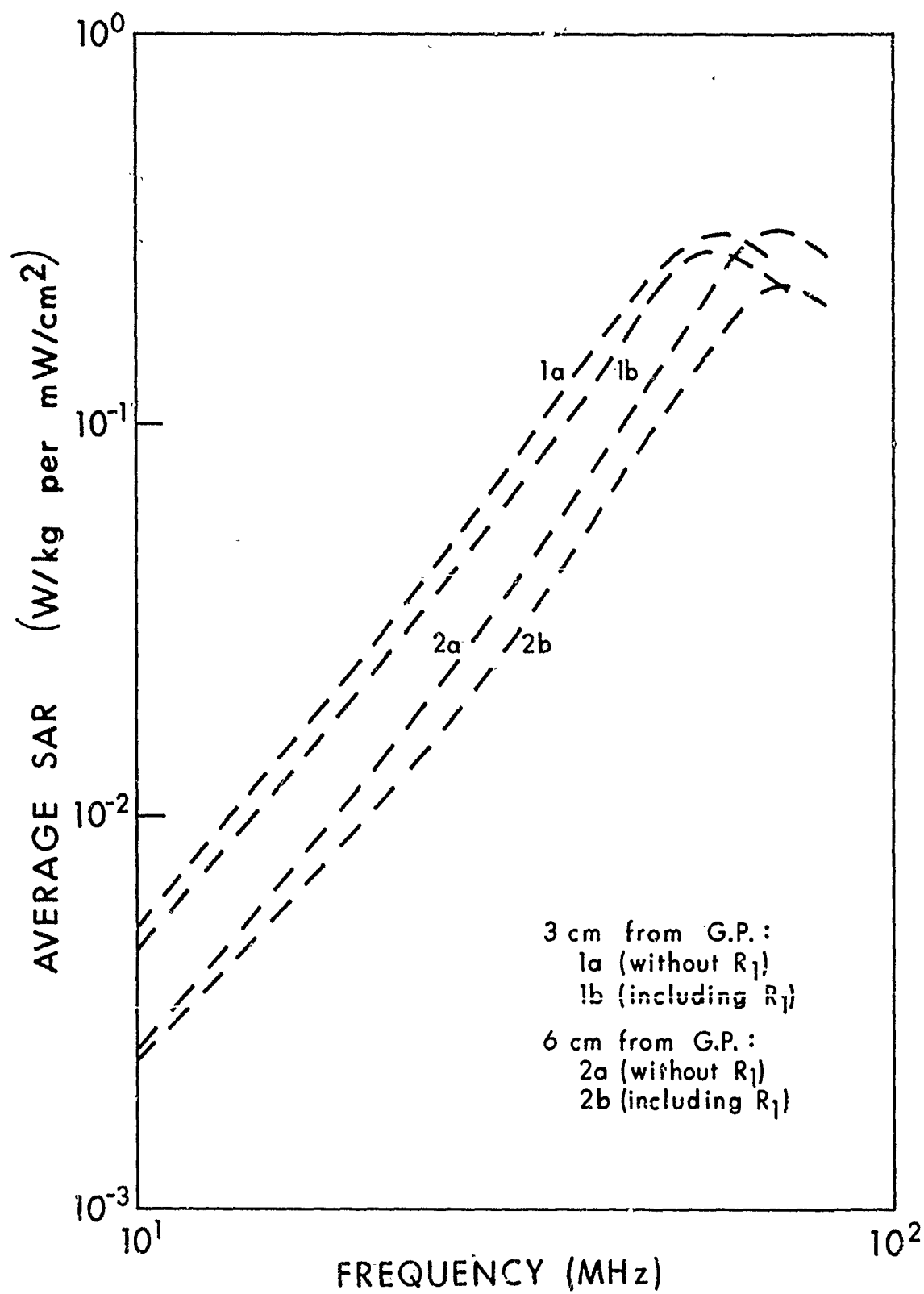
Figure 5.4. Calculated effect of grounding resistance on SAR of man model placed at a distance from ground plane.

To provide more quantitative information about penetration in nonplanar objects, we have made some calculations that show how power absorption is distributed over the volume of the object as a function of frequency for spheres, cylinders, and spheroids irradiated by planewaves. These calculations are based on the following procedure. First, the object is divided into M small equal-volume elements ΔV. Then P_n, the power absorbed in each ΔV, is calculated and ranked in order from greatest power absorbed to least. Next, the total power absorbed in N of the ΔVs is calculated by summing the ranked P_n's from highest toward least:

$$P_N = \sum_{n=1}^{N} P_n \qquad (5.21)$$

The number N is selected so that

$$P_N = 0.9 \, P_M \qquad (5.22)$$

where P_M is the total power absorbed in the object, given by

$$P_M = \sum_{n=1}^{M} P_n \qquad (5.23)$$

Then the volume fraction V_F is defined as that fraction of the volume in which 90% of the power is absorbed:

$$V_F = \frac{N\Delta V}{M\Delta V} = \frac{N}{M} \qquad (5.24)$$

As the curves in Figures 5.5 and 5.6 show, V_F is nearly unity at low frequencies but decreases to a very small number at high frequencies.

Although like calculations are not practical for a shape closer to the human body, the similarity of the curves for the objects shown indicates that similar results would be expected for the human body. Curves for spheres, cylinders, and planar half-space all show that the penetration decreases rapidly with frequency, and at the higher frequencies almost all of the power is absorbed in a small percentage of the volume near the surface.
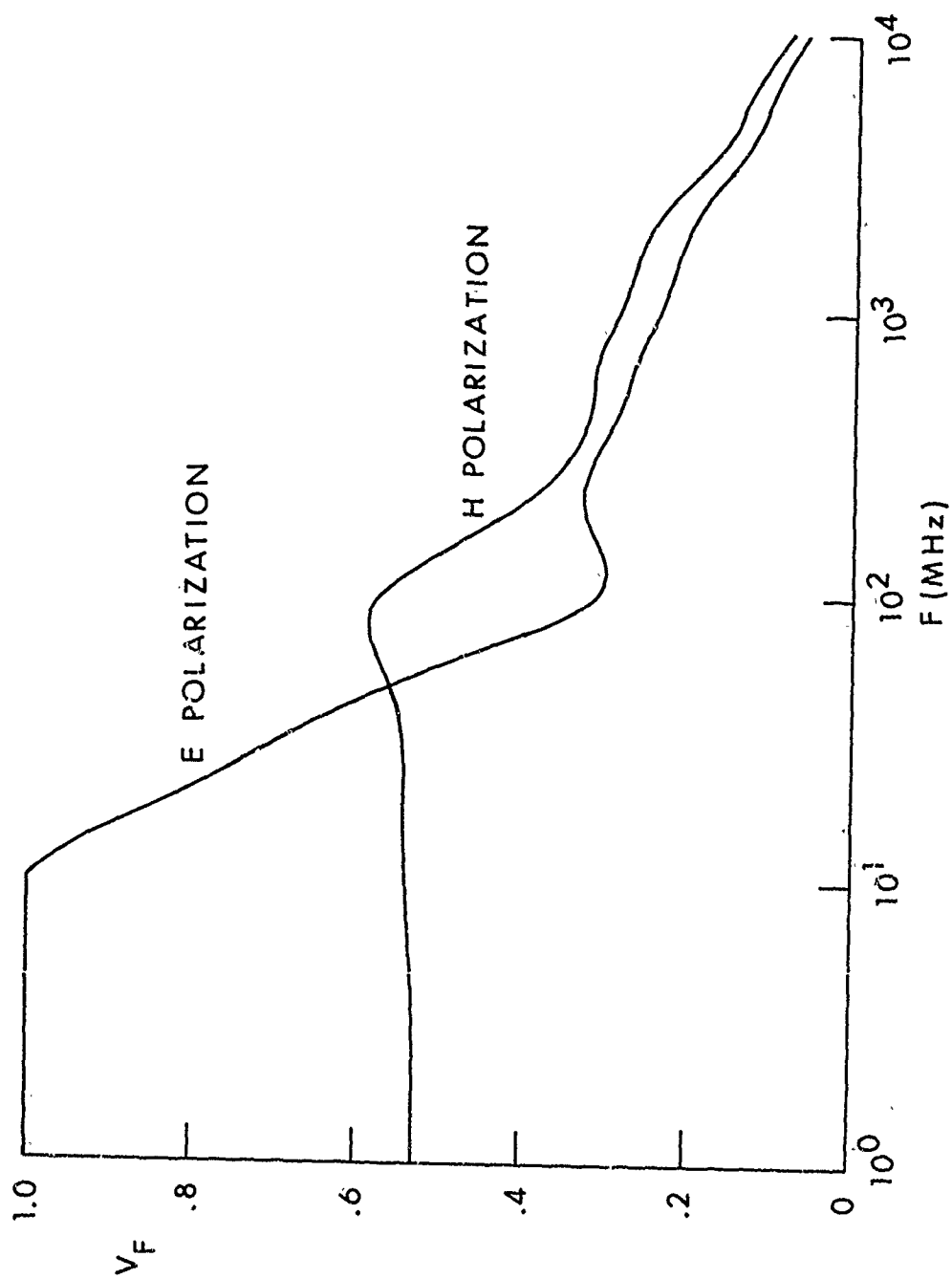
Figure 5.5. The volume fraction, V_F, as a function of frequency for a cylindrical model of an average man. V_F is the fraction of the volume in which 90% of the power is absorbed (see p. 5.15).
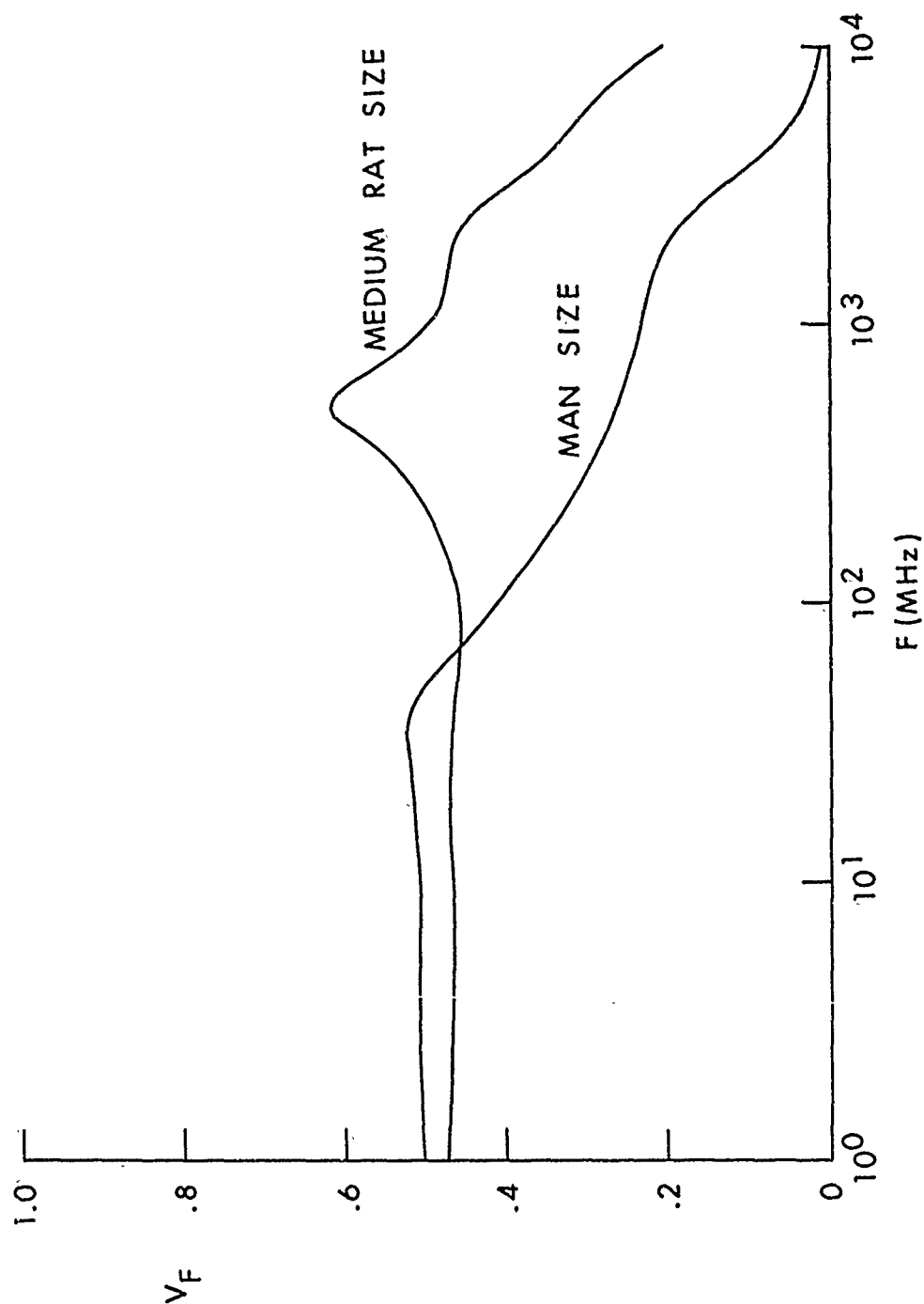
Figure 5.6. The volume fraction, V_F, as a function of frequency for two spheres of muscle material. V_F is the fraction of the volume in which 90% of the power is absorbed (see p. 5.15).

5.1.2. Near-Field Dosimetry

The methods used to calculate near-field SARs are similar to those used to calculate planewave SARs. Since the basic methods were described in Section 5.1.1, the comments here are directed mostly toward the differences required in using the techniques in near-field analyses.

Long-Wavelength Approximation--The long-wavelength approximation used for planewave calculations has been useful for some near-field calculations in spheroids. In the approximation for near fields, the incident near field is averaged along the major axis of the spheroid; the SARs calculated this way are surprisingly close to those calculated by more accurate methods. The advantage of the long-wavelength approximation is its relative simplicity.

Extended-Boundary-Condition Methods--By expanding the incident near fields in spherical harmonics, we have been able to use the EBCM for calculating near-field SARs. Since these calculations are more complex than those for planewaves, the EBCM may not be useful up to 80 MHz for near-field calculations, as it is for planewave calculations.

Iterative-Extended-Boundary-Condition Method--Expanding the incident near fields in spherical harmonics allows use of the IEBCM, which greatly extends the range of calculations possible with the EBCM, just as for planewave calculations.

Cylindrical Approximation--In planewave dosimetry, the SAR calculated for a cylinder was a good approximation to that calculated for a spheroid in the frequency range where the wavelength was short compared to the length of the spheroid. Similarly, the same approximation was valid for near-field calculations and was used in calculating SARs at frequencies above resonance for data in this report. In fact, for sources very close to an absorber, the cylindrical approximation is even better for near fields than for far fields. For the cylindrical models SAR calculations were made by the classical eigenfunction expansion method.

Planewave Spectrum Method—Chatterjee et al. (1980a, 1980b, 1980c, 1982b) expressed incident near fields in terms of a spectrum of planewaves and then used the moment method to calculate local and average SARs in a block model of man. Some of their data are summarized in Chapter 6.

5.1.3. Sensitivity of SAR Calculations to Permittivity Changes

Since there is some variability in the permittivity of people and other animals and some uncertainty in the measurement of permittivity of tissue-equivalent materials, knowing something about SAR sensitivity to permittivity changes is important. Figure 5.7 shows calculated average SAR as a function of frequency for several permittivity values in a prolate spheroidal model of an average man. For this case the SAR is not extremely sensitive to changes in permittivity. This appears to be generally true.

5.1.4. Relative Absorption Cross Section

Although commonly used in electromagnetics, particularly in describing the properties of objects detected by radar, the concepts of absorption cross section and scattering cross section apparently have not been used much by the bioelectromagnetics community. The basic concept of absorption cross section is explained here, and some examples of relative absorption cross sections are given.

The term "absorption cross section" (AC) is defined as the ratio of the total power absorbed by a target exposed to EM radiation to the incident-power density. The AC has the dimension of area and can be expressed in terms of the average SAR as

$$AC = \frac{SAR \times M}{P_{in}} \qquad (5.25)$$

where P_{in} is the incident power density and M is the mass of the object exposed to EM fields.
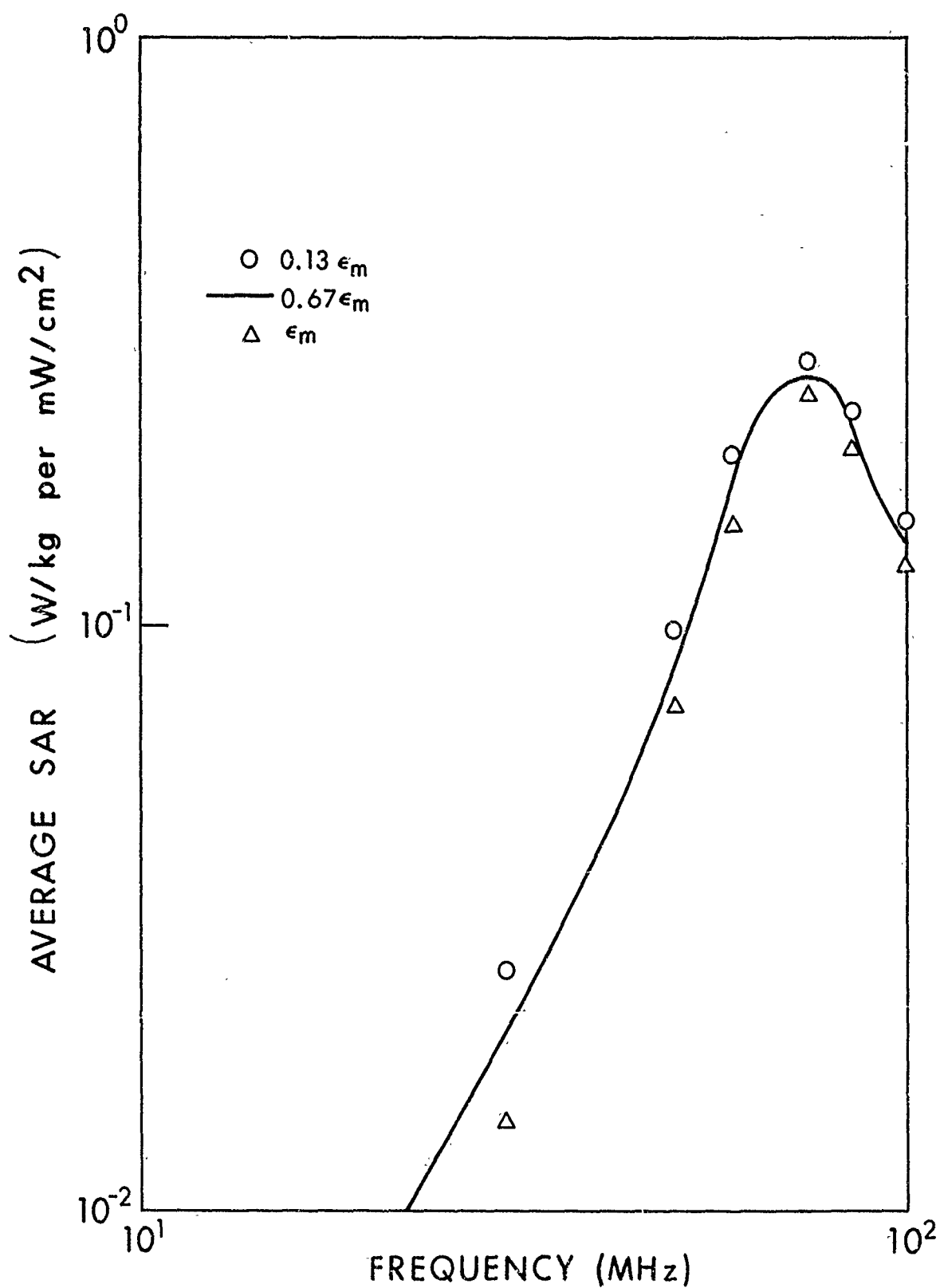
Figure 5.7. Calculated average SAR in a prolate sphercidal model of an average man, as a function of frequency for several values of permittivity. ε_m is the permittivity of muscle tissue.

The relative absorption cross section (RAC) is defined as the ratio of the AC to the geometrical cross section G, where G is the body's cross-sectional area projected onto a plane perpendicular to the direction of propagation of the incident wave (e.g., $G = \pi a^2$ for a sphere of radius a). The RAC is a dimensionless number and is a measure of the object's ability to absorb EM energy. For an arbitrarily shaped body, the RAC depends on the orientation of the body with respect to the polarization of the EM fields. In terms of the average SAR, it can be expressed as

$$RAC = \frac{SAR \times M}{P_{in} \times G} \qquad (5.26)$$

The relative scattering cross section (RSC) is defined as

$$RSC = \frac{P_{sc}}{P_{in} \times G} \qquad (5.27)$$

where P_{sc} is the total power scattered by the object. The RSC shows how effective the geometric cross section is in scattering the power it intercepts. Graphs of the RAC are shown in Figure 5.8 for prolate spheroidal models of an average man, a rabbit, and a medium-sized rat--in the frequency range from $10-10^5$ MHz and for the most highly absorbing polarization, E polarization. The data in Figure 5.8 show that the RAC is a strong function of frequency and shape; also, near resonance the effective cross-sectional area in terms of total energy absorbed is greater than the geometric cross section of the body. Figure 5.9 shows the RAC and the RSC for a prolate spheroidal model of a medium rat.

At low frequencies the RSC varies as f^4; this is called the Rayleigh scattering region. Rayleigh scattering is independent of the shape of the object. Also at low frequencies the size of the object is small compared to a wavelength, the object does not interact strongly with the EM fields, and the RAC and RSC are therefore both very small. Near resonance, where the length of the object is about a half-wavelength, the interaction is very strong and both the RAC and the RSC are greater than unity. For the model of Figure 5.9, near resonance the RSC is greater than the RAC, which means that this model is a more effective scatterer than absorber.
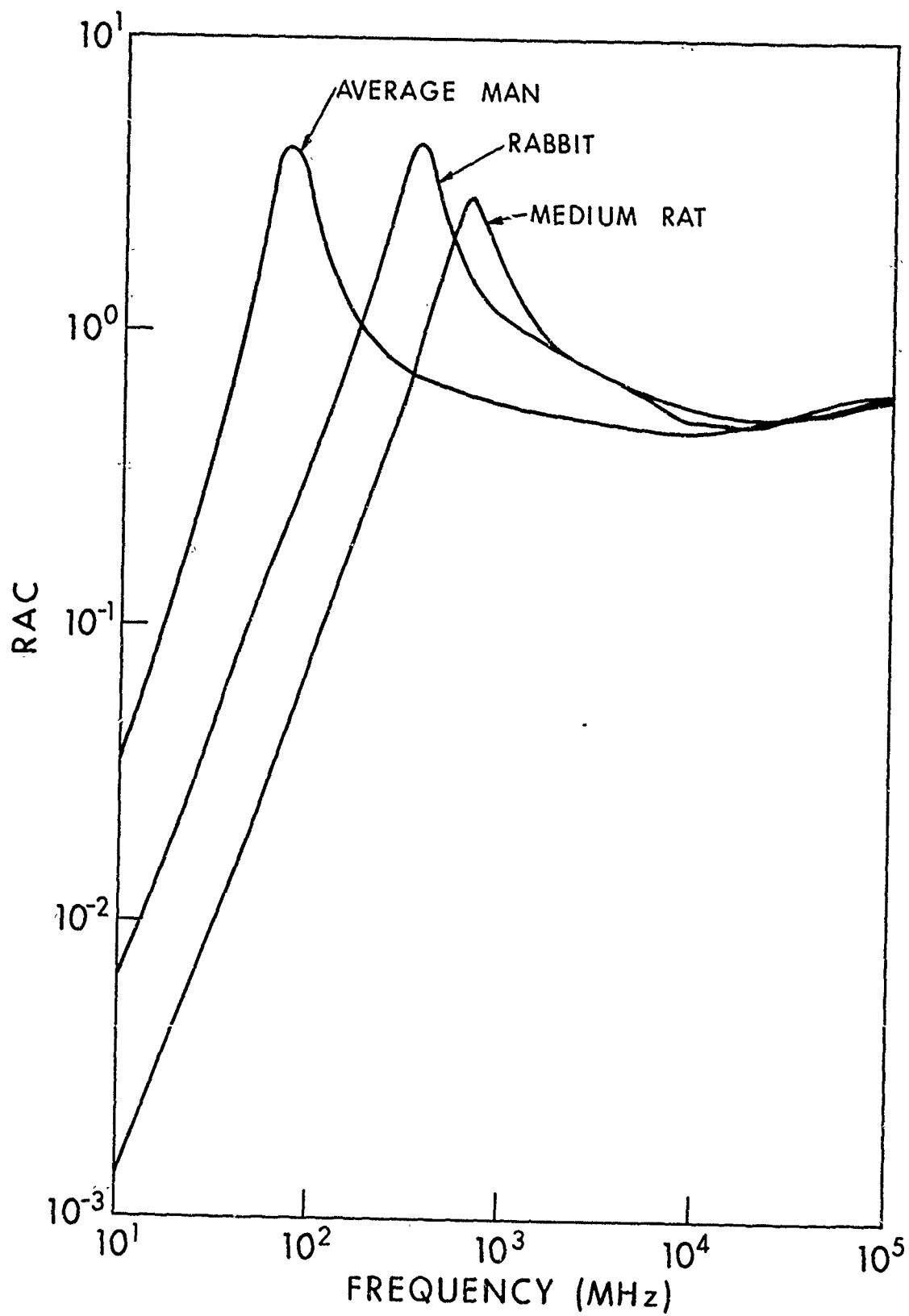
Figure 5.8.   Relative absorption cross section in prolate spheroidal models of an average man, a rabbit, and a medium-sized rat—as a function of frequency for E polarization.
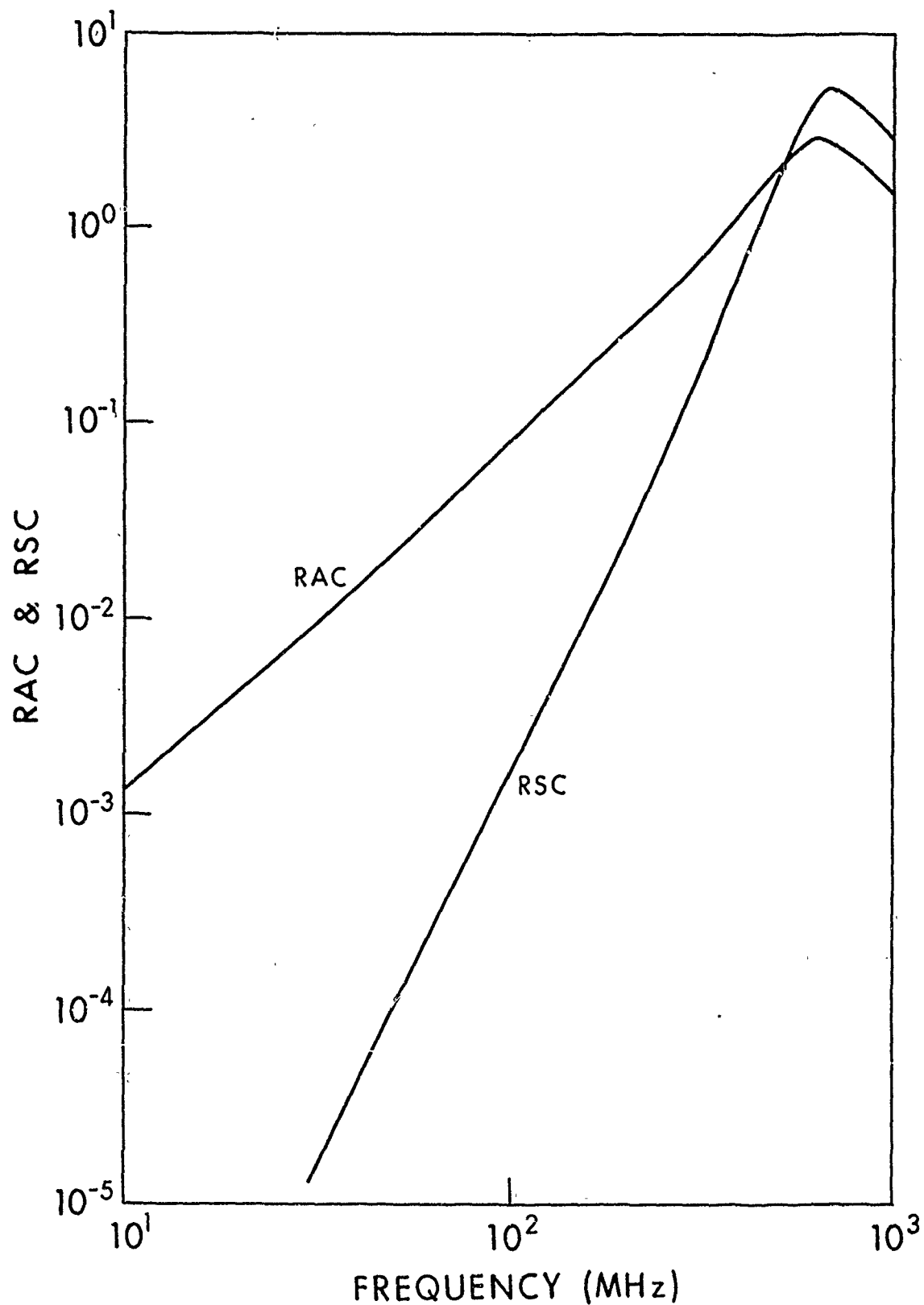
Figure 5.9. Comparison of relative scattering cross section (RSC) and relative absorption cross section (RAC) in a prolate spheroidal model of a medium rat--for planewave irradiation, E polarization.

The three graphs shown in Fig. 5.8 would lie almost on top of each other if they were normalized to the resonant frequencies, which suggests a possibility of a universal RAC graph. Our calculations showed, however, that the graphs are probably not close enough to make a universal curve useful except possibly for very approximate estimates.

5.1.5. Qualitative Dosimetry

Since calculating dosimetric data is usually difficult, time consuming, and expensive, obtaining the desired dosimetric information for a given experiment or application is not always possible. Often, therefore, just having a rough estimate of the dosimetric results to be expected would be useful, both to decide whether further work is justified and to guide and check experiments. This is especially true for near-field dosimetry.

Researchers doing experiments that involve near-field irradiation are apt to find that the near-field SAR curves in this handbook do not correspond closely to those for their irradiation conditions. Near-field radiation varies greatly from source to source, and we have no ready way to normalize the calculated SARs to the incident fields, as we have for planewave irradiation. Consequently it is not practical to give a set of normalized near-field SAR curves to use for predicting SARs in specific experiments, as it is for planewave SARs. However, by having near-field SARs for some typical simple sources (as given in Chapter 6), along with qualitative explanations of how the near-field SARs are related to the incident fields, we can at least predict relative values of SARs for given exposure conditions. In this section, some of the basic characteristics of EM fields described in Chapter 3 are used to develop in more detail some techniques for estimating relative values of SARs, both for far-field and near-field irradiation. These techniques are based on two qualitative relations described earlier: the boundary conditions on the E-field and the magnetic flux intercepted by the absorber.

Estimating Values of Internal Fields—As explained in Chapter 3, at a boundary between two media with different complex permittivities, the E-field must satisfy the following two boundary conditions:

$$E_{1p} = E_{2p} \qquad\qquad (5.28)$$

$$\varepsilon_1 E_{1n} = \varepsilon_2 E_{2n} \qquad\qquad (5.29)$$

where E_{1p} and E_{2p} are components parallel to the boundary, and E_{1n} and E_{2n} are components perpendicular to the boundary, as shown in Figure 5.10. It is important to remember that Equations 5.28 and 5.29 are valid only at a point on the boundary. From Equation 5.29, we can see that $E_{2n} = \varepsilon_1 E_{1n}/\varepsilon_2$; and if $\varepsilon_2 \gg \varepsilon_1$, then $E_{2n} \ll E_{1n}$. Thus if E_{1n} is the field in free space and E_{2n} is the field in an absorber, the internal field at the boundary will be much weaker than the external field at the boundary when $\varepsilon_2 \gg \varepsilon_1$ and the fields are normal to the boundary. Also, from Equation 5.28, we see that the external field and the internal field at the boundary are equal when the fields are parallel to the boundary. These two results will be used extensively in explaining relative energy absorption.
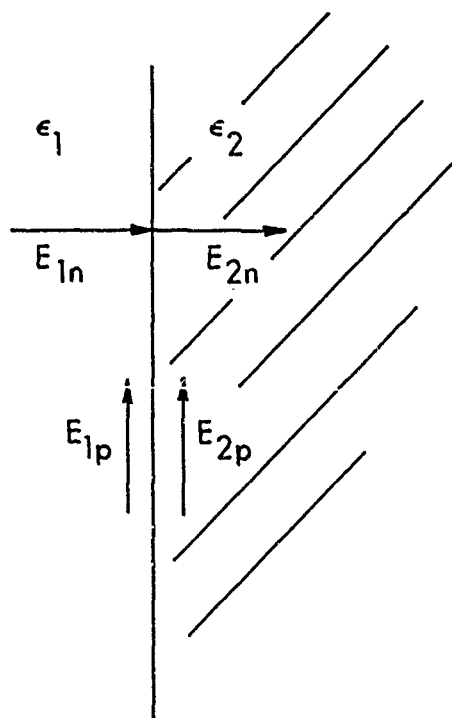
Figure 5.10. Field components at a boundary between two media having different complex permittivities, ε_1 and ε_2.

Boundary conditions are not as important on the H-field as on the E-field for explaining relative energy absorption in biological materials because they are usually nonmagr tic $(\mu = \mu_o)$ and have no significant effect on the H-field itself at the boundary. Another relation between the incident H-field and the internal E-field, however, is useful in explaining qualitatively the relative strengths of internal fields.

From the integral form of Maxwell's equation,

$$\oint E \cdot d\ell = -\mu \int \frac{\partial H}{\partial t} \cdot dS \qquad (5.30)$$

For the very special case of a lossy dielectric cylinder in a uniform H-field, Equation 5.30 can be solved by deducing from the symmetry of the cylinder and fields that E will have only a ϕ component that will be constant around a circular path, such as the one shown dotted in Figure 5.11. For E constant along the circular path, and H uniform, Equation 5.30 reduces to

$$2\pi r E_\phi = -\mu \frac{\partial H}{\partial t} \pi r^2$$

$$E_\phi = -\mu \frac{\partial H}{\partial t} \frac{r}{2} \qquad (5.31)$$

Thus, Equation 5.30 shows that E is related to the rate of change of the magnetic flux intercepted by the object; and Equation 5.31 shows that for the very special case of Figure 5.11, the E-field circulates around the H-field and is directly proportional to the radius. For this example the circulating E-field (which produces a circulating current) would be larger for a larger cross section intercepted by the H-field. The generalized qualitative relation that follows from Equation 5.30 is that the circulating field is in some sense proportional to the cross-sectional area that intercepts the H-field. This result is very useful in qualitative explanations of relative energy-absorption characteristics; however, this qualitative explanation cannot be used indiscriminantly.
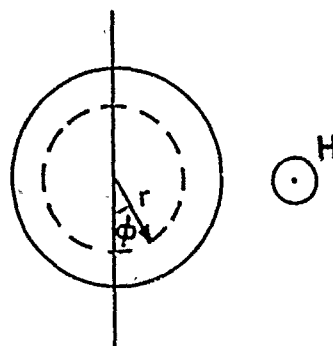
Figure 5.11. A lossy dielectric cylinder in a uniform magnetic field.

The qualitative relations obtained above from the boundary conditions on E and the circulating E-fields produced by H can be used to explain the relative energy-absorption characteristics in terms of some relations that are strictly valid only at low frequencies. The qualitative explanations thus derived, however, appear to be useful at higher frequencies also.

At lower frequencies the internal fields can be thought of as being generated by the incident E and incident H separately. That is, there will be two sets of internal E-fields: one generated by the incident E and one generated by the incident H. The total internal E-field is the sum of these two internal E-fields, i.e.,

$$E_{in} = E_e + E_h \tag{5.32}$$

where

E_e = The internal E-field generated by E_{inc} (incident E-field)

E_h = The internal E-field generated by H_{inc} (incident H-field)

E_{in} = The total internal E-field

E_e = The magnitude of the vector field E_e (with similar notation for E_h, E_{in}, and other vectors)

At low frequencies E_e can be calculated from E_{inc}, and E_h from H_{inc}, and the two are added as in Equation 5.32 to obtain E_{in}. This procedure cannot be followed, however, at the higher frequencies, where the E- and

H-fields are strongly coupled together by Maxwell's equations. Instead, E_e and E_h are strongly interactive and must be calculated simultaneously. However, the qualitative explanations based on the separate calculations of E_e and E_h and the use of Equation 5.32 seem to have some validity at higher frequencies, perhaps even up to resonance in some cases.

The basis for qualitative explanations of the relative strength of E_{in} can be based on two qualitative principles (QP):

QP1. E_e is stronger when E_{inc} is mostly _parallel_ to the boundary of the object and _weaker_ when E_{inc} is mostly _perpendicular_ to the boundary of the object.

QP2. E_h is _stronger_ when H_{inc} intercepts a _larger_ cross section of the object and _weaker_ when H_{inc} intercepts a _smaller_ cross section of the object.

Figure 5.12 shows some examples of qualitative evaluations of internal fields based on these principles. For clarity only simple objects are shown in the illustrations, but the principles can be used with more complicated shapes (e.g., the human body). The dependence of the planewave SAR on polarization can be explained on the basis of QP1 and QP2, as illustrated by the summary in Table 5.1 (refer to Figure 3.37 for the orientations of the incident fields for each polarization).
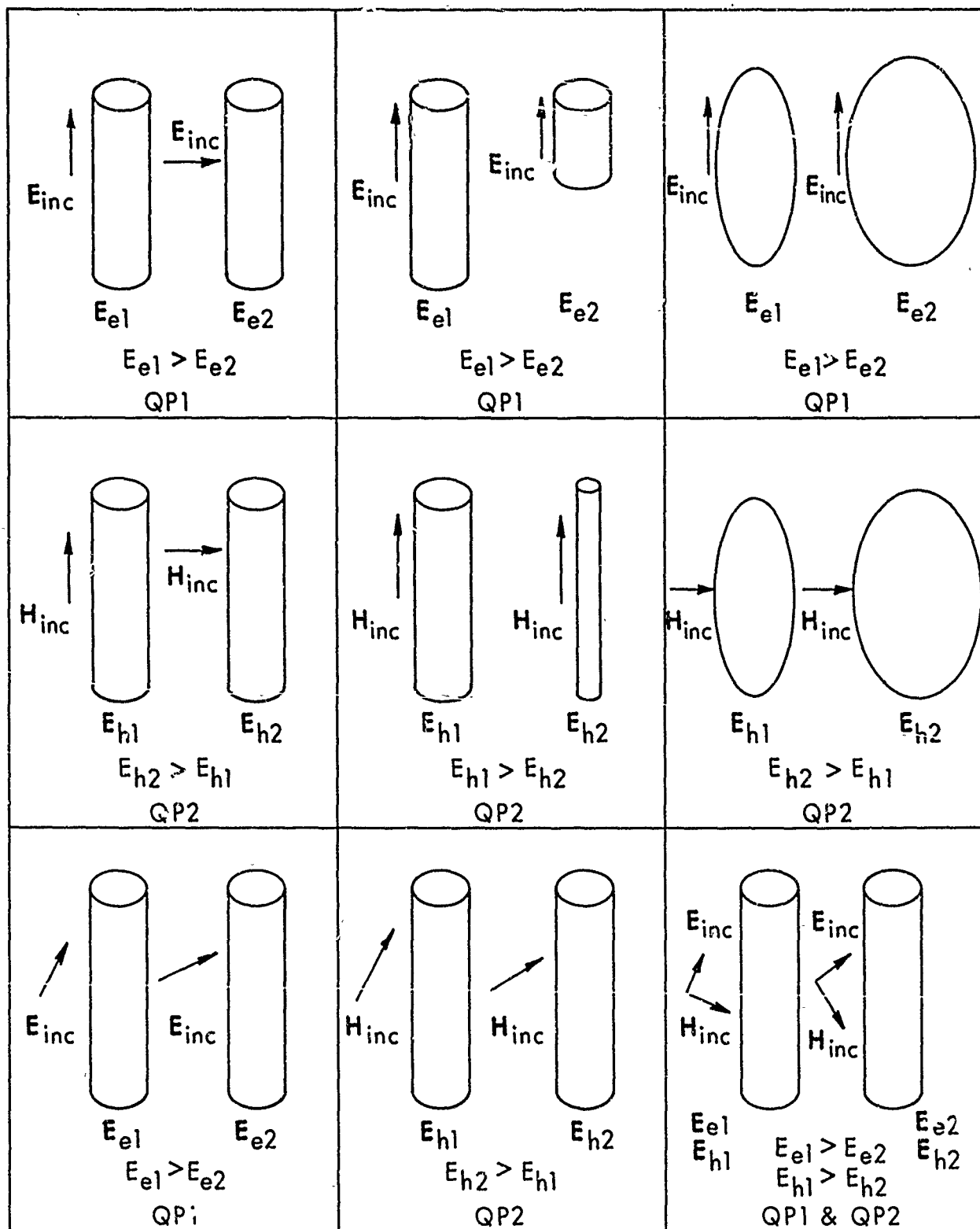
Figure 5.12. Qualitative evaluation of the internal fields based on qualitative principles QP1 and QP2. E_e is the internal E-field generated by E_{inc}, the incident E-field, and E_h is the internal E-field generated by H_{inc}, the incident H-field.

- 5.29 -

TABLE 5.1   APPLICATION OF QP1 AND QP2 TO PLANEWAVE SARS

	E_{inc}	H_{inc}	E_e	E_h	Relative SAR
E polarization	Mostly parallel	Intercepts large cross section	Strong	Strong	Highest
K polarization	Mostly normal	Intercepts large cross section	Weak	Strong	Middle
H polarization	Mostly normal	Intercepts small cross section	Weak	Weak	Lowest

Since E_e and E_h are both strong for E polarization, its relative SAR is the highest. The weak E_e and E_h make the relative SAR of H polarization the lowest, with that of K polarization between the two. Note that for H polarization the cross section intercepted by H_{inc} is circular, also smaller than the elliptical cross section intercepted by H_{inc} in E and K polarization.

From the limited amount of available near-field absorption data, QP1 and QP2 appear also to be very useful in explaining near-field dosimetric characteristics. For example, consider Figure 8.20, the measured relative SAR in man and monkey spheroidal models irradiated by a short electric monopole antenna on a ground plane. At first it may seem surprising that the SAR increases more slowly than $(\lambda/d)^2$, since the magnitude of the E- and H-fields is expected to increase more rapidly than λ/d in the near-field region. However, the reasons for the shape of the SAR curve may be found from Figure 8.21, which shows the behavior of the measured fields of the antenna (designated E_{inc} and H_{inc} with respect to an absorber). The direction of the H_{inc} does not change with d, but the magnitude of H_{inc} increases faster than λ/d for $d/\lambda < 0.3$. The direction of E_{inc}, however, changes significantly with d. In the far field, the angle α between E_{inc} and the long axis of the spheroid is zero; but at $d/\lambda = 0.1$, it is about $70°$. According to QP1, this change in angle has a significant effect on E_e. Thus the change in SAR with d/λ results from three factors:

1. E_e increases as the magnitude of E_{inc} increases.
2. E_e decreases as α increases.
3. E_h increases as the magnitude of H_{inc} increases.

Even though E_h increases faster than λ/d, E_e increases much more slowly than λ/d because of the combination of factors 1 and 2. The average SAR, which is proportional to E_{in}^2, does not increase as fast as $(\lambda/d)^2$ because E_e affects E_{in} more than E_h does. On the other hand, since the monkey-size spheroid is relatively shorter and fatter than the man-size spheroid, E_h has a stronger effect on E_{in} for the monkey than for the man. Consequently, the SAR for the monkey increases more rapidly as d decreases than does the SAR for the man.

Similarly, the variation of the relative SARs in Figure 6.31 can be explained in terms of the antenna-field behavior, as shown in Figures 6.37–6.39. In Figure 6.31 the relative SAR curves for 10, 27.12, 50, and 100 MHz lie very close together, while those for 200 and 300 MHz differ significantly for some values of d/λ. The reasons for this can be seen from Figures 6.37–6.39:

1. E_{inc} is slightly lower at 200 MHz and significantly lower at 300 MHz than at the other frequencies.
2. H_{inc} is lower at 200 and 300 MHz than at the other frequencies.
3. The angle α of E_{inc} with the z axis is significantly higher at 200 and 300 MHz than at the other frequencies.

E_{inc} is not the strongest factor since it is not much less at 200 than at 100 MHz, but the relative SAR is significantly less at 200 MHz than at 100. The dominant factor is α. According to QF1, as α increases, the SAR decreases. The effect of α can be seen from the 300-MHz curve which begins to rise rapidly at $y/\lambda = 0.3$, where α decreases steeply. A surprising aspect of the correspondence between incident-field characteristics and the relative SAR characteristics is that the correlation was based on the values of the incident fields at only one point in space.

Some other important SAR characteristics are the differences between the relative SARs for K and H polarization (Figures 6.32, 6.33) as compared to E polarization (Figure 6.31). Although the variation of the E_{inc} with respect to λ/y (as shown in Figure 6.37) for $0.15 < y/\lambda < 0.5$ is slower than λ/y, the relative SARs for an absorber at distance d from the dipole for both H and

K polarizations vary faster than $(\lambda/d)^2$ in this region (as seen in Figures 6.32 and 6.33). From the nature of the incident fields (as shown in Figures 6.37-6.39), E_h appears to dominate for K and H polarizations, while E_e dominates for E polarization. The same behavior is shown in a different way in Figure 5.13, where the calculated average SAR for a prolate spheroidal model of an average man is shown as a function of $\eta = E_{inc}/\eta_o H_{inc}$, the normalized field impedance, with E_{inc} constant at 1 V/m. The curves show the characteristic behavior that results when the impedance deviates from the planewave case ($\eta = 1$). Since E_{inc} is constant, small η means large H_{inc}; thus, for a very small η, H_{inc} dominates and E polarization and K polarization become equivalent.

The important information furnished by the curves in Figure 5.13 is that the SAR changes significantly with the H_{inc} field for K and H polarizations, but changes very little with the H_{inc} for E polarization in the range $0.5 < \eta < 1.5$, which, according to Figure 6.40, is the range of interest. This means that the contribution of the H_{inc} to the average SAR dominates for K and H polarizations, while the contribution of the E_{inc} dominates for E polarization, as explained by Durney et al. (1975) and in the report by the National Council on Radiation Protection and Measurements (1981). Thus, for K and H polarization, the SAR in the long-wavelength region follows the H_{inc} variation and therefore lies above the $(\lambda/d)^2$ variation, as shown in Figures 6.32 and 6.33.

Further insight at low frequencies is provided by the information in Figure 5.14, which shows the ratio of the SAR produced by E_e to that produced by E_h for a 0.07-m^3 prolate spheroidal model at 27.12 MHz for each of the three polarizations. For a/b < 3.5, E_h dominates in all three polarizations; but for a/b > 3.5, E_e dominates in E polarization and E_h dominates in H and K polarization. This is shown only for a conductivity of 0.4 S/m and at low frequencies, but it appears that E_h usually dominates in H and K polarization, while E_e dominates in longer, thinner models for E polarization. Note that QP1 and QP2 cannot be used to compare E_e and E_h for different polarizations; they can be used only to compare the E_e for one set of conditions to the E_e for another set, and the E_h for one set of conditions to the E_h for another set.
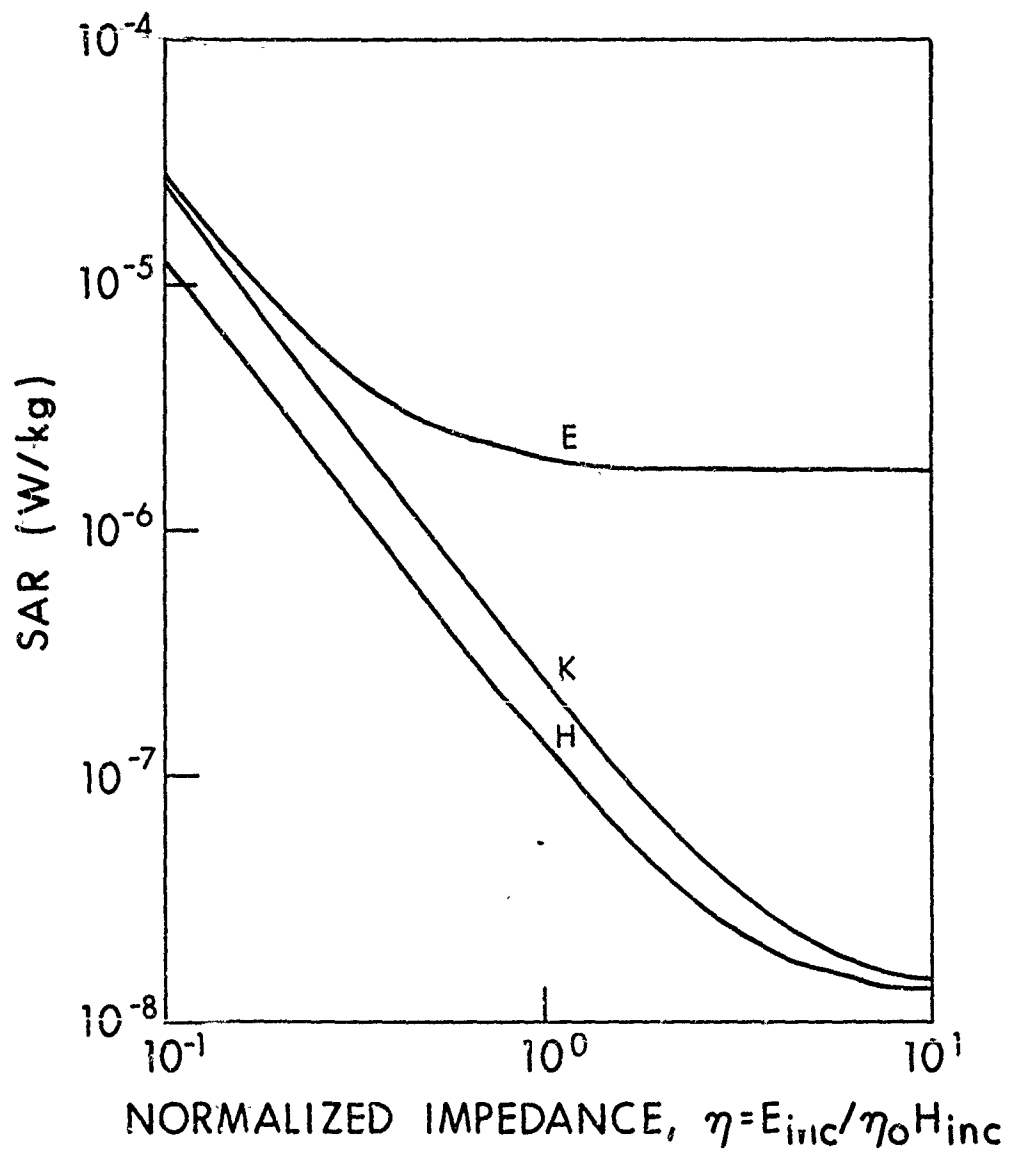
Figure 5.13. Average SAR in a prolate spheroidal model of an average man as a function of normalized impedance for each of the three polarizations. (a = 0.875 m, b = 0.138 m, f = 27.12 MHz, σ = 0.4 S/m, incident E-field is 1 V/m.)
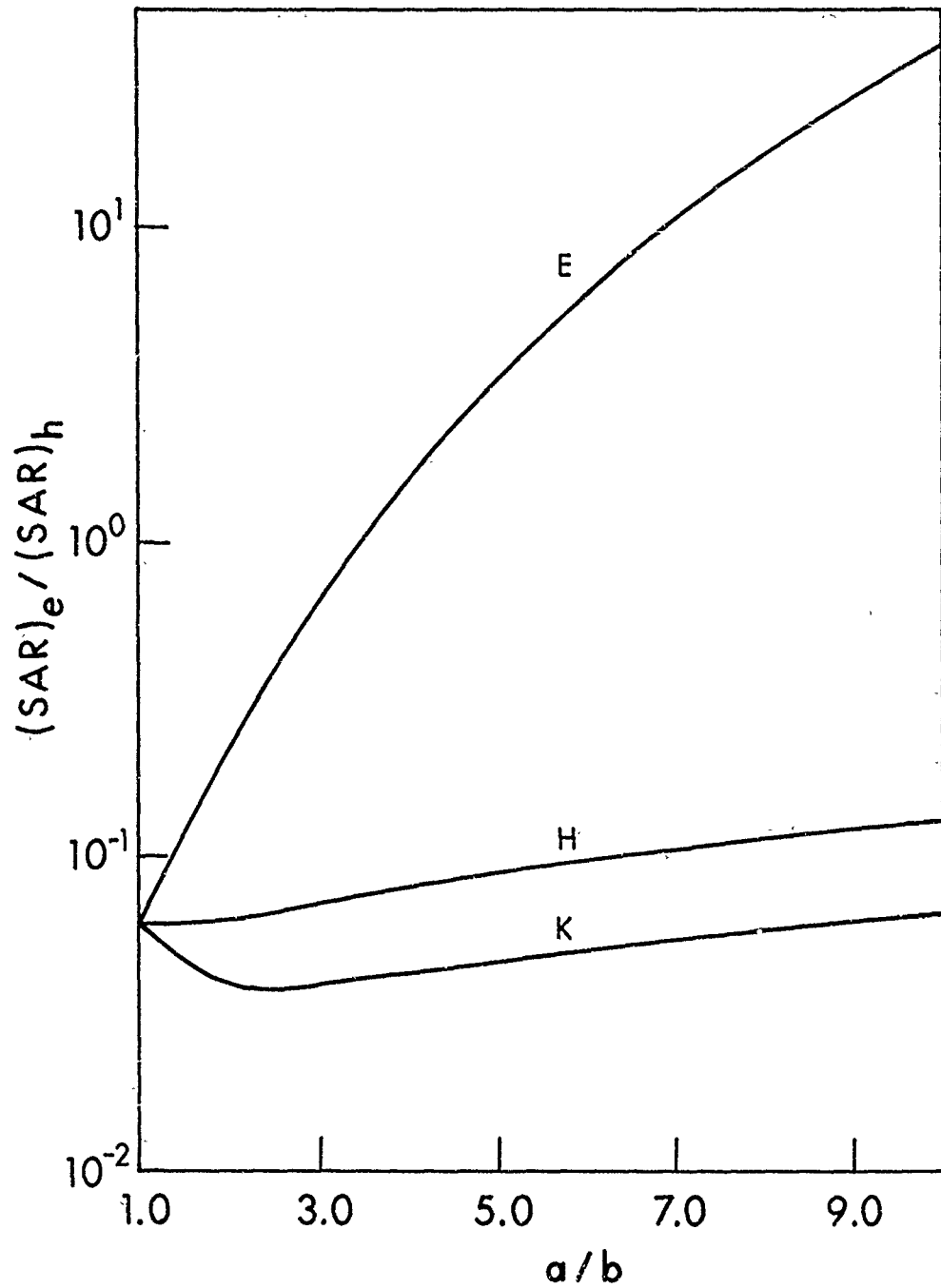
Figure 5.14. Ratio of $(SAR)_e$ to $(SAR)_h$ of a 0.07-m^3 prolate spheroid for each polarization as a function of the ratio of the major axis to the minor axis of the spheroid at 27.12 MHz, $\sigma = 0.4$ S/m.

5.2. DATA FOR MODELS OF BIOLOGICAL SYSTEMS

The average weight and height and the calculated values of semiaxes b and c for ellipsoidal and prolate spheroidal models are given in Tables 5.2 through 5.4. Except items for the Long Evans or Sprague-Dawley rat, IC Swiss Webster mouse, and chicken and quail eggs, which are based on a few measurements in our laboratory, weight and height data were compiled by averaging values contained in the following references: Colliers Encyclopedia, 1971; Dreyfuss, 1967; Encyclopedia Britannica, 1966; Encyclopedia Americana, 1975; Grizmek's Animal Life Encyclopedia, 1975; Jordan, 1969; Walker et al., 1964. The tissue of all the species is assumed to be 1 g/cm^3. The cylindrical models have the same weight and height as the prolate spheroidal models.

TABLE 5.2.   AVERAGE WEIGHT AND LENGTH AND CALCULATED VALUE OF b
FOR PROLATE SPHEROIDAL MODELS OF ANIMALS AND EGGS

Species	Average weight (kg)	Average length, 2a (cm)	b (cm)
Rhesus monkey	3.5	40.0	6.46
Squirrel monkey	1.1	23.0	4.78
Dogs			
German shepherd	32.0	90.0	13.03
Brittany spaniel	15.9	68.8	10.50
Beagle	13.5	57.0	10.63
Rabbit	1.0	40.0	3.45
Guinea pig	0.58	22.0	3.55
Small rat	0.11	14.0	1.94
Medium rat	0.32	20.0	2.76
Large rat	0.52	24.0	3.22
Small mouse	0.015	5.4	1.15
Medium mouse	0.020	7.0	1.17
Large mouse	0.025	7.6	1.25
Pupae (blow fly or mealworm)	1.96×10^{-4}	1.5	0.25
Chicken egg	0.060	5.8	2.22
Quail egg	0.010	3.0	1.26

TABLE 5.3. AVERAGE WEIGHT AND HEIGHT AND CALCULATED VALUES OF
b AND c FOR ELLIPSOIDAL MODELS OF HUMAN-BODY TYPES

Species	Average weight (kg)	Average height, 2a (m)	b (m)	c (m)
Average man	70.00	1.75	0.195	0.098
Average ectomorphic (skinny) man	47.18	1.76	0.160	0.080
Average endomorphic (fat) man	141.00	1.76	0.225	0.170
Average woman	61.14	1.61	0.200	0.091
Small woman	43.09	1.45	0.180	0.079
Large woman	88.45	1.73	0.215	0.114
10-year-old child	32.20	1.38	0.143	0.078
5-year-old child	19.50	1.12	0.120	0.069
1-year-old child	10.00	0.74	0.095	0.068

TABLE 5.4. AVERAGE WEIGHT AND HEIGHT AND CALCULATED VALUE OF b
FOR PROLATE SPHEROIDAL MODELS OF HUMAN-BODY TYPES

Species	Average weight (kg)	Average height, 2a (m)	b (m)
Average man	70.00	1.75	0.138
Average ectomorphic (skinny) man	47.18	1.76	0.113
Average endomorphic (fat) man	141.00	1.76	0.195
Average woman	61.14	1.61	0.135
Small woman	43.09	1.45	0.120
Large woman	88.45	1.73	0.156
10-year-old child	32.20	1.38	0.106
5-year-old child	19.50	1.12	0.091
1-year-old child	10.00	0.74	0.080

5.3. TABULATED SUMMARY OF PUBLISHED WORK IN THEORETICAL DOSIMETRY

Theoretical studies of the SAR in biological models have been of increasing interest in recent years. The analyses started with simple geometrical models, such as homogeneous planar and spherical models. More complicated numerical methods have now been used, and calculations are available for inhomogeneous realistic models of man.

In general the SAR depends on body shape, frequency, polarization, E and H vector fields, presence of ground plane and reflectors, and dielectric composition. The shape of the model basically dictates the appropriate expansion functions to be used in an analytical solution. Frequency, on the other hand, determines the method of solution. Other factors, such as excitation and layering, can be included by extending the appropriate technique.

In Table 5.5 we summarize the theoretical techniques used to calculate the SAR in models of man and animals. The table is divided into three basic divisions according to how complex the model's shape is. The one-dimensional models are the simplest and are particularly useful at higher frequencies where the body curvature can be neglected. Such models, however, cannot predict body resonance that occurs in three-dimensional models. The two-dimensional models are basically single or multilayered cylindrical geometries suitable to simulate limbs. The three-dimensional case includes models of idealized shapes, such as spheres, spheroids, and ellipsoids, as well as more realistic block models of man.

TABLE 5.5. COMPARISON OF THEORETICAL METHODS USED IN LITERATURE TO CALCULATE THE POWER ABSORPTION BY BIOLOGICAL MODELS

Shape	Dimensions	Excitation	Method	Frequency Range	Reference*	Remarks
A. One-dimensional models						
Infinite plane tissue layers (isotropic)	Multilayers	Planewave	Transmission-line model	Unlimited	a	Good only at high frequencies where the body curvature can be neglected. Can predict λ/4 type resonances but not body resonance.
	Two layers	Rectangular aperture	Fourier transform technique and field matching on common boundaries	433-2450 MHz	b, c	Used to calculate relative heating patterns.
(Anisotropic)	Multilayers	Planewave	Transmission-line model (together with Thévenin's theorem)	0.001-100 MHz	d	Used to calculate effects of tissue anisotropy (at low frequencies) on microwave fields and power absorption. Small effects observed at higher frequencies (above 10 MHz).
Semi-infinite homogeneous slab	One layer	Nonperiodic electric field with TE and TM components	Planewave spectrum analysis	All calculations at 2450 MHz	e	Near-field analysis of aperture sources.
	Six layers	E-polarized planewave	Optical refraction— Snell's law	Up to 3.0 GHz	f	Layering increases average SAR; an enhancement factor needed to correct results from homogeneous models.
Homogeneous semi-infinite slab and multi-layered slab	—	Near field of a source leaking radiation	Planewave-spectrum approach	2450 MHz	g, h	For fields nearly constant over at least a free-space wavelength, energy deposition equal to or less than that resulting from planewave exposure. In the analysis, coupling of target to source not taken into account.
B. Two-dimensional models						
Infinite circular cylinder	Length ℓ = 1.75 m, radius a = 11.3 cm; ℓ = 14 cm, a = 1.58 cm	Planewave	Mode-matching technique and geometrical optics	300-6000 MHz; 25-50 GHz	i, j	In good agreement with geometrical optics at the high-frequency limit.
	Radius such that $\sqrt{\epsilon-1}\, k_o a < 2.4$	Coaxial loop antenna	Long-wavelength approximation method	Depends on $\sqrt{\epsilon-1}\, k_o a < 2.4$	k	Formulation simple to use, but valid results are in low-frequency range. Power absorption coefficient is plotted against loop dimensions and cylinder radius.

Model	Source	Method	Frequency	Ref	Remarks
5- and 10-cm-radius cylinders in presence of a reflector	Planewave TE and TM with k vector normal to plane of a reflector	Point-matching method combined with imaging	Up to 1 GHz	ℓ	SAR calculated as function of frequency and distance from reflector.
Radius: 2.24–24 cm	Planewave E and H polarization	a. Geometrical optics approximation b. Mode-matching technique	20–100 GHz	j	At higher frequencies the two methods give same result. Average SAR results tally with those from prolate spheroidal models at higher frequencies.
Multilayered infinite circular cylinder	———	Planewave	Mode-matching technique and moment method	433–2450 MHz	m, n	Microwave heating calculated in simulated human thigh.
Three layers	Direct contact aperture source (TE$_{10}$ mode)	Field expansion in terms of three-dimensional cylindrical waves and matching the boundary conditions	433–2450 MHz	o	Microwave heating calculated in phantom models of human limbs exposed to a direct-contact aperture source.
Multilayered cylinders of arbitrary cross section	a = 1.5 b, a = 0.239 m, b = 0.159 m for elliptical cylinder	Planewave	Surface integral equations derived via vector Green's theorem and boundary condition	All calculations at 300 MHz	p	Calculations made for one- and two-layered circular and elliptical cylinders.
17.5- × 19-cm triple-layered model	Planewave TM	Finite element	433 MHz	q	Finite element method and variational calculus used to approximately calculate internal fields. Results presented only for normalized inside field.
Multilayered infinite circular cylinders	Outer radius 11.28 cm	Planewave E and H polarization		10 MHz–10 GHz	r	Absorption effects due to clothing are negligible below 2 GHz. Layering changes average SAR values in the 0.4- to 8-GHz frequency range.
Homogeneous infinite cylinder	62.6 × 62.6 cm	Planewave E polarization	Stacked two-dimensional spectral iterative technique (SIT)	915 MHz, 2450 MHz	s	Method based on modeling the body by a set of planar parallel slabs and utilizing a convolution-type relationship between a current distribution on any slab and the field due to this current. Calculated data for the SAR distribution are given for two infinite planar layers, a cylindrical muscle structure, and a thin muscle box.

* References are listed at end of table.

TABLE 5.5. (continued)

Shape	Dimensions	Excitation	Method	Frequency Range	Reference	Remarks
Homogeneous infinite circular cylinder	Radius = 5 cm	Near field of electric and magnetic line sources	Mode-matching technique	27, 100, and 300 MHz	t	With proper choice of geometry and polarization of the sources, it is possible to have deep penetration with maximum heating at the center and to move the maximum around.
Inhomogeneous infinite cylinders with arbitrary cross section	Cross section of a human torso	EM planewave and a solenoidal field	Galerkin's method with linear basis function	Low-frequency region	u	Arbitrarily shaped polygonal cells are used to allow more accurate modeling of complex objects without excessive matrix sizes.
		Annular phased array system	Moment method with pulse basis function	70 MHz	v	SAR distribution calculated in two-dimensional models. Cross sections of the human body. Numerical results agree with measured values in central region of the cross section.

C. Three-dimensional models

Shape	Dimensions	Excitation	Method	Frequency Range	Reference	Remarks
Finite planar model	16 × 12 × 4 cm for a fat muscle tissue block and 3 × 0.5 × 0.5 λ for a muscle	Planewave	Tensor integral equation for the electric field inside the body	Results presented up to 2.45 GHz	w	Method applicable for heterogeneous biological bodies.
Finite circular cylinder	Height/radius $\ell/r_o = 12.68$	E-polarized planewave	a. Antenna theory b. Curve fitting used along with circuit theory	1-60 MHz	x	For human model in direct contact with a ground plane, an order-of-magnitude enhancement in SAR value may occur at frequencies below resonance. Enhancement rapidly decreases as model moves away from ground plane. Separation distance of about 7.5 cm from ground plane is sufficient to restore free-space absorption characteristics.
Spherical model	Radius of the sphere r = 10 cm	Planewave	Mie theory	10-10,000 MHz	y, z	Examined distribution of generated heat.
	r = 25.57 cm	Planewave	Mie theory	1-20 MHz	aa, bb	Power deposition in a spherical model of man ~70 kg.

Model	Source	Method	Frequency	Ref.	Description
r = 5 cm	Planewave	Mie theory	10-12,000 MHz	cc	Distribution of heating potential.
r = 10 cm	Planewave	Mie theory	100-10,000 MHz		Type of nonuniformity described in a radius-frequency diagram. Localized heating for 8 cm < a < 0.1 cm in the frequency range 300 MHz < f < 12 GHz is described.
2 < r < 50 cm, experimental results for r = 3 and 7 cm	Planewave	Mie theory	915 and 2450 MHz	dd	Used to calculate heating patterns in mammalian brains. Selective absorption also indicated.
Human head (7-cm radius) and infra-human head	E-polarized planewave	Tensor integral equation method	918 MHz for infrahuman head; 2450 MHz for human head	ee	Comparison made between heating of spherical and realistic models of humans and infrahuman heads. Lower EM heating induced in brain of realistic model than spherical model. Skull's bony structure tends to attenuate heating of the brain, including the eyes.
Primate cranial structure of rhesus macaque monkey	Planewave	Mie theory	Most of the results, 3 GHz	ff	Results given of average SAR and mean square electric field in equatorial plane.
Human skull, r = 7-10 cm	Planewave	Mie theory	0.1-3 GHz	gg	Additional SAR peak recognized at about 2.1 GHz. This is due to the $\lambda/4$ impedance matching effect which was also recognized in planar model (Schwan, 1968).
Human and animal heads, r = 3.3-10 cm	Planewave	Mie theory	0.1-10 GHz	hh	Energy distribution examined in three spheres —3.3-, 6-, and 10-cm radii—with emphasis on strong localized heating.
Outer radius maximum value = 6.6 cm	Planewave	Mie theory	Results presented, 433 < f < 6000 MHz	ii	Examined SAR distribution in different layers.
Multilayered spherical model. Six-layered cranial structure of maximum radius 3.3 cm	a. Current loop $\hat{\rho} \, I \, \hat{z}$ b. Electric dipole $\hat{m} \, I \, \hat{z}$, both axially above the model	State-space formulation	Results only at 3 GHz	jj, kk	Model allows for an idealized continuously inhomogeneous structure. Heat potential distributions are calculated.

TABLE 5.5. (continued)

Shape	Dimensions	Excitation	Method	Frequency Range	Reference	Remarks
Prolate spheroid	a = 1 m and a/b = 7.73, volume = 0.07 m³ and a/b up to 10	Planewave magnetic, electric, and cross polarization	Perturbation theory, based on expanding all fields in a power series of $-jk$	Up to 30 MHz	ℓℓ	Used to calculate the first-order internal electric field and SAR.
	0.02 < a < 0.0875 m, 2 < a/b < 6.34	Planewave magnetic, electric, and cross polarization	Perturbation analysis	Up to 30 MHz for man model; up to 1 GHz for mouse model	d	Average SAR presented as function of angle of incidence.
	3 < a < 10 cm, a/b = 3.6	Planewave cross polarization	Using the vector spheroidal wave function expansion	100 and 2450 MHz	mm, nn	Results presented for 915 and 2450 MHz. In Lin and Wu (1977), peak SAR was plotted for f = 10-3000 MHz for a = 3 cm and b = 2 cm.
	Up to man-size model a = 0.875, a/b = 6.34	Planewave	Extended boundary condition method	At and slightly past resonance (~60 MHz for 2/3 muscle tissue of man-size model)	oo, pp	Good results up to resonance for average-man model. Frequency limited because of ill-conditioned matrix. For lower dielectric constants, the method can be used up to higher frequency limits.
	Man and animal sizes	Planewave	Geometrical optics	20-100 GHz for man model, f > 80 GHz for rat model	i, qq	Based on dividing surface of prolate spheroid into small planar subareas, all power transmitted into the spheroid is assumed to be absorbed and secondary internal reflections are neglected. Lower frequency limit is based on convergence within 20% of Mie solution for sphere with a radius = b of the spheroid.
	a/b = 6.34, a = 0.875 m, weight = 70 kg	E-polarized planewave	Empirical curve-fitting procedure	10 MHz-10 GHz	rr	Provides simple empirical formula for calculating average SAR over broad-frequency band. Formula is only for E-polarized planewaves.
		Planewave E, H, and K polarization	Geometrical optics approximation	6 GHz and beyond	ss	Method valid only in the frequency range where the body dimensions >> λ.
	1.25 < a/b < 1.5, 0.297 < a < 0.335 m, volume = 0.07 m³	Planewave E, H, and K polarization	Point-matching technique	Up to resonance of 130 MHz	tt	Absorbed power density plotted for spherical-like model. Solution does not converge for a/b > 1.5.

Shape	Parameters	Source	Method	Frequency		Remarks
	a/b = 6.34, a = 0.875 m, volume = 0.07 m³	Near field of electric dipole, E and K polarization	Extended boundary condition method	Results at 27 MHz	uu	For E polarization, average SAR oscillates around its planewave value. For K polarization, SAR distribution suggests possible enhancement at regions of small radius of curvature.
	a/b = 6.34, a = 0.875 m, weight = 70 kg	Electric dipole located parallel to major axis of spheroid	Long-wavelength approximation method	Results at 27 MHz	vv	Analysis useful where long-wavelength approximation is valid but wave impedances are not 377 Ω, and for near-field irradiation in which incident fields are quasi-uniform.
		Near field of a short electric dipole	Long-wavelength analysis	27.12 MHz	ww	Average SARs in a prolate spheroidal model of man are essentially the same as those for a block model of man at 27.12 MHz, even in near fields. For purposes of average SAR, this allows use of the simpler and less expensive prolate spheroidal calculations
		Near fields of aperture sources	Extended boundary condition method	27 MHz	xx, yy	Average SAR and the SAR distribution due to near fields of large and small aperture sources are given. Calculated results conform to the understanding previously obtained from studying irradiation of the spheroidal models by EM planewaves and by near fields of various elementary radiation sources.
Spherically capped cylinder	The average man model and the small rat model	EM planewave	Surface integral equation	80 MHz to 2.45 GHz	zz	Average SAR curves for E, H, and K polarizations intersect at a frequency just above resonance, about 800 MHz for man models. This may be useful in cases where the average SAR must be independent of animal position.
Prolate spheroid	• a/b = 6.34, a = 0.875 m, weight = 70 kg • a/b = 3.1, a = 20 cm, weight = 3.5 kg • a/b = 3, a = 3.5 cm, weight = 20 g	Small co-axial loop antenna	Extended boundary condition method	10-600 MHz	ab	SAR distribution and average SAR are plotted as a function of separation distance from the loop. For distances less than 5 λ, average SAR values oscillate about the far-field value.
	a/b = 6.34, a = 0.875 m, weight = 70 kg	Small loop antenna of arbitrary orientation	Extended boundary condition method	27 and 45 MHz	ac	Average SAR and SAR distributions are calculated as a function of separation distance from antenna. Results for separation distances larger than λ/2 agree well with those obtained from planewave exposure case.

TABLE 5.5. (continued)

Shape	Dimensions	Excitation	Method	Frequency Range	Reference	Remarks
Prolate spheroid	a/b = 6.34, a = 0.875 m, weight = 70 kg	Planewave E and K polarizations	Iterative extended boundary condition method	27-300 MHz	ad, ae	An iterative procedure for improving stability and extending frequency range of the extended boundary condition method (EBCM). Calculated data for SAR distribution and average SARs in the resonance and postresonance frequency range are presented.
Axisymmetric cranial structure	height = 22.6 cm, volume = 4189 cm^3	EM planewave	Finite element method	1 and 3 GHz	af	Model composed of upper concentric spheres and lower concentric spheroids. Curves for SAR distribution in brain region are presented for detached model of the human cranial structure
Ellipsoidal model	Man model a = 0.875 m, volume = 0.07 m^3, and b/c = 2	Planewave	Perturbation technique	1-30 MHz for man model	ag	First-order analysis valid for long-wavelength a/λ < 0.1. Curves of SAR vs. frequency show SAR to be strong function of size and orientation of the ellipsoid in the incident field. Strongest absorption was found when electric-field vector of the incident planewave was along the longest dimension of the ellipsoid.
	Man and animal model 0.05 < 2a < 1.8, 1.7 < a/b < 4.5, and 1.3 < b/c < 2	Planewave	Perturbation technique	Up to 30 MHz for man model and to 1 GHz for the mouse	ah	Data used to extrapolate results of observed irradiation effects in animals to those expected to be observed in humans.
Ellipsoid	Model of breast carcinoma embedded in nonabsorbing dielectric	Planewave	Boundary value solution in spheroidal coordinates	Results at 2450 MHz, 5.8 GHz, 10 GHz	ai	Three-dimensional and densitographic pictures of electromagnetic-field distribution with locations of hot spots shown.
Body-of-revolution model	Sphere resting on base of conical body; total height = 1.78 m	Vertically and horizontally polarized planewave	Surface integral equation method	Results at 30, 80, and 300 MHz	aj	Strongest power deposition is for field polarized along longest dimension and for frequencies near the first resonance (i.e., 80 MHz); hot spots predicted in neck region.

Model	Dimensions	Exposure	Method	Frequency	Code	Remarks
Block model of man	Height = 1.7 m, 120 cells; cell size was kept smaller than $\lambda_o/4$	Planewave	Tensor integral equation method	Up to 500 MHz	ak, al	Integral equation solved by dividing the body into N cells, assuming a constant field inside each cell, and solving for the 3N unknowns using point matching. Also, hot spots are illustrated.
	Height = 1.7 m, 180 cells; cell size < 10 cm	Planewave	Moment-method solution of electric-field integral equation	Up to 200 MHz	am	Chen and Guru's work (1977) extended by a. Using interpolant between field values at cell centers before carrying out the volume integral. b. Choosing cell sizes and locations for realistic model of man.
Block model	Height = 1.75 m, weight = 70 kg	E-polarized planewave	Image theory and moment method	Less than 100 MHz	an	Experimental data support numerical results. Resonant frequency shifts from 77 MHz in free space to 47 MHz when standing on a ground plane. An order-of-magnitude enhancement in SAR values is predicted at frequencies below 30 MHz.
			Moment method	10-600 MHz	am	Numerical calculations of absorbed energy deposition made for human model constructed with careful attention to both biometric and anatomical diagrams.
		Planewave, vertical, and horizontal polarization	Tensor integral equation method	Up to 500 MHz	ao	Results for average SAR are compared with existing experimental results. Resonance and the effect of body heterogeneity on the induced field are studied.
Inhomogeneous block model of man	Height = 1.75 m, weight = 70 kg	Planewave	Moment method with pulse basis function	27.12 MHz and 77 MHz	ap	Whole-body and part-body average SAR for man in free space and under grounded conditions are given as function of angle of incidence. In general for frequencies considered, average SAR varies smoothly with angle between the extrema.
Block model of man	Height = 1.75 m, weight = 70 kg	Near-field exposure	An empirical relationship	Less than 350 MHz	aq	Empirical formula for average SAR in man under a two-dimensional near-field exposure. Average SAR is lower for near-field exposure than for planewave irradiation conditions.
Block model and cylindrical model of man	Height = 1.75 m, weight = 70 kg	Near field of resonant thin-wire antenna	Moment method and finite element method	45 MHz, 80 MHz, and 200 MHz	ar, as	Temperature distribution in cylindrical model of man is calculated by a finite element solution of the transient heat conduction equation in which the internal heat generation is due to metabolism and absorption of EM energy. At least 50 W incident power is required before the body experiences any significant thermal effect from the near-zone antenna fields.

TABLE 5.5. (continued)

Shape	Dimensions	Excitation	Method	Frequency Range	Reference	Remarks
Block model	Height = 1.68 m, max diameter = 0.36 m; height = 2.22 cm, max diameter = 3.8 cm	Uniform RF magnetic field	Solution of vector potential by moment method	10-750 MHz	at	Electric fields induced by RF magnetic field inside a sphere, finite circular cylinders, and phantom models of humans are calculated. Calculated data are verified by experimental values and existing theoretical results.
	Height = 1.7 m, weight = 68 kg	Near field of a dipole antenna	Moment method with pulse basis function	27, 80, and 90 MHz	au	Average SAR in the body as a function of antenna-body spacing is calculated at 27 MHz. Calculated SAR-distribution data agree qualitatively with the experiment values.
Inhomogeneous block model	Height = 1.75 m, weight = 70 kg	Near field of an RF sealer	Moment method with pulse basis function	Less than 350 MHz	av	Planewave spectrum approach used to calculate average SAR and SAR distribution in an inhomogeneous block model of man for a prescribed two-dimensional leakage electric field. Average SAR under near-field conditions is always less than or equal to the far-field planewave value.
Inhomogeneous block model of man	Height = 1.75 m, weight = 70 kg	Planewave E polarization	Moment method with pulse basis functions	27.12 MHz	aw	Average SAR and SAR distributions are obtained for man models with 180-1132 cells by the moment method with pulse basis function. Calculated values of average SAR increase with the number of cells used.

REFERENCES:

a. Schwan, 1968
b. Guy, 1971b
c. Guy and Lehmann, 1966
d. Johnson et al., 1975
e. Chatterjee, 1979
f. Barber et al., 1979
g. Chatterjee et al., 1980a
h. Chatterjee et al., 1980b
i. Durney et al., 1976
j. Massoudi et al., 1979a
k. Yoneyama et al., 1979
l. Ruppin, 1979
m. Ho, 1975a
n. Ho et al., 1969
o. Ho et al., 1971
p. Wu and Tsai, 1977
q. Neuder and Meijer, 1976
r. Massoudi et al., 1979b
s. Kastner and Mittra, 1983
t. Morita and Andersen, 1982
u. Hill et al., 1983
v. Iskander et al., 1982a
w. Livesay and Chen, 1974
x. Iskander et al., 1979
y. Anne et al., 1960
z. Kritikos and Schwan, 1972

aa. Johnson and Guy, 1972
bb. Lin et al., 1973b
cc. Kritikos and Schwan, 1975
dd. Lin et al., 1973a
ee. Rukspollmuang and Chen, 1979
ff. Shapiro et al., 1971
gg. Joines and Spiegel, 1974
hh. Weil, 1975
ii. Neuder et al., 1976
jj. Hizal and Tosun, 1973
kk. Hizal and Baykal, 1978
ll. Durney et al., 1975
mm. Lin and Wu, 1977
nn. Wu and Lin, 1977
oo. Barber, 1977a
pp. Barber, 1977b
qq. Rowlandson and Barber, 1977
rr. Durney et al., 1979
ss. Rowlandson and Barber, 1979
tt. Ruppin, 1978
uu. Iskander et al., 1980
vv. Massoudi et al., 1980
ww. Massoudi et al., 1981
xx. Lakhtakia et al., 1983a
yy. Lakhtakia et al., 1982a
zz. Massoudi et al., 1982

ab. Lakhtakia et al., 1982b
ac. Lakhtakia et al., 1981
ad. Iskander et al., 1983
ae. Iskander et al., 1982b
af. Morgan, 1981
ag. Massoudi et al., 1977a
ah. Massoudi et al., 1977b
ai. Zimmer and Gros, 1979
aj. Wu, 1979
ak. Chen and Guru, 1977b
al. Chen et al., 1976
am. Hagmann et al., 1979a
an. Hagmann and Gandhi, 1979
ao. Chen and Guru, 1977c
ap. Hagmann et al., 1981
aq. Chatterjee et al., 1982a
ar. Spiegel, 1982
as. Spiegel et al., 1980
at. Lee and Chen, 1982
au. Karimullah et al., 1980
av. Chatterjee et al., 1980c
aw. Deford et al., 1983

CHAPTER 6. CALCULATED DOSIMETRIC DATA

6.1. CALCULATED PLANEWAVE DOSIMETRIC DATA FOR AVERAGE SAR

Calculated dosimetric data for the average SAR of humans and various animals irradiated by planewaves with incident-power density of 1 mW/cm^2 in free space are presented in Figures 6.1-6.30.

Figure 6.1 shows the average SAR for the six standard polarizations in an ellipsoidal model of an average man. The average SAR in ellipsoidal models of different human-body types, for EKH polarization, are compared in Figure 6.2.

Figures 6.3-6.19 show the average SAR for the three standard polarizations in prolate spheroidal and cylindrical homogeneous models of humans and test animals in the frequency range 10 MHz-100 GHz. These data were calculated by several different techniques, as described in Section 5.1.1 and shown in Figure 5.1. For frequencies below 10 MHz, the $1/f^2$ principle can be applied to the 10-MHz SAR data to determine SARs at lower frequencies. See Chapter 8 for a comparison of calculated and measured values.

The data in Figures 6.20-6.22 illustrate the effects of tissue layers on average SAR, in contrast to the data for homogeneous models in the previous figures. These data were calculated for a man model consisting of multiple cylinders, each cylinder representing a body part such as an arm or leg (Massoudi et al., 1979b). For a cylindrical model with layers that simulate skin and fat, the average SAR is different from the homogeneous models only for frequencies above about 400 MHz, where the wavelength is short enough that a resonance occurs in a direction transverse to the layers. The frequencies at which the resonances occur are primarily a function of the thicknesses of the layers and are not affected much by the overall size of the body. Figures 6.23 and 6.24 show the relationships between the frequency at which the peaks in average SAR due to the transverse resonance occur and the thicknesses of the layers.

Figures 6.25-6.30 show average SARs as a function of frequency for a few models irradiated by circularly and elliptically polarized planewaves.
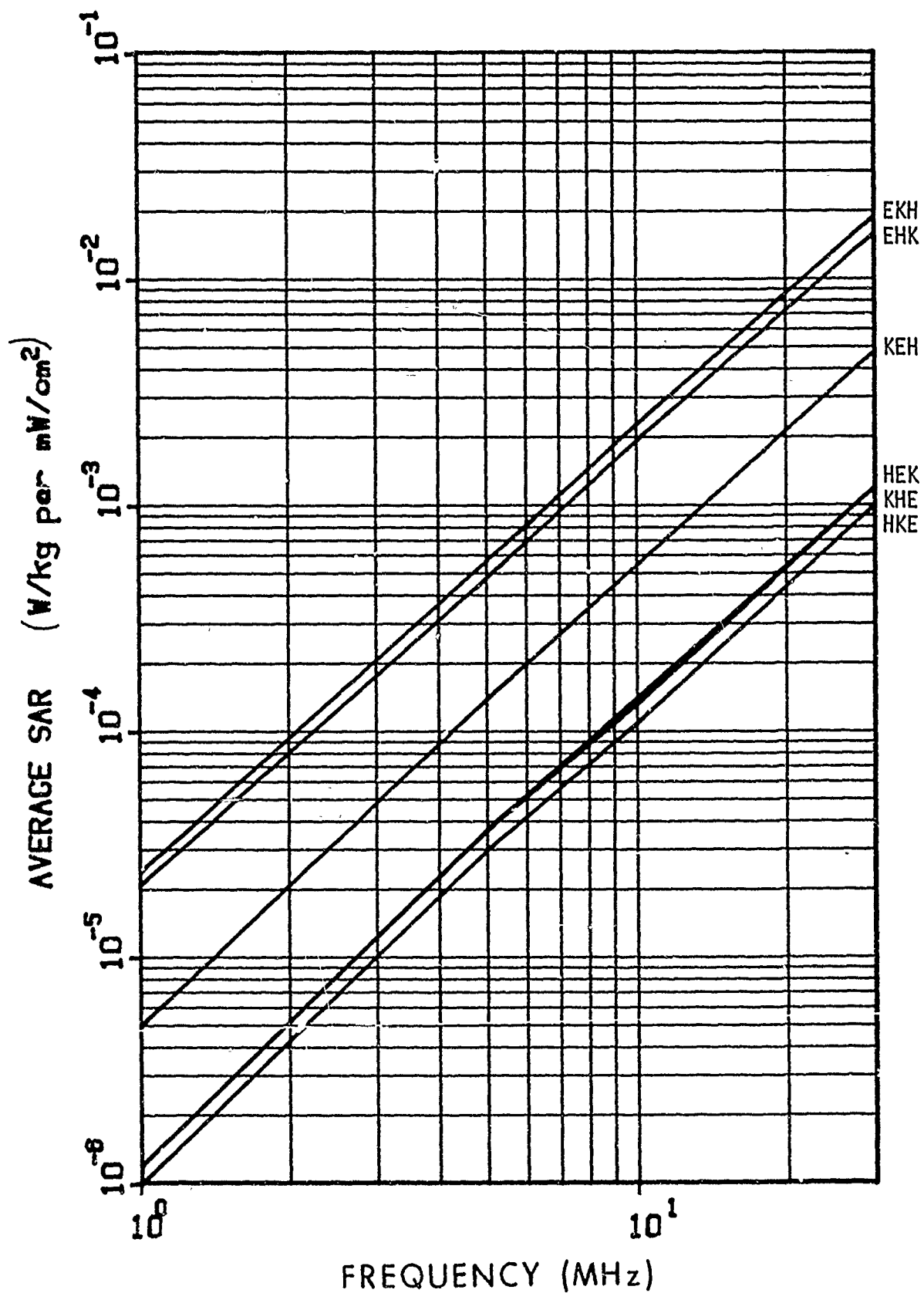
Figure 6.1. Calculated planewave average SAR in an ellipsoidal model
of an average man, for the six standard polarizations;
a = 0.875 m, b = 0.195 m, c = 0.098 m, V = 0.07 m³.
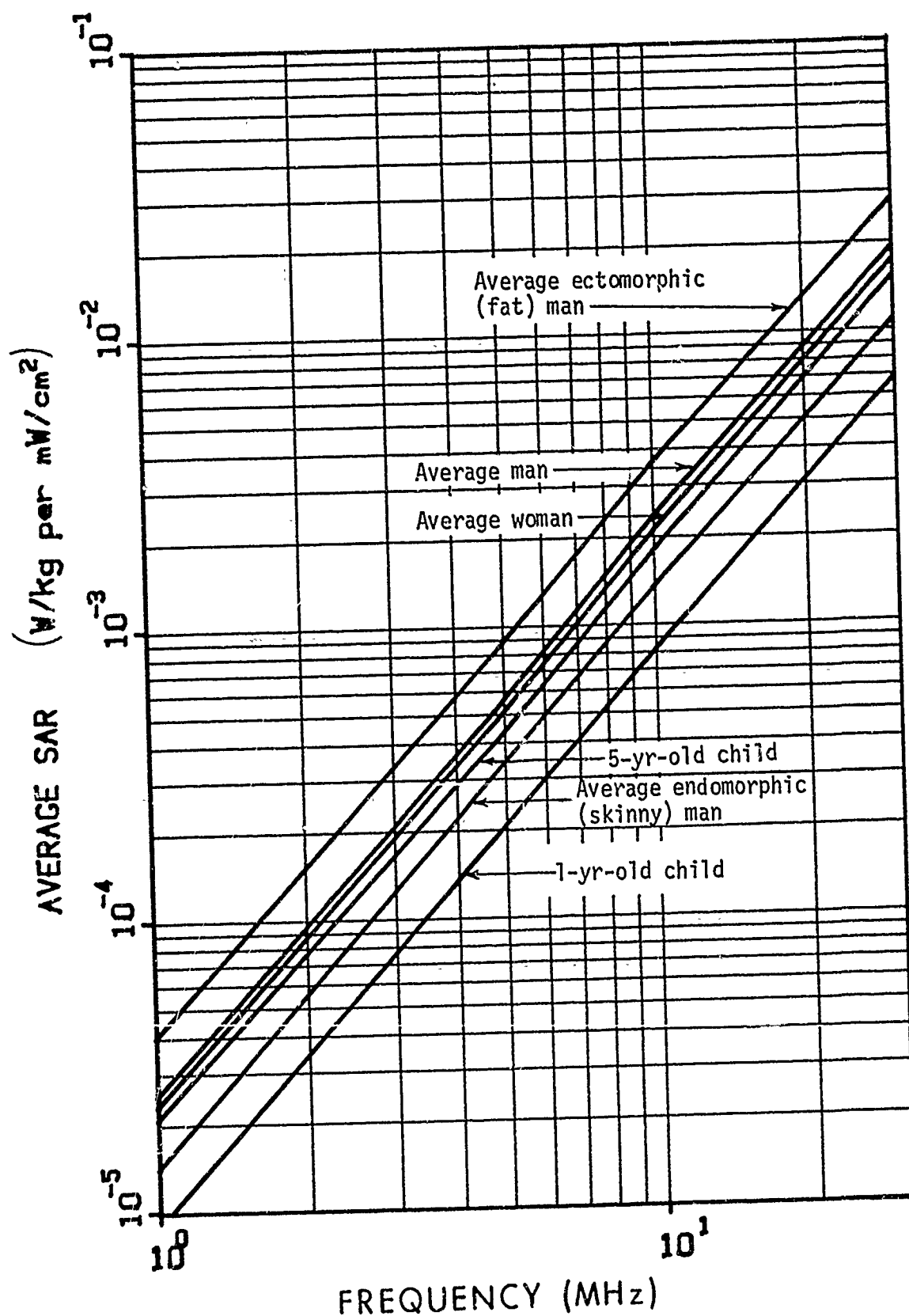
Figure 6.2.   Calculated planewave average SAR in ellipsoidal models of different human-body types, EKH polarization.
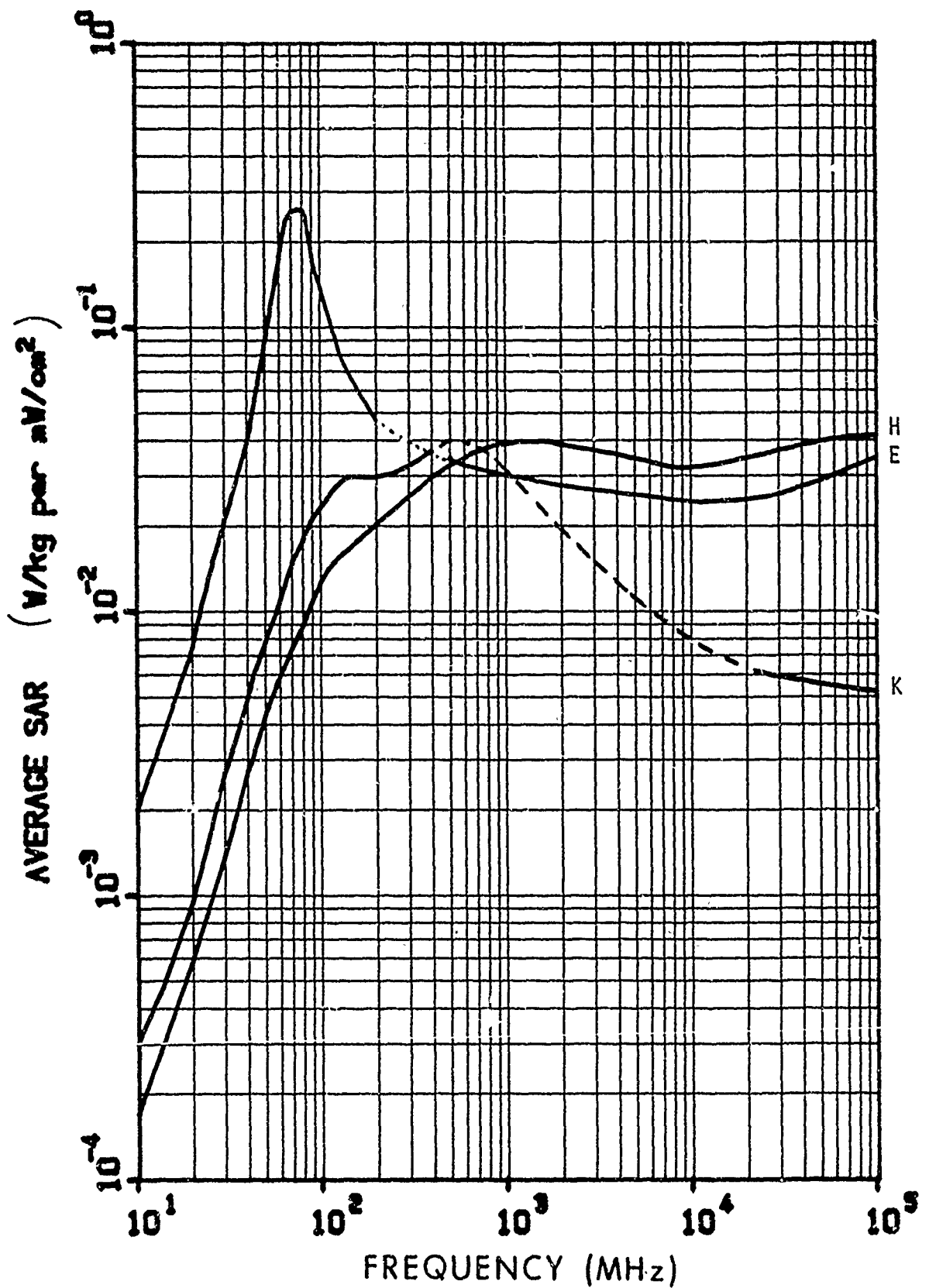
Figure 6.3. Calculated planewave average SAR in a prolate spheroidal model of an average man for three polarizations; a = 0.875 m, b = 0.138 m, V = 0.07 m^3. The dotted line is calculated from Equation 5.1; the dashed line is estimated values.
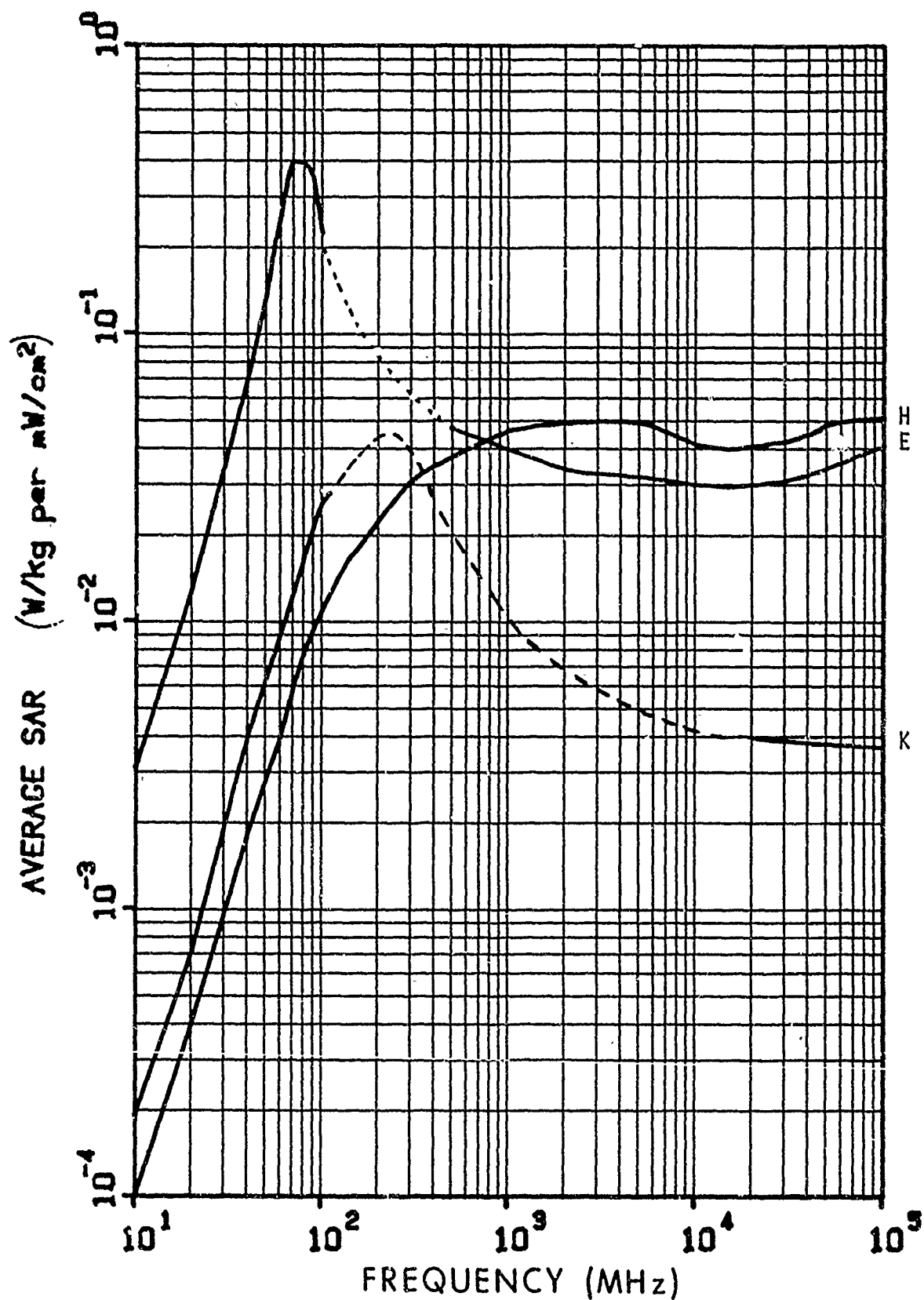
Figure 6.4. Calculated planewave average SAR in a prolate spheroidal model of an average ectomorphic (skinny) man for three polarizations; a = 0.88 m, b = 0.113 m, V = 0.04718 m³. The dotted line is calculated from Equation 5.1; the dashed line is estimated values.
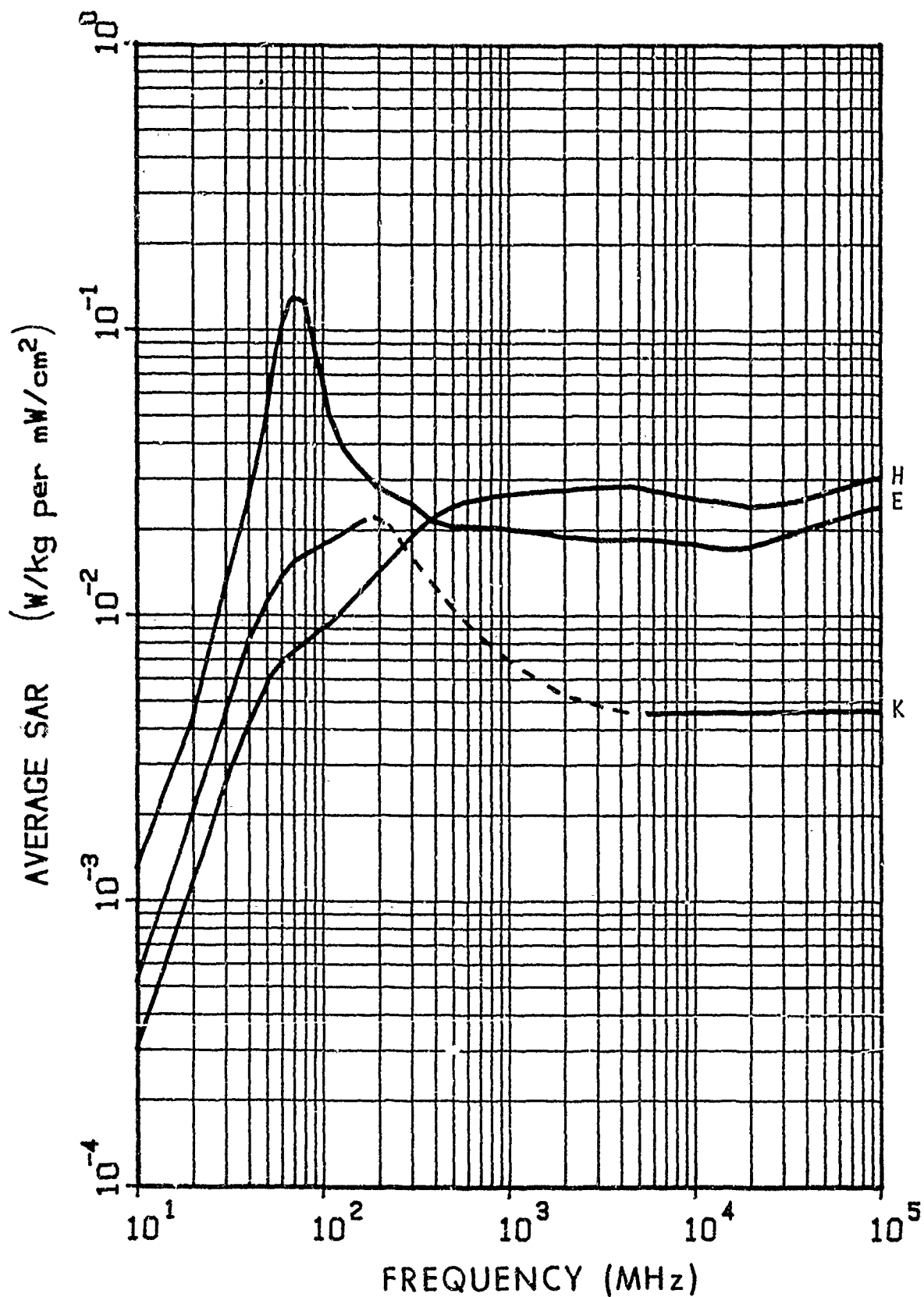
Figure 6.5. Calculated planewave average SAR in a prolate spheroidal model of an average endomorphic (fat) man for three polarizations; a = 0.88 m, b = 0.195 m, V = 0.141 m^3. The dashed line is estimated values.
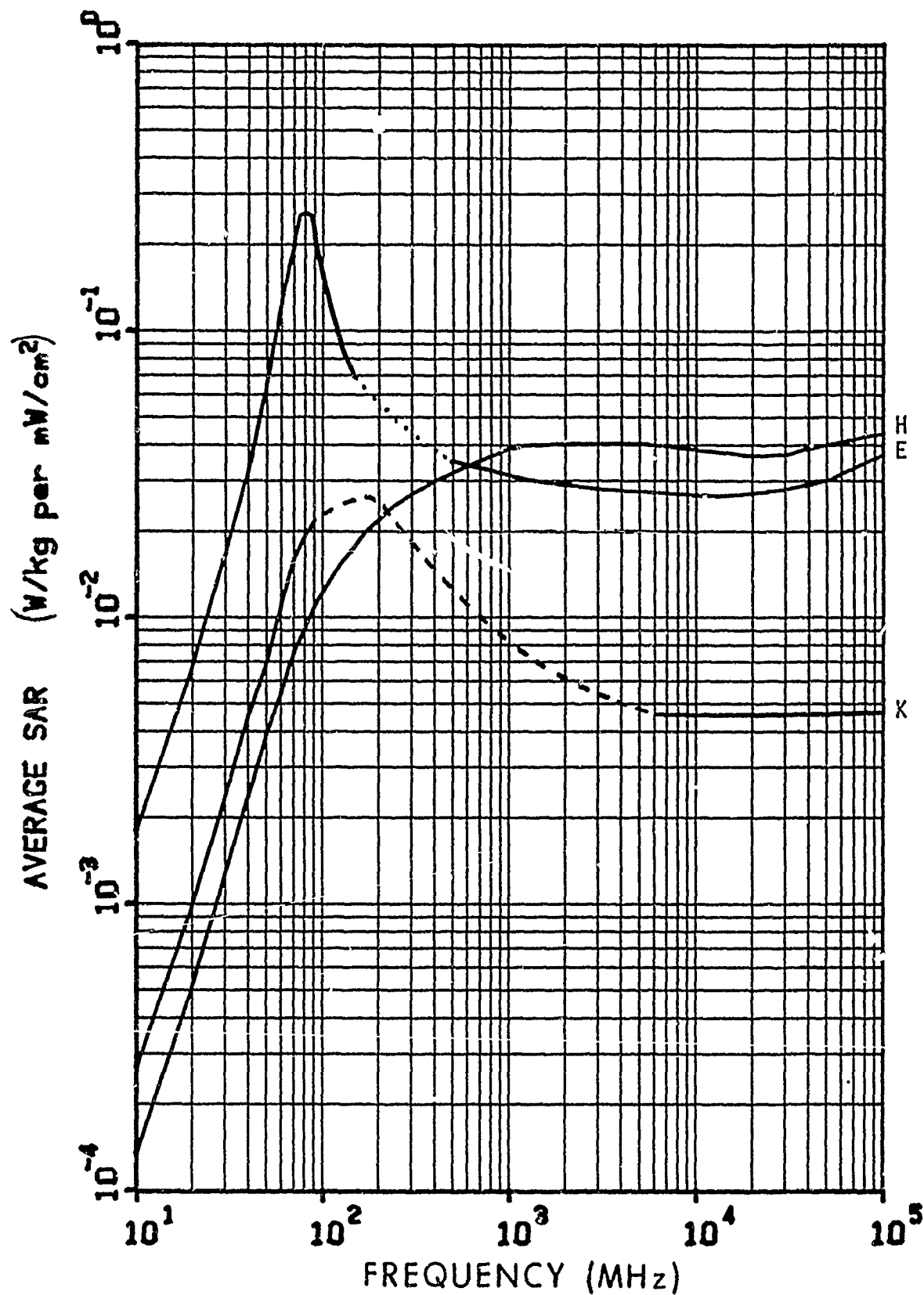
Figure 6.6. Calculated planewave average SAR in a prolate spheroidal model of an average woman for three polarizations; a = 0.805 m, b = 0.135 m, V = 0.06114 m^3. The dotted line is calculated from Equation 5.1; the dashed line is estimated values.
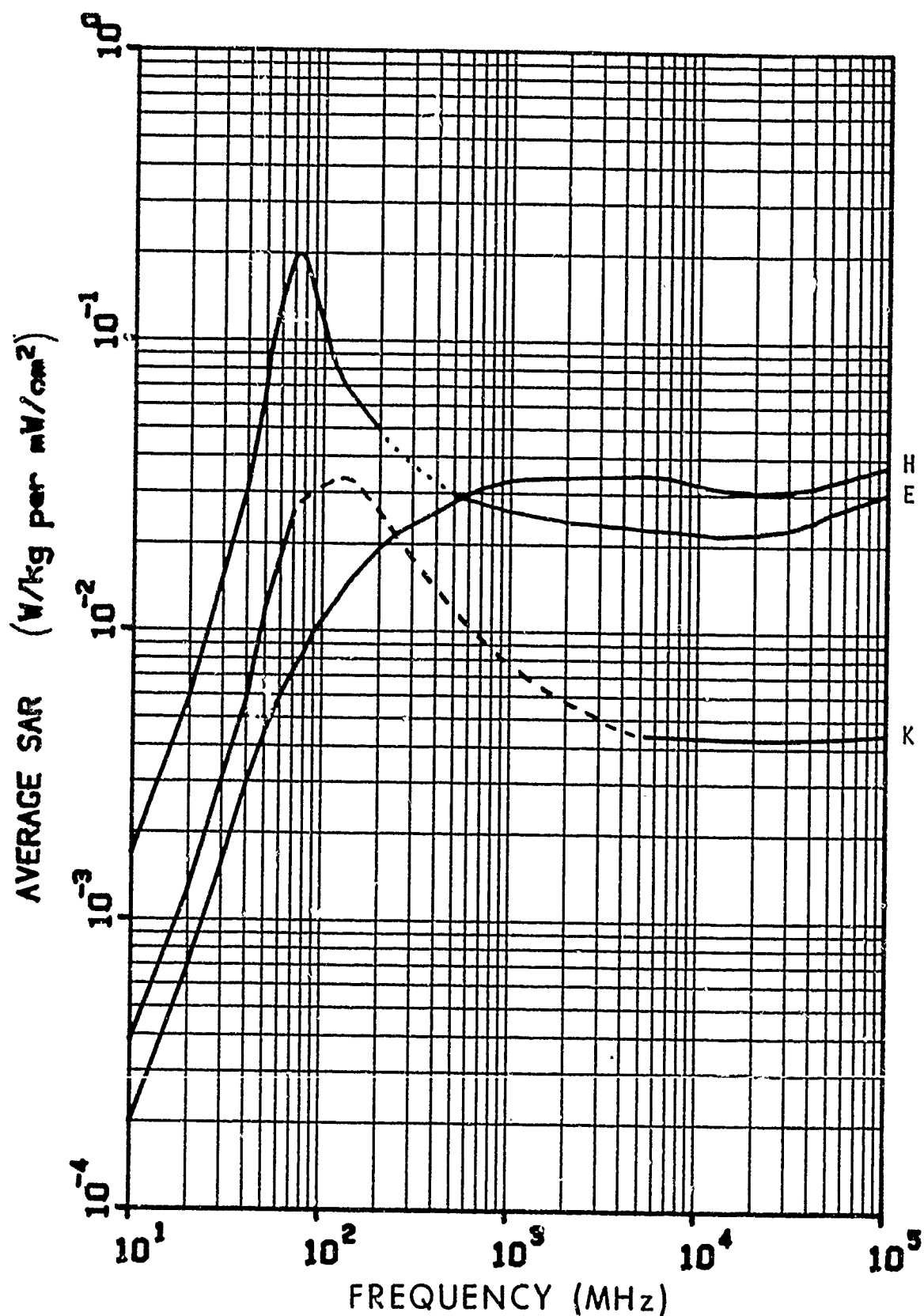
Figure 6.7. Calculated planewave average SAR in a prolate spheroidal model of a large woman for three polarizations; a = 0.865 m, b = 0.156 m, V = 0.08845 m^3. The dotted line is calculated from Equation 5.1; the dashed line is estimated values.
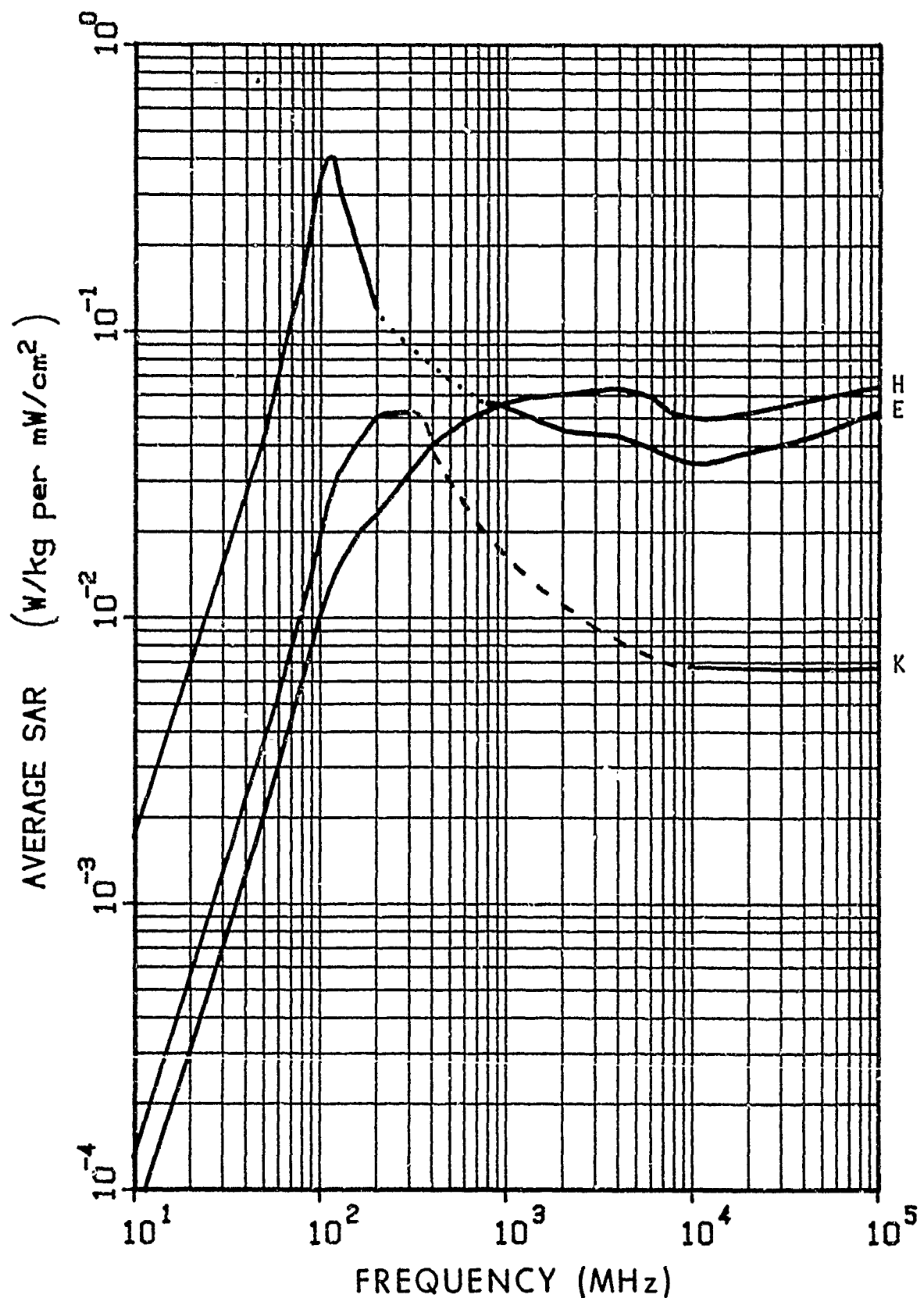
Figure 6.8. Calculated planewave average SAR in a prolate spheroidal model of a 5-year-old child for three polarizations; a = 0.56 m, b = 0.091 m, V = 0.0195 m^3. The dotted line is calculated from Equation 5.1; the dashed line is estimated values.
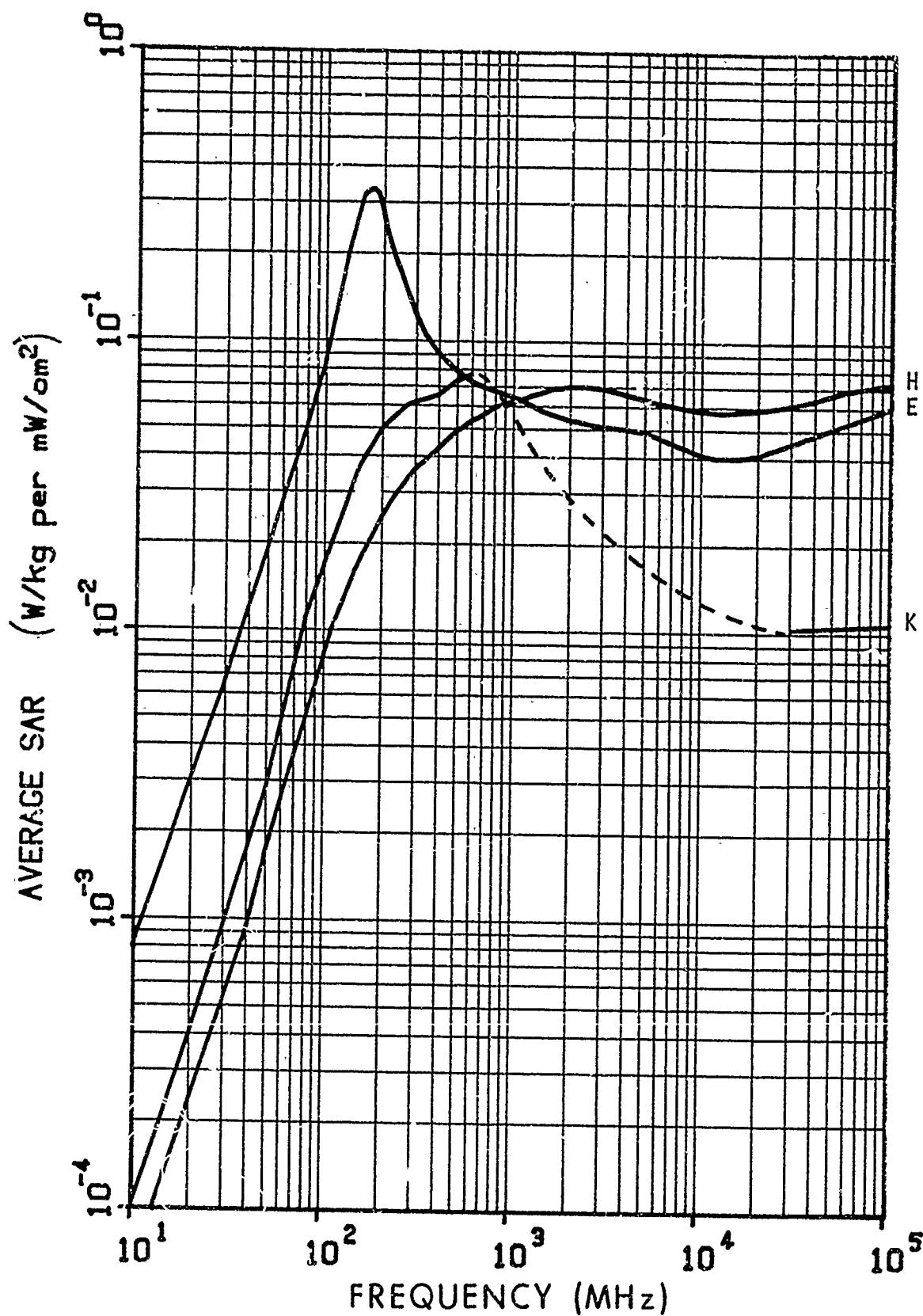
Figure 6.9. Calculated planewave average SAR in a prolate spheroidal model of a 1-year-old child for three polarizations; a = 0.37 m, b = 0.08 m, V = 0.01 m^3. The dashed line is estimated values.
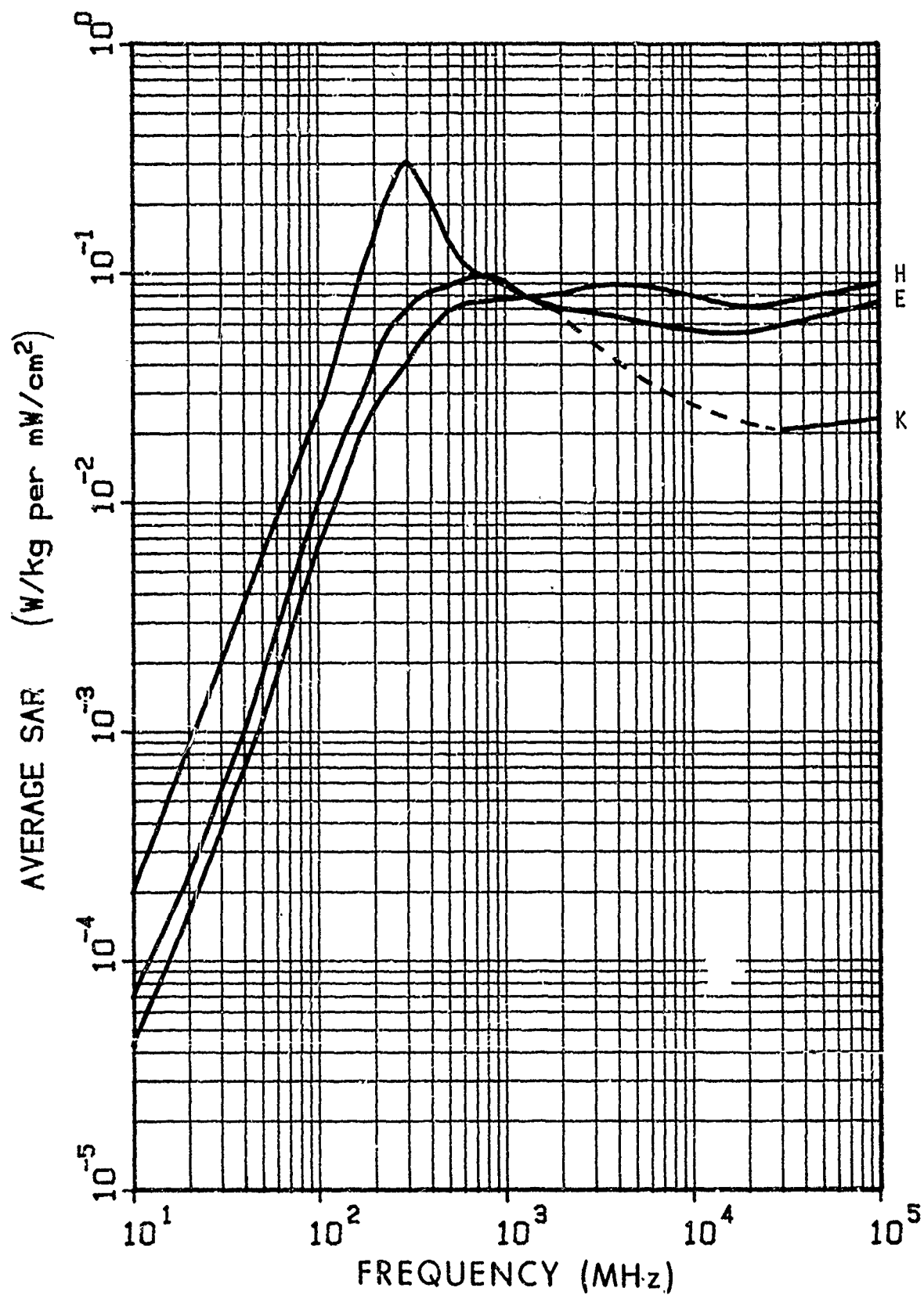
Figure 6.10. Calculated planewave average SAR in a prolate spheroidal model of a sitting rhesus monkey for three polarizations; a = 0.2 m, b = 0.0646 m, $V = 3.5 \times 10^{-3}$ m^3. The dashed line is estimated values.
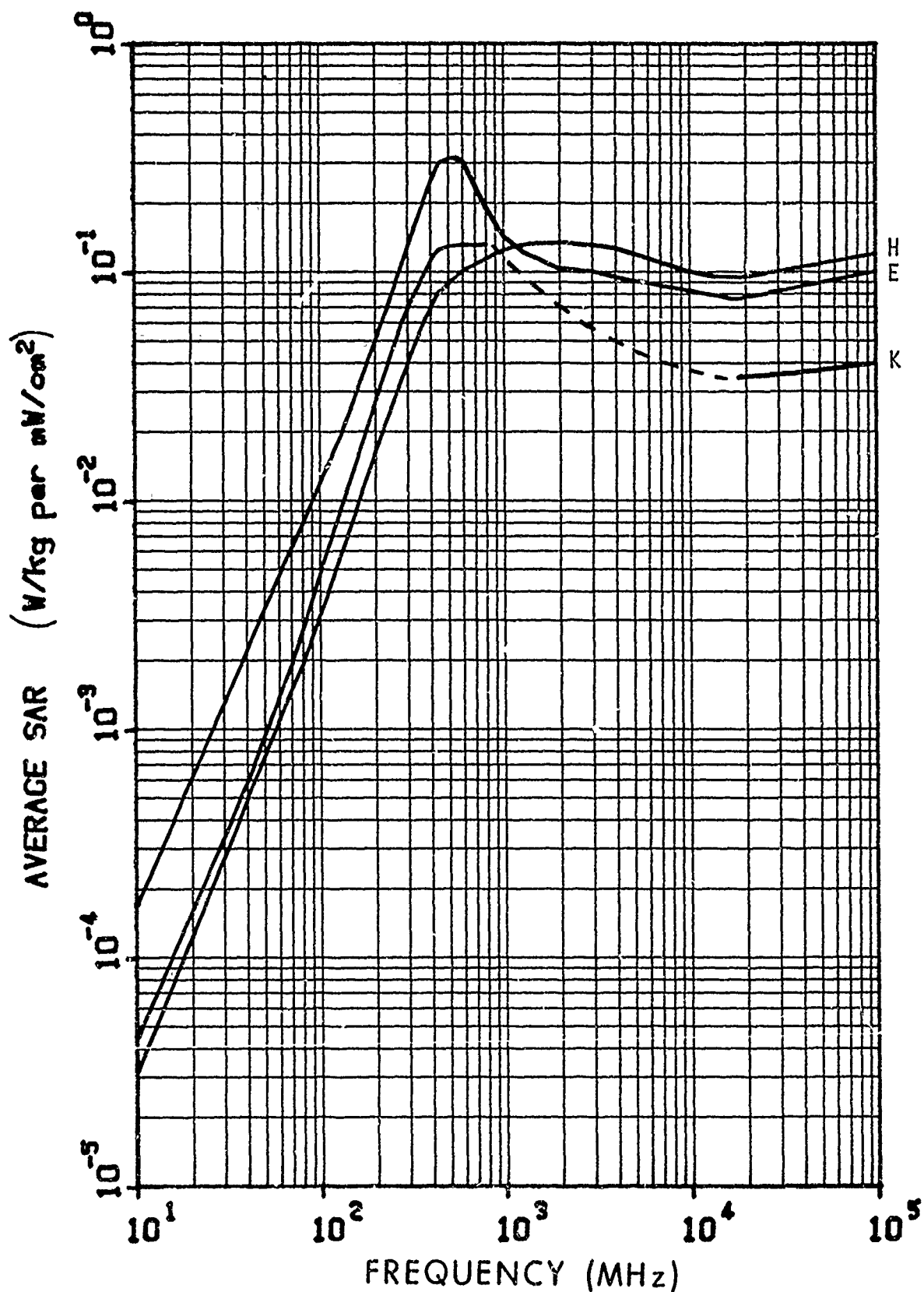
Figure 6.11. Calculated planewave average SAR in a   prolate spheroidal
model of a squirrel monkey for three polarizations; a =
0.115 m, b = 0.0478 m, V = 1.1 × 10^{-3} m^3. The dashed line
is estimated values.
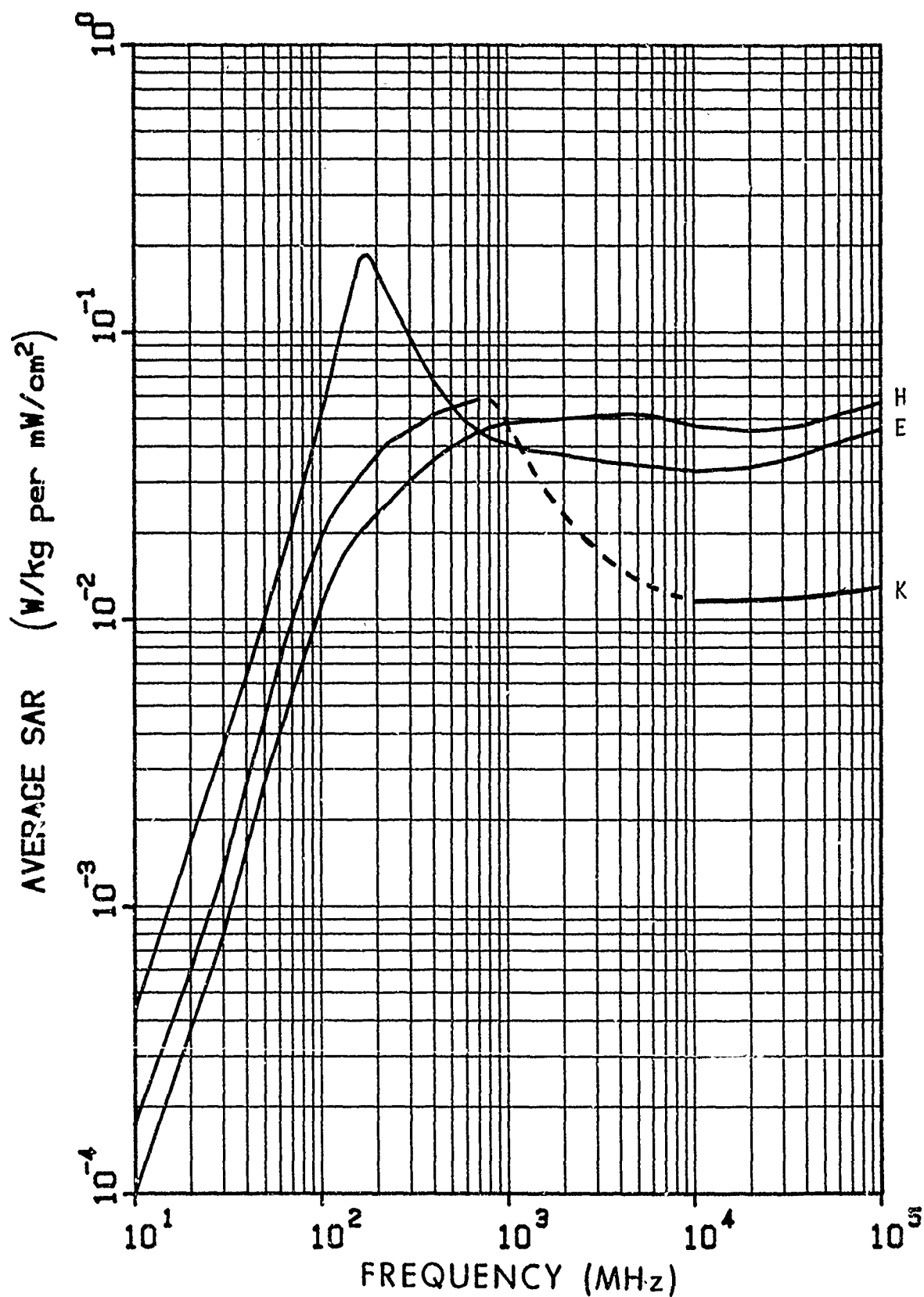
Figure 6.12. Calculated planewave average SAR in a prolate spheroidal
model of a Brittany spaniel for three polarizations; a =
0.344 m, b = 0.105 m, V = 0.0159 m^3. The dashed line is
estimated values.

- 6.13 -
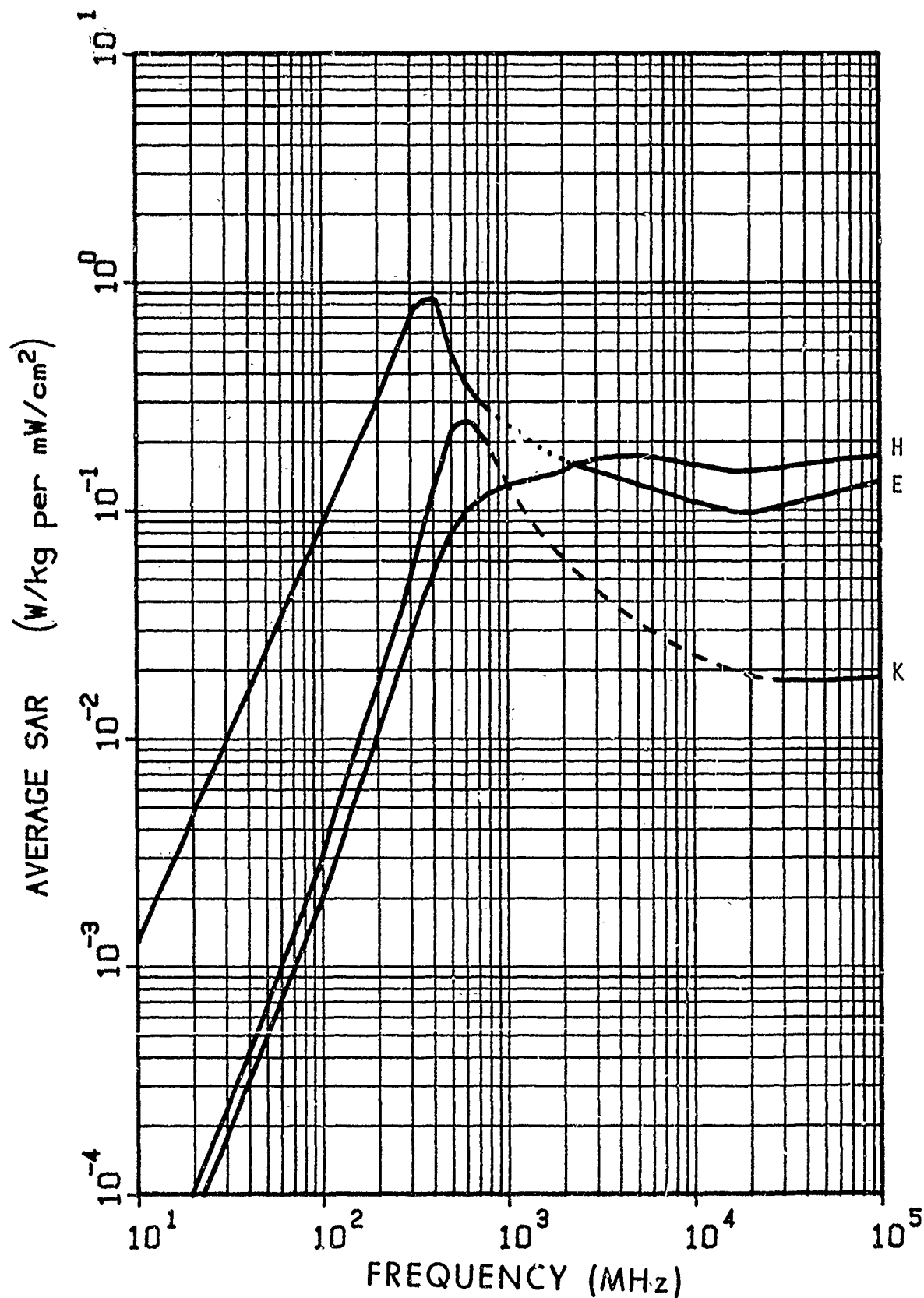
Figure 6.13. Calculated planewave average SAR in a prolate spheroidal model of a rabbit for three polarizations; a = 0.2 m, b = 0.0345 m, V = 1 × 10⁻³ m³. The dotted line is calculated from Equation 5.1; the dashed line is estimated values.
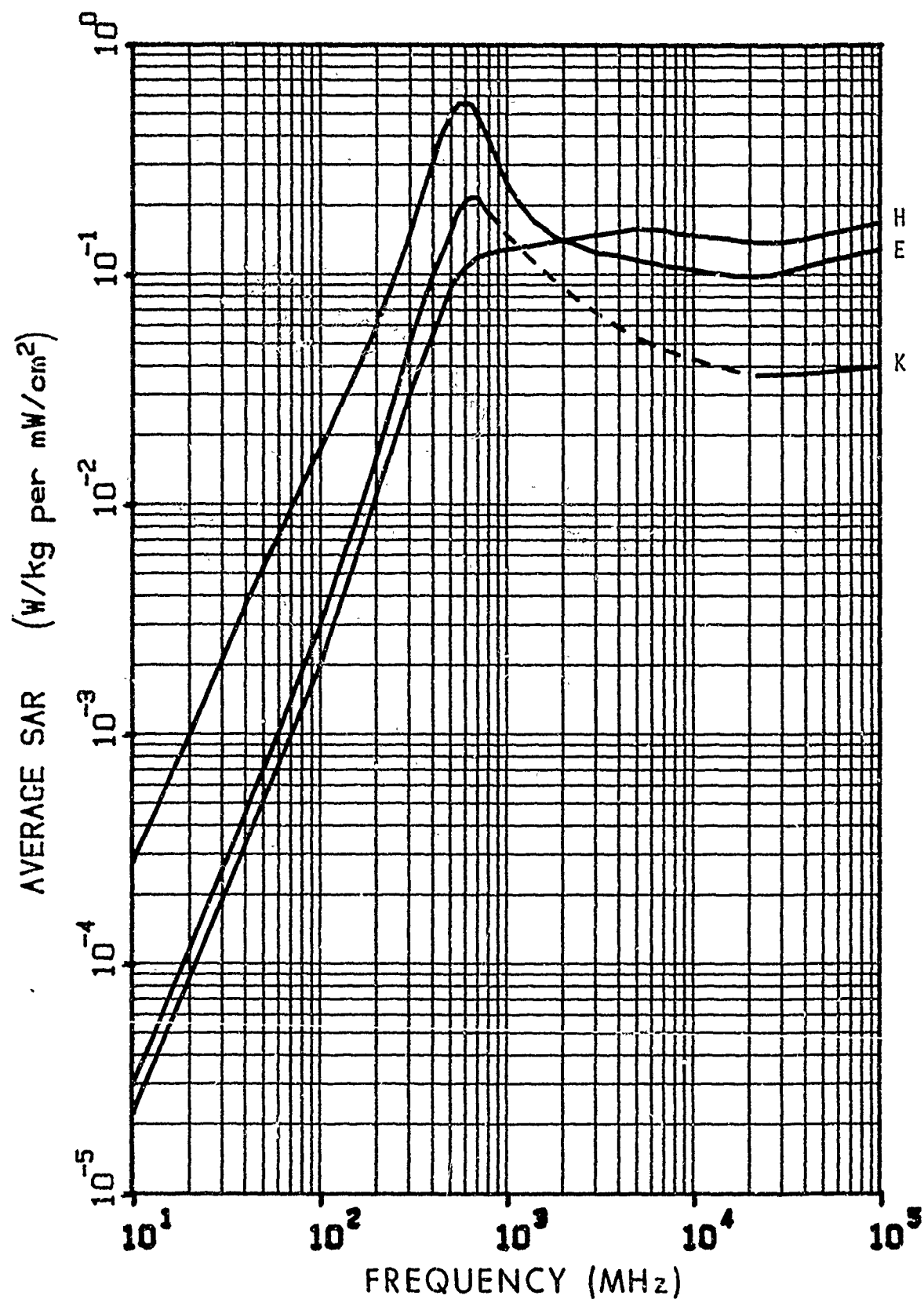
Figure 6.14. Calculated planewave average SAR in a prolate spheroidal model of a guinea pig for three polarizations; $a = 0.11$ m, $b = 0.0355$ m, $V = 5.8 \times 10^{-4}$ m^3. The dashed line is estimated values.

AVERAGE SAR $\left(\text{W/kg per mW/cm}^2\right)$

FREQUENCY (MHz)

10^1

H
E

K
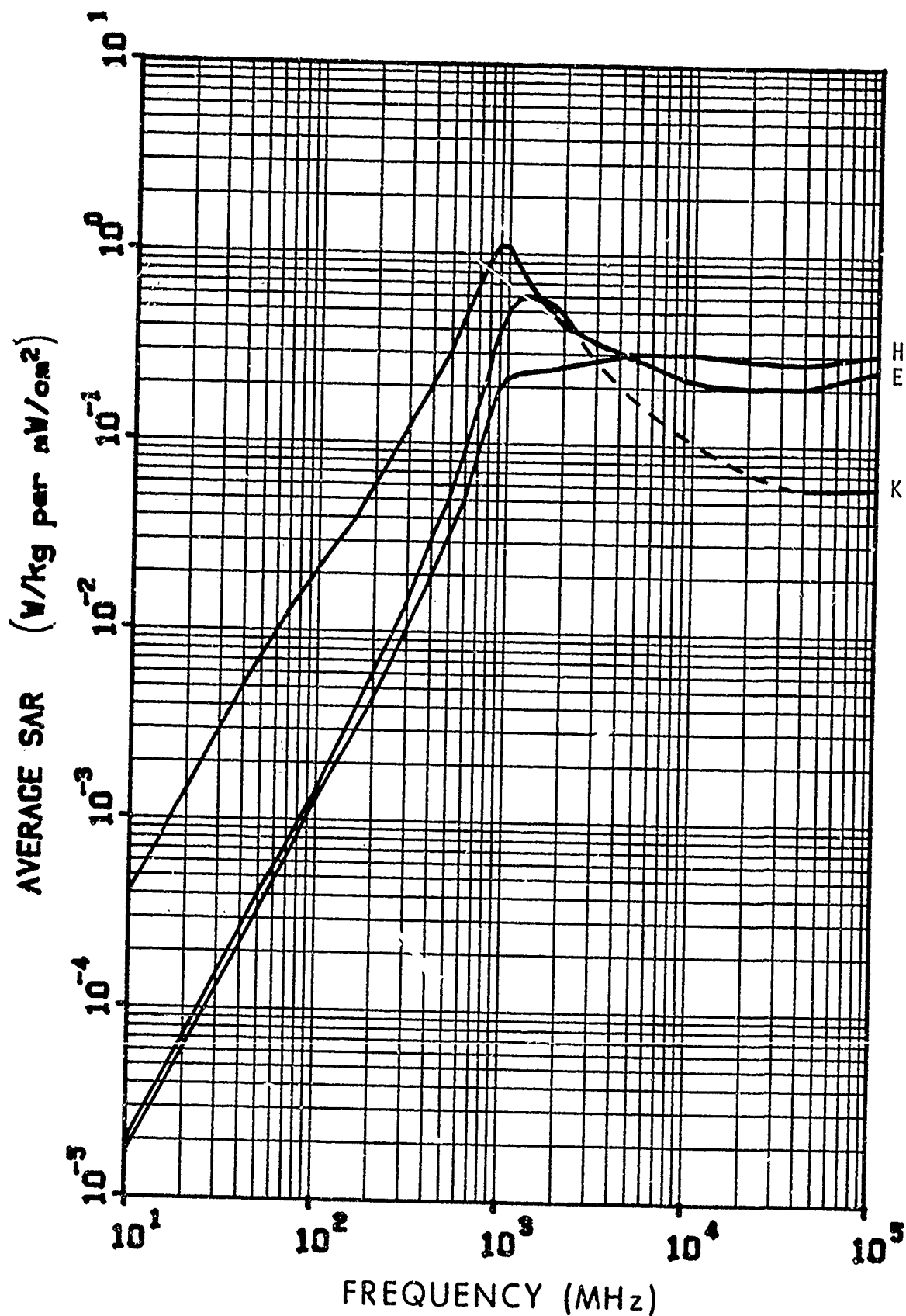
Figure 6.15. Calculated planewave average SAR in a prolate spheroidal model of a small rat for three polarizations; a = 0.07 m, b = 0.194 m, V = 1.1 × 10⁻⁴ m³. The dashed line is estimated values.
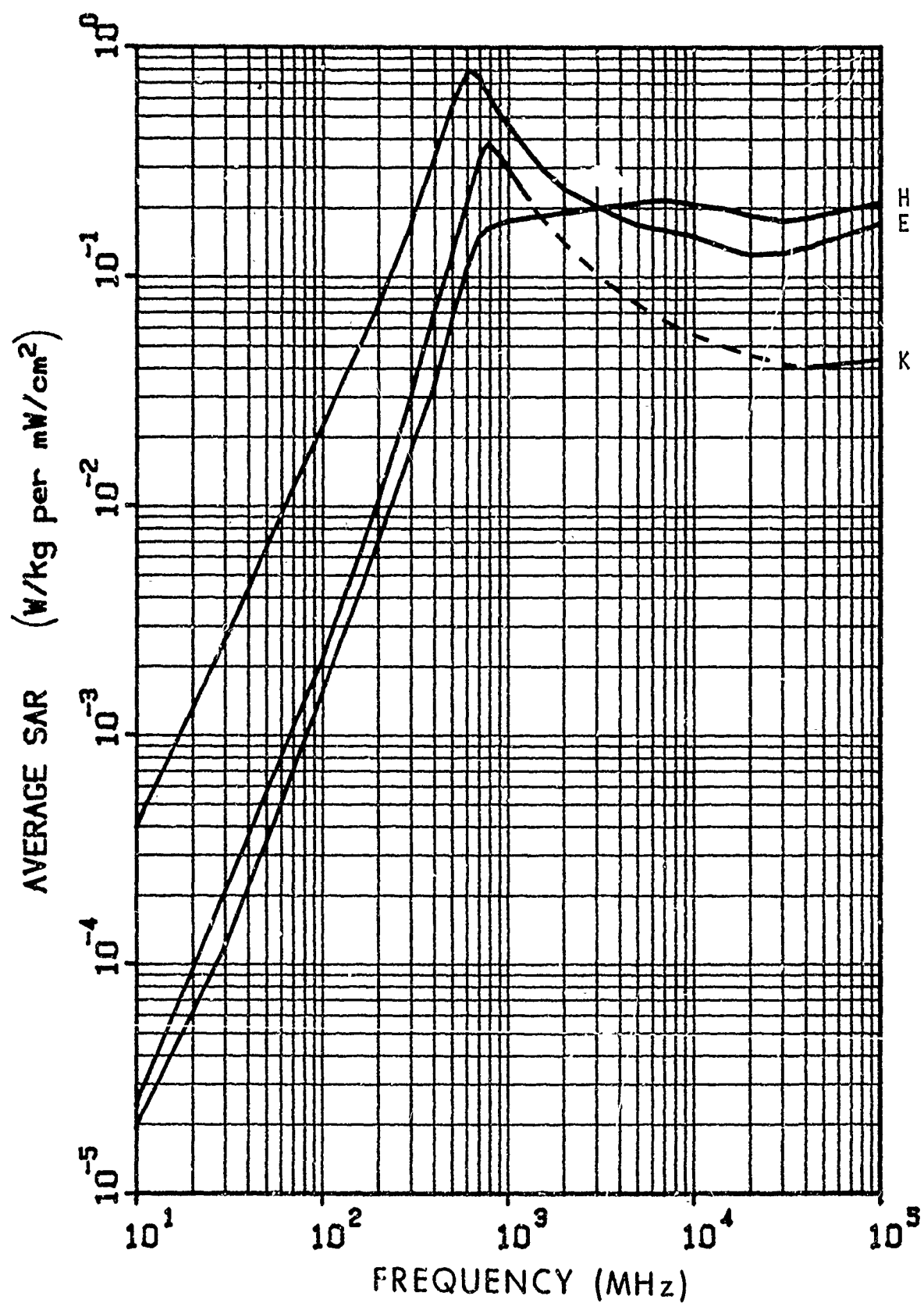
Figure 6.16. Calculated planewave average SAR in a prolate spheroidal model of a medium rat for three polarizations; a = 0.1 m, b = 0.0276 m, V = 3.2×10^{-4} m³. The dashed line is estimated values.
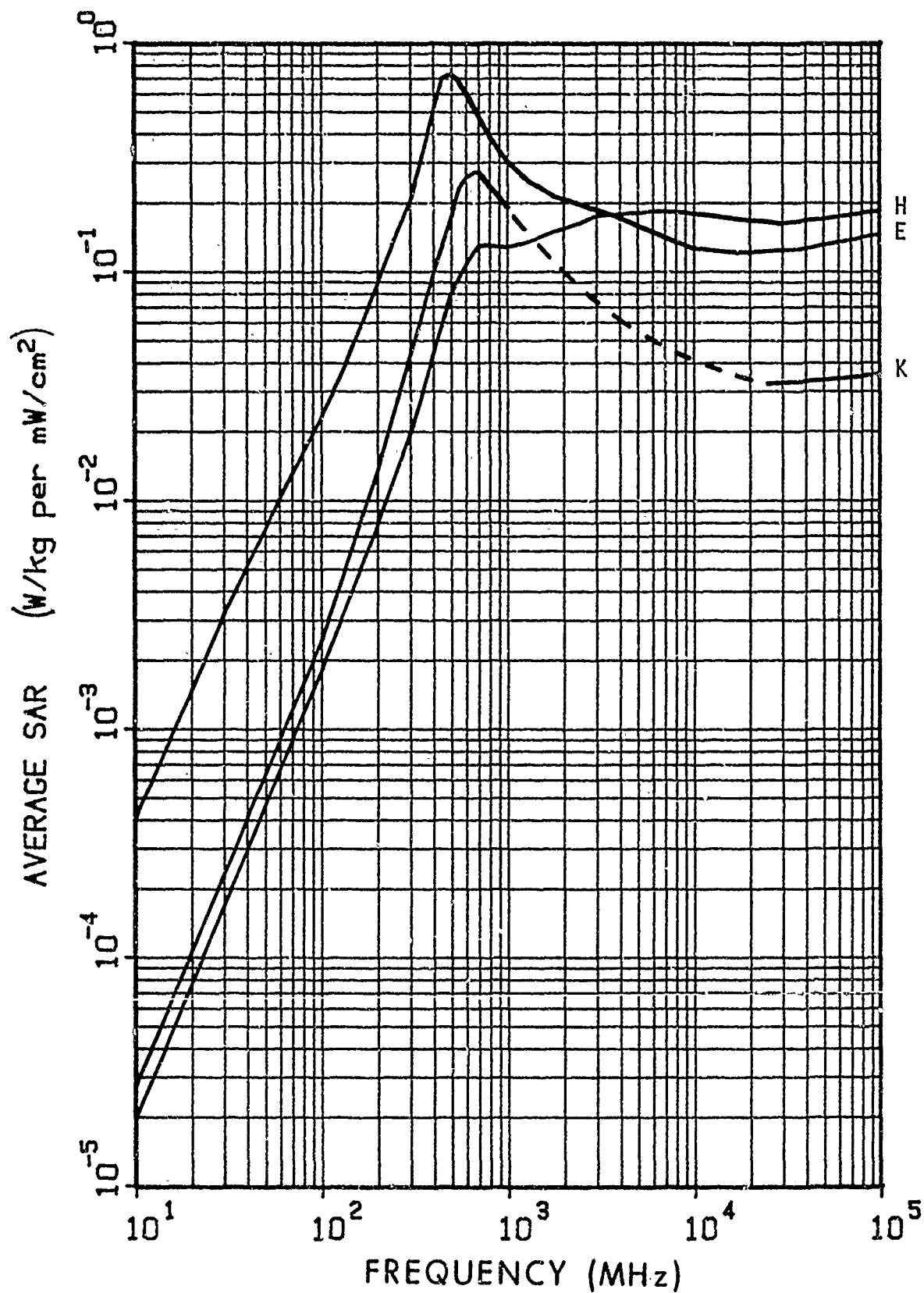
Figure 6.17. Calculated planewave average SAR in a prolate spheroidal model of a large rat for three polarizations; a = 0.12 m, b = 0.0322 m, V = 5.2 × 10^{-4} m^3. The dashed line is estimated values.
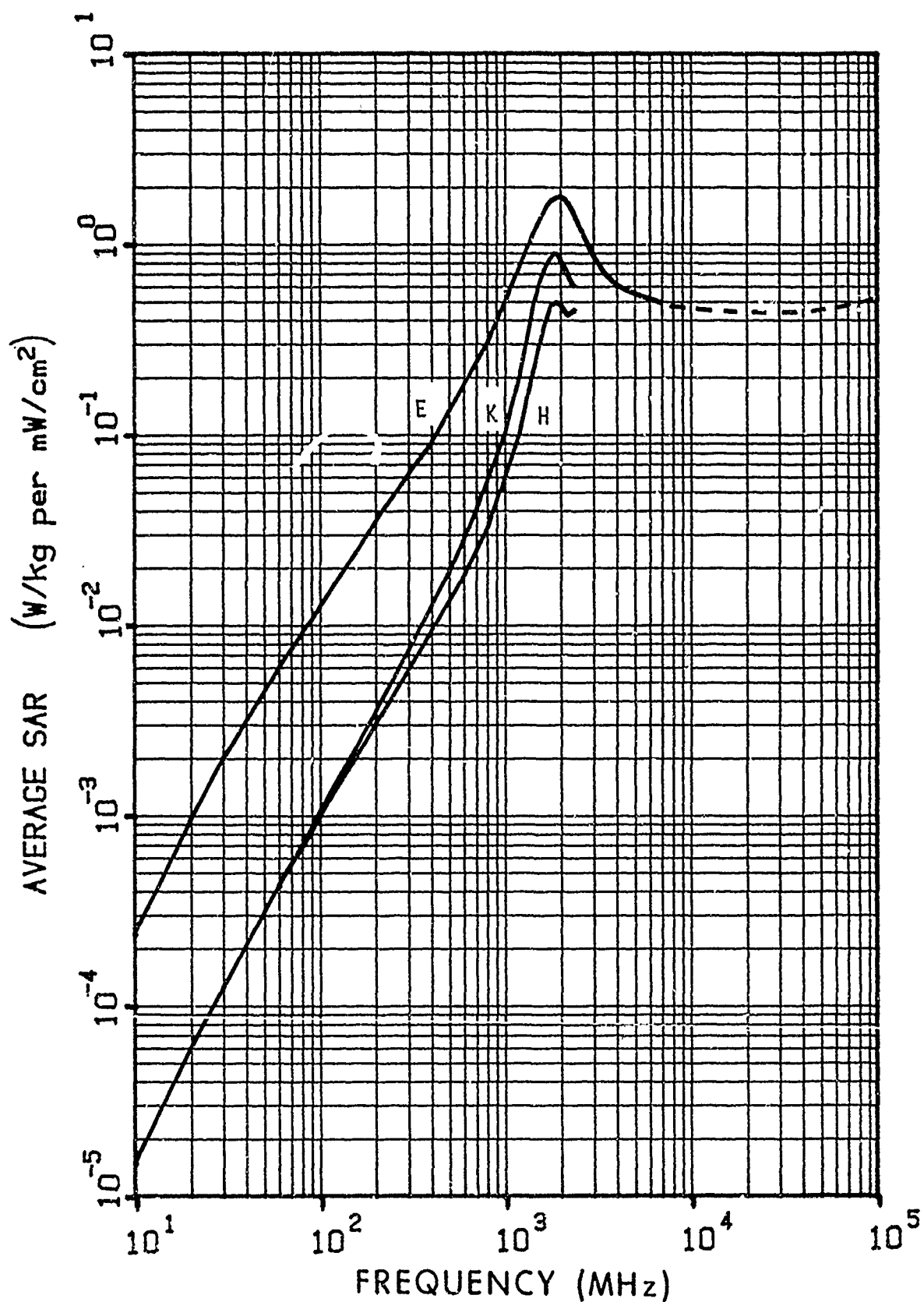
Figure 6.18. Calculated planewave average SAR in a prolate spheroidal model of a medium mouse for three polarizations; a = 3.5 cm, b = 1.17 cm, V = 20 cm^3. The dashed line is estimated values.
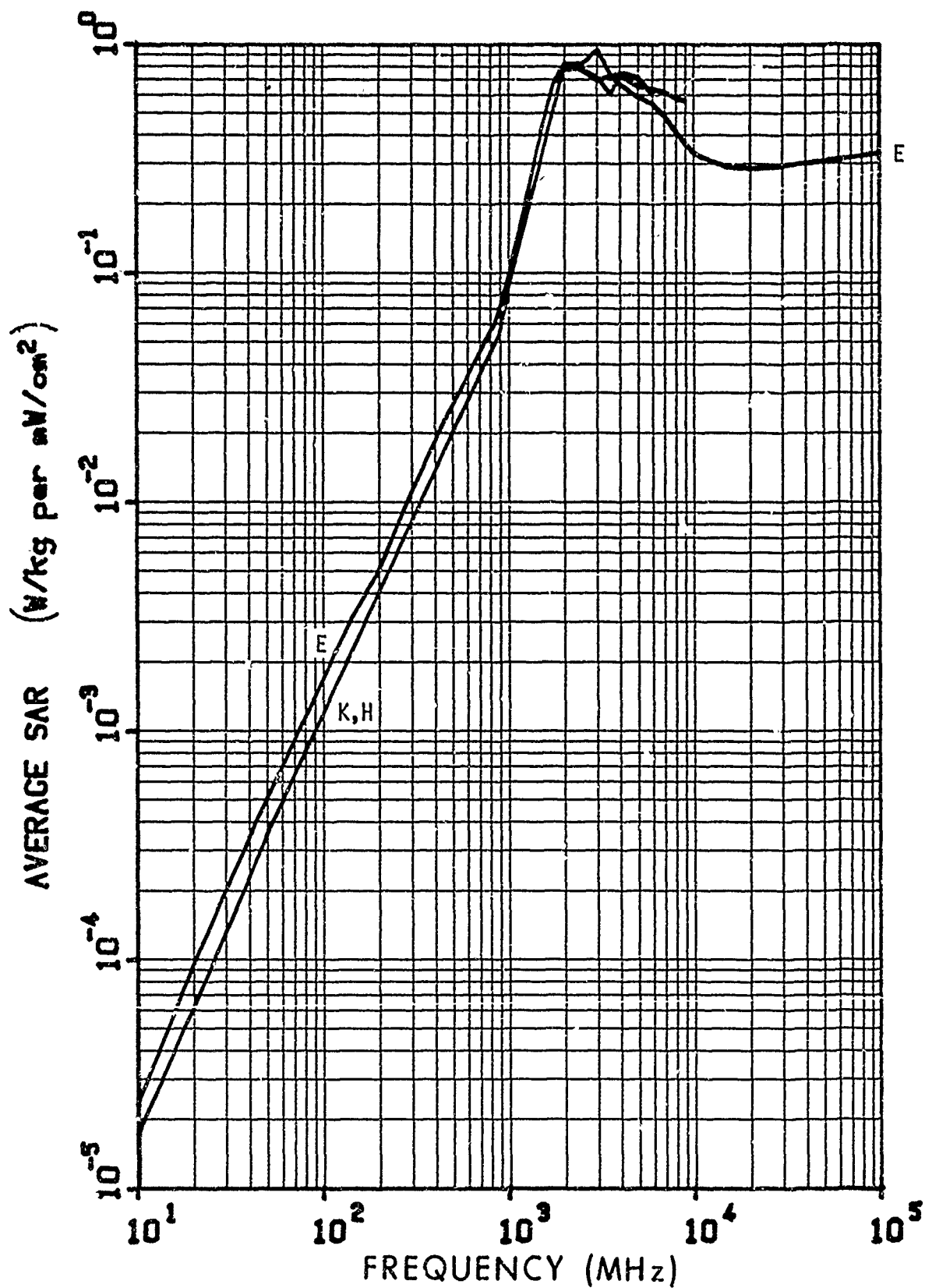
Figure 6.19. Calculated planewave average SAR in a prolate spheroidal model of a quail egg for three polarizations; $a = 1.5$ cm, $b = 1.26$ cm, and $V = 10$ cm^3.
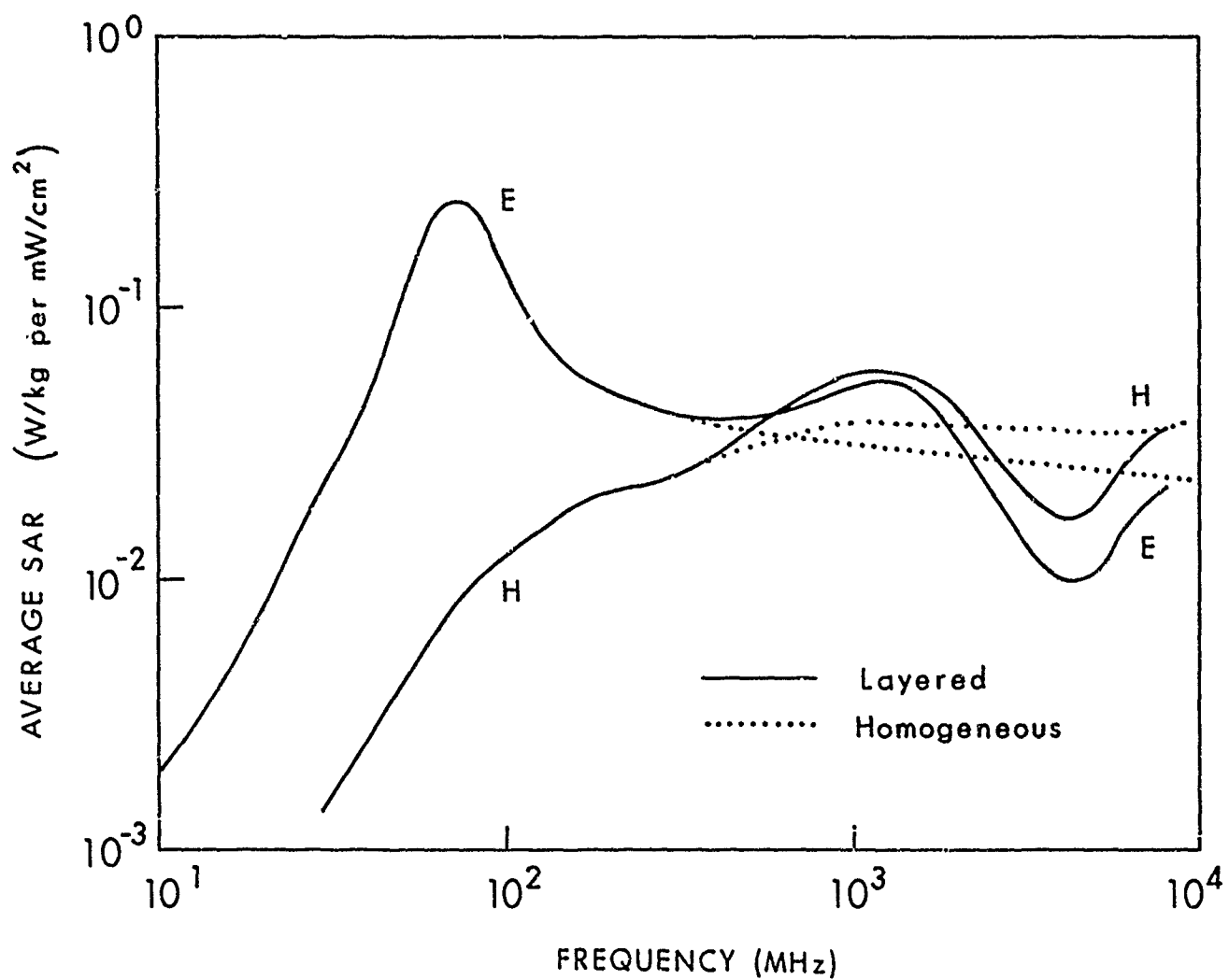
Figure 6.20. Calculated planewave average SAR in homogeneous and multi-layered models of an average man for two polarizations.
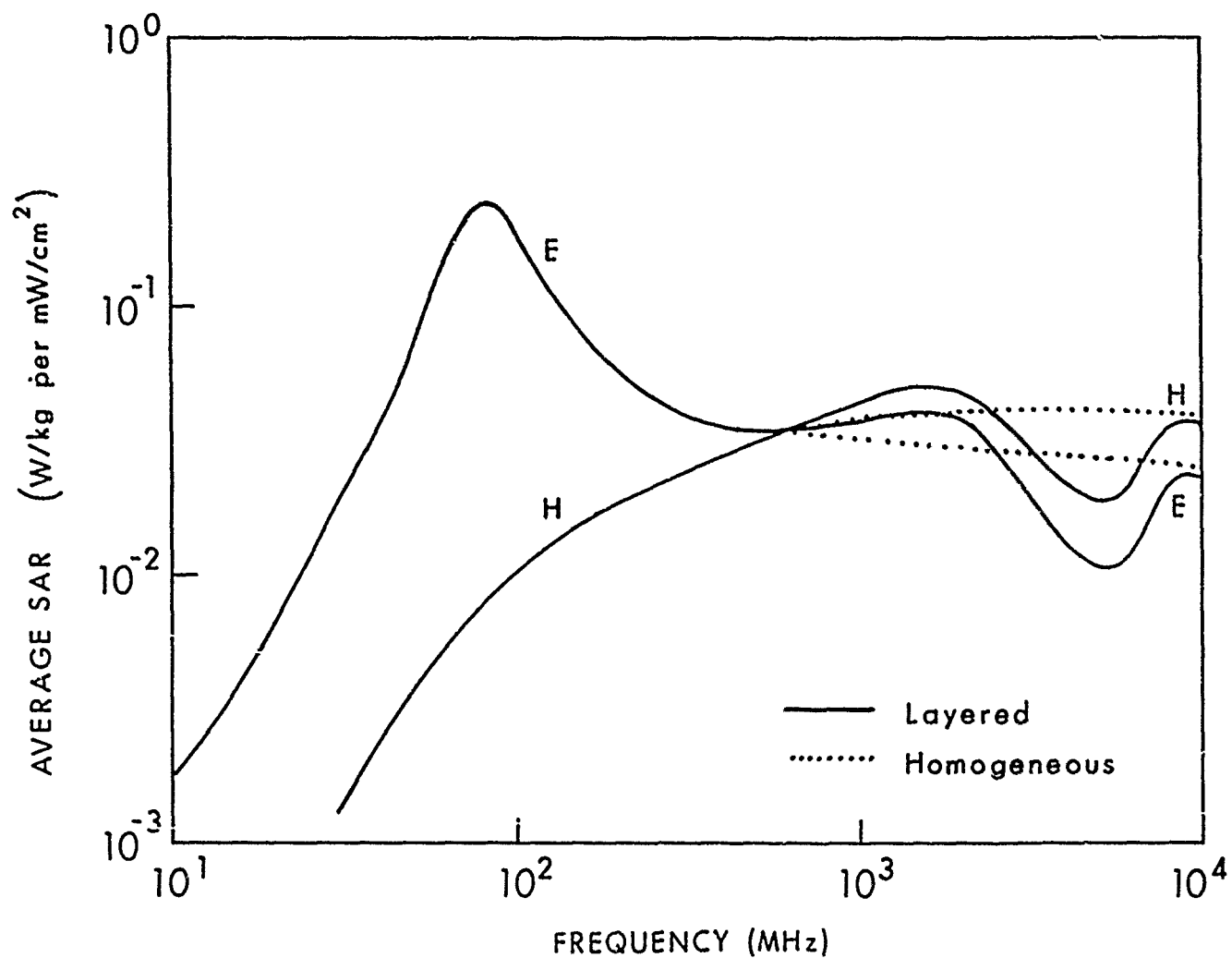
Figure 6.21. Calculated planewave average SAR in homogeneous and multi-layered models of an average woman for two polarizations.
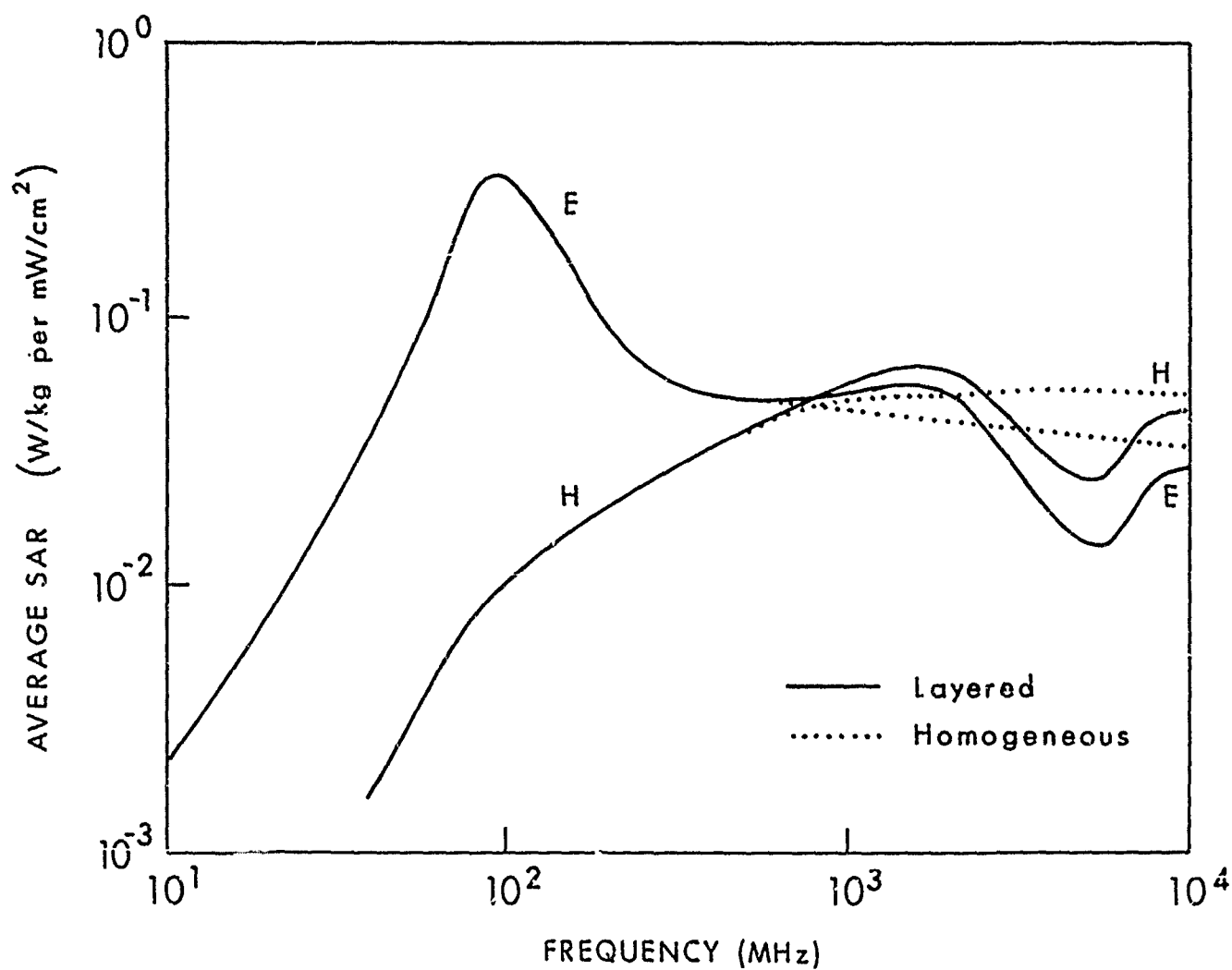
Figure 6.22. Calculated planewave average SAR in homogeneous and multi-layered models of a 10-year-old child for two polarizations.
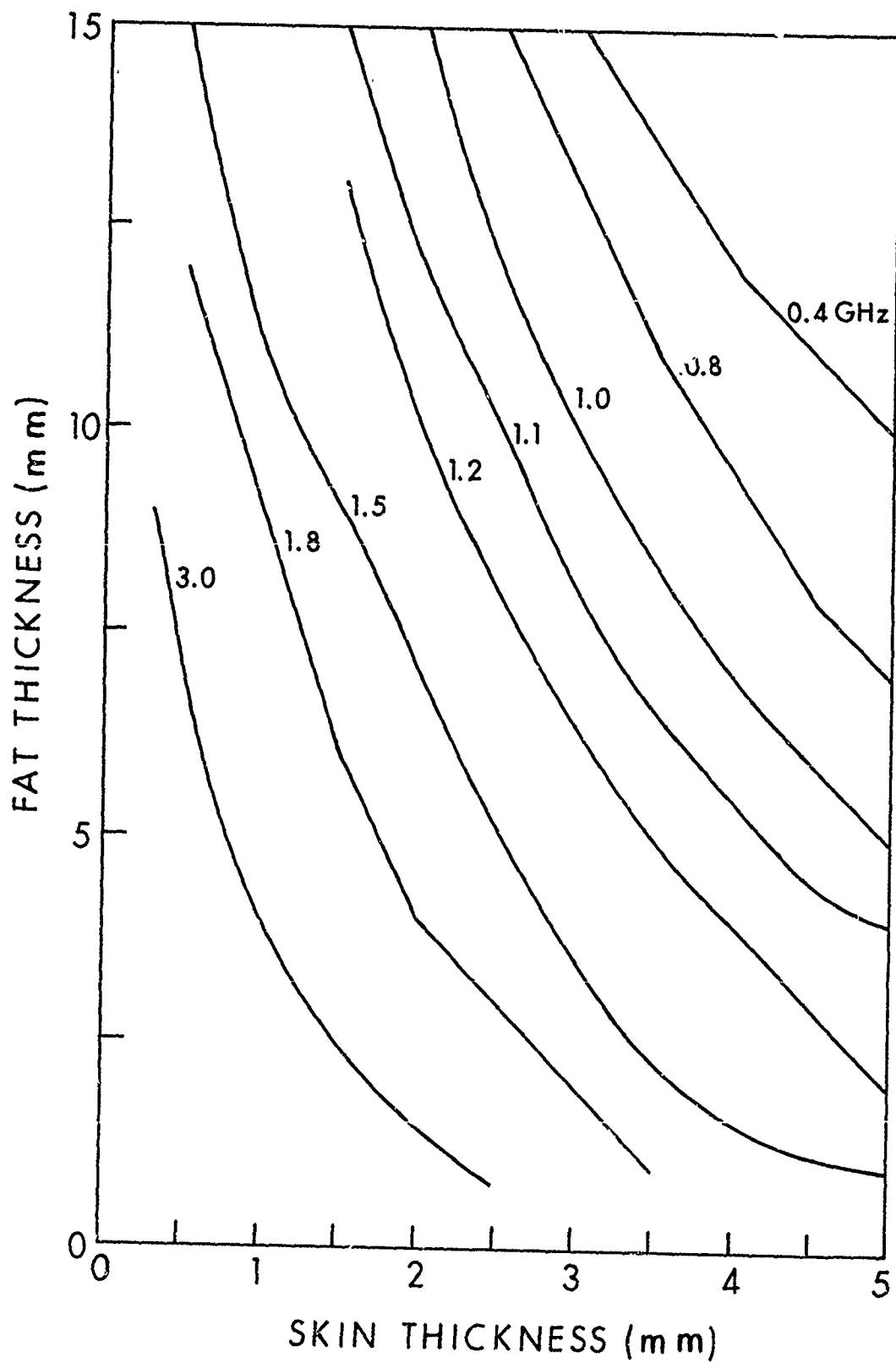
Figure 6.23. Layering resonance frequency as a function of skin
and fat thickness for a skin-fat-muscle cylindri-
cal model of man, planewave H polarization. The
outer radius of the cylinder is 11.28 cm.
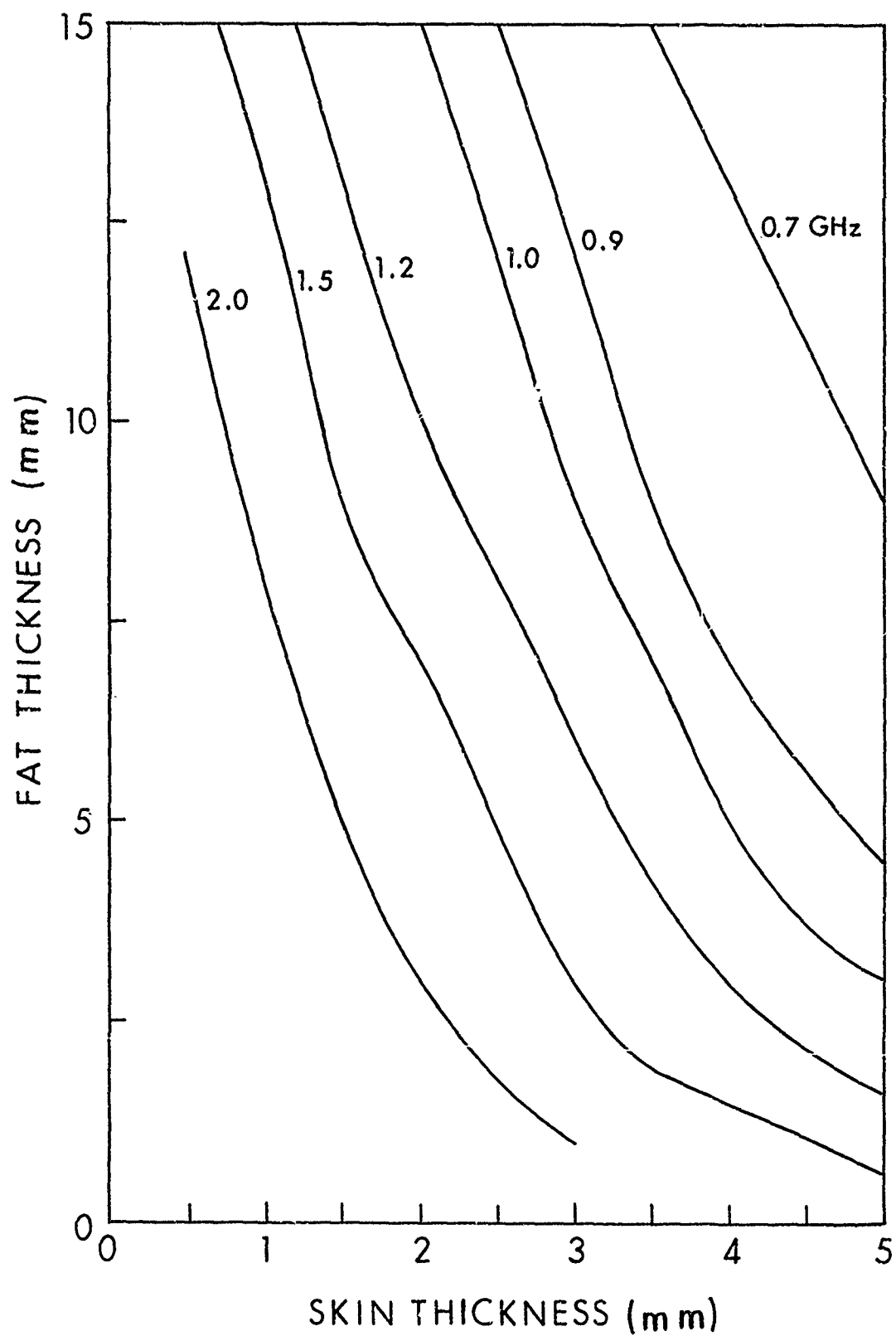
Figure 6.24. Layering resonance frequency as a function of skin and fat thickness for a skin-fat-muscle cylindrical model of man, planewave E polarization. The outer radius of the cylinder is 11.28 cm.
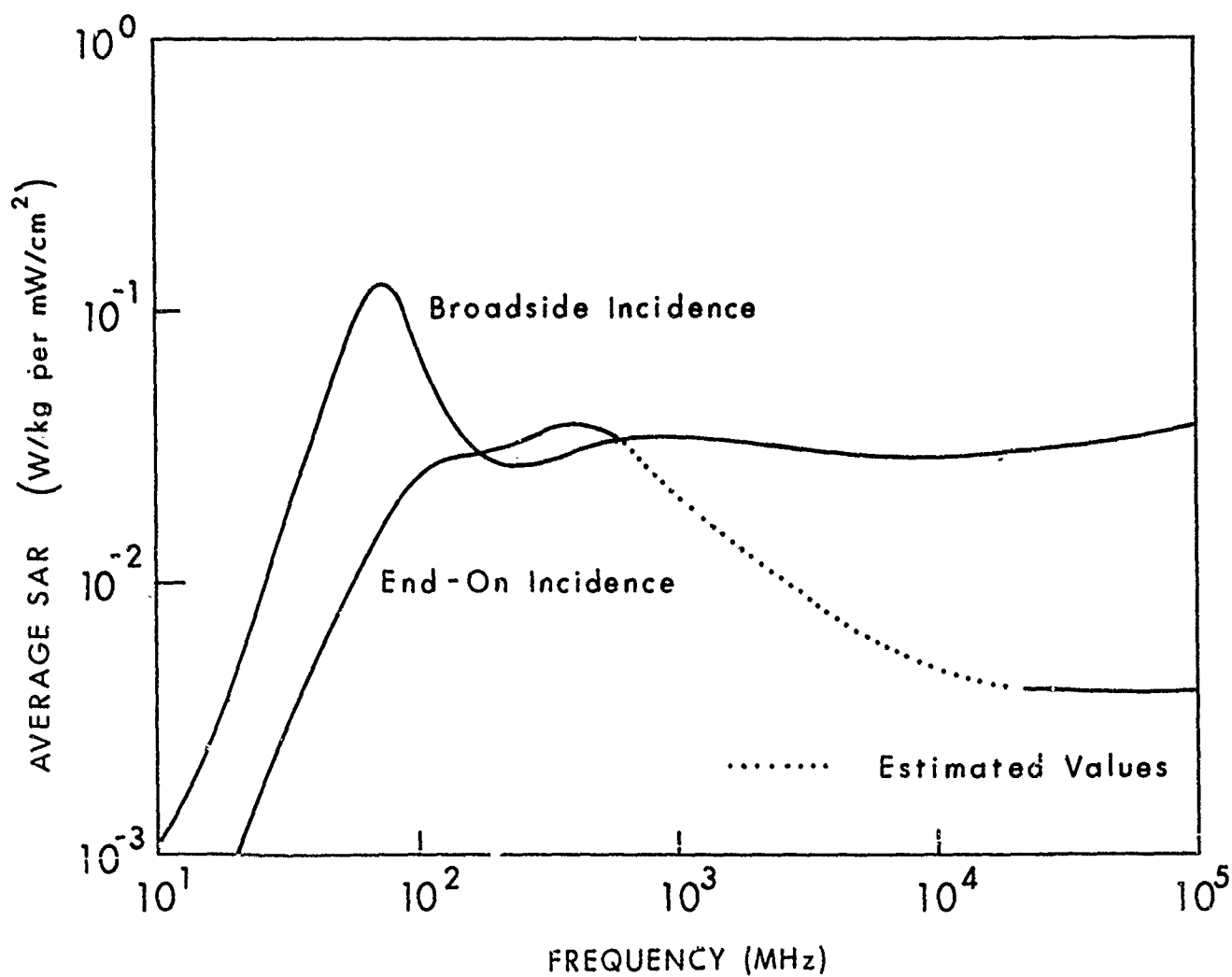
Figure 6.25.   Calculated planewave average SAR in a prolate spheroidal model of an average man   irradiated   by a circularly polarized wave, for two orientations; $a = 0.875$ m, $b = 0.138$ m, $V = 0.07$ m^3.
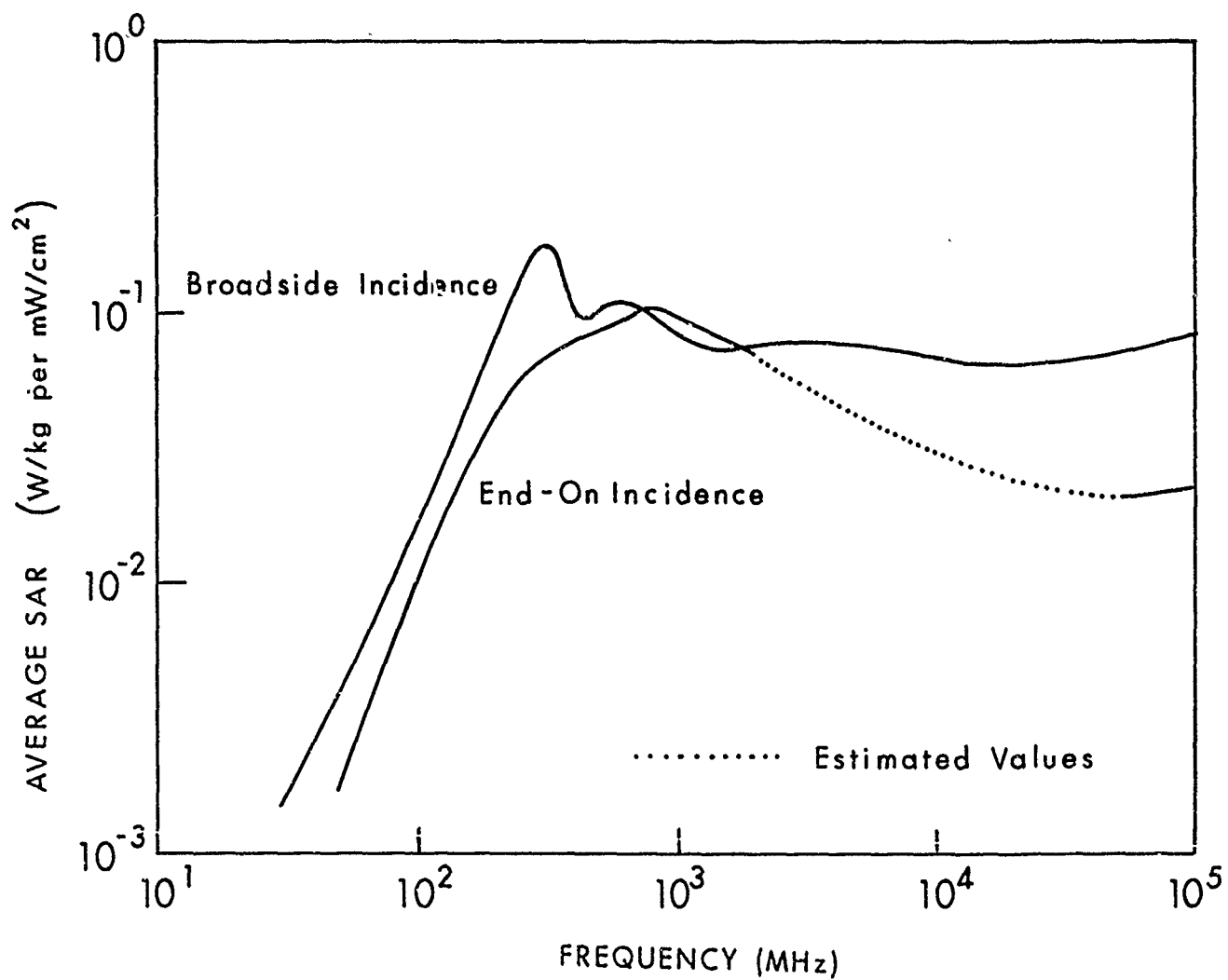
Figure 6.26. Calculated planewave average SAR in a prolate spheroidal model of a sitting rhesus monkey irradiated by a circularly polarized wave, for two orientations; $a = 0.2$ m, $b = 0.0646$ m, $V = 3.5 \times 10^{-3}$ m^3.
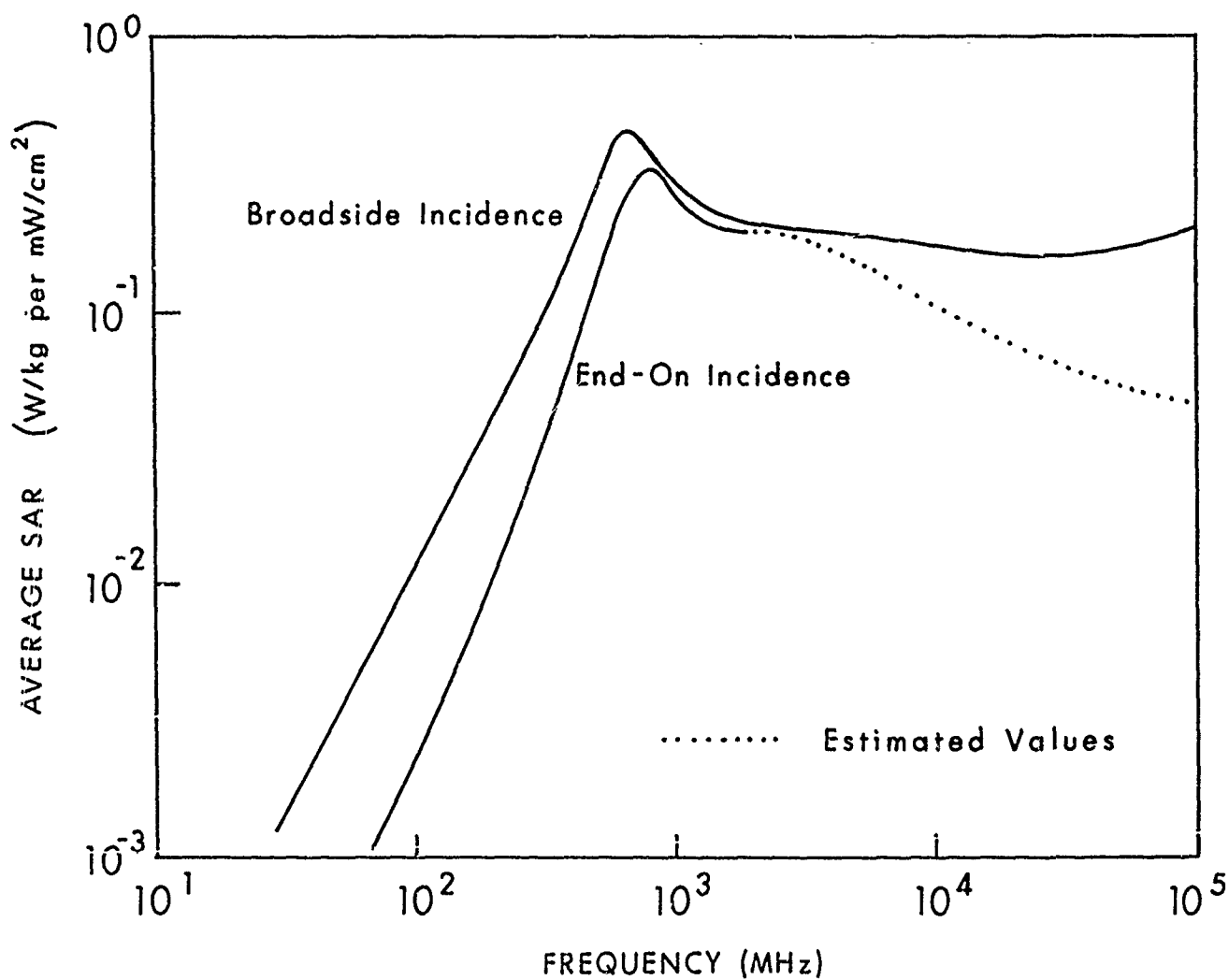
Figure 6.27. Calculated planewave average SAR in a prolate spheroidal model of a medium rat irradiated by a circularly polarized wave, for two orientations;   a = 0.1 m, b = 0.0276 m, V = 3.2 × 10^{-4} m^3.
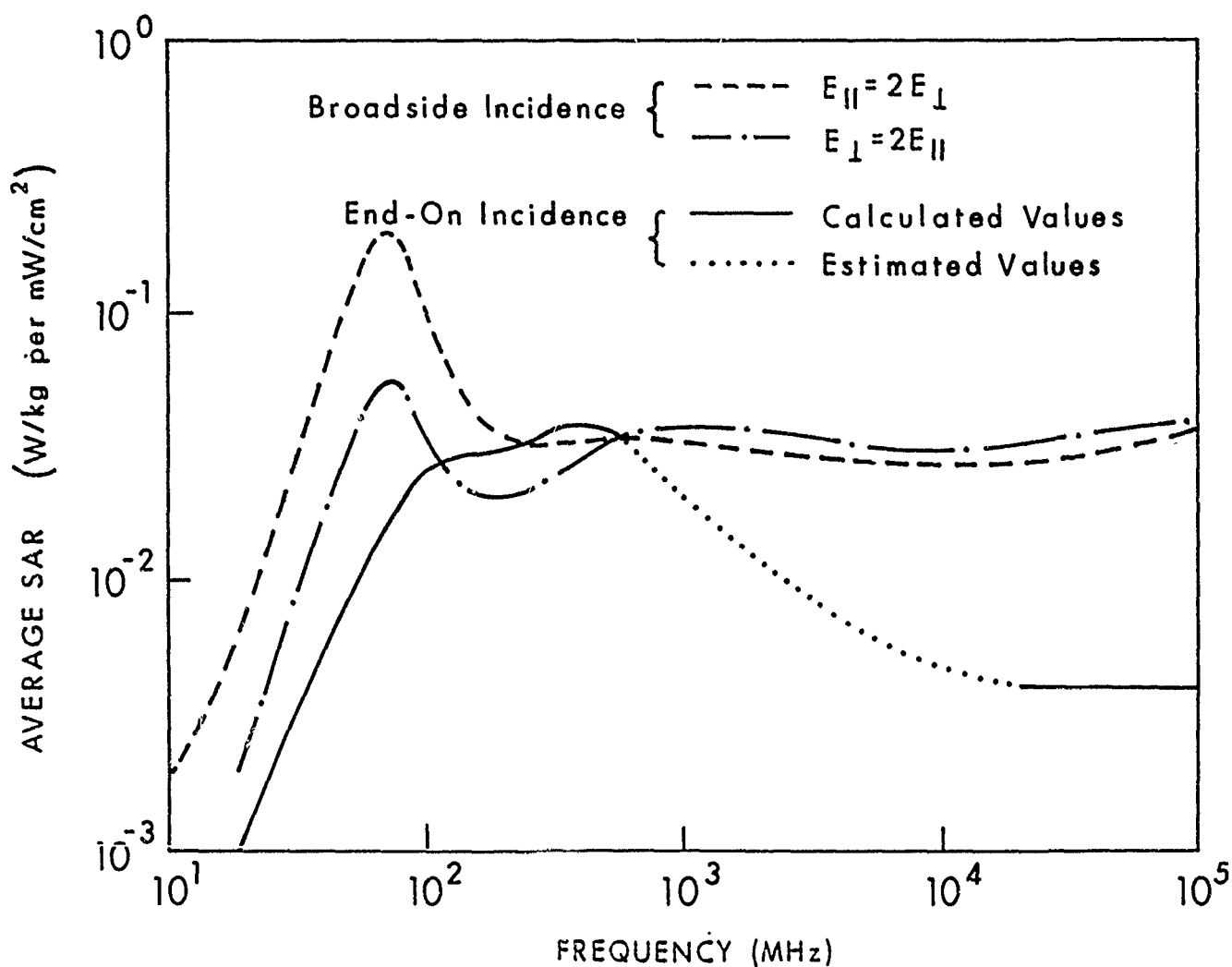
Figure 6.28. Calculated planewave average SAR in a prolate spheroidal model of an average man irradiated by an elliptically polarized wave, for two orientations; $a = 0.875$ m, $b = 0.138$ m, $V = 0.07$ m^3.
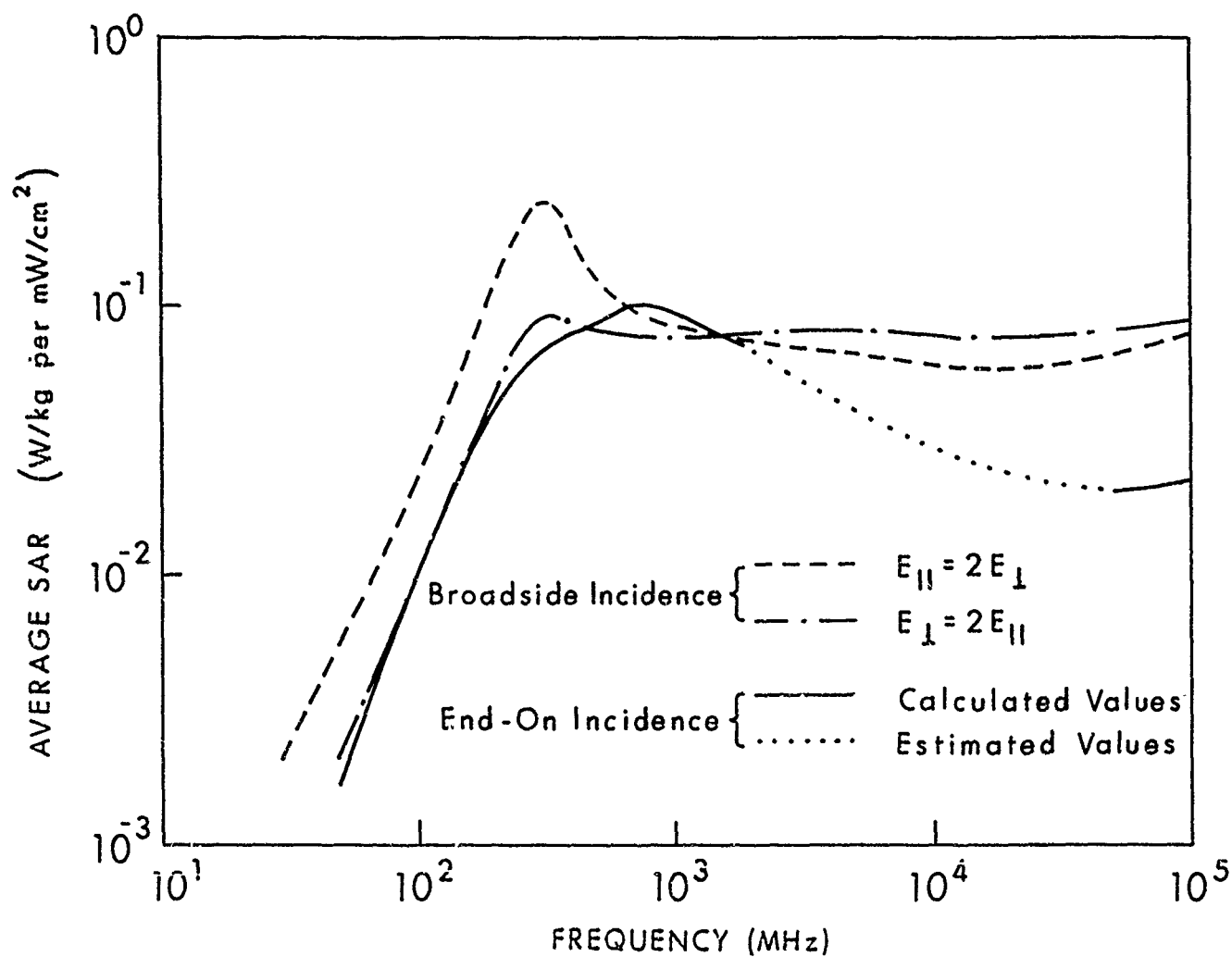
Figure 6.29. Calculated planewave average SAR in a prolate spheroidal model of a sitting rhesus monkey irradiated by an elliptically polarized wave, for two orientations; $a = 0.2$ m, $b = 0.0646$ m, $V = 3.5 \times 10^{-3}$ m³.
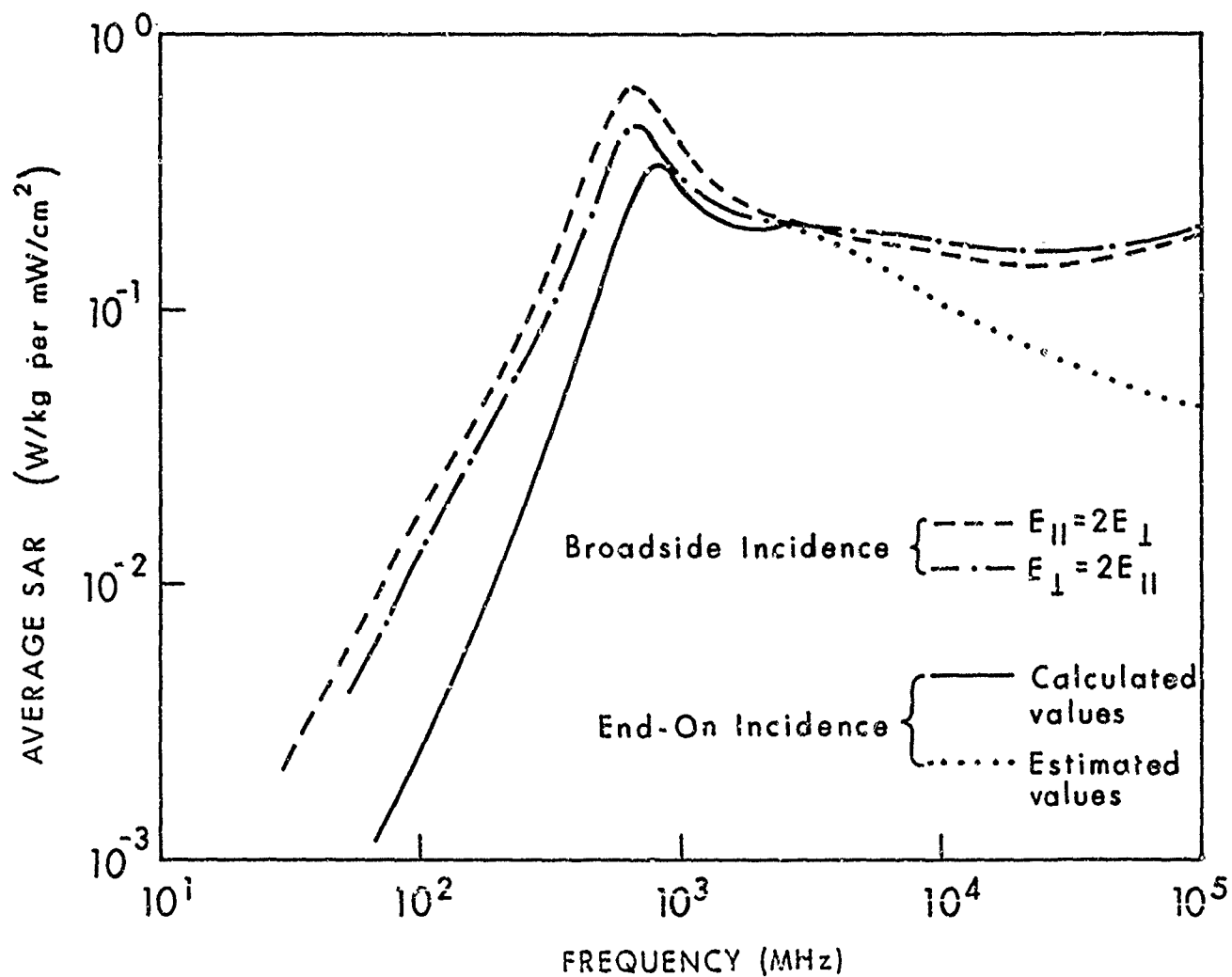
Figure 6.30. Calculated planewave average SAR in a prolate spheroidal model of
a medium rat irradiated by an elliptically polarized wave, for
two orientations; a = 0.1 m, b = 0.0276 m, V = 3.2 × 10^{-4} m^3.

6.2. CALCULATED NEAR-FIELD DOSIMETRIC DATA FOR AVERAGE SAR

6.2.1. Short-Dipole and Small-Loop Irradiators

Figures 6.31-6.36 show the calculated average SAR in prolate spheroidal models of an average man and a medium rat irradiated by the near fields of a short electric dipole. The radiation characteristics of the dipole are shown in Figures 6.37-6.40. Figures 6.41-6.42 show the average SAR, as a function of frequency and dipole-to-body spacing, in spheroidal models of an average man exposed to the near fields of a short electric dipole and a short magnetic dipole respectively.

To emphasize the near-field absorption characteristics, the average SAR in Figures 6.31-6.36 for all frequencies is normalized to unity at a distance of one wavelength from the source. The relative SAR curves thus obtained lie close together and oscillate around the $(\lambda/d)^2$ curve that describes the approximate variation of the far-field absorption characteristics as a function of distance from the source. Of particular interest is the possible reduction in the average SAR below the far-field value. In other words, although the reactive fields are stronger near the source, they are absorbed at a rate less than that for planewaves (far fields). This was first observed by Iskander et al., then verified experimentally and explained in terms of the variation of the incident electric and magnetic fields (Iskander et al., 1981). A detailed explanation of the relationship between the average SAR and the incident field is given in Section 3.3. These qualitative relations show that in spite of the complex characteristics of the near fields, including arbitrary angle between E and H and a wave impedance that is different from 377 Ω, the near-field absorption characteristics can still be explained on the same basis as the far-field SARs.
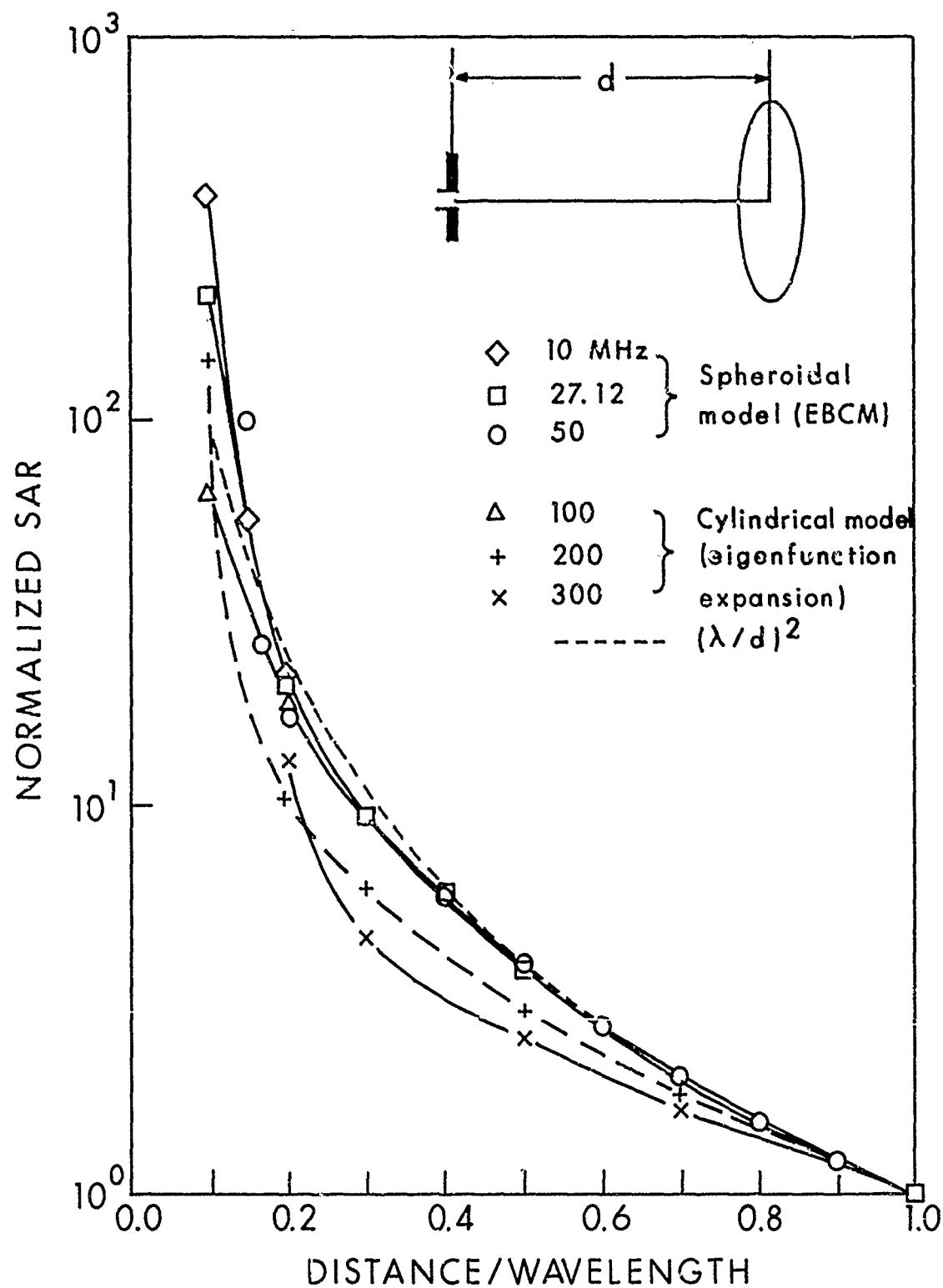
Figure 6.31. Calculated normalized average SAR as a function of
the electric dipole location for E polarization
in a prolate spheroidal model of an average man.
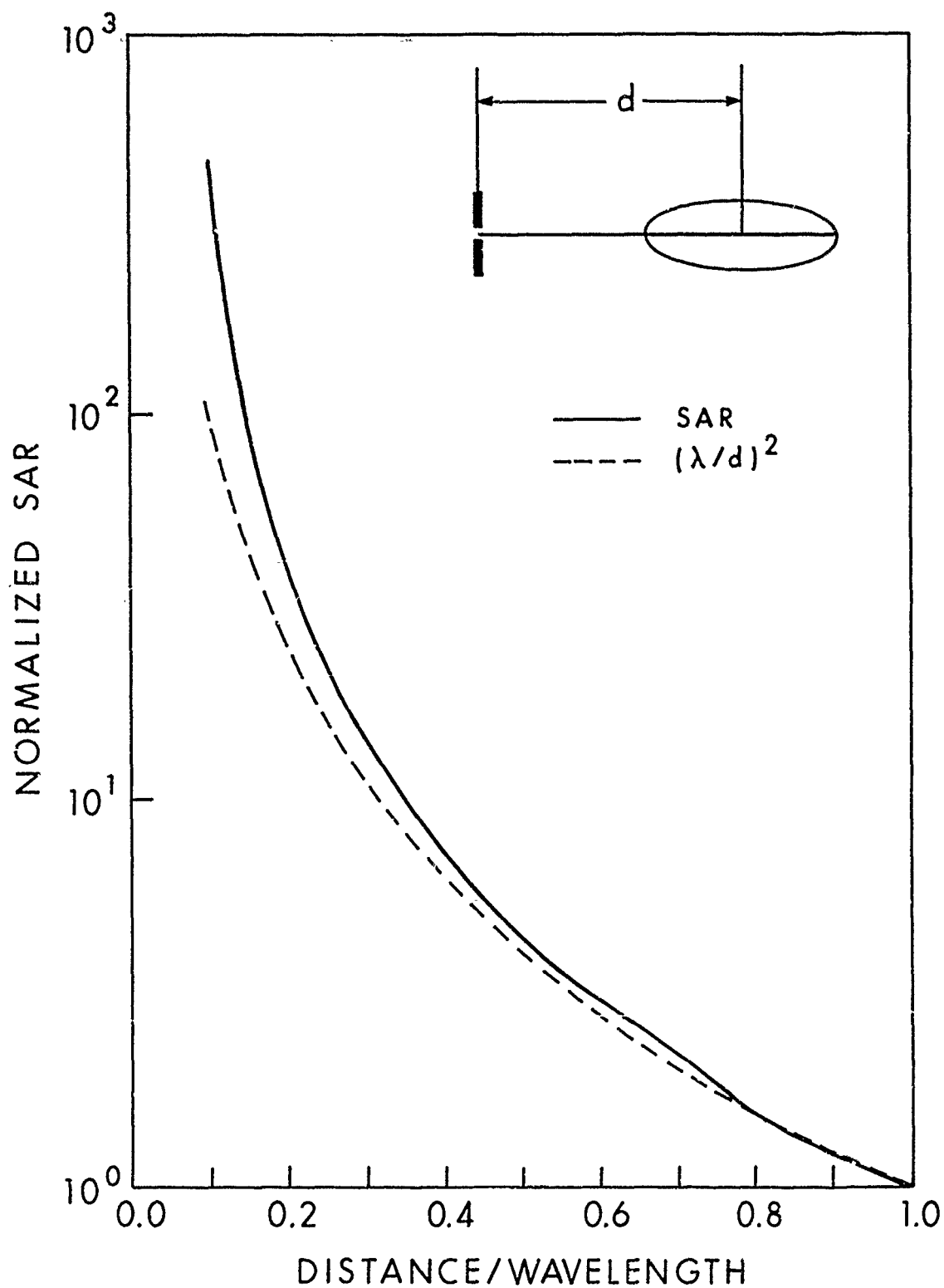
Figure 6.32.   Calculated average SAR (by long-wavelength approximation) as
                a function of the electric dipole location for K polarization
                at 27.12 MHz in a prolate spheroidal model of an average man.

- 6.34 -
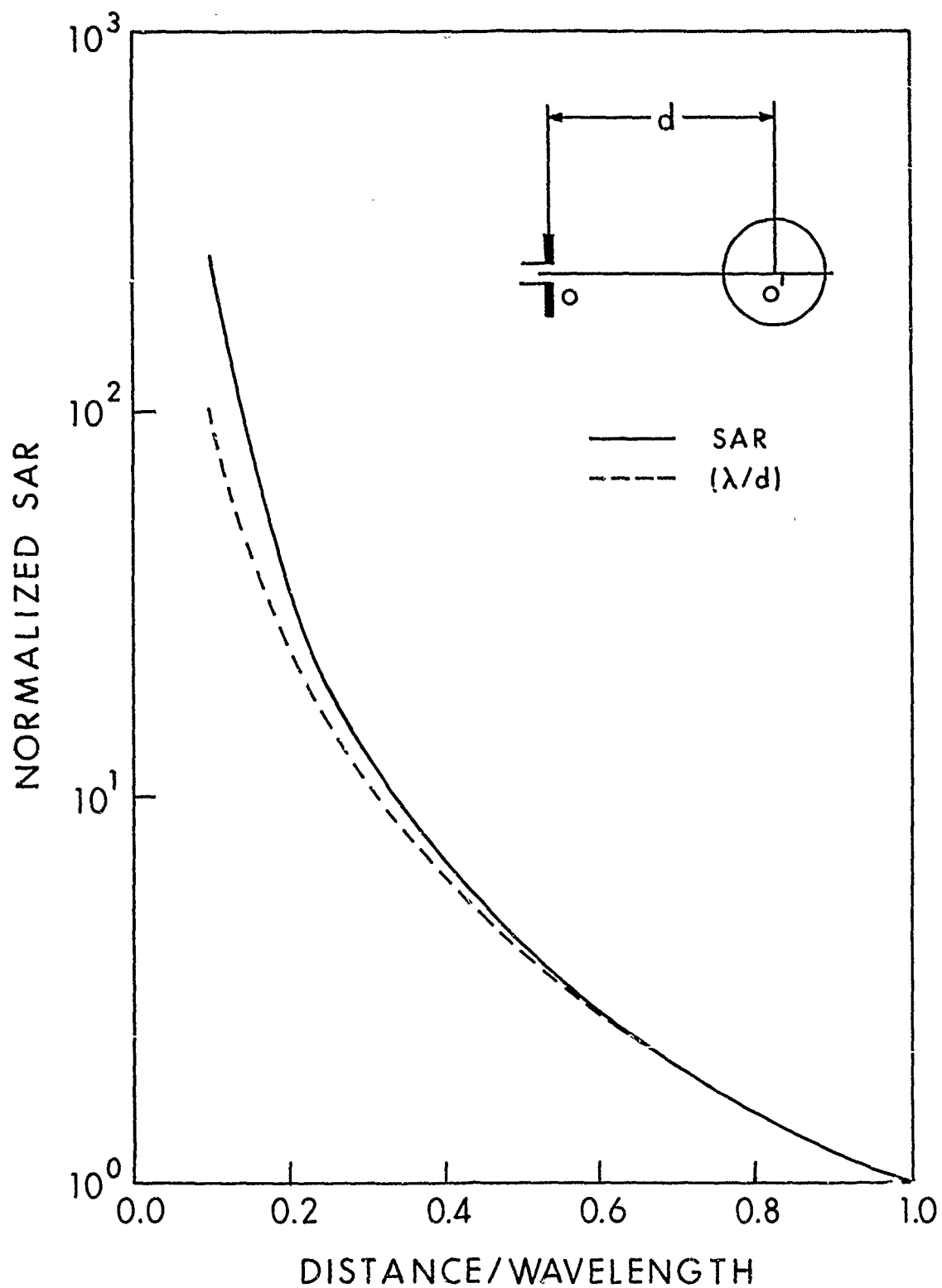
Figure 6.33. Calculated average SAR (by long-wavelength approximation) as
a function of the electric dipole location for H polarization
at 27.12 MHz in a prolate spheroidal model of an average man.
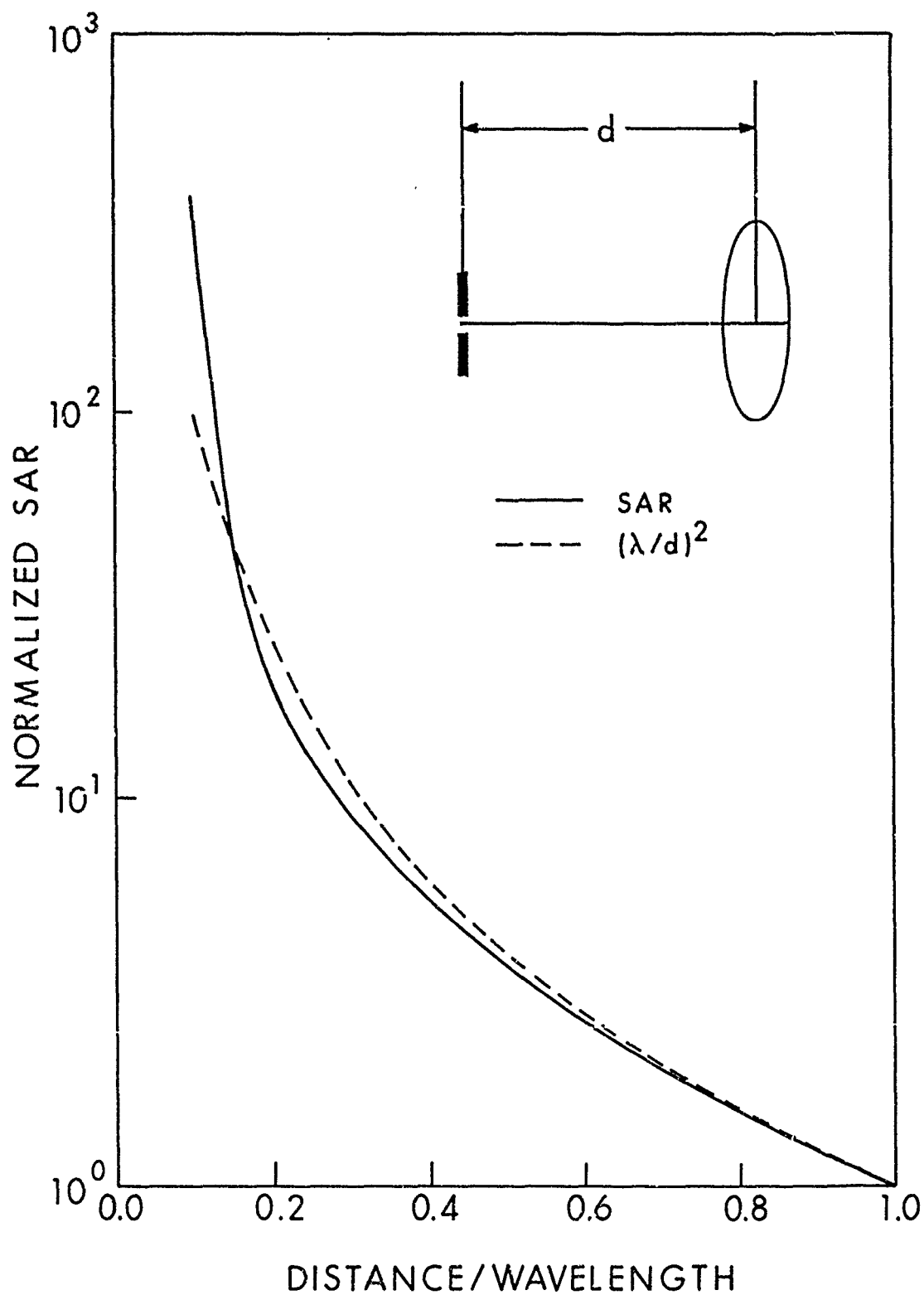
Figure 6.34. Calculated average SAR (by long-wavelength approximation) as a function of the electric dipole location for E polarization at 100 MHz in a prolate spheroidal model of a medium rat.
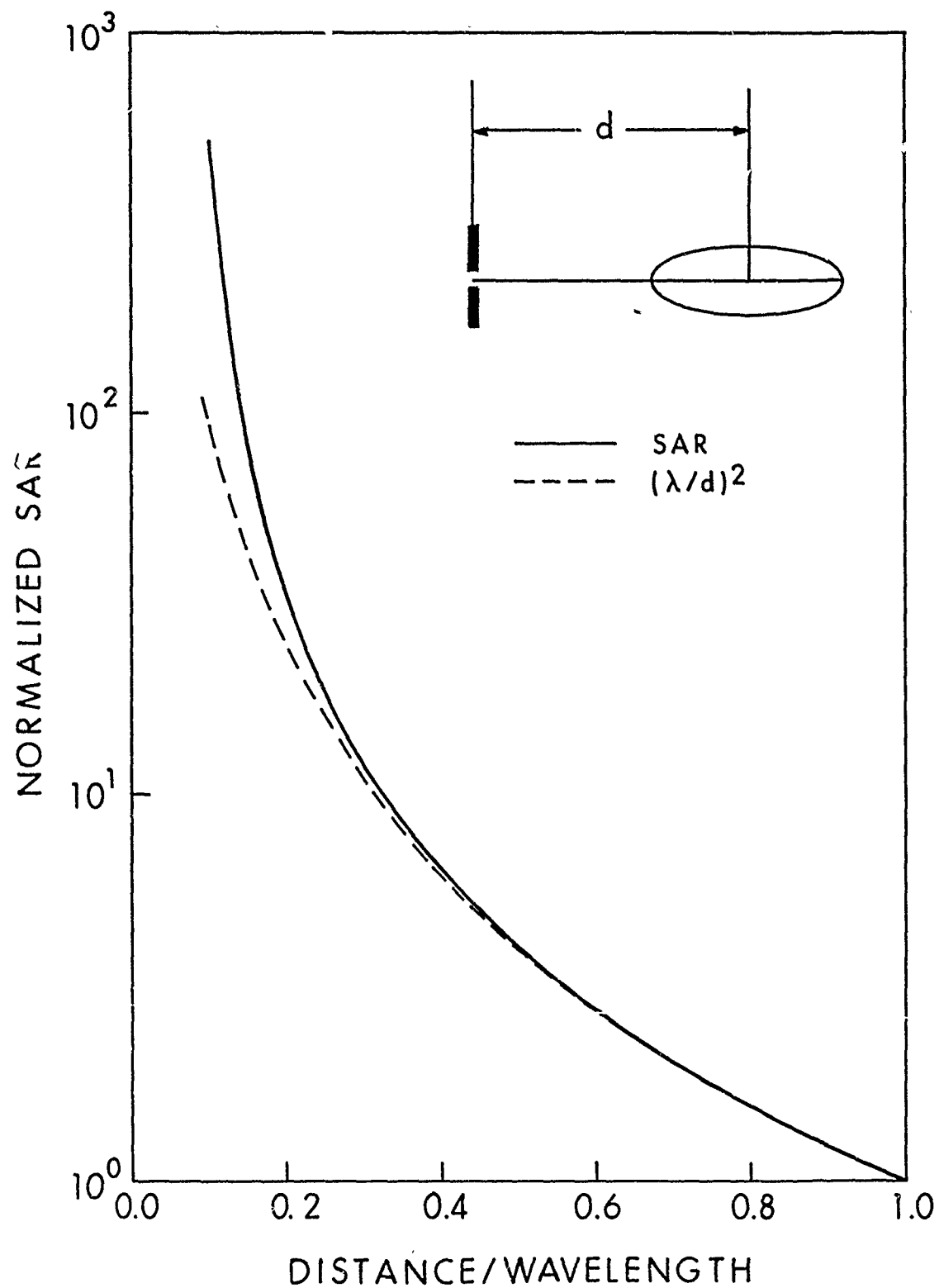
Figure 6.35. Calculated average SAR (by long-wavelength approximation) as
a function of the electric dipole location for K polarization
at 100 MHz in a prolate spheroidal model of a medium rat.

- 6.37 -
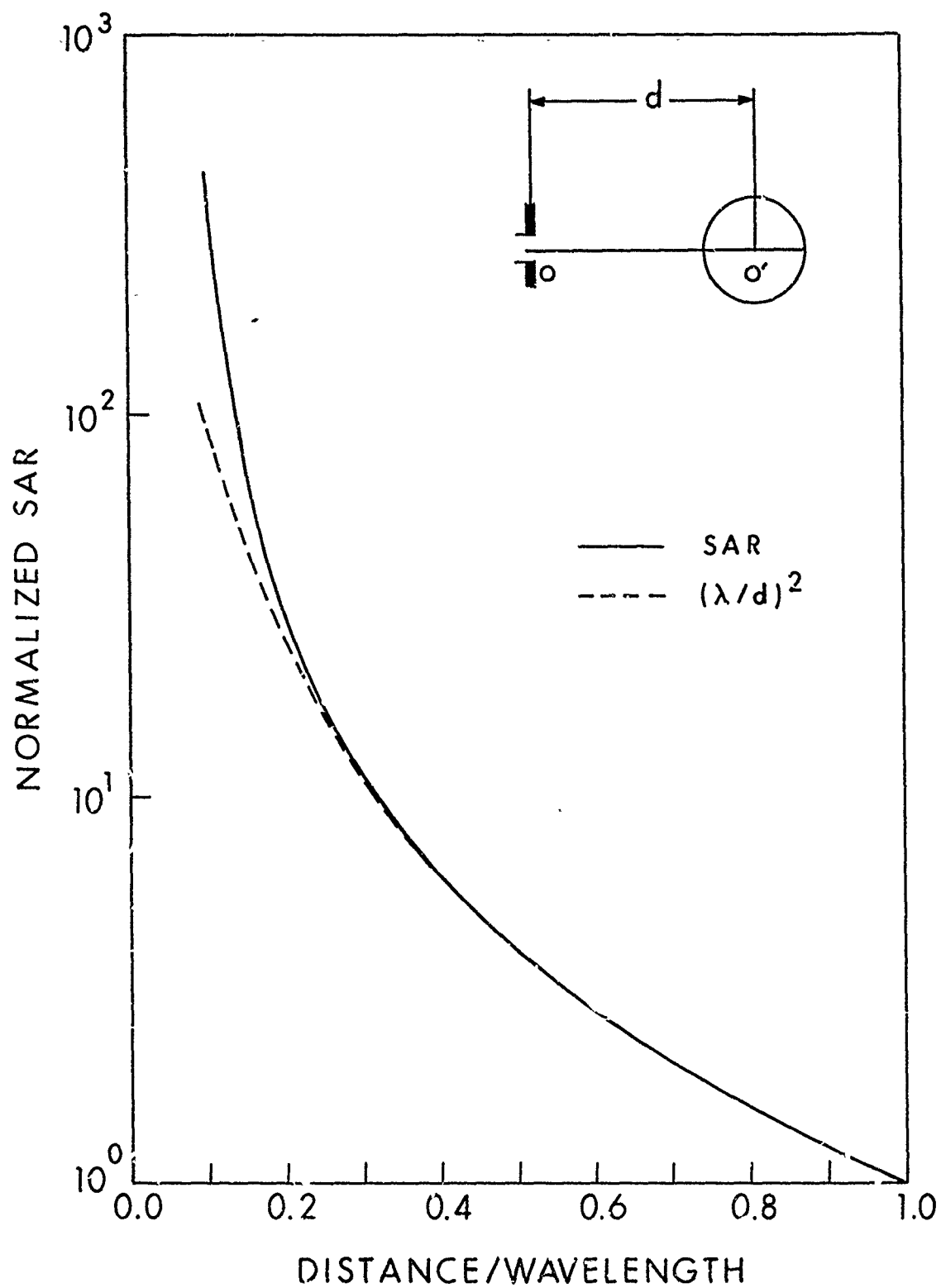
Figure 6.36. Calculated average SAR (by long-wavelength approximation) as a function of the electric dipole location for H polarization at 100 MHz in a prolate spheroidal model of a medium rat.
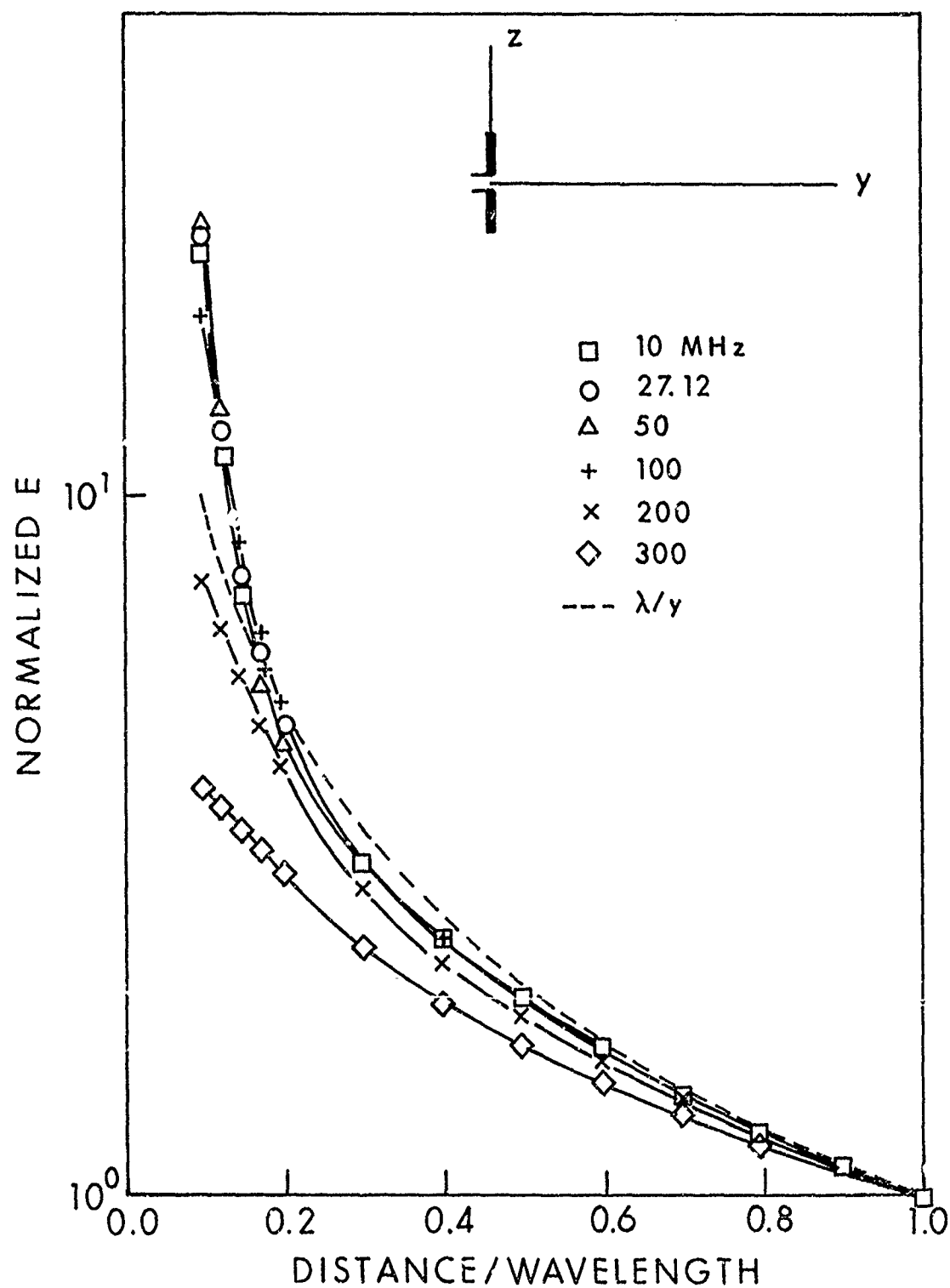
Figure 6.37. Calculated normalized E-field of a short electric dipole, as a function of y/λ at $z = 30$ cm.
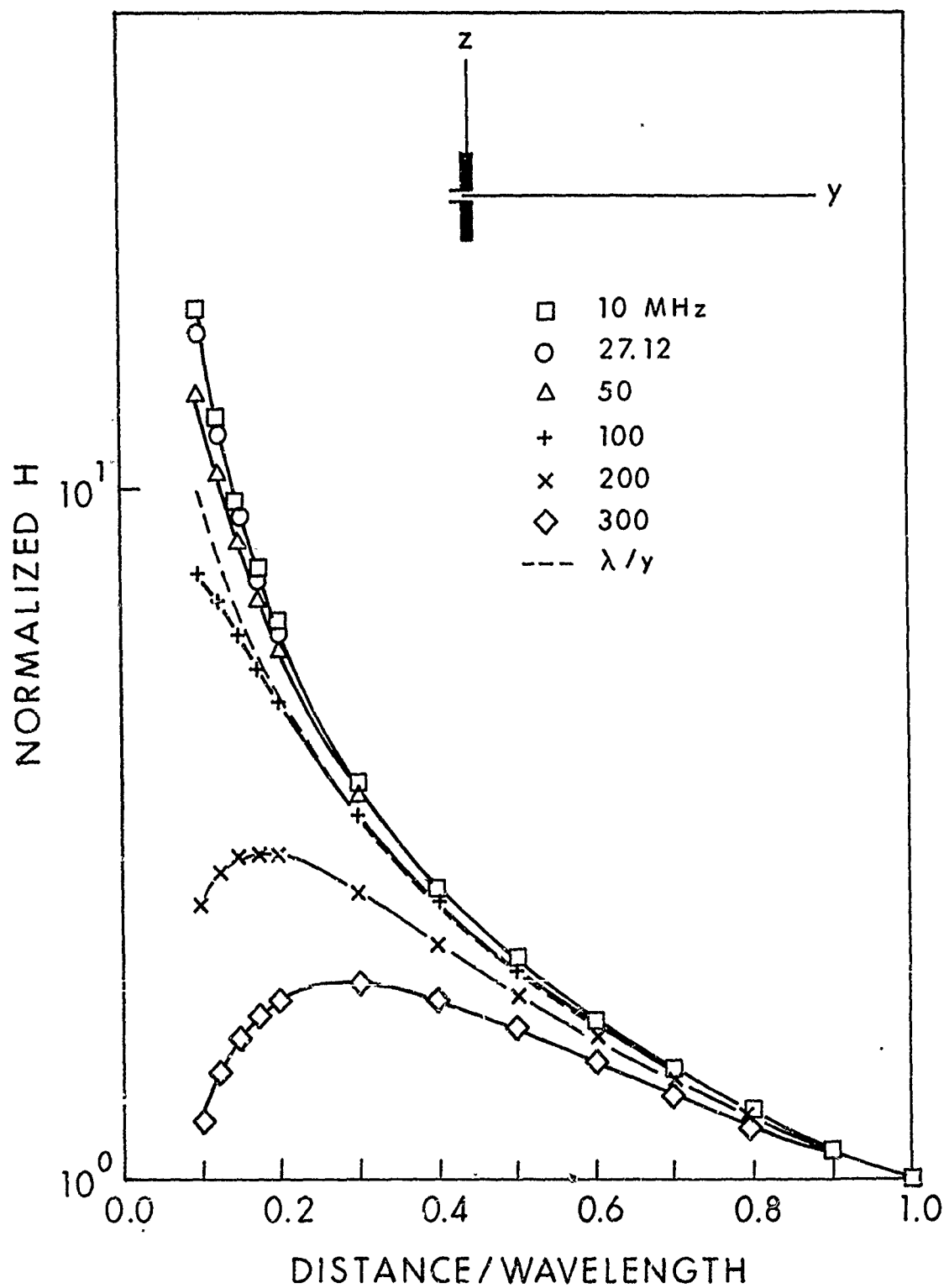
Figure 6.38. Calculated normalized H-field of a short electric
dipole, as a function of y/λ at $z = 30$ cm.
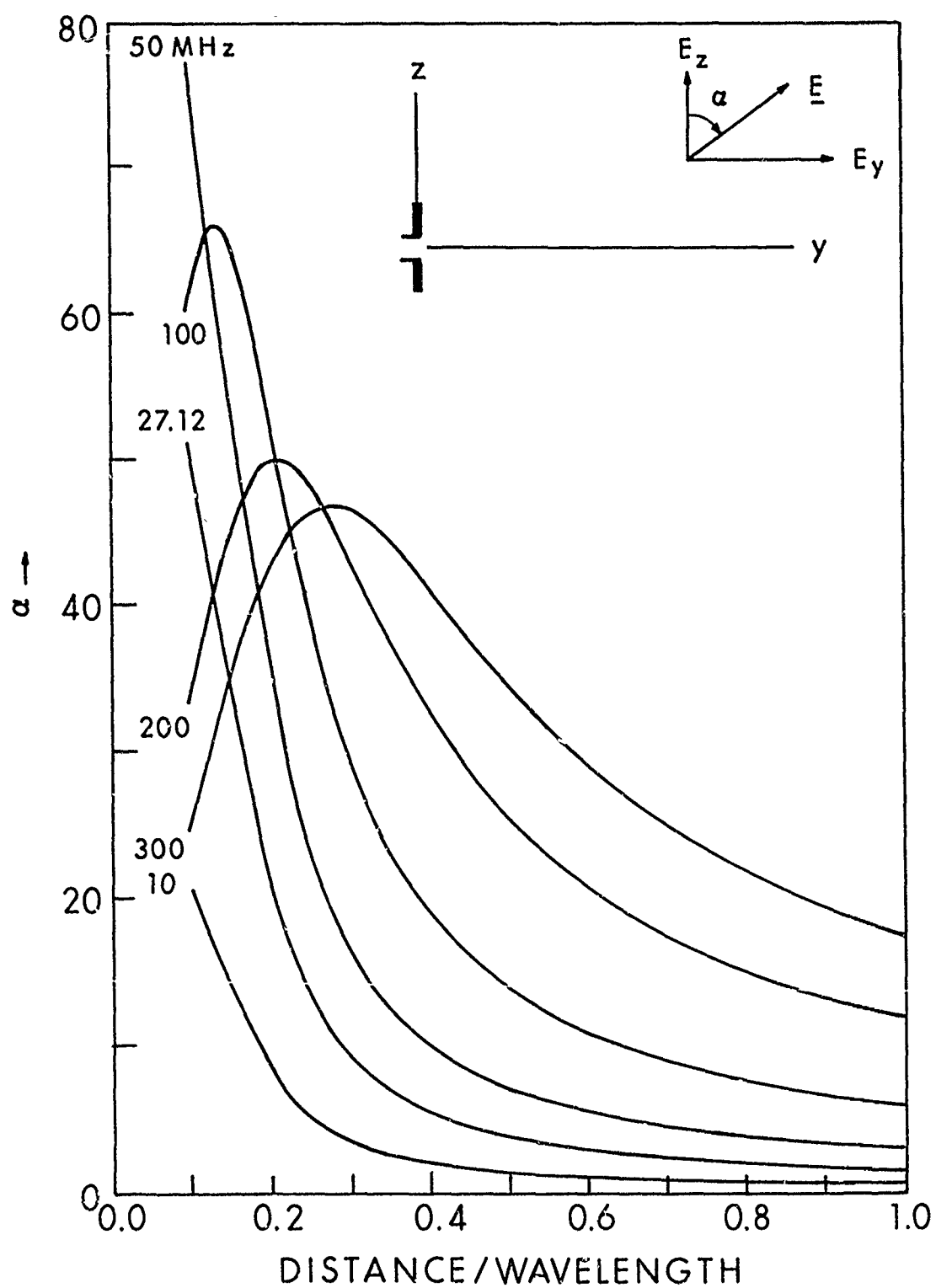
Figure 6.39. Calculated variation of α as a function of y/λ, at z = 30 cm, for a short electric dipole.
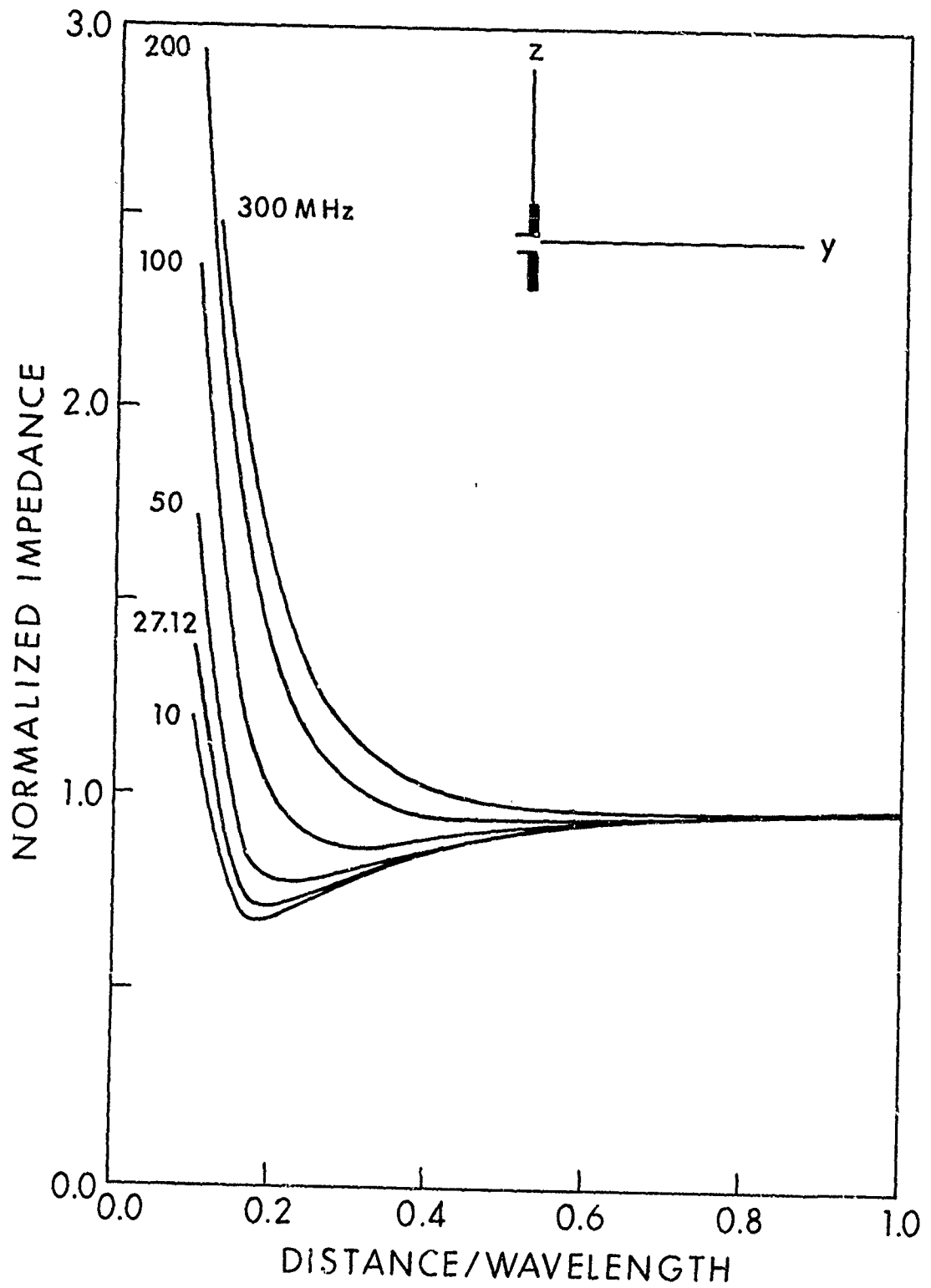
Figure 6.40.   Calculated normalized field impedance of a short
electric dipole, as a function of y/λ at z = 30 cm.
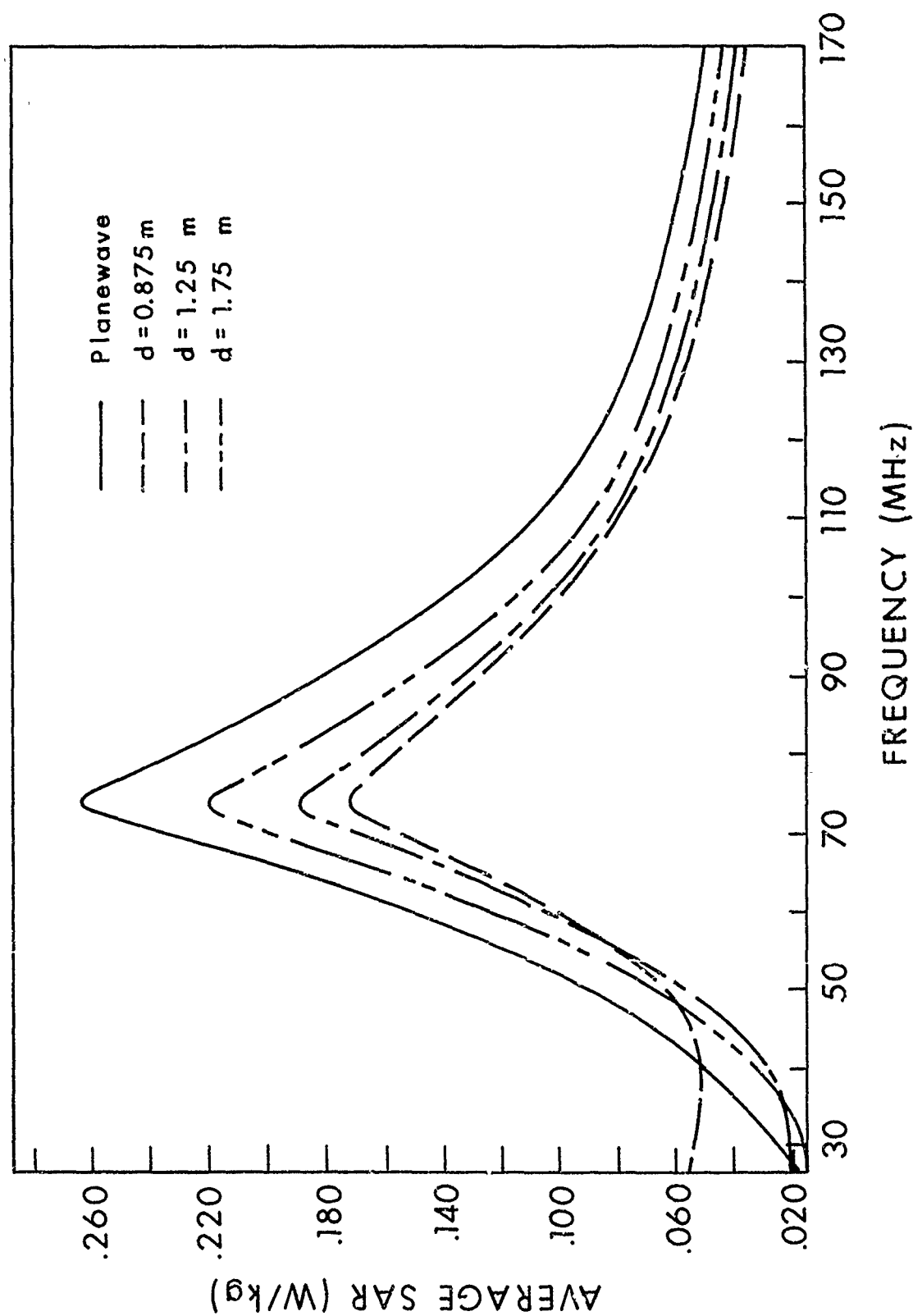
Figure 6.41. Calculated average SAR in a prolate spheroidal model of an average man irradiated by the near fields of a short electric dipole, as a function of the dipole-to-body spacing, d.
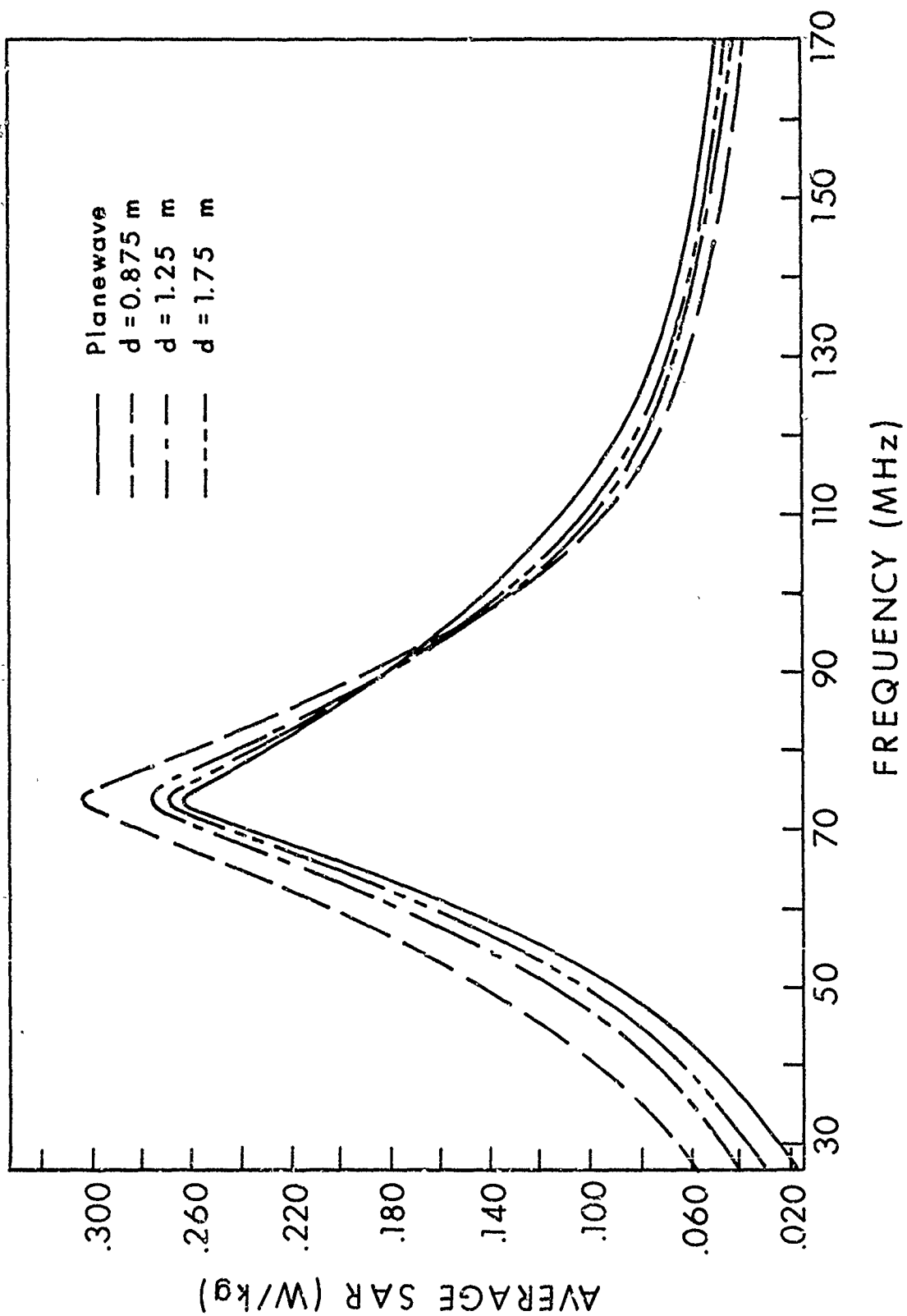
Figure 6.42. Calculated average SAR in a prolate spheroidal model of an average man irradiated by the near fields of a small magnetic dipole, as a function of the dipole-to-body spacing, d.

- 6.44 -

6.2.2. Aperture Fields

Chatterjee et al. (1980a, 1980b, 1980c) have calculated values of both local and average SARs in planar and block models of man by expressing the incident fields in terms of an angular spectrum of planewaves. Some of their data for the model of Figure 6.43 and incident E-field of Figure 6.44 are shown in Figures 6.45 and 6.46. Figure 6.44 shows the incident E_z measured near a 27.12-MHz RF sealer. They assumed no variation of the fields in the y direction, and calculated the E_x that would satisfy Maxwell's equations for the measured E_z. Since the magnitude but not the phase of E_z was measured, they assumed that E_z had a constant phase over the measured region. Average whole-body and partial-body SAR values are shown in Figures 6.45 and 6.46 for an incident field having a half-cycle cosine variation as a function of the width of that field distribution. As the width of the aperture gets large compared to a wavelength, the SAR values approach those for an incident planewave.

To test the sensitivity of the calculations to the variation of phase of the incident field, Chatterjee et al. calculated the SARs as a function of an assumed phase variation in E_z. Figures 6.47-6.49 indicate that the SARs are not highly sensitive to the E_z phase variation. This is an important result. Measuring the phase of an incident field is difficult; if a reasonable approximation can be made on the basis of measuring only the magnitude of the incident field, near-field dosimetry will be much easier than if phase measurement is necessary. Chatterjee et al. have also compared the SARs calculated from the measured incident field and from a half-cycle cosine distribution that is a best fit to the measured field distribution. The results indicate that a reasonably approximate SAR might be obtained by using a convenient mathematical function to approximate the actual field distribution.

An important result of this work is that the calculated SARs for the incident-field distributions used in the calculations were all less than the calculated SARs for the corresponding planewave incident fields.

yz: plane of the
incident
$\vec{E}$-field
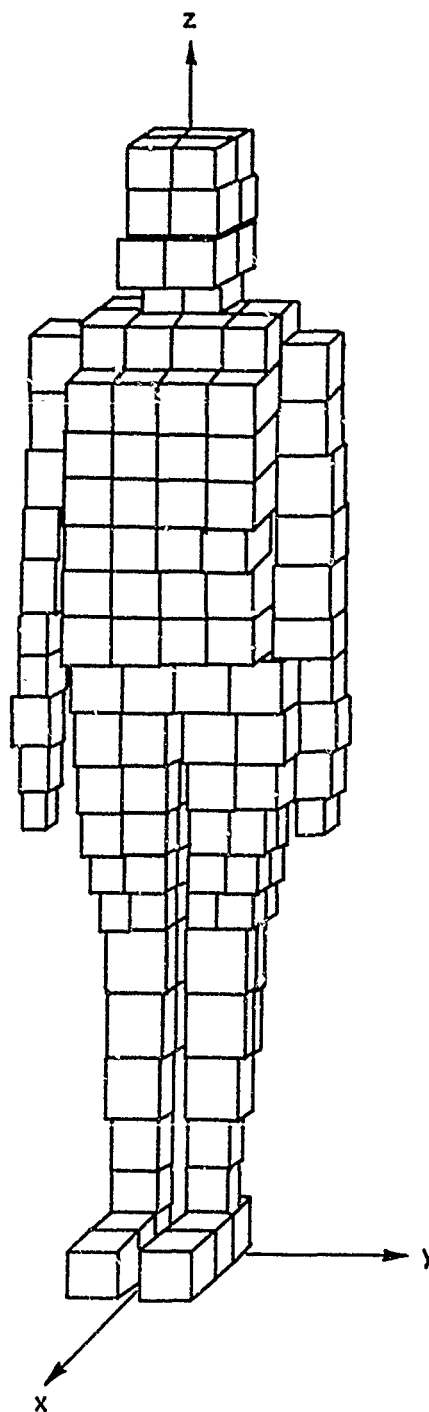
Figure 6.43. The block model of man used by Chatterjee et al. (1980a,
1980b, 1980c) in the planewave spectrum analysis.
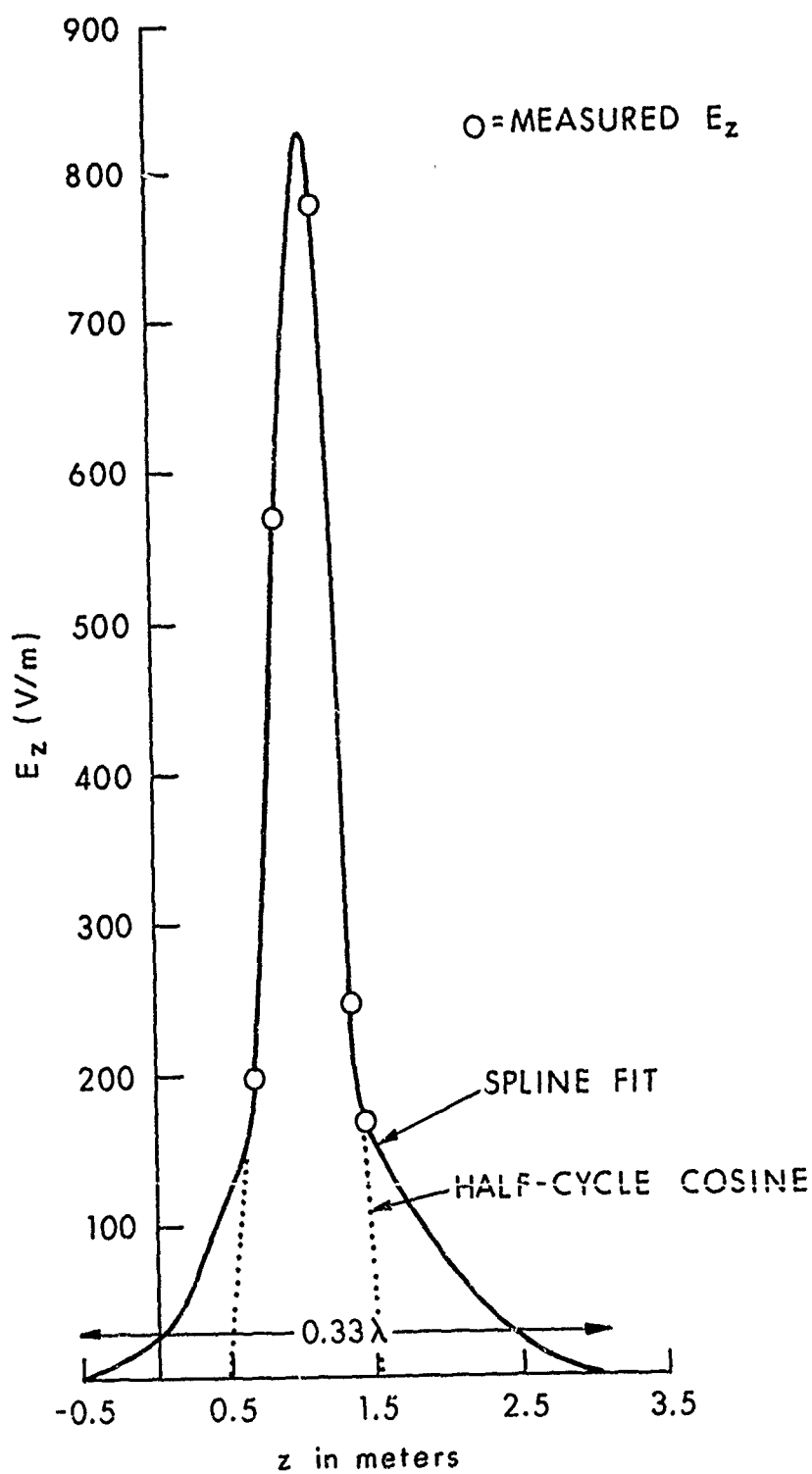
Figure 6.44. Incident-field E_z from a 27.12-MHz RF sealer, used by Chatterjee et al. (1980a, 1980b, 1980c) in the planewave angular-spectrum analysis.
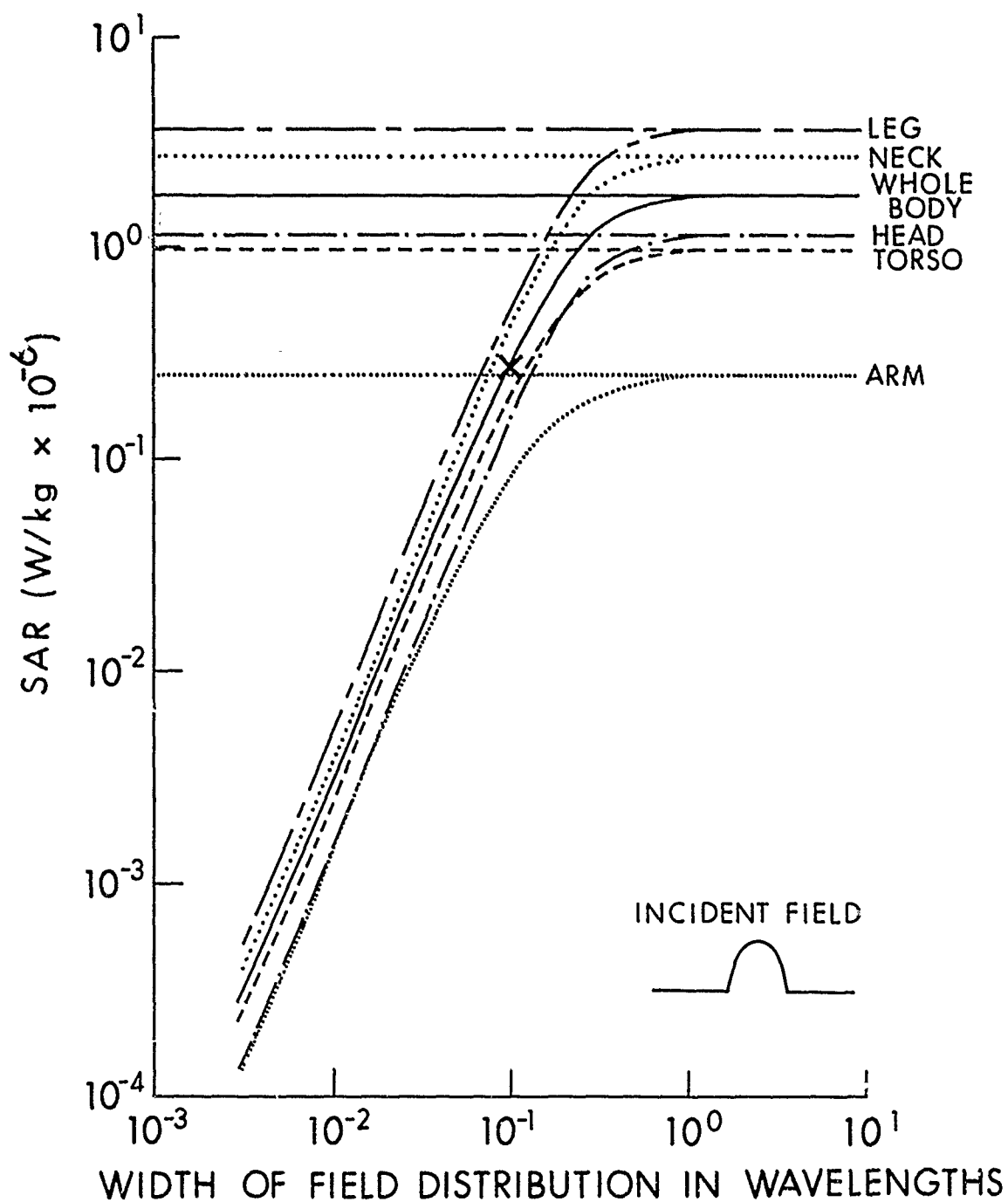
Figure 6.45.   Average whole- and part-body SAR in the block model
of man placed in front of a half-cycle cosine field,
E_z;   frequency = 27.12 MHz, $E_z\big|_{max}$ = 1 V/m.   Calcu-
lated by Chatterjee et al. (1980a, 1980b, 1980c).
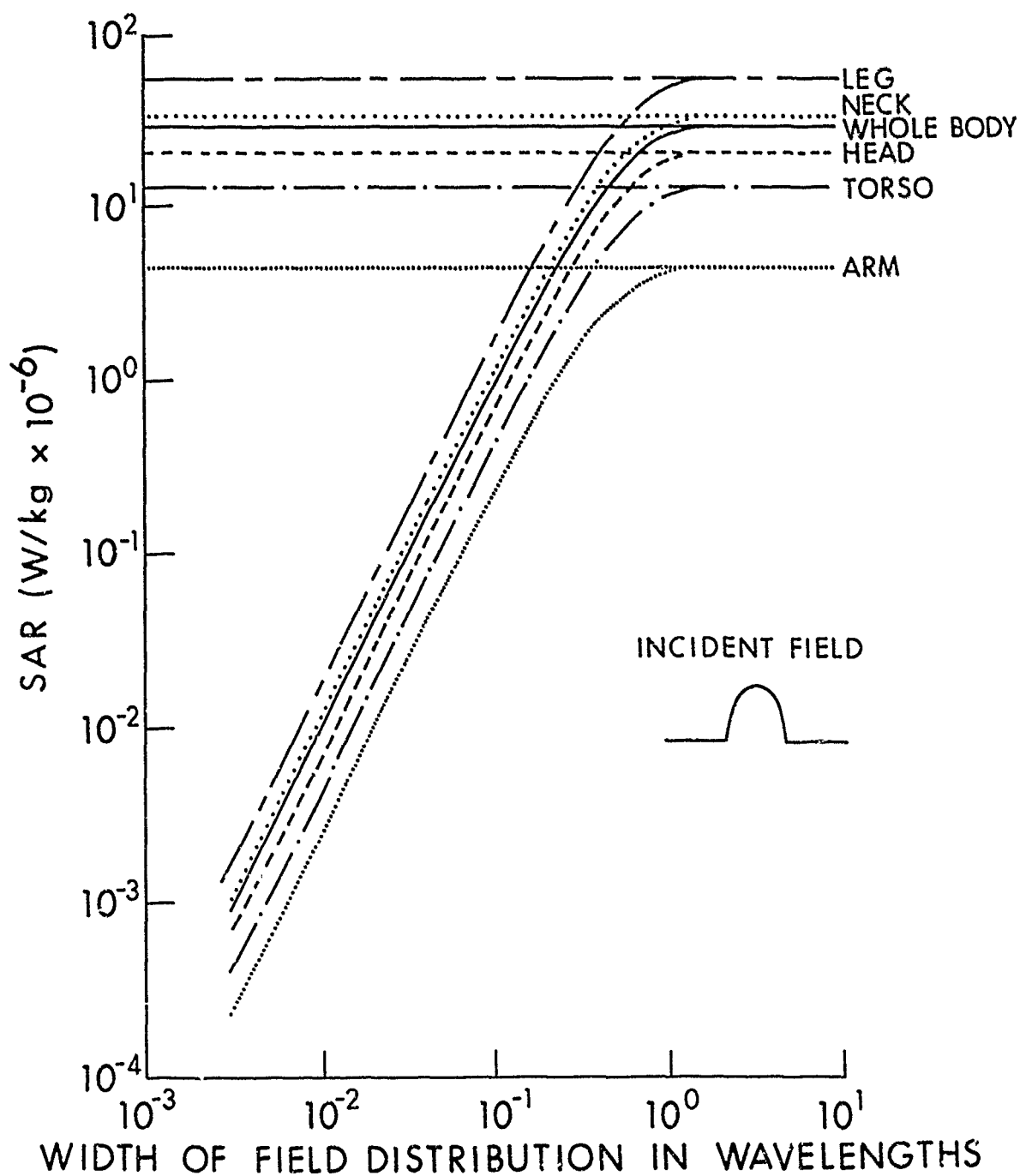
Figure 6.46. Average whole- and part-body SAR in the block model
of man placed in front of a half-cycle cosine field,
E_z; frequency = 77 MHz, $E_z\big|_{max}$ = 1 V/m. Calcu-
lated by Chatterjee et al. (1980a, 1980b, 1980c).
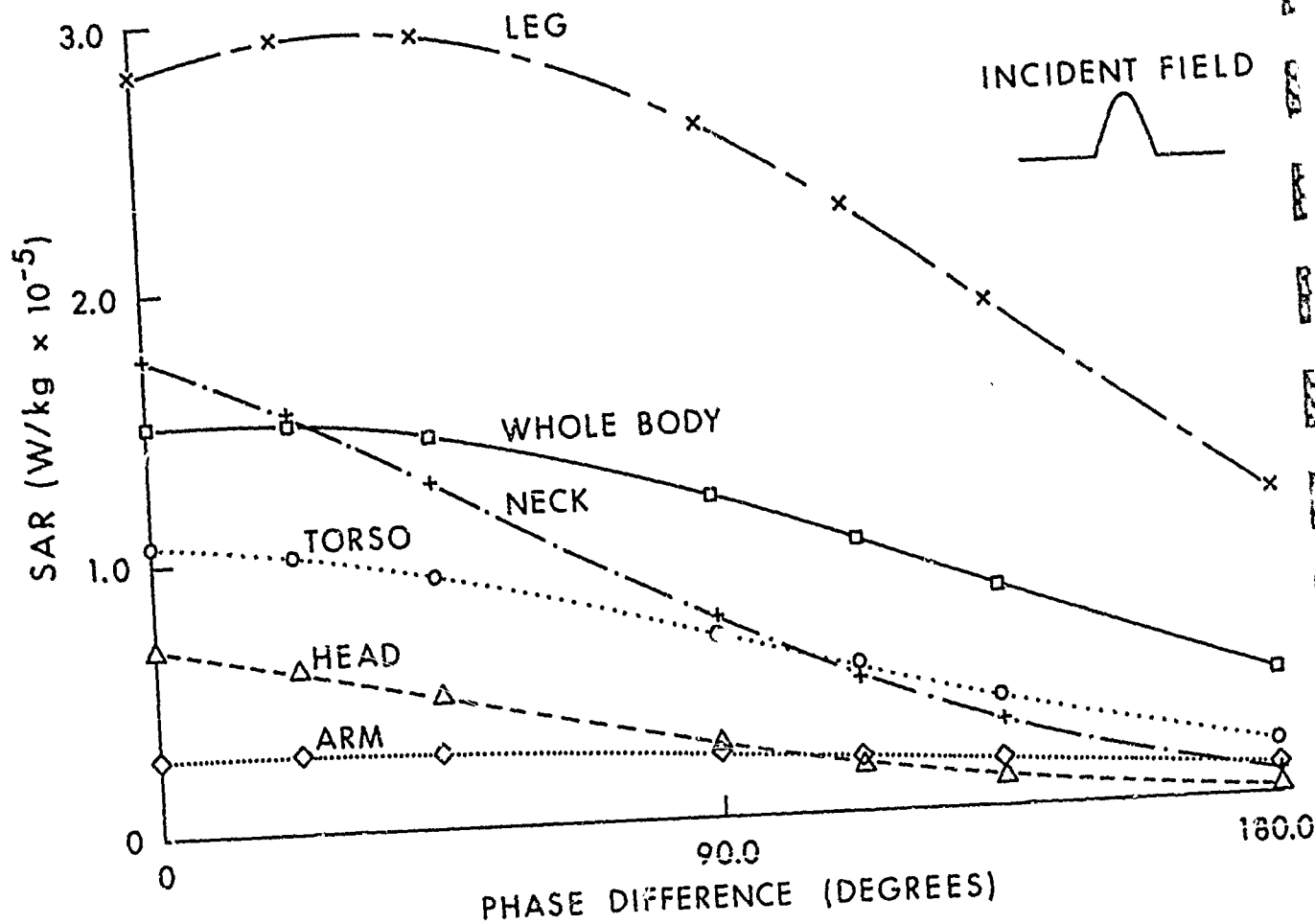
Figure 6.47. Whole- and part-body SAR at 77 MHz in the block model of man as a function of an assumed linear antisymmetric phase variation in the incident E_z; $E_z\big|_{max} = 1$ V/m. Calculated by Chatterjee et al. (1980a, 1980b, 1980c).
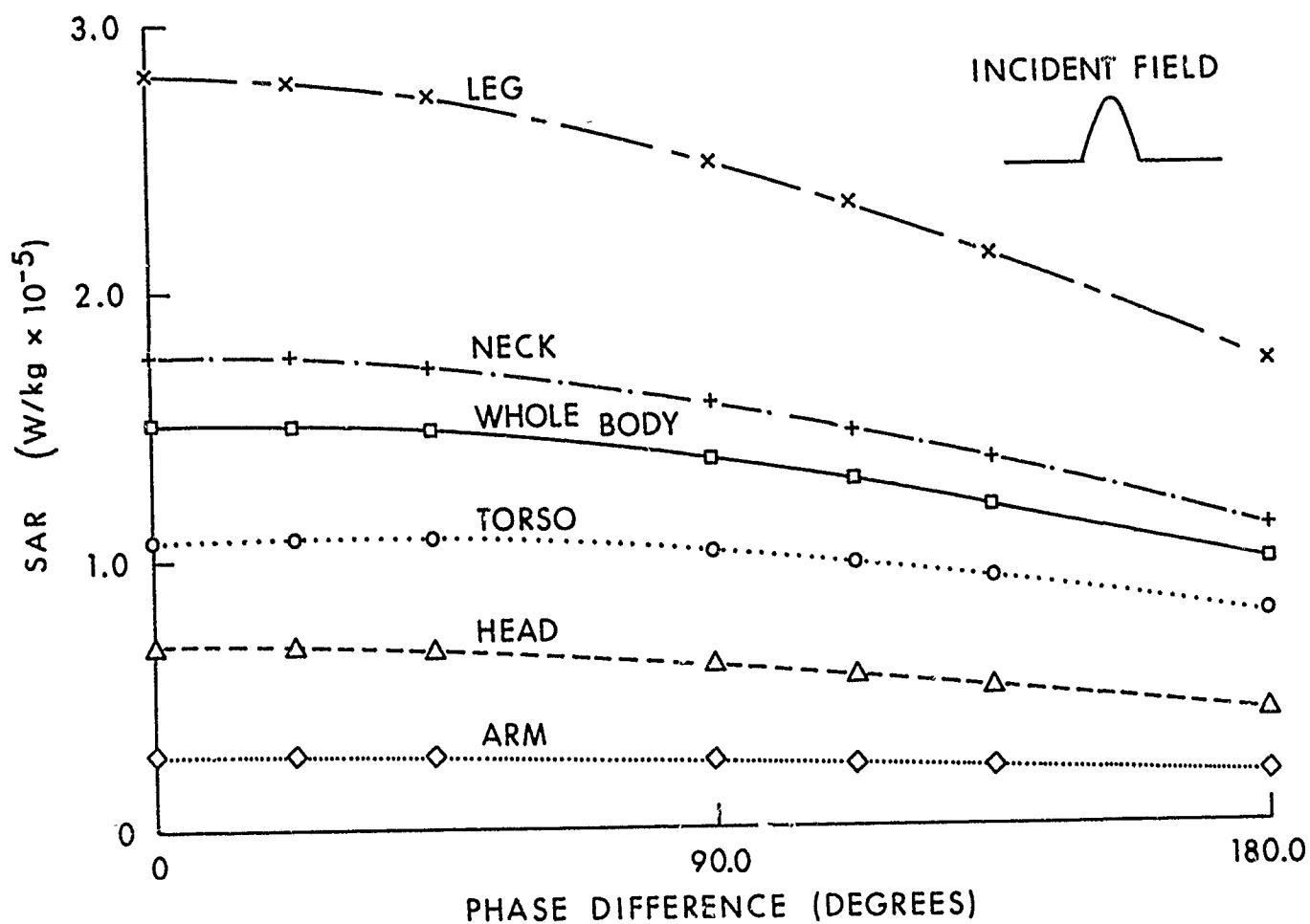
Figure 6.48. Whole- and part-body SAR at 77 MHz in the block model of man as a function of an assumed linear symmetric phase variation in the incident E_z; $E_z\big|_{max}$ = 1 V/m. Calculated by Chatterjee et al. (1980a, 1980b, 1980c).
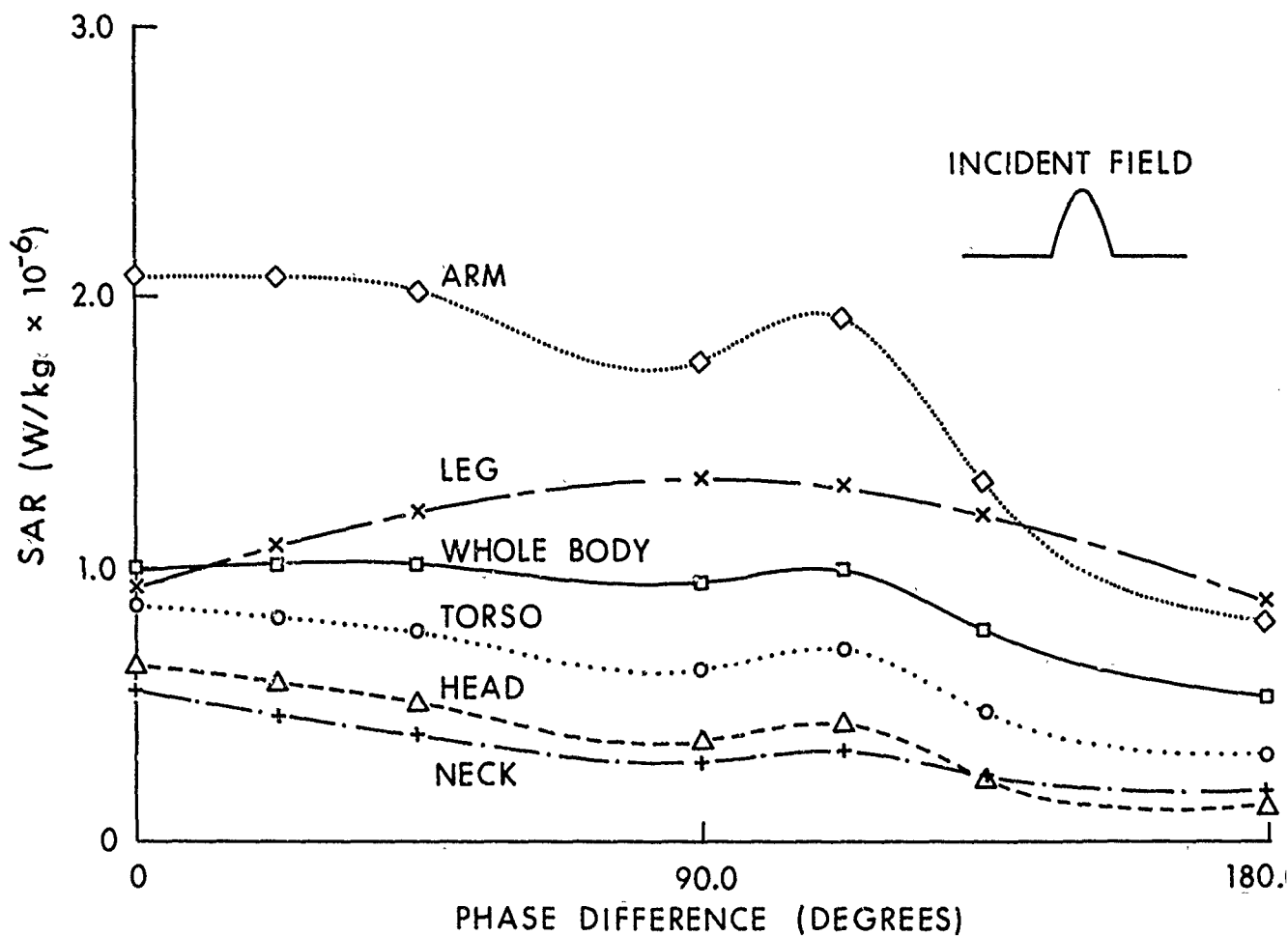
Figure 6.49. Whole- and part-body SAR at 350 MHz in the block model of man as a function of an assumed linear antisymmetric phase variation in the incident E_z; $E_z\big|_{max} = 1$ V/m. Calculated by Chatterjee et al. (1980a, 1980b, 1980c).

- 6.52 -

CHAPTER 7. EXPERIMENTAL DOSIMETRY

Except for Section 7.2.6, this chapter was written by S. J. Allen, then Project Scientist, U.S. Air Force School of Aerospace Medicine. He adapted Section 7.1 from material written by Arthur W. Guy, Ph.D., Professor of Bioengineering, University of Washington. Dr. Guy's material was later published in an IEEE reprint volume (Osepchuk, 1983).

7.1. HISTORY OF EXPERIMENTAL DOSIMETRY

Early dosimetric techniques were developed when electromagnetics were first used in physical medicine. Attempts to quantify exposures consisted of measuring the radiofrequency output current to the electrode or coil applicators of short-wave diathermy equipment. This technique proved to be inadequate, and Mittleman et al. (1941) conceived and conducted the first true RF dosimetry by quantifying the temperature rise in exposed tissue in terms of volume-normalized rate of absorbed energy, expressed in watts per 1,000 cm^3. Little use was made of this work by personnel involved either in microwave therapy or later in bioeffects research. Virtually all reported biologic effects were related to incident-power density, making it difficult, if not impossible, to correlate data from animal experiments to those expected in man.

In the early 1950s Schwan (1948, 1953, 1954), Schwan and Piersol (1953), Schwan and Li (1957), and Cook (1951, 1952) developed the foundation for later analytical work by characterizing the properties of biological tissues. This allowed Schwan and co-workers to use simple models consisting of plane layers of simulated muscle, fat, and skin to analyze microwave fields and their associated patterns of heating in exposed tissues (Schwan and Piersol, 1953; Schwan and Li, 1956; Schwan, 1956a, 1958, 1960). Such predictions were confirmed by Lehmann et al. (1962, 1965) in the early 1960s.

During the period of triservices-supported research, beginning in the mid-1950s and continuing through 1960, preliminary experimental approaches to microwave dosimetry were made. Schwan (1959) and his colleagues described methods that could be used to fabricate tissue-equivalent phantom models and portions of the human anatomy and to experimentally measure energy absorption

during exposure to microwave radiation (Salati and Schwan, 1959). Mermagen (1960) reported using tissue-equivalent phantoms to study energy-absorption characteristics as a function of animal position in a near-field exposure. He recommended measurement of watts per cubic centimeter in an absorber whose dielectric constant is similar to that of tissue and whose volume would represent a finite attenuation of microwave beams, again similar to that of tissue.

Franke (1961) made the first analyses of biologic models that revealed frequency dependencies in the coupling of electromagnetic fields to electrically small bodies. These analyses were discussed later in Pressman's book (1970). The models Franke used varied from circular cylinders to prolate spheroids of homogeneous muscle-equivalent dielectric. Volume-normalized energy absorption rate and heat produced in prolate spheroidal models of man were determined at lower RF frequencies, using quasi-static mathematical solutions. In other theoretical studies, Schwan's group used spherical models to determine relative absorption cross sections as a function of frequency of the incident RF field (Anne et al., 1960). The absorptive cross section varied widely with frequency, reaching a maximum at the model's resonant frequency. From the mid to late 1960s, Guy and his colleagues (Guy and Lehmann, 1966; Guy et al., 1968) developed and used more realistic tissue-simulating models for experimental measurements of field coupling.

In the late 1960s Justesen and King (1969) introduced mass-normalized RF dosimetry using phantom models in laboratory bioeffects research. During the same time period Guy and colleagues (Guy et al., 1968; Guy, 1971a), through the technique of thermography, developed distributive dosimetry measurement of the anatomical distribution of local SARs in biological models and in the bodies of small mammals. Mumford (1969) pointed out the importance of considering environmental factors such as temperature and humidity rather than focusing only on dosimetric quantities.

The 1970s saw a significant increase in the development of experimental and theoretical approaches to definition of SAR in man and animals. Gandhi et al. (Gandhi, 1975a; Gandhi and Hagmann, 1977a; Gandhi et al., 1977) initiated the first in a succession of analytical and empirical studies of electrical and geometrical constraints on SAR. An animal's orientation with respect to

the vectors of an incident planewave proved to be a powerful controlling influence on the quantity of energy absorbed in an RF field.

During the 1970s numerous new techniques and exposure devices were developed. The twin-cell calorimeter developed by Hunt et al. (1980) and Phillips et al. (1975) allowed accurate measurement of whole-body SAR, as did the continuous integration of momentary energy absorption rates via differentiation of transmitted and reflected power in a special environmentally controlled waveguide system developed by Ho et al. (1973). A transverse electro-magnetic (TEM) mode chamber--developed by Mitchell (1970) at the U.S. Air Force School of Aerospace Medicine (USAFSAM)--allowed, for the first time, measurement of SAR in large animals (monkeys, pigs, and dogs) in uniform and well-defined fields, thus letting SAR be compared with incident-power density. Guy and Chou (1975) and Guy et al. (1979) developed a circularly polarized cylindrical-waveguide exposure system that enabled precise control of SARs and virtually continuous irradiation of small animals that are fed and watered and have their excrement accumulated with minimal disturbance of the field.

Theoretical work and the development of instrumentation for quantifying electromagnetic-field interactions with biological materials increased substantially in the 1970s, with many important developments. Interactions of planewave sources with layered tissues were studied (Guy, 1971; Ho et al., 1971; Ho, 1975b, 1977). New and novel instruments provided better characterization of exposure fields (Aslan, 1971; Bowman, 1972; Hopfer, 1972; Bassan and Herman, 1977; Bassen, 1977). More sophisticated mathematical and physical models of biological tissues and anatomical structures generated a much better understanding of absorptive characteristics of tissues of differing composition and geometry.

Theoretical human-head models that consisted of a "brain" and spherical shells to simulate the skull and scalp led to Shapiro's observation that electrical "hot spots" (localized regions of intensified energy absorption) could occur deep within the brain at frequencies associated with resonance (Shapiro et al., 1971). Due to the high dielectric constant and the spherical shape of the head, focusing of the field caused considerably less RF-energy absorption at the surface of the head. The theoretical results were expanded

- 7.3 -

and verified experimentally to predict energy absorption by animal and human bodies of a wide range of sizes and exposed at various frequencies (Johnson and Guy, 1972; Ho and Guy, 1975; Ho and Youmans, 1975; Kritikos and Schwan, 1975; Lin et al., 1973b; Weil, 1975; Joines and Spiegel, 1974). Better and more detailed analyses were developed for various geometric objects that simulate bodies of man and animals; i.e., cylinders (Massoudi et al., 1979a; Ho, 1975a, 1976; Wu, 1977), prolate spheroids (Durney et al., 1975; Johnson et al., 1975; Barber, 1977a), and ellipsoids (Massoudi et al., 1977a, 1977b, 1977c).

Theoretical analyses were verified experimentally via thermography (Johnson and Guy, 1972; Guy et al., 1974a, 1974b), newly developed calorimetric techniques (McRee, 1974; Allis et al., 1977; Blackman and Black, 1977), special temperature-sensing probes composed of microwave-transparent materials such as fiber-optics guides (Rozzell et al., 1974; Gandhi and Rozzell, 1975; Johnson and Rozzell, 1975; Cetas, 1976) and high-resistance leads (Bowman, 1976; Larsen et al., 1979), and differential power-measurement techniques (Allen, 1975; Allen et al., 1975, 1976). Cetas (1977) has reviewed and discussed the relative merits of these different techniques. Also, probes were developed to directly measure electric fields within exposed tissues (Bassen et al., 1977b; Cheung, 1977). The microwave transparent materials used for new dosimetry instrumentation were also used in recording physiological signals from live laboratory animals under microwave exposure (Chou et al., 1975; Tyazhelov et al., 1977; Chou and Guy, 1977b).

Numerical studies in conjunction with high-speed computers were developed along with sophisticated programs for calculating the electromagnetic fields and the associated heating patterns in arbitrarily shaped bodies (Chen and Guru, 1977a, 1977b, 1977c; Neuder, 1977; Gandhi and Hagmann, 1977a; Hagmann et al., 1977, 1978, 1979a). Mathematical models included the effects of convective cooling via blood flow in calculating steady-state temperatures for various parts of the body, including critical organs such as the eyes and the brain (Chan et al., 1973; Emery et al., 1975, 1976a). The continued development and use of phantom models has contributed significantly to our understanding of energy absorption in biological bodies (Guy, 1971a; Guy et al., 1974a, 1974b, 1977; Allen, 1975; Allen et al., 1975, 1976; Cheung and

Koopman, 1976; Chou and Guy, 1977a, 1977b; Balzano et al., 1978a, 1978b). For a brief summary of the theoretical methods and experimental work found in the literature, see Sections 5.3 and 7.3.

When simultaneously applied in various laboratories, these new developments of the 1970s allowed the microwave hearing, or "Frey effect," to be quantified and understood as a complex thermal acoustic phenomenon--which for nonbiological materials had been quantified by the physicists more than a decade earlier (Chou et al., 1975; Guy et al., 1975b; Foster and Finch, 1974; White, 1963; Gournay, 1966).

The collective advances in RF radiation dosimetry culminated in publication of the first dosimetry handbook for RF radiation by C. C. Johnson and colleagues of the University of Utah and USAFSAM (1976). The collective results were empirically cast in a succinct form by Durney et al. (1979). Subsequent editions of the handbook were supported and published by USAFSAM to maintain documentation of advancements in the overall state of knowledge in RF dosimetry (Durney et al., 1978, 1980).

7.2. MEASUREMENT TECHNIQUES

7.2.1. Dosimetry Requirements

Inadequate dosimetry or description of experimental design has been a common shortcoming of many radiofrequency bioeffect experiments performed in the past. Without adequate dosimetric definition, experiments cannot be replicated nor can the information gained from the experiment be used to define the expected consequences of equivalent human exposures.

To facilitate compilation of the minimum required data, researchers at USAFSAM, Brooks Air Force Base, Texas, developed an RFR Bioeffects Research Data Sheet (Figure 7.1). The form indicates what information should be recorded, and all the information is very important to those desiring to replicate an experiment or evaluate it. The required data are divided into four basic areas of concern as follows:

1. <u>Description and condition of experimental data.</u> Date and time of exposure are important for evaluating seasonal and diurnal effects. Provide a

DATA SHEET
RFR BIOEFFECTS RESEARCH

Date _____

Time of day _____

Experimental subject (including species, where applicable) _____

Subject mass _____ g   Subject age _____

Subject size: Length _____ cm Width _____ cm Breadth _____ cm

Subject temperature: Before   _____ °C

                           During   _____ °C

                           After   _____ °C

Environmental conditions: Temperature   ____ +/- ____ °C

                           Relative humidity ____ +/- ____ %

Other relevant environmental conditions   _____

Polarization of subject with respect to field _____

Polarization of field _____

Radiofrequency_____ Exposure time _____

Generator output ____ +/- ____ watts Incident field ____ +/- ____ mW/cm^2, V/m, A/m

Type of generator _____ Method used to determine _____

Manufacturer _____ Model _____ Average SAR _____ W/kg

Type of antenna _____ Peak SAR _____ W/kg

Manufacturer _____ Model _____ Method used to determine _____

Modulated, pulsed, or CW exposure

    If pulsed: Pulse repetition frequency _____ Hz

                  Pulse width _____ ms/µs

                  Duty factor _____

    If modulated: Modulation frequency _____ Hz

                  Percent modulation _____

Exposure device (diagram if applicable) _____

Subject-holding device (diagram if applicable) _____

Condition of subject during exposure _____

Equivalent human exposure: Frequency _____

                            Incident power density _____

Figure 7.1. A data sheet for RFR bioeffects research.

detailed description of the experimental subject, including the type of animals and their source. If biological substances are being investigated, note the source and method of preparation. A physical description of the experimental subject--including mass, length, width, and breadth--is the minimum data needed for theoretical evaluation of the SAR expected in the subject. These data are particularly important in the case of in vitro exposures such as cell suspensions and isolated tissues. In such cases define both the size of the biologic material and the nature of the surrounding suspension. If nonperturbing temperature probes are available, monitor and record the temperature of the experimental subject during exposure; if not, use available standard temperature-monitoring devices to measure the temperature of the subject prior to and immediately after exposure.

2. Environmental conditions. Environmental conditions can affect the subject's temperature-regulation capabilities and response to radiation. Measure and report the mean, minimum, and maximum values. Note any unusual environmental factors such as extreme lighting conditions, presence of noxious fumes, and use of hypobaric or hyperbaric conditions. Take care not to place environment-recording instruments in the RF fields; this can lead to inaccurate readings as well as perturbation of the exposure fields.

3. Definition of RFR exposure, including localized SAR. Define the RFR exposure conditions with as much precision as possible. Polarization can be defined as in Section 3.3.5. In the case of an unrestrained animal, note whether the orientation is random or preferred. "Polarization of the field" means whether the field is linearly, circularly, or elliptically polarized. Record the directions of the k and E vectors. If a frequency spectrum analyzer is available, record the width of the exposure frequency band and any anomalies introduced by pulse characteristics. Measure and record the drift of the generator output, and report average and extremes. Determine the uniformity of the exposure field by mapping the field in the volume to be occupied by the subject; always do this without the subject in the field but with the subject-holding device in the same position as during exposure. Measure the incident fields by methods such as the dipole antenna, loop antenna, standard-gain horn, and broad-band isotropic RF monitor. Methods for measuring SARs may include calorimetry, localized temperature measurement,

differential power techniques, or thermographic measurement in cadavers or models. Rate the condition of the subject (restrained, unrestrained, anesthetized, or unanesthetized).

4. _Equivalence of animal exposure to that expected for man under similar exposure conditions._ Determine the equivalent human-exposure frequency by finding the equivalent point on the SAR-versus-frequency curve (see Section 6.1) or determine an approximate equivalent from the following equation (see Chapter 2):

$$f_h = f_a \frac{\ell_a}{\ell_h} \tag{7.1}$$

where

f_h = equivalent human exposure frequency

f_a = animal exposure frequency

ℓ_a = length of animal

ℓ_h = length of human

Then use f_h to determine the average SAR expected in man at this frequency by reading the SAR for the appropriate polarization from the appropriate figure in Section 6.1. Determine the equivalent exposure by

$$P_e = \frac{SAR_a}{SAR_h} \tag{7.2}$$

where

P_e = equivalent human exposure $\left(mW/cm^2\right)$

SAR_a = average SAR in exposed animal (W/kg)

SAR_h = average SAR in human expected at equivalent frequency $\left(W/kg \text{ per } mW/cm^2\right)$

7.2.2. Holding Devices for Experimental Subjects

Because RF fields interact with dielectric materials, select with care the holding devices for experimental subjects. A variety of materials in common use include Lucite, Plexiglas, glass, Teflon, and a number of foam materials. Avoid all electrical conductors because they cause major

perturbations in RF fields. The magnitude of the perturbation produced by subject-holding devices varies with the exposure frequency, electrical properties, mass, geometry, and orientation of the material. At 30 MHz a massive Lucite cage causes only minor perturbations of the fields, while at 10 GHz the same cage causes extreme field attenuation and perturbation of the fields. Glass rods and sheets of Lucite cause major perturbations in the 1- to 10-GHz frequency band if the materials are aligned in the same direction as the E-field; however, if these materials are aligned for minimum E-field aperture, the field perturbations will be minimal. SAR measurements have shown that dielectric interfaces can cause large deviations in localized SAR in tissue cultures exposed in test tubes. This is particularly true at the hemispherical surface at the bottom of a standard test tube for certain frequencies. Avoid potential problems with tissue cultures by properly orienting the test tube (less perturbation is observed for H polarization than E polarization) or by circulating or agitating the exposed material.

Experimenters at USAFSAM have found that rodent holders constructed from a rectangular section of Lucite, with numerous perforations for ventilation and with blocks of low-loss foam material filling the two open ends, can be used for planewave fields where the field is incident on the blocks of foam material. This device provides animal restraint with minimal field perturbation and minimal stress on the animal.

Since experimental conditions, availability of materials, and experimental objectives vary widely, detailed discussion of subject-holding devices is not appropriate. Experimenters should select the best materials available, test far-field perturbation at the frequencies of interest, and use only materials found to cause minimum perturbation. The quantity of dielectric material must be kept to a minimum, as should the use of electrical conductors. If materials that perturb the fields are used, they should not be aligned with the E vector. When the device is completed, measurements should be made to quantify the amount of field perturbation that it causes.

7.2.3. Exposure Devices

The commonly used planewave and near-field exposure devices are briefly reviewed in this section.

Planewave Exposure Devices--Anechoic chambers are the most used exposure devices. With an appropriate antenna system, these chambers provide versatile exposure conditions for bioeffects experiments. At lower frequencies, however, the size becomes prohibitive and the cost is generally high.

The TEM-mode chamber offers the advantages of being versatile in size, relatively inexpensive, and relatively broad-banded. It can be instrumented to measure SAR continuously with only three power meters, incident-power density is easily measured, and polarizat'on effects can be measured. Since the TEM-mode chamber is particularly suitable for lower frequency exposures, it also complements the anechoic chamber. At higher frequencies (above 500 MHz), however, the size of the TEM-mode chamber must be significantly smaller to ensure that higher-order modes are cut off, which limits the usable exposure space. On the other hand, at these higher frequencies the anechoic chamber is generally reasonable in size and affordable in price.

When constructing a TEM chamber, pay special attention to the tapered transitions to ensure good impedance matches. Impedance mismatches cause standing waves in the chamber that may not be detected by power meters at the input and output ports. You can detect mismatches either by measuring time-domain reflection or by mapping the E-and H-fields inside the chamber. In every case, map the fields inside the chamber to ensure single-mode operation.

When higher-order modes and standing waves are not present, the E-field strength between the plates in the chamber can be found from

$$E = V/d \qquad\qquad (7.3)$$

and

$$V = \left(PZ_o\right)^{1/2} \qquad\qquad (7.4)$$

where

V = the rms voltage between the center conductor and the outer conductor of the line

P = the input power in watts

Z_o = the characteristic impedance of the chamber

The equivalent incident planewave power density can be found from

$$P_{inc} = E^2/3770 \ mW/cm^2 \qquad (7.5)$$

with the E-field in rms V/m.

Other planewave exposure devices include the <u>circular waveguide</u> and <u>cell culture irradiator.</u> Circular-waveguide exposure devices are relatively inexpensive and small in size, and they can be instrumented to constantly monitor the SAR in the exposed animal. These devices are power efficient and can provide almost continuous exposure of animals over long periods of time. This system is also desirable for chronic exposures of a large number of animals; however, incident-power density in the waveguide is difficult to measure. Five stable power meters are required to measure SAR; present designs limit the size of the experimental subject to that of a large rat, and the circular polarization of the field limits the advantage of being able to determine polarization effects. This is also a narrow-band device, and present models operate at 918 and 2450 MHz.

Cell-culture irradiators have the advantages of low cost, small size, and extremely good power efficiency; but they suffer from narrow-band operation, lack of field-measuring capability, and high gradient fields. To eliminate effects of hot spots with these devices, be sure to circulate the cell-culture fluid.

Near-Field Exposure Devices--Near-field exposure devices basically provide E- and H-fields that can be controlled independently in phase and magnitude at the position of the exposed model so that any field impedance condition can be simulated. The following is a brief description of some common exposure devices.

One type of near-field exposure device is a <u>resonant cavity</u>. Guy et al. (1974b) designed a resonant cavity for TM_{110} and TE_{102} mode resonance at 144 MHz. Each mode is fed by a separate probe, with variable control of the relative phase and amplitude of the power delivered to the feeds. The exposed subject is typically oriented in the center of the cavity, at the position of maximum E-field and zero H-field for the TM_{110} mode and maximum H-field and zero E-field for the TE_{102} mode. The resultant E- and H-fields are, therefore, in space quadrature and independently controllable in phase and magnitude at the position of the exposed model so that any field impedance condition can be simulated.

Another exposure device is the <u>near-field synthesizer</u> developed by the National Bureau of Standards (NBS) (Greene, 1974); this device also can produce fields of several combinations. It consists of two parallel plates that produce a uniformly distributed E-field between them, and a loop inductor between the plates can provide an H-field parallel to the axis of the loop. The loop can also be rotated over any angle with respect to the plate, so the relative orientation between E- and H-fields can be varied from parallel to perpendicular.

An interesting comparison between the dosimetric results on scaled phantoms obtained using the resonant cavity and the near-field synthesizer is described by Guy et al. (1976a).

<u>Anechoic chambers</u> also can be used for the near-field exposures of phantoms and experimental animals (Iskander et al., 1978, 1981). Using different radiation sources and varying the distance between the source and the exposed subject allows a large variety of near-field exposures to be obtained. For simple sources (e.g., electric dipoles and loop antennas), the E- and H-fields at the location of the subject can be calculated. In general, however, particularly for more complicated sources, measuring these fields with suitable E- and H-field probes is advantageous.

7.2.4. Incident-Field Measurements

The procedure for measuring the RF incident fields at the location of the subject basically depends on the exposure conditions. For planewave or

far-field exposures, apart from polarization and direction of propagation, only the incident-power density has to be measured. The planewave power density can be determined from the measured magnitude of the E- or H-field. In the near field, however, the E- and H-fields are not necessarily in phase or related by a constant wave impedance. Therefore, the magnitude and the direction of each E- and H-field must be measured independently at several points in the exposure region.

Depending on the type of detector, two basic techniques are used for monitoring RFR levels: (1) devices that measure power by sensing a temperature change due to energy absorption (thermocouple types) and (2) devices that use diodes to produce a current or voltage related to the electromagnetic energy. The thermocouple type of device has the advantage of accurate measurement in pulsed fields and a linear response with the incident-power density. The readout is accomplished by RF heating, however, so the instrument has a slow response and is susceptible to drift with environmental temperature, particularly in the lower ranges. The diode detector devices have the advantage of being extremely sensitive; they also have the major disadvantage of a limited dynamic range caused by the diodes' nonlinear response.

For planewave incident-power density measurements, several instruments are available, such as General Microwave, Holaday, Narda, and NBS EDM series. With all of these an orthogonal antenna system is used, and the antenna outputs are summed to provide a readout related to total incident-power density. Take care when choosing an instrument to assure that appropriate range and pulse characteristics are known and that the instrument will respond to these field parameters. In making these measurements, measure the fields over the volume to be occupied by the experimental subject, first in empty space and then with the subject-holding device in place. This ensures that the effect of the subject-holding device is negligible. When using a single antenna, manually rotate it to measure each of the three orthogonal components of the field; then square each of these three components and add them to obtain the square of the total field. For linear polarization, first rotate the antenna to the position of a maximum reading; then take the other two orthogonal measurements from that reference. This will usually result in the first reading being considerably larger than the other two, thus

decreasing errors caused by inexact antenna positioning for the second and third measurements.

Small dipole and loop antennas such as those produced by NBS are useful for measuring E- and H-field intensities in the near field (Green, 1975). A diode at the antenna detects the signal, and high-resistance leads connect the diode to a high-impedance voltmeter for readout. Alternatively, an optical telemetry system can be used to replace the long high-resistance leads (Bassen et al., 1977a). For both systems these devices can be constructed in most laboratories, with the advantage of low cost and good stability. They can be accurately calibrated for frequencies up to 400 MHz in TEM-mode cells available commercially (Crawford, 1974). At higher frequencies, however, the calibration is usually made inside anechoic chambers and in terms of calibrated antennas because of the very limited available calibration space in the TEM-mode cells. For the H-field probe, a small loop antenna with a series diode may not be adequate for near-field measurements because the E-field causes too large a voltage across the diode. A Moebius loop with a series diode reduces this problem significantly, at the same time providing twice the sensitivity of the diode-loaded circular loop (Duncan, 1974).

7.2.5. Measurement of Specific Absorption Rates

The SAR measurement is very useful in dosimetry. In cases where non-uniform exposures occur or where incident-power density cannot be measured, SAR is the only measurement that allows definition of the RF exposures. There are five basic techniques for measuring the SAR in biological systems and phantoms:

1. Differential power measured in a closed exposure system
2. Rate of temperature change measured with noninterfering probes
3. Calorimetric techniques
4. Thermographic techniques
5. Implantable E-field probes

The latter four methods are also suitable for near-field SAR measurements.

Differential-Power Technique--For the differential-power technique, use directional couplers and power meters on all input and output ports of the

exposure device. In the case of waveguide and TEM-mode exposure devices, monitor the input, output, and reflected powers and determine the absorbed power by

$$P_E = P_I - P_O - P_R \qquad (7.6)$$

where

P_E = power (watts) absorbed by empty exposure device

P_I = input power (watts)

P_O = output power (watts)

P_R = reflected power (watts)

Then place the sample in the exposure device and determine P_S, the power absorbed by both the sample and exposure device, in a similar manner. Determine the total absorbed power for the sample by taking the difference between P_E and P_S. To determine the SAR, divide the total absorbed power by the mass of the sample.

The accuracy of these measurements can be improved by electronically measuring differential power: Use a differential amplifier or, for even more accuracy, connect the output of the power meters to an A-to-D converter and computer. Controlling temperature of the couplers and power meter heads also will improve the stability of the measurements.

The fields in a circular waveguide system can be quantified by differential-power determination of the SAR in the animal being exposed. To do this, subtract from the input power the power reflected out of the two transmitting and the two output ports. This requires five power meters.

Noninterfering Temperature-Probe Techniques--With the advent of RF noninterfering probes, a whole new field of SAR distribution determinations in realistic phantoms, cadavers, and live animals has become a reality. High-resolution systems using thermistor detectors on high-resistance lead wires can reliably measure 0.01°C temperature changes in high-level RF fields. Lossy-line systems work best for frequencies above 100 MHz. For high fields below 100 MHz, line burnout may be a problem. Fiber-optic readouts are

usable across the RF spectrum with minimal interference problems, but present instruments suffer from instability. Having the most sensitive technique possible is important if SAR distribution is to be measured. Less sensitive techniques require larger temperature rises, and more smearing of the SAR pattern will occur. Therefore, keep exposure time to a minimum to obtain minimum error from heat flow within the subject. Measure temperature rises in °C per minute; and for tissue and tissue-equivalent material, convert these data to SAR by

$$1°C/min = 58.6 \text{ W/kg} \qquad (7.7)$$

which is based on a specific heat of tissue of 0.84.

This measurement technique is the most accurate for assessing SAR distribution in phantoms and cadavers, allows temperature regulation to be measured in live animals, and is inexpensive. The major disadvantage is the time required to define the SAR in large or complex geometrical bodies. With the advent of systems with multiple temperature probes (Christensen and Volz, 1979), this problem has been largely reduced.

Calorimetric Techniques--Calorimetric techniques prove extremely useful in measuring whole-body SAR for animal phantoms and cadavers. Two techniques are now in practice: twin-well and dewar.

Twin-well calorimetry yields accurate results and requires little effort of the experimenter after initial setup and calibration. Difficulties include long run times for making one measurement (approximately 1 day for a large rat), complexity or multiple thermocouple readouts that make it difficult to detect failure in one or two thermocouples, and relatively high cost.

The dewar calorimeter technique is relatively inexpensive, is simple (calibration and operation anomalies are easily resolved), and requires a relatively short time for one reading (from 30 min for a mouse to 1 h for a rat). Accurate SAR determinations can be made with this technique, but they require experimenters to exercise extra precautions.

To check for heat loss during exposure, compare an SAR measurement immediately after exposure with a measurement that was delayed by a period

equal to the exposure time. Water is usually used as the heat transfer medium; use just enough to allow total immersion of the cadaver. Adjust the water temperature to approximately 0.5°C below the ambient air temperature; and after inserting the exposed animal, adjust the resultant temperature by varying exposure time to obtain a temperature rise of approximately 1°C. This achieves maximum stability in terms of calorimeter drift. When thermal equilibrium is reached (i.e., when the change in T is less than 0.01°C during a 15-min period), measure the final temperature, T_F, and use it to evaluate T_e for each cadaver:

$$T_e = [(Z_p + M_e \cdot C_e)(T_F - T_i)]/(M_s \cdot C_s) + T_F \qquad (7.8)$$

where

T_e = rationalized temperature of the cadaver upon insertion in the calorimeter

M_s = mass of the cadaver (kg)

C_s = specific heat of the cadaver $(J \cdot kg^{-1} \cdot K^{-1})$

M_e = mass of water in calorimeter (kg)

C_e = specific heat of water $(J \cdot kg^{-1} \cdot K^{-1})$

T_i = temperature of calorimeter just before insertion of cadaver (°C)

T_F = final temperature of calorimeter (°C)

Z_p = heat capacity of calorimeter $(J \cdot K^{-1})$

The SAR in $W \cdot kg^{-1}$ is determined by

$$SAR = C_s[T_e(\text{exposed}) - T_e(\text{control})]/\text{exposure time in seconds} \qquad (7.9)$$

where

C_s = 3448 for a rat or mouse

C_e = 4185

The readout of the calorimeter can be automated by direct computer readout; this also facilitates computations.

Thermographic Techniques--A scanning thermographic camera can be used to provide detailed SAR distribution in phantoms and cadavers in a short time. Suitable material to separate sections of the phantom or cadaver must be used, and readout after termination of exposure must be rapid. If the output of the thermographic camera is put into a computer, average SAR can be easily computed. Personnel at the University of Washington have developed this technique which is described in detail by Guy (1971a). The technique has proven valuable in assessing SAR distribution for laboratory animals and models of man. The procedure originally involved using a thin sheet of plastic to facilitate separating the halves of the phantom; thus the procedure was limited to symmetrical models exposed to a linearly polarized field (E-field parallel to the interface) to avoid interrupting any induced currents that would normally flow perpendicular to the median plane of separation (Guy, 1971a). For near-field measurements, however, the procedure was modified by replacing the plastic sheet with a silk screen, thus allowing easy separation without loss of electrical continuity (Guy et al., 1975a). The major disadvantage of this technique is the high cost of the required equipment.

Implantable Electric-Field Probes--Miniature electric-field probes with fiber-optics readout were developed by Bassen et al. (1977a). This system can be used to determine the E-field in a cadaver or phantom exposed to RF fields. The same equation used to determine E-fields from SAR (page 2.1) can be used to determine SAR if the E-field is measured and the dielectric properties of the subject are known. The advantages of this technique include instant readout (allowing SAR distribution to be determined by scanning techniques) and accurate measurements in low-level fields (this technique being at least 10 times as sensitive as any technique previously discussed). The primary problems include probe rigidity (requiring straight insertion into the subject) and frequency-range limitation. The use of orthogonal probes simplifies measurements, but single-axis probes can be used. Subminiature probes (2-mm diameter) are under development. A review of implantable E-field probes is given by Bassen et al. (1983).

Use of Phantoms to Measure SAR--SAR can be measured in animal cadavers; but measuring in phantoms is sometimes more convenient, more reproducible, and almost as accurate. A mold of RF-transparent foam material can be made in the shape of the phantom to be investigated, and the mold filled with a tissue-equivalent material. Researchers in the Department of Rehabilitation Medicine, University of Washington School of Medicine, have developed materials to simulate muscle, brain, fat, and bone for various frequency ranges (Guy, 1971a; Chou et al., 1984).

Tables 7.1-7.4 summarize the directions for preparing the simulated tissue material, Tables 7.5-7.7 list the composition and properties, and Table 7.8 gives sources for the ingredients. Figures 7.2 and 7.3 show the electrical properties as a function of frequency and temperature.

Tables 7.9-7.11 give directions for other tissue-equivalent materials, developed at the University of Ottawa (Hartsgrove and Kraszewski, 1984). The material in Table 7.9 includes hydroxyethylcellulose to make preparation easier and to provide stability of the material over longer periods of time. Table 7.10 describes a more liquid material that has electrical properties equivalent to tissue.

Knowledge of thermal properties of tissue-equivalent materials is useful in determining how fast thermal diffusion will cause heating patterns to change. Leonard et al. (1984) determined the thermal properties of some common tissue-equivalent materials. Tables 7.12 and 7.13 list formulas for other muscle- and fat-equivalent materials for the 10-50-MHz frequency range, also the thermal and electrical properties. These materials, in which barium titanate is used instead of aluminum powder, were designed to have a lower thermal diffusivity to minimize smearing of the heating patterns.

TABLE 7.1.   DIRECTIONS FOR PREPARING SIMULATED MUSCLE MATERIAL
FOR 13.56-100 MHz (Guy, 1971a; Chou et al., 1984)

1. Weigh all ingredients and determine percentages by weight.

2. Mix aluminum powder, TX-150, and salt; pour in 14-20°C water and mix with
    a 4-in. shear stirrer rotating at 1200 rpm for 45-120 s on a variable-
    speed drill press until all of the polyethylene powder is wet. Add one
    drop of household liquid detergent to help wet the polyethylene powder.

3. Because air bubbles are easily formed in this mixture, constantly rotate
    the bucket and move it up and down to ensure proper mixing. When the
    mixture starts to set (thicken), slow the drill press to about 800 rpm to
    avoid formation of air bubbles (essential!). The setting time of TX-150
    varies by factory batch, so proper water temperature and mixing time must
    be determined by experience. If the mixture is not stirred long enough,
    the aluminum powder will sink; if stirred too long, the mixture will be
    too hard to pour.

4. Pour the mixture into the mold, slowly, to allow air bubbles to escape
    from the mixture.

TABLE 7.2.   DIRECTIONS FOR PREPARING SIMULATED MUSCLE MATERIAL
FOR 200-2450 MHz (Guy, 1971a; Chou et al., 1984)

1. Weigh all ingredients and determine percentages by weight.

2. Mix ingredients except TX-150 in 14-20°C water with a 4-in. shear stirrer
    rotating at 450 rpm on a variable-speed drill press until all polyethylene
    powder is wet. Add one drop of household liquid detergent to help wet the
    polyethylene powder.

3. Add TX-150 and increase drill press speed to 1200 rpm.

4. Mix for about 45-120 s. When the mixture becomes thick, slow the drill
    press to about 800 rpm to avoid generating air bubbles. Since the setting
    time of TX-150 varies with factory batch, proper water temperature and
    mixing time must be determined by experience. If stirred too long, the
    mixture will become too hard to pour; if not stirred enough, the polyethy-
    lene powder will float.

5. Pour the mixture into the mold, slowly, to allow air bubbles to escape
    from the mixture.

TABLE 7.3.   DIRECTIONS FOR PREPARING SIMULATED BRAIN MATERIAL FOR
915 AND 2450 MHz (Guy, 1971a; Chou et al., 1984)

1.   Weigh all ingredients and determine percentages by weight.

2.   Mix all ingredients except TX-150 in 14-20°C water with a 4-in. shear
     stirrer rotating at 450 rpm on a variable-speed drill press until all
     polyethylene powder is wet. Add one drop of household liquid detergent to
     help wet the polyethylene powder.

3.   Add TX-150 and increase drill press speed to 1200 rpm.

4.   Mix for about 45-120 s. When the mixture becomes thick, slow the drill
     press to about 800 rpm to avoid generating air bubbles. Since the setting
     time of TX-150 varies with factory batch, proper water temperature and
     mixing time must be determined by experience. If stirred too long, the
     mixture may be filled with air; if not stirred enough, the polyethylene
     powder will float. The larger amount of polyethylene powder in this
     mixture makes it more difficult to determine the correct stirring time.

5.   When the mixture looks soupy, pour it into a plastic bag and let it set;
     then force it into the mold.

TABLE 7.4.   DIRECTIONS FOR PREPARING SIMULATED FAT AND BONE MATERIALS
FOR 915 AND 2450 MHz (Guy, 1971a; Chou et al., 1984)

1.   Weigh all ingredients and determine percentages by weight.

2.   For a small quantity, place everything but the catalyst in a 1-qt round
     ice-cream carton with a fitted aluminum base and stir until blended. Use
     a small drill press as a stirring machine, a drill stand for 1/4- and 3/8-
     in. drills, a 1000-rpm 1/4-in. drill, a 2-in. shear stirrer, and a verti-
     cally oscillating-rotating table. The period of vertical oscillation and
     rotation is about 1 s. When the ingredients are blended, add the catalyst
     and continue stirring for 20 min; then pour the mixture. For large mix-
     tures, use a 4-in. shear stirrer, a larger (industrial size) drill press,
     a stainless-steel can 8 in. in diameter and 12 in. high, and a heavier
     vertically oscillating-rotating table. Table rotation is 40 rpm, and
     vertical oscillation 50 rpm.

3.   Coat molds with paraffin wax to ease removal. Due to internal heat,
     excess wax will melt and float on the model. After 3 h of setting, the
     models will be firm and can be removed from the molds. Machine the top
     and bottom of the final casting to remove air pockets and settled aluminum
     powder.

TABLE 7.5. COMPOSITION AND PROPERTIES OF SIMULATED BRAIN, FAT, AND BONE TISSUE AT MICROWAVE FREQUENCIES (Guy, 1971a)

COMPOSITION

Simulated	TX-150	Polyethelene Powder	H_2O	NaCl
Brain	7.01%	29.80%	62.61%	0.52823%

	Laminac 4110	Aluminum Powder	Acetylene Black	P-102
Fat and bone	85.20%	14.5%	0.24%	0.375%

ELECTRICAL PROPERTIES

	Frequency (MHz)	Relative Permittivity	Conductivity (S/m)	Loss Tangent
Brain	915	34.37	0.730	0.442
	2450	33.56	1.266	0.2713
Fat and Bone	915	5.61	0.0665	0.233
	2450	4.51	0.172	0.187

PHYSICAL PROPERTIES

	Specific Heat	Specific Density
Brain	0.83	0.96
Fat and bone	0.29-0.37	1.29-1.38

TABLE 7.6. COMPOSITION AND ELECTRICAL PROPERTIES OF SIMULATED MUSCLE FOR 13.56-2450 MHz (Chou et al., 1984)

Frequency (MHz)	Actual Muscle Tissue (37°C)		Phantom Muscle Tissue (22°C)						
	Dielectric Constant ϵ'	Conductivity σ(S/m)	Dielectric Constant ϵ'	Conductivity σ(S/m)	TX-150 (%)	Polyethylene Powder (%)	Aluminum Powder (%)	H_2O (%)	NaCl (%)
2450	47.0	2.17	47.4 ± 0.9	2.17 ± 0.08	8.46	15.01	---	75.48	1.051
915	51.0	1.28	51.1 ± 0.6	1.27 ± 0.02	8.42	15.44	---	75.15	0.996
750	52.0	1.25	52.5 ± 0.6	1.26 ± 0.04	8.42	15.44	---	75.15	0.996
433	53.0	1.18	53.5 ± 0.5	1.21 ± 0.01	8.42	15.44	---	75.15	0.996
300	54.0	1.15	54.8 ± 0.7	1.17 ± 0.01	8.42	15.44	---	75.15	0.996
200	56.5	1.00	56.7 ± 0.7	1.06 ± 0.02	8.39	15.79	---	74.92	0.894
100	71.7	0.89	71.5 ± 1.1	0.89 ± 0.01	9.81	---	2.12	87.59	0.482
70	84.0	0.79	84.7 ± 0.5	0.76 ± 0.01	10.36	---	2.72	86.50	0.424
40.68	97.0	0.68	97.9 ± 3.8	0.70 ± 0.02	9.68	---	9.20	80.82	0.303
27.12	113.0	0.60	113 ± 3.0	0.62 ± 0.02	9.70	---	9.06	80.97	0.270
13.56	149.0	0.62	149 ± 3.0	0.62 ± 0.03	9.69	---	9.15	80.88	0.280

TABLE 7.7. ELECTRICAL PROPERTIES OF SIMULATED MUSCLE TISSUE FOR
13.56-2450 MHz AT THREE TEMPERATURES (Chou et al., 1984)

Frequency (MHz)	15 ± 1°C		22 ± 1°C		30 ± 1°C	
	Dielectric Constant ε'	Conductivity σ(S/m)	Dielectric Constant ε'	Conductivity σ(S/m)	Dielectric Constant ε'	Conductivity σ(S/m)
2450	49.3 ± 1.3	2.09 ± 0.02	47.0 ± 0.9	2.17 ± 0.08	46.0 ± 0.3	2.43 ± 0.02
915	53.1 ± 0.7	1.10 ± 0.02	51.1 ± 0.6	1.27 ± 0.02	50.3 ± 0.4	1.47 ± 0.04
750	53.6 ± 0.6	1.09 ± 0.04	52.5 ± 0.6	1.26 ± 0.04	50.7 ± 1.0	1.43 ± 0.03
433	54.9 ± 0.7	1.07 ± 0.03	53.5 ± 0.5	1.21 ± 0.01	51.3 ± 0.8	1.38 ± 0.03
300	56.9 ± 0.6	1.06 ± 0.01	54.8 ± 0.7	1.17 ± 0.01	52.4 ± 0.7	1.36 ± 0.04
200	59.8 ± 0.6	0.91 ± 0.02	56.7 ± 0.7	1.06 ± 0.02	54.8 ± 1.0	1.21 ± 0.04
100	80.2 ± 1.2	0.76 ± 0.01	71.5 ± 1.1	0.89 ± 0.01	67.3 ± 1.3	1.03 ± 0.02
70	88.1 ± 0.7	0.67 ± 0.01	84.7 ± 0.5	0.76 ± 0.01	80.7 ± 2.8	0.92 ± 0.02
40.68	106.0 ± 2.0	0.60 ± 0.04	97.9 ± 3.8	0.70 ± 0.02	88.6 ± 4.7	0.84 ± 0.04
27.12	118.0 ± 5.0	0.51 ± 0.01	113.0 ± 3.0	0.62 ± 0.02	109.0 ± 1.0	0.72 ± 0.01
13.56	167.0 ± 4.0	0.52 ± 0.02	149.0 ± 3.0	0.62 ± 0.03	141.0 ± 2.0	0.77 ± 0.02

TABLE 7.8. SOME SOURCES[*] OF MATERIALS USED TO CONSTRUCT
PHANTOM MODELS (Guy, 1971a; Chou et al., 1984)

TX-150   Oil Center Research, P. O. Box 71871, Lafayette, LA
                                    70501.

Polyethylene Powder   Wadco California, Inc., 2102 Curry St., Long Beach,
(20 mesh, low density)   CA 90805. Attention: Henry Schymanitz.

Laminac 4110   Fiberlay, Inc., 1158 Fairview North, Seattle, WA
                                    98102. (An American Cyanamid resin product.)

NaCl (Merk reagent grade) Merk & Company, Inc., Rahway, NJ 07065

Aluminum Powder   J. T. Baker Chemical Company, Phillipsburg, NJ
(Baker's USP)   08865. (Do not substitute industrial powder; it
                                    lacks particle uniformity and purity, which
                                    affects the catalytic reaction.) Caution:
                                    Aluminum powder is highly flammable. Be careful
                                    in storing and handling it.

P-102 (60% methyl ethyl   Fiberlay, Inc., 1158 Fairview North, Seattle, WA
      ketone peroxide)   98102

Acetylene Black   Shawinigan Products Corporation, Empire State Build-
                                    ing, 350 5th Ave., New York, NY 10001

---

[*] The sources in this table are given only as examples. Equivalent materials
    may be obtained from other sources.
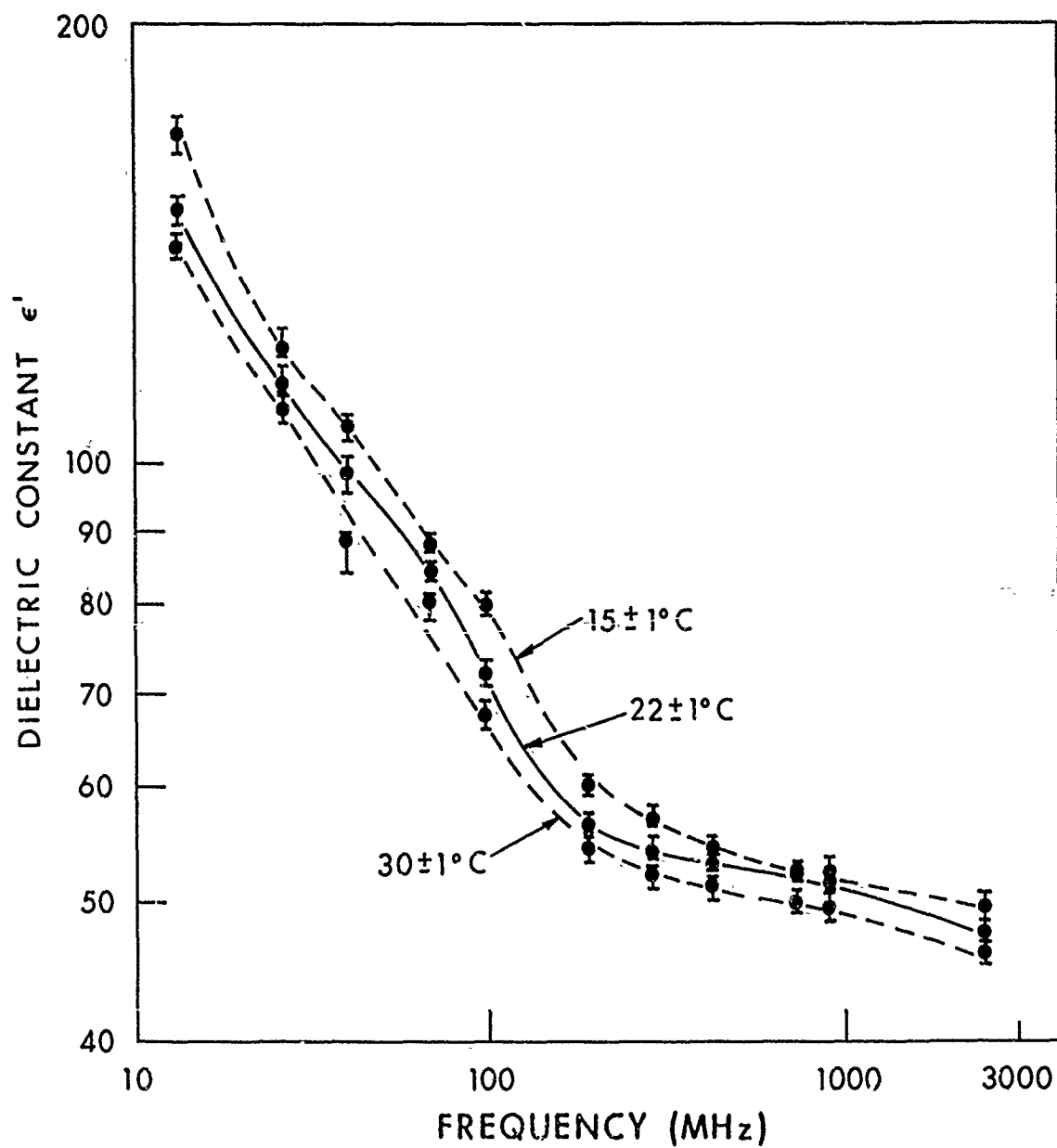
Figure 7.2. Relative permittivity of simulated muscle tissue versus frequency for three temperatures (Chou et al., 1984).
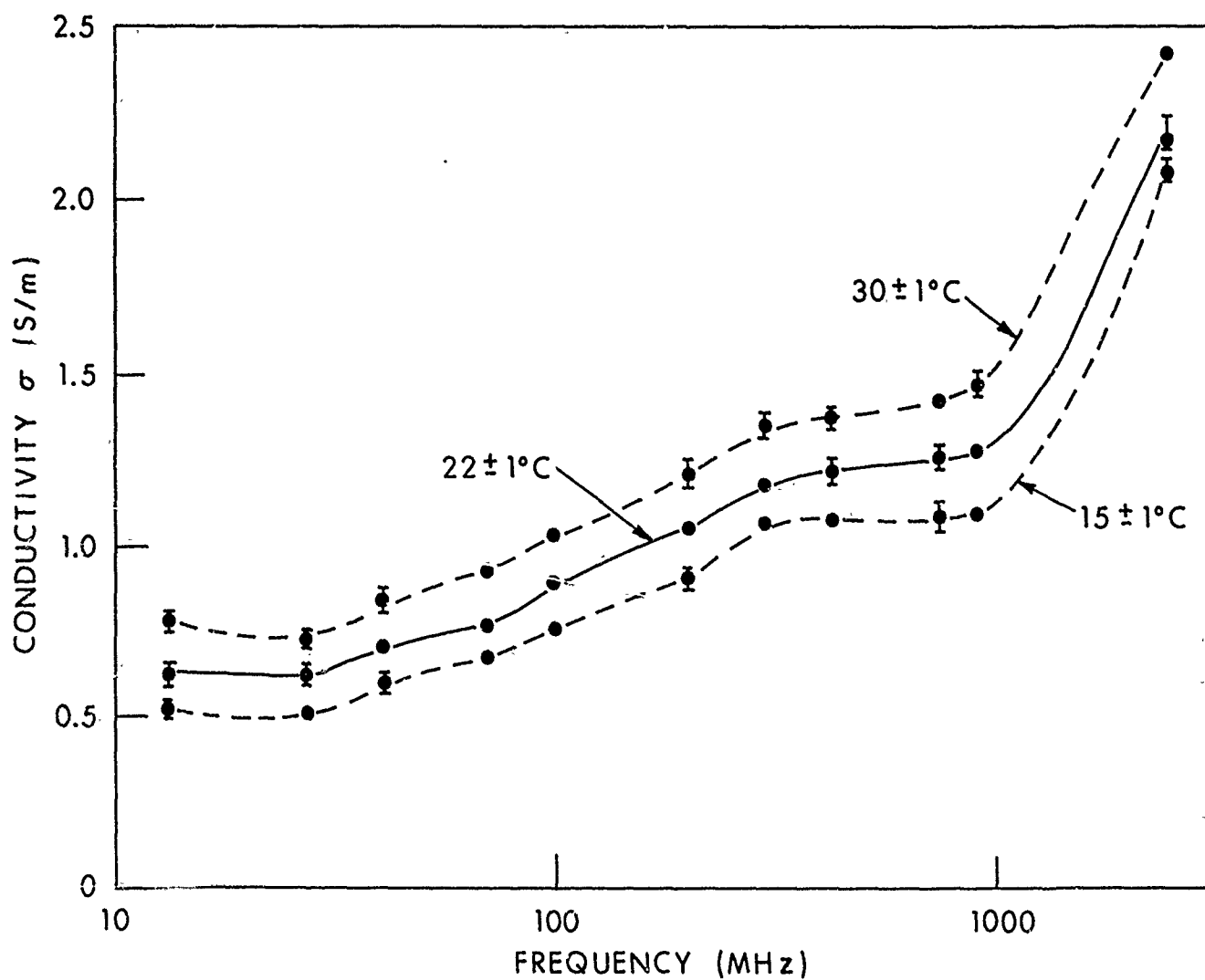
Figure 7.3. Electrical conductivity of simulated muscle tissue versus frequency for three temperatures (Chou et al., 1984).

TABLE 7.9 COMPOSITION AND ELECTRICAL PROPERTIES OF TISSUE-EQUIVALENT MATERIALS (Hartsgrove and Kraszewski, 1984)

Frequency (MHz)	ε'	σ (S/m)	Percent by Weight				
			Aluminum Powder	NaCl	Polyethylene Powder	H_2O	HEC*
27.12	103.0	0.649	9.3	0.16	–	87.44	3.0
40.68	96.1	0.671	6.9	0.18	–	88.82	3.0
70	83.0	0.679	–	0.27	–	96.63	3.0
100	69.3	0.81	–	0.34	5	91.6	3.0
200	62.6	0.97	–	0.5	4	92.4	3.0
300	57.0	1.09	–	0.55	12	84.4	3.0
433	55.5	1.27	–	0.8	15	81.1	3.0
750	51.2	1.29	–	0.75	17	79.2	3.0
915	48.2	1.58	–	1.0	20	75.9	3.0
2450	48.0	2.34	–	0.92	22	74.0	3.0

TABLE 7.10. COMPOSITION AND ELECTRICAL PROPERTIES OF A LIQUID THAT HAS THE ELECTRICAL PROPERTIES OF TISSUE (Hartsgrove and Kraszewski, 1984)

Frequency (MHz)	ε'	σ (S/m)	Percent by Weight			
			NaCl	Sugar	H_2O	HEC*
100	70.5	0.875	0.38	10	87.5	2.0
200	62.0	0.979	1.8	40	56.1	2.0
300	58.7	1.006	2.3	45	50.6	2.0
433	53.7	1.146	2.5	47	48.4	2.0
750	53.6	1.42	1.9	41	55.0	2.0
915	49.2	1.57	3.0	45	49.9	2.0
2450	53.9	2.32	–	34	63.9	2.0

* Hydroxyethylcellulose

TABLE 7.13. SIMULATED FAT MATERIAL

COMPOSITION

Material	Percentage by Weight
Polyester resin (Allied Chemical No. 32033)	77
Carbon powder (Cabot XC-72)	1
Barium titanate (Alfa)	22

ELECTRICAL PROPERTIES (PRELIMINARY)

f(MHz)	ε'	σ(S/m)
11	18	0.025
27	16	0.025
43	14	0.025

THERMAL PROPERTIES

Thermal conductivity	$0.20 \ \frac{W}{m \cdot K}$
Specific heat	$1.16 \times 10^3 \ \frac{J}{kg \cdot K}$
Thermal diffusivity	$0.115 \times 10^{-6} \ \frac{m^2}{S}$

- 7.31 -

PRECEDING PAGE BLANK

7.2.6. Scaled-Model Techniques

Although measurements in models made of tissue-equivalent material are valuable for determining the internal distribution of SARs and E-fields, making measurements in full-size models of people and larger animals is often difficult. A useful alternative is to make measurements on smaller models at higher frequencies and then relate these measured values to corresponding values that would occur in the full-size models. This process is called scaling.

Measurements on scaled models offer several advantages over measurements on full-size models:

1. In the smaller models less electromagnetic generator power is required to produce measurable temperature rises. In full-size models excessive amounts of power are often required to produce measurable temperature rises, especially enough rise to measure heating patterns accurately in the presence of thermal diffusion.

2. Use of several scaled models permits measurements at more frequencies. Since most electromagnetic generators with sufficient power are narrow-band, measurements in full-size models can usually be made only over a very narrow frequency band.

3. Scaled models are smaller, easier to handle, and less expensive than full-size models.

Mathematical Basis for Measurements on Scaled Models—The derivation of relations between quantities in the full-size and scaled system is outlined here. Readers interested only in the results should skip to the next subsection.

Since scaling is based on the linearity of Maxwell's equations, it is valid only for linear materials. With respect to typical measurements of SAR and E-field distributions, biological materials are linear. Scaling is valid for inhomogeneous materials—materials whose properties vary from point to point—as long as the material is linear at each point.

To derive the relations between measurements in the full-size and scaled models, let each point in full-size model A (Figure 7.4) be described by coordinates x, y, and z and each point in scaled model $\tilde{A}$ be described by
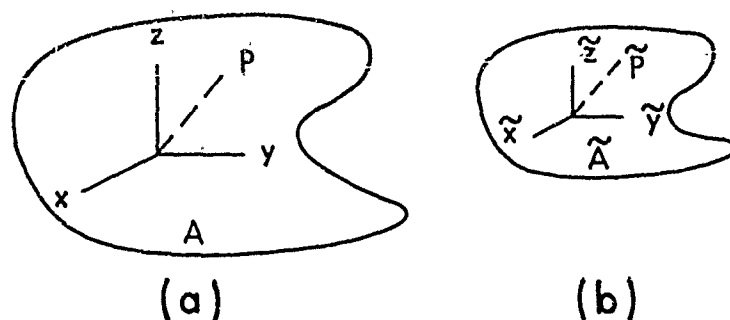
Figure 7.4. Schematic diagram illustrating the coordinate system used in the scaling procedure. (a) Full-size object with coordinate system x, y, z; (b) scaled model with coordinate system $\tilde{x}, \tilde{y}, \tilde{z}$.

coordinates $\tilde{x}$, $\tilde{y}$, and $\tilde{z}$. Each point in $\tilde{A}$ is obtained by reducing the coordinates of a point in A by the scale factor S. Therefore, the coordinate values are related by

$$x = S\tilde{x} \qquad (7.10)$$

$$y = S\tilde{y} \qquad (7.11)$$

$$z = S\tilde{z} \qquad (7.12)$$

Since four fundamental quantities--mass, length, time, and charge--are required to describe an electromagnetic-field quantity, three scale factors in addition to S are required to relate quantities in $\tilde{A}$ to those in A. Scale factors for E- and H-fields, however, are more convenient than those for mass and charge. Hence the following additional three scale factors have traditionally been used:

$$E(x, y, z, t) = \alpha \, \tilde{E}(\tilde{x}, \tilde{y}, \tilde{z}, \tilde{t}) \qquad (7.13)$$

$$H(x, y, z, t) = \beta \, \tilde{H}(\tilde{x}, \tilde{y}, \tilde{z}, \tilde{t}) \qquad (7.14)$$

$$t = \gamma \tilde{t} \qquad (7.15)$$

where E is electric field; H is magnetic field; t is time; and α, β, and γ are the corresponding scale factors.

Desired relationships between quantities in full-size and scaled systems can be found from Maxwell's equations because the fields in both systems must satisfy them. For simplicity, development of the relationships will be described for sinusoidal steady-state electromagnetic fields. This is appropriate because most measurements in biological systems are of sinusoidal steady-state quantities. For this case, the fields in the full-size system must satisfy

$$\nabla \times E(x, y, z, t) = j\omega\mu^* H(x, y, z, t) \qquad (7.16)$$

$$\nabla \times H(x, y, z, t) = j\omega\varepsilon_o (\varepsilon' - j\varepsilon'') E(x, y, z, t) \qquad (7.17)$$

where μ^* is the complex permeability and $\varepsilon' - j\varepsilon''$ is the complex relative permittivity (see Sections 3.2.6, 3.3.3, and 4.1). The effective conductivity, σ, is related to ε'' by

$$\sigma = \omega\varepsilon_o \varepsilon'' \qquad (7.18)$$

Fields in the scaled model, on the other hand, must satisfy

$$\tilde{\nabla}x \ \tilde{E}(\tilde{x}, \tilde{y}, \tilde{z}, \tilde{t}) = -j\tilde{\omega}\tilde{\mu}^* \tilde{H}(\tilde{x}, \tilde{y}, \tilde{z}, \tilde{t}) \qquad (7.19)$$

$$\tilde{\nabla}x \ \tilde{H}(\tilde{x}, \tilde{y}, \tilde{z}, \tilde{t}) = j\tilde{\omega}\varepsilon_o (\tilde{\varepsilon}' - j\tilde{\varepsilon}'') \tilde{E}(\tilde{x}, \tilde{y}, \tilde{z}, \tilde{t}) \qquad (7.20)$$

where $\tilde{\nabla}x$ indicates differentiations with respect to $\tilde{x}$, $\tilde{y}$, $\tilde{z}$.

If the scaled model is an accurate simulation of the full-size system, then substituting the transformations relating scaled-model quantities to the full-size model should transform Equations 7.19 and 7.20 into 7.16 and 7.17 respectively. Substituting Equations 7.10-7.15 into 7.19 and 7.20 gives

$$\nabla \times E(x,\ y,\ z,\ t) = -j\omega \frac{\gamma\alpha\tilde{\mu}^*}{S\beta} H(x,\ y,\ z,\ t) \qquad (7.21)$$

$$\nabla \times H(x,\ y,\ z,\ t) = j\omega \frac{\gamma\beta}{S\alpha} \left(\tilde{\varepsilon}' - j\tilde{\varepsilon}''\right) E(x,\ y,\ z,\ t) \qquad (7.22)$$

Note that

$$\tilde{\omega} = \gamma\omega \qquad (7.23)$$

$$\tilde{\nabla}x = S\nabla x \qquad (7.24)$$

Equations 7.21 and 7.22 will be the same as 7.16 and 7.17, respectively, if

$$\frac{\gamma\alpha}{S\beta} \tilde{\mu}^* = \mu^* \qquad (7.25)$$

$$\frac{\gamma\beta}{S\alpha} \left(\tilde{\varepsilon}' - j\tilde{\varepsilon}''\right) = \varepsilon' - j\varepsilon'' \qquad (7.26)$$

If material properties and scaling factors are selected so that Equations 7.25 and 7.26 are true, then measured quantities in the scaled model can be related to those in the full-size system, because Equations 7.19 and 7.20, which describe fields in the scaled system, are equivalent to Equations 7.16 and 7.17, respectively, which describe fields in the full-size system.

Scaling factors can be chosen as follows. First, since biological materials are essentially nonmagnetic, the μ^* and $\tilde{\mu}^*$ are both approximately equal to μ_o. Therefore, from Equation 7.25,

$$\frac{\gamma\alpha}{S\beta} = 1 \qquad (7.27)$$

Second, it is most convenient to have both the full-size and the scaled models surrounded by air. Then Equation 7.26 must be valid when both $\tilde{\varepsilon}' - j\tilde{\varepsilon}''$ and $\varepsilon' - j\varepsilon''$ represent air; that is, $\tilde{\varepsilon}' = \varepsilon' = 1$, $\tilde{\varepsilon}'' = \varepsilon'' = 0$. From Equation 7.26 for this condition,

$$\frac{\gamma\beta}{S\alpha} = 1 \qquad (7.28)$$

- 7.35 -

Equations 7.27 and 7.28 together require

$$\alpha = \beta \qquad (7.29)$$

$$\gamma = S \qquad (7.30)$$

The specified conditions thus far have been based on making field pat-
terns correspondingly similar in full-size and scaled models by requiring
solutions to Maxwell's equations in the two cases to correspond. Complete
specification of electromagnetic fields requires the fields to satisfy
Maxwell's equations _and_ boundary conditions. The next step, then, is to
specify α and β from boundary conditions. This is equivalent to adjusting the
intensity of the electromagnetic sources in the two systems. The usual prac-
tice is to set

$$\alpha = \beta = 1 \qquad (7.31)$$

which is equivalent to making the intensity of the source fields in the two
systems equal. This can be seen from Equations 7.13 and 7.14, which are valid
for all pairs of coordinate points (x, y, z, t) and $(\tilde{x}, \tilde{y}, \tilde{z}, \tilde{t})$. Let the
corresponding points be far enough away from the object so that scattered
fields are negligibly small and only source fields are present. Then,
$\alpha = \beta = 1$ corresponds to the source fields in the two systems having equal
intensities. This assumes that the sources in the two systems are correspond-
ingly similar. Since scattered-field intensities are proportional to source-
field intensities, the interpretation that "setting $\alpha = \beta = 1$ is equal to
making the source intensities equal" is valid at all points but easier to
understand at points where the scattered fields are negligible.

With the scaling parameters specified by Equations 7.30 and 7.31, mea-
sured quantities in the scaled model can be related to measurements in the
full-size model. Local SAR is of particular interest. From Equation 3.49,
the SAR at a point in the full-size model is

$$SAR = \omega \varepsilon_o \varepsilon'' |E|^2 / \rho_m = \sigma |E|^2 / \rho_m \qquad (7.32)$$

where ρ_m is mass density. The relationship with the effective conductivity, σ, is usually used. From Equations 7.26, 7.30, and 7.31,

$$\epsilon'' = \tilde{\epsilon}'' \tag{7.33}$$

Relating ϵ'' and $\tilde{\epsilon}''$ to σ and $\tilde{\sigma}$ (see Equation 7.18),

$$\frac{\sigma}{\omega\epsilon_o} = \frac{\tilde{\sigma}}{\tilde{\omega\epsilon}_o}$$

Using Equation 7.23 gives

$$\sigma = \tilde{\sigma}/\gamma \tag{7.34}$$

and using Equation 7.30 gives

$$\sigma = \tilde{\sigma}/S \tag{7.35}$$

From Equations 7.32, 7.13, and 7.34, the general relationship for SAR is

$$SAR = \frac{\tilde{\sigma}\left|\tilde{E}\right|^2 \alpha^2}{\gamma\rho_m} \tag{7.36}$$

$$SAR = \frac{\alpha^2 \tilde{\rho}_m}{\rho_m \gamma} \widetilde{SAR} \tag{7.37}$$

When both models are in air and the intensities of the sources are equal (so Equations 7.30 and 7.31 apply) and for the usual case when $\rho_m = \tilde{\rho}_m$, Equation 7.37 reduces to

$$SAR = \frac{\widetilde{SAR}}{S} \tag{7.38}$$

From Equation 7.38, the scaled-model SAR is seen to be higher than that in the full-size model by scale factor S. This is often a significant advantage because it generally means that making measurements in a scaled model

requires less generator power. This is particularly important when temperature measurements are made because it means that less power is required to get a measurable temperature rise in a scaled model than in a full-size model.

Another quantity that sometimes is of interest is the Poynting vector. The scaling relationship is easily obtained from Equations 7.13 and 7.14:

$$\mathbf{E} \times \mathbf{H} = \alpha\beta \ \tilde{\mathbf{E}} \times \tilde{\mathbf{H}} \tag{7.39}$$

Applications of Scaling Relationships--The general scaling relationships derived above are summarized in Table 7.14 in terms of the various factors. The relationships for commonly used values of the scale factors are given in Table 7.15. In practice, the scaling factor is usually determined by the desired irradiation frequency of the full-size model and the frequency at which the scaled model could be irradiated. For example, the SAR distribution at 13.56 MHz in a 0.52-m-diameter spherical model of equivalent muscle tissue might be desired, and a generator with sufficient power for measurements at 100 MHz is available. The appropriate scale factor, S, and the other parameters are given in the example in Table 7.15.

Adjusting the conductivity of the model material is often important in scaling techniques, as illustrated in Table 7.15. This can usually be done by varying the amount of NaCl in the mixture. Fortunately the amount of NaCl can be varied enough to adjust σ without affecting ε' drastically. Figure 7.5 shows conductivity as a function of percentage of NaCl for various percentages of the gelling agent TX-150 (see Section 7.2.5). Doubling the percentage of TX-150 has a relatively small effect on the conductivity, which is largely controlled by the percentage of NaCl. Figures 7.6 and 7.7 show the conductivity values as a function of percentage of NaCl. These graphs can be used to simulate muscle tissue in saline form for a wide range of frequencies and scale factors.

TABLE 7.14. GENERAL SCALING RELATIONSHIPS

Full-Size Model	Scaled Model	Relationships
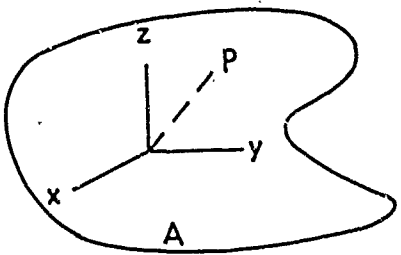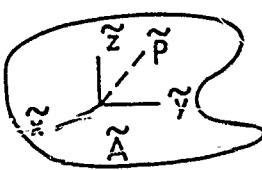
	Full-Size Model	Scaled Model	Relationships
Coordinates	x, y, z	$\tilde{x}, \tilde{y}, \tilde{z}$	$x = S\tilde{x}$
			$y = S\tilde{y}$
			$z = S\tilde{z}$
Mass density	ρ_m	$\tilde{\rho}_m$	
Time	t	$\tilde{t}$	$t = \gamma\tilde{t}$
Frequency	f	$\tilde{f}$	$f = \tilde{f}/\gamma$
Radian frequency	ω	$\tilde{\omega}$	$\omega = \tilde{\omega}/\gamma$
Fields	$E(x,y,z,t)$	$\tilde{E}(\tilde{x},\tilde{y},\tilde{z},\tilde{t})$	$E(x,y,z,t) = \alpha\,\tilde{E}(\tilde{x},\tilde{y},\tilde{z},\tilde{t})$
	$H(x,y,z,t)$	$\tilde{H}(\tilde{x},\tilde{y},\tilde{z},\tilde{t})$	$H(x,y,z,t) = \beta\,\tilde{H}(\tilde{x},\tilde{y},\tilde{z},\tilde{t})$
Complex relative permittivity	$\epsilon' - j\epsilon''$	$\tilde{\epsilon}' - j\tilde{\epsilon}''$	$\epsilon' - j\epsilon'' = \dfrac{\gamma\beta}{S\alpha}\left(\tilde{\epsilon}' - j\tilde{\epsilon}''\right)$
Effective conductivity	σ	$\tilde{\sigma}$	$\sigma = \tilde{\sigma}/\gamma$
Poynting vector	$E \times H$	$\tilde{E} \times \tilde{H}$	$E \times H = \alpha\beta\,\tilde{E} \times \tilde{H}$
SAR	$\sigma|E|^2/\rho_m$	$\tilde{\sigma}|\tilde{E}|^2/\tilde{\rho}_m$	$SAR = \dfrac{\alpha^2\tilde{\rho}_m}{\rho_m\gamma}\,\widetilde{SAR}$

TABLE 7.15. SCALING RELATIONSHIPS FOR TYPICAL
VALUES OF SCALING PARAMETERS

CONDITIONS

1. Both the full-size and scaled models are in air.

2. Both models are nonmagnetic $\left(\mu^* = \tilde{\mu}^* = \mu_o\right)$.

3. Both models are irradiated by similar sources with correspondingly equal intensities. That is, at corresponding points (x, y, z) and $(\tilde{x}, \tilde{y}, \tilde{z})$, $E(x,y,z) = \tilde{E}(\tilde{x},\tilde{y},\tilde{z})$ and $H(x,y,z) = \tilde{H}(\tilde{x},\tilde{y},\tilde{z})$.

4. The models have equal mass densities $\left(\rho_m = \tilde{\rho}_m\right)$.

RELATIONSHIPS

	Quantity in the Full-Size Model	Quantity in the Scaled Model	Relationships
Coordinates	x	$\tilde{x}$	$x = S\tilde{x}$
	y	$\tilde{y}$	$y = S\tilde{y}$
	z	$\tilde{z}$	$z = S\tilde{z}$
Frequency	f	$\tilde{f}$	$f = \tilde{f}/S$
Complex relative	ε'	$\tilde{\varepsilon}'$	$\varepsilon' = \tilde{\varepsilon}'$
permittivity	ε''	$\tilde{\varepsilon}''$	$\varepsilon'' = \tilde{\varepsilon}''$
Conductivity	σ	$\tilde{\sigma}$	$\sigma = \tilde{\sigma}/S$
SAR	SAR	$\widetilde{SAR}$	$SAR = \widetilde{SAR}/S$

TABLE 7.15 (continued)

EXAMPLE

Measured SAR distribution in a 0.52-m-diameter spherical model of muscle-equivalent tissue at 13.56 MHz is desired. A generator operating at a frequency of 100 MHz is available. Design a scaled model for appropriate measurements.

The scale factor is determined by the two frequencies:

$S = \tilde{f}/f = 100 \text{ MHz}/13.56 \text{ MHz} = 7.38$.

	Full-Size Model	Scaled Model
Sphere diameter	$d = 52$ cm	$\tilde{d} = d/S = 52/7.38 = 7.05$ cm
Frequency	$f = 13.56$ MHz	$\tilde{f} = Sf = 7.38 \times 13.56 = 100$ MHz
Permittivity	$\varepsilon' = 149$	$\tilde{\varepsilon}' = \varepsilon' = 149$
Conductivity	$\sigma = 0.62$ S/m	$\tilde{\sigma} = S\sigma = 7.38 \times 0.62 = 4.58$ S/m
SAR	(Calculated) $SAR = \widetilde{SAR}/S = 4/7.38 = 0.54$ W/kg	(Measured) $\widetilde{SAR} = 4$ W/kg
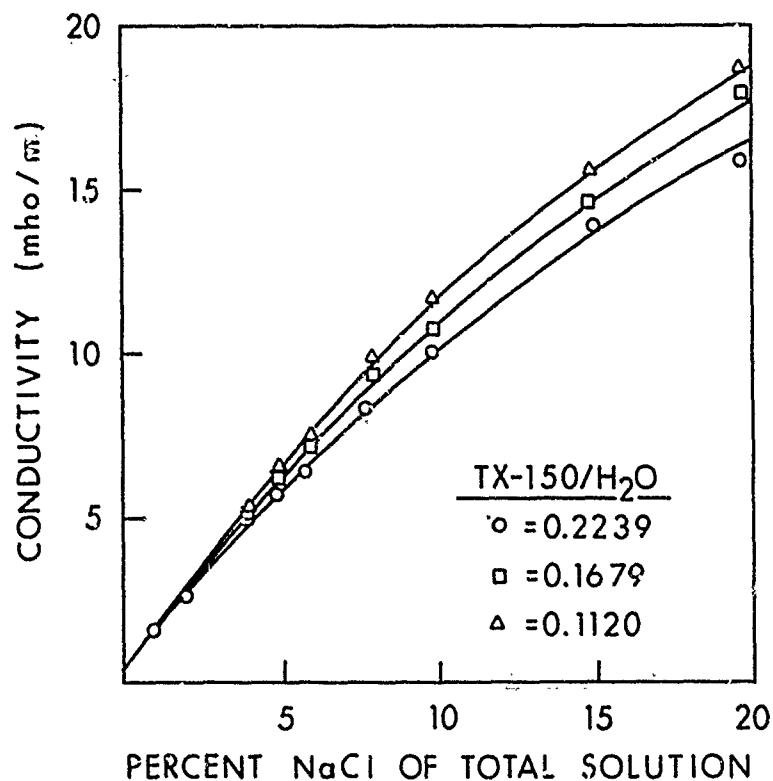
Figure 7.5. Electrical conductivity of phantom muscle as a function of NaCl and TX-150 contents measured at 100 kHz and 23°C.
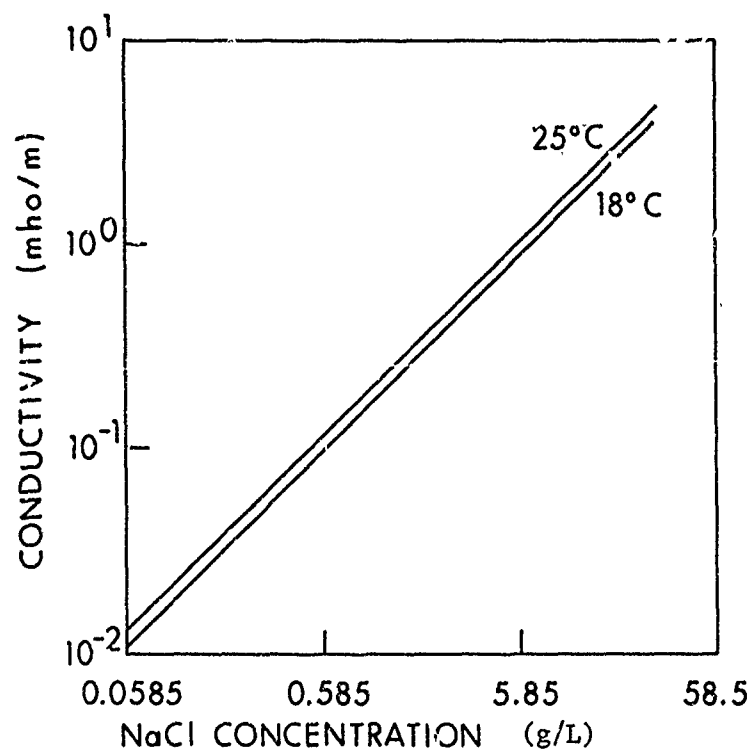
Figure 7.6. Electrical conductivity of saline solution as a function of the aqueous sodium chloride concentration.
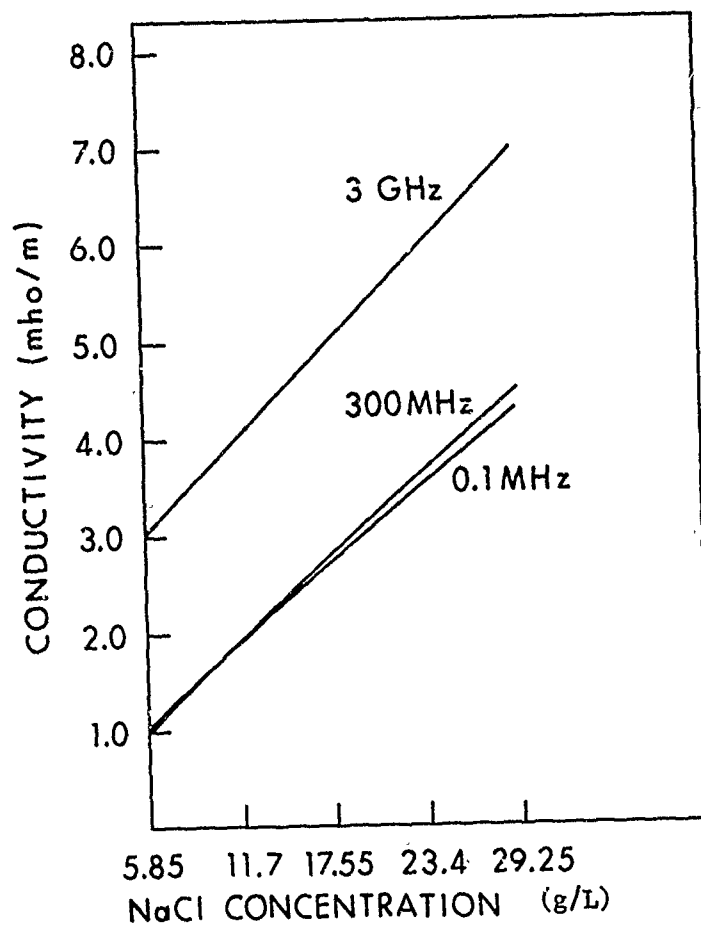
Figure 7.7. Electrical conductivity of saline solution as a function of the NaCl concentration at 25°C.

Table 7.16 shows nine compositions that can be used to simulate muscle material over a wide range of parameters. For example, to get a conductivity of $\tilde{\sigma}$ = 4.6 S/m, Figure 7.5 shows that the NaCl concentration should be about 3.5% of the total mixture. From Table 7.16, we see that mixture VIII could be adjusted to accommodate the 0.4% difference needed in NaCl concentration. The ε' for the mixtures in Table 7.16 are all about that of water. In many cases the ε'' for biological tissue is the dominant factor in determining the SAR, especially at frequencies from 10 to 20 MHz, and the value of ε' is not critical to the measurements.

TABLE 7.16.   COMPOSITIONS OF THE NINE MIXTURES USED
FOR MEASURING DIELECTRIC PROPERTIES

| | Percent by Weight | | | |
Mixture	H_2O	NaCl	TX-150	Polyethylene Powder
I	75	13.0	12.0	0
II	75	11.1	7.9	6.0
III	75	9.8	8.2	7.0
IV	75	9.0	8.0	8.0
V	75	5.45	10.55	9.0
VI	75	4.45	10.55	10.0
VII	75	4.0	10.5	10.5
VIII	75	3.9	10.1	11.0
IX	75	2.0	10.0	13.0

7.3.   TABULATED SUMMARY OF PUBLISHED WORK IN EXPERIMENTAL DOSIMETRY

Table 7.17 contains a summary of published work in experimental dosimetry, including references.

TABLE 7.17. A SUMMARY OF AVAILABLE EXPERIMENTAL DATA ON FIELDS AND SAR MEASUREMENTS IN BIOLOGICAL PHANTOMS AND TEST ANIMALS IRRADIATED BY ELECTROMAGNETIC FIELDS

Object Exposed	Frequency Range	Radiation Source Characteristics	Polarization	Dosimetric Parameter	Measurement Technique	Reference	Summary of Results
Saline-filled rectangular phantoms 45.7 × 78.8 × 25 cm	10-30 MHz	Planewave, CW	KHE	Maximum and average SAR	Differential power measurement	a	Experimental data demonstrate the square-law dependence of SAR on frequency of RF source in the HF band, and linear relationship between P_{in} and SAR.
• 190-560-g rats • Water-filled cylindrical phantoms 190 and 290 g (17-cm long by 3.8-cm diameter) • 29-g mice	2450 MHz	Multimodal resonating cavity, pulse repetition rate = 120 Hz, pulse width = 2.5 ns	Unspecified	Mass absorption density (mJ/g), area absorption density (mJ/cm²) and latency to convulsion	Calorimetric technique	b	Absorbed dose measurements in phantoms are compared with those in rats. At a given power level, mean latency to convulsion is proportional to the weight of rats. Latency to convulsion in rats and mice as function of SAR is given.
• 190-560-g rats • Water-filled cylindrical phantoms 190 and 290 g	2880 MHz	Far field	Unspecified	Mass absorption density (mJ/g) and area absorption density (mJ/cm²)	Calorimetric technique	c	SAR measurements in phantoms are compared with those in rats.
• 96-390 Wistar rats • 25-g mice • Brain-phantom prolate spheroids (a/b up to and including 5.75)	285-4000 MHz	Planewave (two-plate stripline)	E, H, and K	SAR	Insertion loss measurement	d e f	For rats, mice, and spheroidal phantoms, E polarization is the most absorbing, H polarization the least, and K polarization slightly more absorbing than the H. For rats, in K polarization the frequencies of peak absorption and the maximum absorption at these values demonstrate $Wl^{1/3}$ and $Wl^{2/3}$ dependencies, respectively, upon the weight of the animal. In phantom spheres the peak SAR occurs in a resonant region where $k_a = 0.55-0.59$.
• Rhesus monkeys (anesthetized) • 3.5-kg prolate spheroid monkey phantoms • 70-kg prolate spheroid human phantoms	1-50 MHz	Far-field exposure chamber	E, H, and K	SAR	Differential power measurements	f g	Average SAR increases approximately as the frequency squared, for all phantoms as well as monkey exposures. Experimental data on spheroidal phantoms are in good agreement with theoretical data calculated by long-wavelength analysis (Durney et al., 1975). Comparisons are made between measured SAR data on monkeys and calculated data on ellipsoidal models (Massoudi et al., 1977a).

* References are listed at end of table.

TABLE 7.17 (continued)

Object Exposed	Frequency Range	Radiation Source Characteristics	Polarization	Dosimetric Parameter	Measurement Technique	Reference	Summary of Results
Tissue-equivalent materials simulating rats 1, 4, 10, 12, 30, and 60 d old	2450 MHz	Rectangular waveguide, TE$_{10}$ mode, CW	Tail-on (0°) and head-on (180°) to direction of incident wave. Also, stepwise variations from 0° to 180°	SAR and SAR distribution	Thermography from SAR distribution and insertion-loss measurement for average SAR	h	For 180° orientation, the head area, including the brain, absorbs the most microwave energy. In the opposite orientation, the tail and abdominal regions absorb the maximum. Total SAR changes only slightly between 0° and 180° orientations. SAR is lowest at 90° orientation angle.
• 25-30-g mice (8.5 cm long) • 100-125-g rats (16 cm long) • 380-420-g rats (22.5 cm long, excluding tail)	710-3000 MHz	Standard-gain horns	E and H	Latency to tonic-clonic convulsion	Observation via closed-circuit television and elapsed time recorded on a printout counter	i	E polarization produces consistently shorter convulsion latencies. An inverse relationship between frequency and animal size was observed over the range of frequencies and sizes tested.
• Rats (60-440 g) • Mice (35-50 g)	2450 MHz	Horn antenna (free-field exposure)	---	SAR	Calorimetric technique	j	Simultaneous exposures of groups of animals in varying numbers and various configurations have been made. SAR data as a function of position and weight are presented. Position of animal in an exposure matrix significantly affects the SAR.
Mice (4 wk old)	918 MHz	Rectangular waveguide (24.8 × 12.4 cm)	---	SAR	Differential power measurements	k	During 8-h irradiation sessions, a reduction in SAR after the initial hour of each session was observed for both female and male groups of mice exposed to a 5-W forward power but not for a 2.5-W forward power.
Spheres of simulated muscle tissue (3.3-cm and 8-cm radii)	450, 915, and 2450 MHz	Planewave (horn antenna)	---	Spatial distribution of E-field	Miniature isotropic probes	ℓ m	Spatial distribution of E-field within spheres is compared with theoretically predicted values. Some internal dosimetric techniques are compared. Measured data are obtained with implantable probe in living cat's brain.

Sample	Frequency	Setup	Polarization	Quantity	Method	Findings	Ref.
Saline-filled and biological phantom figurines (dolls 12.1, 18.4, 22.3, and 23.5 cm tall)	500, 985, and 2450 MHz	TEM parallel-plate chamber and free space	EHK, EKH, KHE, and KEH	SAR distribution	Temperature-rise measurement	Measured SAR data for dolls are scaled to obtain SAR values for humans as function of L/λ. For E polarization, (a) SAR observed for $L/\lambda = 0.37$; (b) hot spots observed in neck region; (c) maximum whole-body absorption under grounded conditions observed at a frequency about one-half that of ungrounded body; (d) zone of maximum SAR is ankle region for a grounded doll.	n o p
• Saline-filled (0.9% NaCl) figurines (7.6, 10.2, 12.7, 15.2, 20.3, 25.4, 33, and 40.6 cm high) • Saline-filled prolate spheroid ($L/2b = 6$)	500, 710, 987, and 2450 MHz	Free space	EKH, KEH, and HEK	SAR	Temperature-rise measurements	For EHK polarization, SAR dependence on frequency (f) is (a) an f^2 type for frequencies well below resonance ($L/\lambda < 0.1\text{-}0.2$); (b) an $f^{2.75}$ to f^3 type at sub-resonant region ($0.2 < L/\lambda < 0.36$); (c) a $1/f$ type for supraresonant region. For $f \gg f_r$ the relative absorption coefficient asymptotically approaches the optical value (1-power reflection coefficient).	o q
Saline-filled figurines (10.2, 12.7, 15.2, and 20.3 cm tall)	150-1500 MHz	Monopole-above-ground radiation chamber	EKH	SAR	Temperature-rise measurements	Projected SARs for a human being of height L, with feet in conductive contact with ground, are given as a function of L/λ. Peak SAR occurs at a frequency about one-half the value for the ungrounded condition.	o q
Saline-filled figurines	987 and 2450 MHz	Monopole antenna in front of flat and corner reflectors	---	SAR	Temperature-rise measurements	Enhancement factor as a function of L/λ for different size figurines, near both a flat reflector and 90° corner reflector, are presented. Tremendous enhancements in SAR are observed for targets that are placed in proximity to reflecting surfaces.	n q
Rats (averaged mass near 100 g)	987 MHz	Monopole antenna in a 90° corner reflector	---	Time to convulsion	---	Times to convulsion of rats incident wave of 3~ to 20~/cm2 power densities confirm some of the predictions of enhanced SAR in the presence of reflecting surfaces.	q

TABLE 7.17. (continued)

Object Exposed	Frequency Range	Radiation Source Characteristics	Polarization	Dosimetric Parameter	Measurement Technique	Reference	Summary of Results
Prolate spheroid phantoms: 330 g (17 × 6.1 cm) 301 g (13.2 × 6.6 cm)	918 MHz	Cylindrical waveguide excited with circularly polarized TE_{11}-mode field configuration	Major axis of the spheroid, both parallel and perpendicular to waveguide axis	Average SAR, peak SAR, and SAR distribution	Thermographic methods and differential power measurements	r	Thermographic SAR measurements on exposed spheroidal phantoms are presented. Average and peak SAR values show very little change with orientation of phantoms.
A sacrificed 388-g rat	918 MHz	Cylindrical waveguide excited with circularly polarized TE_{11}-mode field configuration	Axial head, axial tail, and transverse illuminations	SAR distribution	Thermographic methods	r	Computer-processed thermograms showing iso-SAR lines normalized for 1-W input in three orientations.
132-490-g anesthetized and freely moving rats	918 MHz	Cylindrical waveguide excited with circularly polarized TE_{11}-mode field configuration	---	Mean SAR	Differential power measurement	r	For both moving and anesthetized rats, the mean SAR remains relatively constant with low standard deviation.
Spherical phantoms, 6-11.1-cm diameters	VHF	Resonant cavity	---	SAR distribution, peak SAR	Thermographic techniques	s, t	Thermograms show SAR distribution inside phantoms exposed to electric, magnetic, and combinations of electric and magnetic fields in the near-field synthesizer. Peak SAR data for phantoms exposed in near-field synthesizer are compared with those of the resonant cavity. Peak SAR values are also given for phantoms exposed in stripline chamber and microwave brain deactivator. For short exposure time and temperature rise of more than 2°, measurements made in near-field synthesizer on tissue-equivalent spheroids agree well with theory (Durney et al., 1975) and values measured in the resonant cavity.
• Prolate spheroidal phantoms with semimajor axes of 6.82-19.6 cm and aspect ratios (a/b) of 2-7.73	19 MHz	Near-field synthesizer	E, K, and H				
	19 MHz	Stripline exposure apparatus					
• 1/4.62 scale human, 37.7 cm tall	1600 MHz	Planewave					
• 40-g mouse and its phantom	2450 MHz	Microwave brain deactivator					

Specimen	Frequency	Exposure device	Polarization	Dosimetric quantity	Measurement	Results	
Inhomogeneous saline-filled rectangular phantom (8 × 6 × 2 cm)	2370 MHz	Planewave	KEH	SAR	E-field measurement	SAR due to vertical component of induced E-field as a function of conductivity of the central region was measured and experimental data compared with theoretical values. At 2370 MHz, an optimal conductivity exists for the local region to gain the most effective EH heating.	u v
18 rats simultaneously exposed	2.6 GHz	Standard gain horn	R	Average SAR	Calorimetric technique	Power density levels at positions near the center of the array were higher than those near the edge.	w
Erythrocyte membrane	2.45 GHz and 12.5–18 GHz	Horn antenna	---	SAR	Temperature-rise measurements	At all frequencies and power levels tested, increased loss of either hemoglobin or K^+ from microwave-irradiated-rabbit RBCs should be ascribed to thermal effects on the stability and/or permeability of erythrocyte membrane.	x
25-g mice to 45-g mice	31–34 MHz, 62–68 MHz	90° corner reflector with quarter-wavelength monopole	---	SAR	Colonic temperature elevation and calorimetric method of average-SAR measurement	Extremely high rates of absorption in the presence of reflecting surfaces were confirmed.	q
Guinea pigs, rabbits, mice, cacti	X-band microwave frequency range	Rectangular horn antenna	---	Power density	Changes of power density	Significant changes in radiation pattern occurred as result of presence of biological specimen.	w
20.3-cm saline-filled dolls and various orientations to E	2450 and 987 MHz	---	E, K	SAR	---	Whole-body SARs varied smoothly from E- to K-orientation values as body orientation was altered between the two extreme positions in this plane.	y
Frog sciatic nerves, cat saphenous nerves, rabbit vagus nerves, rat diaphragm muscles	2450 MHz	S-band waveguide	H, K	SAR, and nerve conduction and contraction	Fiber-optic probe for temperature measurements	When the temperature of nerves and muscles exposed to EM fields was kept constant, no change in conduction characteristics or contraction was observed.	z
Scaled figurines 20.3, 25.4, 33, and 40.5 cm long and Long Evans rats	285 MHz, 355.6 MHz, 462.3 MHz, 569 MHz	---	E, K	SAR	Calorimetric technique and temperature-rise measurements	Head resonance was observed in each case.	aa

TABLE 7.17. (continued)

Object Exposed	Frequency Range	Radiation Source Characteristics	Polarization	Dosimetric Parameter	Measurement Technique	Reference	Summary of Results
Four 300-g male Walter Reed strain rats	2450 MHz, 987 MHz	Exposed rectangular waveguide	0°, 90°, 180°, 270°, within waveguide	Spatial distribution of heat loading and pattern of succinic dehydrogenase	Temperature-rise measurements and cytochemical measurement	bb	Data obtained suggest that further exploration of frequency parameter could lead to extremely rapid method of sacrifice with simultaneous inactivation of brain enzymes in unrestrained rats.
100-g rats placed 3λ/2 in front of 90° corner reflector	987 MHz, 2650 MHz	90° corner reflector	----	Time to convulsion	----	y	Departure of only 10% between projected and observed values; may be even lower for heavier animals.
Eleven rats 420-450 g	200-700 MHz	Single brass monopole (λ/4 long, 1.2-cm diameter)	E	Rise in temperature and change in behavior	Temperature-rise measurements	cc	Showed increasingly larger rise in body temperature and increasing tendency for behavioral disruption to occur in animals as frequency was increased from 200 to 500 MHz.
Adult male CFI mice	2450 MHz	Inside a rectangular waveguide	----	Specific heat dissipation rate	Calorimetric technique	dd	Indicated increased heat-dissipation rate of animals (compared to sham) for average absorbed dose rates above 12 mW/g.
Pupae of the insect Tenebrio molitor L	1.3, 5.95, and 10 GHz	Right-angle, waveguide E bends	E, K, and H	SAR distribution	Thermographic imaging system	ee	At X band, waveguide-irradiated insects experienced localized SAR values significantly higher than whole-body average SAR.
Phantom model of man	0.5, 0.75, 2, and 2.5 GHz	EM standing wave	E	Electric-field distribution	Implantable electric-field probe	ff	Distribution of measured electric field is compared with distribution of theoretical results obtained numerically from the moment-method solution of electric-field integral equation with pulse basis functions. Agreement between the experiment and theory tends to deteriorate at lower frequencies.

Model/Subject	Frequency	Source	Orientation	Measured quantity	Technique		Comments
Human volunteers	18.5 MHz	TEM cell	EKH, EHK, KEH, KHE, HEK, and HKE	Average SAR	Insertion-loss technique	gg	First set of human whole-body average SAR is presented for three subjects exposed in free space to 11 µW/cm2 at 18.5 MHz. Measured average SARs for the two principal E-orientations (EKH and EHK) are larger than the published predictions by a factor of 2 or 3.
Saline-filled reduced-scale figurines	610-795 MHz	Leakage fields of parallel-plate applicator	---	Average SAR internal electric field	Temperature-rise measurements and electric-field measurements	hh	Experimental results using reduced-scale figurines for whole-body average SAR agree well with results obtained from the empirical relationship (Chatterjee et al., 1980). For near-field leakage-type exposures, internal E-fields and average SARs are considerably smaller than for far-field exposure conditions.
3.3-cm-radius muscle-equivalent sphere, M. mulatta head	1.2 GHz	Far field of a standard-gain horn	E and H	Rate of temperature rise	Temperature-rise measurements	ii	Thermal response model accurately predicts temperature distribution in muscle-equivalent spheres and in detached/attached M. mulatta heads. Orientation of M. mulatta cadaver body with respect to EM-field vectors significantly affects temperature distribution in the head.
Conducting models of swine and rat	60 Hz	Electric field of strength 9.5 kV/m	---	Induced current measurements	---	jj	Body shape has a major influence on fields actually experienced by a man or animal exposed to a 60-Hz electric field.
Muscle-equivalent model of sitting rhesus monkey	1.29 GHz and 225 MHz	Rectangular horn antenna	E	SAR distribution and average SAR	Temperature-rise measurement, calorimetric and thermographic technique	kk, ll	Measured average SAR is about three times that predicted for a prolate spheroidal model of similar mass, at 1.29 GHz. However, at 225 MHz, very close agreement between theory and experiment is seen.

TABLE 7.17. (continued)

Object Exposed	Frequency Range	Radiation Source Characteristics	Polarization	Dosimetric Parameter	Measurement Technique	Reference	Summary of Results
Scaled phantom models of humans and test animals	57.3 MHz	TE_{101} mode rectangular resonant cavity	—	SAR	Thermographic technique	mm	Instrumentation system is developed for determining relationship between the applied uniform electric-field intensity at 60 Hz and the pattern of internal electric currents induced in exposed models. The 60-Hz field exposures are simulated by exposing scale models to 57.3-MHz fields of high strength on a resonant cavity.
Muscle-equivalent full-sized model of man	2 GHz	Horn antenna	E	Average SAR and SAR distribution	Calorimetric and temperature-rise measurement	nn	Relatively high SAR values are found in the limbs compared to the axis of the trunk of the model. Measured average SAR values are about three times higher than that estimated theoretically for a prolate spheroidal model of man.
Full-size muscle-equivalent human model	1.29 GHz	Far field of a standard gain horn	E	SAR distribution	Temperature-rise measurement	oo	Temperature rise is measured at front surface and several depths within the phantom. Based on these measurements, an approximate average-SAR value is obtained which agrees well with theoretical predictions based on absorption in the prolate spheroidal model of man.
Saline-filled prolate spheroidal phantom	400 MHz	Near field of a dipole source	E	Average SAR	Temperature-rise measurement	pp	Although relative SAR increases as distance from antenna decreases, the rate of increase of SAR values is slower than $(\lambda/d)^2$, which is the characteristic variation of the far-field absorption produced by an electrically short dipole.
Human volunteer	3 to 41 MHz	TEM cell	EKH and EHK	Average SAR	Insertion-loss technique	qq	Measured average SAR, at 10 MHz, exceeds the average of the standard model calculations by a factor of 3 for free space and a factor of 4 for ground conditions.

REFERENCES

a. Allen, 1975

b. Phillips et al., 1975

c. Gandhi, 1974

d. Gandhi, 1975a

e. Gandhi, 1975c

f. Allen et al., 1975

g. Allen et al., 1976

h. Leicher-Preka and Ho, 1976

i. Schrot and Hawkins, 1976

j. Kinn, 1977

k. Ho et al., 1977

l. Bassen, 1977

m. Bassen et al., 1977b

n. Gandhi, 1975b

o. Gandhi and Hagmann, 1977a

p. Gandhi et al., 1976

q. Gandhi et al., 1977

r. Guy and Chou, 1976

s. Chou and Guy, 1977

t. Guy et al., 1976

u. Chen and Guru, 1977a

v. Guru and Chen, 1977

w. Bigu del Blanco and Romero-Sierra, 1978

x. Peterson et al., 1979

y. Gandhi, 1980

z. Chou and Guy, 1978

aa. Hagmann et al., 1979b

bb. Meyerhoff et al., 1979

cc. D'Andrea et al., 1977

dd. Ho and McManaway, 1977

ee. Olsen and Hammeur, 1982

ff. Chen et al., 1982

gg. Hill, 1982

hh. Chatterjee et al., 1982b

ii. Rurr and Krupp, 1980

jj. Kaune and Phillips, 1980

kk. Olsen et al., 1980

ll. Olsen and Grinur, 1982

mm. Guy et al., 1982

nn. Olsen, 1982

oo. Olsen, 1979

pp. Iskander et al., 1981

qq. Hill, 1984

CHAPTER 8. EXPERIMENTAL DOSIMETRIC DATA

Experimental data from the literature on the average SAR, SAR distribu-
tions, and the temperature-rise distributions on some test animals, human
subjects, and phantom models, along with some calculated data, are shown in
Figures 8.1-8.47 and Tables 8.1-8.4. References are given in the figure
captions and table headings.

Of particular interest is the comparison between measured and calculated
values of average SAR. Figures 8.1A and 8.1B show a summary of measured
values reported in the literature compared with calculations of average SAR in
a block model of an average man. The data lead to the following observations:

1. Values measured in figurines by Gandhi et al. (1977) are very close
   to calculated values for frequencies up to about 600 MHz.

2. Values measured in figurines by Guy et al. (1984) are about a factor
   of 2 higher than calculated values for frequencies up to about
   resonance, and above resonance are about equal tr calculated values.

3. Values measured in human subjects by Hill (1984), just below reso-
   nance in a large TEM cell, are higher than values measured by others
   in figurines. Also, the values Guy et al. (1984) measured in human
   subjects, using VLF techniques, are higher than those they measured
   in figurines. All these human-subject data are a factor of 2-4
   higher than calculated values.

4. The value at 27.12 MHz calculated in the 1132-cell inhomogeneous
   block model (DeFord et al., 1983) is about 2 times larger than that
   calculated in the 180-cell homogeneous block model and about the
   same as that measured in figurines by Guy et al. (1984).

5. In summary, one set of measured data agrees reasonably well with
   calculated values; three other sets of measured data and DeFord's
   calculated datum are all higher than the other calculated values by
   a factor of 2-4.
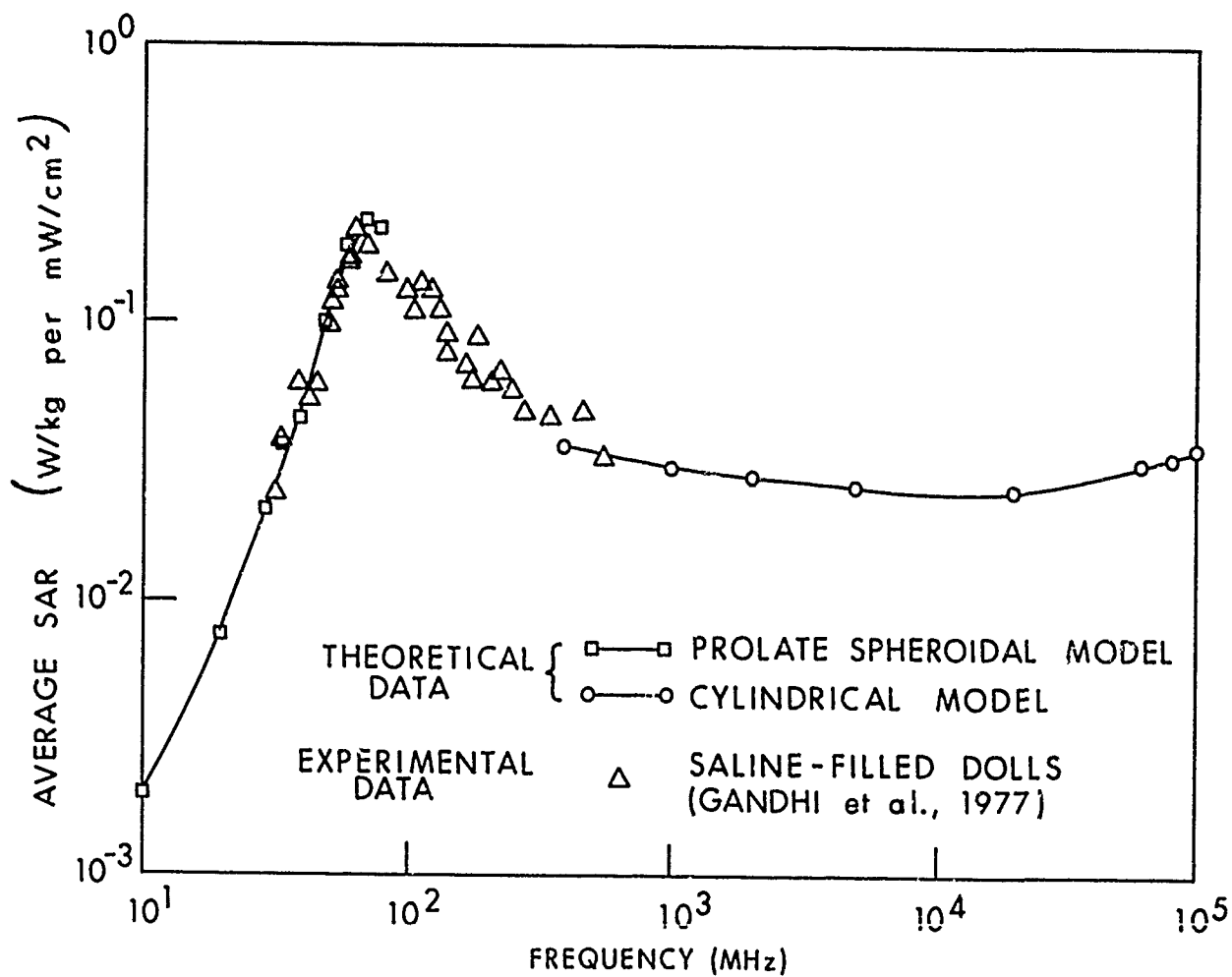
Figure 8.1A. Comparison of measured (experimental) and calculated (theoreti-
cal) SAR values for an average man in free space, E polarization.
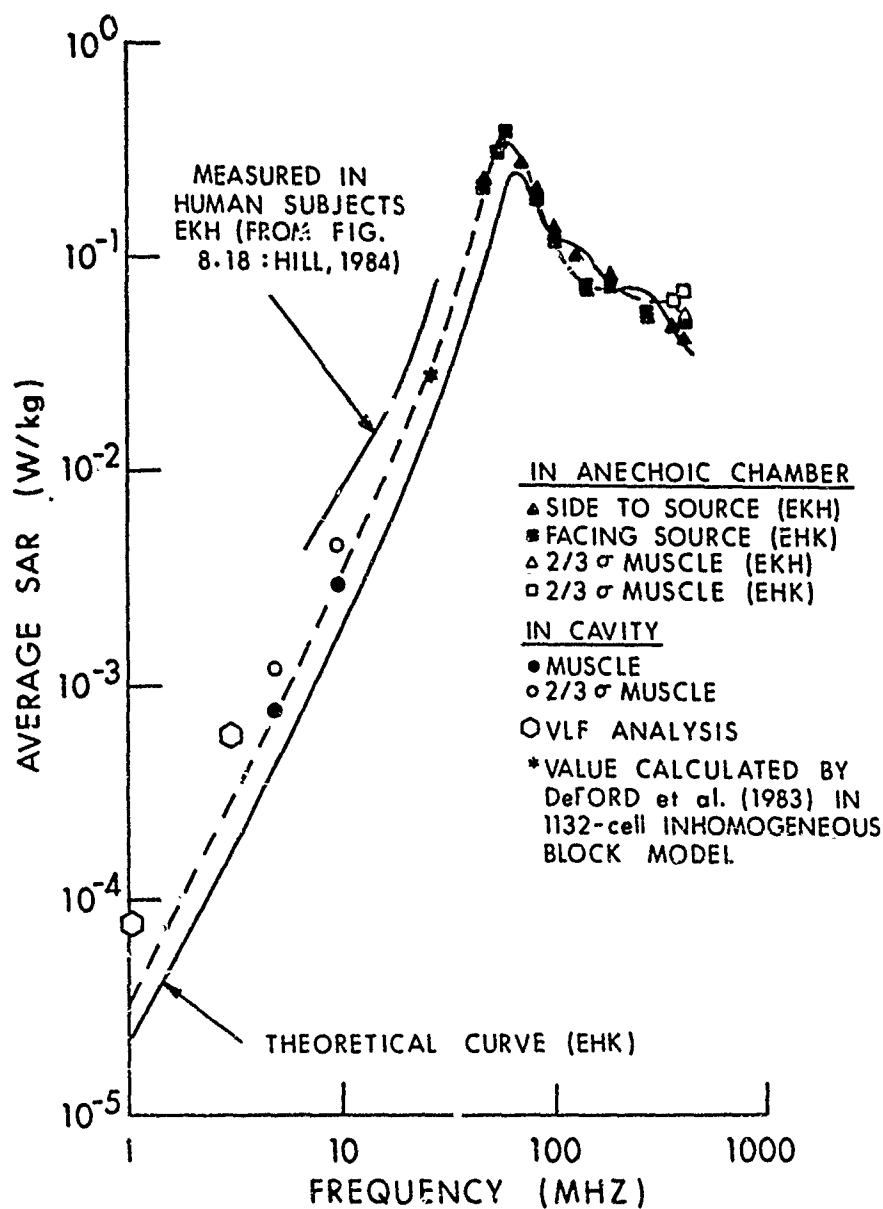
Figure 8.1E. Comparison of measured and calculated SAR values for an average man in free space, H and K polarizations. The figure is basically that of Guy et al. (© 1984 IEEE), showing their measurements on scaled figurines compared with the theoretical curve (180-cell block model) and two VLF measurements on human subjects. An approximate average of measured values on human subjects by Hill has been added, also a single value in a 1132-cell inhomogeneous block model of man as calculated by DeFord et al.

- 8.3 -

A possible explanation of the higher values lies in the very nonuniform distribution of SAR within the body, as explored extensively with thermographic techniques by Guy et al. (1976b, 1984) and illustrated by Figures 8.32 to 8.46. Measured local SAR values are as much as 13 times greater than average SAR values at 450 MHz. In particular the legs, which are relatively thinner and longer than the main trunk of the body, absorb significantly more than the average (see Figures 8.36, 8.46); the reason is explained qualitatively in Section 5.1.5. Since using pulse functions with the moment method to calculate local SAR in block models has been unsatisfactory (Massoudi et al., 1984), average-SAR calculation by the same method may not adequately include the higher local absorption in the legs, thus resulting in lower values of average SAR. Calculated average SARs in prolate spheroidal models, which are very close to those calculated in the block model, also would not account for higher absorption in the legs. Thus the calculated average SARs in both block and spheroidal models might be low because the calculations do not adequately include locally high SAR values. More calculated and measured values are needed to clarify the results.
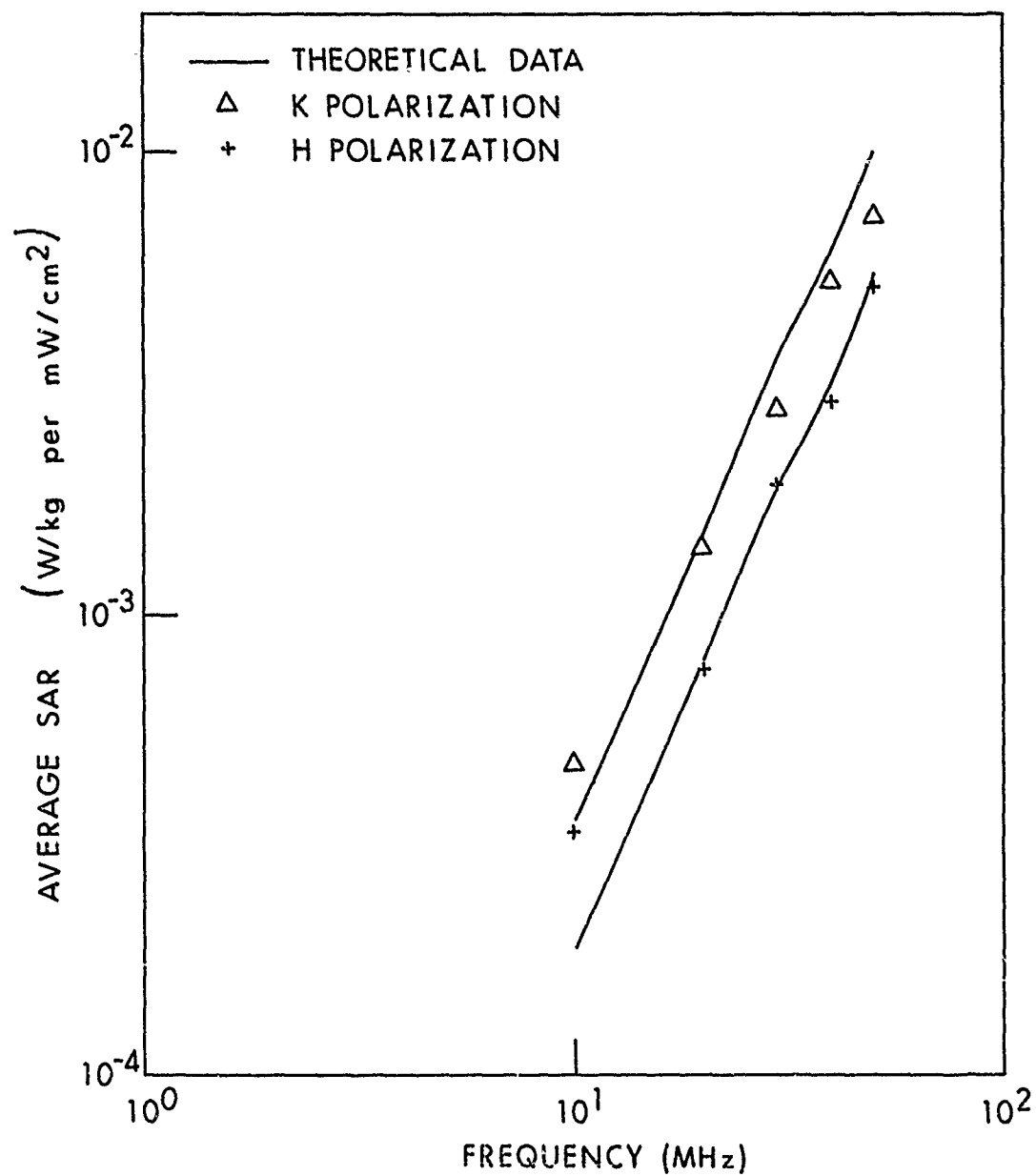
Figure 8.2.   Calculated   and   measured values   of the average SAR
for a human prolate spheroidal phantom; a = 0.875 m,
b = 0.138 m, V = 0.07 m³ (Allen et al., 1975).

- 8.5 -
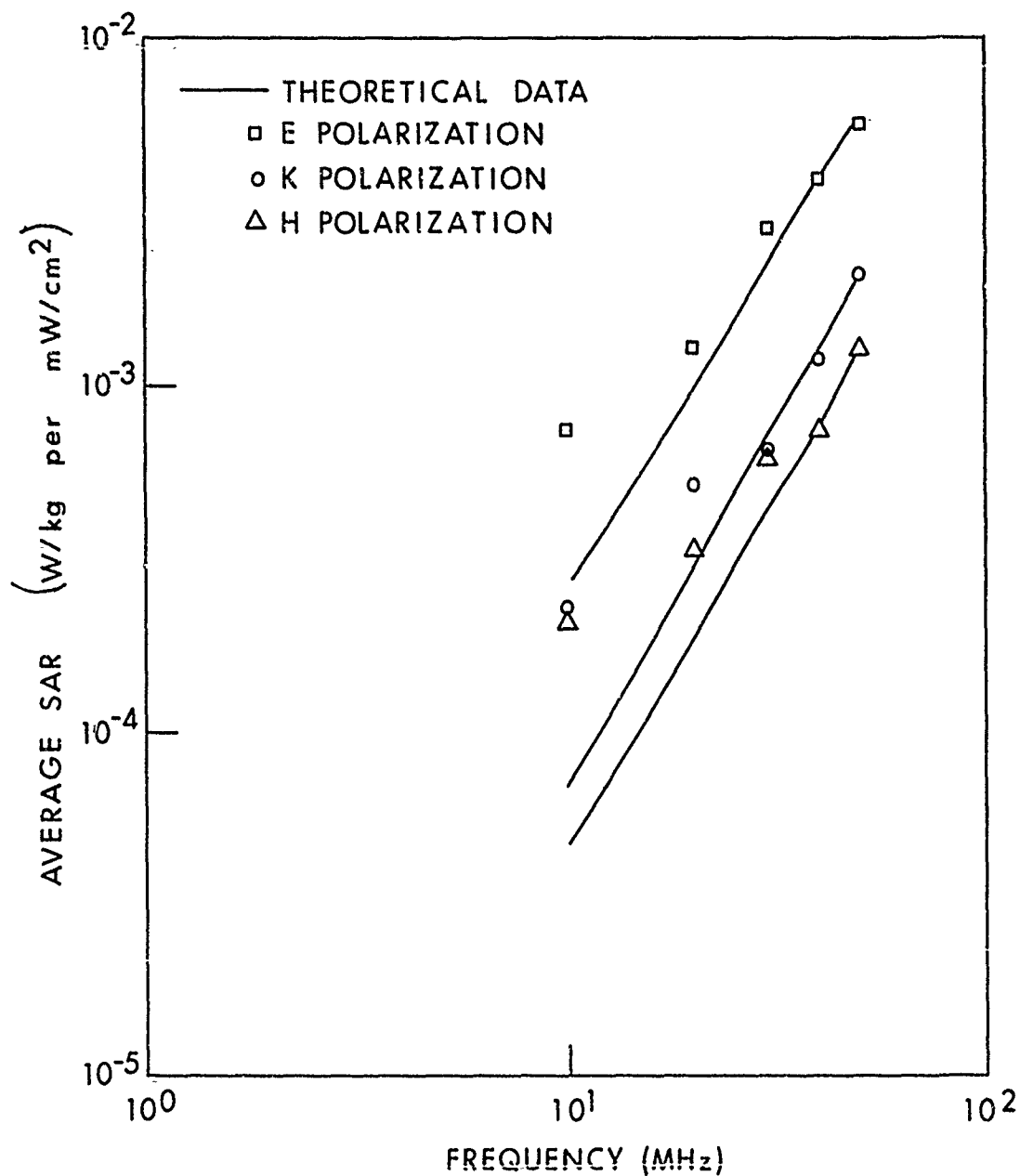
Figure 8.3. Calculated and measured values of the average SAR for a prolate spheroidal phantom of a sitting rhesus monkey; a = 0.2 m, b = 6.46 cm, $V = 3.5 \times 10^{-3}$ m^3 (Allen et al., 1975).
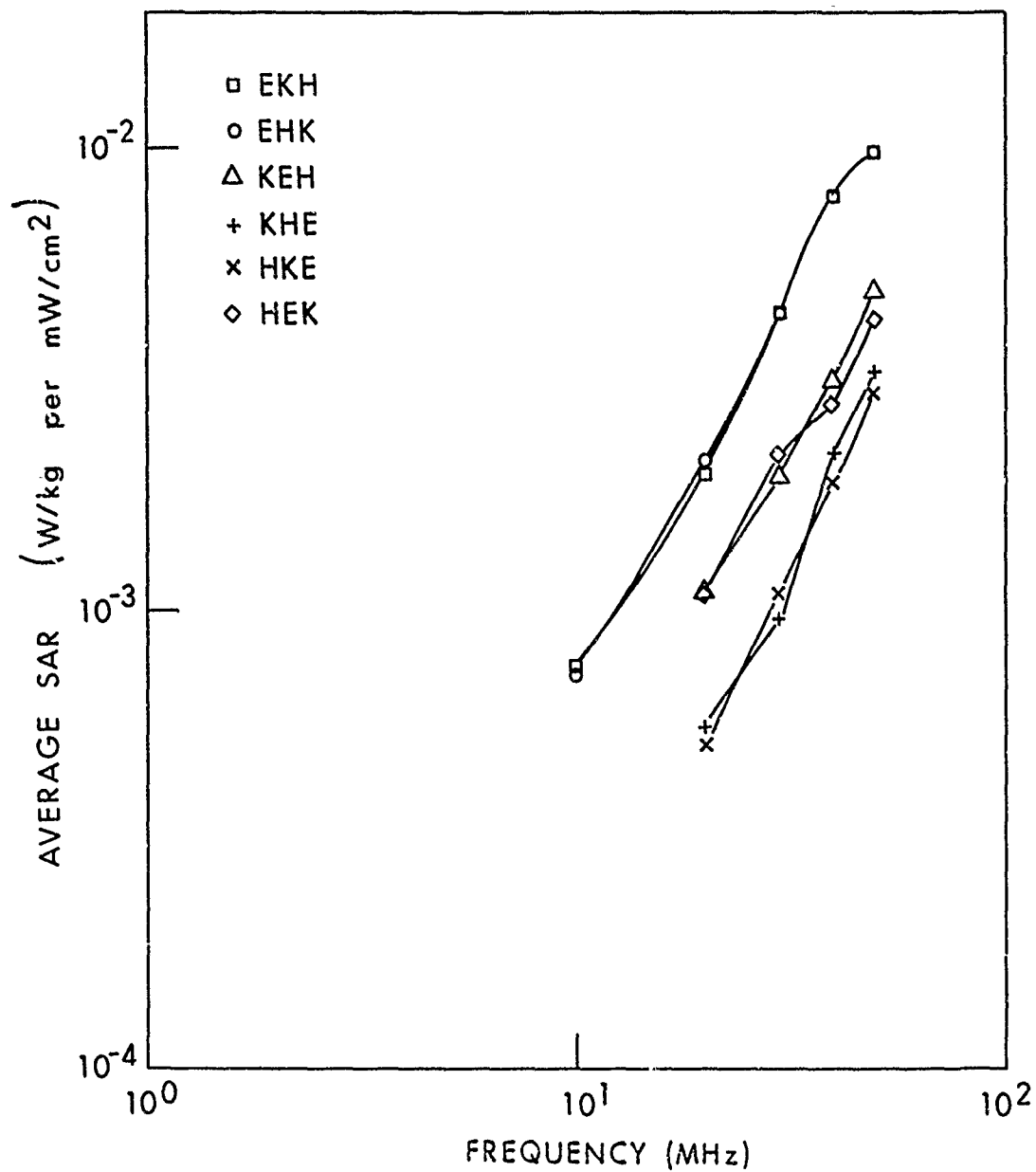
Figure 8.4. Measured values of the average SAR for a live, sitting rhesus monkey, for six standard polarizations (Allen et al., 1976).
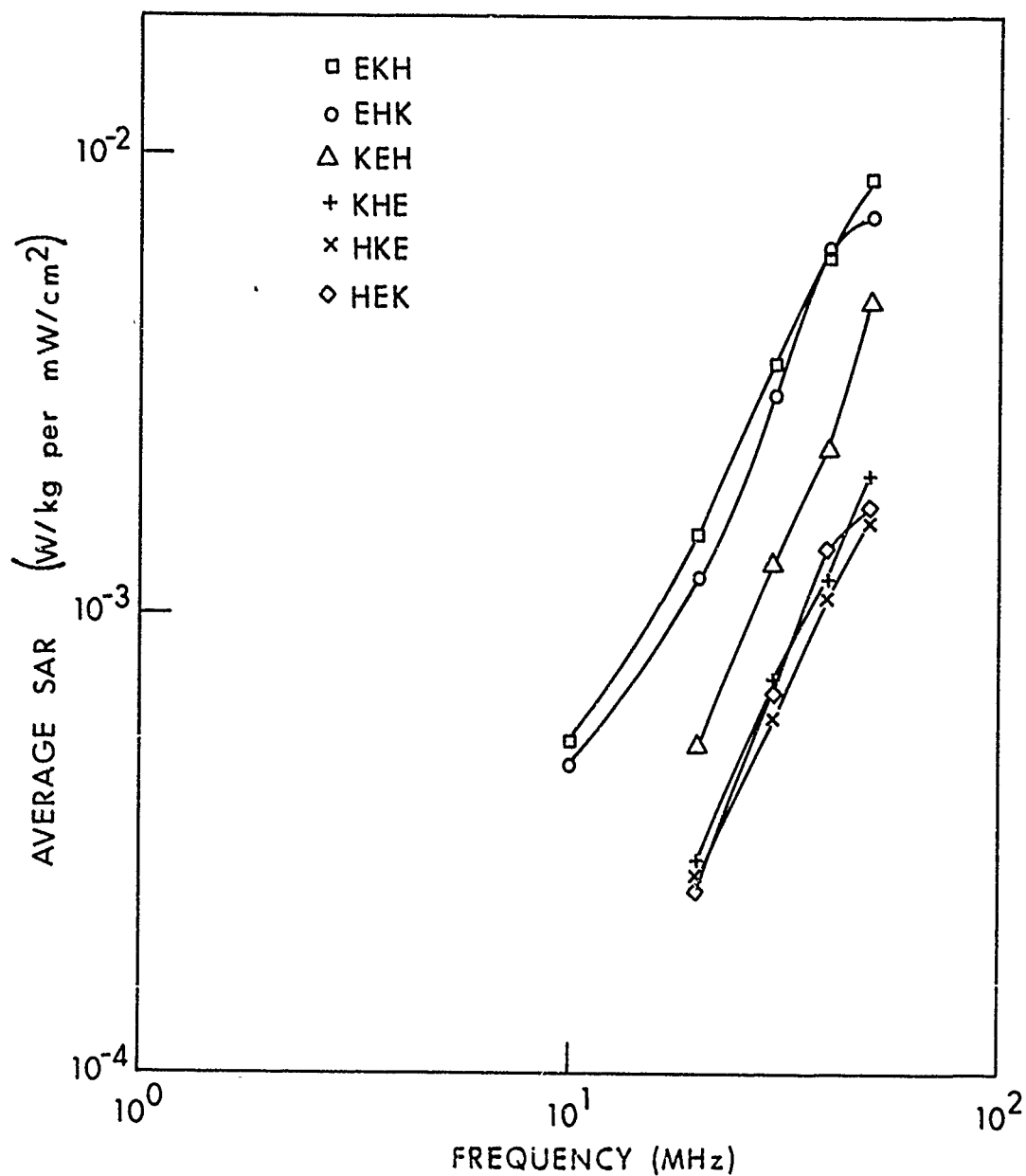
Figure 8.5. Measured values of the average SAR for saline-filled ellipsoidal phantoms, for six standard polarizations; a = 20 cm, b = 7.92 cm, c = 5.28 cm, σ = 0.64 S/m (Allen et al., 1976).
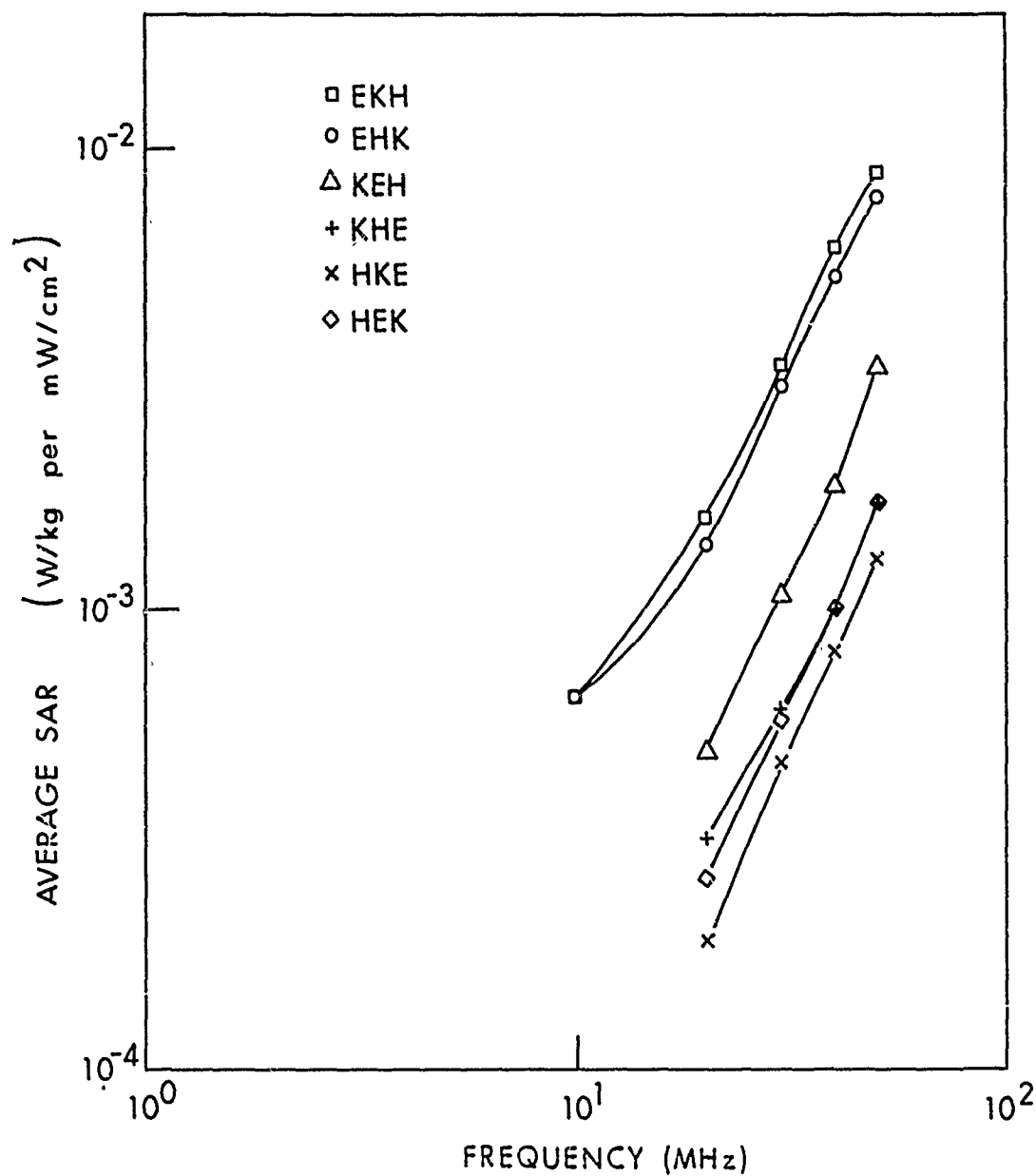
Figure 8.6. Measured values of the average SAR for saline-filled ellipsoidal phantoms, for six standard polarizations; a = 20 cm, b = 7.92 cm, c = 5.28 cm, σ = 0.54 S/m (Allen et al., 1976).
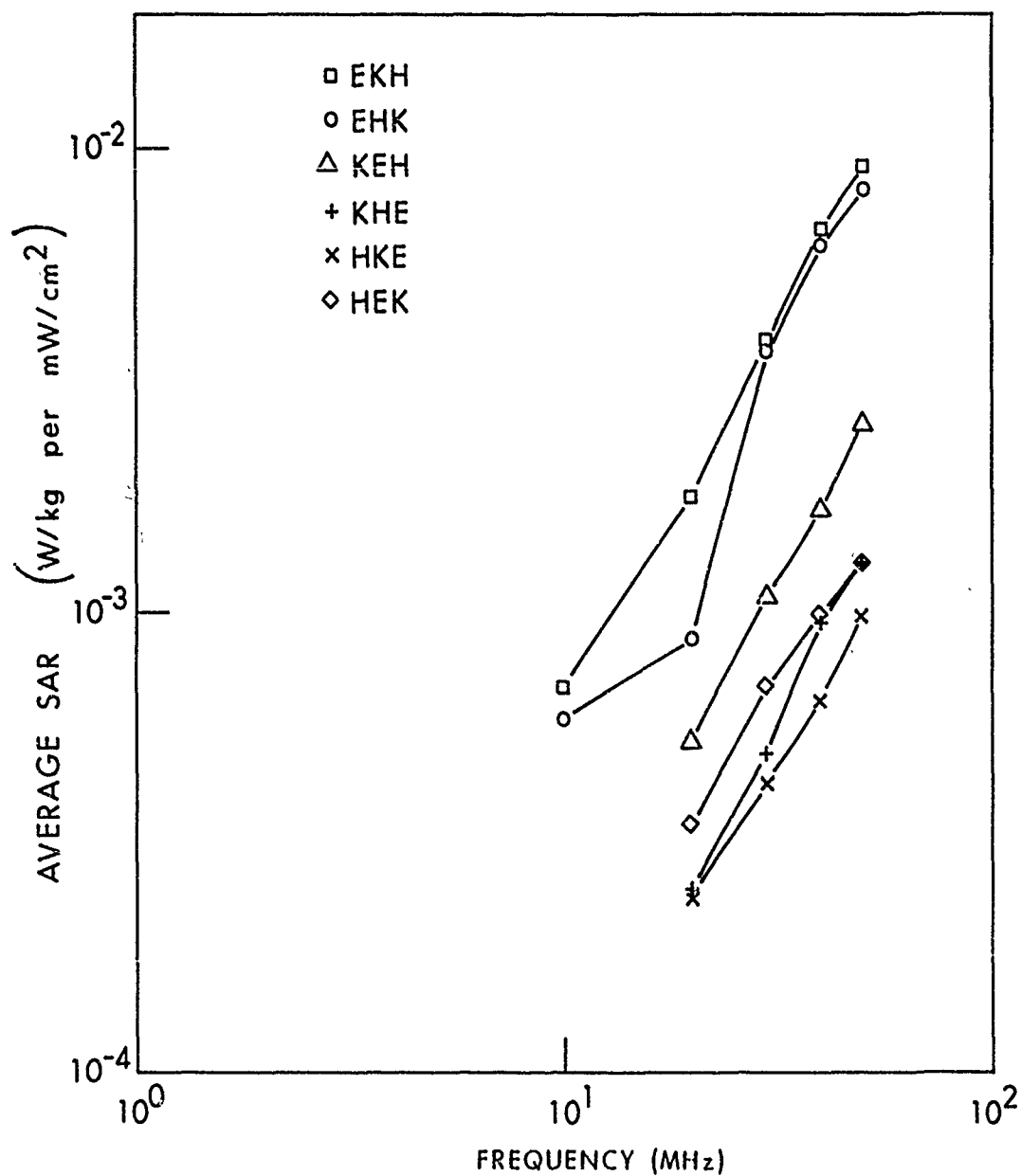
Figure 8.7. Measured values of the average SAR for saline-filled ellipsoidal
phantoms, for six standard polarizations; a = 20 cm, b = 7.92 cm,
c = 5.28 cm, σ = 0.36 S/m (Allen et al., 1976).
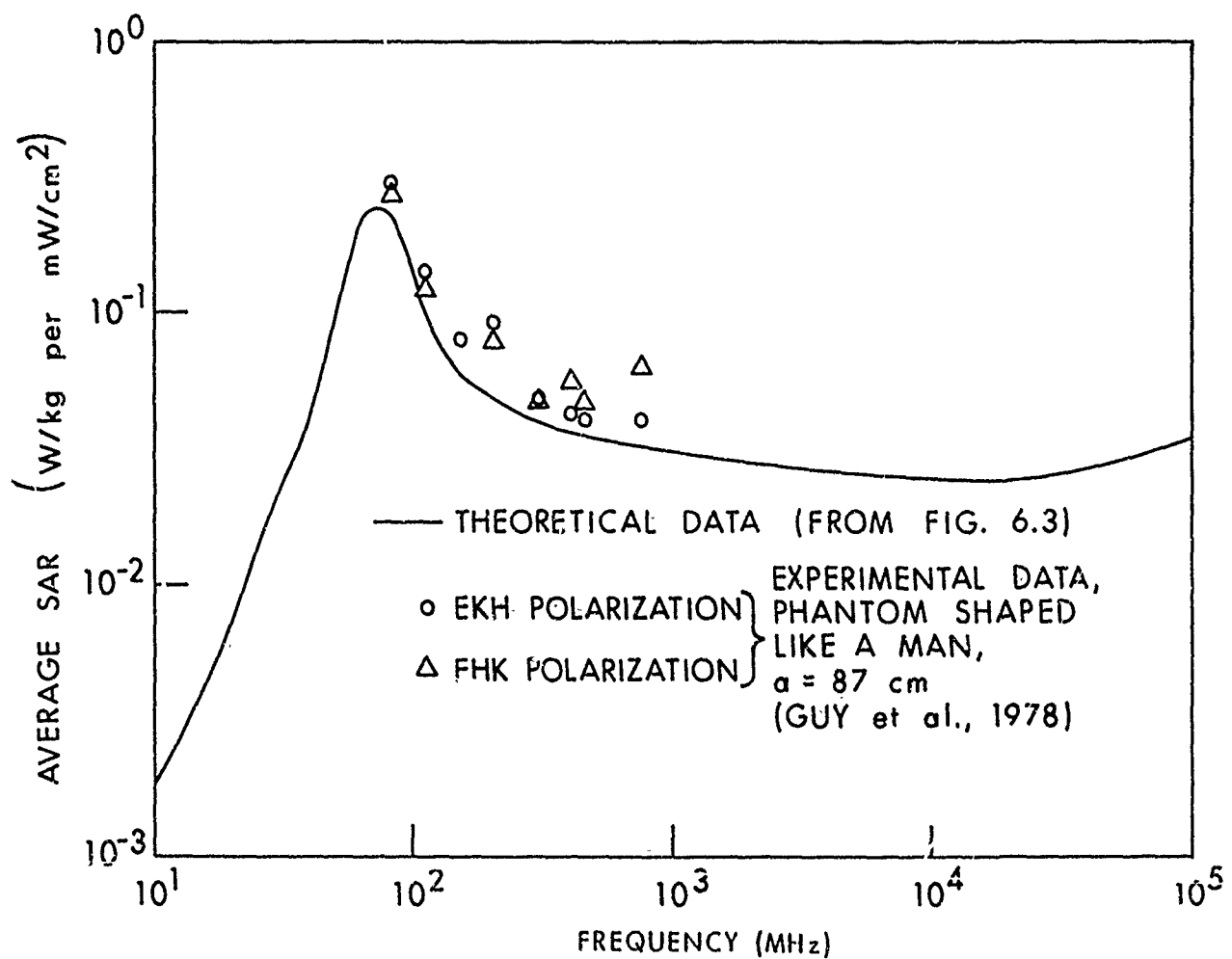
Figure 8.8. Calculated and measured values of the average SAR
for models of an average man, E polarization.
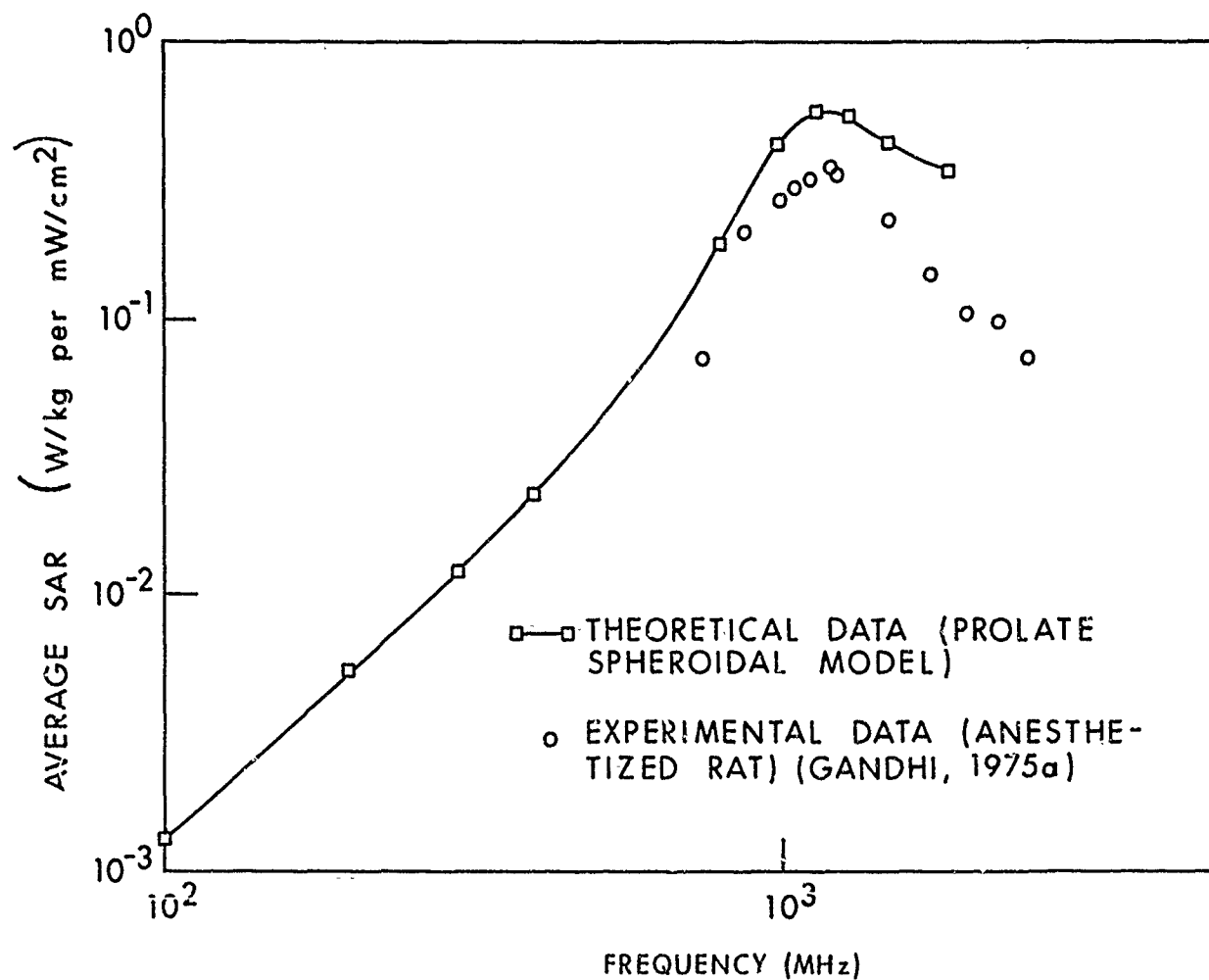
Figure 8.9. Calculated and measured values of the average
SAR for a 96-g rat, K polarization.
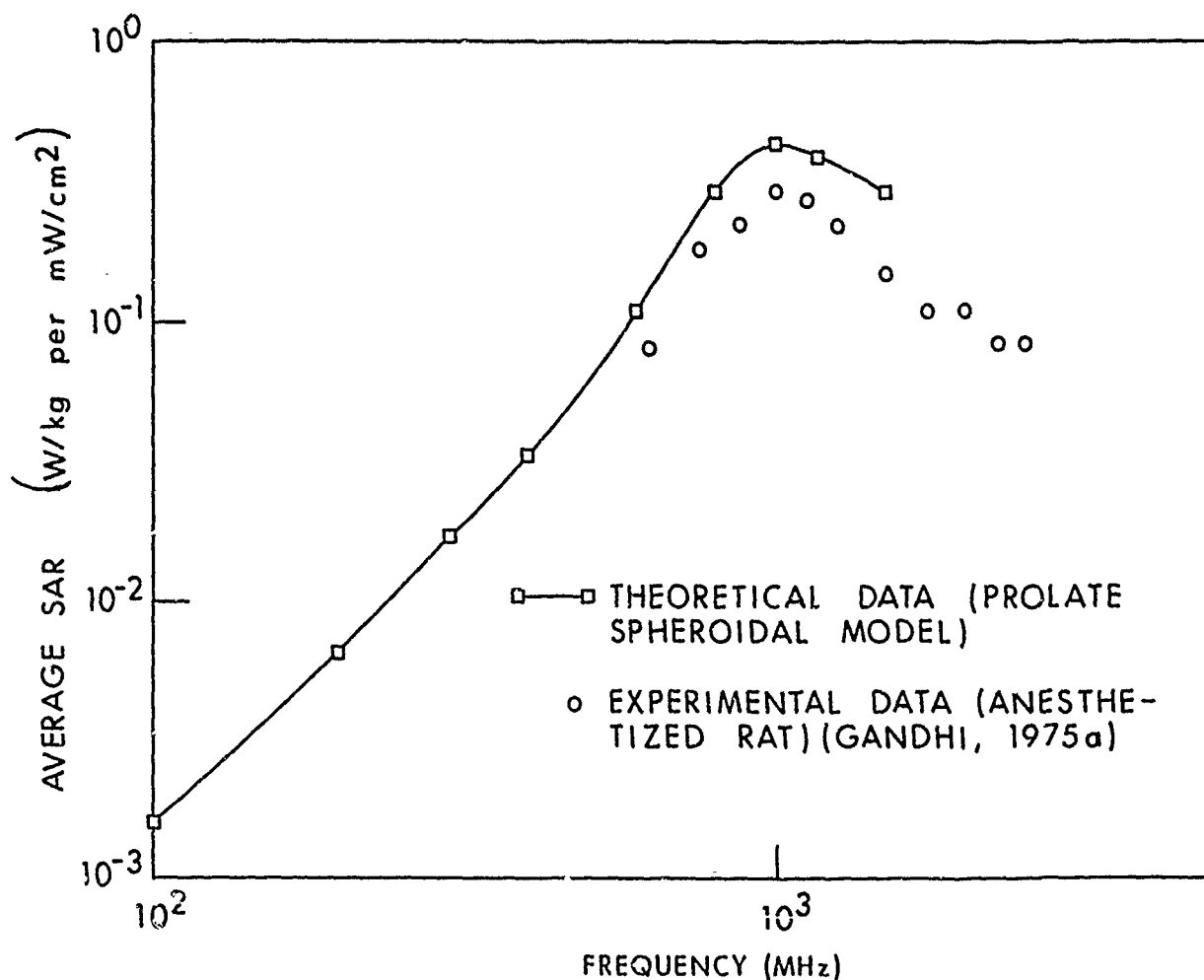
Figure 8.10. Calculated and measured values of the average SAR for a 158-g rat, K polarization.
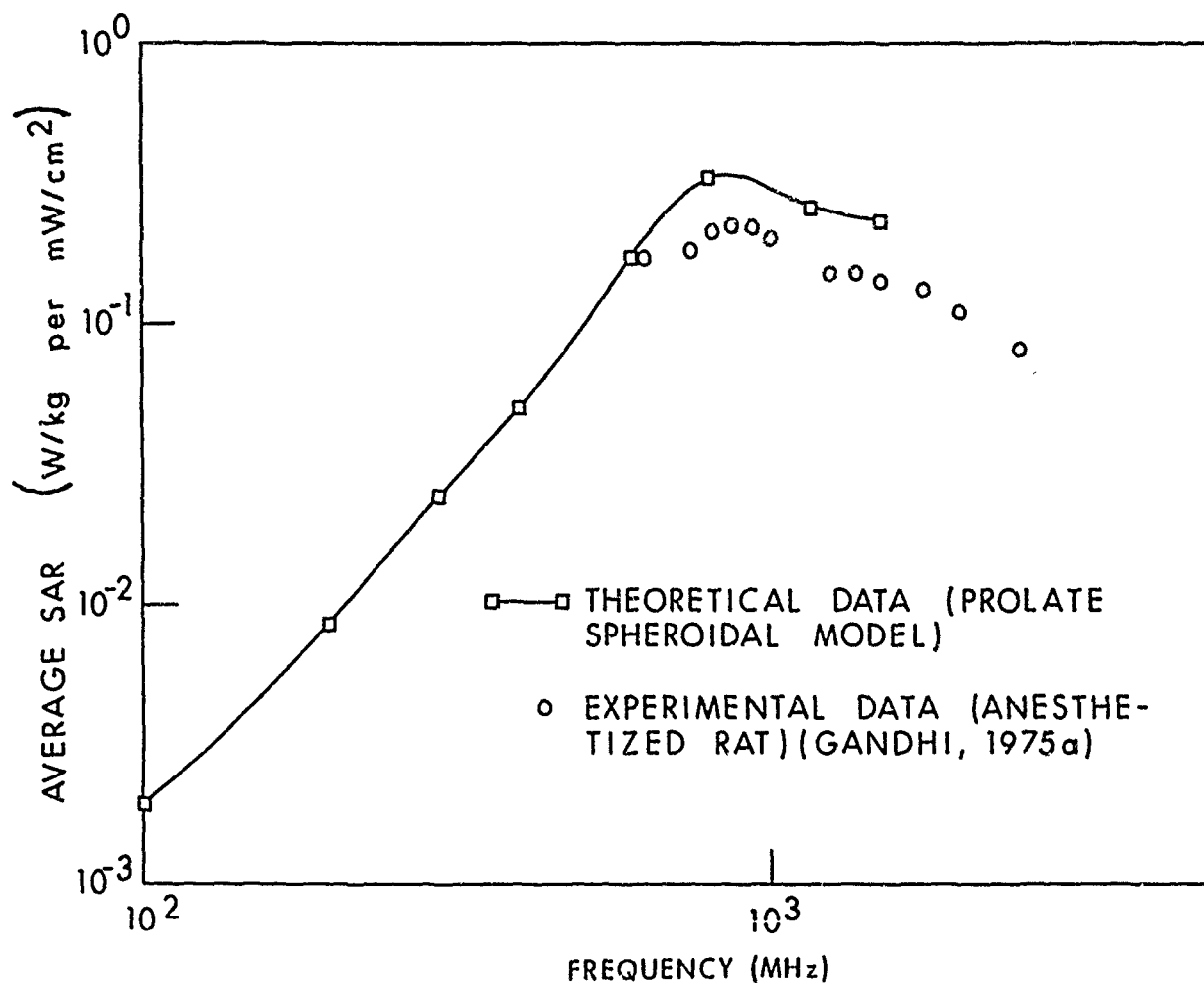
Figure 8.11.   Calculated and measured values of the average
SAR for a 261-g rat, K polarization.
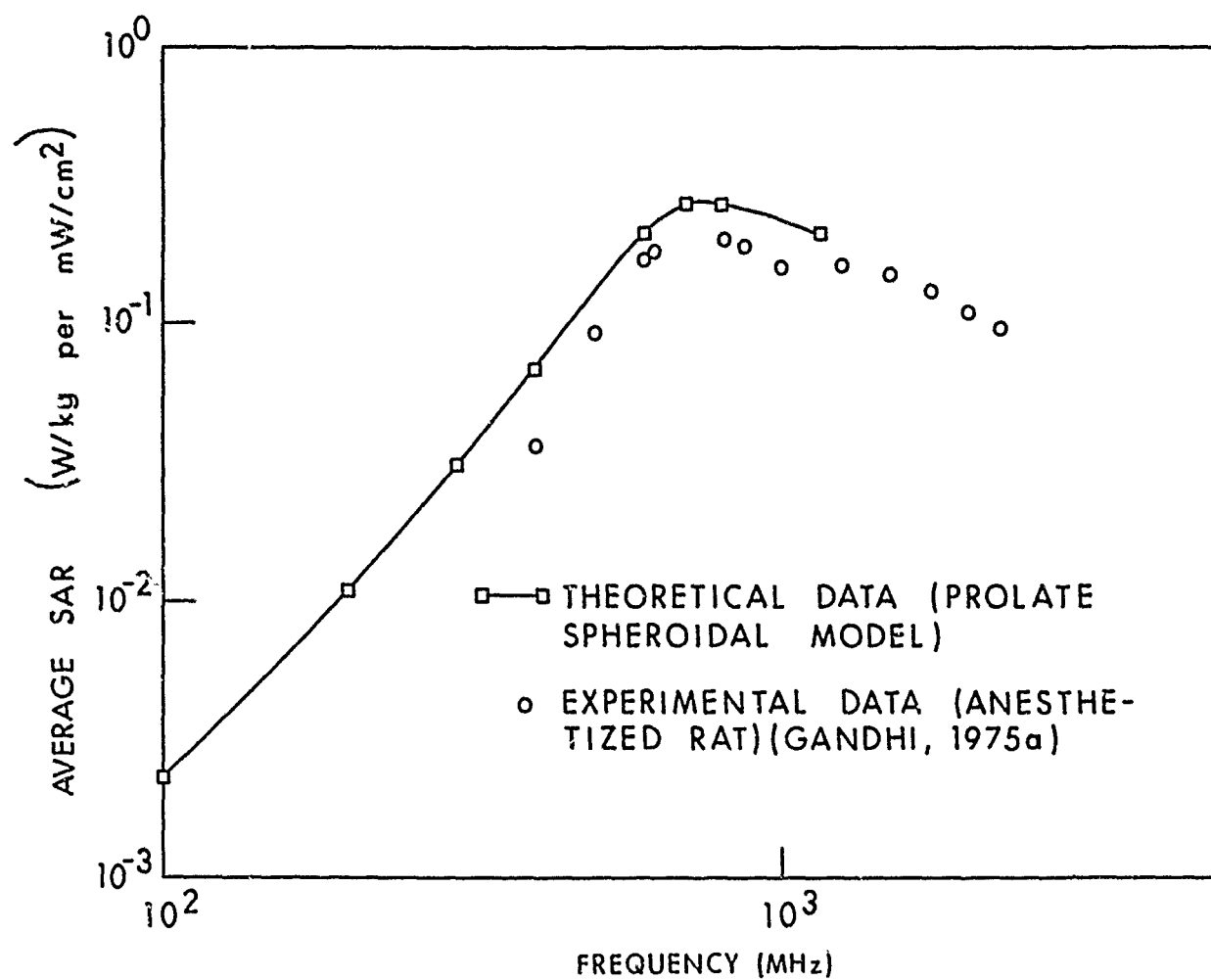
Figure 8.12. Calculated and measured values of the average SAR for a 390-g rat, K polarization.
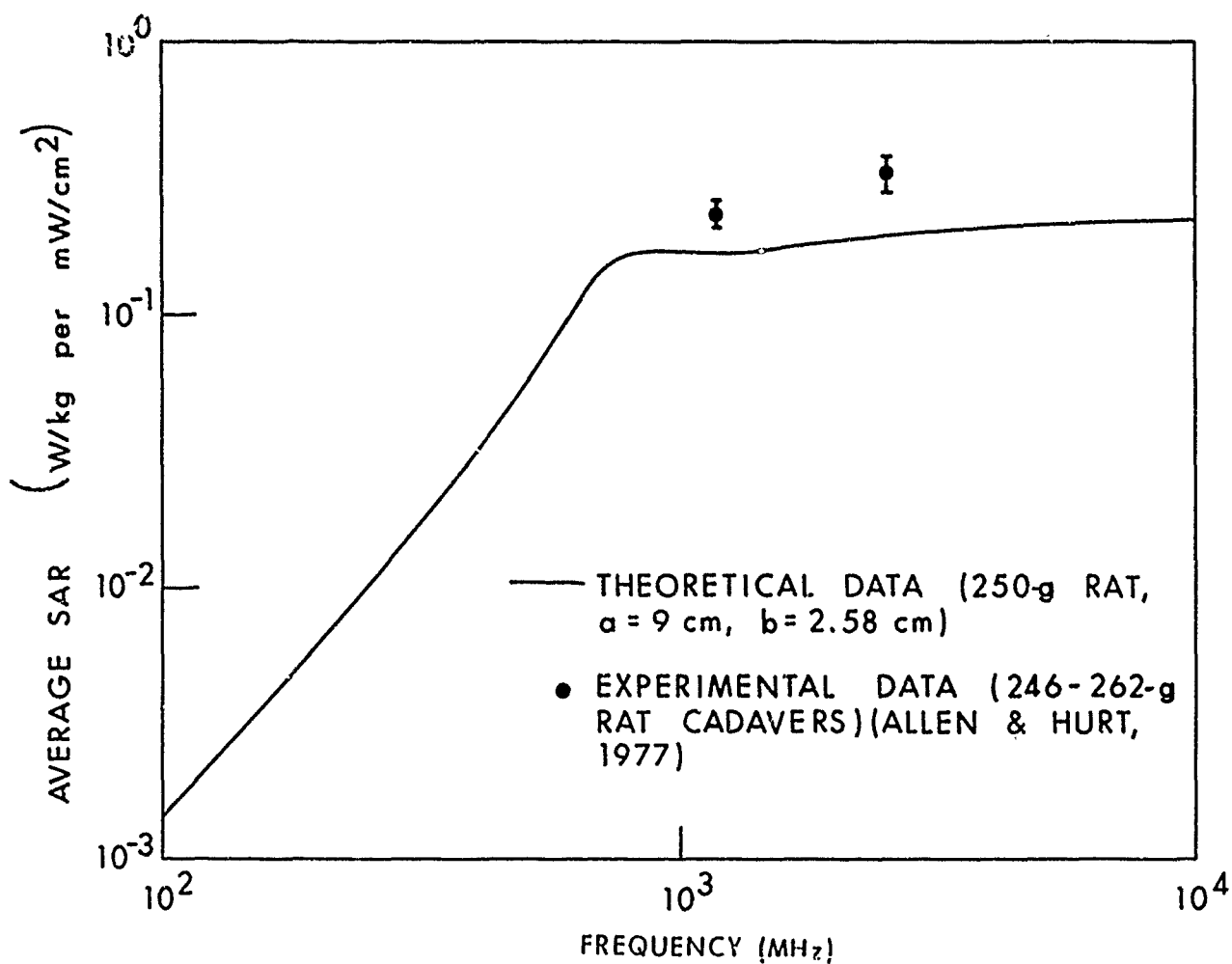
Figure 8.13. Calculated and measured values of the average
SAR for models of a rat, H polarization.
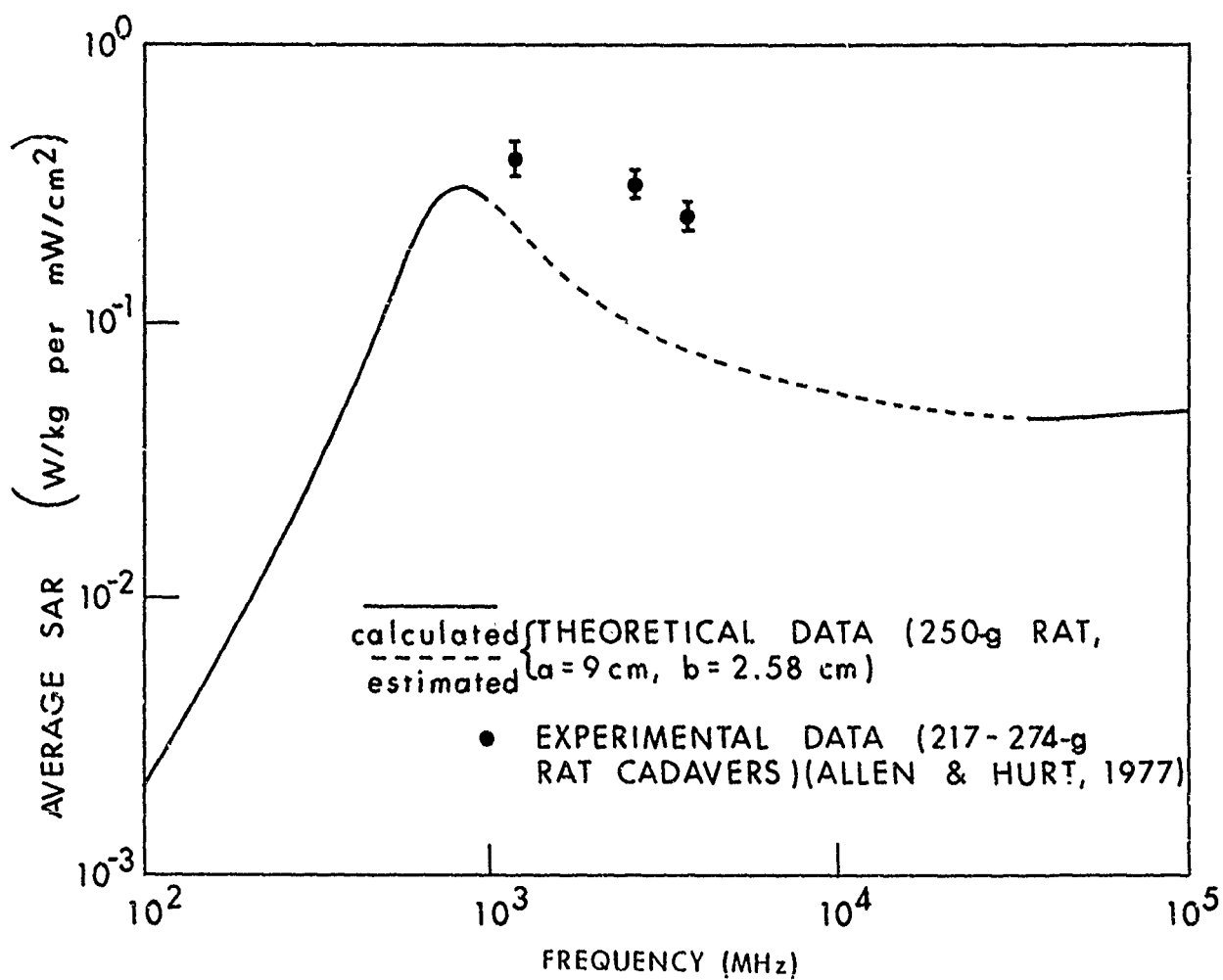
Figure 8.14.   Calculated and measured values of the average
SAR for models of a rat, K polarization.
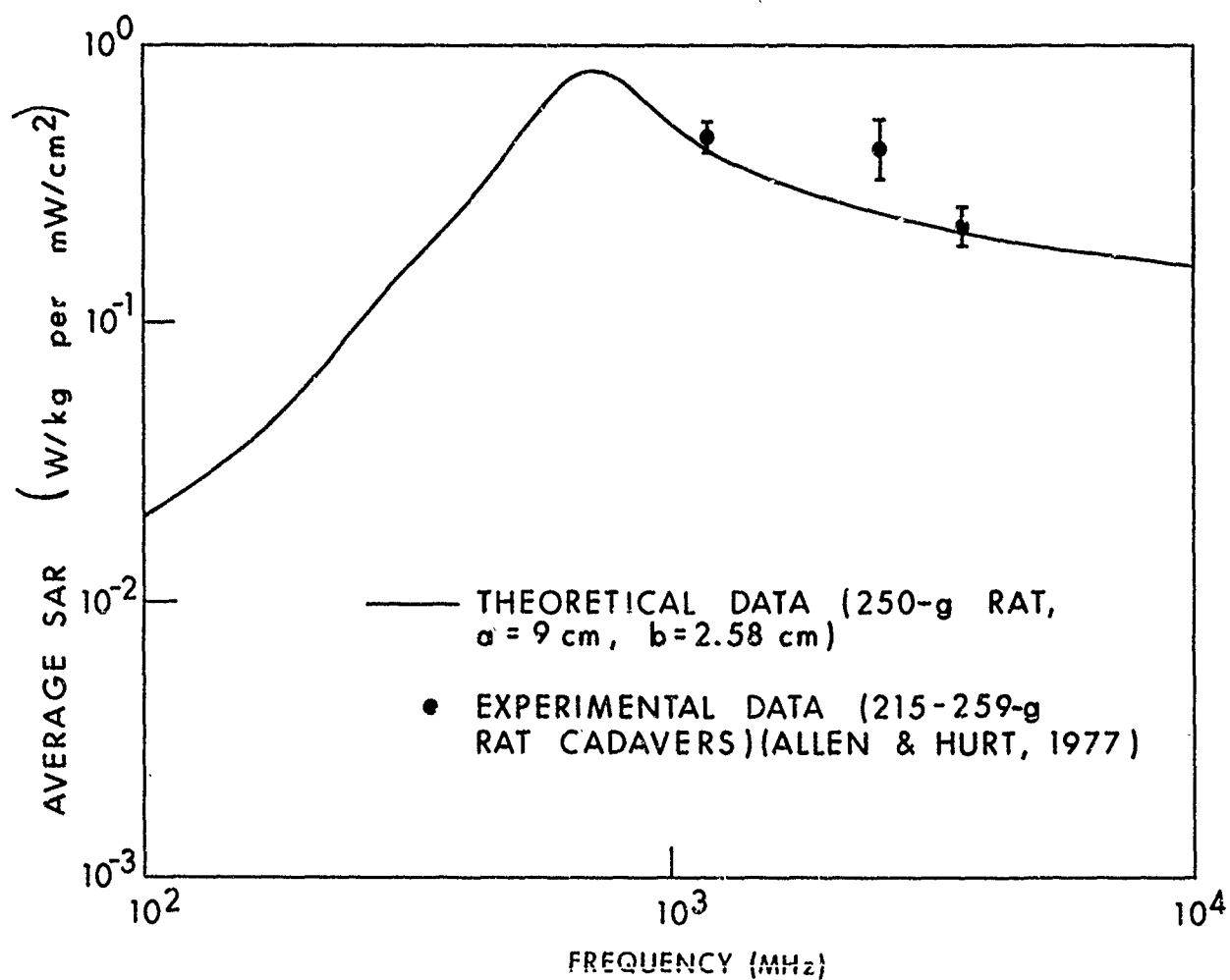
Figure 8.15. Calculated and measured values of the average
SAR for models of a rat, E polarization.
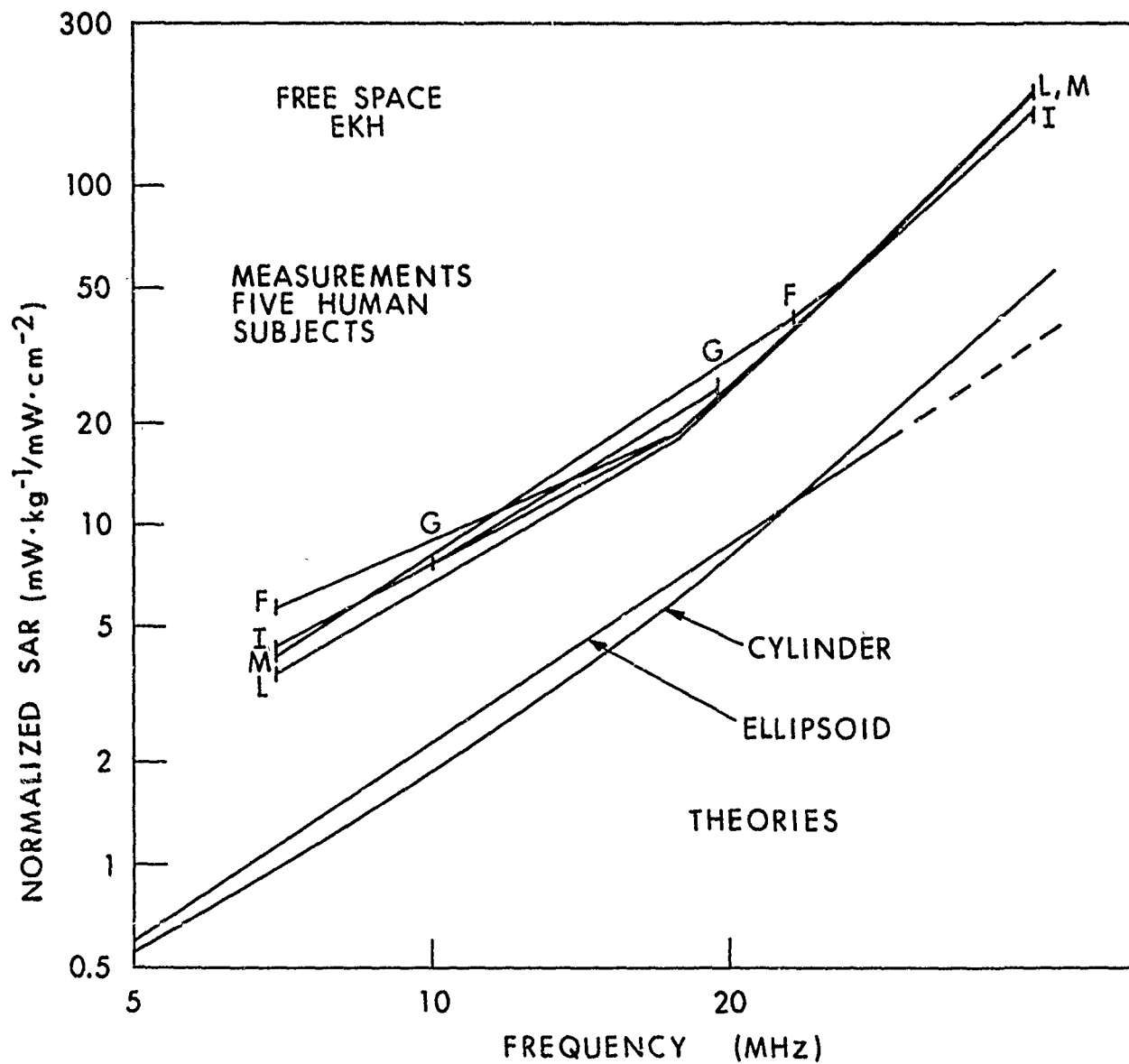
Figure 8.16. Comparison of free-space absorption rates of five human subjects with each other and with two standard theories (Hill, 1984).
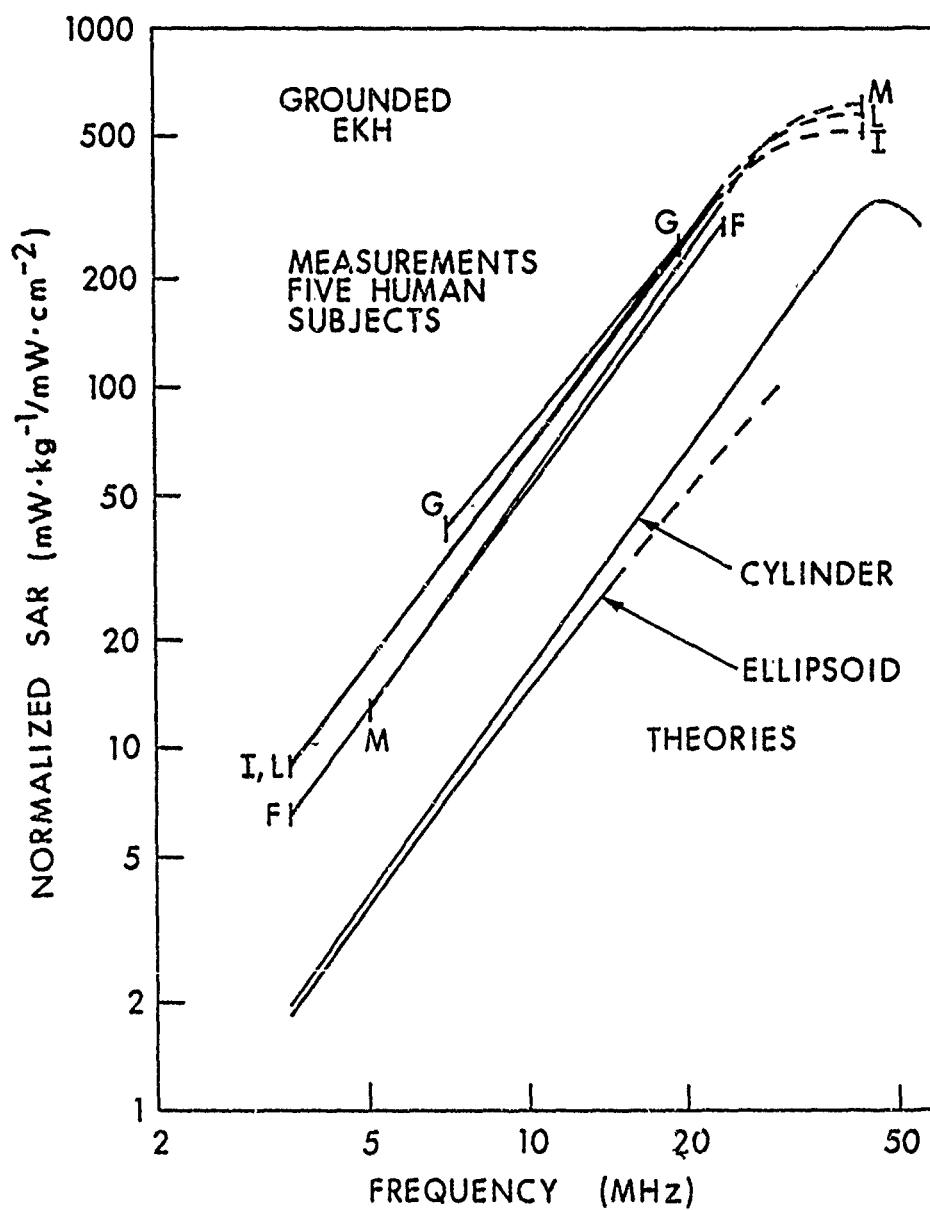
Figure 8.17. Comparison of the grounded absorption rates of five human subjects with each other and with two standard theories (Hill, 1984).
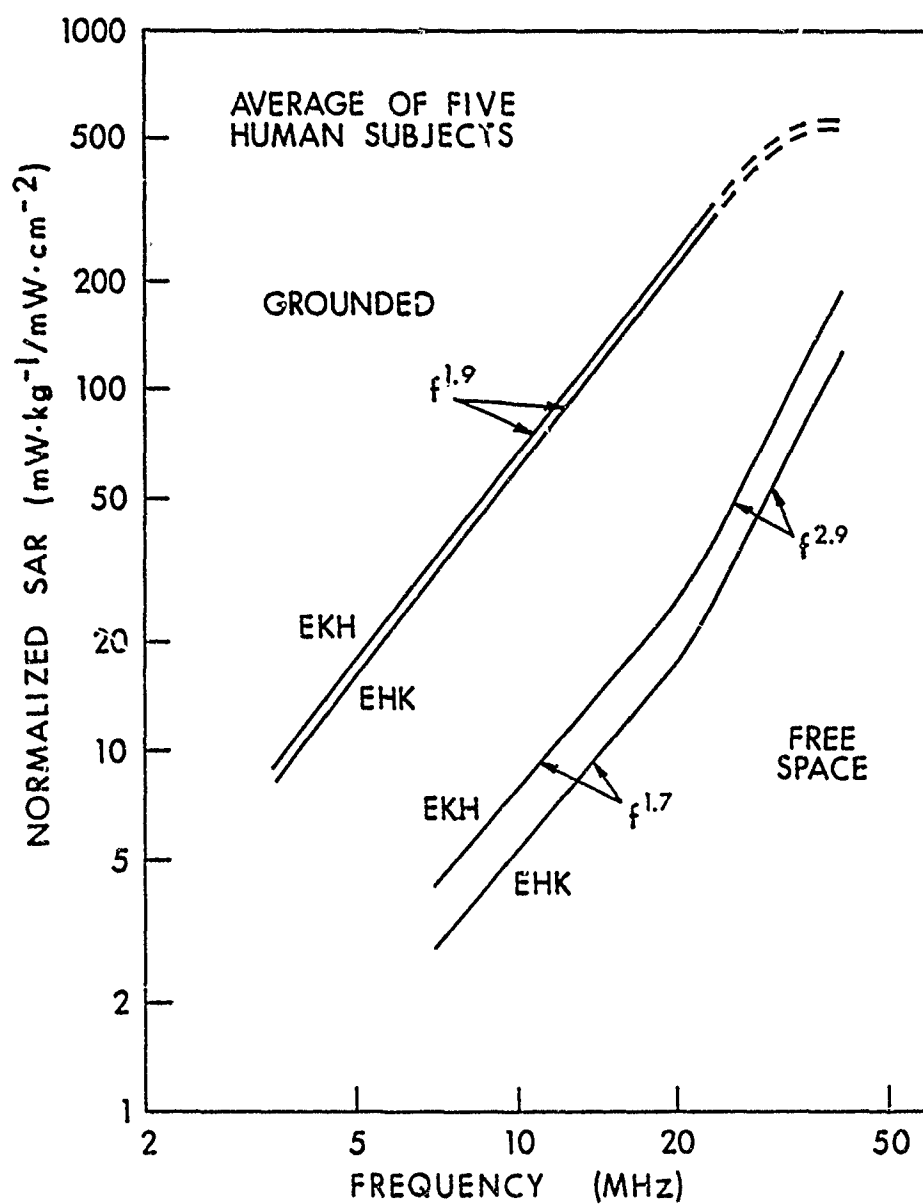
Figure 8.18. The frequency dependence of the average absorption rates for five human subjects in the EKH and EHK orientations under both free-space and grounded conditions (Hill, 1984).

- 8.21 -
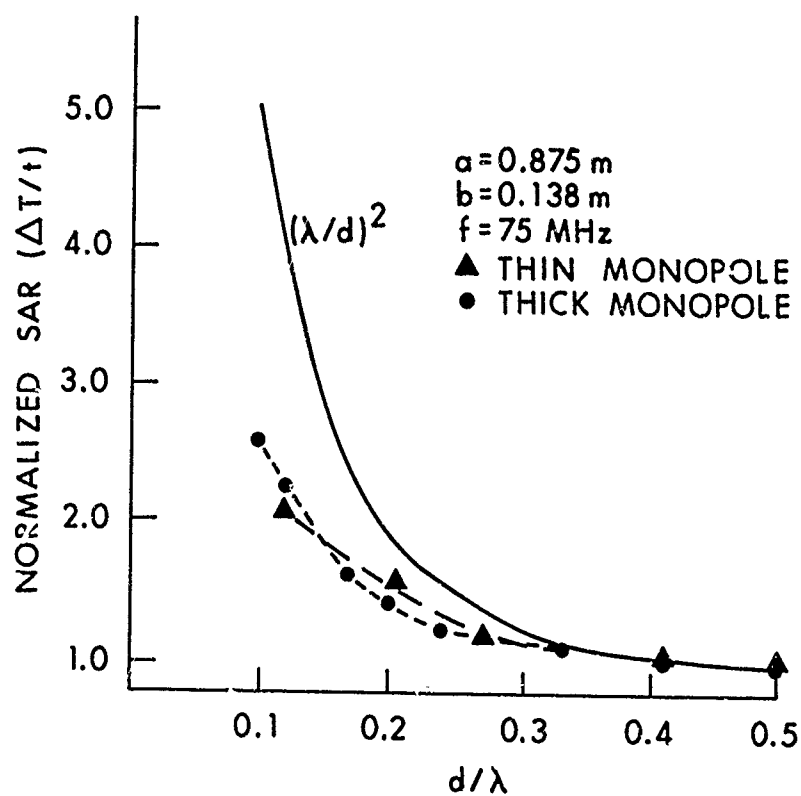
Figure 8.19. Measured relative SARs in scaled saline spheroidal models of man. To emphasize the differences in the absorption characteristics, the values are normalized with respect to their far-field value at $d/\lambda = 0.5$. ΔT is the temperature rise in the saline solution after exposure for time t (Iskander et al., 1981).
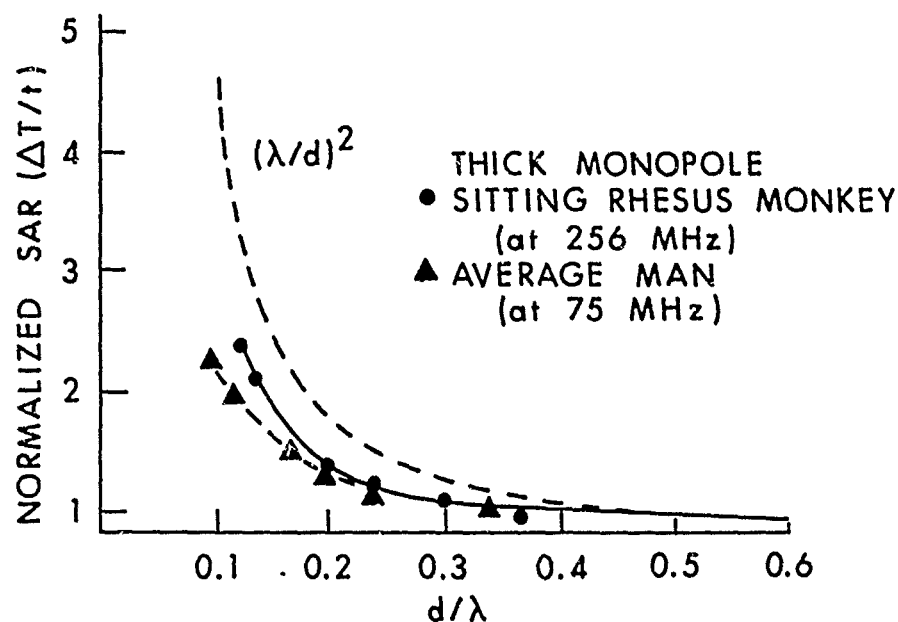
Figure 8.20. Measured relative SARs in scaled saline spheroidal models versus distance. SAR values for the different models are normalized with respect to their planewave value. ΔT is the temperature rise in the saline solution after exposure for time t (Iskander et al., 1981).
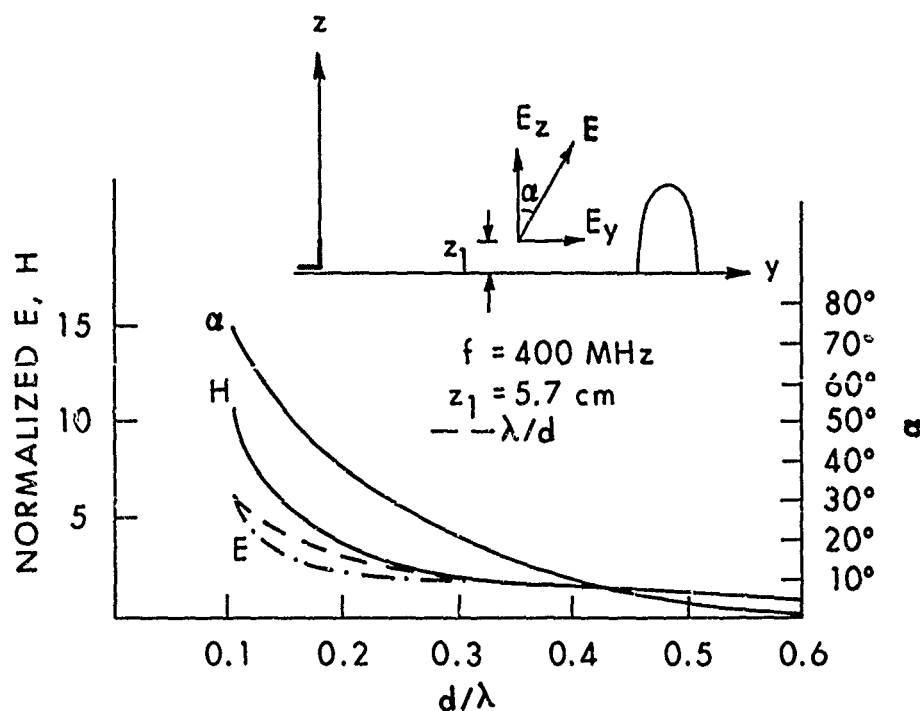
Figure 8.21. Measured relative fields versus distance for the thick monopole on a ground plane. The values of E and H are normalized with respect to their values at $d/\lambda = 0.6$ (Iskander et al., 1981).
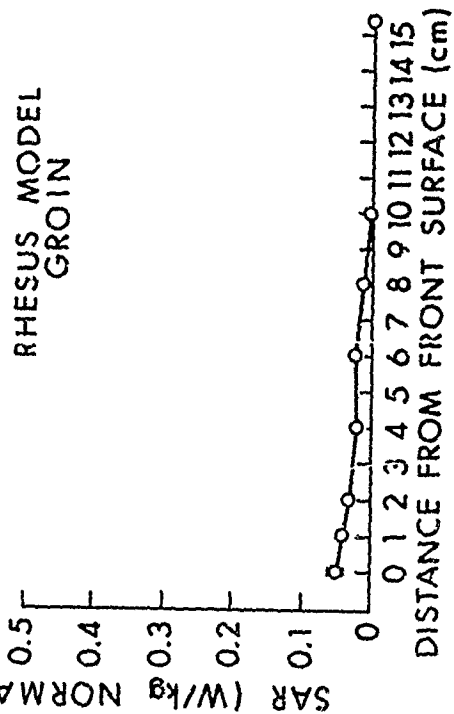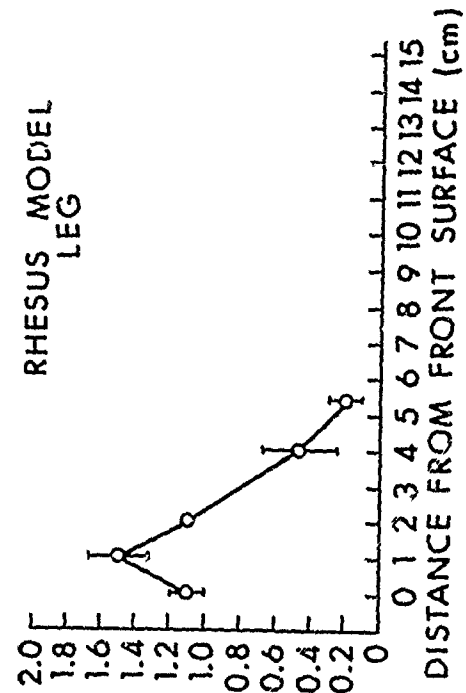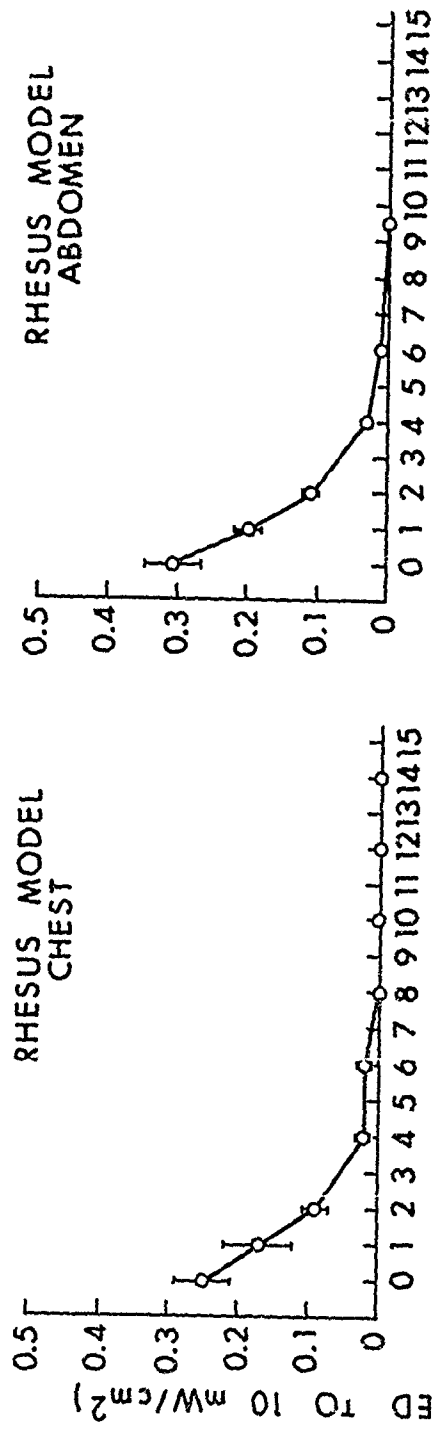
RHESUS MODEL
ABDOMEN

RHESUS MODEL
LEG

RHESUS MODEL
CHEST

RHESUS MODEL
GROIN

DISTANCE FROM FRONT SURFACE (cm)

SAR (W/kg NORMALIZED TO 10 mW/cm²)
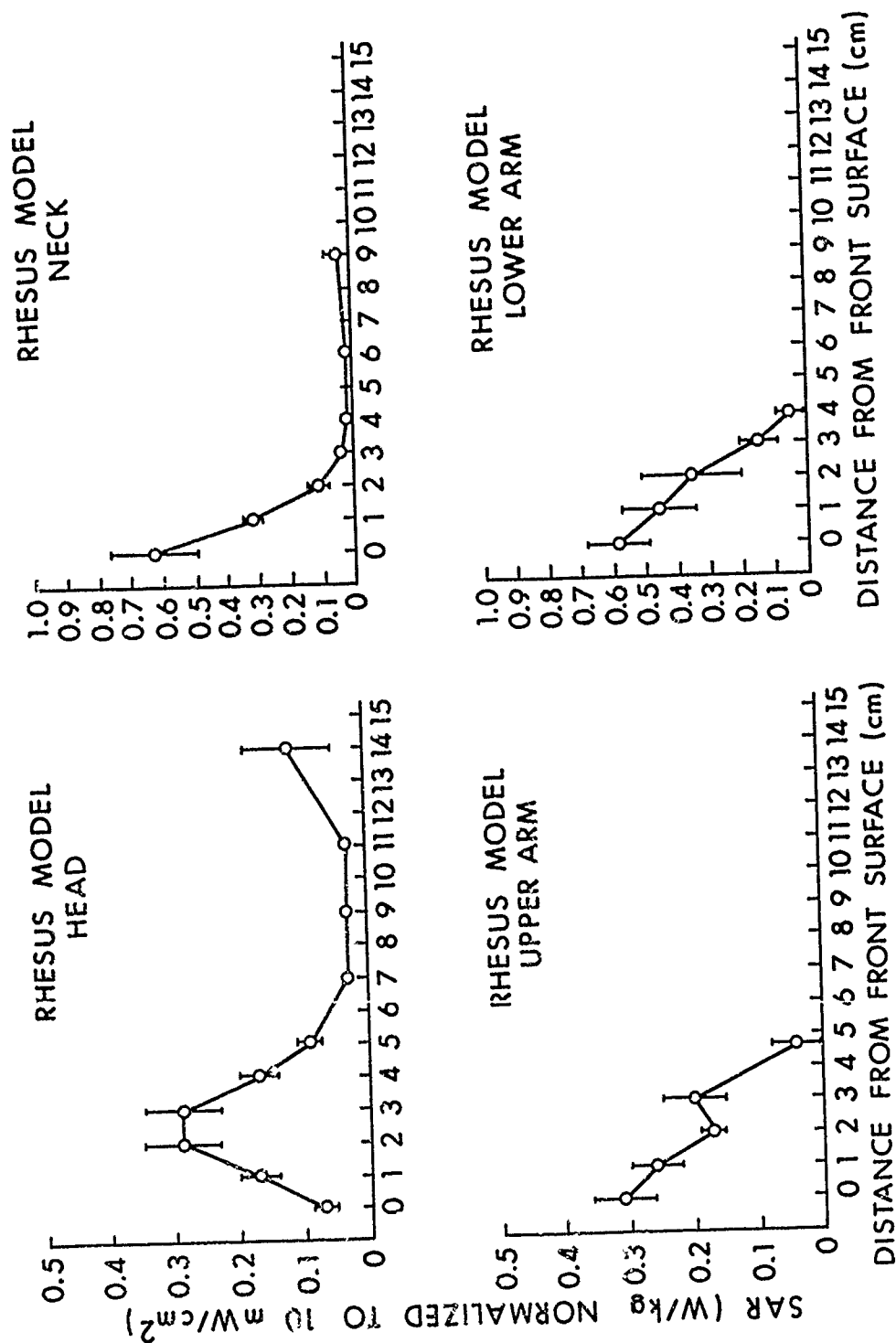
Figure 8.22. Microwave absorption profiles for rhesus monkey model. Irradiation frequency was 1.29 GHz. Vertical bars represent ± in the calculated value of the SAR (Olsen et al., 1980).
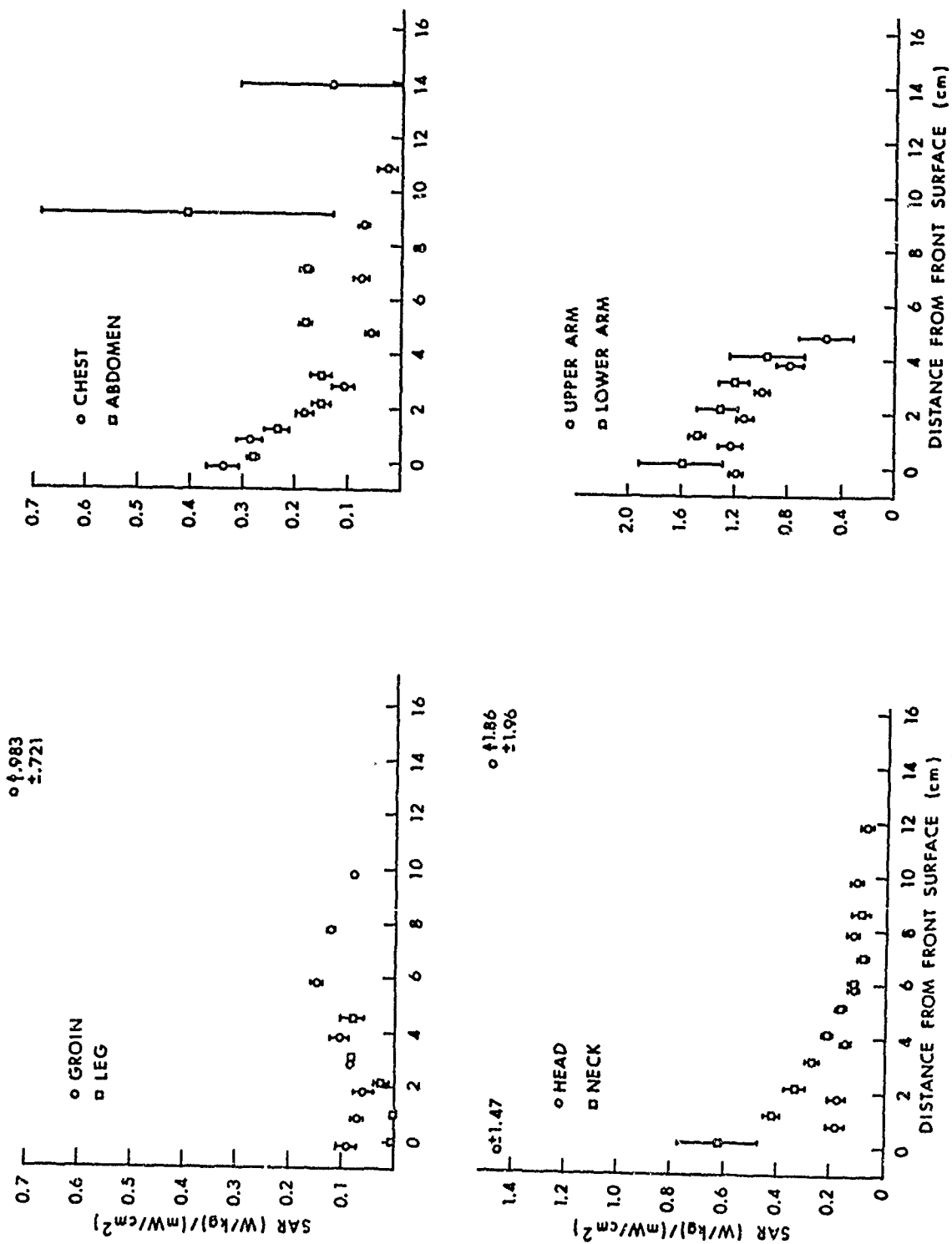
Figure 8.23. Profiles of electromagnetic absorption in the sitting rhesus model at 225 MHz. Vertical bars represent ±1 SD (N = 3) in calculated mean SAR (Olsen and Griner, 1982).
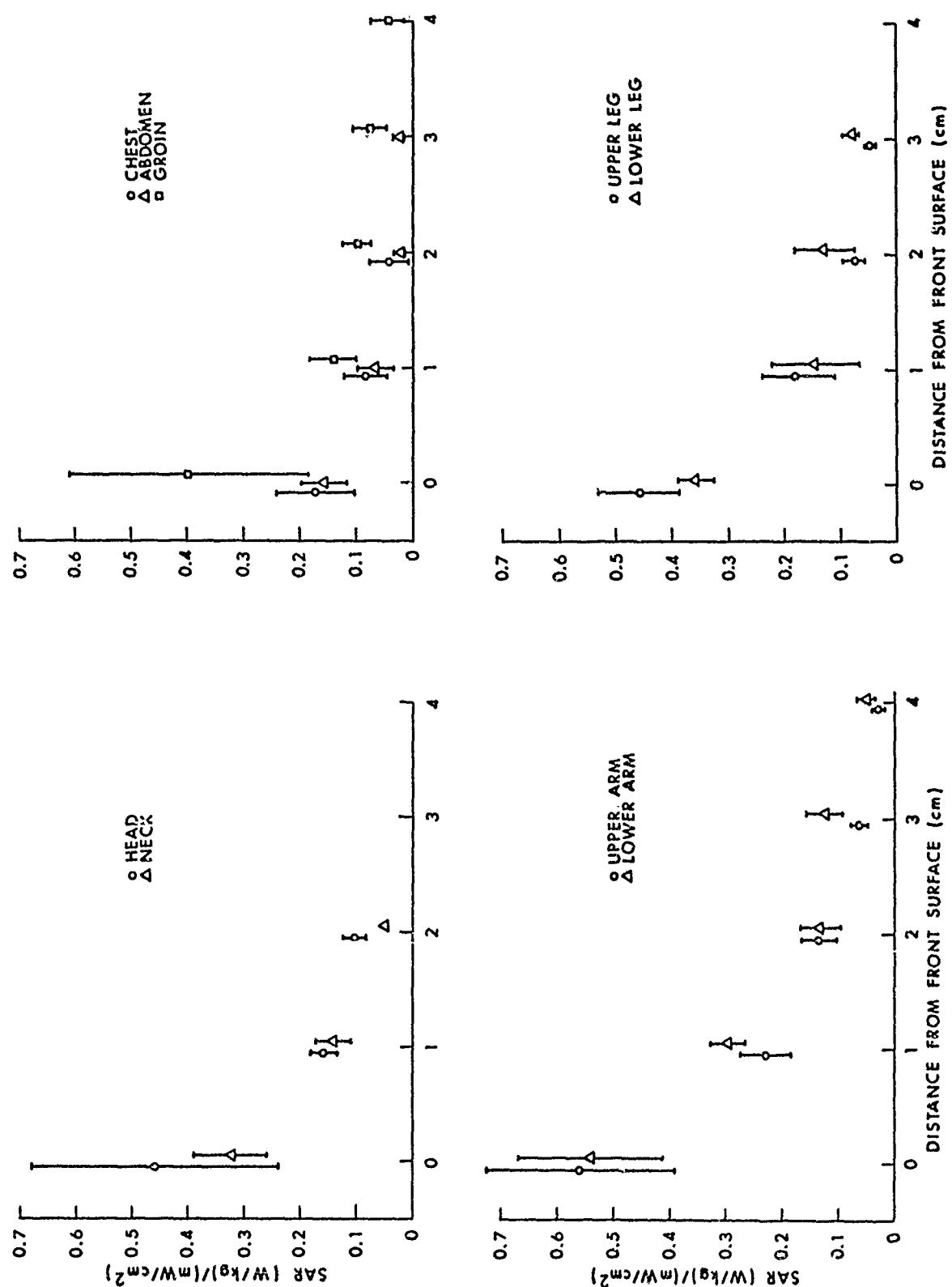
Figure 8.24. Normalized microwave absorption profiles in man-size model at 2.0 GHz. Vertical bars represent: ±1 SD of the mean SAR. Minimum N, 3; average N, 5 (Olsen, 1982).
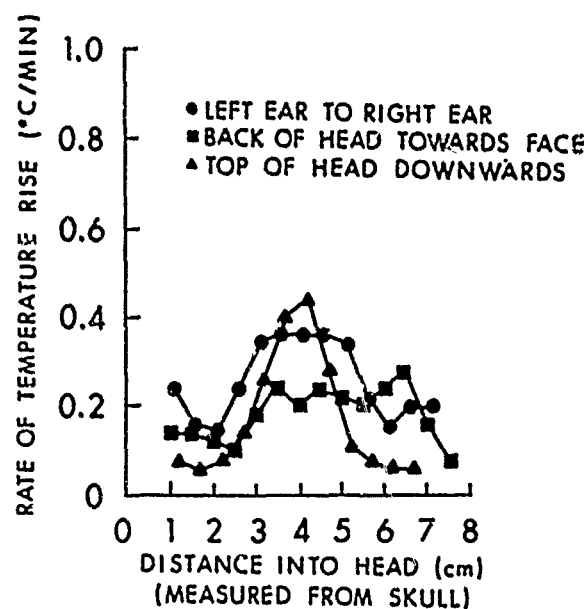
Figure 8.25. Rate of temperature rise from RFR exposure in the face of a detached M. mulatta head; 1.2 GHz, CW, 70 mW/cm^2, far field (Burr and Krupp, 1980).
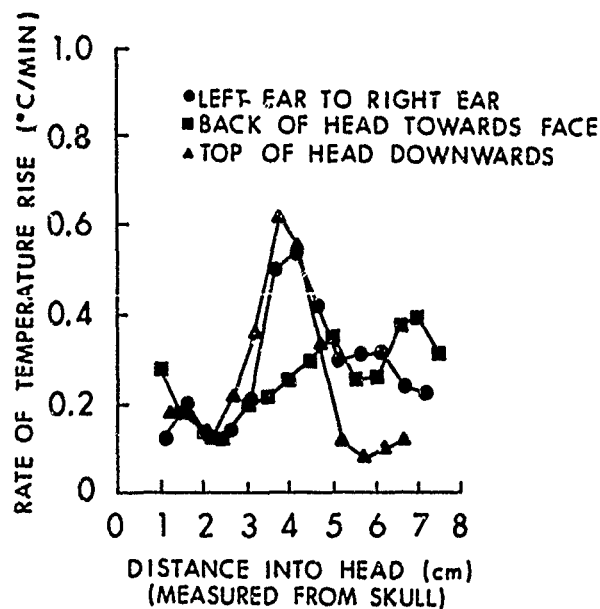
Figure 8.26. Rate of temperature rise from RFR exposure at the right side of a detached M. mulatta head; 1.2 GHz, CW, 70 mW/cm^2, far field (Burr and Krupp, 1980).
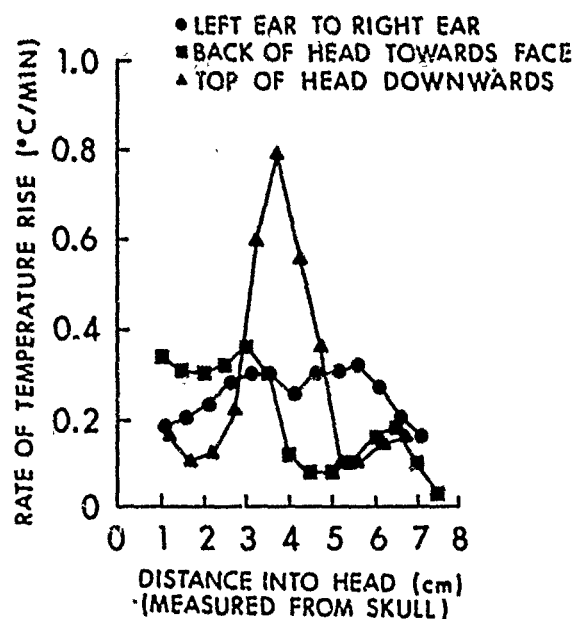
Figure 8.27. Rate of temperature rise from RFR exposure at the back of a detached M. mulatta head; 1.2 GHz, CW, 70 mW/cm^2, far field (Burr and Krupp, 1980).
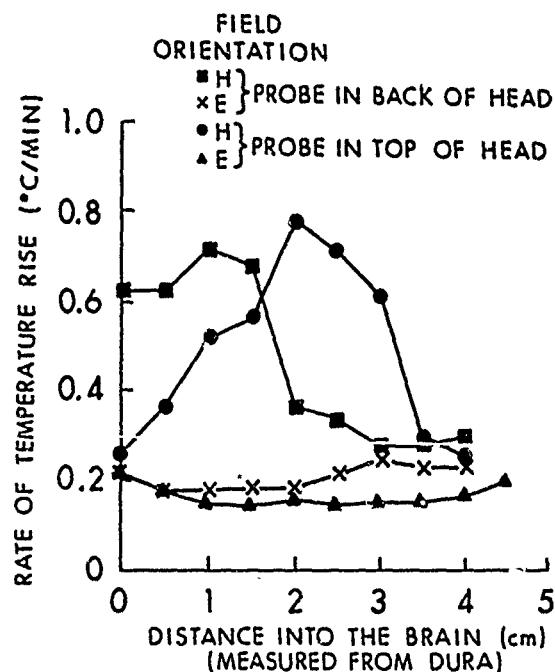
Figure 8.28. Rate of temperature rise from RFR exposure to the back of an M. mulatta cadaver head (with body attached); 1.2 GHz, CW, 70 mW/cm^2, far field. Temperature rise shown for animal's body oriented parallel with the E- and H-fields (Burr and Krupp, 1980).
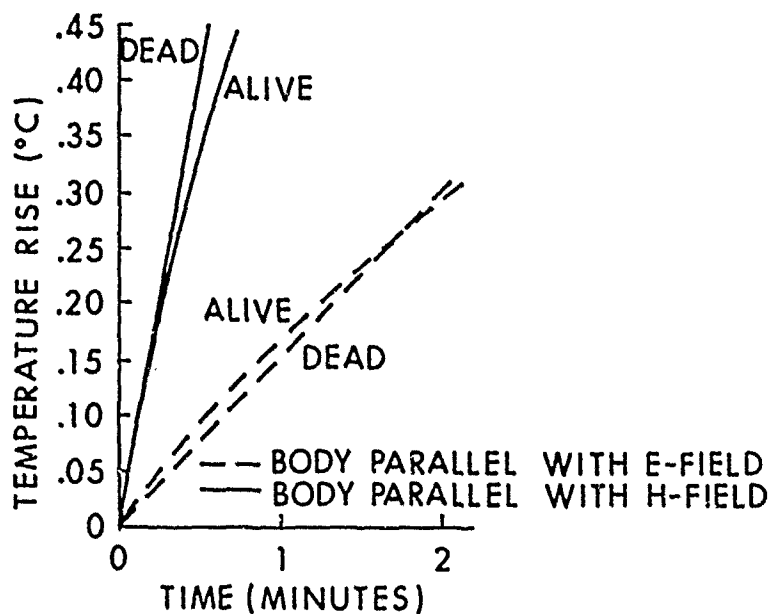
Figure 8.29. Temperature rise (at 2.0 cm into the top of the head) of an M. mulatta exposed to 70 mW/cm², 1.2 GHz, CW, RFR, in the far field (Burr and Krupp, 1980).
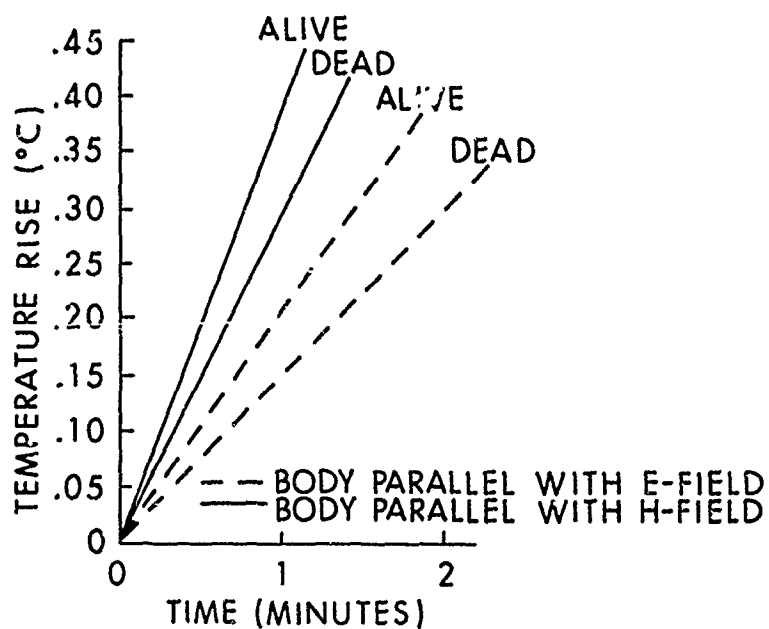
Figure 8.30. Temperature rise (at 3.5 cm into the top of the head) of an M. mulatta exposed to 70 mW/cm², 1.2 GHz, CW, RFR, in the far field (Burr and Krupp, 1980).
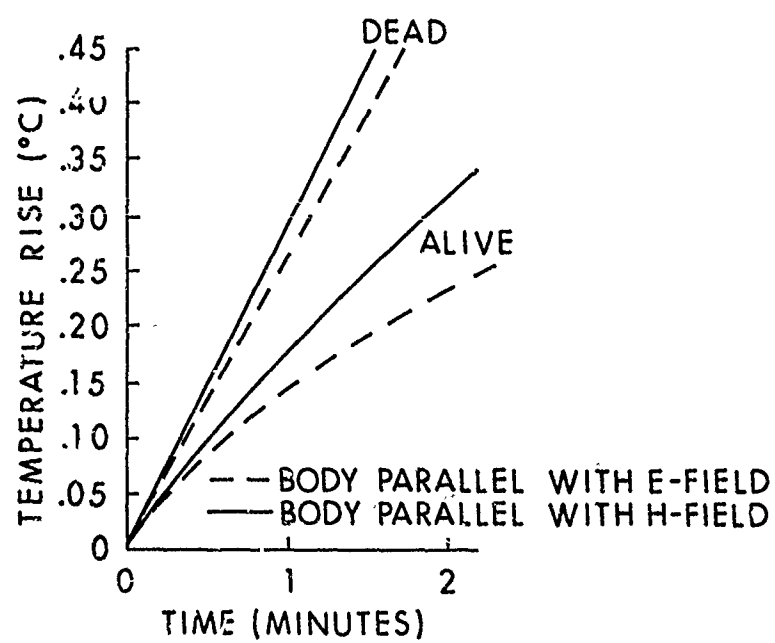
Figure 8.31. Temperature rise (at 3.5 cm into the back of the nead) of an M. mulatta exposed to 70 mW/cm^2, 1.2 GHz, CW, RFR, in the far field (Burr and Krupp, 1980).

SPHERE   R=25.6cm $E^2=1V^2/m^2$ sf=5.95   f=24.1MHz
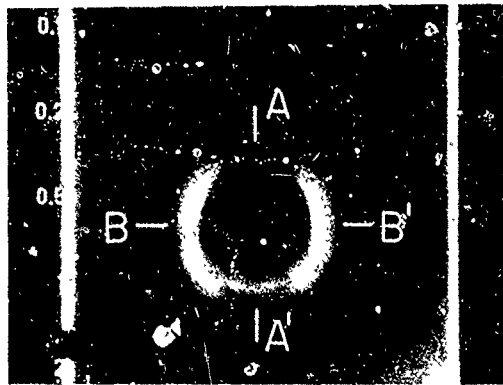
INTENSITY SCAN
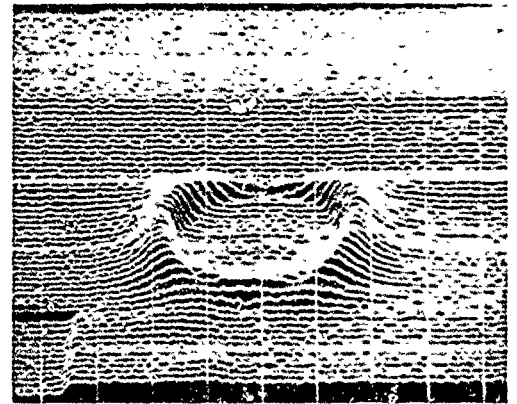
PROFILE SCAN
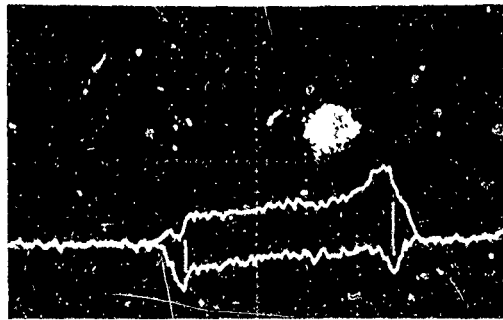
A-A' SCAN
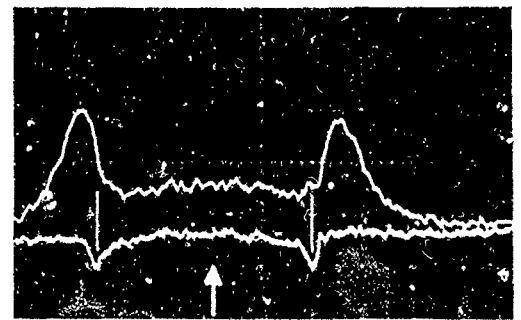
B-B' SCAN

MEASURED W=26.4nW/kg   THEORETICAL W=25.1nW/kg

Figure 8.32.   Thermographic results of exposing a 4.3-cm-radius sphere
to 144-MHz TM_{110} electric field in a rectangular reso-
nant cavity simulating a 25.6-cm-radius sphere exposed
to 24.1 MHz: vertical divergence = 2°C, horizontal
divergence = 2 cm (Guy et al., 1976b) (© 1976 IEEE).

- 8.32 -

SPHERE   R=25.6cm $H^2 = 1 A^2/m^2$ sf = 5.95   f = 24.1 MHz
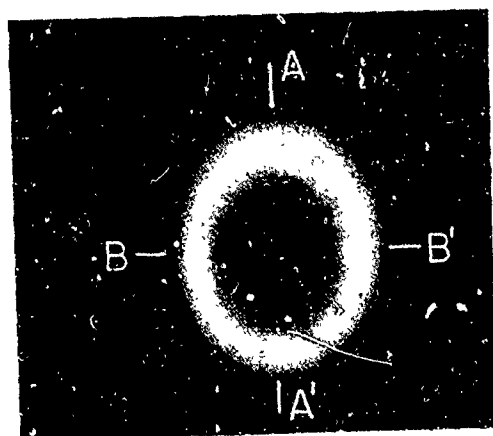
INTENSITY SCAN
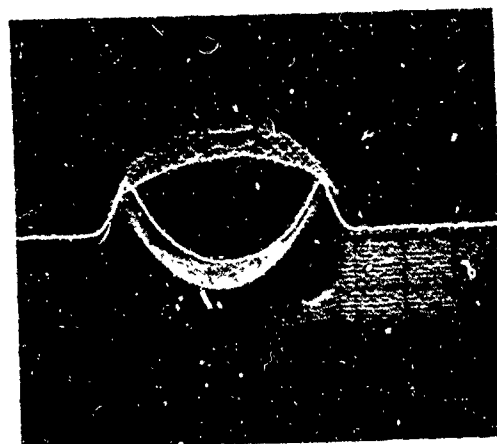
PROFILE SCAN
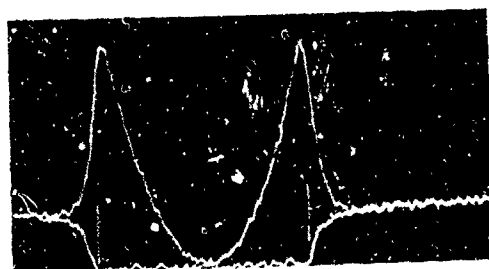
A'-A SCAN
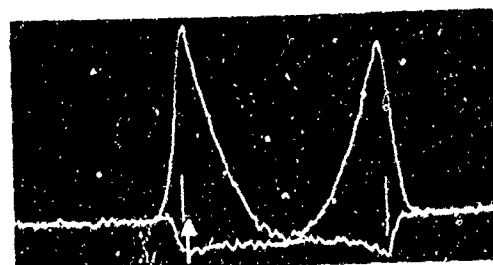
B-B' SCAN

MEASURED W=0.366 W/kg   THEORETICAL W=0.359 W/kg

Figure 8.33.   Thermographic results of exposing a 4.3-cm-radius sphere to 144-MHz TE_{102} magnetic field in a rectangular resonant cavity simulating a 25.6-cm-radius sphere exposed to 24.1 MHz: vertical divergence = 2°C, horizontal divergence = 2 cm (Guy et al., 1976b) (© 1976 IEEE).

ELLIPSE   a=74.8cm a/b=5.0 $E^2=1V^2/m^2$ sf=5.95   f=24.1MHz
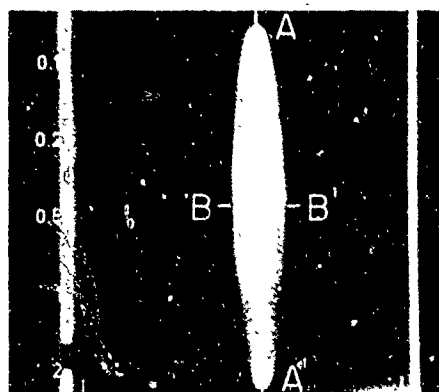
INTENSITY SCAN
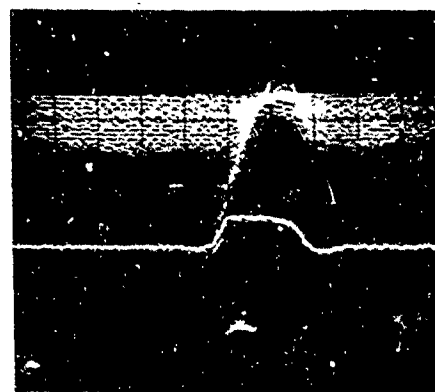
PROFILE SCAN
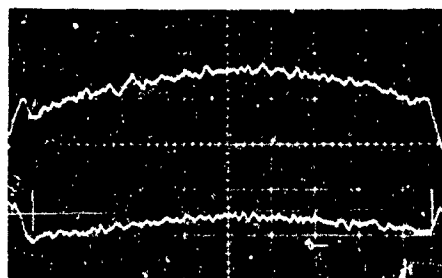
A'-A SCAN
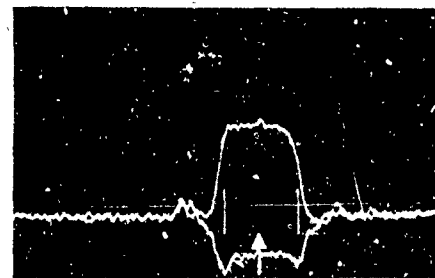
B-B' SCAN

MEASURED W=1.15μW/kg   THEORETICAL W=0.99μW/kg

Figure 8.34. Scale-model thermograms and calculated peak SAR for 70-kg, 5/1 prolate spheroid (a = 74.8 cm) exposed to 24.1-MHz electric field parallel to the major axis: vertical divergence = 2°C, horizontal divergence = 2.65 cm (Guy et al., 1976b) (© 1976 IEEE).

ELLIPSE   a=74.8cm a/b=5.0   H²=I A²/m²   sf=5.95   f=24.IMHz
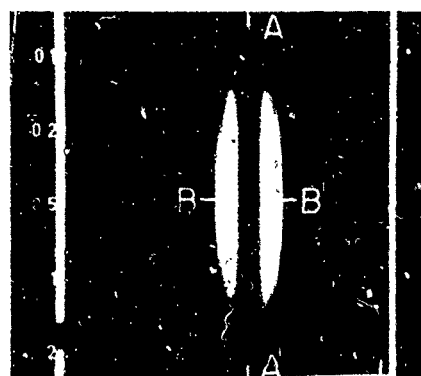
INTENSITY SCAN
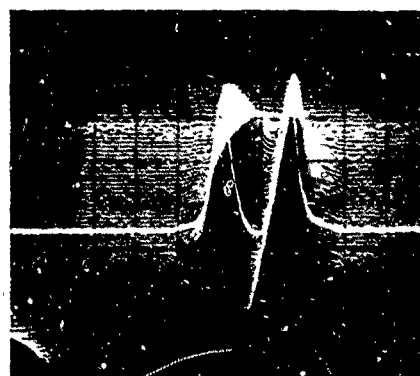
PROFILE SCAN
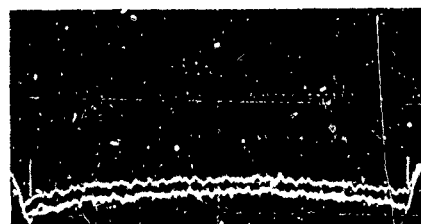
A'-A SCAN
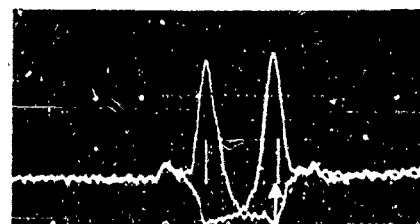
B-B' SCAN

MEASURED W=0.502 W/kg   THEORETICAL W=0.427 W/kg

Figure 8.35. Scale-model thermograms and calculated peak SAR for 70-kg, 5/1 prolate spheroid (a = 74.8 cm) exposed to 24.1-MHz magnetic field perpendicular to the major axis: vertical divergence = 2°C, horizontal divergence = 2.65 cm (Guy et al., 1976b) (© 1976 IEEE).

MAN   FRONT   h=1.74m $E^2=1V^2/m^2$ sf=4.62   f=31.0MHz

A B
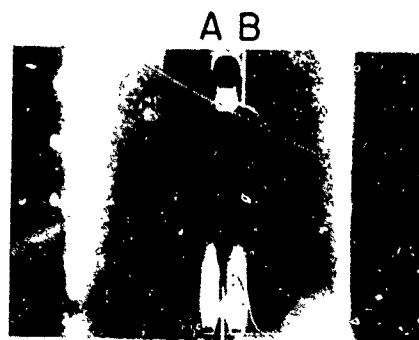
A' B'

INTENSITY SCAN
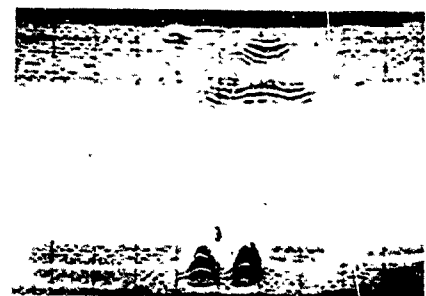
PROFILE SCAN

A'-A
W=25.2μW/kg
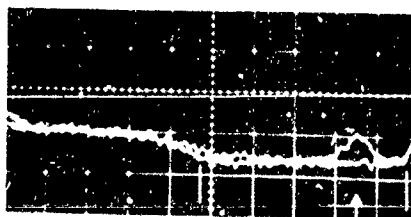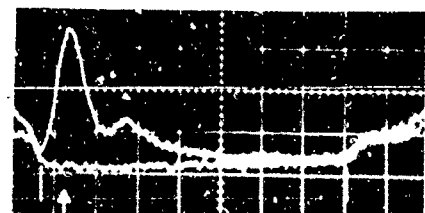
B'-B
W=134μW/kg

Figure 8.36.   Scale-model thermograms and measured peak SAR for
70-kg, 1.74-m-height frontal-plane man model ex-
posed to 31.0-MHz electric field parallel to the
long axis: vertical divergence = 2°C, horizontal
divergence = 4 cm (Guy et al., 1976b) (© 1976 IEEE).

MAN   FRONT   h=1.74m E^2=1V^2/m^2 sf=4.62   f=31.0MHz
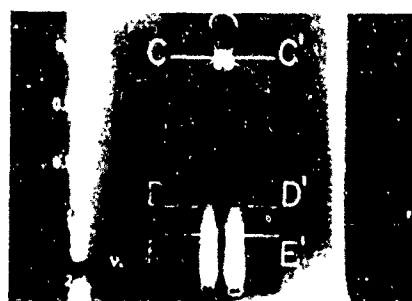
INTENSITY SCAN

C-C'
W=29.6μW/kg

D-D'
W=25.7μW/kg

E-E'
W=54.1μW/kg
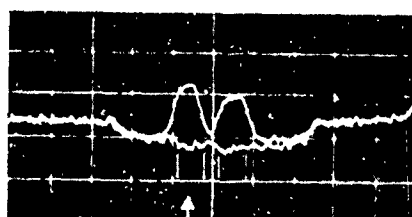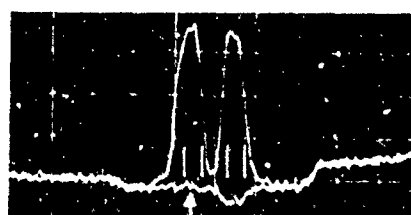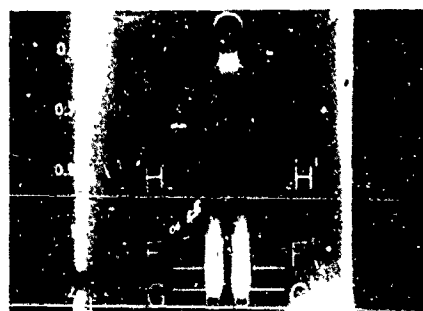
INTENSITY SCAN

F-F'
W=50.2 μW/kg

G-G'
W=149μW/kg
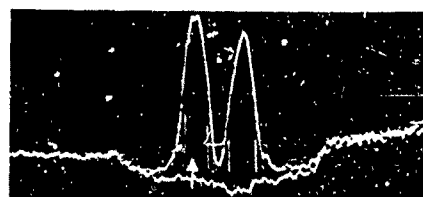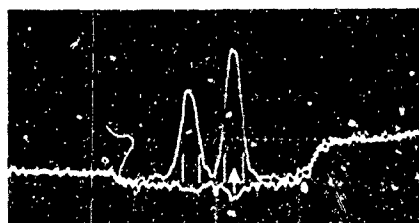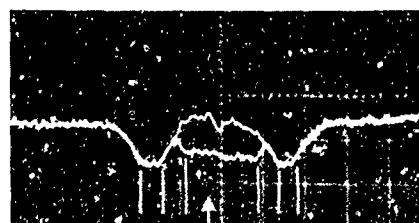
H-H'
W=11.7μW/kg

Figure 8.36.   (Continued)

- 8.37 -

MAN   FRONT   h=1.74m $H^2 = 1A^2/m^2$ sf=4.62   f=31.0 MHz

INTENSITY SCAN

PROFILE SCAN

A'-A
W=1.88 W/kg

B'-B
W=2.52 W/kg
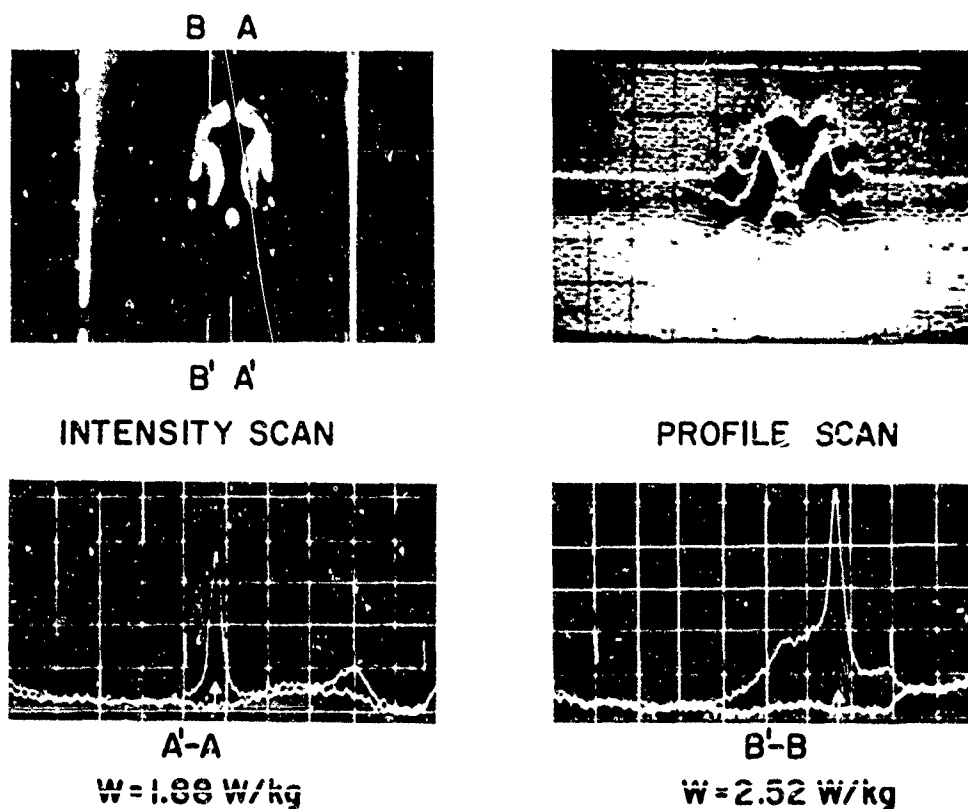
Figure 8.37. Scale-model thermograms and measured peak SAR for 70-kg, 1.74-m-height frontal-plane man model exposed to 31.0-MHz magnetic field perpendicular to the major axis: vertical divergence = 2°C, horizontal divergence = 4 cm (Guy et al., 1976b) (© 1976 IEEE).

MAN   FRONT   h=1.74m $H^2 = 1A^2/m^2$ sf=4.62   f=31.0MHz

C

C'

INTENSITY SCAN

C'-C
W=1.32 W/kg
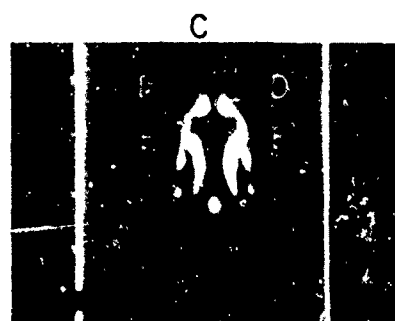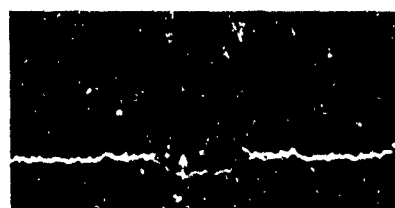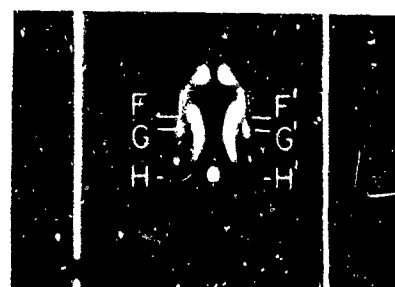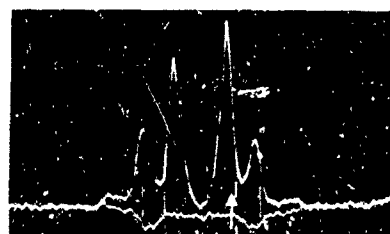
D-D'
W=1.13 W/kg

E-E'
W=0.54 W/kg

E"-E'"
W=0.55W/kg

INTENSITY SCAN

F-F'
W=2.22 W/kg
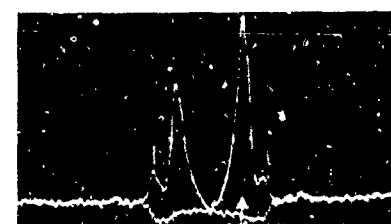
G-G'
W=1.51 W/kg
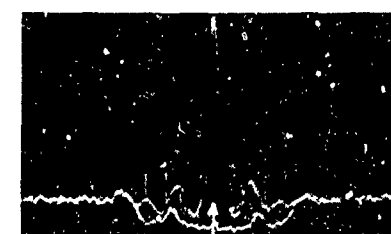
H-H'
W=1.56 W/kg

Figure 8.37. (Continued)

MAN   SIDE   h=1.74 m $H^2 = 1 A^2/m^2$ sf=4.62   f=31.0MHz
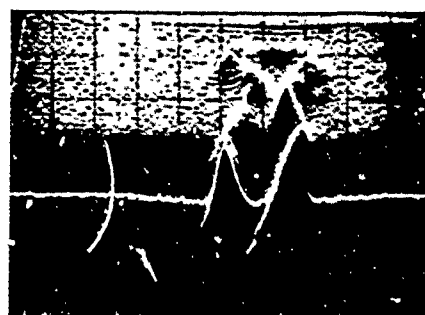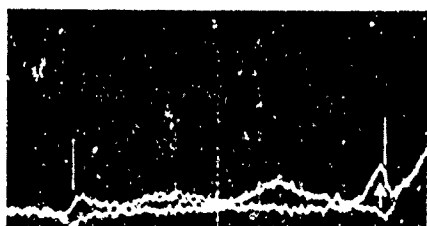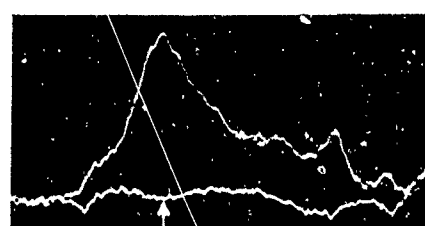
Figure 8.38. Scale-model thermograms and measured peak SAR for 70-kg, 1.74-m-height medial-plane man model exposed to 31.0-MHz magnetic field perpendicular to the median plane: vertical divergence = 2°C, horizontal divergence = 2.65 cm (Guy et al., 1976b) (© 1976 IEEE).

MAN   SIDE   h=1.74 m $H^2 = 1A^2/m^2$ sf=4.62   f=31.0MHz
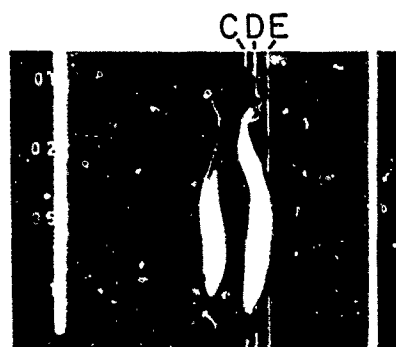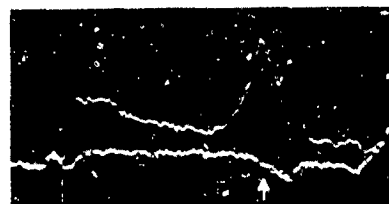
INTENSITY SCAN

C–C'
W=0.485 W/kg
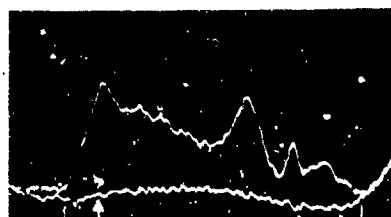
D'–D
W=0.442 W/kg
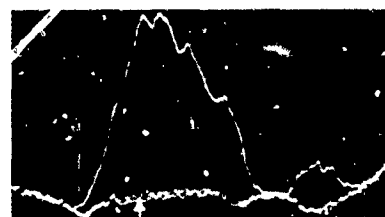
E'–E
W=0.724 W/kg
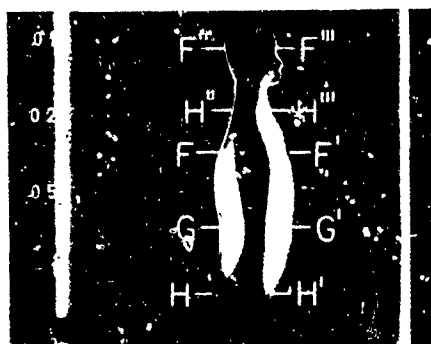
INTENSITY SCAN
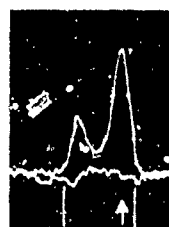
F·–F'
W=0.497 W/kg
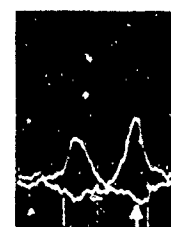
F"–F"'
W=0.166 W/kg
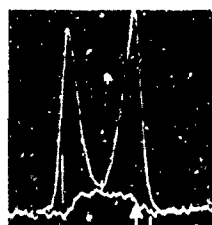
G–G'
W=0.702 W/kg
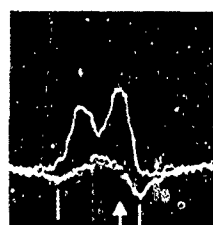
H–H'
W=0.223 W/kg
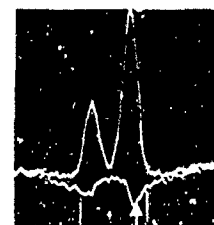
H"–H"'
W=0.422 W/kg

Figure 8.38.   (Continued)

MAN SIDE h=1.74 m $E^2 = 1V^2/m^2$ sf=4.62 f=31.0MHz
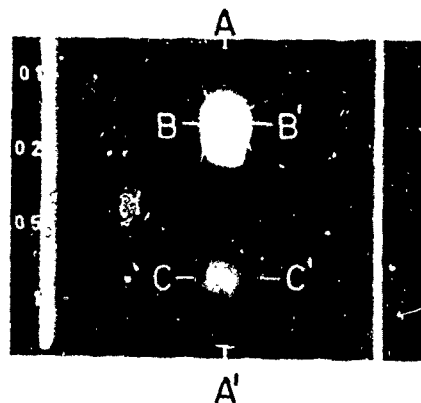
PROFILE SCAN

INTENSITY SCAN

A'-A
W=24.1 μW/kg

B-B'
W=21.5 μW/kg
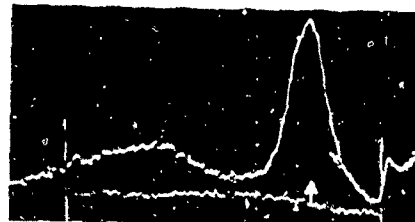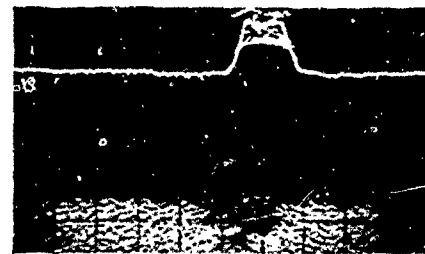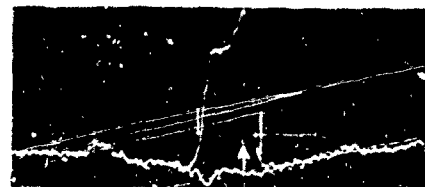
C-C'
W=8.2 μW/kg

Figure 8.39. Scale-model thermograms and measured peak SAR for 70-kg, 1.74-m-height medial-plane man model exposed to 31.0-MHz electric field parallel to the major axis: vertical divergence = 2°C, horizontal divergence = 2.65 cm (Guy et al., 1976b) (© 1976 IEEE).
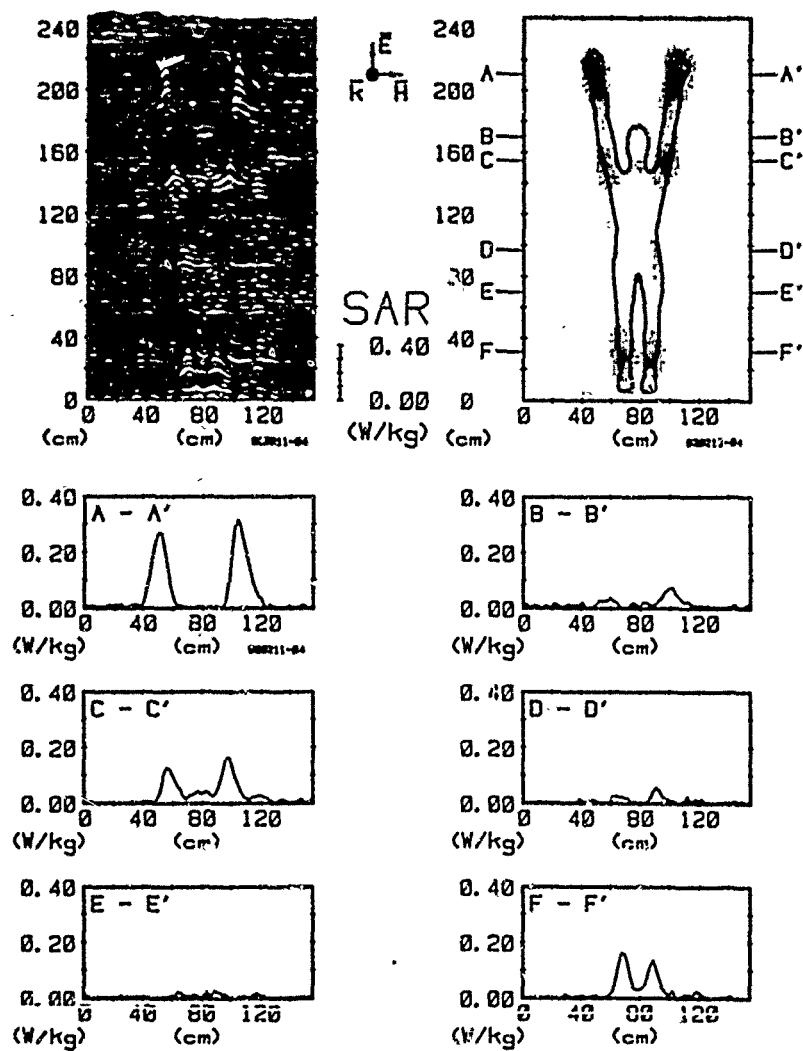
Figure 8.40. Computer-processed whole-body thermograms expressing SAR patterns for man with arms up, exposed to 1-mW/cm^2 450-MHz radiation with EHK polarization (Guy et al., 1984) (© 1984 IEEE).
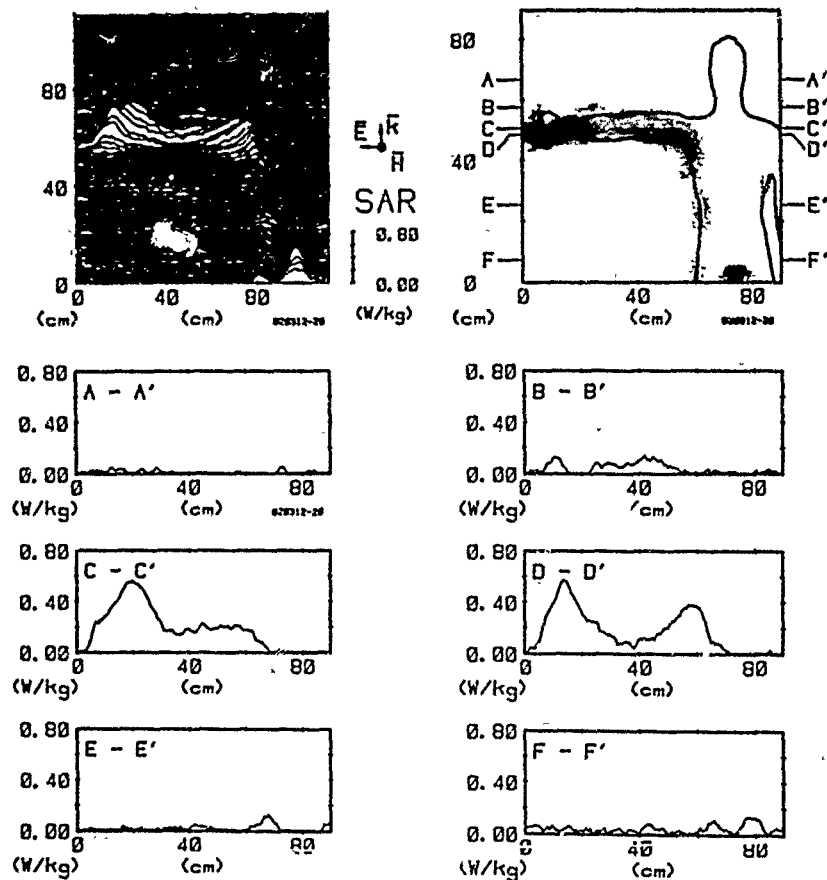
Figure 8.41. Computer-processed whole-body thermograms expressing SAR patterns for man with one arm extended, exposed to 1-mW/cm^2 450-MHz radiation with KEH polarization (Guy et al., 1984) (© 1984 IEEE).
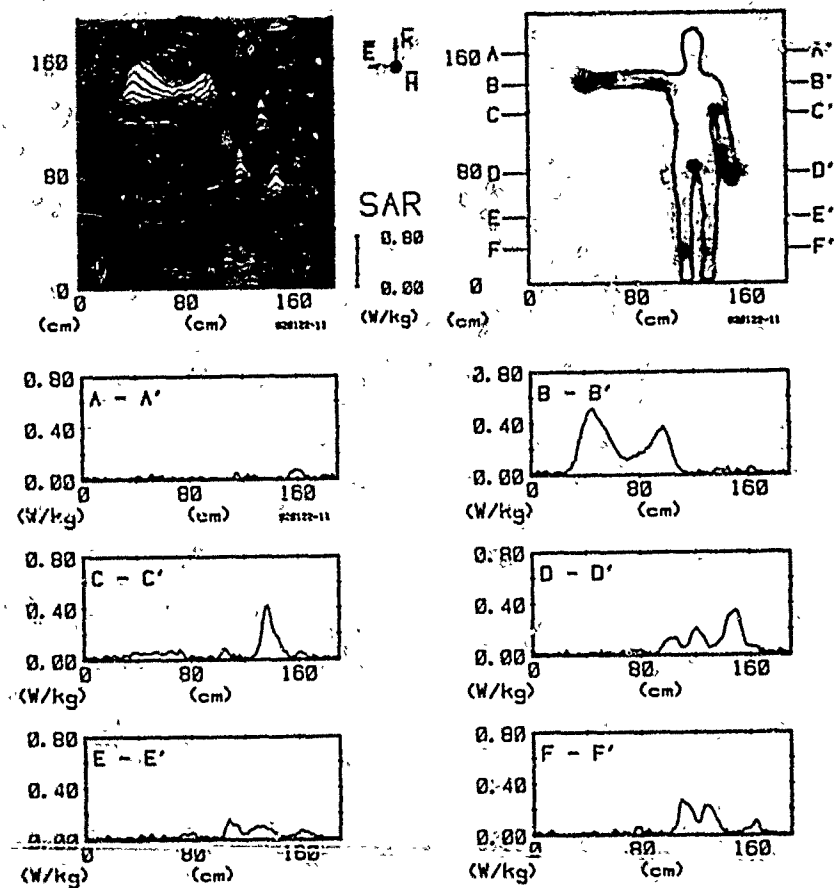
Figure 8.42. Computer-processed upper-body thermograms expressing SAR patterns
for man with one arm extended, exposed to 1-mW/cm^2 450-MHz radi-
ation with KEH polarization (Guy et al., 1984) (© 1984 IEEE).
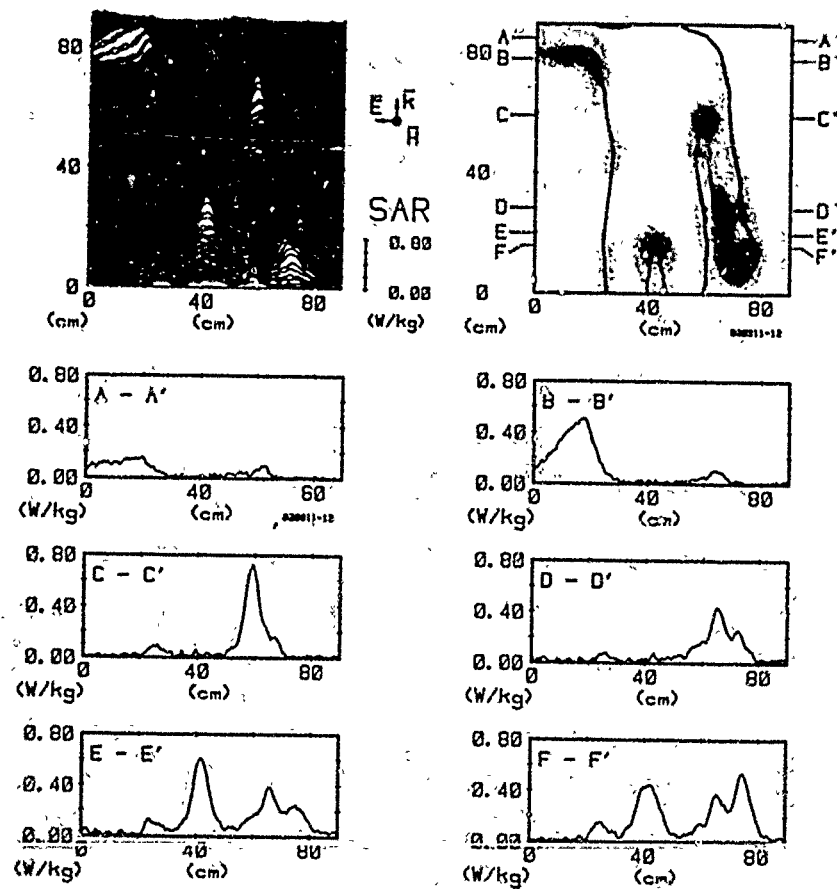
Figure 8.43. Computer-processed midbody thermograms expressing SAR patterns for man with one arm extended, exposed to 1-mW/cm^2 450-MHz radiation with KEH polarization (Guy et al., 1984) (© 1984 IEEE).
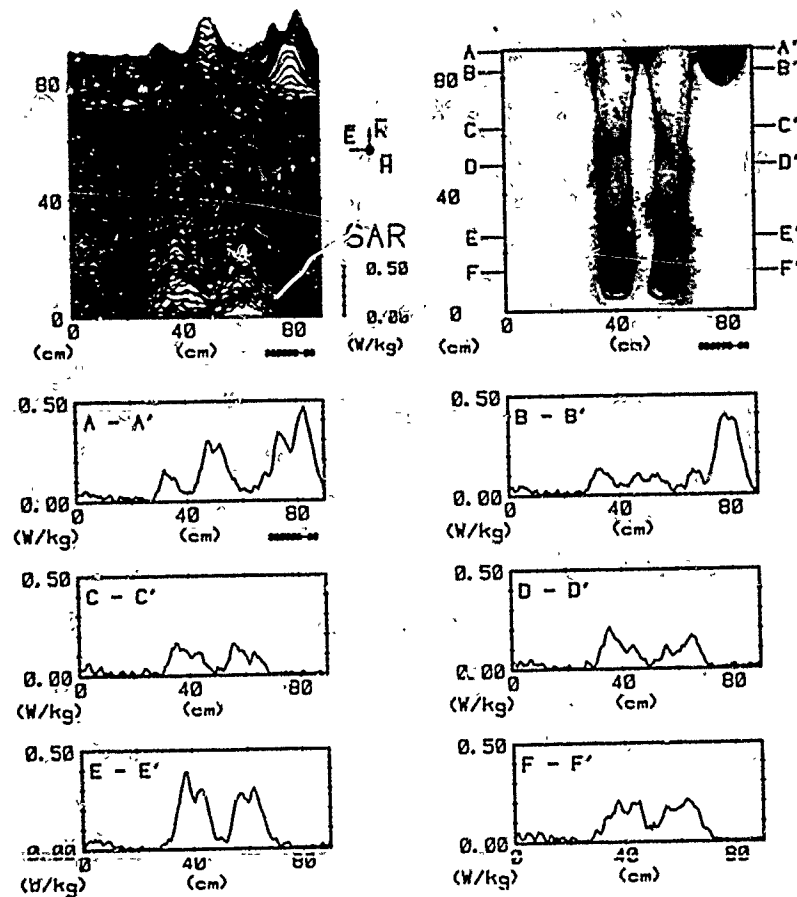
Figure 8.44. Computer-processed lower-body thermograms expressing SAR patterns for man with one arm extended, exposed to 1-mW/cm^2 450-MHz radiation with KEH polarization (Guy et al., 1984) (© 1984 IEEE).
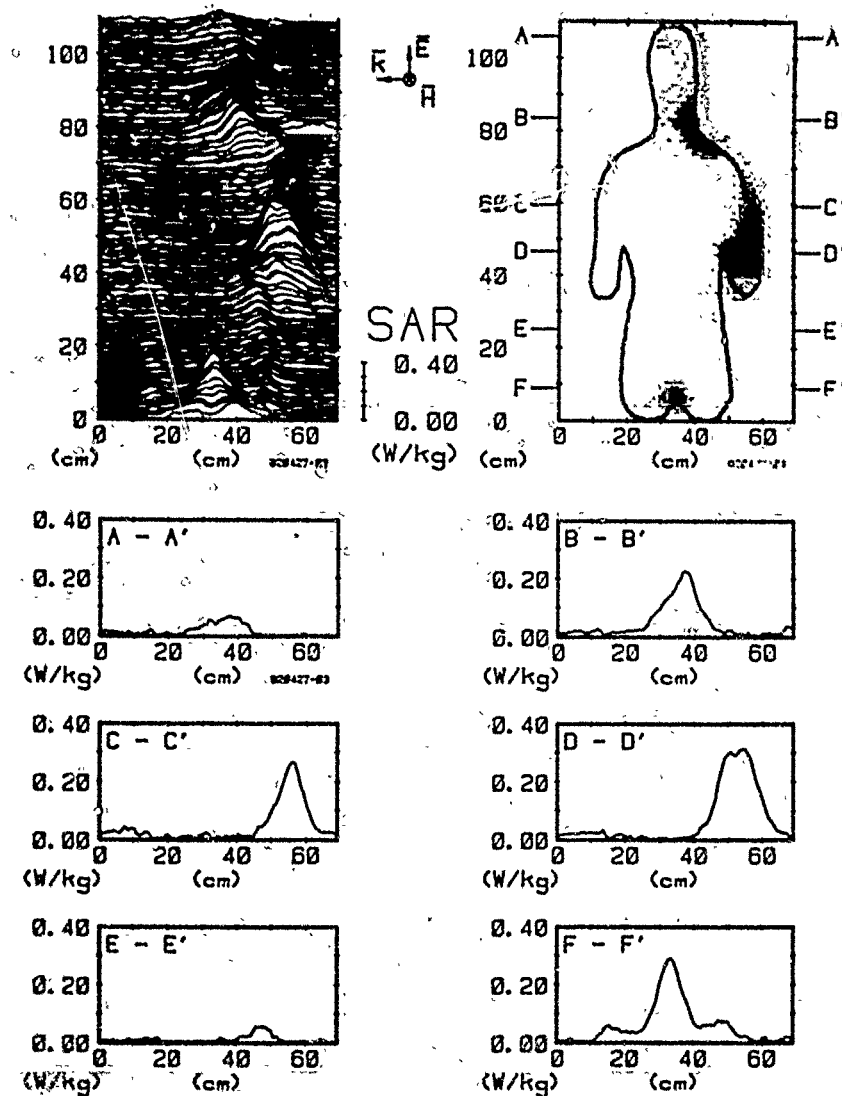
Figure 8.45. Computer-processed whole-body thermograms expressing SAR patterns for man sitting (frontal plane), exposed to 1-mW/cm^2 450-MHz radiation with EKH polarization (Guy et al., 1984) (© 1984 IEEE).
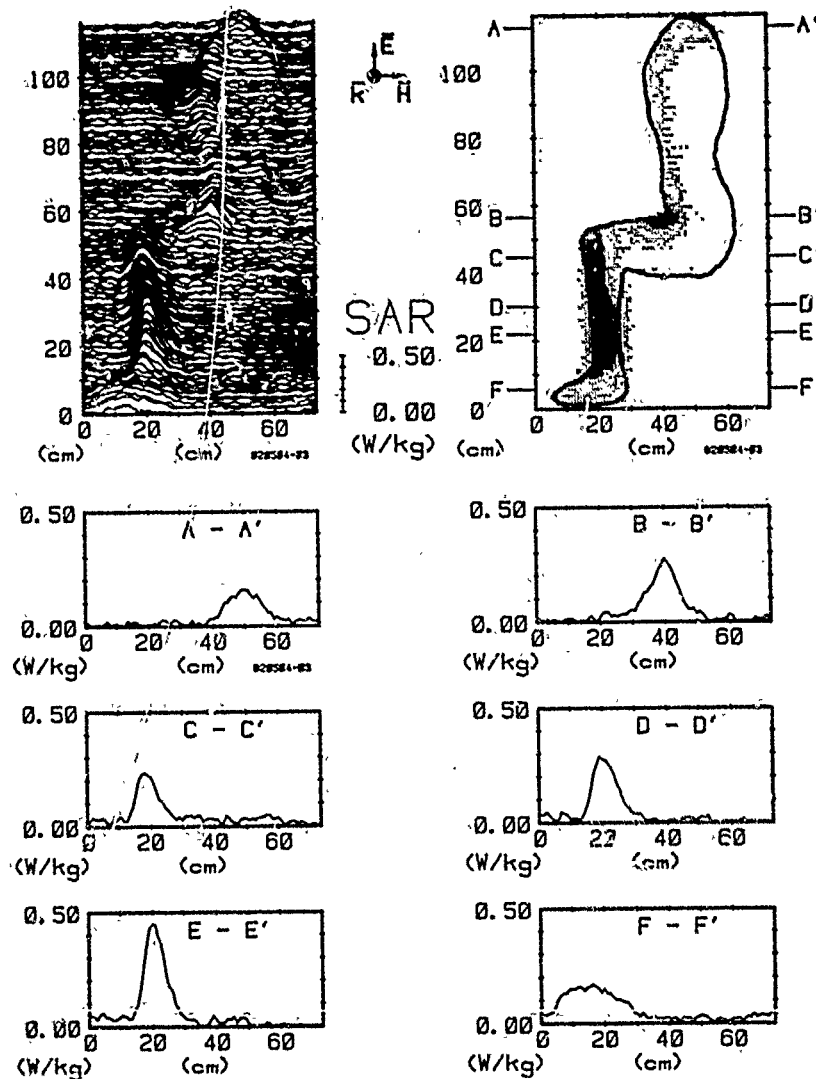
Figure 8.46. Computer-processed whole-body thermograms expressing SAR patterns for man sitting (sagittal plane through leg), exposed to 1-mW/cm² 450-MHz radiation with EHK polarization (Guy et al., 1984) (© 1984 IEEE).
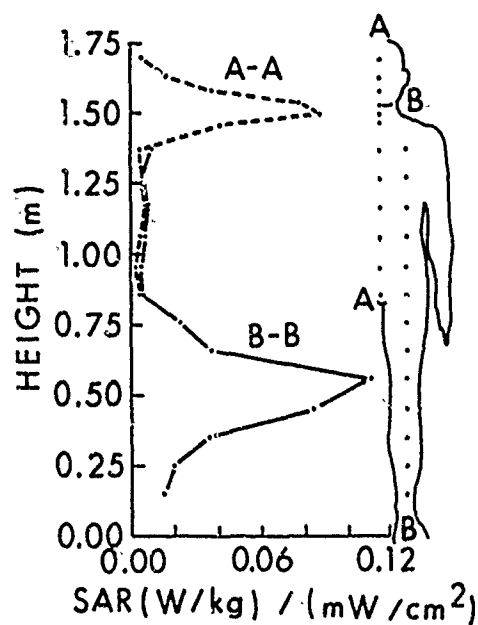
Figure 8.47. SAR distribution along an average man-model height for two cross sections; 1-mW/cm^2 incident-power density on the surface of the model, frequency 350 MHz E∥L, K back to front (Krazewski et al., 1984) (© 1984, IEEE).

TABLE 8.1. MEASURED AND CALCULATED VALUES OF AVERAGE
SAR FOR MICE (Allen and Hurt, 1977)

Number of Animals	F(GHz)	Average Weight (g)	Polarization	Average SAR $(W/kg)/(mW/cm^2)$	
				Measured	Calculated (Empirical)
5	2.6	35.0	E	0.92 ± 18%	0.8[*]
1	2.6	35.0	K	0.52	---
3	2.6	24.4	E	1.19 ± 10%	1.0
3	2.6	23.7	E	1.11 ± 7%	1.0

[*] Interpolated value to avoid a step function discontinuity at f_{02} around 2.6 GHz.

TABLE 8.2. MEASURED AND CALCULATED VALUES OF AVERAGE SAR FOR PROLATE
SPHEROIDAL MODELS OF MAN AND TEST ANIMALS (Guy et al., 1978)

Model	a(cm)	b(cm)	F(MHz)	Polarization	Average SAR $(W/kg)/(mW/cm^2)$	
					Measured	Calculated
Average man	87.5	13.8	80	E	0.211	0.22
Average man	87.5	13.8	80	H	0.010	0.009
Rhesus monkey	20.0	6.46	400	E	0.191	0.21
Rhesus monkey	20.0	6.46	400	H	0.0627	0.054
Squirrel monkey	11.5	4.78	700	E	0.234	0.24
Medium rat	10.0	2.76	915	E	0.517	0.49
Man[*]	89.5	----	1290	E	0.031	0.03

[*] Phantom shaped like a man, weight about 75 kg (Olsen, 1977).

TABLE 8.3. WHOLE-BODY AVERAGE SAR FOR SALINE-FILLED FIGURINES UNDER NEAR-FIELD EXPOSURE CONDITIONS. EXPERIMENTAL FREQUENCY = SIMULATED FREQUENCY × (HEIGHT OF MAN/HEIGHT OF FIGURINE) (Chatterjee et al., 1982b)

Simulated Frequency for Man (MHz)	Model Size (cm)	Experimental Frequency (MHz)	Physical Parameters for the Fields at the Simulated Frequency (m)		Average SAR (±SD) μW/kg for Maximum $E_v = 1$ V/m rms		SAR for Planewave Irradiation (μW/kg)†
			Δ_v^*	δ_h^*	Experimental# N = 5	Empirical Equation	
71	20.3	610	0.14	1.28	1.0 (±0.029)	1.2	58.4
77	20.3	663	0.484	1.32	1.7 (±0.029)	1.8	58.6
88	20.3	760	0.622	1.66	2.6 (±0.081)	3.8	52.0
96	25.4	663	0.388	1.06	1.4 (±0.075)	1.3	48.0
110	25.4	760	0.496	1.32	2.0 (±0.067)	2.4	39.2
115	33.0	610	0.212	0.657	0.42 (±0.064)	0.46	36.0
125	33.0	663	0.298	0.814	0.66 (±0.045)	0.58	33.4
143	33.0	760	0.256	0.816	0.38 (±0.040)	0.46	35.0
150	33.0	795	0.276	0.742	0.54 (±0.0035)	0.42	26.0
176	40.6	760	0.207	0.690	0.20 (±0.050)	0.19	22.6

* Obtained by measurement.

Average of three measurements; standard deviation less than ±5%, calculated from 4180 $\Delta T/$ (irradiation time in seconds).

† Obtained numerically for an incident field of rms magnitude 1 V/m.

TABLE 8.4. INTERNAL ELECTRIC FIELD IN THE ABDOMIN — REGION OF PHANTOM FIGURINES AS A FRACTION OF THE MAXIMUM INCIDENT ELECTRIC FIELD (JUST IN FRONT OF THE FIGURINE) FOR NEAR-FIELD EXPOSURE CONDITIONS (Chatterjee et al., 1982b)

Simulated Frequency for Man (MHz)	Figurine Size (cm)	Experimental Frequency (MHz)	Δ_v/λ	Δ_h/λ	Internal $|\bar{E}|$/Incident $|E_v|^*$ Near Field		Far Field[‡] (Numerical)
					Experimental[†]	Numerical[‡]	
77	25.4	530	0.18	0.40	0.070	0.070	0.42
77	20.3	663	0.16	0.40	0.049	0.059	0.42
110	25.4	760	0.18	0.43	0.033	0.060	0.29
150	40.6	663	0.09	0.30	0.022	0.025	0.14
150	33.0	795	0.10	0.45	0.040	0.042	0.14

* BRH electric-field probes were used for internal and external field measurements (courtesy of Howard Bassen).

† Average of three measurements, standard deviation less than 5%.

‡ Obtained by averaging calculated values of $|\bar{E}|$ for the abdominal cells of the 180-cell block model of man.

CHAPTER 9. DOSIMETRY IN THE VERY-LOW-FREQUENCY AND MEDIUM-FREQUENCY RANGES

In the frequency range from 10 kHz to 3 MHz, which includes the very-low-frequency (VLF) and medium-frequency (MF) bands, other dosimetric data may be more important than the SARs given in Chapters 6 and 8. Exposure fields (even relatively intense ones) at the low frequencies produce relatively inconsequential amounts of absorbed energy but may cause electric shocks and RF burns. Since the shocks and burns are more directly related to current density and total current, these quantities are probably more useful dosimetric data than SARs in the VLF-MF ranges.

Dosimetry in the VLF-MF bands thus consists primarily of relating current densities in the exposed bodies to the exposure fields. Important factors in this relationship are the presence of nearby objects, especially conducting objects such as automobiles, and the exposed person's contact with the objects. The impedance between the exposed person and ground is useful in relating the current densities to the exposure field. This section contains information about methods of calculating and measuring impedances and current densities, and summaries of such data. Most of the information was obtained from work reported under USAFSAM contracts with Guy and Chou (1982) and Gandhi and Chatterjee (1982).

9.1. METHODS

Most objects of interest are small compared to a wavelength in the VLF-MF ranges, so quasi-static analyses are useful for obtaining dosimetric information. In the quasi-static approximation, the calculated results at one frequency are directly applicable to all frequencies for which the approximation is valid. Fortunately this includes the 60-Hz range, where a great deal of theoretical and experimental dosimetry has been done. All of these 60-Hz results can be applied to the VLF-MF bands. The basic reason is explained by Kaune and Gillis (1981), among many others. They showed, from the quasi-static approximation to Maxwell's equations, that the field internal to a living subject is very small compared to the external field, which means that the perturbed external field and the induced surface-charge density are

independent of the permittivity of the body tissues. The induced surface charge causes internal currents that depend directly on the electrical properties of the body tissue, but the total conduction current passing through any section of the body is independent of the tissue characteristics (Kaune and Gillis, 1981; Deno, 1977). This also means that the total induced volume charge in the body is negligible compared to the total induced surface charge. The induced current in the body is directly proportional to frequency.

Several approaches have been used to calculate induced currents and energy absorption, but experimental measurements have proved to be more accurate. The methods described here consist of calculating currents, current densities, potential distributions, resistances, and local and average SARs from measured impedances and fields. The only polarization considered here is the one that causes the greatest absorption; as indicated in Chapters 6 and 8, that is the polarization in which E is parallel to the long dimension of the body.

9.1.1. Calculation of Current

In the quasi-static approximation, the total charge, q, on an object close to ground is given by

$$q = EhC_{og} \qquad (9.1)$$

where E is the E-field magnitude in the absence of the object, h is the effective height of the object, and C_{og} is the capacitance between the object and ground. The current, I_{sc}, induced on the object by E when the object is short-circuited to ground is given by

$$I_{sc} = j\omega q \qquad (9.2)$$

where $j\omega$ corresponds to the time derivative in the sinusoidal steady-state case, and ω is the radian frequency of E. Writing C_{og} as

$$C_{og} = \frac{S\varepsilon_o}{h} \qquad (9.3)$$

where S is an effective surface area and ε_o is the permittivity of free space, and combining Equations 9.1, 9.2, and 9.3 gives for the magnitude of I_{sc},

$$I_{sc} = \omega\varepsilon_o ES \qquad (9.4)$$

An approximate value for S may be obtained from the geometrical relation shown in Figure 9.1. Using this calculated value for S gives

$$I_{sc} = 0.09 \, h^2 Ef \qquad (9.5)$$

where h is the height in meters, E is the E-field magnitude in kilovolts per meter, f is the frequency in kilohertz, and I_{sc} is in milliamperes.

Deno (1977) measured the short-circuit current and the distribution of current at 60 Hz in a metallized mannequin consisting of insulated material covered with copper foil. Breaks in the copper foil were used to measure current distribution. By measuring short-circuit currents near powerful VLF-MF transmitting stations, Guy and Chou (1982) showed that the determination of currents at 60 Hz is applicable to the VLF-MF band.

Gandhi and Chatterjee (1982) used a Norton's equivalent circuit to represent the body and from it calculated the total current in the human body to be

$$I_h = I_{sc}[1/R_h + j\omega C_h]/[(1/R_h + 1/R_{og}) + j\omega(C_h + C_{og})] \qquad (9.6)$$

where R_{og} is leakage resistance of the body to ground, and R_h and C_h are equivalent body resistance and capacitance respectively. Combining Equations 9.6 and 9.4 gives the current in a person exposed to an electric field, E.

$$\text{AREA} = S = \pi r^2 = \pi (h \tan 35.7°)^2$$

$$I_{sc} = 0.09 h^2 E f$$
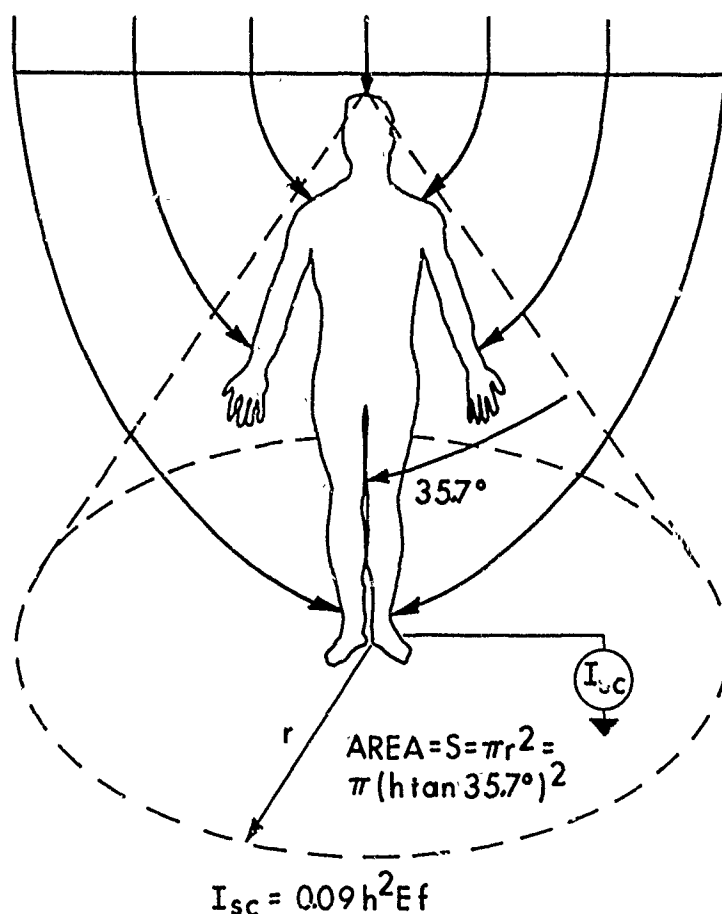
Figure 9.1.   Relationship between effective area and short-circuit current $\left(I_{sc}\right)$ for exposed human figure (Guy and Chou, 1982).

9.1.2.   Measurement of Body Potential and Dimensions

In baboons the equipotential planes occur perpendicular to the long axis of the body when the incident E-field is parallel to the long axis (Frazier et al., 1978; Bridges and Frazier, 1979), so the potential distribution inside the body can be predicted from the surface potential.   While applying a harmless low-level VLF current through volunteers' bodies, Guy and Chou (1982) measured the surface potential distribution.   They measured the circumference and maximum dimensions of the subject's body and limbs as a function of position every 5 cm from the feet to the head, and then assumed an elliptical
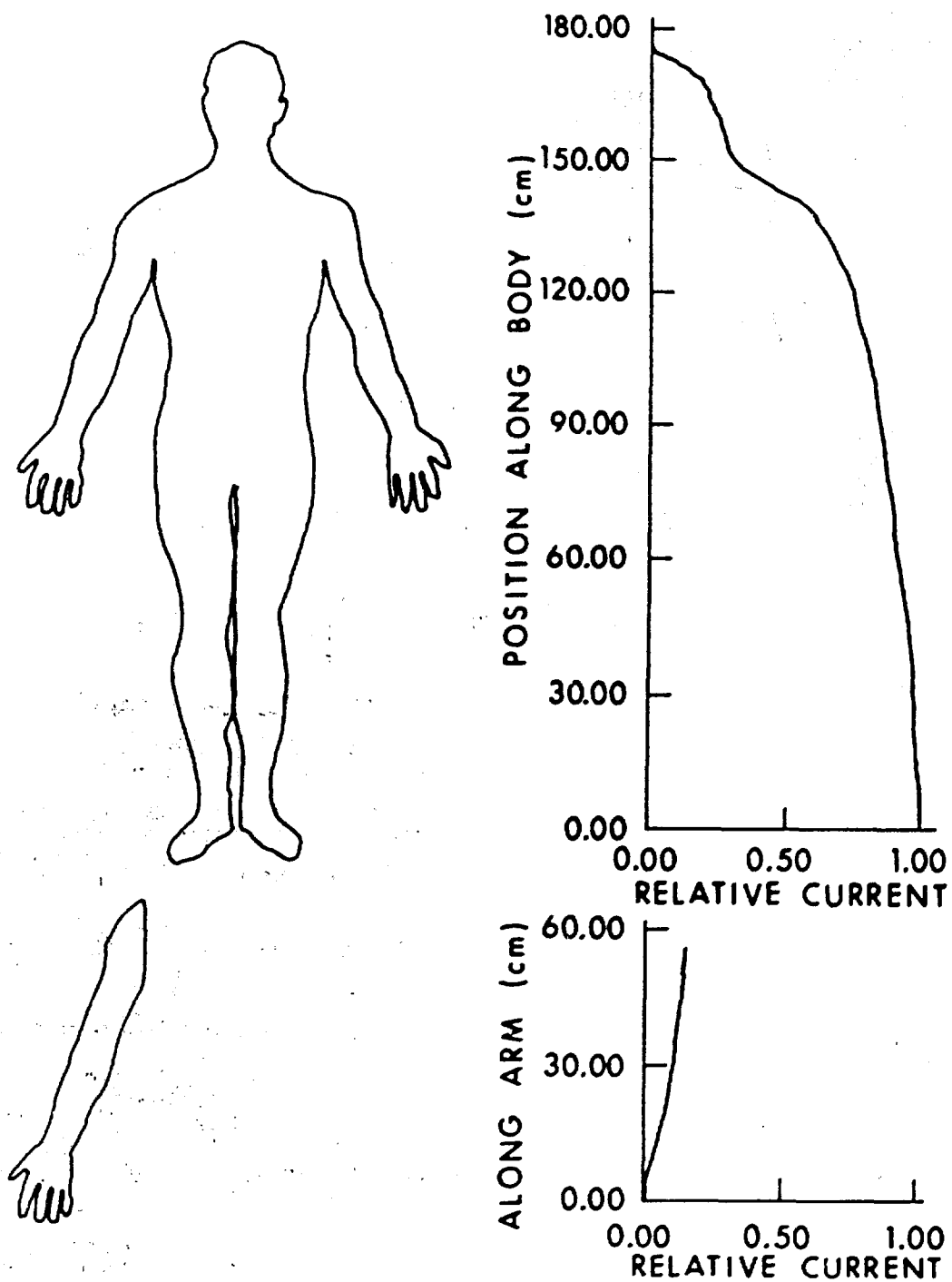
Figure 9.2.   Relative surface-current distribution in grounded man exposed
to VLF–MF fields [after Deno, 1977 (Guy and Chou, 1982)].
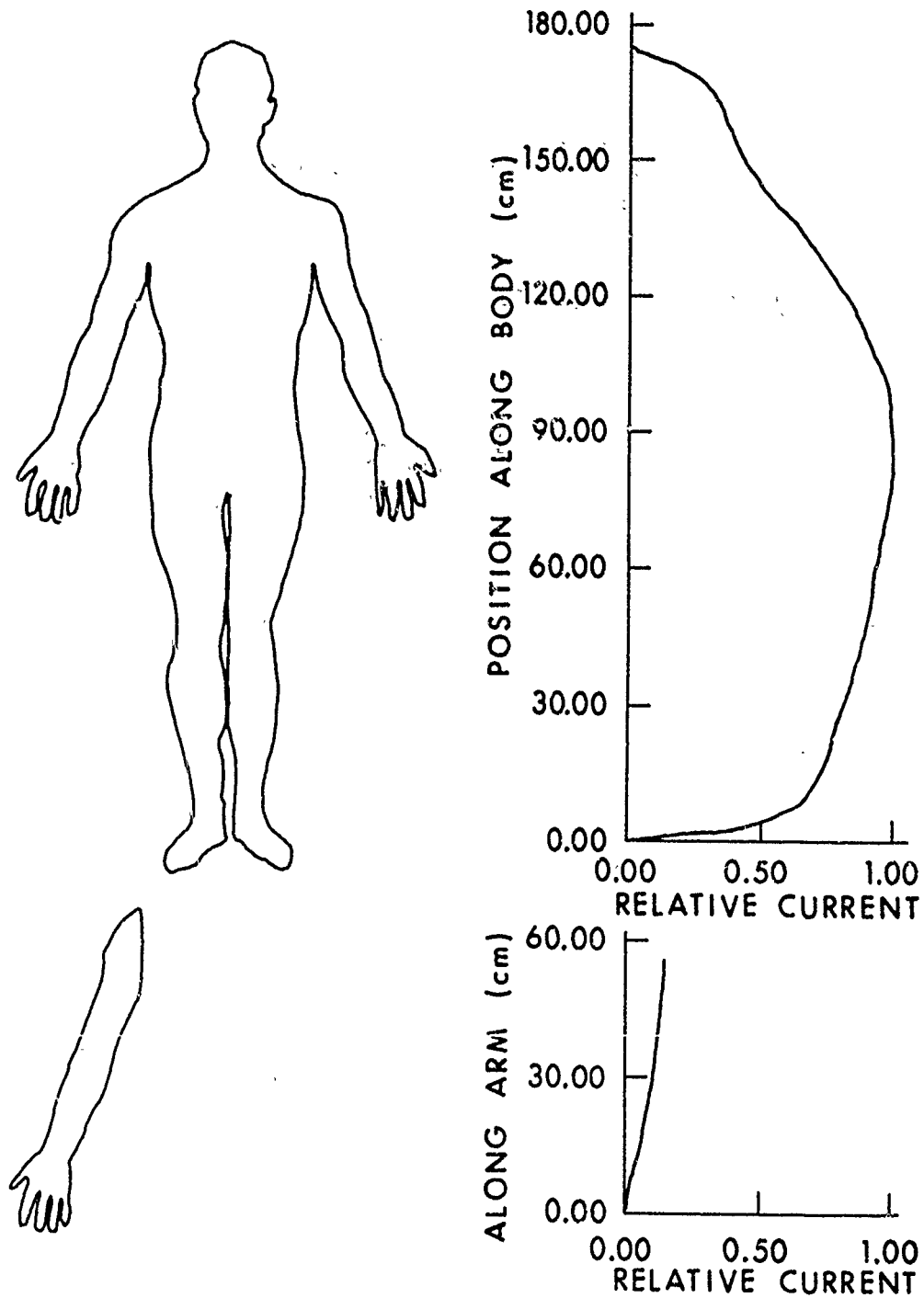
Figure 9.3. Relative surface-current distribution in man exposed in free space to VLF-MF electric fields [after Deno, 1977 (Guy and Chou, 1982)].
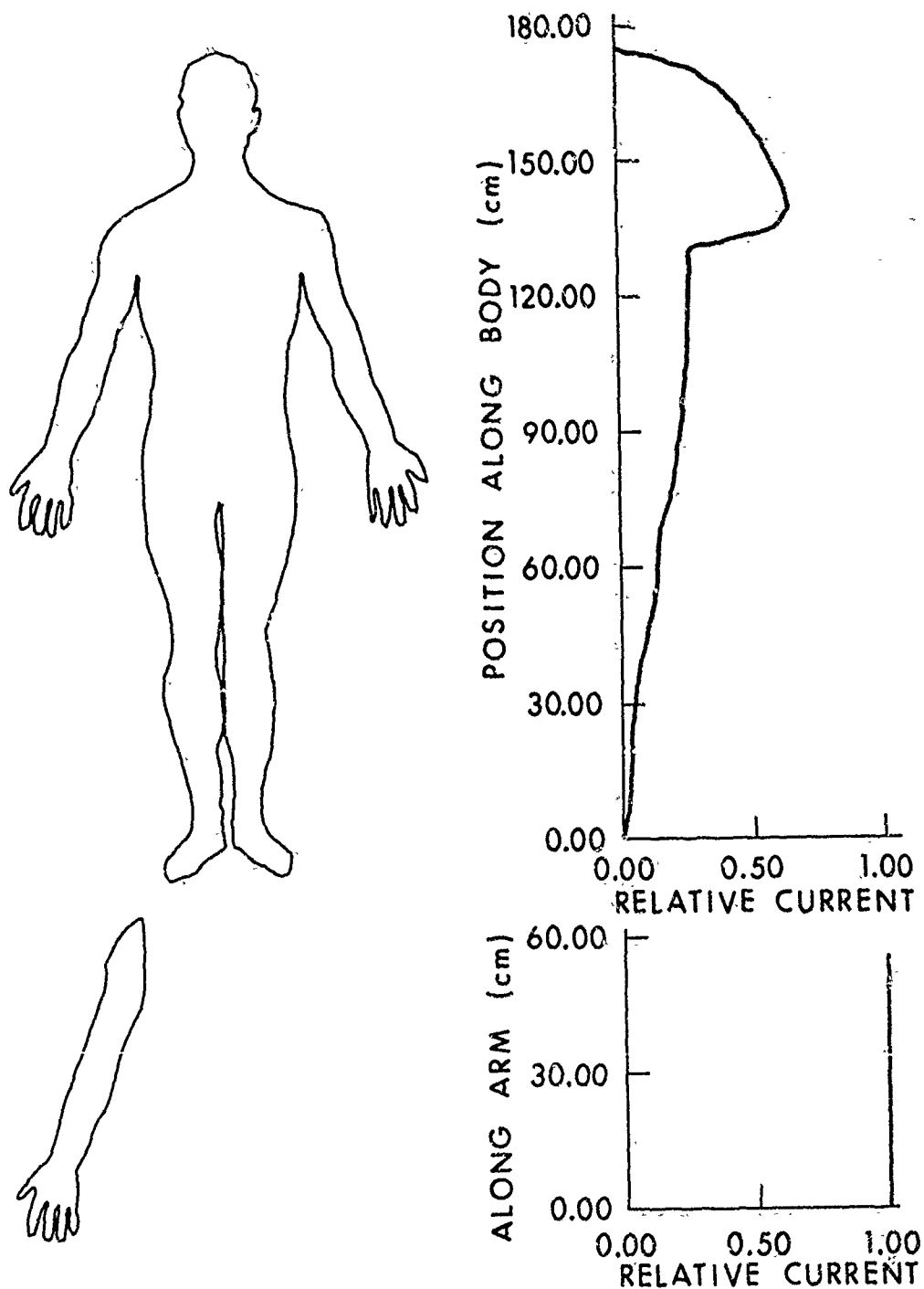
Figure 9.4. Relative surface-current distribution in man exposed to VLF-MF electric fields with feet insulated and hand grounded [after Deno, 1977 (Guy and Chou, 1982)].

Tables 9.1 and 9.2 summarize, respectively, the effects of currents on humans and some values specified in safety standards. Table 9.3 gives currents in various parts of the body, based on 60-Hz work by Kaune (1980). Table 9.4 gives short-circuit currents for various objects exposed to VLF-MF fields, based on 60-Hz work. Tables 9.5-9.7 show data measured in VLF-MF fields. The plot of these data in Figure 9.5 compares very well with values calculated from Equation 9.5.

TABLE 9.1. SUMMARY OF ELECTRIC-CURRENT EFFECTS ON HUMANS (Guy and Chou, 1982)

Electric Shock		0.06-kHz Current (mA)	10.0-kHz Current (mA)	Spark Discharge Energy
No sensation in hand	Men	0.4	7	
	Women	0.3	5	
Threshold of perception	Men	1.1	12	0.12 mJ
	Women	0.7	8	C = 1000 pF
				V = 350 V
Shock--not painful	Men	1.8	17	0.5-1.5 mJ
	Women	1.2	11	C = 1000 pF
				V = 0.7-1.2 kV
Painful shock; muscle control	Men	9.0	55	
	Women	6.0	37	
	Children	5.0	27	
Painful shock; let-go threshold	Men	16.0	75	
	Women	10.5	50	
Severe shock	Men	23.0	94	
	Women	15.0	63	

Threshold for radiofrequency burns: 200 mA

TABLE 9.2. MAXIMUM 60-Hz CURRENTS ALLOWED TO HUMAN BODY BY
NATIONAL ELECTRICAL CODE (mA) AND EQUIVALENT
LEVELS AT OTHER FREQUENCIES (Guy and Chou, 1982)

Source	Maximum 60 Hz	Equivalent 10 kHz	Equivalent 50 kHz	Equivalent 100 kHz
Portable appliances	0.5	5	20	40
Fixed appliances	0.75	8	32	64
Vehicles under transmission lines	0.5	27	--	--

ANSI C95.1-1982 Standard: maximum SAR = 0.4 W/kg average, 8.0 W/kg peak.

TABLE 9.3. CURRENT AND CURRENT DENSITY IN MAN EXPOSED TO VLF-MF [f(kHz)]
1-kV/m ELECTRIC FIELDS (based on Kaune, 1980) (Guy and Chou, 1982)

Section	$I(\mu A)$	Area (cm^2)	$J(\mu A/cm^2)$
Neck	78 f	85	0.91 f
Chest	200 f	630	0.32 f
Arm	37 f	95	0.38 f
Pelvis	220 f	540	0.42 f
Thigh	120 f	200	0.62 f
Ankle	130 f	40	3.3 f

TABLE 9.4. SHORT-CIRCUIT CURRENTS FOR OBJECTS EXPOSED TO VLF-MF
[f(kHz)] 1-kV/m ELECTRIC FIELDS (Guy and Chou, 1982)

Object	I(ma)	Object	I(ma)
Tractor	1.0 f	10-m vertical wire	2.08 f
Car	1.47 f	20-m vertical wire	7.72 f
Jeep	1.8 f	10-m crane	7.1 f
Bus	6.5 f	30-m crane	44.0 f
Truck	9.6 f	100-m horizontal wire	3.8 f
5-m vertical wire	0.561 f	Man	0.26 f

TABLE 9.5. COMPARISON OF MEASURED AND THEORETICAL SHORT-CIRCUIT
BODY CURRENT FOR MAN EXPOSED TO VLF-MF ELECTRIC
FIELDS WITH FEET GROUNDED (Guy and Chou, 1982)

Location and E-Field Strength	Frequency (kHz)	Measured Current (mA/(kV/m))	Theoretical Current (mA/(kV/m))
Wet asphalt Haiku, Hawaii, Omega Station, E = 1 kV/m, height of subject = 1.77 m	10.2	2.9	2.88
Lualualei, Hawaii, Naval VLF Station, E = 1 to 2 kV/m, height of subject = 1.77 m	23.4	6.75	6.60
Jim Creek, Washington Naval VLF Station, E = 487 V/m, Subject No. 1 (height = 1.77 m) (weight = 80 kg)	24.8	6.0	6.60
Subject No. 2 (height = 1.77 m) (weight = 65 kg)	24.8	5.6	6.60
Subject No. 3 (height = 1.68 m)[*] (weight = 64 kg)	24.8	6.22	6.60
Right hand over head Subject No. 1	24.8	7.23	7.39
Subject No. 2	24.8	6.27	7.39
Subject No. 3	24.8	6.97	7.39
Lualualei, Hawaii, Naval LF Station, E = 76 V/m, height of subject = 1.77 m	146.08	35.5	41.2
Broadcast stations, Las Vegas, Nevada by Tell et al. (1979) E = 0.1-63 V/m height of subject = 1.68 m[*]	720.0	216.0	203.0
	920.0	316.0	259.0
	1145.0	366.0	322.0
	1350.0	405.0	380.0
	1470.0	560.0	414.0

[*] Current corrected for height of 1.77 m.

TABLE 9.6. MEASURED BODY CURRENTS [mA/(kV/m)] TO GROUND FOR SUBJECTS
            EXPOSED UNDER DIFFERENT CONDITIONS TO 24.8-kHz VLF ELECTRIC
            FIELDS [WASHINGTON VLF (Guy and Chou, 1982)]

Condition and E-Field Strength (Wet Asphalt)	Hands Down	One Hand Up	Both Hands Up	Crouch
E = 487 V/m				
Bare feet				
Subject No. 1 (height = 1.77 m)	6.0	7.23	8.19	3.14
Subject No. 2 (height = 1.77 m)	5.6	6.80	7.62	2.77
Subject No. 3 (height = 1.68 m)	5.24	6.30	7.02	2.46
Rubber-sole shoes				
Subject No. 1	3.20	3.72	4.00	1.46
Subject No. 2	3.78	4.44	4.93	1.56
Subject No. 3	2.6	3.10	3.39	1.21
Leather-sole shoes				
Subject No. 1	4.52	5.46	5.91	2.34
Feet grounded to ground strip				
Subject No. 3	5.9	--	--	--
Feet insulated, hand grounded to ground strip	6.63	--	--	--
E = 1.46 kV/m				
Subject No. 2	6.44	7.67	8.70	2.95

TABLE 9.7. COMPARISON OF MEASURED AND THEORETICAL PERSON-TO-VEHICLE CURRENT RESULTING FROM VLF-MF ELECTRIC-FIELD EXPOSURE (Guy and Chou, 1982)

Type of Vehicle and Exposure Conditions	Frequency (kHz)	Measured Current (mA/(kV/m))	Theoretical Short-Circuit Current (mA/(kV/m))
Stanza; short-circuit current wet asphalt, E = 0.92 kV/m open-circuit voltage, measured = 240 V, theory = 307 V	10.2	12.7	15.0
Bare feet	10.2	11.5	---
Wet ground; short-circuit current, E = 1 kV/m	23.4	28.0	32.5
Bare feet	23.4	29.7	---
Impala; short-circuit current to ground strip, E = 0.487 kV/m; open-circuit voltage, measured = 230 V	24.8	37.6	---
Bare feet, wet asphalt	24.8	25.7	---
Volkswagen van; short-circuit current, wet asphalt E = 0.92 kV/m	10.2	18.8	18.4
Bare feet	10.2	19.0	---
Leather shoes	10.2	12.6	---
Leather shoes, dry asphalt	10.2	4.9	---
Rubber beach sandles, wet asphalt	10.2	2.1	---
Chevrolet sports van; short-circuit current, E = 0.92 kV/m	10.2	18.5	18.4
Bare feet	10.2	18.4	---
Leather shoes, dry asphalt	10.2	4.0	---
Beach sandles	10.2	0.8	---
Dodge trademan 300 van; short-circuit current, E = 1 kV/m, open-circuit V = 415, wet ground	23.4	65.0	42.5
Bare feet	23.4	65.0	---
Leather shoes	23.4	25.0	---
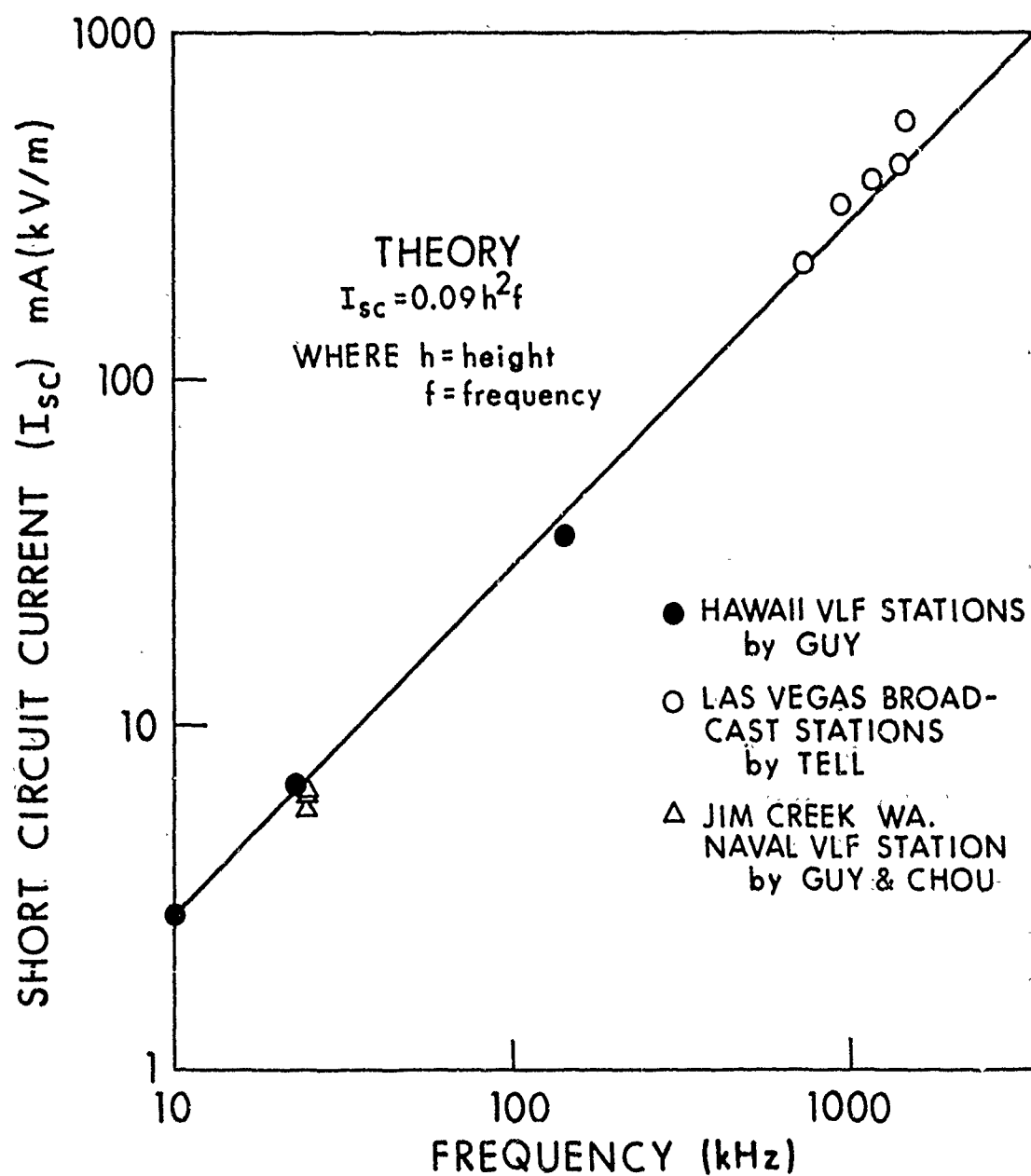
Figure 9.5. Comparison of theoretical and measured short-circuit body
current of grounded man exposed to VLF-MF electric field
that is parallel to body axis (Guy and Chou, 1982).

- 9.15 -

Figures 9.6-9.8 show results by Gandhi and Chatterjee (1982) of human body resistance, threshold perception and let-go currents and corresponding unperturbed incident E-fields that would produce these threshold currents for various conditions. Perception current is defined as the smallest current at which a person feels a tingling or pricking sensation due to nerve stimulation. Let-go current is defined as the maximum current at which a human is still capable of releasing an energized conductor using muscles directly stimulated by that current. Tables 9.8-9.10 show values of threshold perception measured with an experimental setup like the one illustrated in Figure 9.9. Either a copper-disk or a brass-rod electrode was used in the measurements. Table 9.11 gives calculated values of currents through the wrist and finger for a maximum SAR of 8 W/kg.

Table 9.12 shows the body dimensions calculated by Guy and Chou for one person. Figures 9.10-9.17 show their calculated current distributions for the current distributions of Figures 9.2-9.4. The data in Figures 9.10-9.17 are for exposure of a subject with feet electrically grounded, in free space, with feet insulated but hands grounded, and with feet grounded but one hand contacting a large object such as a vehicle. To calculate values of current, current density, and potential in a subject contacting one of the specific objects in Table 9.4, multiply the values in Figures 9.10-9.17 by the short-circuit object currents in Table 9.4. Calculations for objects not given in Table 9.4 can be made by looking up methods for calculating the effective surface area, S, in the literature (for example, Deno, 1977; Transmission-Line Reference Book, 1979) using Equation 9.5 to calculate I_{sc}, and proceeding as described above.
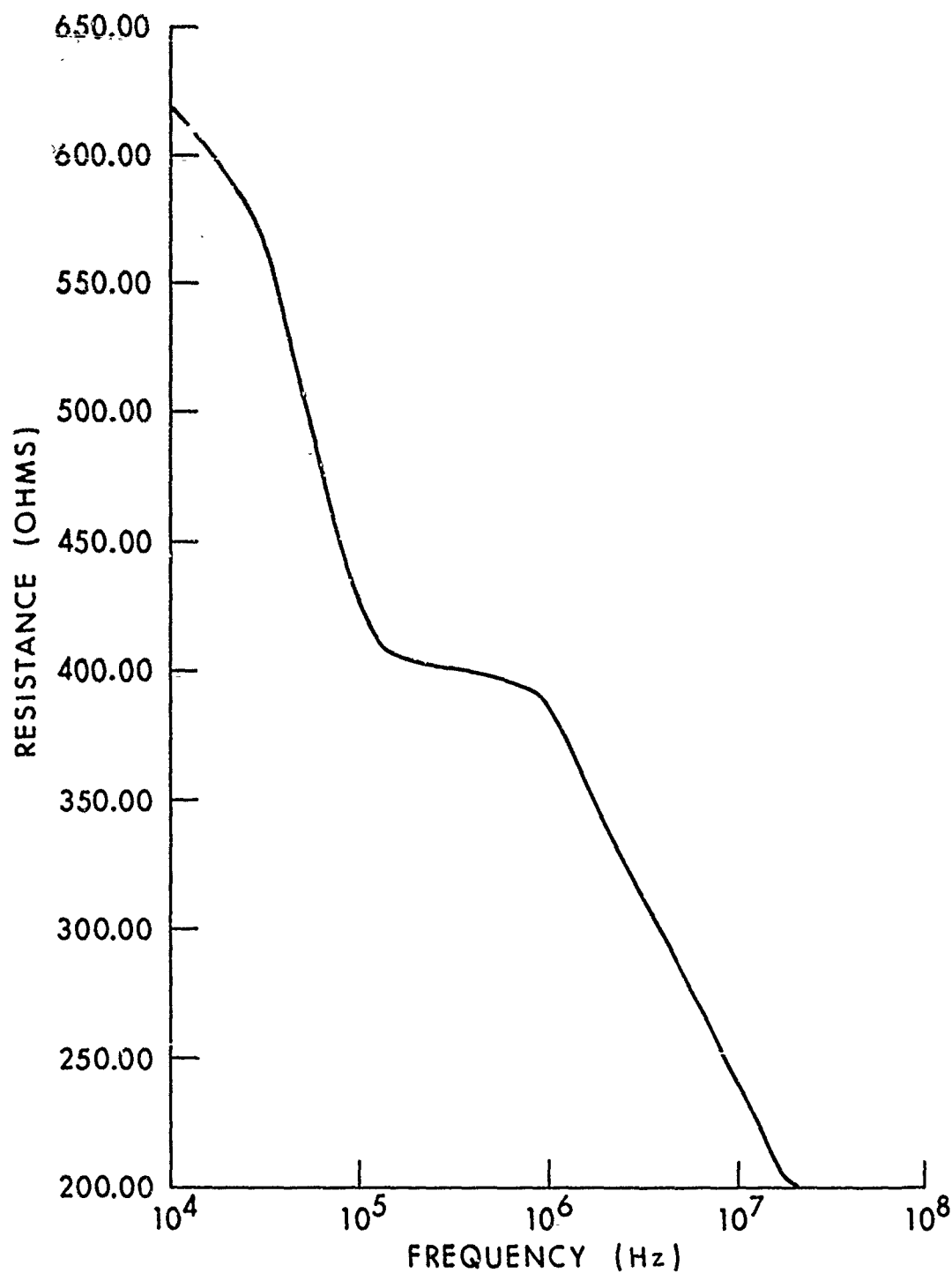
Figure 9.6. Average values of the human body resistance, R_h, (see Equation 9.6) assumed for the range 10 kHz to 20 MHz (Gandhi and Chatterjee, 1982).
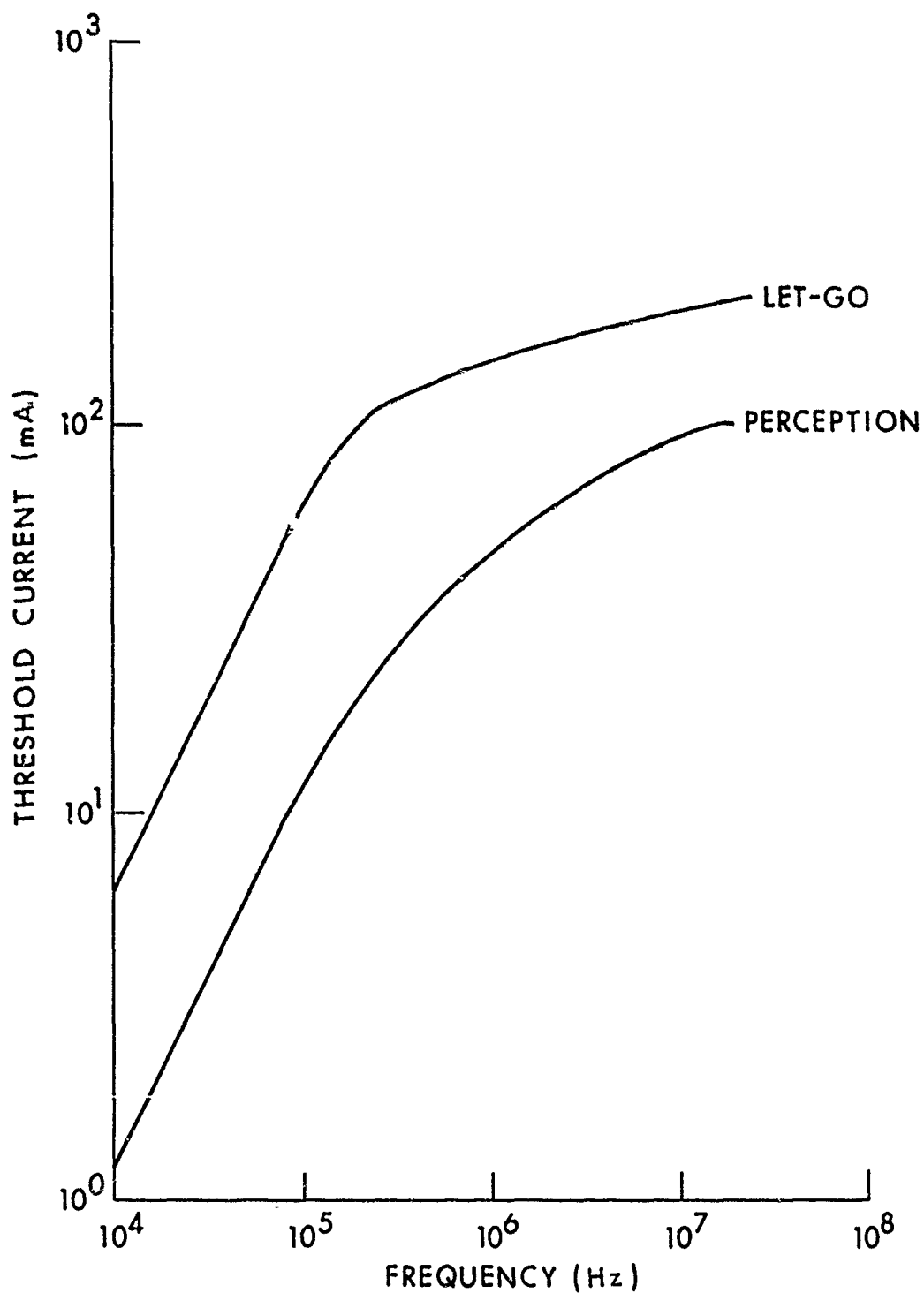
Figure 9.7. Perception and let-go currents for finger contact for a 50th percentile human as a function of frequency assumed for the calculations (Gandhi and Chatterjee, 1982). [These were obtained as a composite of the experimental data of Dalziel and Mansfield (1950), Dalziel and Lee (1969), and Rogers (1981).]
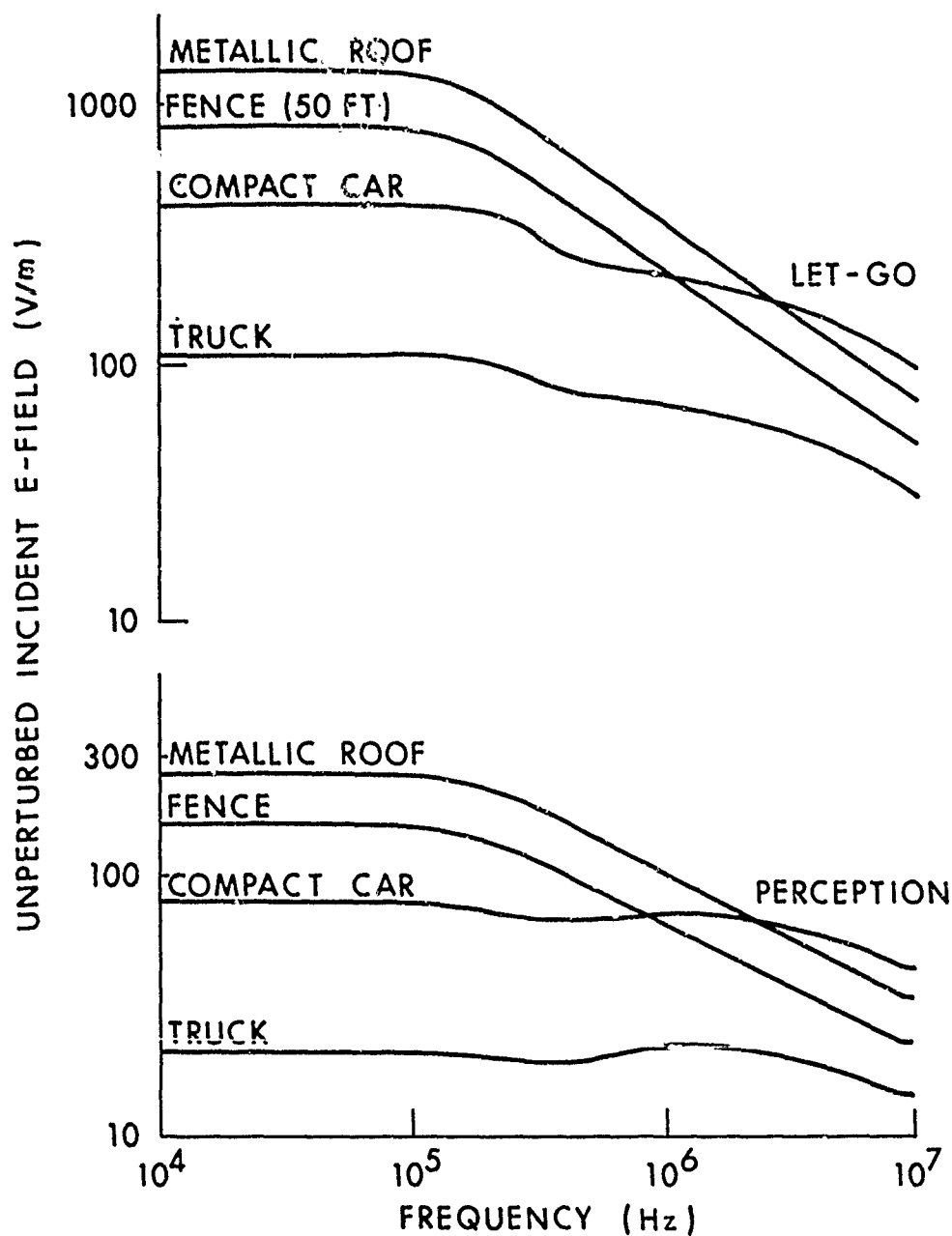
Figure 9.8. Unperturbed incident E-field required to create threshold perception and let-go currents in a human for conductive finger contact with various metallic objects, as a function of frequency (Gandhi and Chatterjee, 1982).

TABLE 9.8. THRESHOLD CURRENTS FOR PERCEPTION WHEN IN CONTACT WITH THE COPPER-PLATE ELECTRODE AND THRESHOLD INCIDENT ELECTRIC FIELDS FOR PERCEPTION WHEN IN CONTACT WITH VARIOUS METALLIC OBJECTS (Gandhi et al., 1984)

Frequency kHz	Threshold Current for Perception (Copper-Plate Electrode) mA	Series Impedance $(R_s - jX_s)$ of a Human	Threshold Incident E-Field for Perception (V/m)						
			Car C_g=800 pF S =26.4 m²	Tractor C_g=700 pF S =18 m²	Jeep C_g=900 pF S =32.4 m²	Wagon C_g=1200 pF S =39 m²	Truck C_g=1000 pF S =101.9 m²	Bus C_g=2000 pF S =117 m²	Metallic Roof C_g=105 pF S =8.39 m²
10	5.43	1250 - j782	385.4	562.7	315.5	266.4	100.9	92.7	1172.6
30	13.55	1004 - j385	329.2	478.6	270.6	231.5	86.9	83.8	976.6
100	74.55	775 - j151	581.5	829.5	484.5	432.8	157.8	176.3	1619.5
300	102.5	699 - j194	388.3	532.3	337.8	337.0	114.4	165.6	767.9
1000	100.25	766 - j135	287.0	373.7	260.3	282.9	87.9	154.1	258.5

* Average value for eight male subjects.

TABLE 9.9. STATISTICAL ANALYSIS OF MEASURED DATA ON THRESHOLD
CURRENTS FOR PERCEPTION WITH SUBJECTS BAREFOOT
AND WITH THE WRISTBAND (Gandhi et al., 1984)

Frequency (kHz)

	(Barefoot)					(Wristband)				
	10	30	100	300	1000	10	30	100	300	1000
N	7	8	7	8	8	5	6	4	7	4
Mean	5.40	14.0	77.4	105.1	93.7	5.46	13.1	71.7	99.9	106.8
±SD	0.92	3.1	22.5	29.7	13.1	0.99	0.5	15.9	28.2	16.7
N	5		6		4		8		5	
r	0.89		0.22		0.98		0.75		0.80	

Overall; N = 28; r = +0.95; p < 0.01

TABLE 9.10. THRESHOLD CURRENTS FOR PERCEPTION WHEN IN GRASPING CONTACT
WITH THE BRASS-ROD ELECTRODE AND THRESHOLD EXTERNAL
ELECTRIC FIELDS FOR PERCEPTION WHEN IN CONTACT WITH A
COMPACT CAR (C_g = 800 pF) (Gandhi et al., 1984)

Frequency (kHz)	Threshold Current[*] mA	Threshold External E-Field V/m
10	12.5	870
30	45.0	1036
100	315.0	2246
300	NA	
1000	NA	

[*] Average of values for two subjects.

NA -- The threshold currents are higher than currents available from the
Krohn-Hite model BR7500, 75-W amplifier.
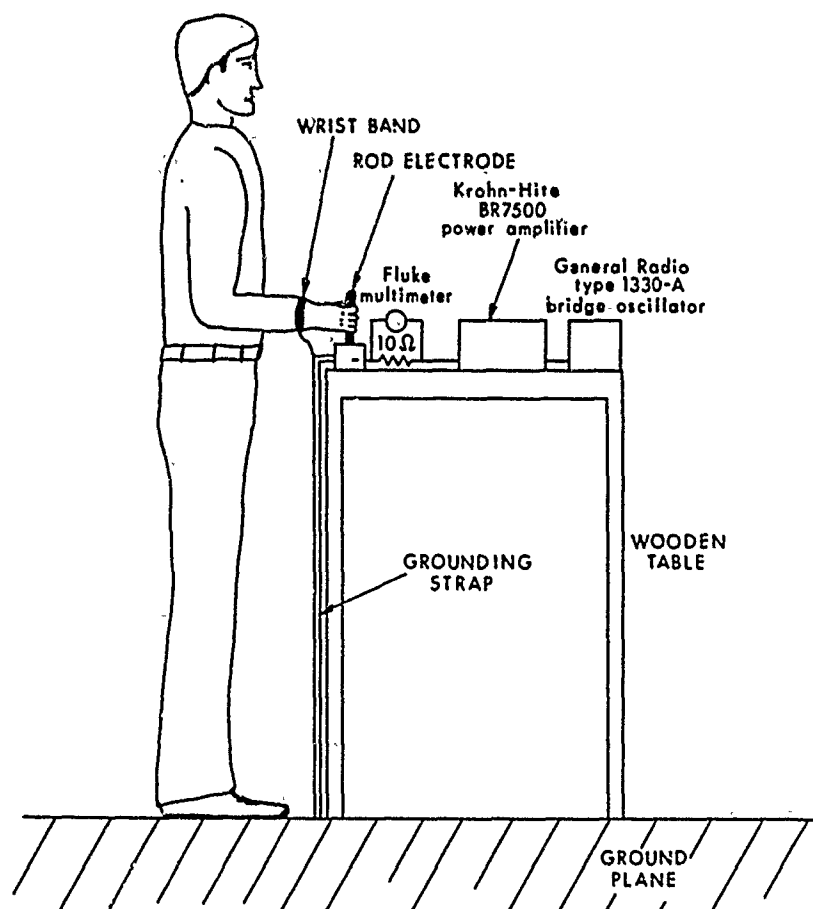
Figure 9.9. Experimental arrangement for measuring threshold currents for perception and let-go (Gandhi and Chatterjee, 1982).

TABLE 9.11. CURRENTS THROUGH THE WRIST AND FINGER FOR MAXIMUM SAR = 8 W/kg. (Cross-sectional areas are for nonbony regions of respective parts of the body.) (Gandhi et al., 1984)

			Current (mA)	
Frequency (kHz)	Conductivity of Muscle* (S/m)	Current Density (A/m^2)	Wrist (cross-sectional area = 17×10^{-4} m^2)**	Finger (cross-sectional area = 1.22×10^{-4} m^2)†
10	0.132	32.5	55.2	3.96
100	0.494	62.9	106.9	7.67
1000	0.550	66.3	112.7	8.09

* From Durney et al., 1980.
** A. C. Eycleshymer, 1911.
† J. Sobotta and F. H. J. Figge, 1967.

TABLE 9.12.

TABLE 9.12.   DIMENSIONS OF BODY USED FOR VLF-MF EXPOSURE MODEL (Guy and Chou, 1982)

Position (cm)	Circumference (cm)	Max Dim. (cm)	Min Dim. (cm)	Area (cm^2)
175	2.50	0.41	0.39	0.50
170	49.44	8.05	7.68	194.28
165	56.13	9.52	8.30	248.37
160	52.69	9.52	7.07	211.41
155	40.97	7.09	5.89	131.31
150	75.89	6.84	15.65	336.19
145	108.43	14.06	19.95	881.32
140	104.33	23.00	4.73	341.56
135	96.80	20.34	7.80	498.36
130	96.79	16.32	14.44	739.97
125	96.08	16.03	14.51	730.99
120	93.48	15.85	13.83	688.97
115	90.19	15.67	12.90	635.18
110	91.61	15.88	13.16	656.22
105	92.86	16.14	13.28	673.38
100	95.20	16.92	13.15	698.82
95	96.71	17.56	12.86	709.64
90	85.86	15.44	11.62	563.77
85	57.20	9.48	8.71	259.42
80	56.54	9.32	8.66	253.75
75	54.15	9.09	8.12	231.88
70	51.44	8.63	7.72	209.32
65	46.02	8.09	6.47	164.35
60	41.54	7.28	5.87	134.16
55	38.22	6.43	5.72	115.42
50	35.65	5.93	5.40	100.68
45	34.75	5.47	5.59	96.09
40	37.78	5.93	5.59	113.53
35	39.20	6.20	6.09	122.30
30	34.69	5.04	6.27	94.42
25	29.53	5.01	5.96	68.78
20	26.18	4.13	4.37	54.53
15	22.93	4.14	4.20	40.03
10	24.04	4.55	3.08	41.78
5	40.97	8.04	2.92	113.98
0	64.40	13.95	4.51	272.57
55	33.75	5.47	5.27	90.56
50	30.90	4.31	5.46	73.89
45	29.53	4.45	4.94	69.01
40	27.75	4.51	4.33	51.22
35	26.70	4.87	3.52	53.90
30	26.76	4.47	4.03	56.66
25	27.15	4.76	3.83	57.28
20	25.22	4.68	3.20	47.16
15	22.35	3.48	3.63	39.73
10	19.39	3.18	2.99	29.86
5	19.64	3.44	2.77	29.99

Weight of subject = 79.5 kg
Calculated weight = 79.4 kg
(Based on dimension and specific gravity of 1.06)

POSITION ALONG BODY (cm)

ALONG ARM (cm)
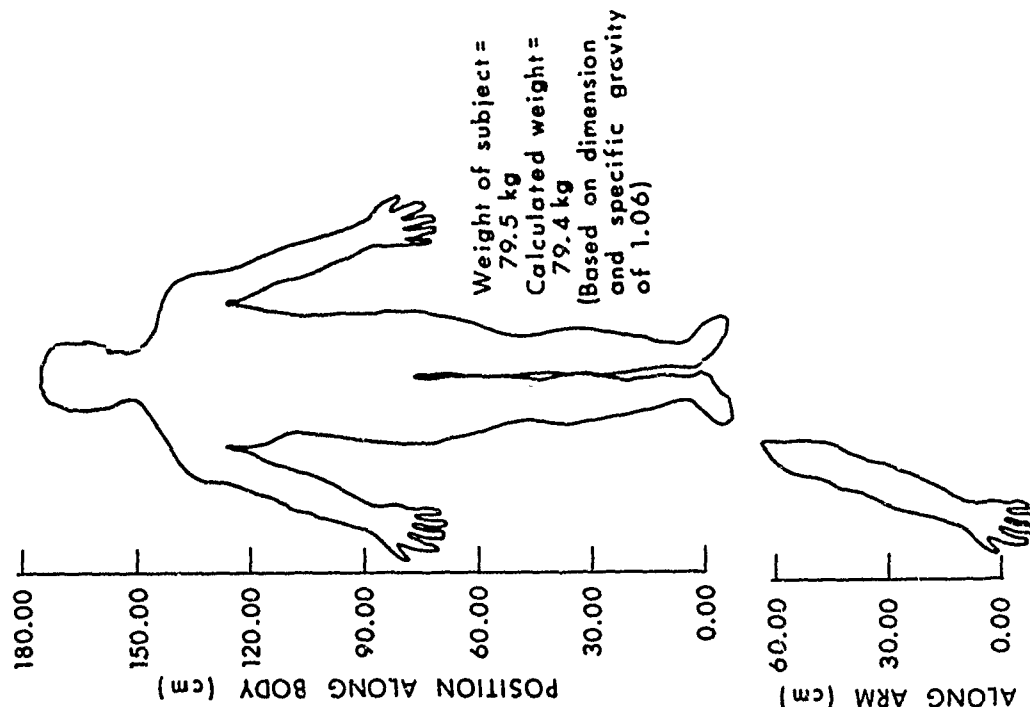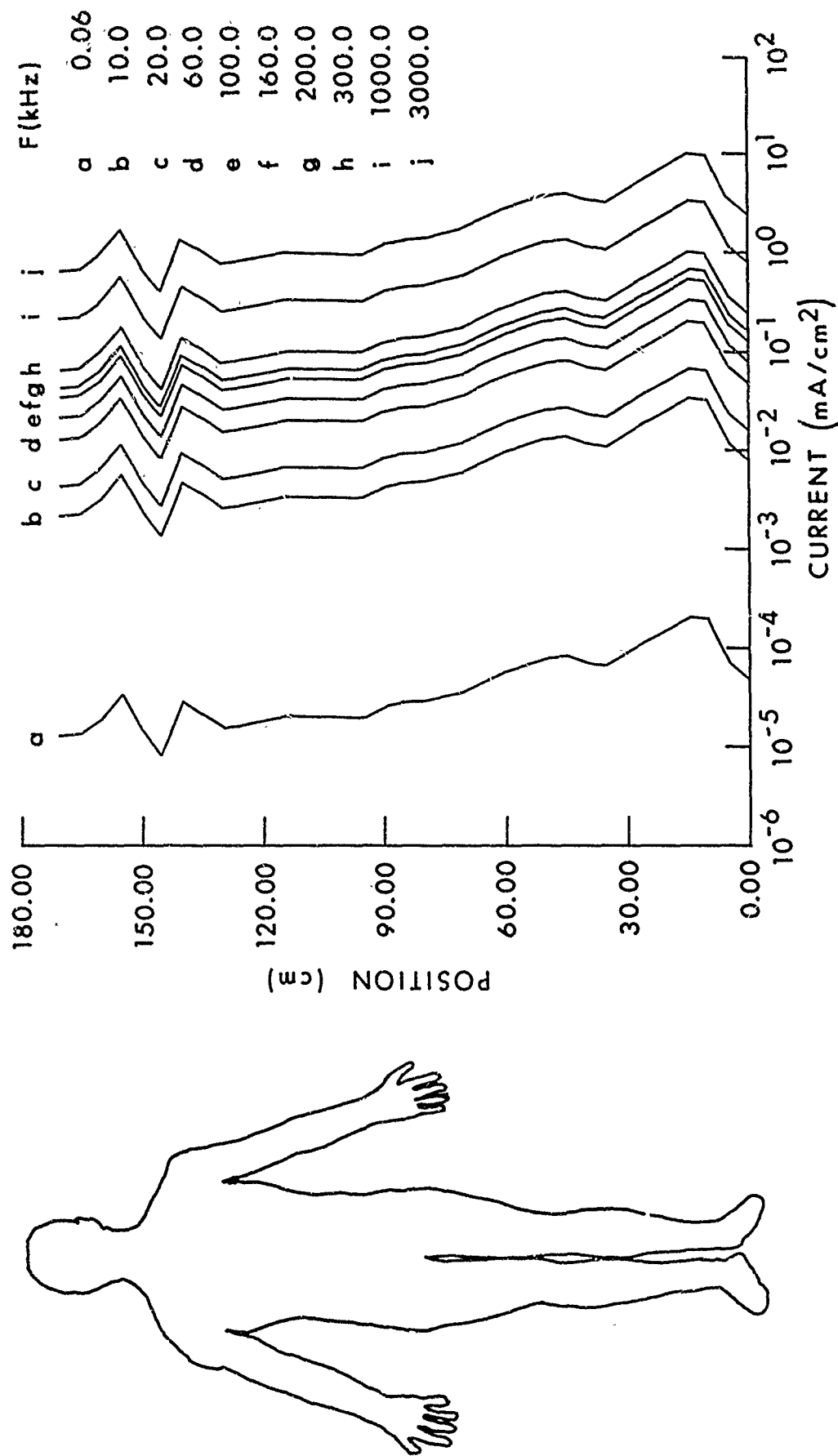
Figure 9.10. Calculated current distributions as a function of position in man exposed to 1-kV/m VLF-MF fields with feet grounded (Guy and Chou, 1982).
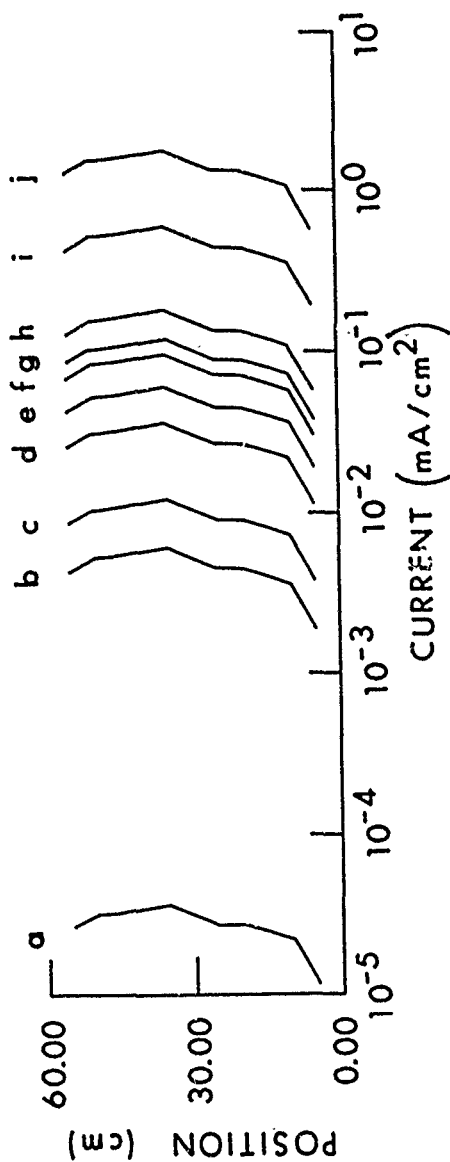
Figure 9.11. Calculated current density flowing through one arm. The exposure condition is the same as that of Figure 9.10 (Guy and Chou, 1982).
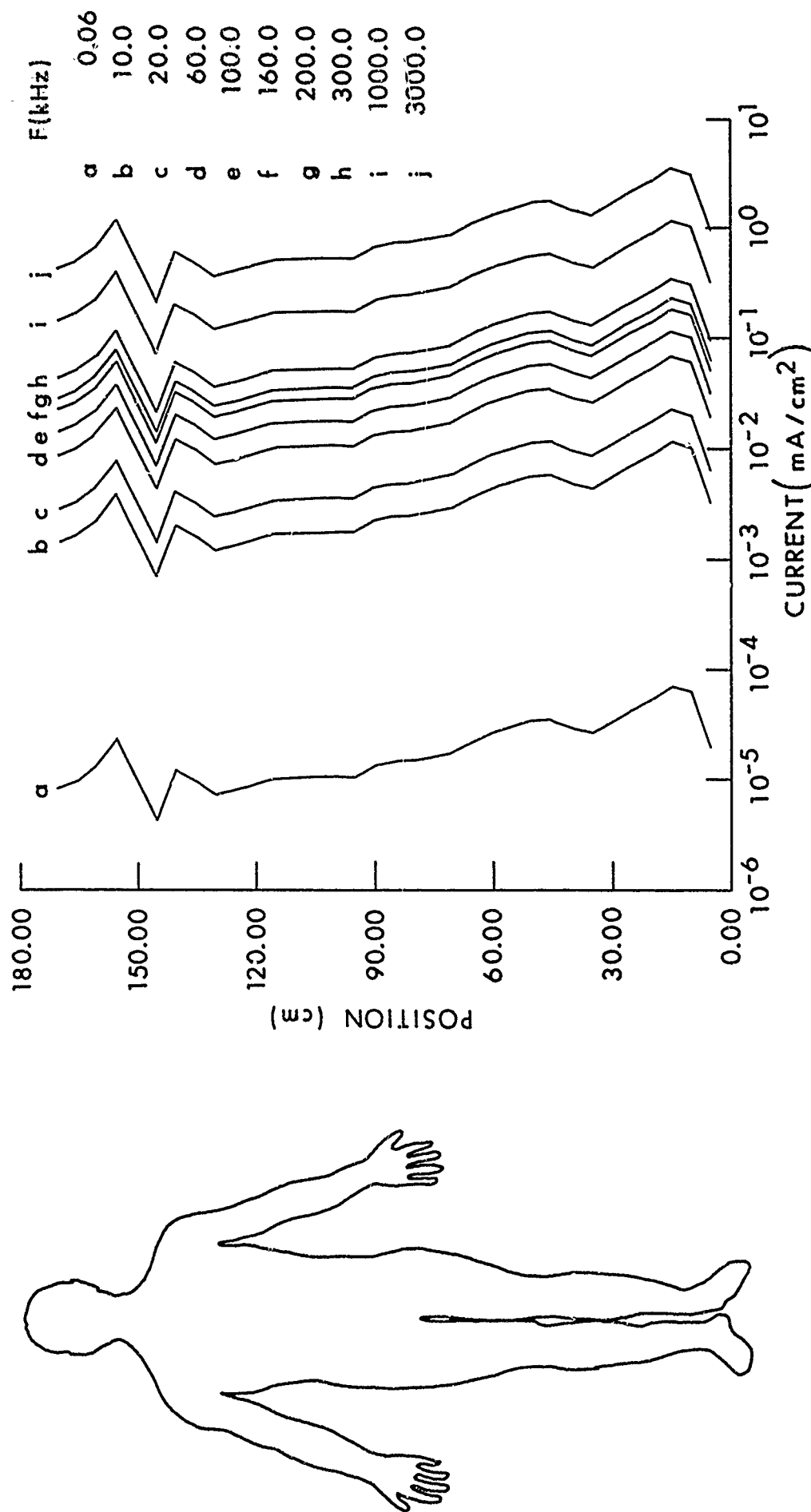
Figure 9.12. Calculated current distribution as a function of position in man exposed to 1-kV/m VLF-MF fields in free space (Guy and Chou, 1982).
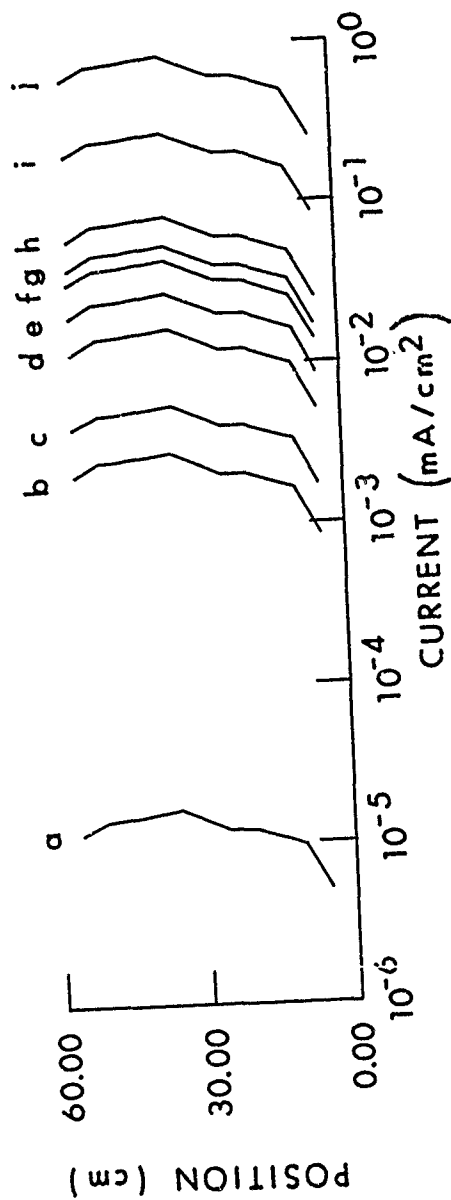
Figure 9.13. Calculated current density flowing through one arm. The exposure condition is the same as for Figure 9.12 (Guy and Chou, 1982).
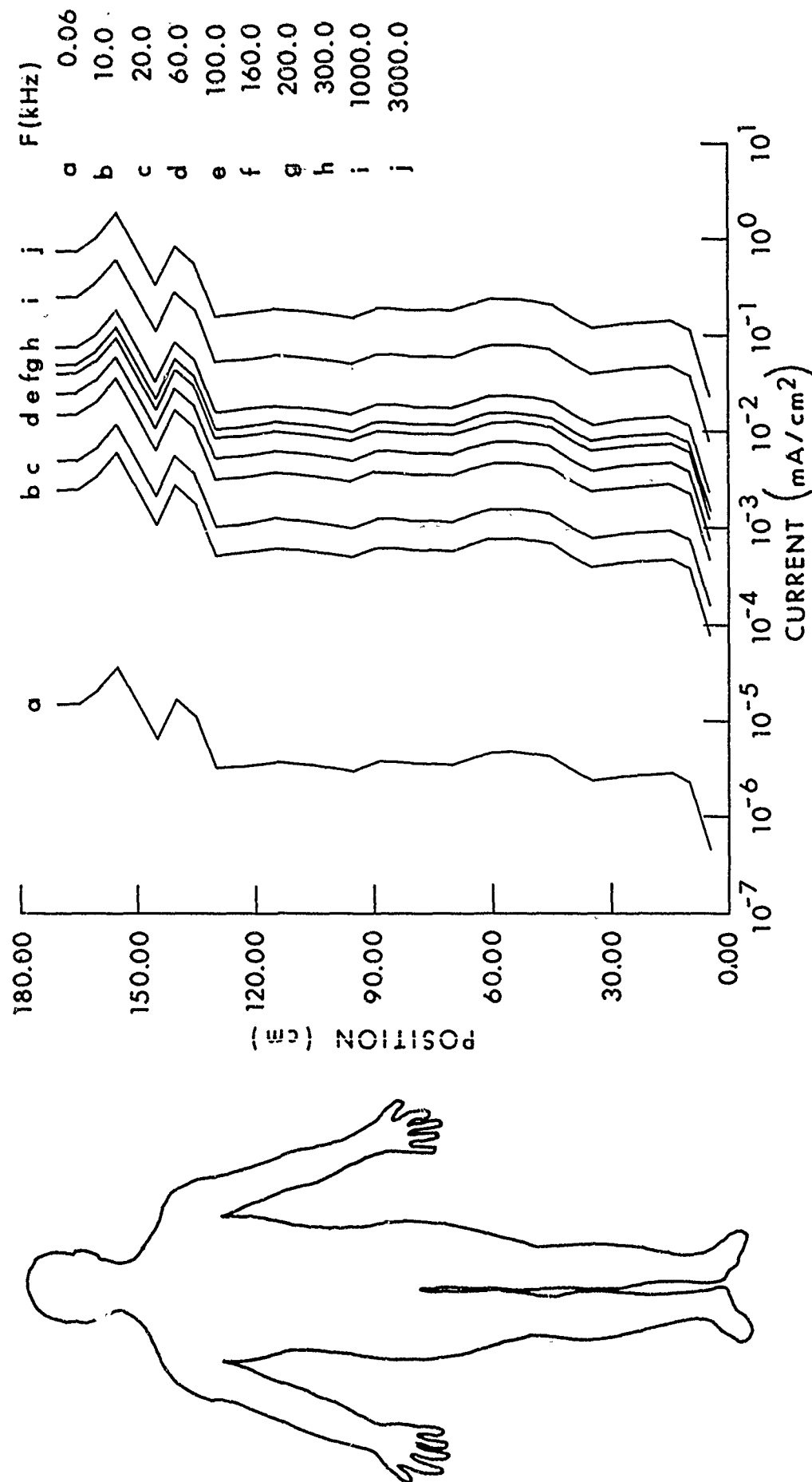
Figure 9.14. Calculated current distributions as a function of position in man exposed to 1-kV/m VLF-MF fields with feet insulated but hands grounded (Guy and Chou, 1982).
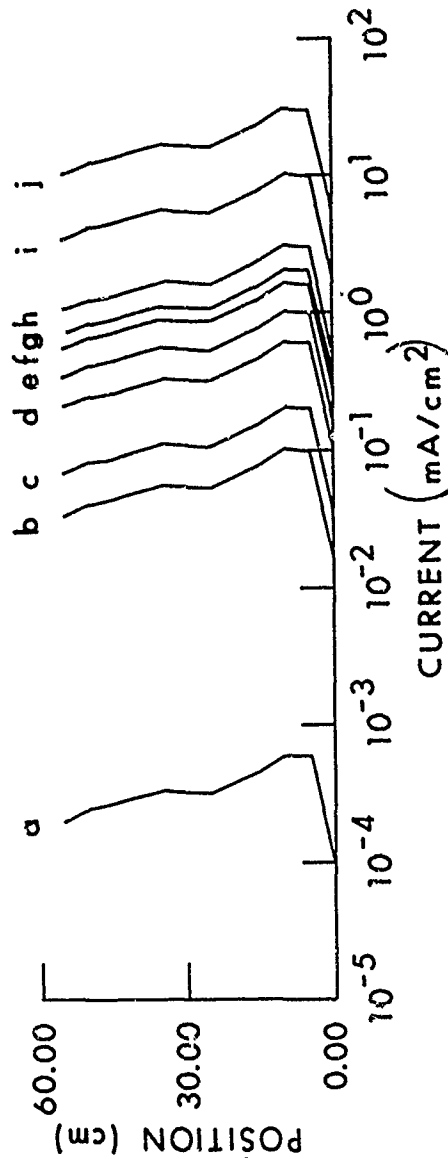
Figure 9.15. Calculated current density flowing through one arm. Exposure condition is the same as for Figure 9.14 (Guy and Chou, 1982).

- 9.29 -
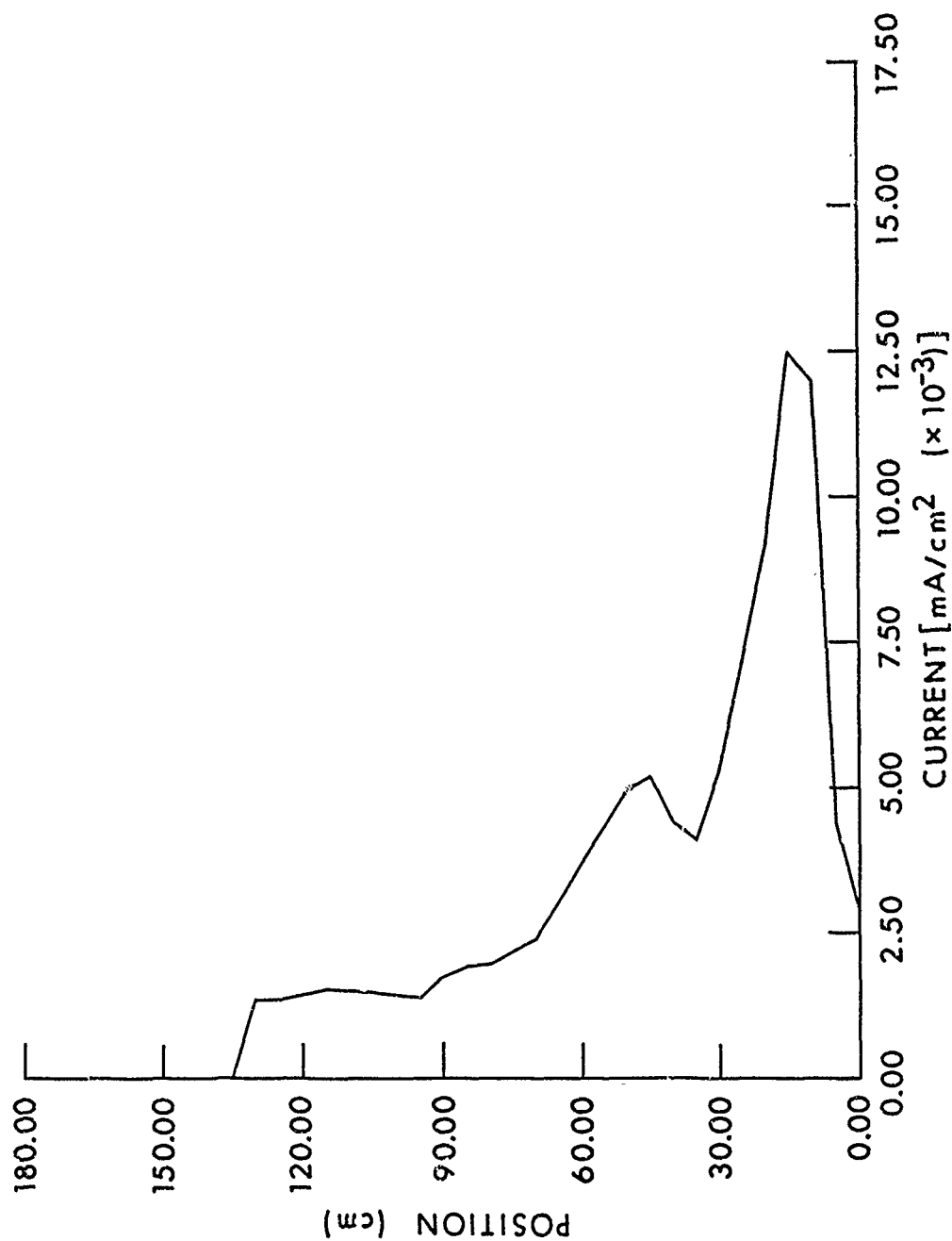
Figure 9.16. Calculated current distribution as a function of position in man with hand contacting a large object and with feet grounded. A 1-mA current is assumed to be flowing through the arm, thorax, and legs of the subject to ground, F = 60 Hz (Guy and Chou, 1982).
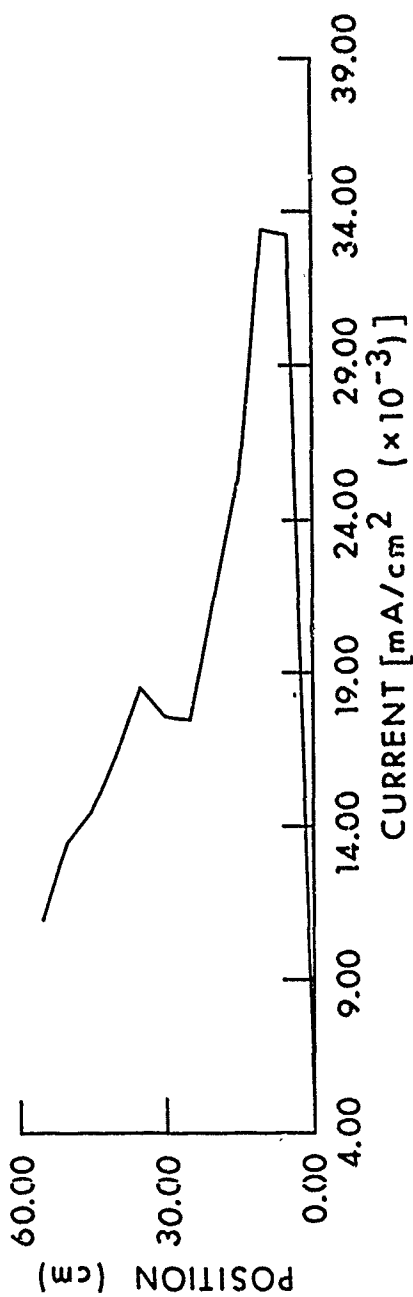
Figure 9.17. Calculated current density flowing through one arm. Exposure condition is same as for Fig. 9.16 (Guy and Chou, 1982).

CURRENT [mA/cm² (×10⁻³)]

POSITION (cm)

Table 9.13 gives regional and average SARs for various exposure conditions. Figure 9.18 shows measured values of the imaginary component of the permittivity (Tables 9.14 and 9.15; see Section 3.2.6 for the relationships of permittivity, conductivity, and loss factor) along with values of the real and imaginary components given in the first edition of this handbook. Figures 9.19 and 9.20 show average SARs of Table 9.13 compared with theoretical values. Further power absorption calculations are given in Table 9.16.

Figure 9.21 shows the maximum electric-field strength below levels of 1000 V/m that would violate any of the following conditions:

1. The maximum current through any body member contacting ground or an object should not exceed levels equivalent to those allowed by the National Electric Safety Code in the frequency range where shock hazards may occur.

2. Total possible current entering the body should not exceed 200 mA, for prevention of RF burns.

3. The 0.4-W/kg average and 8-W/kg maximum SAR recommended by the ANSI C95.1-1982 Standard shall not be exceeded.

According to the calculated data of Guy and Chou (1982), none of the conditions would be violated for exposure of persons isolated in free space at E-field strengths of 1 kV/m or below. Other conditions are shown in Figure 9.21.

TABLE 9.13. DISTRIBUTION OF POWER ABSORPTION (WATTS) IN MAN EXPOSED TO VLF-MF FIELDS: 1-kV/m EXPOSURE, E-FIELD PARALLEL LONG AXIS, 1-mA CURRENT ASSUMED FOR CONTACT WITH OBJECT (Guy and Chou, 1982)

	Feet Grounded	Free Space	Hand Grounded	Hand Contact with Object
Frequency = 0.060 kHz				
Lower leg	3.28E − 08	4.33E − 09	3.44E − 11	1.23E − 04
Upper leg	7.09E − 09	1.65E − 09	6.80E − 11	3.05E − 05
Lower torso	2.64E − 09	7.50E − 10	6.27E − 11	1.30E − 05
Midtorso	4.29E − 09	1.06E − 09	2.95E − 10	2.24E − 05
Upper torso	1.41E − 09	2.91E − 10	4.73E − 10	0.00E − 01
Neck	6.60E − 10	2.80E − 10	6.73E − 10	0.00E − 01
Head	4.76E − 10	2.30E − 10	5.80E − 10	0.00E − 01
Lower arm	4.53E − 10	9.46E − 11	6.47E − 08	2.00E − 04
Upper arm	1.06E − 09	2.21E − 10	3.81E − 08	1.18E − 04
Whole body	5.09E − 08	8.91E − 09	1.05E − 07	5.06E − 04
Avg SAR (W/kg)	6.41E − 10	1.12E − 10	1.32E − 09	6.38E − 06

TABLE 9.13. (continued)

	Feet Grounded	Free Space	Hand Grounded	Hand Contact with Object
Frequency = 10 kHz				
Lower leg	8.49E − 04	1.12E − 04	8.90E − 07	1.14E − 04
Upper leg	1.75E − 04	4.08E − 05	1.67E − 06	2.72E − 05
Lower torso	5.72E − 05	1.62E − 05	1.35E − 06	1.01E − 05
Midtorso	8.26E − 05	2.05E − 05	5.65E − 06	1.55E − 05
Upper torso	3.95E − 05	8.07E − 06	1.41E − 05	0.00E − 01
Neck	2.03E − 05	8.47E − 06	2.03E − 05	0.00E − 01
Head	1.03E − 05	5.02E − 06	1.25E − 05	0.00E − 01
Lower arm	1.20E − 05	2.51E − 06	1.70E − 03	1.89E − 04
Upper arm	2.89E − 05	6.03E − 06	1.04E − 03	1.16E − 04
Whole body	1.28E − 03	2.20E − 04	2.80E − 03	4.72E − 04
Avg SAR (W/kg)	1.61E − 05	2.77E − 06	3.52E − 05	5.49E − 06
Frequency = 20 kHz				
Lower leg	3.27E − 03	4.31E − 04	3.42E − 06	1.10E − 04
Upper leg	7.14E − 04	1.67E − 04	6.86E − 06	2.77E − 05
Lower torso	2.13E − 04	6.03E − 05	4.98E − 06	9.42E − 06
Midtorso	3.14E − 04	7.78E − 05	2.15E − 05	1.48E − 05
Upper torso	1.38E − 04	2.83E − 05	4.87E − 05	0.00E − 01
Neck	8.81E − 05	3.78E − 05	9.08E − 05	0.00E − 01
Head	4.34E − 05	2.11E − 05	5.25E − 05	0.00E − 01
Lower arm	4.67E − 05	9.75E − 06	6.61E − 03	1.83E − 04
Upper arm	1.12E − 04	2.35E − 05	4.05E − 03	1.13E − 04
Whole body	4.94E − 03	8.56E − 04	1.09E − 02	4.58E − 04
Avg SAR (W/kg)	6.22E − 05	1.08E − 05	1.37E − 04	5.77E − 06
Frequency = 60 kHz				
Lower leg	2.75E − 02	3.62E − 03	2.88E − 05	1.03E − 04
Upper leg	5.67E − 03	1.32E − 03	5.40E − 05	2.44E − 05
Lower torso	2.00E − 03	5.68E − 04	4.74E − 05	9.88E − 06
Midtorso	2.29E − 03	5.72E − 04	1.53E − 04	1.20E − 05
Upper torso	1.13E − 03	2.31E − 04	4.08E − 04	0.00E − 01
Neck	7.44E − 04	3.18E − 04	7.63E − 04	0.00E − 01
Head	3.24E − 04	1.58E − 04	3.90E − 04	0.00E − 01
Lower arm	3.84E − 04	8.03E − 05	5.47E − 02	1.69E − 04
Upper arm	9.09E − 04	1.90E − 04	3.28E − 02	1.01E − 04
Whole body	4.09E − 02	7.06E − 03	8.93E − 02	4.19E − 04
Avg SAR (W/kg)	5.15E − 04	8.89E − 05	1.12E − 03	5.28E − 06

TABLE 9.13. (continued)

	Feet Grounded	Free Space	Hand Grounded	Hand Contact with Object
Frequency = 100 kHz				
Lower leg	7.37E - 02	9.71E - 03	7.72E - 05	9.93E - 05
Upper leg	1.47E - 02	3.43E - 03	1.40E - 04	2.28E - 05
Lower torso	4.52E - 03	1.28E - 03	1.06E - 04	8.02E - 06
Midtorso	6.50E - 03	1.62E - 03	4.45E - 04	1.22E - 05
Upper torso	3.01E - 03	6.17E - 04	1.07E - 03	0.00E - 01
Neck	1.98E - 03	8.48E - 04	2.04E - 03	0.00E - 01
Head	8.44E - 04	4.11E - 04	1.02E - 03	0.00E - 01
Lower arm	9.96E - 04	2.08E - 04	1.45E - 01	1.61E - 04
Upper arm	2.17E - 03	4.53E - 04	7.82E - 02	8.69E - 05
Whole body	1.08E - 01	1.86E - 02	2.28E - 01	3.91E - 04
Avg SAR (W/kg)	1.37E - 03	2.34E - 04	2.87E - 03	4.92E - 06
Frequency = 160 kHz				
Lower leg	1.79E - 01	2.36E - 02	1.87E - 04	9.42E - 05
Upper leg	3.46E - 02	8.03E - 03	3.26E - 04	2.09E - 05
Lower torso	1.13E - 02	3.21E - 03	2.67E - 04	7.84E - 06
Midtorso	1.56E - 02	3.89E - 03	1.06E - 03	1.15E - 05
Upper torso	8.52E - 03	1.74E - 03	3.09E - 03	0.00E - 01
Neck	4.63E - 03	1.93E - 03	4.64E - 03	0.00E - 01
Head	2.08E - 03	1.01E - 03	2.52E - 03	0.00E - 01
Lower arm	2.41E - 03	5.04E - 04	3.53E - 01	1.53E - 04
Upper arm	5.17E - 03	1.08E - 03	1.86E - 01	8.09E - 05
Whole body	2.63E - 01	4.50E - 02	5.52E - 01	3.69E - 04
Avg SAR (W/kg)	3.32E - 03	5.66E - 04	6.95E - 03	4.64E - 06
Frequency = 200 kHz				
Lower leg	2.66E - 01	3.51E - 02	2.79E - 04	8.98E - 05
Upper leg	5.97E - 02	1.40E - 02	5.76E - 04	2.32E - 05
Lower torso	1.54E - 02	4.37E - 03	3.57E - 04	6.81E - 06
Midtorso	2.29E - 02	5.68E - 03	1.58E - 03	1.08E - 05
Upper torso	1.47E - 02	3.00E - 03	5.41E - 03	0.00E - 01
Neck	7.22E - 03	2.96E - 03	7.10E - 03	0.00E - 01
Head	2.73E - 03	1.33E - 03	3.29E - 03	0.00E - 01
Lower arm	3.55E - 03	7.42E - 04	5.30E - 01	1.47E - 04
Upper arm	7.06E - 03	1.47E - 03	2.54E - 01	7.07E - 05
Whole body	4.00E - 01	6.86E - 02	8.03E - 01	3.48E - 04
Avg SAR (W/kg)	5.03E - 03	8.64E - 04	1.01E - 02	4.39E - 06

TABLE 9.13. (continued)

	Feet Grounded	Free Space	Hand Grounded	Hand contact with Object
Frequency = 300 kHz				
Lower leg	6.35E – 01	8.37E – 02	6.65E – 04	9.51E – 05
Upper leg	1.27E – 01	2.96E – 02	1.20E – 03	2.19E – 05
Lower torso	3.90E – 02	1.11E – 02	9.16E – 04	7.68E – 06
Midtorso	5.62E – 02	1.40E – 02	3.84E – 03	1.17E – 05
Upper torso	2.58E – 02	5.28E – 03	9.16E – 03	0.00E – 01
Neck	1.70E – 02	7.30E – 03	1.76E – 02	0.00E – 01
Head	7.28E – 03	3.55E – 03	8.77E – 03	0.00E – 01
Lower arm	8.59E – 03	1.80E – 03	1.25E + 00	1.55E – 04
Upper arm	1.87E – 02	3.91E – 03	6.75E – 01	8.33E – 05
Whole body	9.35E – 01	1.60E – 01	1.97E + 00	3.74E – 04
Avg SAR (W/kg)	1.18E – 02	2.02E – 03	2.48E – 02	4.71E – 06
Frequency = 1000 kHz				
Lower leg	6.14E + 00	8.09E – 01	6.43E – 03	8.28E – 05
Upper leg	1.23E + 00	2.85E – 01	1.16E – 02	1.90E – 05
Lower torso	3.77E – 01	1.07E – 01	8.86E – 03	6.68E – 06
Midtorso	5.42E – 01	1.35E – 01	3.71E – 02	1.02E – 05
Upper torso	2.51E – 01	5.14E – 02	8.92E – 02	0.00E – 01
Neck	1.65E – 01	7.06E – 02	1.70E – 01	0.00E – 01
Head	7.03E – 02	3.43E – 02	8.47E – 02	0.00E – 01
Lower arm	8.30E – 02	1.73E – 02	1.21E + 01	1.34E – 04
Upper arm	1.81E – 01	3.78E – 02	6.52E + 00	7.25E – 05
Whole body	9.04E + 00	1.55E + 00	1.90E + 01	3.25E – 04
Avg SAR (W/kg)	1.14E – 01	1.95E – 02	2.40E – 01	4.10E – 06
Frequency = 3000 kHz				
Lower leg	5.12E + 01	6.75E + 00	5.36E – 02	7.66E – 05
Upper leg	1.02E + 01	2.38E + 00	9.68E – 02	1.76E – 05
Lower torso	2.99E + 00	8.47E – 01	7.00E – 02	5.88E – 06
Midtorso	4.48E + 00	1.11E + 00	3.08E – 01	9.36E – 06
Upper torso	2.09E + 00	4.28E – 01	7.44E – 01	0.00E – 01
Neck	1.38E + 00	5.89E – 01	1.42E + 00	0.00E – 01
Head	5.86E – 01	2.85E – 01	7.06E – 01	0.00E – 01
Lower arm	6.91E – 01	1.44E – 01	1.01E + 02	1.24E – 04
Upper arm	1.50E + 00	3.14E – 01	5.42E + 01	6.70E – 05
Whole body	7.51E + 01	1.28E + 01	1.58E + 02	3.01E – 04
Avg SAR (W/kg)	9.46E – 01	1.62E – 01	1.99E + 00	3.79E – 06
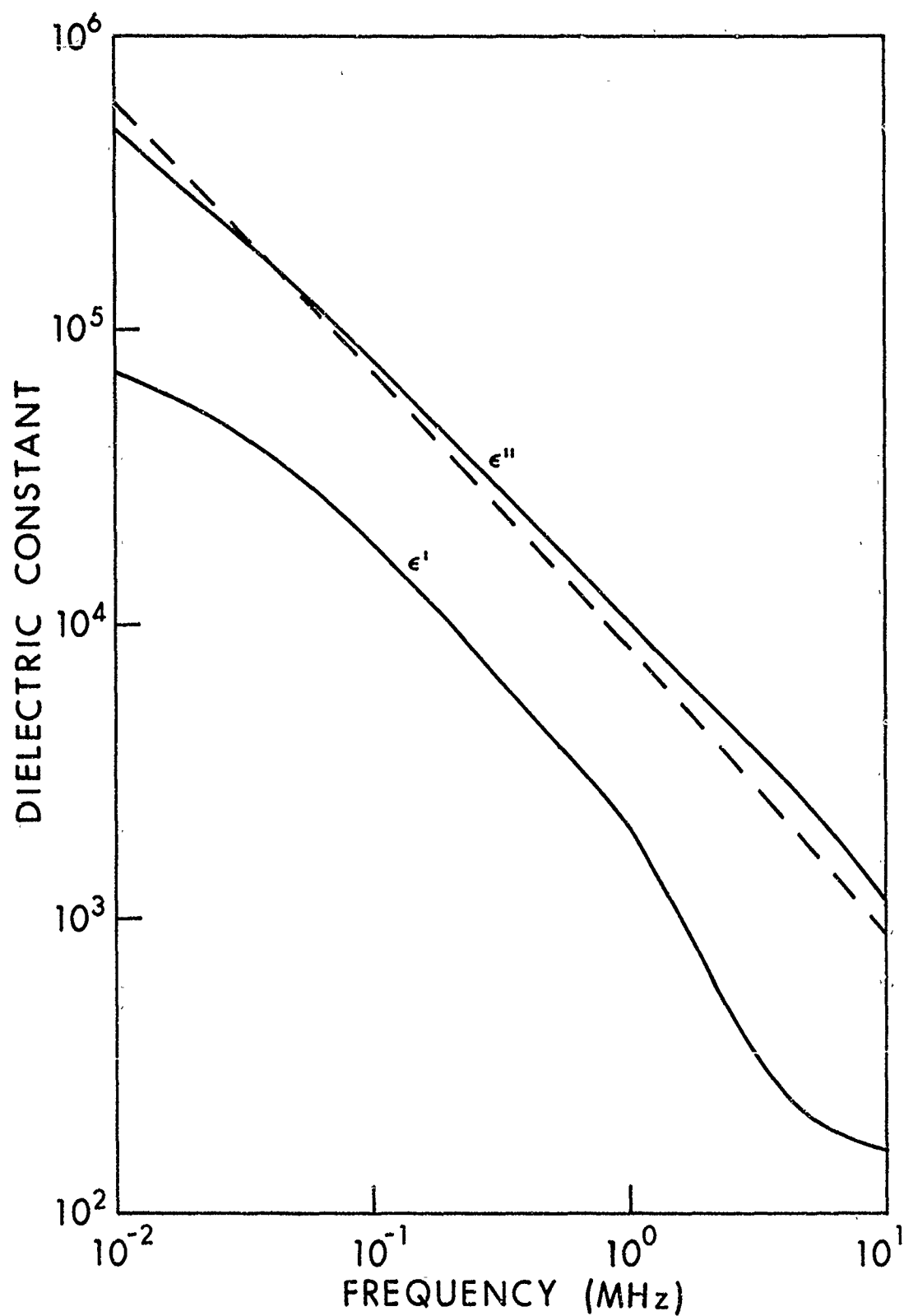
Figure 9.18. Real part, ε', and imaginary part, ε", of the dielectric con-
stant for high-water-content tissue. The dashed line is mea-
sured values (Guy and Chou, 1982). The other lines are values
given in the first edition of this handbook.

- 9.36 -

TABLE 9.14. AVERAGE APPARENT CONDUCTIVITY OF MAN BASED ON WHOLE-BODY IN VIVO MEASUREMENTS (S/m) (Guy and Chou, 1982)

Frequency (kHz)	Feet Grounded	Free Space	Hand Grounded	In Contact with Object
0.060	0.300	0.294	0.346	0.353
10.000	0.333	0.331	0.360	0.379
20.000	0.344	0.340	0.371	0.390
60.000	0.374	0.371	0.407	0.427
100.000	0.391	0.392	0.442	0.458
160.000	0.413	0.414	0.468	0.485
200.000	0.425	0.424	0.502	0.513
300.000	0.409	0.409	0.461	0.478
1000.000	0.470	0.470	0.530	0.549
3000.000	0.509	0.510	0.573	0.594

TABLE 9.15. AVERAGE APPARENT LOSS FACTOR OF MAN BASED ON WHOLE-BODY IN VIVO MEASUREMENTS (Guy and Chou, 1982)

Frequency (kHz)	Feet Grounded	Free Space	Hand Grounded	In Contact with Object
0.060	8.990E + 07	8.806E + 07	1.035E + 08	1.058E + 08
10.000	5.981E + 05	5.956E + 05	6.480E + 05	6.812E + 05
20.000	3.089E + 05	3.056E + 05	3.330E + 05	3.509E + 05
60.000	1.119E + 05	1.113E + 05	1.218E + 05	1.279E + 05
100.000	7.035E + 04	7.043E + 04	7.940E + 04	8.230E + 04
160.000	4.637E + 04	4.654E + 04	5.255E + 04	5.449E + 04
200.000	3.817E + 04	3.813E + 04	4.512E + 04	4.612E + 04
300.000	2.448E + 04	2.451E + 04	2.761E + 04	2.862E + 04
1000.000	8.442E + 03	8.453E + 03	9.528E + 03	9.876E + 03
3000.000	3.047E + 03	3.056E + 03	3.433E + 03	3.562E + 03
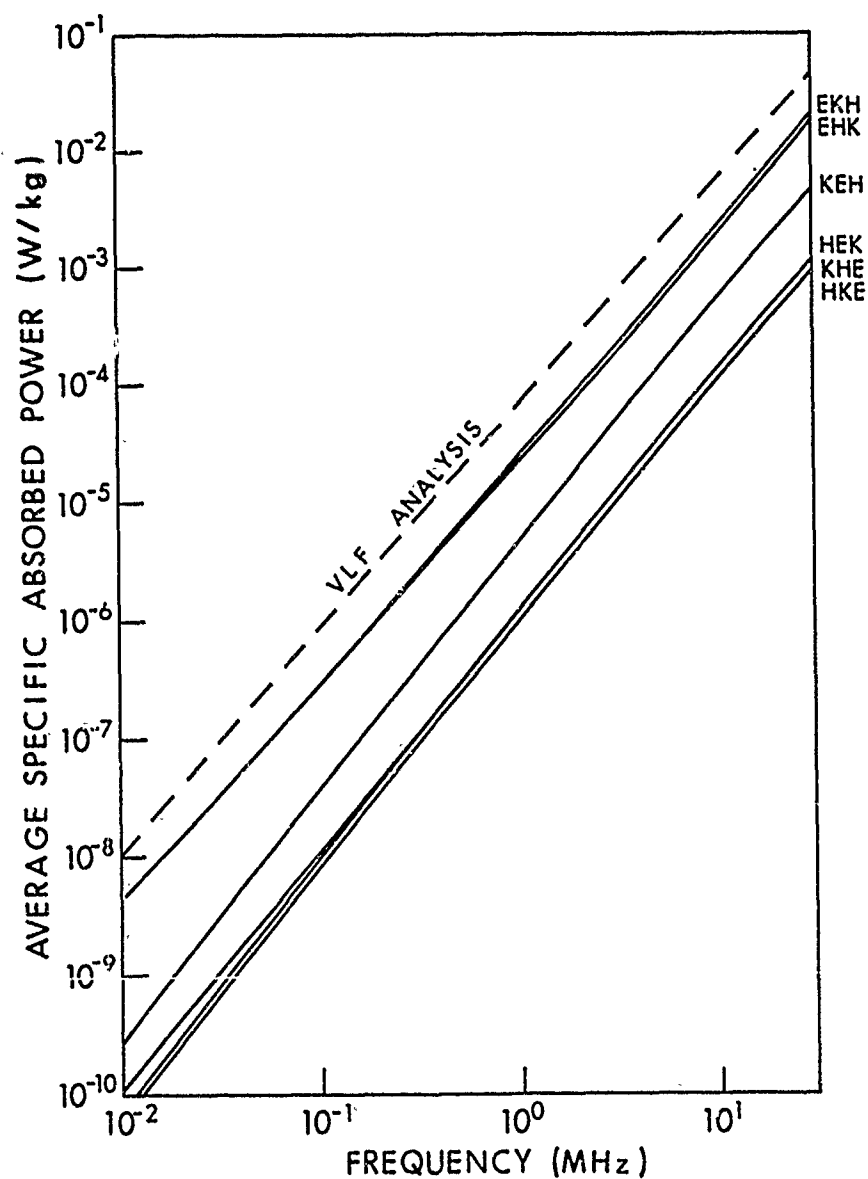
Figure 9.19. Comparison of calculated average SAR (obtained from VLF analysis) with average SAR (reported in the first edition of this handbook) of average absorbed power in an ellipsoidal model of an average man (Guy and Chou, 1982).
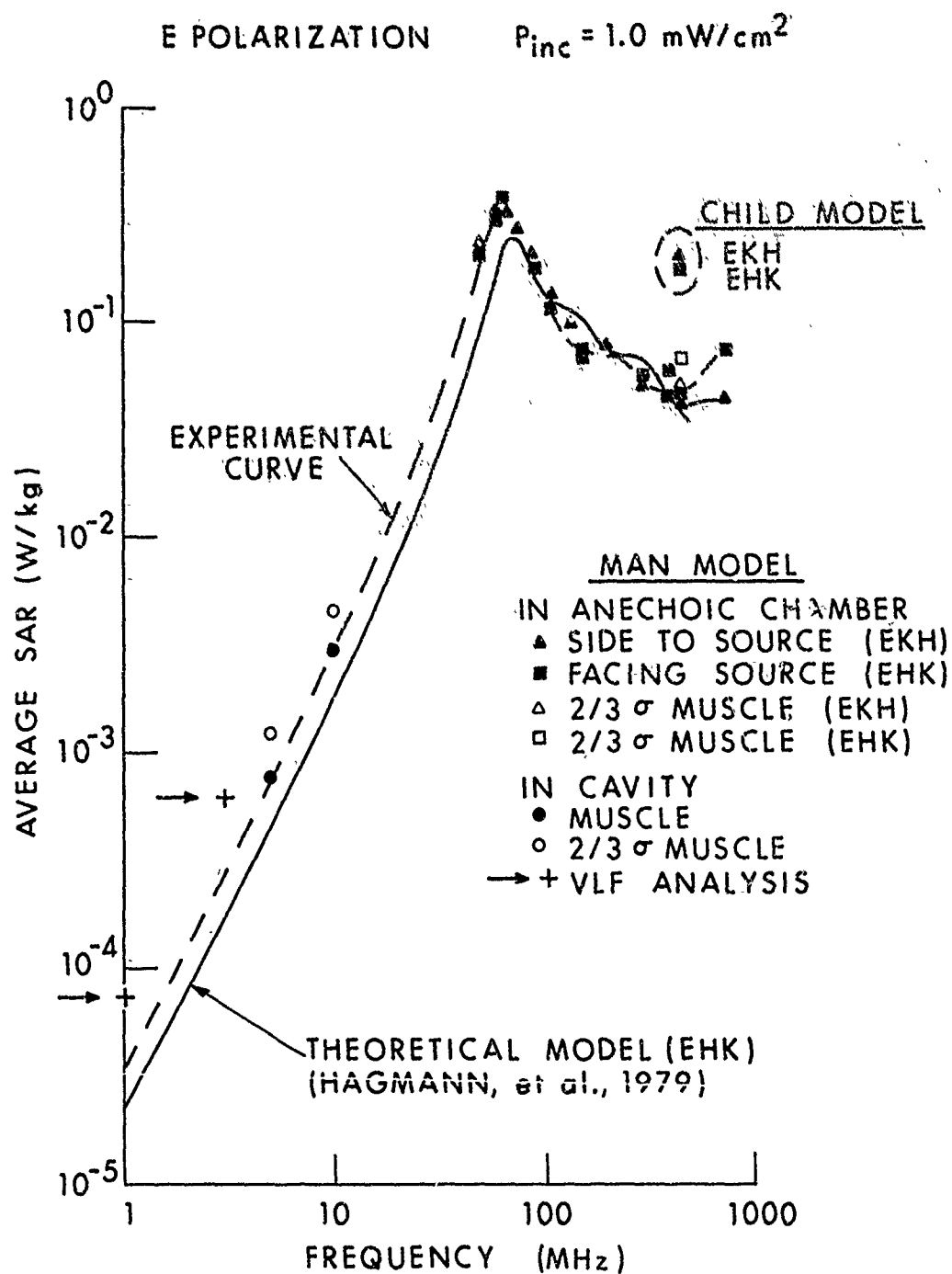
Figure 9.20. Comparison of theoretical and experimentally measured whole-body average SAR for realistic man models exposed at various frequencies. The experimental curve is measured results in scaled human-shaped models at simulated VLF frequencies (Guy and Chou, 1982).

TABLE 9.16.   DISTRIBUTION OF POWER ABSORPTION (WATTS) IN MAN, WITH
              FEET GROUNDED, EXPOSED TO 1-kV/m VLF-MF FIELDS WHILE IN
              CONTACT WITH VEHICLE (Guy and Chou, 1982)

	Car	Jeep Wagon	School Bus	Semitruck
Frequency = 0.060 kHz				
Lower leg	9.56E − 07	1.43E − 06	1.87E − 05	4.08E − 05
Upper leg	2.37E − 07	3.56E − 07	4.64E − 06	1.01E − 05
Lower torso	1.02E − 07	1.52E − 07	1.98E − 06	4.33E − 06
Midtorso	1.74E − 07	2.62E − 07	3.41E − 06	7.44E − 06
Upper torso	0.00E − 01	0.00E − 01	0.00E − 01	0.00E − 01
Neck	0.00E − 01	0.00E − 01	0.00E − 01	0.00E − 01
Head	0.00E − 01	0.00E − 01	0.00E − 01	0.00E − 01
Lower arm	1.55E − 06	2.33E − 06	3.04E − 05	6.63E − 05
Upper arm	9.16E − 07	1.37E − 06	1.79E − 05	3.91E − 05
Whole body	3.94E − 06	5.91E − 06	7.70E − 05	1.68E − 04
Avg SAR (W/kg)	4.96E − 08	7.44E − 08	9.70E − 07	2.12E − 06
Frequency = 10 kHz				
Lower leg	2.47E − 02	3.71E − 02	4.84E − 01	1.06E + 00
Upper leg	5.87E − 03	8.80E − 03	1.15E − 01	2.50E − 01
Lower torso	2.19E − 03	3.29E − 03	4.29E − 02	9.35E − 02
Midtorso	3.36E − 03	5.04E − 03	6.57E − 02	1.43E − 01
Upper torso	0.00E − 01	0.00E − 01	0.00E − 01	0.00E − 01
Neck	0.00E − 01	0.00E − 01	0.00E − 01	0.00E − 01
Head	0.00E − 01	0.00E − 01	0.00E − 01	0.00E − 01
Lower arm	4.08E − 02	6.12E − 02	7.98E − 01	1.74E + 00
Upper arm	2.50E − 02	3.75E − 02	4.89E − 01	1.07E + 00
Whole body	1.02E − 01	1.53E − 01	1.99E + 00	4.35E + 00
Avg SAR (W/kg)	1.28E − 03	1.93E − 03	2.51E − 02	5.48E − 02
Frequency = 20 kHz				
Lower leg	9.52E − 02	1.43E − 01	1.86E + 00	4.06E + 00
Upper leg	2.39E − 02	3.59E − 02	4.68E − 01	1.02E + 00
Lower torso	8.14E − 03	1.22E − 02	1.59E − 01	3.47E − 01
Midtorso	1.28E − 02	1.91E − 02	2.49E − 01	5.44E − 01
Upper torso	0.00E − 01	0.00E − 01	0.00E − 01	0.00E − 01
Neck	0.00E − 01	0.00E − 01	0.00E − 01	0.00E − 01
Head	0.00E − 01	0.00E − 01	0.00E − 01	0.00E − 01
Lower arm	1.59E − 01	2.38E − 01	3.10E + 00	6.76E + 00
Upper arm	9.73E − 02	1.46E − 01	1.90E + 00	4.15E + 00
Whole body	3.96E − 01	5.94E − 01	7.74E + 00	1.69E + 01
Avg SAR (W/kg)	4.99E − 03	7.48E − 03	9.75E − 02	2.13E − 01

TABLE 9.16. (continued)

	Car	Jeep Wagon	School Bus	Semitruck

Frequency = 60 kHz

	Car	Jeep Wagon	School Bus	Semitruck
Lower leg	8.00E – 01	1.20E + 00	1.56E + 01	3.41E + 01
Upper leg	1.90E – 01	2.84E – 01	3.71E + 00	8.09E + 00
Lower torso	7.69E – 02	1.15E – 01	1.50E + 00	3.28E + 00
Midtorso	9.32E – 02	1.40E – 01	1.82E + 00	3.98E + 00
Upper torso	0.00E – 01	0.00E – 01	0.00E – 01	0.00E – 01
Neck	0.00E – 01	0.00E – 01	0.00E – 01	0.00E – 01
Head	0.00E – 01	0.00E – 01	0.00E – 01	0.00E – 01
Lower arm	1.31E + 00	1.97E + 00	2.57E + 01	5.60E + 01
Upper arm	7.87E – 01	1.18E + 00	1.54E + 01	3.35E + 01
Whole body	3.26E + 00	4.89E + 00	6.37E + 01	1.39E + 02
Avg SAR (W/kg)	4.10E – 02	6.15E – 02	8.03E – 01	1.75E + 00

Frequency = 100 kHz

	Car	Jeep Wagon	School Bus	Semitruck
Lower leg	2.15E + 00	3.22E + 00	4.20E + 01	9.15E + 01
Upper leg	4.93E – 01	7.39E – 01	9.63E + 00	2.10E + 01
Lower torso	1.73E – 01	2.60E – 01	3.39E + 00	7.39E + 00
Midtorso	2.64E – 01	3.97E – 01	5.17E + 00	1.13E + 01
Upper torso	0.00E – 01	0.00E – 01	0.00E – 01	0.00E – 01
Neck	0.00E – 01	0.00E – 01	0.00E – 01	0.00E – 01
Head	0.00E – 01	0.00E – 01	0.00E – 01	0.00E – 01
Lower arm	3.49E + 00	5.23E + 00	6.81E + 01	1.49E + 02
Upper arm	1.88E + 00	2.82E + 00	3.67E + 01	8.01E + 01
Whole body	8.44E + 00	1.27E + 01	1.65E + 02	3.60E + 02
Avg SAR (W/kg)	1.06E – 01	1.59E – 01	2.08E + 00	4.53E + 00

Frequency = 160 kHz

	Car	Jeep Wagon	School Bus	Semitruck
Lower leg	5.21E + 00	7.81E + 00	1.02E + 02	2.22E + 02
Upper leg	1.16E + 00	1.73E + 00	2.26E + 01	4.93E + 01
Lower torso	4.33E – 01	6.50E – 01	8.47E + 00	1.85E + 01
Midtorso	6.36E – 01	9.54E – 01	1.24E + 01	2.71E + 01
Upper torso	0.00E – 01	0.00E – 01	0.00E – 01	0.00E – 01
Neck	0.00E – 01	0.00E – 01	0.00E – 01	0.00E – 01
Head	0.00E – 01	0.00E – 01	0.00E – 01	0.00E – 01
Lower arm	8.48E + 00	1.27E + 01	1.66E + 02	3.62E + 02
Upper arm	4.48E + 00	6.71E + 00	8.75E + 01	1.91E + 02
Whole body	2.04E + 01	3.06E + 01	3.99E + 02	8.70E + 02
Avg SAR (W/kg)	2.57E – 01	3.85E – 01	5.02E + 00	1.10E + 01

TABLE 9.16.   (continued)

	Car	Jeep Wagon	School Bus	Semitruck
Frequency = 200 kHz				
Lower leg	7.76E + 00	1.16E + 01	1.52E + 02	3.31E + 02
Upper leg	2.00E + 00	3.00E + 00	3.91E + 01	8.53E + 01
Lower torso	5.89E - 01	8.83E - 01	1.15E + 01	2.51E + 01
Midtorso	9.31E - 01	1.40E + 00	1.82E + 01	3.97E + 01
Upper torso	0.00E - 01	0.00E - 01	0.00E - 01	0.00E - 01
Neck	0.00E - 01	0.00E - 01	0.00E - 01	0.00E - 01
Head	0.00E - 01	0.00E - 01	0.00E - 01	0.00E - 01
Lower arm	1.27E + 01	1.91E + 01	2.49E + 02	5.43E + 02
Upper arm	6.11E + 00	9.16E + 00	1.19E + 02	2.61E + 02
Whole body	3.01E + 01	4.52E + 01	5.89E + 02	1.28E + 03
Avg SAR (W/kg)	3.79E - 01	5.69E - 01	7.42E + 00	1.62E + 01
Frequency = 300 kHz				
Lower leg	1.85E + 01	2.77E + 01	3.62E + 02	7.89E + 02
Upper leg	4.25E + 00	6.37E + 00	8.31E + 01	1.81E + 02
Lower torso	1.49E + 00	2.24E + 00	2.92E + 01	6.37E + 01
Midtorso	2.28E + 00	3.43E + 00	4.47E + 01	9.74E + 01
Upper torso	0.00E - 01	0.00E - 01	0.00E - 01	0.00E - 01
Neck	0.00E - 01	0.00E - 01	0.00E - 01	0.00E - 01
Head	0.00E - 01	0.00E - 01	0.00E - 01	0.00E - 01
Lower arm	3.01E + 01	4.51E + 01	5.88E + 02	1.28E + 03
Upper arm	1.62E + 01	2.43E + 01	3.17E + 02	6.91E + 02
Whole body	7.28E + 01	1.09E + 02	1.42E + 03	3.10E + 03
Avg SAR (W/kg)	9.17E - 01	1.37E + 00	1.79E + 01	3.91E + 01
Frequency = 1000 kHz				
Lower leg	1.79E + 02	2.68E + 02	3.50E + 03	7.63E + 03
Upper leg	4.10E + 01	6.15E + 01	8.02E + 02	1.75E + 03
Lower torso	1.44E + 01	2.17E + 01	2.82E + 02	6.16E + 02
Midtorso	2.21E + 01	3.31E + 01	4.31E + 02	9.40E + 02
Upper torso	0.00E - 01	0.00E - 01	0.00E - 01	0.00E - 01
Neck	0.00E - 01	0.00E - 01	0.00E - 01	0.00E - 01
Head	0.00E - 01	0.00E - 01	0.00E - 01	0.00E - 01
Lower arm	2.90E + 02	4.35E + 02	5.68E + 03	1.24E + 04
Upper arm	1.57E + 02	2.35E + 02	3.06E + 03	6.68E + 03
Whole body	7.03E + 02	1.05E + 03	1.38E + 04	3.00E + 04
Avg SAR (W/kg)	8.86E + 00	1.33E + 01	1.73E + 02	3.78E + 02

TABLE 9.16. (continued)

	Car	Jeep Wagon	School Bus	Semitruck
Frequency = 3000 kHz				
Lower leg	1.49E + 03	2.23E + 03	2.91E + 04	6.36E + 04
Upper leg	3.42E + 02	5.12E + 02	6.68E + 03	1.46E + 04
Lower torso	1.14E + 02	1.72E + 02	2.24E + 03	4.88E + 03
Midtorso	1.82E + 02	2.73E + 02	3.56E + 03	7.76E + 03
Upper torso	0.00E − 01	0.00E − 01	0.00E − 01	0.00E − 01
Neck	0.00E − 01	0.00E − 01	0.00E − 01	0.00E − 01
Head	0.00E − 01	0.00E − 01	0.00E − 01	0.00E − 01
Lower arm	2.42E + 03	3.63E + 03	4.73E + 04	1.03E + 05
Upper arm	1.30E + 03	1.95E + 03	2.55E + 04	5.55E + 04
Whole body	5.85E + 03	8.77E + 03	1.14E + 05	2.49E + 05
Avg SAR (W/kg)	7.37E + 01	1.10E + 02	1.44E + 03	3.14E + 03
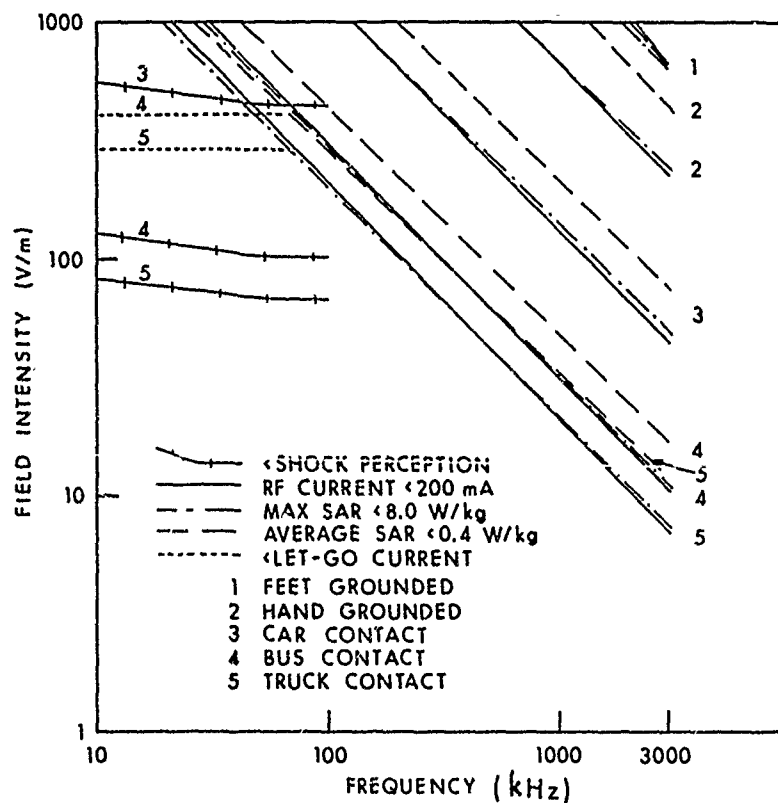
Figure 9.21. Required restrictions of VLF-MF electric-field strength to prevent biological hazards related to shock, RF burns, and SAR exceeding ANSI C95.1 criteria (Guy and Chou, 1982).

CHAPTER 10. THERMAL RESPONSES OF MAN AND ANIMALS

This chapter was revised by Eleanor R. Adair, Ph.D., Associate Fellow, John B. Pierce Foundation Laboratory, Yale University. It includes material written by James L. Lords, Ph.D., and David K. Ryser, Ph.D., from previous editions of this handbook and new material added by Dr. Adair.

10.1. INTRODUCTION

The study of thermoregulation--the responses that maintain a constant internal body temperature--has flourished since Claude Bernard (1865) first demonstrated that the temperature of the blood varies in different parts of the body. Bernard established that food taken into the body is metabolized in the tissues and that the bloodstream distributes the released energy throughout the body. The relative constancy of the internal body temperature was part of his concept of the constancy of the milieu intérieur, a necessity for optimal functioning and health of the organism. He pointed out that the vasomotor nerves control the transfer of heat from deep in the body to the skin and that this is a mechanism of the utmost importance to thermoregulation in homeotherms. Bernard's discoveries underlie the modern science of thermophysiology and help us to understand how man and animals can remain relatively independent of the thermal environment, even when that environment contains potent or unusual thermal stressors.

Thermal loads on the body can result from changes in metabolic heat production and from changes in the characteristics of the environment (temperature, ambient vapor pressure, air movement, insulation, and other environmental variables that may alter the skin's temperature). Thermalizing energy deposited in body tissues by exposure to radiofrequency electromagnetic radiation can be a unique exception to the normal energy flows in the body, although metabolic activity in skeletal muscle can deposit large amounts of thermal energy directly into deep tissues.

All living organisms respond vigorously to changes in body temperature. Cold-blooded animals, called ectotherms because they derive thermal energy mainly from outside the body, regulate their body temperatures largely through behavioral selection of a preferred microclimate. Warm-blooded animals, called endotherms because they can produce heat in their bodies and

dissipate it to the environment through physiological processes, often rely largely on behavioral thermoregulation. Behavior is important to thermoregulation because it is mobilized rapidly and aids the conservation of body energy and fluid stores. When behavioral responses--which include the thermostatic control of the immediate microenvironment--are difficult or impossible, the body temperature of endothermic species is regulated by the autonomic mechanisms that control heat production, the distribution of heat within the body, and the avenues and rate of heat loss from the body to the environment.

Other descriptive terms currently used include "temperature conformer" for ectotherm and "temperature regulator" for endotherm. Some thermal physiologists prefer a different classification, based on the quality of the thermoregulation: A homeotherm normally regulates its body temperature within rather narrow limits by varying its metabolic rate, heat and moisture loss, or position in the environment; a poikilotherm may allow its body temperature to vary over a considerable range, and regulates that variation by its position in the environment. Complications for the latter scheme arise when one considers hibernators (endotherms that periodically become poikilothermic) or ectotherms that are effectively homeothermic by virtue of efficient behavioral thermoregulation. The terms "endotherm" and "ectotherm" are used in the material that follows.

10.2. HEAT EXCHANGE BETWEEN ORGANISM AND ENVIRONMENT

Radiofrequency radiation may be regarded conveniently as part of the thermal environment to which man and other endotherms may be exposed. Figure 10.1 is a schematic representation of the sources of heat in the body and of the different routes by which thermal energy may be transferred between the body and the environment. Heat is produced in the body through metabolic processes (M) and may also be passively generated in body tissues by absorption of RFR (A_{RFR}). If the body temperature is to remain stable, this thermal energy must be continually transferred to the environment. As outlined above, the balance between the production and loss of thermal energy is so regulated by behavioral and autonomic responses that minimal variation occurs in the body temperature of an endotherm.

Energy may be lost (Figure 10.1) by evaporation of water from the respiratory tract (E_{res}) or from the skin (E_{sw}), by dry-heat transfer from the skin surface via radiation (Q_r) or convection (Q_c), and by doing work (W = force × distance) on the environment. Heat transfer by conduction is usually insignificant in most species unless they are recumbent. When the environment is thermally neutral, dry-heat loss predominates in the form of convective transfer to the air and radiant transfer to the surrounding surfaces. A small amount of heat is always lost by the diffusion of water through the skin (not shown in the figure).
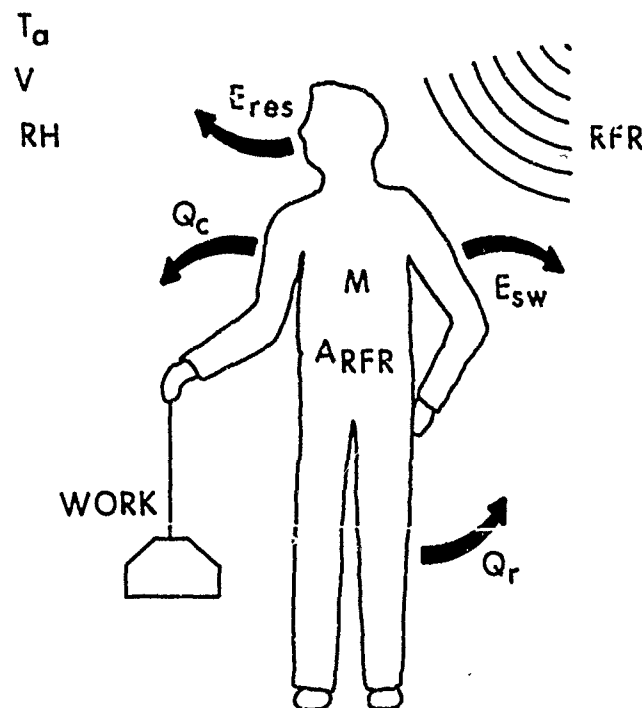
Figure 10.1. A schematic diagram of the sources of body heat (including radiofrequency radiation) and the 'r ortant energy flows between man and the environment. The body is in thermal equilibrium if the rate of heat loss equals the rate of heat gain. Figure modified from Berglund (1983).

When the temperature of the environment rises above thermoneutrality, or during vigorous exercise or defervescence, the evaporation of sweat (E_{sw}) dissipates large amounts of body heat. Evaporative water loss through sweating occurs in man, the great apes, certain other primates, and a few other species such as horses and camels. Many animals—such as dogs, cats, and rabbits—use panting (increased respiratory frequency coupled with copious saliva production) to lose heat by evaporation. Other species, such as the rodents, have no such physiological mechanisms and must rely on behavioral responses which include seeking shade, burrows, or aqueous environments and/or grooming their bodies with water, urine, or saliva to aid evaporative cooling. Table 10.1 includes several thermoregulatory characteristics of certain animals.

The rate of heat loss from an endotherm is governed by the thermal characteristics of the environment, as indicated in Figure 10.1; these include not only the air temperature (T_a) but also the air movement (v) and humidity (RH). Two other environmental variables that affect heat transfer (not shown in the figure) are the mean radiant temperature of surrounding surfaces, especially those close to the body, and the amounts of insulation (fur, fat, feathers, clothing).

When the thermal energy produced in the body (including that derived from absorbed RFR) is equal to that exchanged with the environment, the body is said to be in thermal balance. Under these conditions the body temperature remains stable. When heat production exceeds heat dissipation, thermal energy is stored in the body and the body temperature rises (hyperthermia). On the other hand, when more heat is transferred to the environment than can be produced or absorbed, the body temperature falls (hypothermia).

TABLE 10.1.   THERMOREGULATORY CHARACTERISTICS OF ANIMALS

Species	Body Temperature (°C) Normal	Min.	Max.	Thermoregulatory Mechanisms Sweating	Shivering	Panting	Thermo-preferendum[a] (°C)	Thermo-neutral Zone (°C)	Air-Temperature Survival Limits (°C) Low	High
Man*[b] Homo sapiens	37	27	42	Yes	Yes	No	23-26 (50% RH)	25-28	0	50
Rhesus monkey[c] Macaca mulatta	36-39	25	43	Yes	Yes	No	—	25-31	—	40
Patas monkey[d] Erythrocebus patas	38-40	—	42-43	Yes	Yes	No	—	20-40	<0	>55
Squirrel monkey[e] Saimiri sciureus	38-39	25	43	Yes	Yes	No	35-36	26-35	0	40
Dog[f] Canis familiaris	38-39	24	42	No	Yes	Yes	12-16	18-25	-80**	42-58
Cat[g] Felix domesticus	38-39	19	42	No	Yes	Yes	—	32-38	-10	41
Domestic pig[h] Sus scrofa	36.5-37	—	42	No	Yes	Yes	30-32[†]	15-27	-27	35
Sheep (fleeced)[h] Ovis aries	38-39	—	42	Yes	Yes	Yes	—	10-20	-45	32
Rabbit[i] Oryctolagus cuniculus	39	20	42	No	Yes	Yes	—	15-25	-29	32
Guinea pig[i] Cavis porcellus	39	17	43	No	Yes	Yes	29	30-31	-15	32
Rat[jk] Rattus norvegicus	37-38	20	42	No	Yes	No	29-30	28-30	-3	40
Mouse[j] Mus musculus	37	20	42-44	No	Yes	No	32	30-33	-5	37

* Assumes man is lightly clothed, sedentary in still air.
** Value for Alaskan husky is well below that for most other subspecies.
† Values given are for young animals.
a Cabanac, M. (1983)
b Elizondo, R. (1977)
c Johnson, G. S., and Elizondo, R. S. (1979)
d Mahoney, S. (1980)

e Stitt, J. T., and Hardy, J. D. (1971)
f Adams, T. C. (1971)
g Adams, T., et al. (1970)
h Whittow, G. C. (1971)
i Gonzalez, R. R., et al. (1971)
j Hart, J. S. (1971)
k Berry, J. J., et al. (1984)

10.3. THE THERMOREGULATORY PROFILE

The particular thermoregulatory effector response mobilized at any given time, and its vigor, will depend on the prevailing thermal environment. The ambient temperature is frequently the only environmental variable specified in research reports, but the specification of air movement and relative humidity is equally important. Figure 10.2, a schematic thermoregulatory profile of a typical endotherm, illustrates how the principal autonomic responses of heat production and heat loss depend on the ambient temperature. The responses are considered to be steady state rather than transient, and the ambient air is considered to have minimal movement and water content. Three distinct zones can be defined in terms of the prevailing autonomic adjustment. Below the lower critical temperature (LCT), thermoregulation is accomplished by changes in metabolic heat production, other responses remaining at minimal strength. As the ambient temperature falls further and further below the LCT, heat production increases proportionately. In a cool environment RF energy absorbed by an endotherm will spare the metabolic system in proportion to the field strength and will have no effect on other autonomic responses.

At ambient temperatures above the LCT, metabolic heat production is at the low resting level characteristic of the species, evaporative heat loss is minimal, and changes in thermal conductance accomplish thermoregulation. Conductance is a measure of heat flow from the body core to the skin and reflects the vasomotor tone of the peripheral vasculature. As the constricted peripheral vessels begin to dilate, warm blood from the body core is brought to the surface so that the heat may be lost to the environment by radiation and convection. These vasomotor adjustments take place within a range of ambient temperatures, called the thermoneutral zone (TNZ), that is peculiar to each species. Insofar as they are known, the TNZs for animals commonly used in the laboratory are indicated in Table 10.1. If an endotherm at thermoneutrality is exposed to RFR, augmented vasodilation may occur so that the heat generated in deep tissues can be quickly brought to the skin surface for dissipation to the environment.

The upper limit of the TNZ is known as the upper critical temperature (UCT). At this ambient temperature the endotherm is fully vasodilated and
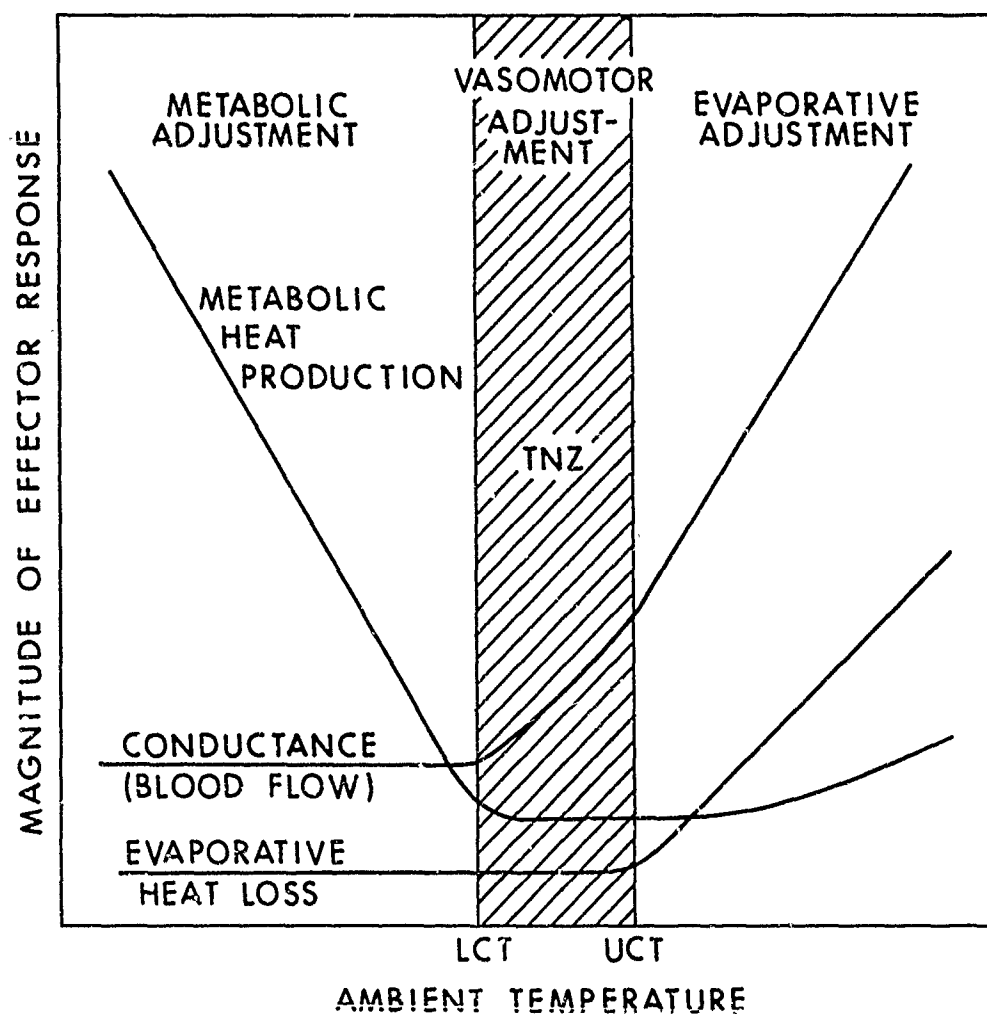
Figure 10.2. Thermoregulatory profile of a typical endothermic
organism to illustrate the dependence of principal
types of autonomic responses on environmental tem-
perature. LCT = lower critical temperature; UCT =
upper critical temperature; TNZ = thermoneutral zone.

dry-heat loss (by convection and radiation) is maximal. Further increases in ambient temperature provoke the mobilization of heat loss by evaporation, either from the skin (sweating) or the respiratory tract (panting). Man and certain other mammals have the ability to sweat copiously to achieve thermo-regulation in hot environments. It is reasonable to assume that if these species were exposed to RFR at ambient temperatures above the UCT, their sweating rate would increase in proportion to the field strength. Other mammals, notably the rodents, neither sweat nor pant and when heat stressed must depend on behavioral maneuvers to achieve some degree of thermoregula-tion; if the opportunity for behavioral thermoregulation is curtailed, these animals can rapidly become hyperthermic when heat stressed. The basic thermo-regulatory profile of the selected laboratory animal must therefore be con-sidered in detail as part of the experimental design of any research into the biological consequences of exposure to RFR; changes in any measured thermo-regulatory response will depend on the functional relationship between that response and the prevailing ambient temperature. Other types of responses also may be indirectly affected by the thermoregulatory profile if they inter-fere with efficient thermoregulation (e.g., food and water consumption).

Man exhibits profound adaptability in the face of environmental thermal stress, particularly in warm environments. Figure 10.3 illustrates some of the fundamental data collected by Hardy and DuBois (1941) for nude men and women exposed in a calorimeter to a wide range of ambient temperatures. Because of the vigorous responses of heat production and heat loss, the rectal temperature varies less than 1°C across a 20°C range of calorimeter tempera-ture. The TNZ is extremely narrow, occurring at about 28°C in the calorimeter and closer to 30°C in the natural environment. Above the TNZ, evaporative heat loss (whole-body sweating) is initiated that can attain rates of 2-3 L/h and up to 10-15 L/d (Wenger, 1983). Assuming normal hydration, it is diffi-cult to increase metabolic heat production (by exercise) to levels that cannot be dissipated by sweating, unless the ambient temperature or vapor pressure is very high. Since human evaporative heat loss is controlled by both peripheral and internal thermal signals (Nadel et al., 1971), only an extraordinarily hostile thermal environment, which includes a source of RFR, can be expected to seriously threaten man's thermoregulatory system. Way et al. (1981)
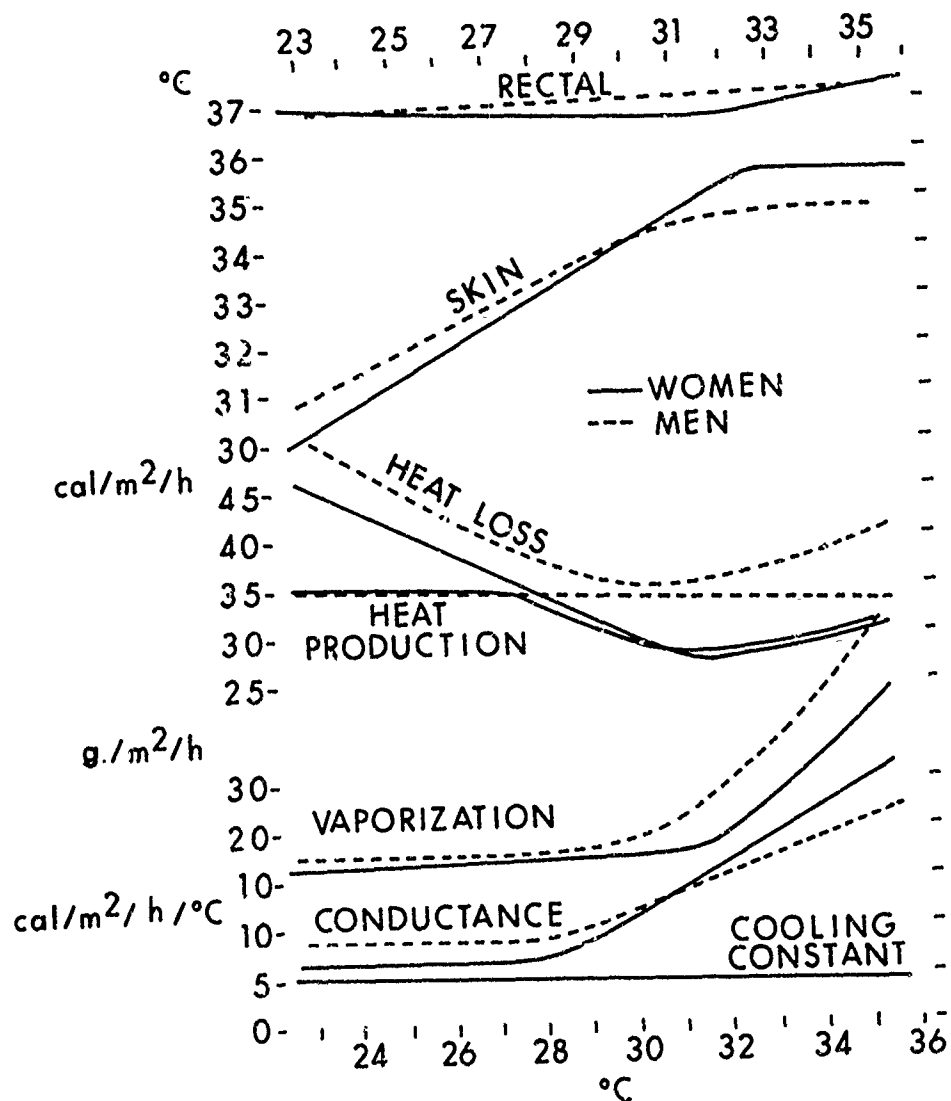
Figure 10.3. Thermoregulatory profile of nude humans equilibrated in a calorimeter to different ambient temperatures. Data adapted from Hardy and DuBois (1941).

and others (Stolwijk, 1983) have predicted minimal increases in brain and body temperatures during local absorption of significant amounts of RF energy, because of the rapid mobilization of evaporative heat loss and a significant increase in tissue blood flow. Under the assumption that RF exposure provides a thermal stress comparable to exercise (Nielsen and Nielsen, 1965) or an ambient temperature well above the TNZ, such response changes would be predicted from knowledge of the human thermoregulatory profile in Figure 10.3. On the other hand, significant temperature elevations in certain body sites (e.g., the legs, arms, and neck) have been predicted by a two-dimensional heat-transfer model of man exposed to a unilateral planewave at resonant and near-resonant frequencies (Spiegel et al., 1980). These predictions should be verified in animal models or, preferably, in human subjects exposed to comparable fields.

10.4. BODY HEAT BALANCE

The most important principle involved in the study of autonomic thermoregulation of endotherms is the first law of thermodynamics--the law of conservation of energy (Bligh and Johnson, 1973). In the steady state the heat produced in the body is balanced by the heat lost to the environment, so heat storage is minimal. This relationship can be expressed by a heat-balance equation:

$$M \pm W = R + C + E \pm S \tag{10.1}$$

in which

       M = rate at which thermal energy is produced through metabolic processes

       W = power, or rate at which work is produced by or on the body

       R = heat exchange with the environment via radiation

       C = heat exchange with the environment via convection

       E = rate of heat loss due to the evaporation of body water

       S = rate of heat storage in the body

All terms in Equation 10.1 must be in the same units, e.g., watts (the unit used throughout this handbook). Physiologists commonly express these quantities in kilocalories per hour, which can be converted to watts by multiplying by 1.163, the conversion factor. As Equation 10.1 is written, negative values of R, C, and E may all cause a rise in the body temperature; positive values may cause a fall. Work (W) is positive when accomplished by the body (e.g., riding a bicycle), and this potential energy must be subtracted from metabolic energy (M) to find the net heat (H) developed within the body. When W is negative (e.g., walking downstairs), this heat is added to M. While W may be a significant factor for humans or beasts of burden, it may be considered negligible for other endotherms, particularly in a laboratory setting. Usually evaporative heat loss (E) is positive; when E is negative, condensation occurs and thermal injury is possible.

Because heat exchange by radiation, convection, or evaporation is always related in some way to the surface area of the body, each term in Equation 10.1 is usually expressed in terms of energy per unit surface area, e.g., watts per square meter. The most commonly used measure of the body surface area of humans is that proposed by DuBois (1916),

$$A_D = 0.202 \ w^{0.425} \ h^{0.725} \tag{10.2}$$

where

A_D = DuBois surface in square meters

w = body mass in kilograms

h = height in meters

As noted by Kleiber (1961), h for similar body shapes is proportional to a mean linear dimension equal to $w^{1/3}$. Therefore, to compare humans of different sizes, Equation 10.2 may be generalized as

$$A_D = k_1 \ w^{0.425} \ k_2 \ w^{1/3 \times 0.725}$$

$$= k_1 \ k_2 \ w^{(0.425 + 0.242)}$$

$$= k_1 \ k_2 \ w^{2/3} \tag{10.3}$$

The ratio of surface area to body mass varies between species, so it is difficult to establish a general rule for the determination of surface area. Many methods have been devised for the direct measurement of the surface area of experimental animals, most of which are inaccurate to some degree. In nearly all cases, the surface area is some function of $w^{2/3}$.

Although Equation 10.1 has no term for heat transfer through <u>conduction</u> (which is usually insignificant under normal conditions), conduction combined with mass transfer forms the significant mode of heat transfer called <u>convection</u>. Convective heat transfer in air (C) is a linear function of body surface area (A), and the convective heat transfer coefficient $\left(h_c\right)$ is a function of ambient air motion to the 0.6 power $\left(v^{0.6}\right)$. The amount of heat the body loses through convection depends on the difference between the surface temperature of the skin $\left(\bar{T}_{sk}\right)$ and the air temperature, usually taken as the dry-bulb temperature $\left(T_{db}\right)$. The value of the heat-transfer coefficient depends on certain properties of the surrounding medium, such as density and viscosity, as well as a shape/dimension factor for the body. Clothing complicates the analysis and is often evaluated in terms of insulation (clo) units.

Heat transfer by <u>radiation</u> is independent of ambient temperature. The wavelengths of the radiation exchanged between two objects are related to their respective surface temperatures; the net heat transfer by radiation is proportional to the difference between their absolute temperatures to the fourth power and to the relative absorptive and reflective properties of the two surfaces. In general, the net radiant-heat exchange (where h_r = radiant-heat-transfer coefficient) between a nude man and the environment involves estimation of the mean radiant temperature (MRT). MRT $\left(\text{alternate symbol } T_r\right)$ can be derived from the temperature $\left(T_g\right)$ of a blackened hollow sphere of thin copper (usually 0.15-m diameter) having heat-transfer characteristics similar to those for the human body (Woodcock et al., 1960):

$$\text{MRT} = \left(1 + 0.222 \ v^{0.5}\right)\left(T_g - T_{db}\right) + T_{db} \quad °C \quad\quad (10.4)$$

Clothing complicates this analysis as it does heat transfer by other modes. Heating by RFR may further complicate the analysis of radiant-heat exchange

between a man and his environment, although Berglund (1983) has demonstrated that this complex situation can be analyzed by conventional methods.

The final avenue of heat loss available to man is that due to the evaporation of water. The latent heat of vaporization of water at normal body temperature is 0.58 kcal/g; the body loses this amount of heat when water is evaporated from its surfaces. Water from the respiratory surfaces is continually being lost in the expired air. Water also continually diffuses through the skin; this is called insensible water loss or insensible perspiration. These two avenues contribute equally to a heat loss that totals about 25% of the resting metabolic heat production of a man in a thermoneutral environment. However, the major avenue of evaporative heat loss in man is sweating, which depends on the vapor pressures of the air and the evaporating surface and is thus a direct function of both dry bulb (T_{db}) and wet bulb (T_{wb}) temperatures. When $T_{db} = T_{wb}$, the air is at 100% relative humidity and thus no water can be evaporated from the skin surface; at less than 100% relative humidity, evaporation can occur. The interrelationships between these variables can be determined from a standard psychrometric chart (ASHRAE Handbook, 1981). In Equation 10.1, E represents the evaporative cooling allowed by the environment (E_{max}) and is in no way related to the level of evaporative cooling required (E_{req}) by the man.

10.5. METABOLIC RATES OF MAN AND ANIMALS

Because the metabolic heat production per unit body mass, or "specific metabolic rate," varies greatly with body size and proportion (somatotype), several measures of this variable are in wide use. Figure 10.4 is a log-log plot of metabolic heat production versus body mass for several animals and man. The solid line with a slope of 0.75 reveals a strong correlation between body mass raised to the 0.75 power and metabolic heat production. This empirical observation has prompted researchers to adopt power per unit body mass, in units of watts per kilogram, as the standard metric for animal metabolic rate.
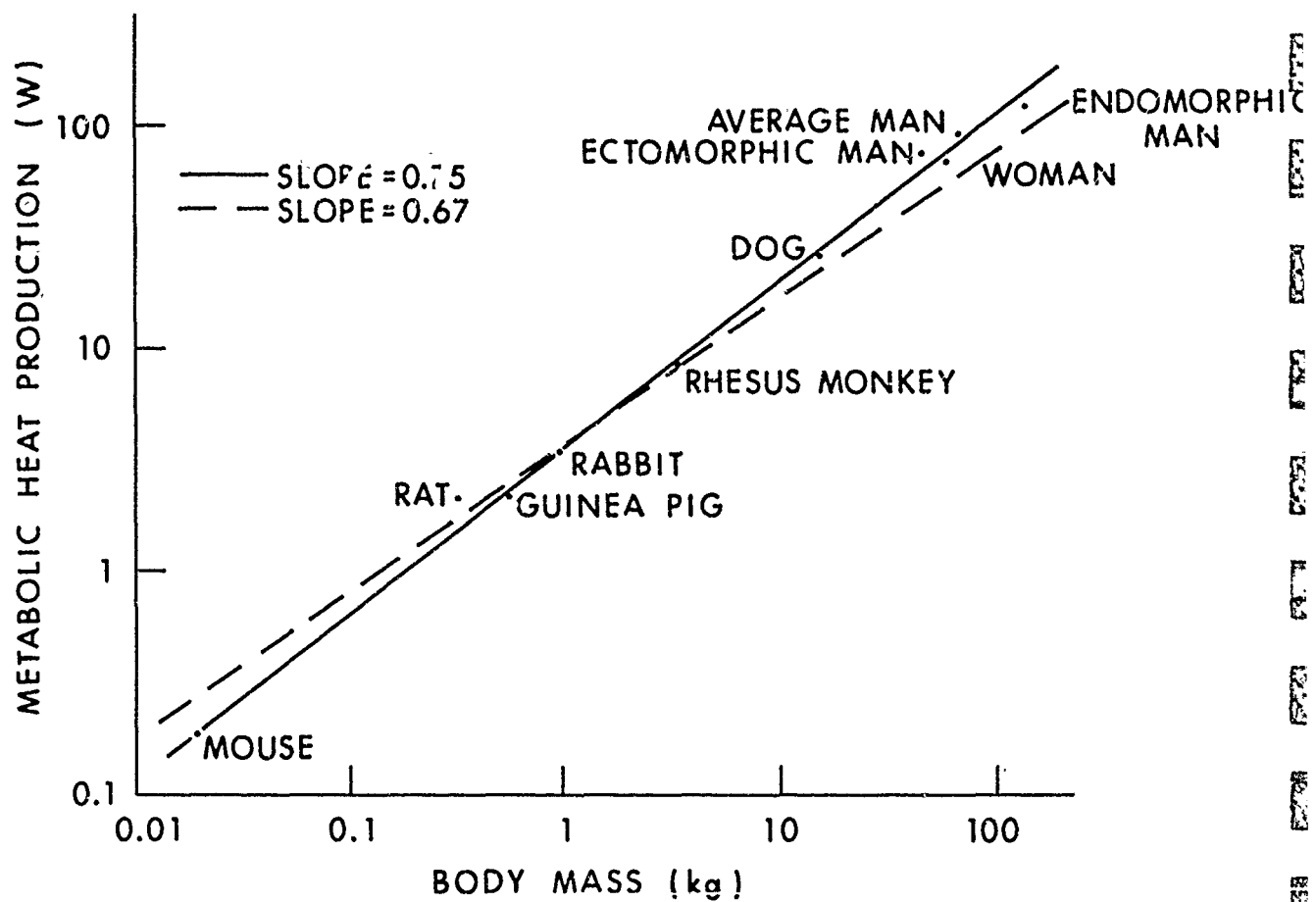
Figure 10.4. Logarithm of total metabolic heat production plotted against logarithm of body mass. (Data taken from Tables 10.2 and 10.4.)

The metabolic heat production (M) of placental animals (most mammals) can be estimated by the following formula:

$$M = 3.39 \, w^{0.75} \quad W \tag{10.5}$$

where w is the mass of the animal in kilograms. Another useful equation relates the metabolic heat produced by the body to the rate of oxygen consumption (ASHRAE Handbook, 1981):

$$M = [0.23(RQ) + 0.77](5.87)(\dot{V}_{O_2})(60/A_D) \quad W/m^2 \tag{10.6}$$

where

RQ = the respiratory quotient, or ratio of $\dot{V}_{CO_2}$ produced to $\dot{V}_{O_2}$ inhaled; RQ in man may vary from 0.83 (resting) to over 1.0 (heavy exercise)

$\dot{V}_{O_2}$ = oxygen consumption in liters/minute at standard conditions (0°C, 760 mmHg)

5.87 = the energy equivalent of 1 L of oxygen at standard conditions in watt-hours/liter when RQ = 1.

Formulas for the metabolic heat production of other classes of animals can be found in an article by Gordon (1977).

Another widely accepted form for expressing metabolic heat production is power per unit surface area. The dashed line in Figure 10.4, with a slope of 0.67, represents how surface area increases with mass for geometrically similar shapes. This corresponds to the approximate formula for the body surface area (SA) of these animals:

$$SA = 0.09 \, w^{0.67} \quad m^2 \tag{10.7}$$

Although surface area does not describe the animal data as well as $w^{0.75}$, it is as suitable a measure as any for human metabolic heat production. For accurate calculations of human metabolic heat production, the DuBois area (Equation 10.2) should be used.

10.5.1. Human Data

Metabolic heat production (M) is often called "metabolic rate" (MR). Table 10.2 lists resting metabolic rates for normal healthy humans of varying age and somatotype. The specific metabolic rate (SMR; W/kg) is clearly seen to be a function of body size and shape.

The basal metabolic rate (BMR) is defined as the heat production of a human in a thermoneutral environment (33°C), at rest mentally and physically and at a time exceeding 12 h from the last meal. The standard BMR for man is about 250 ml O_2/min, or 84 W, or 0.8 MET $\left(\text{where 1 MET} = 58.2 \text{ W/m}^2 \right)$. The BMR also corresponds to about 1.2 W/kg for a 70-kg "standard" man. The BMR is altered by changes in active body mass, diet, and endocrine levels but probably not by living in the heat (Goldman, 1983). In resting man most of the heat is generated in the core of the body—the trunk, viscera, and brain—despite the fact that these regions represent only about one-third of the total body mass. This heat is conducted to the other body tissues, and its elimination from the body is controlled by the peripheral vasomotor system.

Table 10.3 shows the wide variation of metabolic rates during various activities. All of these data are given for a healthy normal 20- to 24-yr-old male except as noted. The range of metabolic rate for humans—considering work performed and assorted physiological variables such as age, sex, and size—is roughly 40 to 800 W/m^2 (1 to 21 W/kg for "standard" man), depending on physical fitness and level of activity. The influence of age and sex on the metabolic rate of humans is shown in Figures 10.5 and 10.6. Other factors that may influence the metabolic rate are endocrine state, diet, race, pregnancy, time of day, and emotional state. If deep-body temperature is altered, from either heat storage in warm environments or febrile disease, a comparable change occurs in the metabolic rate (Stitt et al., 1974). Similar changes occur when deep-body temperature rises during exposure to RFR (Adair and Adams, 1982).

TABLE 10.2. RESTING METABOLIC RATES FOR NORMAL HEALTHY HUMANS OF SPECIFIC AGE AND SOMATOTYPE (adapted from Ruch and Patton, 1973)

	Average Weight (kg)	Average Height (m)	Body Surface Area (m^2)	Metabolic Rate W	Metabolic Rate (W/m^2)	Metabolic Rate (W/kg)
Man (20-24 yr old)						
Average	70.00	1.75	1.85	88.2	47.7	1.26
Ectomorphic	47.18	1.76	1.57	74.9	47.7	1.59
Endomorphic	141.00	1.76	2.50	119.3	47.7	0.85
Woman (20-24 yr old)						
Average	61.14	1.61	1.64	70.4	42.9	1.15
Ectomorphic	43.09	1.45	1.31	56.2	42.9	1.30
Endomorphic	88.45	1.73	2.02	86.7	42.9	0.98
Average male child						
10 yr old	32.20	1.38	1.12	64.5	57.6	2.00
5 yr old	19.50	1.12	0.78	48.0	61.6	2.46
1 yr old	10.00	0.74	0.43	27.5	64.0	2.75

TABLE 10.3. VARIATION OF METABOLIC RATE WITH ACTIVITY FOR A NORMAL 20-24-YEAR-OLD MALE[*] (adapted from Ruch and Patton, 1973)

Activity	Metabolic Rate (W)	Metabolic Rate (W/m^2)	Metabolic Rate (W/kg)	METS[**]
Sleeping	75	41	1.1	0.7
Resting quietly (~basal conditions)	88.2	48	1.3	0.8
Sitting upright	110	58	1.5	1.0
Standing, clerical work (Newburgh, 1949)	130	70	1.8	1.2
Walking 3 mph	300	160	4.3	2.7
Bicycling	540	290	7.7	5.0
Swimming	750	410	11.0	7.0
Maximum sustained exercise	750	410	11.0	7.0
Running (sprinting)	1300	700	18.0	12.0
Maximum peak exercise (Astrand and Rodahl, 1970):				
Average male	850-1600	460-860	12-23	
Average female	700-1100	410-700	11-18	
Trained male athlete	2000	1080	29.0	

[*] Female included under "maximum peak exercise."
[**] 1 MET = 58.2 W/m^2 (this column is not included in Ruch and Patton, 1973).
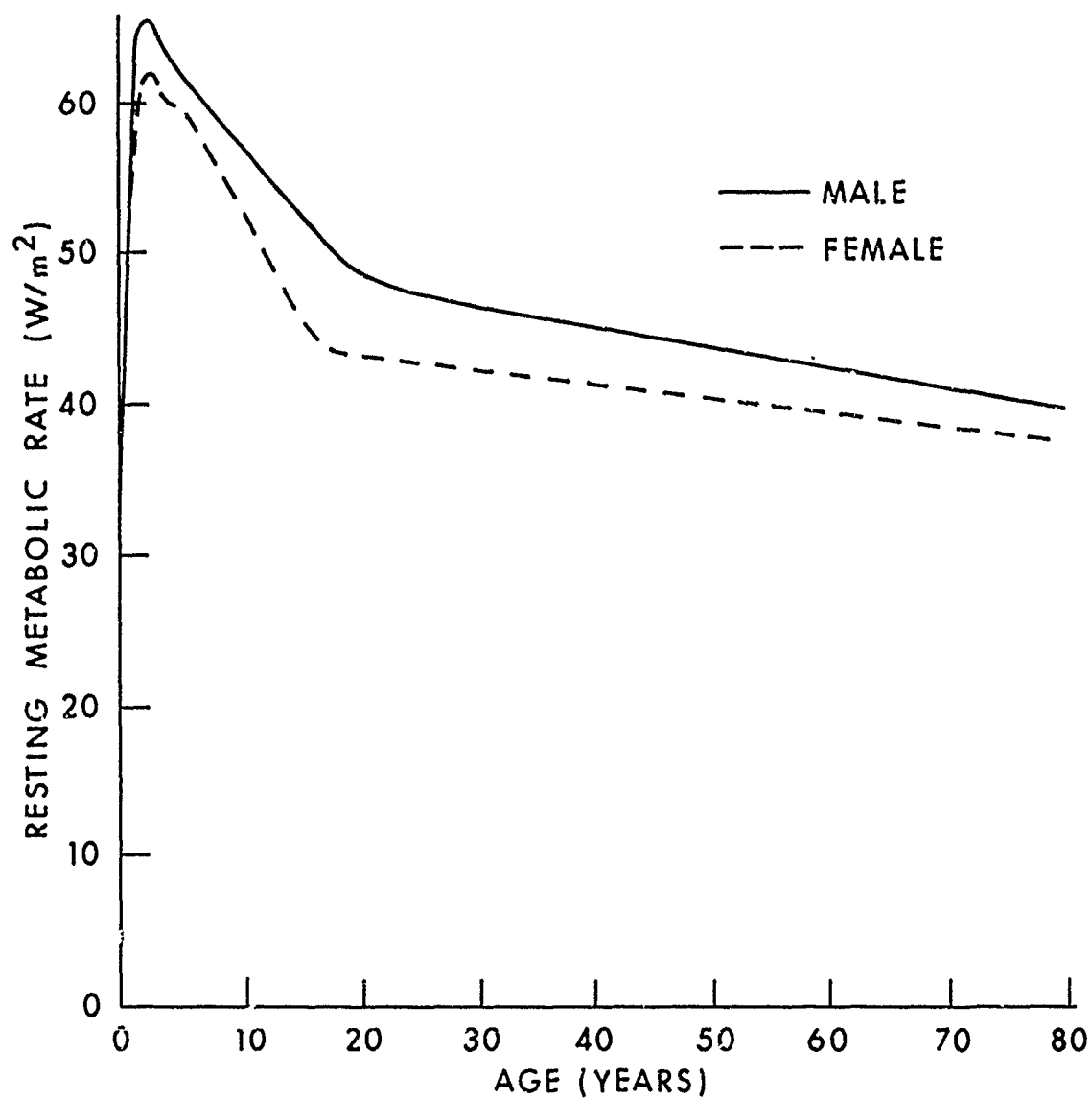
Figure 10.5.   Variation of human resting metabolic rate (RMR),
              with age and sex, expressed as power per unit
              surface area.   Data from Ruch and Patton (1973).
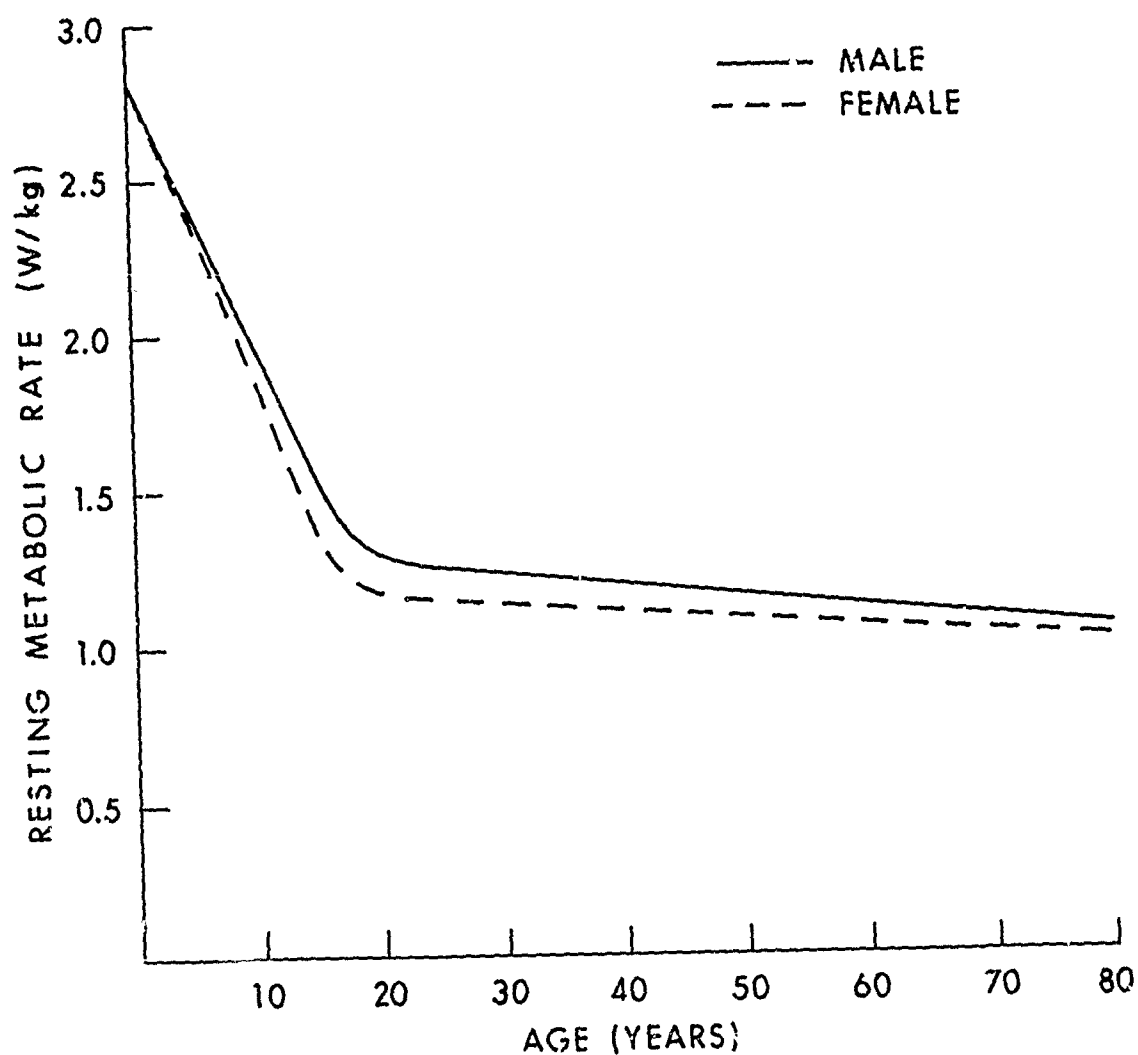
Figure 10.6. Variation of human resting metabolic rate (RMR),
with age and sex, expressed as power per unit body
mass. Data from Figure 10.5 converted by means
of average height and weight in Dreyfuss (1967).

10.5.2. Animal Data

Resting metabolic rates (MR) for some adult laboratory animals are shown in Table 10.4 in three different forms: total MR for the weight given, specific MR, and standardized MR.

TABLE 10.4. RESTING METABOLIC RATES FOR ADULT LABORATORY ANIMALS

Animal (Reference)	Average Weight (kg)	Metabolic Rate[*]		
		W	W/kg	$W/kg^{0.75}$
Rhesus monkey[**] (Bourne, 1975)	3.5	8.26	2.36	4.34
Squirrel monkey (Rosenblum and Cooper, 1968)	1.1	4.93	4.47	4.59
Baboon[**] (Bourne, 1975)	13.0	40.7	2.26	4.66
Dog (Benedict, 1938)				
German shepherd	32.0	44.20	1.38	3.29
Brittany spaniel	15.9	26.20	1.65	3.29
Beagle	13.5	23.20	1.72	3.29
Rabbit (Heilbrun, 1952)	1.0	3.57	3.57	3.57
Guinea pig[**] (Altman and Dittmer, 1968)	0.58	2.26	3.83	3.40
Rat[**] (Altman and Dittmer, 1968)				
Small	0.11	0.94	8.51	4.90
Medium	0.32	2.08	6.51	4.90
Large	0.52	3.00	5.77	4.90
Mouse (Pennycuik, 1967)				
Small	0.015	0.15	10.00	3.50
Medium	0.020	0.19	9.31	3.50
Large	0.025	0.22	8.88	3.50

[*] W = total MR for given weight; W/kg = specific MR; $W/kg^{0.75}$ = standardized MR.

[**] MR data given as totals for 24-h period.

A rough idea of metabolic heat production can be gained from an animal's oxygen consumption $\left(\dot{V}_{O_2}\right)$ by using the formula

$$M = 335 \; \dot{V}_{O_2} \qquad W \qquad\qquad (10.8)$$

where $\dot{V}_{O_2}$ = liters of oxygen consumed per minute. The energy equivalent of oxygen is approximately 4.8 kcal/L O_2 for a typical animal diet, and the respiratory quotient (RQ) is approximately 0.85.

10.6. AVENUES OF HEAT LOSS

Changes in vasomotor tonus and evaporation of body water through active sweating (or panting in certain endotherms) are both mechanisms of body heat loss. As detailed in Section 10.3 (Figures 10.2 and 10.3), vasomotor control normally operates to regulate the body temperature when an endotherm is in a thermoneutral environment, i.e., within the TNZ. Sweating (or panting) is activated in warmer environments and during exercise and defervescence.

10.6.1. Vasomotor Control

Convective heat transfer via the circulatory system is controlled by the sympathetic nervous system. Below the LCT, vasoconstriction of the peripheral vasculature in arm, leg, and trunk skin minimizes heat loss from the skin, leaving a residual conductive heat flow of 5-9 W/m per °C difference between body core and skin. For a body in the TNZ, when the peripheral vessels are vasodilated, each liter of blood at 37°C that flows to the skin and returns 1°C cooler allows the body to lose about 1 kcal, or 1.16 W·h, of heat (Hardy, 1978). During vigorous exercise in the heat, peripheral blood flow can increase almost tenfold; this increase is essential to eliminate the increased metabolic heat produced in the working muscles.

Tissue conductance (K) represents the combined effect of two channels of heat transfer in the body--conductive heat transfer through layers of muscle and fat and convective heat transfer by the blood. Tissue thermal conductance is defined as the rate of heat transfer per unit area during a steady state when a difference of 1°C is maintained across a layer of tissue $\left(W/m^2 \cdot °C\right)$

Johnson, 1973). Although K cannot be measured directly in the human organism, it can be estimated for resting humans under the assumption that all the heat is produced in the core of the body and is transferred to the skin and thence to the environment. Thus

$$H_L = K\left(T_{re} - \bar{T}_{sk}\right) \qquad W/m^2 \qquad (10.9)$$

in which H_L represents the heat loss (neglecting that lost through respiration), T_{re} is rectal or core temperature, and $\bar{T}_{sk}$ is the average skin temperature. In the cold (22-28°C), conductance is minimal for both men and women, ranging between 6 and 9 $W/m^2 \cdot °C$. In warm environments conductance increases rapidly, and women show a faster increase than men (Cunningham, 1970; also see Figure 10.3).

10.6.2. Sweating

Evaporation of sweat from the skin surface efficiently removes heat even in environments warmer than the skin. In this case, evaporative heat loss must take care of both metabolic heat and that absorbed from the environment by radiation and convection. We have no reason to believe that thermalizing energy from absorbed RFR will be dealt with any differently than heat produced by normal metabolic processes or absorbed by exposure to warm environments.

Normal secretory functioning of the approximately 2.5 million sweat glands on the skin of a human being is essential to the prevention of dangerous hyperthermia. Secretion is controlled by the sympathetic nervous system and occurs when the ambient temperature rises above 30-31°C or the body temperature rises above 37°C. Local sweating rate also depends on the local skin temperature (Nadel et al., 1971). Physically fit individuals and those acclimated to warm environments sweat more efficiently and at a lower internal body temperature than normal (Nadel et al., 1974). Dehydration or increased salt intake will alter plasma volume and decrease sweating efficiency (Greenleaf, 1973).

The maximum sweat rate for humans and the length of time it can be maintained are limited. The maximum rate of sweat production by an average

man is about 30 g/min. If the ambient air movement and humidity are low enough for all this sweat to be evaporated, the maximum cooling will be about 675 W/m^2; however, conditions are not usually this ideal--some sweat may roll off the skin or be absorbed by layers of clothing. A more practical limit of cooling is 350 W/m^2, or 6 METS, which represents about 17 g/min for the average man (ASHRAE Handbook, 1981).

10.7. HEAT-RESPONSE CALCULATIONS

10.7.1. Models of the Thermoregulatory System

The operating characteristics of the thermoregulatory system appear to be similar to those of an automatic control system involving negative feedback. The body temperature of endotherms appears to be regulated at a set, or reference, level. Temperature sensors located in the skin and various other parts of the body detect temperature perturbations and transmit this information to a central integrator, or controller, that integrates the sensory information, compares the integrated signal with the set point, and generates an output command to the effector systems for heat production or loss. The responses thus mobilized tend to return the body temperature back to the set level.

These hypothetical constructs aid our understanding of thermoregulatory processes and let us formulate simulation models that can be used to predict human response to a wide variety of thermal stressors. Models have been of many types, from verbal descriptions to highly sophisticated electrical analogs and mathematical models. Hardy (1972) gives a comprehensive account of the development of modeling in thermal physiology. Many simulation models have been used to predict human responses to RFR (Farr et al., 1971). Of particular relevance are the theoretical models of Mumford (1969) and Guy et al. (1973) that use a heat-stress index to describe man's response to particular environmental and RF heat loads. A model by Emery et al. (1976b) uses several sweat rates to calculate the thermal response of the body to absorbed RFR. A model of Stolwijk and Hardy (1966) has been combined with simulations of RFR energy deposition by Stolwijk (1980) and Way et al. (1981) to

demonstrate that the rise in local temperatures in the human body, especially in the brain, may be much less than anticipated during the localized deposition of RF energy, even when the radiation is focused on the hypothalamus. Greatly enhanced evaporative heat loss, skin blood flow, and conductance serve to protect individual body tissues during RFR energy deposition. On the other hand, a two-dimensional, combined RF-heat-transfer model developed by Spiegel et al. (1980) predicts rapid localized temperature increments in the thigh of a nude male resting at thermoneutrality and exposed to 80 MHz at 50 mW/cm^2, and similar temperature increments in the steady state at power densities as low as 10 mW/cm^2. Adding to this model the altered tissue blood flow for temperatures in excess of 40°C may modify these predictions.

10.7.2. Data for Heat-Response Calculations

Much is known about the upper limits of human tolerance to hot, humid environments that contain no source of RFR (Givoni and Goldman, 1972; Provins et al., 1962). Knowing what the human tolerance time would be for a given SAR would be useful. This section describes calculations of the approximate SAR that will produce a critical internal body temperature in a standard man exposed for 60 min in a specified hot and humid environment.

The body's two physiological mechanisms that deal with heat stress, vasomotor and sudomotor, are each a complex function of many variables. The problem can be simplified, however, if we assume that the body is calling upon its maximum thermoregulatory capacity. Under most conditions of severe thermal stress, evaporative cooling is limited by the evaporation rate, not the sweat rate since the maximum sweat rate is over 2 L/h. If the psychrometric conditions (air temperature, relative humidity, and air velocity), skin temperature, and clothing characteristics are known, the heat storage in the body can be calculated by the fundamental heat-balance equation (10.1).

Agreement is not complete on the physiological criteria that best describe the limits of human thermal tolerance. Several researchers (Ellis et al., 1964; Craig et al., 1954; Goldman et al., 1965; Wyndham et al., 1965) have used a rectal temperature (T_{re}) of 39.2°C as a useful criterion for setting the upper level of heat-stress tolerance in clinical trials. Others

have advocated the use of more subjective criteria such as faintness and loss of mental and physical ability (Bell and Walters, 1969; Bell et al., 1965; Machle and Hatch, 1947). Since quantitative calculations based on such subjective criteria are not practical, for the purposes of the following calculations we have defined a T_{re} of 39.2°C as the danger level for man. With this definition, the critical rate of heating for a 1-h period is that which will cause a rise in T_{re} of 2.2°C/h, assuming a normal beginning rectal temperature of 37°C and neglecting any temporal lag in the T_{re} response.

We utilized data for the change in mean skin temperature $(\bar{T}_{sk})$ as a function of time collected in an experiment recorded by Ellis et al. (1964), in which a healthy 28-yr-old male exposed to a hot, humid environment was judged by observers to have reached his tolerance limit in 61 min. His final rectal temperature was 39.4°C. His skin temperature rose bimodally from 36.9 to 38.4°C during the first 20 min of exposure, then increased more slowly to 39.3°C in the next 41 min because of the onset of sweating.

If these data for T_{re} and $\bar{T}_{sk}$ are assumed to be generally true for a man heat stressed to his tolerance point in 1 h, we should be able to calculate lesser amounts of heat storage imposed on the body by less severe environmental conditions that permit greater rates of evaporative cooling. Also, substituting an equivalent amount of heat energy absorbed during exposure to RFR for metabolic energy seems reasonable. Such an equivalence was demonstrated by Nielsen and Nielsen (1965) when they measured identical thermoregulatory responses to exercise and to diathermic heating. This assumption would be expected to be valid for RFR at frequencies up to the postresonance region (perhaps up to about 1 GHz for the average man), but might not be valid at higher frequencies where the RFR causes primarily surface heating. Consequently, the results calculated in the next section are restricted to radiation conditions where the RF heating does not occur primarily on the surface. The substituted equivalent RFR heat load, expressed in watts per kilogram of body mass, is designated the SAR_{60}--the specific absorption rate that would produce a rectal temperature of 39.2°C in the irradiated subject in 60 min. The SAR_{60} is intended to represent the <u>maximum SAR</u> that a healthy average man can tolerate, with regard to thermal considerations alone, for 60 min in a given environment, assuming both that the capacity to thermoregulate is

normal and that the other criteria for metabolic rate, posture, clothing, and behavior specified below are valid.

10.7.3. Calculations

For the following calculations the required parameters for man and the environment are listed in Table 10.5. Standard values obtained from physiology texts (Kerslake, 1972; Mountcastle, 1974; Newburgh, 1949; Ruch and Patton, 1973) are given for the sample calculations. The symbols, units, and conversion factors used in this section conform for the most part to the uniform standards proposed by Gagge et al. (1969).

The calculations are based on a modification of the fundamental heat-balance equation (10.1) which neglects the work factor (W), groups together the terms for dry-heat losses (R + C), and incorporates the electromagnetic power absorbed (P):

$$M + P = (R + C) + E + S$$

or

$$S = M - (R + C) - E + P \tag{10.10}$$

in which all symbols are as previously defined. The total heat load is given by

$$H = \Delta T_{re} c_p w \quad \text{kcal} \tag{10.11}$$

where ΔT_{re} is the change in rectal temperature caused by heat load H. The evaporation rate is given by

$$E = h_e A_w \left(P_{sk} - P_a \right) + 0.0023 \, M \left(44 - P_a \right) \quad W \tag{10.12}$$

The dry-heat losses due to radiation and convection can be represented by

$$(R + C) = \left(h_r A_r + h_c A_c \right) \left(\overline{T}_{sk} - T_a \right) \quad W \tag{10.13}$$

TABLE 10.5. SPECIFICATION OF PARAMETERS USED IN CALCULATING SAR_{60}

Parameters for a Standard Physiological Man	Symbol and Numerical Value
Mass	$w = 70$ kg
Height	$h = 1.75$ m
Surface area	$A_D = 1.85$ m^2
Convection, radiation area	$A_r = A_c = 1.3$ m^2
Wetted area	$A_w = 1.7$ m^2
Rate of metabolic heat production	M
Sitting at rest	$M = 110$ W or 1.57 W/kg
With thermal stress, $T_{re} = 37°C$	$M = 120$ W or 1.71 W/kg
At $T_{re} = 39.2°C$	$M = 153$ W or 2.18 W/kg
Average M over 1-h period	$\bar{M} = 137$ W or 1.96 W/kg
Critical rectal temperature	$T_{re} = 39.2°C$
Normal rectal temperature	$T_{re} = 37°C$
Specific heat of body	$c_p = 0.83$ (kcal/°C·kg)

Psychrometric Conditions	Symbol and Numerical Value
Wind velocity	$v = 1.35$ m/s
Evaporation coefficient	$h_e = 21$ W/(m^2·torr)
Convective coefficient	$h_c = 9.5$ W/(m^2·°C)
Radiation coefficient	$h_r = 8$ W/(m^2·°C)
Ambient temperature range	$T_a = 30$ to $68°C$
Relative humidity	$\phi_a = 0.8, 0.5, 0.2$
Saturated ambient water-vapor pressure	P_{wa} is given in referenced tables in units of torr as a function of T_a
Ambient water-vapor pressure	$P_a = \phi_a \cdot P_{wa}$
Saturated skin-vapor pressure	P_{sk} is given in referenced tables in units of torr as a function of $\bar{T}_{sk}$

Combining Equations 10.10, 10.12, and 10.13 and using values from Table 10.5 results in

$$S = M - [0.0023 \, M(44 - P_a) + 36(P_{sk} - P_a)] - 23(\bar{T}_{sk} - T_a) + P \qquad W \qquad (10.14)$$

This equation is first solved for the particular psychrometric conditions of interest with no RF power absorbed ($P = 0$). Over a 1-h period, the heat load due to the environment alone is given by

$$H = \int_0^{60 \text{ min}} S \cdot dt \qquad (10.15)$$

The solution is -60 kcal when $T_a = 40°C$ and $\phi_a = 0.8$. By Equation 10.11, the heat load that causes a 2.2°C rise in T_{re} was 128 kcal for this particular man.

The power, P, that will cause a 2.2°C rise in T_{re} in 1 h is the difference between H and 128 kcal.

$$P = 1.16 \, \frac{W}{kcal/h} \, (128 - H)$$

$$P = 218 \; W$$

The SAR_{60} is simply

$$SAR_{60} = \frac{P}{70 \text{ kg}} = 3.11 \, \frac{W}{kg}$$

By using the SAR curves for an average man, we can plot the incident power density that will produce the SAR_{60} for any given frequency and polarization, as shown in Figure 10.7. The calculated SAR_{60} values plotted on this graph represent the worst possible case for man, which is, according to the data for the prolate spheroidal model, E polarization at resonance (70 MHz).

In Figure 10.7 the intercept of each curve with the horizontal axis indicates the ambient conditions (temperature and relative humidity) that will produce a rectal temperature of 39.2°C with no irradiation. For example, with a relative humidity of 80% and an ambient temperature of 42°C, the SAR_{60} is zero--which means that under these conditions a rectal temperature of 39.2°C

- 10.28 -

will occur in 1 h with no irradiation. Similarly, the curve shows that if the ambient temperature were 41°C and the relative humidity 80%, the SAR_{60} would be 1.25 W/kg--under these conditions a rectal temperature of 39.2°C would be reached in 60 min. The other curves in the figure indicate that the same SAR (1.25 W/kg) would occur at 49°C and 50% relative humidity and at 63°C and 20% relative humidity. From the ordinate on the right, we read that at this SAR_{60}, the incident power density for E polarization at resonance would be 5 mW/cm^2. The incident power densities at other frequencies and/or polarizations can be determined by using the dosimetric curves to find what power density produces an SAR of 1.25 W/kg for the given frequency and polarization in question.
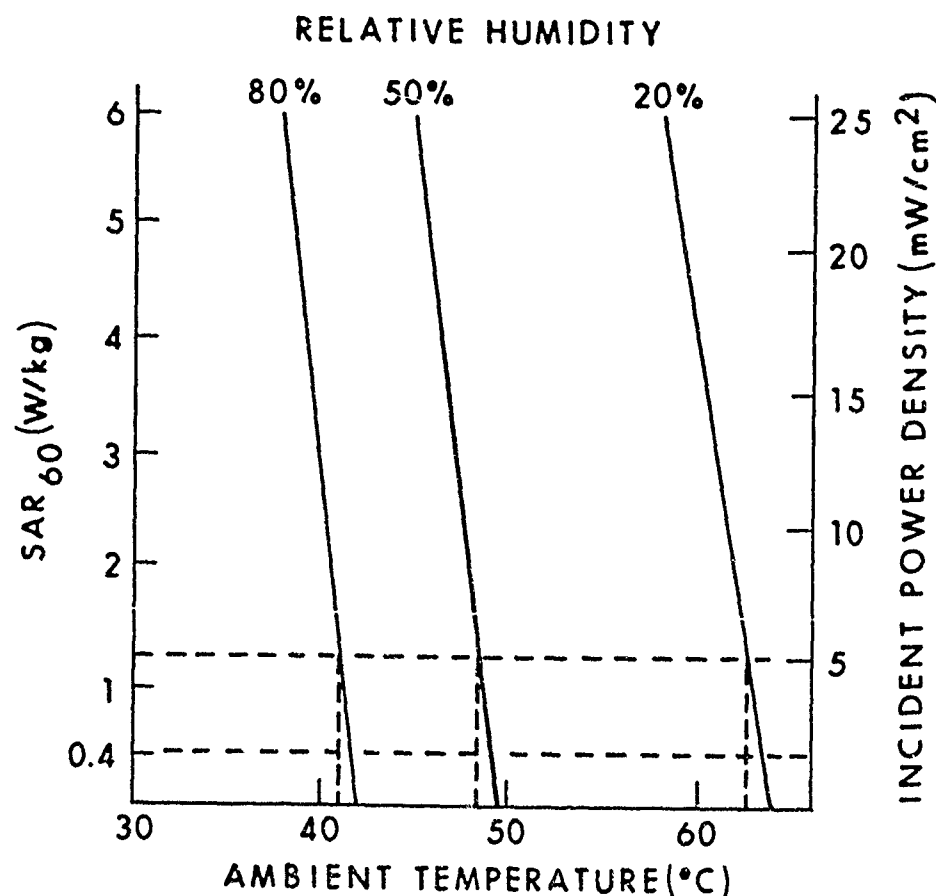
Figure 10.7.   Calculated SAR_{60} values in an average man, unclothed and quiet, irradiated by an electromagnetic planewave with E polarization at resonance (about 70 MHz). Dashed horizontal lines indicate the psychrometric conditions (in still air) that yield an SAR_{60} of 1.25 W/kg and 0.4 W/kg at this frequency.

If the ambient temperature were 41°C and the relative humidity only 20%, a very high SAR would be required to produce a rectal temperature of 39.2°C in 60 min, a value too high to be read from Figure 10.7. This shows that, as expected, in warm environments the relative humidity has a great effect on the body's ability to dissipate an added thermal burden by evaporation. We strongly emphasize that the SAR_{60} is only an estimate of the upper limit of thermal tolerance for a healthy nude man. Many other factors must be considered, not the least of which is the great disparity in thermoregulatory response from individual to individual.

Figure 10.7 shows the relative independence of the SAR_{60} on the prevailing ambient temperature at any given ambient humidity level. Thus at such moderate SARs, hyperthermic levels of body temperature can be expected only if the body is already operating at near-critical environmental conditions. Under such hostile conditions even small increases in metabolic heat production, such as very light work, will also initiate an increase in the body temperature. The basis for RF exposure guidelines currently in force, 0.4 W/kg, is also indicated on the curves in Figure 10.7 under the assumption of a 60-min average time. (The 6-min averaging time specified in the current guidelines is far too short to achieve a thermal steady state such as that represented in Figure 10.7.) The reduction in ambient temperature required, at any relative humidity, to accommodate an SAR_{60} of 0.4 W/kg is less than can be precisely achieved or measured, given present technology; therefore, no temperature or humidity factors should be used to adjust 0.4-W/kg RF exposures.

A healthy person exposed to the environments represented in the SAR curves would be expected to experience considerable thermal discomfort along with the rise in core temperature, rise in heart rate, and profuse sweating. All of these responses would increase over time until, at about 60 min, the person would be on the verge of collapse and exhibiting the unpleasant but reversible symptoms reported in experiments on human heat tolerance.

Because of the approximations used in the calculations described here and the great differences in thermoregulatory response found from person to person, we emphasize that the calculated data given in this handbook are intended to serve only as guidelines and to give a qualitative indication of anticipated responses.

CHAPTER 11. RADIOFREQUENCY RADIATION SAFETY STANDARDS

This chapter was written by John C. Mitchell, Chief, Radiation Physics Branch, Radiation Sciences Division, USAF School of Aerospace Medicine, Brooks Air Force Base, Texas 78235-5301.

11.1. INTRODUCTION

The development and application of devices that emit radiofrequency radiation have significantly increased the quality of life throughout the world. Yet the beneficial aspects of RF/microwave technology have been somewhat overshadowed in recent years by the public's fear of potential adverse effects. This fear, in turn, has led to increased RFR research (resulting in a much better understanding of the interaction of RFR fields and biological systems) and to new RFR safety guidelines. The new exposure standards are based on what is known about the frequency-dependent nature of RFR energy deposition in biological systems and about any biological effects. In general, the new guidelines provide an added margin of safety over those previously used.

Inherent health risks from RFR exposures are directly linked to absorption and distribution of RFR energy in the body, and the absorption and distribution are strongly dependent on body size and orientation and on frequency and polarization of the incident radiation, as indicated by the data in Chapters 6 and 8. Both theoretical and experimental dosimetric data show that RFR absorption approaches maximum when the long axis of the body is both parallel to the E-field vector and equal to four-tenths of the wavelength of the incident RFR field. Thus a 70-kg, 1.75-m human exposed to a planewave RFR field in free-space with the E-field aligned with the long axis of the body, would absorb the most energy at a frequency of about 70 MHz (Chapter 6). If the person were standing in contact with a conducting ground plane (producing a change in the apparent long-axis length), the frequency for maximum RFR absorption would be about 35 MHz. This frequency-dependent behavior is illustrated in Figure 11.1 for several human sizes (using prolate spheroidal models having body masses of 10, 32, and 70 kg). The average whole-body specific

absorption rate in watts per kilogram is plotted as a function of radiation frequency in megahertz for an incident average power density of 1 mW/cm^2.
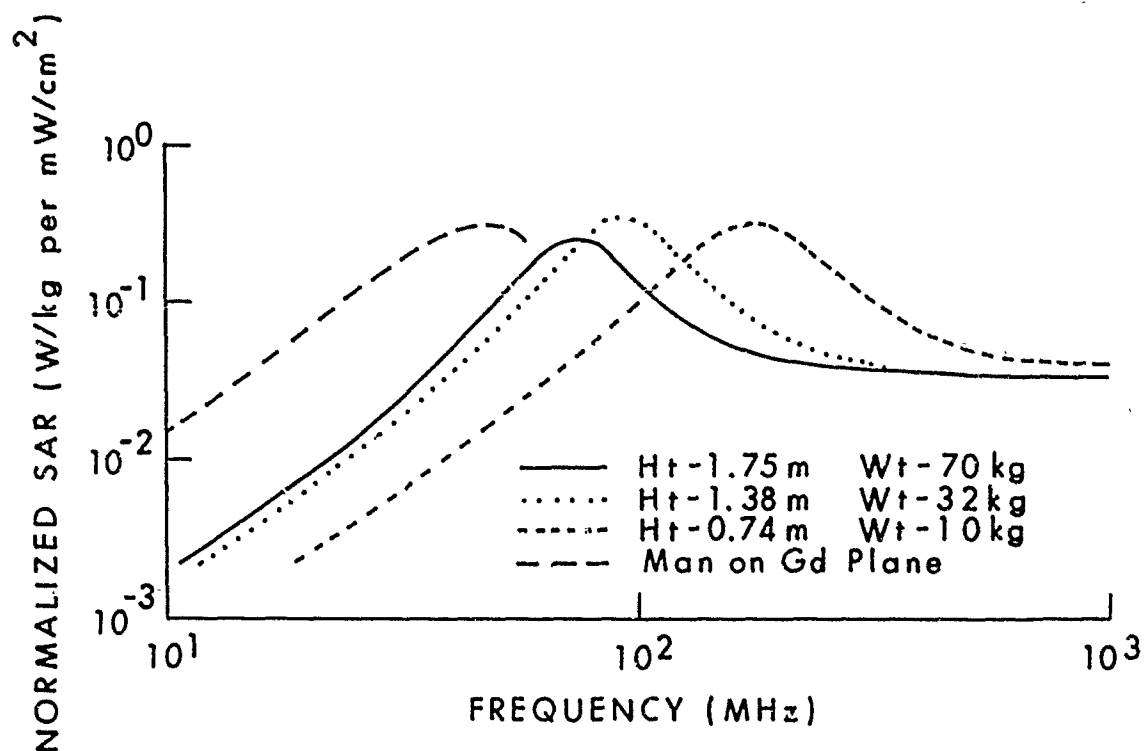
Figure 11.1. Calculated relative RFR absorption in
prolate spheroidal models of humans.

11.2. RFR SAFETY STANDARDS

11.2.1. American National Standards Institute (ANSI) Standard

For more than 20 years the United States and most of the free world used a single field-intensity value to maintain the safety of personnel exposed to RFR. A power density of 10 mW/cm^2, time averaged over any 6-min period, was applied as an acceptable exposure level and generally was thought to include a safety factor of 10. During the past 5-10 years it has become well accepted that the RFR absorption and distribution in humans are strongly dependent on the frequency of the incident radiation, as shown in Figure

11.1.   When ANSI revised its safety standard in 1982, it incorporated this
frequency-dependency concept and used SAR as a common denominator for bio-
logical effects.   The ANSI standard (1 Sep 1982) allows average incident-power
densities from 1 to 100 mW/cm^2 depending on the radiation frequency.   It
limits the average whole-body absorption to 0.4 W/kg or less and the spatial
peak SAR to 8 W/kg as averaged over any 1 g of tissue.

Figure 11.2 illustrates how the ANSI standard was derived.   The relative
power-absorption curves illustrated in Figure 11.1 were used to establish the
shape of the ANSI curve.   It was normalized to 0.4 W/kg because the ANSI
committee, after reviewing the biological effects data base, believed the
threshold for adverse biological effects to be greater than 4 W/kg.   Thus the
0.4 W/kg was selected to include a safety factor of 10.   Table 11.1 shows the
ANSI RFR Protection Guides in terms of the mean squared E- and H-field
strengths and of the equivalent planewave free-space power density as a func-
tion of frequency.
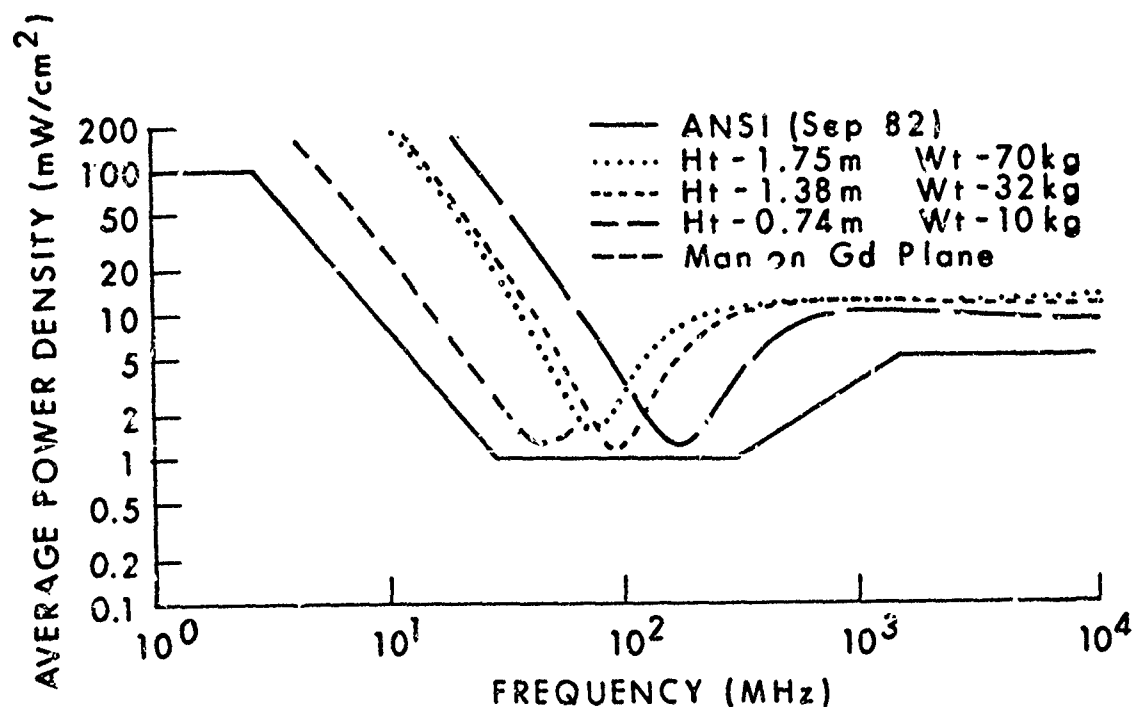
Figure 11.2.   Power densities that limit human whole-body
SAR to 0.4 W/kg compared to ANSI standard.

- 11.3 -

TABLE 11.1. ANSI RADIOFREQUENCY PROTECTION GUIDES

Frequency Range (MHz)	E^2 (V^2/m^2)	H^2 (A^2/m^2)	Power Density (mW/cm^2)
0.3 – 3	400,000	2.5	100
3 – 30	4,000 $(900/f^2)$	0.025 $(900/f^2)$	$900/f^2$
30 – 300	4,000	0.025	1.0
300 – 1,500	4,000 $(f/300)$	0.025 $(f/300)$	$f/300$
1500 –100,000	20,000	0.125	5.0

At the low end of the frequency coverage (<3 MHz), ANSI placed an arbitrary cap at 100 mW/cm^2 rather than extending the frequency-dependent boundary. If the permissible exposure levels were allowed to increase without limit, other phenomena such as corona discharge and electric shock effects could become problems. On the other hand, there was concern that, at the lower frequencies, the 100 mW/cm^2 cap would be too conservative and might place unnecessary operational constraints on some RFR operations.

11.2.2. American Conference of Governmental Industrial Hygienists (ACGIH) TLV

In May 1983, ACGIH published new threshold limit values (TLVs) for RF microwave radiation (ACGIH, 1984). Like the ANSI standard, the ACGIH TLVs limit human absorption to an SAR of 0.4 W/kg or less, averaged over any 6-min period. Unlike the ANSI standard, the TLVs cover the added frequency range from 10 to 300 kHz and from 100 to 300 GHz. Because the TLVs are to be applied in occupational settings, they are based on the assumption that no children (small humans) will be in the workplace. This assumption allows an average incident-power density of 10 mW/cm^2 at frequencies greater than 1 GHz, while maintaining the same 0.4-W/kg whole-body absorption limit. This can be seen from Figure 11.2 if the absorption curve for the 10-kg human is removed. The arbitrary 100-mW/cm^2 cap applied in the frequency range from 10 kHz to 3 MHz appears safe on the basis of whole-body SAR; however, RFR intensities of 100 mW/cm^2 can result in shocks or burns under certain conditions. The 100-mW/cm^2 limit should not restrict many operations but serves as a

reminder that at this level potentially significant shock and burn problems may occur. The ACGIH TLV provides procedures to minimize these problems and reduce operational constraints while maintaining personnel safety. The ACGIH TLVs (Table 11.2) are established as safety guidelines for the workplace. They are intended for use in the practice of industrial hygiene and should be interpreted and applied only by a person trained in this discipline.

TABLE 11.2. ACGIH RADIOFREQUENCY/MICROWAVE THRESHOLD LIMIT VALUES

Frequency	Power Density (mW/cm^2)	E^2 (V^2/m^2)	H^2 (A^2/m^2)
10 kHz to 3 MHz	100	377,000	2.65
3 MHz to 30 MHz	$900/f^2$	$3770 \times 900/f^2$	$900/37.7\ f^2$
30 MHz to 100 MHz	1	3770	0.027
100 MHz to 1000 MHz	$f/100$	$3770 \times f/100$	$f/37.7 \times 100$
1 GHz to 300 GHz	10	37,700	0.265

11.2.3. United States Federal Guidelines

The United States has not established Federal guidelines for RFR exposures. The ANSI and ACGIH voluntary guidelines coupled with those used by the individual services of the Department of Defense and some State and local standards represent the range of RFR safety guidelines applied in the United States in the past few years (U.S. AFOSH Standard 161-9, 1984; Commonwealth of Massachusetts, 1983; Johns Hopkins Applied Physics Laboratory Health and Safety Bulletin, 1984).

11.2.4. International Radiation Protection Association Guidelines

On 8 July 1983 the Executive Council of the International Radiation Protection Association (IRPA) approved interim guidelines on limits of exposure to radiofrequency electromagnetic fields in the frequency range from 100 kHz to 300 GHz (Interim Guidelines, 1984). The International Nonionizing Radiation Committee of IRPA included participants from France, Netherlands, Poland, Denmark, the Federal Republic of Germany, Great Britain, Australia, and the United States of America. Environmental Health Criteria 16 (1981), "Radiofrequency and Microwaves," serves as the primary scientific rationale for the development of the IRPA RFR guidelines. These guidelines apply to RFR exposure of both occupational workers and the general public. The basic limits of exposure for frequencies greater than 10 MHz are expressed in whole-body averaged SAR. For practical purposes, derived limits of exposure are also expressed in average incident-power density. See Table 11.3. The derived limits are extremely conservative in the frequency range 10-30 MHz. This approach, to state the exposure limit in terms of whole-body SAR, represents a departure from current practices; i.e., most new standards express the permissible exposure levels in average incident-power density even though they are based on limiting the whole-body SAR. For occupational workers the IRPA exposure limit for frequencies greater than 10 MHz is 0.4 W/kg when averaged over any 6 min and over the whole body or 4 W/kg when averaged over any 6 min and any 1 g of tissue. For the general public, the IRPA exposure limit is 5 times lower; i.e., 0.08 W/kg when averaged over any 6 min and over the whole body or 0.8 W/kg when averaged over any 6 min and any 1 g of tissue.

TABLE 11.3.   IRPA EXPOSURE LIMITS TO RADIO-
FREQUENCY ELECTROMAGNETIC FIELDS

Frequency MHz		E (V/m)	H (A/m)	Power Density (mW/cm^2)
Occupational				
0.1 –	1	194	0.51	*10
>1 –	10	$194/f^{1/2}$	$0.51/f^{1/2}$	*10/f
>10 –	400	61	0.16	1
>400 –	2,000	$3 \times f^{1/2}$	$0.008 \times f^{1/2}$	f/400
>2,000 –	300,000	137	0.36	5
General Public				
0.1 –	1	87	0.23	*2
>1 –	10	$87/f^{1/2}$	$0.23/f^{1/2}$	*2/f
>10 –	400	27.5	0.073	0.2
>400 –	2,000	$1.375 \times f^{1/2}$	$0.0037 \times f^{1/2}$	f/2,000
>2,000 –	300,000	61	0.16	1

---

* These values are provided for information only and are not to be considered
  for determining compliance.

Figure 11.3 presents a comparison of the ANSI, ACGIH, and IRPA RFR
safety standards plotted as average incident-power density versus frequency.
These standards are based on the same assumption, that 4 W/kg is a reasonable
threshold for adverse biological effects.   Differences in the permissible
incident-power densities as a function of frequency result from the degree of
conservatism applied in each instance.
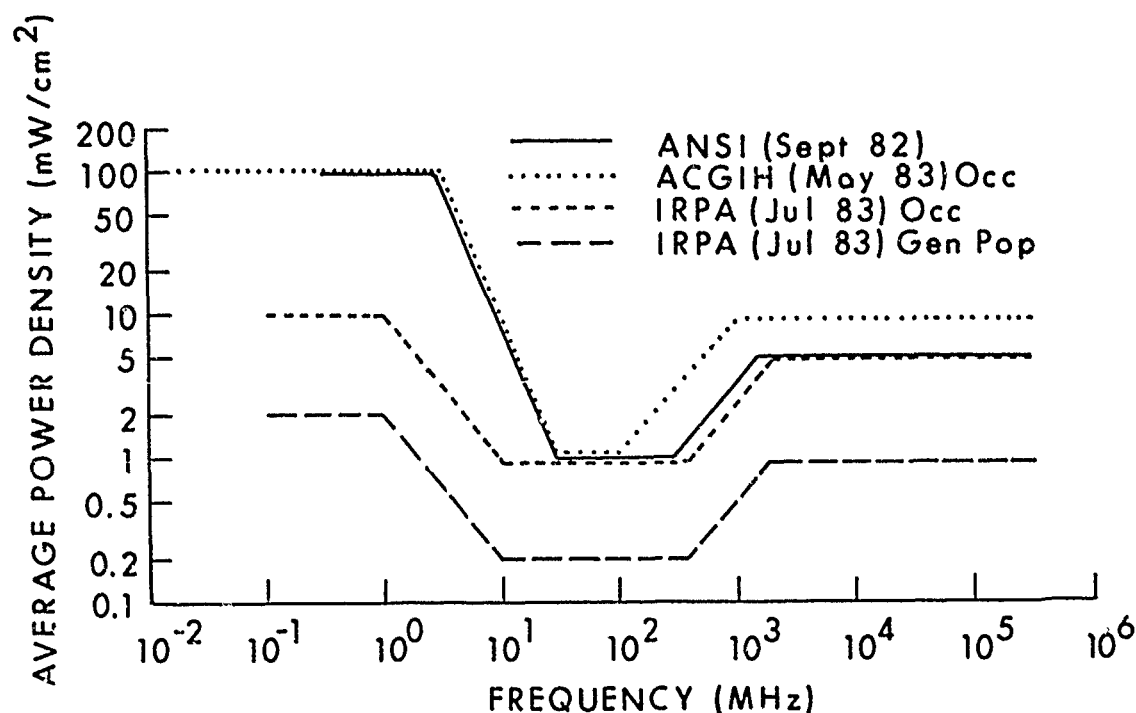
Figure 11.3. Comparison of RFR safety guidelines based on
a threshold of 4 W/kg for adverse effects.

11.3. PHYSICAL CONSIDERATIONS INHERENT IN APPLICATION OF NEW RFR SAFETY GUIDELINES

11.3.1. RFR Penetration and Absorption in Biological Systems

Most biological-effects studies used to establish the current RFR safety guidelines have used small laboratory animals (mice and rats) and 2450-MHz radiation sources. In such studies the RFR energy is deposited throughout the animal's body and includes "hot spots" of RFR absorption that can be 10 to 20 times higher than the average. The bioeffect thresholds were established using worst-case data. The most likely human exposures are much less traumatic because the RFR energy is not generally deposited throughout the body (see Section 5.1). To illustrate this fact, Table 11.4 gives some rough approximations of the penetration depth in biological tissue and the percentage of total body mass (in humans) that might be exposed as a function of

radiation frequency. Depth of penetration is defined as the distance at which the power absorption is e^{-2} (0.135) of the surface value. The results in Table 11.4 are for a cylindrical model of man. Similar information is given in Figure 3.36 for a planar model.

TABLE 11.4. APPROXIMATE RFR PENETRATION AND ABSORPTION IN HUMANS

Radiation Frequency (GHz)	Penetration in Tissue (cm)	% Total-Body Mass Exposed
1	4.05	20.8
2	2.46	15.6
4	1.66	9.2
8	0.65	4.0
10	0.46	2.9
20	0.16	1.0

For example, a standard man exposed to a 1-GHz field might receive a unilateral exposure, penetrating to a depth of ~4 cm, resulting in ~21% of the total-body mass receiving RFR energy. For a 10-GHz exposure the RFR energy might penetrate only ~0.5 cm and result in less than ~3% of the total-body mass receiving RFR energy. In fact, real-world exposure situations are much more complicated because the RFR energy is deposited in a very nonuniform manner that results in hot spots difficult to predict. These so-called hot spots do not relate to temperature excursion but to the fact that the SAR at different locations in the body can vary by an order of magnitude. Nevertheless, the data in Table 11.4 illustrate that in most exposure situations the RFR energy is deposited unilaterally in a relatively small volume of the body; in many exposure situations an appreciable fraction of the body is not subjected to any significant energy deposition. With regards to potential bioeffects of RFR exposures, this is considered an added safety factor for exposures at or below the safety guidelines. The body's thermoregulatory system must still handle the total energy deposited, but such heat loads are minimal (generally less than one-half of the basal metabolic rate) for permissible exposure levels.

11.3.2. Partial Versus Whole-Body Exposures

In most human exposures only a part of the body is exposed at radiation intensities approaching the safety limits. For example, most radar systems propagate radiation beams that are confined to a few degrees in both lateral directions and depend on scanning to cover the surveillance volume. At intensities approaching the maximum permissible values, human exposures normally would occur only close to the source, where the beam size is relatively small. This situation also applies for exposures to leakage fields from microwave ovens and from a wide range of RFR-generation equipment. Such partial-body exposures at intensities that exceed the normal limits are often felt as a warming sensation, giving a person warning to terminate the exposure before it becomes more serious.

11.3.3. Subject and Source Dynamics

The radiation protection guides applied over the frequency range covering whole-body resonant conditions were selected to protect the human under the worst circumstances (ANSI, 1982; ACGIH, 1984). The guides are based on a person's being exposed for 6 min to a free-space planewave field at the radiation frequency equivalent to his or her resonant frequency (dependent on the person's height), with the E-field vector aligned with the long axis of the body, and at the maximum RFR intensity allowed by the guideline. These circumstances seldom, if ever, occur. For example, persons would rarely find themselves in a field having their resonant frequency at the maximum intensity allowed. Even with a measured level equal to the maximum, the isodose intensity contour will not likely be as large as the human. It is also unlikely that a human will maintain erect posture for 6 min at a time. Changes in posture (stooping, bending, squatting) significantly reduce RFR energy absorption. Figure 11.4 shows calculated relative power-absorption curves plotted for a 1.8-m, 70-kg human who has changed his or her effective height by squatting, sitting, and standing with arms both in normal position and raised above the head. As in Figure 11.1, these curves were developed using prolate spheroid models with a constant body mass of 70 kg.
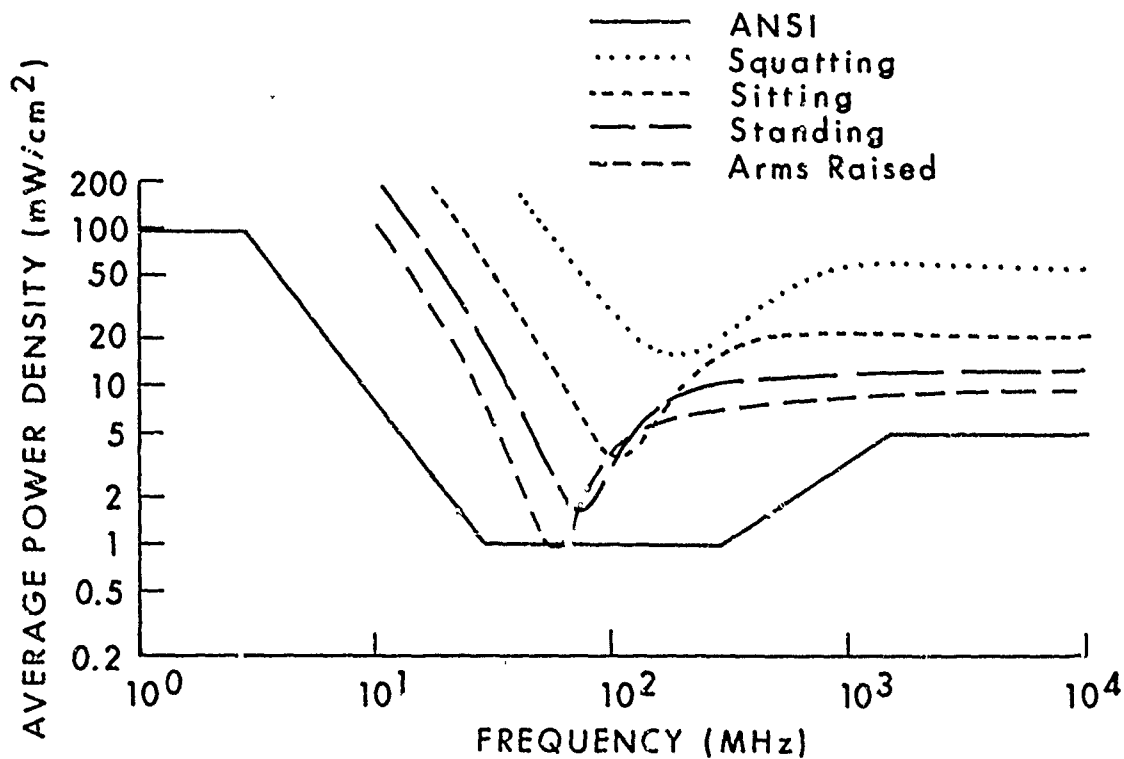
Figure 11.4. Power densities that limit human whole-body
SAR to 0.4 W/kg for a 1.8-m, 70-kg person.

In some jobs people might remain a fixed distance from an RFR source, but in most exposure situations the distance between the source and the person varies considerably--with movement often reducing the amount of RFR energy absorbed. Also, normal thermoregulatory response (blood flow) in living animals minimizes the temperature excursions predicted from static models (Krupp, 1983).

11.4. CONCLUSIONS

Advancements in understanding RFR interactions with living systems, based on dosimetry and biological effects research, are shared commonly throughout the world. Differences in RFR safety guidelines established by different governmental bodies depend largely on the degree of conservatism applied and philosophical approaches taken. These facts are well documented in current reviews of RFR-induced biological effects (ANSI, 1982; ACGIH, 1984; Environmental Health Criteria, 1981; Heynick, 1984; Biological Effects of Radiofrequency Radiation, 1984).

New research to assess the biological effects of RFR exposure has emerged rapidly and in considerable quantity over the past 5 years. Most reported effects are related to thermal insults from specific absorption rates greater than 4 W/kg. The new RFR safety guidelines and their rules of application provide greater safety than those used in the past; they also have a more credible scientific basis.

11.5. FUTURE TRENDS IN RFR-STANDARDS SETTING

The whole-body (averaged) SAR used in developing new frequency-dependent RFR safety standards has been a significant improvement over what was previously used. The SAR relates well to most laboratory studies using small animals subjected to RFR fields at frequencies close to resonant conditions.

At frequencies greater than about 20 GHz and less than about 3 MHz, however, whole-body SAR is not an adequate basis for the RFR safety guidelines. At frequencies greater than 20 GHz, RFR energy deposition in biologic tissue is very superficial (see Table 11.4 and Figure 3.36), and some form of localized SAR may serve as a better safety guideline than a whole-body SAR. New safety guidelines for the 20-300-GHz frequency range will likely emerge in the next few years.

Below about 3 MHz, the RFR absorption in biologic tissue decreases as a function of frequency squared below the resonant point. The actual RFR energy absorption becomes so small in the 10-kHz to 3-MHz frequency range that it can be considered safe at any practical value of incident-power density. However, valid questions remain concerning the potential for shocks and burns. These questions are being studied (as indicated in Chapter 9), and new safety guidelines can be expected in the future.

REFERENCES

ACGIH. Threshold limit values (TLV) for chemical substances and physical agents in the work environment with intended changes for 1983-1984. ISBN: 0-936712-45-7. Ann Am Conf Govern Indus Hygien 8:190-191 (Mar 1984).

Adair, E. R., and B. W. Adams. Adjustments in metabolic heat production by squirrel monkeys exposed to microwaves. J Appl Physiol: Respir Environ Exerc Physiol 52:1049-1058 (1982).

Adams, T. C. Carnivores. In G. C. Whittow (ed.). Comparative Physiology of Thermoregulation, Vol. II. New York: Academic Press, 1971.

Adams, T., et al. Temperature regulation of the unanesthetized cat during mild cold and severe heat stress. J Appl Physiol 29:852-858 (1970).

Afsar, M. N., and J. B. Hasted. Measurements of the optical constants of liquid H_2O and D_2O between 6 and 450 cm^{-1}. J Opt Soc Am 67:902-904 (1977).

Allen, S. J. Measurements of power absorption by human phantoms immersed in radio-frequency fields. Ann NY Acad Sci 247:494-498 (1975).

Allen, S. J., et al. Comparison of theoretical and experimental absorption of radiofrequency power. SAM-TR-75-52, Dec 1975.

Allen, S. J., et al. Measurement of radiofrequency power absorption in monkeys, monkey phantoms, and human phantoms exposed to 10-50 MHz fields. SAM-TR-76-5, Feb 1976.

Allen, S. J., and W. D. Hurt. Development and use of a calorimeter to measure specific absorption rates in small laboratory animals, p. 61. In Abstracts of Scientific Papers. URSI International Symposium on the Biological Effects of Electromagnetic Waves, Airlie, VA, 30 Oct-4 Nov 1977.

Allis, J. W., et al. Measurement of microwave radiation absorbed by biological systems: 1. Analysis of heating and cooling data. Radio Sci 12:1-8 (1977).

Altman, P. O., and D. S. Dittmer (eds.). Metabolism. Bethesda, MD: Fed Am Soc Exp Biol, 1968.

Anne, A., et al. Relative microwave absorption cross sections of biological significance. In Biological Effects of Microwave Radiation. New York: Plenum Press, 1960.

ANSI C95.1-1982. Safety levels with respect to human exposure to radiofrequency electromagnetic fields, 300 kHz to 100 GHz. American National Standards Institute, 1 Sep 1982.

ASHRAE Handbook. Physiological principles, comfort, and health, ch. 8. In 1981 Fundamentals. American Society of Heating, Refrigerating, and Air-Conditioning Engineers, Atlanta, GA, 1981.

Aslan, E. Electromagnetic leakage survey meter. J Microwave Power 6:169-177 (1971).

Astrand, P. O., and K. Rodahl. Textbook of Work Physiology. New York: McGraw-Hill, 1970.

Athey, T. W., et al. Measurement of radiofrequency permittivity of biological tissues with an open-ended coaxial line: Part I. IEEE Trans MTT-30:82-87 (1982).

Balzano, Q., et al. Heating of biological tissue in the induction field of VHF portable radio transmitters. IEEE Trans VT-27:51-56 (1978a).

Balzano, Q., et al. Energy deposition in simulated human operators of 800 MHz portable transmitters. IEEE Trans VT-27:174-181 (1978b).

Baranski, S., and P. Czerski. Biological Effects of Microwaves. Stroudsburg, PA: Dowden, Hutchinson and Ross, Inc., 1976.

Barber, P. W. Electromagnetic power deposition in prolate spheroid models of man and animals at resonance. IEEE Trans BME-24:513-521 (1977a).

Barber, P. W. Resonance electromagnetic absorption by nonspherical dielectric objects. IEEE Trans MTT-25(5):373-381 (1977b).

Barber, P. W., et al. Electromagnetic absorption in a multilayered model of man. IEEE Trans BME-26(7):400-404 (1979).

Bassen, H. I. Internal dosimetry and external microwave field measurements using miniature electric field probes, pp. 136-151. In D. G. Hazzard (ed.). Proc of Symposium on Biological Effects and Measurements of Radio-frequency/Microwaves. Rockville, MD., 16-18 Feb 1977. Washington: U.S. Govt Printing Office, HEW Publ (FDA)77-8026. July 1977.

Bassen, H. I., and W. A. Herman. Precise calibration of plane-wave microwave power density, using power equation techniques. IEEE Trans MTT-25:701-706 (1977).

Bassen, H. I., et al. EM probe with fiber-optic telemetry system. Microwave J 4:35-39 (1977a).

Bassen, H. I., et al. Evaluation of an implantable electric-field probe within finite simulated tissues. Radio Sci 12:15-22 (1977b).

Bassen, H. I., et al. Electric field probes--a review. IEEE Trans AP-31:710-718 (1983).

Bawin, S. M., and W. R. Adey. Sensitivity of calcium binding in cerebral tissue to weak environmental electric fields oscillating at low frequency. Proc Natl Acad Sci USA 73:1999-2003 (1976).

Bawin, S. M., and W. R. Adey. Brain interactions with weak electric and magnetic fields. Neurosci Res Prog Bull 15:1-129 (1977).

Bell, C. R., et al. Safe exposure of men to severe heat. J Appl Physiol 20(2):288-292 (1965).

Bell, C. R., and J. D. Walters. Reactions of men working in hot and humid conditions. J Appl Physiol 27(5):684-686 (1969).

Benedict, F. G. Vital energetics: A study in comparative basal metabolism. Washington: Carnegie Institute of Washington, Publ. 503, 193£.

Berglund, L. G. Characterizing the thermal environment, pp. 15-31. In E. R. Adair (ed.). Microwaves and Thermoregulation. New York: Academic Press, 1983.

Bernard, C. Introduction a l'Etude de la Medecine Experimentale. Paris: Bailliere et Fils, 1865.

Berry, J. J., et al. Thermoregulatory responses of rats to varying environmental temperatures. Aviat Space Environ Med 55:546-549 (1984).

Bigu del Blanco, J., and C. Romero-Sierra. Microwave radiation pattern measurements in the presence of biological specimens. IEEE Trans EMC-20(1; Part 2):248-258 (1978).

Biological effects of radiofrequency radiation. EPA-600/8-83-026A, Final Report, Sep 1984.

Blackman, C. F., and J. A. Black. Measurement of microwave radiation absorbed by biological systems. 2. Analysis by Dewar-flask calorimetry. Radio Sci 12:9-14 (1977).

Blakemore, R. Magnetotactic bacteria. Science 190:377-379 (1975).

Bligh, J., and K. G. Johnson. Glossary of terms for thermal physiology. J Appl Physiol 35:941-961 (1973).

Bourne, G. H. (ed.). The Rhesus Monkey. New York: Academic Press, 1975.

Bowman, R. R. Two isotropic electric-field probes for complicated fields. Proc Microwave Power Symp 5:29-30 (1972).

Bowman, R. R. A probe for measuring temperature in radiofrequency-heated material. IEEE Trans MTT-24:43-45 (1976).

Bridges, J. E., and M. F. Frazier. The effects of 60-Hz electric and magnetic fields on implanted cardiac pacemakers. In EPRI, EPRI EA-1174, 1979.

Burdette, E. C., et al. In vivo probe measurement technique for determining dielectric properties at VHF through microwave frequencies. IEEE Trans MTT-28(4):414-427 (1980).

Burr, J. G., and J. H. Krupp. Real-time measurement to RFR energy distribution in the Macaca mulatta head. J BEMS 1(1):21-34 (1980).

Cabanac, M. Thermoregulatory behavioral responses, pp. 307-357. In E. R. Adair (ed.). Microwaves and Thermoregulation. New York: Academic Press, 1983.

Cetas, T. C. A birefringent crystal optical thermometer for measurements of electromagnetically induced heating, pp. 338-348. In C. C. Johnson and M. L. Shore (eds). Biological Effects of Electromagnetic Waves, Vol. II. Selected papers of '↘ USNC/URSI annual meeting, Boulder, CO, 20-23 Oct 1975. Washington: U.S. Govt Printing Office, HEW Publ (FDA)77-8011, Dec 1976.

Cetas, T. C. Thermometry in strong electromagnetic fields, pp. 261-282. In L. S. Taylor and A. Y. Cheung (eds.). Proc of Workshop on the Physical Basis of Electromagnetic Interactions with Biological Systems, University of Maryland, College Park, MD, 15-17 June 1977.

Chan, A. K., et al. Calculation by the method of finite differences of the temperature distribution in layered tissues. IEEE Trans BME-20:86-90 (1973).

Chang, H-C, and G. Kaffe. Polarization electrolytic solution. I: Theory. J Chem Phys 20:1071-1077 (1952).

Chatterjee, I., et al. A method of calculating electromagnetic absorption under near-field exposure conditions, p. 350. In Abstracts of National Radio Science Meeting, Bioelectromagnetics Symposium, University of Washington, Seattle, WA, 1979.

Chatterjee, I., et al. Planewave spectrum approach for the calculation of electromagnetic absorption under near-field exposure conditions. Bioelectromagnetics 1(4):363-378 (1980a).

Chatterjee, I., et al. Electromagnetic absorption in a multilayered slab model of tissue under near-field exposure conditions. Bioelectromagnetics 1(4):379-388 (1980b).

Chatterjee, I., et al. EM energy deposition in an inhomogeneous block model of man for near-field irradiation conditions. IEEE Trans MTT-28(12):1452-1459 (1980c).

Chatterjee, I., et al. An empirical relationship for electromagnetic energy absorption in man for near-field exposure conditions. IEEE Trans MTT-30(5):838 (1982a).

Chatterjee, I., et al. Numerical and experimental results for near-field electromagnetic absorption in man. IEEE Trans MTT-30(11):2000-2005 (1982b).

Chen, K., et al. Quantification and measurement of induced fields inside finite biological bodies, pp. 19-43. In C. C. Johnson and M. L. Shore (eds.). Biological Effects of Electromagnetic Waves, Vol. II. Selected papers of the USNC/URSI annual meeting, Boulder, CO, 20-23 Oct 1975. Washington: U.S. Govt Printing Office, HEW Publ (FDA)77-8011, Dec 1976.

Chen, K. M., and B. S. Guru. Focal hyperthermia as induced by RF radiation of simulacra with embedded tumors and as induced by EM fields in a model of a human body. Radio Sci 12:27-38 (1977a).

Chen, K. M., and B. S. Guru. Induced EM fields inside human bodies irradiated by EM waves of up to 500 MHz. J Microwave Power 12:173-183 (1977b).

Chen, K. M., and B. S. Guru. Internal EM field and absorbed power density in human torsos induced by 1-500-MHz EM waves. IEEE Trans MTT-26(9):746-755 (1977c).

Chen, K. M., et al. Measurement of induced electric fields in a phantom model of man. Radio Sci 17(5S):495-595 (Sept-Oct 1982).

Cheung, A. Y., and D. W. Koopman. Experimental development of simulated biomaterials for dosimetry studies of hazardous microwave radiation. IEEE Trans MTT-24:669-673 (1976).

Cheung, A. Electric field measurements within biological media, pp. 217-242. In L. S. Taylor and A. Y. Cheung (eds.). Proc of Workshop on the Physical Basis of Electromagnetic Interactions with Biological Systems, University of Maryland, College Park, MD, 15-17 June 1977.

Chou, C. K., et al. Cochlea microphonics generated by microwave pulses. J Microwave Power 10:361-367 (1975).

Chou, C. K., and A. W. Guy. Microwave and RF dosimetry, pp. 165-216. In L. S. Taylor and A. Y. Cheung (eds.). Proc of Workshop on the Physical Basis of Electromagnetic Interactions with Biological Systems, University of Maryland, College Park, MD, 15-17 June 1977a.

Chou, C. K., and A. W. Guy. Quantitation of microwave biological effects, pp. 81-103. In D. G. Hazzard (ed.). Proc of Symposium on Biological Effects and Measurements of Radiofrequency/Microwaves. Rockville, MD, 16-18 Feb 1977. Washington: U.S. Govt Printing Office, HEW Publ (FDA)77-8026, July 1977b.

Chou, C. K., and A. W. Guy. Effects of electromagnetic fields on isolated nerve and muscle preparations. IEEE Trans MTT-26(3):141-147 (1978).

Chou, C. K., et al. Formulas for preparing phantom muscle tissue at various radiofrequencies. Bioelectromagnetics 5:435-441 (1984).

Christensen, D. A., and R. J. Volz. A nonperturbing temperature probe system designed for hyperthermia monitoring, p. 490. In Abstracts of National Radio Science Meeting, Bioelectromagnetics Symposium, University of Washington, Seattle, WA, 1979.

Cole, K. S. Membranes, Iones and Impulses. Berkeley, CA: University of California Press, 1972.

Collett, L. S. Laboratory investigation of overvoltage, ch. 5. In J. R. Wait (ed.). Overvoltage Research and Geophysical Applications. Elmsford, NY: Pergamon Press, Inc., 1959.

Colliers' Encyclopedia, s. v. "beagle," "Brittany spaniel," "dog," 1971.

Commonwealth of Massachusetts, 105 CMR 122.000: Regulations Governing Fixed Facilities Which Generate Electromagnetic Fields in the Frequency Range of 300 kHz to 100 GHz and Microwave Ovens. Massachusetts Register Issue No. 379, Sep 1983.

Cook, H. F. The dielectric behavior of some types of human tissues at microwave frequencies. Br J Appl Phys 2:292-300 (1951).

Cook, H. F. A comparison of dielectric behavior of pure water and human blood at microwave frequencies. Br J Appl Phys 3:249-255 (1952).

Craig, F. N., et al. Heat load and voluntary tolerance time. J Appl Physiol 6:634-644 (1954).

Crawford, M. L. Generation of standard EM fields using TEM transmission cells. IEEE Trans EMC-16:189-195 (1974).

Cunningham, D. J. An evaluation of heat transfer through the skin in the human extremity, pp. 302-315. In J. D. Hardy, A. P. Gagge, and J. A. J. Stolwijk (eds.). Physiological and Behavioral Temperature Regulation. Springfield, IL: Charles C Thomas, 1970.

D'Andrea, J. A., et al. Behavioral and thermal effects of microwave radiation at resonant and nonresonant wavelengths. Radio Sci 12(6S):251-256 (1977).

Dalziel, C. F., and T. H. Mansfield. Effect of frequency on perception currents. AIEE Trans 69 Part II:1162-1168 (1950).

Dalziel, C. F., and W. R. Lee. Lethal electric currents. IEEE Spectrum 6:44-50 (1969).

DeFord, J. F., et al. Moment-method solutions and SAR calculations for inho-
mogeneous models of man with large number of cells. IEEE Trans MTT-31(10):
848-851 (1983).

Deno, D. W. Currents induced in the human body by high-voltage transmission
line electric-field measurement and calculation of distribution and dose.
IEEE Trans PAS-96(5):1517-1527, Sep/Oct (1977).

Devyatkov, N. D. Influence of millimeter-band electromagnetic radiation on
biological objects (transl). Sov Phys USPEKHI 16:568-579 (1974).

Dreyfuss, H. The Measure of Man: Human Factors in Design. New York: Whit-
ney Library of Design, 1967.

Driscoll, D. A. An Investigation of a Theoretical Model of the Human Head
with Application to Current Flow Calculations and EEG Interpretation.
Ph.D. Thesis, University of Vermont, 1970.

DuBois, D., and E. F. DuBois. A formula to estimate approximate surface area
if height and weight are known. Arch Int Med 17:863 (1916).

Duncan, P. H., Jr. Analysis of the moebius magnetic-field sensor. IEEE Trans
EMC-16:83-89 (1974).

Durney, C. H., et al. Long-wavelength analysis of plane wave irradiation of a
prolate spheroid model of man. IEEE Trans MTT-23:246-253 (1975).

Durney, C. H., et al. Comparison of theoretical and experimental absorption
of radiofrequency power. Final report to USAF under contract No. F41609-
76-C-0025, University of Utah, Departments of Electrical Engineering and
Bioengineering, Salt Lake City, UT, Dec 1976.

Durney, C. H., et al. Radiofrequency radiation dosimetry handbook, second
edition. SAM-TR-78-22, May 1978.

Durney, C. H., et al. An empirical formula for broad-band SAR calculations of
prolate spheroidal models of humans and animals. IEEE Trans MTT-27(8):758-
763 (1979).

Durney, C. H. Electromagnetic dosimetry for models of humans and animals: A
review of theoretical and numerical techniques. Proc IEEE 68(1):33-40
(1980).

Durney, C. H., et al. Radiofrequency radiation dosimetry handbook, third
edition. SAM TR-80-32, Aug 1980.

Elizondo, R. Temperature regulation in primates, p 71-118. In D.
Robertshaw (ed.). International Review of Physiology, Environmental Physi-
ology II, Vol. 15. Baltimore: University Park Press, 1977.

Frazier, M. J., et al. Internal body potentials and currents from ELF electric fields and household appliances. In 1978 IEEE International Electromagnetic Compatibility Symposium Record, Atlanta, GA, 26-27 June 1978.

Frey, A. H. Biological function as influenced by low-power modulated RF energy. IEEE Trans MTT-19:153-164 (1971).

Fricke, H. The electric capacity of cell suspensions. Phys Rev 21:708-709 (1923).

Friend, A. W., et al. Low-frequency electric-field-induced changes in the shape and motility of amoebae. Science 187:357-359 (1974).

Froehlich, H. Theory of Dielectrics. Oxford, England: Oxford University Press, 1949.

Froehlich, H. Collective behavior of nonlinearly coupled oscillating fields. J Collective Phen 1:101-109 (1973).

Froehlich, H. The extraordinary dielectric properties of biological materials and the action of enzymes. Proc Natl Acad Sci USA 72:4211-4215 (1975).

Gabriel, C., et al. Dielectric properties of ocular tissues at 37°C. Phys Med Biol 28(1):43-49 (1983).

Gagge, A. P., et al. Proposed standard system of symbols for thermal physiology. J Appl Physiol 27:4.9 (1969).

Gandhi, O. P. Polarization and frequency effects on whole animal absorption of RF energy. Proc IEEE 62:1171-1175 (1974).

Gandhi, O. P. Frequency and orientation effect on whole animal absorption of electromagnetic waves. IEEE Trans BME-22(6):536-542 (1975a).

Gandhi, O. P. Conditions of strongest electromagnetic power deposition in man and animals. IEEE Trans MTT-23(12):1021-1029 (1975b).

Gandhi, O. P. Strong dependence of whole animal absorption on polarization and frequency of radiofrequency energy. Ann NY Acad Sci 247:532-538 (1975c).

Gandhi, O. P., and T. C. Rozzell. Liquid crystal fiberoptic RF probe. Part II: A microwave power probe. Microwave J 18(8):58-59 (1975).

Gandhi, O. P., et al. Distribution of electromagnetic energy deposition in models of man with frequencies near resonance, pp. 44-67. In C. C. Johnson and M. L. Shore (eds.). Biological Effects of Electromagnetic Waves, Vol. II. Selected papers of the USNC/URSI annual meeting, Boulder, CO, 20-23 Oct 1975. Washington: U.S. Govt Printing Office, HEW Publ (FDA)77-8011, Dec 1976.

Frazier, M. J., et al. Internal body potentials and currents from ELF electric fields and household appliances. In 1978 IEEE International Electromagnetic Compatibility Symposium Record, Atlanta, GA, 26-27 June 1978.

Frey, A. H. Biological function as influenced by low-power modulated RF energy. IEEE Trans MTT-19:153-164 (1971).

Fricke, H. The electric capacity of cell suspensions. Phys Rev 21:708-709 (1923).

Friend, A. W., e. al. Low-frequency electric-field-induced changes in the shape and motility of amoebae. Science 187:357-359 (1974).

Froehlich, H. Theory of Dielectrics. Oxford, England: Oxford University Press, 1949.

Froehlich, H. Collective behavior of nonlinearly coupled oscillating fields. J Collective Phen 1:101-109 (1973).

Froehlich, H. The extraordinary dielectric properties of biological materials and the action of enzymes. Proc Natl Acad Sci USA 72:4211-4215 (1975).

Gabriel, C., et al. Dielectric properties of ocular tissues at 37°C. Phys Med Biol 28(1):43-49 (1983).

Gagge, A. P., et al. Proposed standard system of symbols for thermal physiology. J Appl Physiol 27:4.9 (1969).

Gandhi, O. P. Polarization and frequency effects on whole animal absorption of RF energy. Proc IEEE 62:1171-1175 (1974).

Gandhi, O. P. Frequency and orientation effect on whole animal absorption of electromagnetic waves. IEEE Trans BME-22(6):536-542 (1975a).

Gandhi, O. P. Conditions of strongest electromagnetic power deposition in man and animals. IEEE Trans MTT-23(12):1021-1029 (1975b).

Gandhi, O. P. Strong dependence of whole animal absorption on polarization and frequency of radiofrequency energy. Ann NY Acad Sci 247:532-538 (1975c).

Gandhi, O. P., and T. C. Rozzell. Liquid crystal fiberoptic RF probe. Part II: A microwave power probe. Microwave J 18(8):58-59 (1975).

Gandhi, O. P., et al. Distribution of electromagnetic energy deposition in models of man with frequencies near resonance, pp. 44-67. In C. C. Johnson and M. L. Shore (eds.). Biological Effects of Electromagnetic Waves, Vol. II. Selected papers of the USNC/URSI annual meeting, Boulder, CO, 20-23 Oct 1975. Washington: U.S. Govt Printing Office, HEW Publ (FDA)77-8011, Dec 1976.

Gandhi, O. P., et al. Deposition of electromagnetic energy in animals and in models of man with and without grounding and reflector effects. Radio Sci 12:39-48 (1977).

Gandhi, O. P., and M. J. Hagmann. Some recent results on deposition of electromagnetic energy in animals and models of man, pp. 243-260. In L. S. Taylor and A. Y. Cheung (eds.). Proc of Workshop on the Physical Basis of Electromagnetic Interactions with Biological Systems, University of Maryland, College Park, MD, 15-17 June 1977a.

Gandhi, O. P., and M. J. Hagmann. Some recent results on deposition of electromagnetic energy in animals and models of man, p. 51. In Abstracts of Scientific Papers. URSI International Symposium on the Biological Effects of Electromagnetic Waves, Airlie, VA, 30 Oct-4 Nov 1977b.

Gandhi, O. P., et al. Millimeter wave and raman spectra of living cells--some problems and results. Workshop on Mechanisms of Microwave Biological Effects, University of Maryland, College Park, MD, 14-16 May 1979.

Gandhi, O. P. State of the knowledge for electromagnetic absorbed dose in man and animals. Proc IEEE 68(1):24-32 (1980).

Gandhi, O. P., and I. Chatterjee. VLF hazard analysis. Final Report, USAFSAM Contract F33615-78-D-0617. Electrical Engineering Department, University of Utah, Salt Lake City, UT, 10 Aug 1982.

Gandhi, O. P., et al. Very low frequency (VLF) hazard study. Quarterly Report No. 2, USAFSAM Contract No. F33615-83-R-0613. Electrical Engineering Department, University of Utah, Salt Lake City, UT, 15 Feb 1984.

Gavalas-Medici, R., and S. R. Day-Magdaleno. Extremely low frequency, weak electric fields affect schedule-controlled behavior of monkeys. Nature 261:256-259 (1976).

Givoni, B., and R. F. Goldman. Predicting rectal temperature response to work, environment, and clothing. J Appl Physiol 32(6):812-822 (1972).

Goldman, R. F., et al. tolerance of hot, wet environments by resting men. J Appl Physiol 20(2):271-277 (1965).

Goldman, R. F. Acclimation to heat and suggestions, by inference, for microwave radiation, pp. 275-282. In E. R. Adair (ed.). Microwaves and Thermoregulation. New York: Academic Press, 1983.

Gonzalez, R. R., et al. Partitional calorimetry of the New Zealand white rabbit at temperature 5-35°C. J Appl Physiol 31:728-734 (1971).

Goodman, E. M., et al. Effects of extremely low frequency electromagnetic fields on growth and differentiation of Physarum polycephalum. Technical Report Phase I (Continuous Wave). University of Wisconsin-Parkside, Kenosha, WI, 1975.

Goodman, E. M., et al. Effects of extremely low frequency electromagnetic fields on Physarum polycephalum. Technical Report, Office of Naval Research, Contract N-00014-76-C-0180, University of Wisconsin-Parkside, Kenosha, WI, 1976.

Gordan, M. S. Animal Physiology: Principles and Adaptations. New York: Macmillan Company, 1977.

Gournay, L. S. Conversion of electromagnetic to acoustic energy by surface heating. J Acoust Soc Am 40:1322 (1966).

Grant, E. H., et al. The dielectric behavior of aqueous solutions of bovine serum albumin from radiowave to microwave frequencies. J Phys Chem 72:4373-4380 (1968).

Grant, E. H., et al. Dielectric Behavior of Biological Molecules in Solution. Oxford, England: Clarendon, 1978.

Grant, E. H. Determination of bound water in biological materials, p. 113. In L. S. Taylor and A. Y. Cheung (eds.). Proc Workshop Physical Basis of Electromagnetic Interactions with Biological Systems, University of Maryland, College Park, MD, 1979.

Green, F. M. Development and construction of an electromagnetic near-field synthesizer. NBS Technical Note 652, May 1974.

Green, F. M. Development of electric and magnetic near-field probes. NBS Technical Note 658, Jan 1975.

Greenleaf, J. E. Blood electrolytes and exercise in relation to temperature regulation in man, pp. 72-84. In E. Schoenbaum and P. Lomax (eds.). The Pharmacology of Thermoregulation. Basel: Karger, 1973.

Grizmek's Animal Life Encyclopedia. New York: Van Nostrand Reinhold Co., 1975.

Grundler, W., et al. Resonant growth rate response of yeast cells irradiated by weak microwaves. Phys Lett 62A:463-466 (1977).

Guru, B. S., and K. M. Chen. Hyperthermia by local EM heating and local conductivity change. IEEE Trans BME-24(5):473-477 (1977).

Guy, A. W., and J. F. Lehmann. On the determination of an optimum microwave diathermy frequency for a direct contact applicator. IEEE Trans BME-13:76-87 (1966).

Guy, A. W., et al. Studies on therapeutic heating by electromagnetic energy, pp. 26-45. In Thermal Problems in Biotechnology. New York: American Society of Mechanical Engineers, 1968.

Guy, A. W. Analysis of electromagnetic fields induced in biological tissues by thermographic studies on equivalent phantom models. IEEE Trans MTT-19:205-214 (1971a).

Guy, A. W. Electromagnetic fields and relative heating patterns due to a rectangular aperture source in direct contact with bilayered biological tissue. IEEE Trans MTT-19(2):214-223 (1971b).

Guy, A. W., et al. Electromagnetic power deposition in man exposed to high frequency fields and the associated thermal and physiologic consequences. SAM-TR-73-13, Dec 1973.

Guy, A W., et al. Therapeutic applications of electromagnetic power. Proc IEEE 62:55-75 (1974a).

Guy, A. W., et al. Determination of power absorption in man exposed to high frequency electromagnetic fields by thermographic measurements on scale models. IEEE Trans BME-23:361-371 (1974b).

Guy, A. W., et al. A new technique for measuring power deposition patterns in phantoms exposed to EM fields of arbitrary polarization -- example, the microwave oven, pp. 36-40. Proc Microwave Power Symposium, University of Waterloo, Waterloo, Ontario, Canada, May 1975a.

Guy, A. W., et al. Microwave-induced acoustic effects in mammalian auditory systems and physical materials. Ann NY Acad Sci 247:194-218 (1975b).

Guy, A. W., and C. K. Chou. System for quantitative chronic exposure of a population of rodents to UHF fields, pp. 389-410. In C. C. Johnson and M. L. Shore (eds.). Biological Effects of Electromagnetic Waves, Vol. II. Selected papers of the USNC/URSI annual meeting, Boulder, CO., 20-23 Oct 1975. Washington: U.S. Govt Printing Office, HEW Publ (FDA)77-8011, Dec 1976.

Guy, A. W., et al. Critical comparisons of RF field delivery methods to thermal responses of models and experimental animals. University of Washington, Scientific Report No. 10 (final report), 15 June 1976a.

Guy, A. W., et al. Determination of power absorption in man exposed to high frequency electromagnetic fields by thermographic measurements of scale models. IEEE Trans BME-23(5):361-371 (1976b).

Guy, A. W., et al. RF radiation patterns: Human and animal modeling data. Research report. Cincinnati: NIOSH Division of Biomedical and Behavioral Science, DHEW (NIOSH) Publ No. 77-183, 1977.

Guy, A. W., et al. Measurement of power distribution at resonant and nonresonant frequencies in the experimental animals and models. Final report, prepared for USAFSAM by the University of Washington, Seattle, WA, Mar 1978.

Guy, A. W., et al. Circularly polarized 2450-MHz waveguide system for chronic exposure of small animals to microwaves. Special issue: Bioeffects of electromagnetic waves. Radio Sci 14(6S):63-74 (1979).

Guy, A. W., and C. K. Chou. Hazard analysis: Very low frequency through medium-frequencies range. Final Report, USAFSAM Contract F33615-78-D-0617, Task 0065. Bioelectromagnetics Research Laboratory, Department of Rehabilitation Medicine, University of Washington, Seattle, WA, 5 Feb-1 Aug 1982.

Guy, A. W., et al. Determination of electric current distributions in animals and humans exposed to a uniform 60-Hz high-intensity electric field. Bioelectromagnetics 3(1):47-71 (1982).

Guy, A. W., et al. Average SAR and SAR distribution in man exposed to 450-MHz radiofrequency radiation. IEEE Trans MTT-32(8):752-763 (1984).

Hagmann, M. J., et al. Upper bound on cell size for moment-method solutions. IEEE Trans MTT-25:831-832 (1977).

Hagmann, M. J., et al. Improvement of convergence in moment-method solutions by the use of interpolants. IEEE Trans MTT-26(11):904-908 (1978).

Hagmann, M. J., and O. P. Gandhi. Numerical calculation of electromagnetic energy deposition in man with ground and reflector effects. Radio Sci 14(6S):23-29 (1979).

Hagmann, M. J., et al. Numerical calculation of electromagnetic energy deposition for a realistic model of man. IEEE Trans MTT-27(9):804-809 (1979a).

Hagmann, M. J., et al. Head resonance: Numerical solutions and experimental results. IEEE Trans MTT-27(9):809-813 (1979b).

Hagmann, M. J., et al. Dependence of electromagnetic energy deposition upon angle of incidence for an inhomogeneous block model of man under planewave irradiation. IEEE Trans MTT-29(3):252-255 (1981).

Hardy, J. D., and E. F. DuBois. Differences between men and women in their response to heat and cold. Proc Nat Acad Sci 26:389-398 (1941).

Hardy, J. D. Models of temperature regulation--a review, pp. 163-186. In J. Bligh and R. Moore (eds.). Essays on Temperature Regulation. Amsterdam: North Holland, 1972.

Hardy, J. D. Regulation of body temperature in man--an overview, pp. 14-37. In J. A. J. Stolwijk (ed.). Energy Conservation Strategies in Buildings. New Haven, CT: Yale University Printing Service, 1978.

Harrington, R. F., and J. R. Mautz. Green's function for surfaces of revolution. Radio Sci 7(5):603-611 (1972).

Hart, J. S. Rodents, pp. 1-149. In G. C. Whittow (ed.). Comparative Physiology of Thermoregulation, Vol. II. New York: Academic Press, 1971.

Hartsgrove, G. W., and A. Kraszewski. Improved tissue equivalent materials for electromagnetic absorption studies. Sixth Annual Meeting of Bioelectromagnetics Society, Atlanta, GA, 15-19 July 1984.

Hasted, J. B. Aqueous Dielectrics. London, England: Chapman and Hall, 1963.

Heilbrun, L. V. Outline of General Physiology. Philadelphia: W. B. Saunders Co., 1952.

Herrick, J. F., et al. Dielectric properties of tissues important in microwave diathermy. Fed Proc 9:60 (1950).

Heynick, L. N. USAFSAM review and analysis of radiofrequency radiation bioeffects literature, SAM-TR-81-24, Nov 1981; SAM-TR-82-16, May 1982; SAM-TR-84-6, Mar 1984; and SAM-TR-84-17, May 1984.

Hill, D. A. Human whole-body radiofrequency absorption studies using a TEM-cell exposure system. IEEE Trans MTT-30(11):1847-1854 (1982).

Hill, D. A. The effect of frequency and grounding on whole-body absorption of humans in E-polarization radiofrequency. Bioelectromagnetics 5:131-146 (1984).

Hill, N. E. Interpretation of the dielectric properties of water. Trans Faraday Soc 59:344-346 (1963).

Hill, S. C., et al. Numerical calculations of low-frequency TE fields in arbitrarily shaped inhomogeneous lossy dielectric cylinders. Radio Sci 18(3):328-336 (May-June 1983).

Hizal, A., and H. Tosun. State-space formulation of scattering with application to spherically symmetrical objects. Can J Phys 51:549-558 (1973).

Hizal, A., and Y. K. Baykal. Heat potential distribution in an inhomogeneous spherical model of a cranial structure exposed to microwaves due to loop or dipole antennas. IEEE Trans MTT-26(8):607-612 (1978).

Ho, H. S., et al. Electromagnetic heating patterns in circular cylindrical models of human tissue. In Proc Eighth International Conference on Medical and Biological Engineering, Session 27.4, Chicago, IL, 1969.

Ho, H. S., et al. Microwave heating of simulated human limbs by aperture sources. IEEE Trans MTT-19:224-231 (1971).

Ho, H. S., et al. Environmentally controlled waveguide irradiation facility. IEEE Trans MTT-21:837-840 (1973).

Ho, H. S. Dose rate distribution in triple-layered dielectric cylinder with irregular cross section irradiated by plane wave sources. J Microwave Power 10:421-432 (1975a).

Ho, H. S. Contrast of dose distribution in phantom heads due to aperture and planewave sources. Ann NY Acad Sci 247:454-472 (1975b).

Ho, H. S., and A. W. Guy. Development of dosimetry for RF and microwave radiation. II. Calculations of absorbed dose distributions in two sizes of muscle-equivalent spheres. Health Phys 29:317-324 (1975).

Ho, H. S., and H. D. Youmans. Development of dosimetry for RF and microwave radiation. III. Dose rate distribution in tissue spheres due to measured spectra of electromagnetic plane wave. Health Phys 29:325-329 (1975).

Ho, H. S. Energy absorption patterns in circular triple-layered tissue cylinders exposed to planewave sources [calculated for sources of 433, 750, 918, and 2450 MHz]. Health Phys 31:97-108 (1976).

Ho, H. S. Comparison of calculated absorbed dose rate distributions in phantom heads exposed to 2450-MHz and 195-MHz planewave and slot sources, pp. 191-200. In D. G. Hazzard (ed.). Proc of Symposium on Biological Effects and Measurements of Radio Frequency/Microwaves. Rockville, MD, 16-18 Feb 1977. Washington: U.S. Govt Printing Office, HEW Publ (FDA)77-8026, July 1977.

Ho, H. S., et al. Change in average absorbed dose rate of a group of mice under repeated exposure to 915 MHz microwave radiation, pp. 201-215. In D. G. Hazzard (ed.). Proc of Symposium on Biological Effects and Measurements of Radiofrequency/Microwaves, Rockville, MD, 16-18 Feb 1977. Washington: U.S. Govt Printing Office, HEW Publ (FDA)77-8026, July 1977.

Ho, H. S., and M. McManaway. Heat dissipation rate of mice after microwave irradiation. J Microwave Power 12(1):93-100 (1977).

Hopfer, S. The design of broadband resistive (microwave) radiation probes. IEEE Trans IM-21(4):416-424 (1972).

Hunt, E. L., et al. Dosimetry for whole-animal microwave irradiation, pp. 33-36. In J. M. Osepchuk (ed.). Biological Effects of Electromagnetic Radiation. New York: IEEE Press, 1983.

Hurt, W. D. Multiterm Debye dispersion relations for permittivity of muscle. IEEE Trans BME-32(1):60-64 (1985).

Illinger, K. H. Millimeter-wave and far-infrared absorption in biological systems, p. 43. In L. S. Taylor and A. Y. Cheung (eds.). Proc of Workshop of the Physical Basis of Electromagnetic Interactions with Biological Systems, University of Maryland, College Park, MD, 15-17 June 1977.

Interim guidelines on limits of exposure to radiofrequency electromagnetic fields in the frequency range from 100 kHz to 300 GHz. Health Phys J (Apr 1984).

Iskander, M. F., and S. S. Stuchly. A time-domain technique for measurement of the dielectric properties of biological substances. IEEE Trans IM-21:425-429 (1972).

Iskander, M. F., et al. Near-field irradiation of prolate spheroidal models of humans. Presented at the Open Symposium on Biological Effects of Electromagnetic Waves, 19th General Assembly of URSI (Helsinki, Finland), 1-8 Aug 1978.

Iskander, M. F., et al. Approximate calculation of SAR for planewave irradiation of SAR man models near a ground plane. In Proc 1978 Symposium on Electromagnetic Fields and Biological Systems, International Microwave Power Institute, 1979.

Iskander, M. F., et al. Irradiation of prolate spheroidal models of humans in the near-field of a short electric dipole. IEEE Trans MTT-28(7):801-807 (1980).

Iskander, M. F., et al. Measurements of the RF power absorption in spheroidal human and animal phantoms exposed to the near field of a dipole source. IEEE Trans BME-28:258-264 (Mar 1981).

Iskander, M. F., et al. Two-dimensional technique to calculate the EM power deposition pattern in the human body. J Microwave Power 17(3):175-185 (Sep 1982a).

Iskander, M. F., et al. A new iterative procedure to solve for scattering and absorption by dielectric objects. Proc IEEE:1361-1362 (Nov 1982b).

Iskander, M. F., and J. B. DuBow. Time- and frequency-domain techniques for measuring the dielectric properties of rocks: A review. J Microwave Power 18:55-74 (1983).

Iskander, M. F., et al. A new procedure for improving the solution stability and extending the frequency range of the EBCM. IEEE Trans AP-31(2):317-324 (Mar 1983).

Johns Hopkins Applied Physics Laboratory Health and Safety Bulletin, No. 51, 19 Oct 1984.

Johnson, C. C., and A. W. Guy. Nonionizing electromagnetic wave effects in biological materials and systems. Proc IEEE 60:692-718 (1972).

Johnson, C. C., and T. C. Rozzell. Liquid crystal fiberoptic RF probes. Part I: Temperature probe for microwave fields. Microwave J 18(8):55-57 (1975).

Johnson, C. C., et al. Long-wavelength electromagnetic power absorption in prolate spheroidal models of man and animals. IEEE Trans MTT-23:739-747 (1975).

Johnson, C. C., et al. Radiofrequency radiation dosimetry handbook, first edition. SAM-TR-76-35, Sep 1976.

Johnson, G. S., and R. S. Elizondo. Thermoregulation in Macaca mulatta: A thermal balance study. J Appl Physiol: Respir Environ Exerc Physiol 46:268-277 (1979).

Joines, W. T., and R. J. Spiegel. Resonance absorption of microwaves by the human skull. IEEE Trans BME-21:46-47 (1974).

Jones, G. P., et al. Total dielectric saturation observed in polar solution. Chem Phys Lett 4:33-34 (1969).

Jordan, E. L. Animal Atlas of the World. Maplewood, New Jersey: Hammond, Inc., 1969.

Justesen, D. R., and N. W. King. Behavioral effects of low-level microwave irradiation in the closed space situation. Proc Biological Effects and Health Implications of Microwave Radiation Symposium (BRH/DBE 70-2), Richmond, VA, 17-19 Sep 1969.

Kalmijn, A. J. Electroperception in sharks and rays. Nature 212:1232-1233 (1966).

Karimullah, K., et al. Electromagnetic coupling between a thin-wire antenna and a neighboring biological body: theory and experiment. IEEE Trans MTT-28(11):1218-1225 (1980).

Kastner, R., and R. Mittra. A new stacked two-dimensional spectral iterative technique (SIT) for analyzing microwave power deposition. IEEE Trans MTT-31(11):898-904 (1983).

Kaune, W. T., and R. D. Phillips. Comparison of coupling of grounded humans, swine, and rats to vertical 60-Hz electric fields. Bioelectromagnetics 1(2):117-129 (1980).

Kaune, W. T. Interactive effects in 60-Hz electric-field exposure systems. Bioelectromagnetics 2:33-50 (1980).

Kaune, W. T., and M. F. Gillis. General properties of the interaction between animals and ELF electric fields. Bioelectromagnetics 2:1-11 (1981).

Kerslake, D. M. The Stress of Hot Environments. Cambridge, England: Cambridge University Press, 1972.

Kinn, J. B. Whole-body dosimetry of microwave radiation in small animals: The effect of body mass and exposure geometry. Radio Sci 12:61-64 (1977).

Kleiber, M. The Fire of Life. New York: John Wiley and Sons, 1961.

Kraszewski, A., et al. Specific absorption rate distribution in a full-scale model of man at 350 MHz. IEEE Trans MTT-32(8):779-783 (1984).

Kritikos, H. N., and H. P. Schwan. Hot spots generated in conducting spheres by electromagnetic waves and biological implications. IEEE Trans BME-19(1):53-58 (1972).

Kritikos, H. N., and H. P. Schwan. The distribution of heating potential inside lossy spheres. IEEE Trans BME-22:457-463 (1975).

Krupp, J. H. In vivo Temperature Measurements during Whole-body Exposure of Macaca Mulatta to Resonant and Nonresonant Frequencies, pp. 95-107. In E. R. Edair (ed.). Microwaves and Thermoregulations. ISBN: 0-12-044020-2. New York: Academic Press, 1983.

Kucia, H. R. Accuracy limitation in measurements of HF field intensities for protection against radiation hazards. IEEE Trans IM-21(4):412-415 (1972).

Lakhtakia, A., et al. Near-field absorption in prolate spheroidal models of humans exposed to a small loop antenna of arbitrary orientation. IEEE Trans MTT-29(6):588-594 (1981).

Lakhtakia, A., et al. Absorption characteristics of prolate spheroidal models exposed to the near fields of electrically small apertures. IEEE Trans BME(8):569-576 (1982a).

Lakhtakia, A., et al. Irradiation of prolate spheroidal models of humans and animals in the near field of a small loop antenna. Radio Sci:77-84 (1982b).

Lakhtakia, A., et al. Scattering and absorption characteristics of lossy dielectric objects exposed to the near fields of aperture sources. IEEE Trans AP-31(2):111-120 (1983a).

Lakhtakia, A., et al. An iterative extended boundary condition method for solving the absorption characteristic of lossy dielectric objects of larger aspect ratio. IEEE Trans MTT-31:640-647 (1983b).

Larsen, L. E., et al. A microwave compatible MIC temperature electrode for use in biological dielectrics. IEEE Trans MTT-27:673-679 (1979).

Lee, J. H., and K. M. Chen. Eddy currents induced by RF magnetic fields in biological bodies. Radio Sci 17:61-76 (1982).

Lehmann, J. F., et al. Comparison of relative heating patterns produced in tissues by exposure to microwave energy at frequencies of 2450 and 900 megacycles. Arch Phys Med 43:69-76 (1962).

Lehmann, J. F., et al. Comparison of deep heating by microwaves at frequencies of 2456 and 900 megacycles. Arch Phys Med 46:307-314 (1965).

Leicher-Preka, A., and H. S. Ho. Dependence of total and distributed absorbed microwave energy upon size and orientation of rat phantoms in waveguide, pp. 158-168. In C. C. Johnson and M. L. Shore (eds.). Biological Effects of Electromagnetic Waves, Vol. II. Selected papers of the USNC/URSI annual meeting, Boulder, CO, 20-23 Oct 1975. Washington: U.S. Govt Printing Office, HEW Publ (FDA)77-8011, Dec 1976.

Leonard, J. B., et al. Thermal properties of tissue equivalent phantom materials. IEEE Trans BME-31:533-536 (1984).

Lin, J. C., et al. Microwave selective brain heating. J Microwave Power 8:275-286 (1973a).

Lin, J. C., et al. Power deposition in a spherical model of man exposed to 1-20 MHz EM fields. IEEE Trans MTT-21:791-797 (1973b).

Lin, J. C., and C. L. Wu. Indexing of electromagnetic energy absorption by biological objects using prolate spheroidal model, p. 47. In Abstracts of Scientific Papers. URSI International Symposium on the Biological Effects of Electromagnetic Waves, Airlie, VA, 30 Oct-4 Nov 1977.

Livesay, D. E., and K. Chen. Electromagnetic fields induced inside arbitrary shaped biological bodies. IEEE Trans MTT-22(Part II):1273-1280 (1974).

Machle, W., and T. F. Hatch. Heat: Man's exchanges and physiological responses. Physiol Rev 27:200-227 (1947).

Mahoney, S. A. Cost of locomotion and heat balance during rest and running from 0 to 55°C in a patas monkey. J Appl Physiol: Respir Environ Exerc Physiol 49:789-800 (1980).

Massoudi, H., et al. Long-wavelength analysis of planewave irradiation of an ellipsoidal model of man. IEEE Trans MTT-25:41-46 (1977a).

Massoudi, H., et al. Long-wavelength electromagnetic power absorption in ellipsoidal models of man and animals. IEEE Trans MTT-25:47-52 (1977b).

Massoudi, H., et al. Comparison of the average specific absorption rate in the ellipsoidal conductor and dielectric models of humans and monkeys at radio frequencies. Radio Sci 12:65-72 (1977c).

Massoudi, H., et al. Geometrical-optics and exact solutions for internal fields and SARs in a cylindrical model of man as irradiated by an electromagnetic plane wave. Radio Sci 14(6S):35-42 (1979a).

Massoudi, H., et al. Electromagnetic absorption in multilayered cylindrical models of man. IEEE Trans MTT-27(10):825-830 (1979b).

Massoudi, H., et al. Long-wavelength analysis of near-field irradiation of prolate spheroidal models of man and animals. Electron Lett 16(3):99-100 (1980).

Massoudi, H., et al. Comparison of the absorption characteristics of block and prolate spheroidal models of man exposed to near fields of short electric dipole. IEEE Proc:1086-1087 (1981).

Massoudi, H., et al. Postresonance electromagnetic absorption by man and animals. Bioelectromagnetics 3(3):333-339 (1982).

Massoudi, H., et al. Limitation of the cubical block model of man in calculating SAR distributions. IEEE Trans MTT-32:746-752 (Aug 1984).

McRee, D. I. Determination of energy absorption of microwave radiation using the cooling curve technique. J Microwave Power 9:263-270 (1974).

Mermagen, H. Phantom experiments with microwaves at the University of Rochester, pp. 143-152. Proc of Fourth Annual Tri-Service Conference on the Biological Effects of Microwave Radiation, New York University Medical Center, New York, 1960.

Meyerhoff, J. L., et al. Comparison of microwave irradiation at 986 MHz versus 2450 MHz for in vivo inactivation of brain enzymes in rats. IEEE Trans MTT-27(3):267-270 (1979).

Mitchell, J. C. A radiofrequency radiation exposure apparatus. SAM-TR-70-43, July 1970.

Mittlemann, E., et al. Shortwave diathermy power absorption and deep tissue temperature. Arch Phys Ther 22:133-139 (1941).

Morgan, M. A. Finite element calculation of microwave absorption by the cranial structure. IEEE Trans BME-28(10):687-695 (1981).

Morita, N., and J. B. Andersen. Near-field absorption in a circular cylinder from electric and magnetic line sources. Bioelectromagnetics 3(2):253-274 (1982).

Mountcastle, V. B. Medical physiology, Vol. II. St. Louis: C. V. Mosby Co., 1974.

Mumford, W. W. Heat stress due to RF radiation. Proc IEEE 57(2):171-178 (1969).

Nadel, E. R., et al. Importance of skin temperature in the regulation of sweating. J Appl Physiol 31:80-87 (1971).

Nadel, E. R., et al. Mechanisms of thermal acclimation to exercise and heat. J Appl Physiol 37:515-520 (1974).

National Academy cf Sciences-National Research Council. Biological Effects of Electric and Magnetic Fields Associated with Proposed Project Seafarer. Washington, DC, 1977.

National Council on Radiation Protection and Measurements. Radiofrequency electromagnetic fields: Properties, quantities and units, biophysical interaction, and measurements. Washington, DC: Report No. 67, 1 Mar 1981.

Neuder, S. M., and P. H. E. Meijer. Finite element variational calculus approach to the determination of electromagnetic fields in irregular geometry, pp. 193-198. In C. C. Johnson and M. L. Shore (eds.). Biological Effects of Electromagnetic Waves, Vol. II. Selected papers of the USNC/URSI annual meeting, Boulder, CO, 20-23 Oct 1975. Washington: U.S. Govt Printing Office, HEW Publ (FDA)77-8011, Dec 1976.

Neuder, S. M., et al. Microwave power density absorption in a spherical multilayered model of the head, pp. 199-210. In C. C. Johnson and M. L. Shore (eds.). Biological Effects of Electromagnetic Waves, Vol. II. Selected papers of the USNC/URSI annual meeting, Boulder, CO, 20-23 Oct 1975. Washington: U.S. Govt Printing Office, HEW Publ (FDA)77-8011, Dec 1976.

Neuder, S. M. A finite element technique for calculating induced internal fields and power deposition in biological media of complex irregular geometry exposed to planewave electromagnetic radiation, pp. 170-190. In D. G. Hazzard (ed.). Proc of Symposium on Biological Effects and Measurements of Radio Frequency/Microwaves, Rockville, MD, 16-18 Feb 1977. Washington: U.S. Govt Printing office, HEW Publ (FDA)77-8026, July 1977.

Neumann, E., and K. Rosenheck. Permeability changes induced by electric impulses in vesicular membranes. J Memb Biol 10:279-290 (1972).

Newburgh, L. H. Physiology of Heat Regulation and the Science of Clothing. Philadelphia: W. B. Saunders Co., 1949.

Nicholson, A. M., and G. F. Ross. Measurement of the intrinsic properties by time-domain techniques. IEEE Trans IM-19:377-382 (1970).

Nielsen, B., and M. Nielsen. Influence of passive and active heating on the temperature regulation of man. Acta Physiol Scand 64:323-331 (1965).

Novak, B., and F. W. Bentrup. Orientation of fucus egg polarity by electric ac and dc fields. Biophysik 9:253-260 (1973).

Olsen, R. G. Far-field microwave dosimetric measurements in a man-size phantom, p. 60. In Abstracts of Scientific Papers. URSI International Symposium on the Biologi' . Effects of Electromagnetic Waves, Airlie, VA, 30 Oct-4 Nov 1977.

Olsen, R. G. Preliminary studies: Far-field microwave dosimetric measurements of a full-scale model of man. J Microwave Power 14(4):383-388 (Dec 1979).

Olsen, R. G., et al. Far-field microwave dosimetry in a rhesus monkey model. Bioelectromagnetics 1(2):149-160 (1980).

Olsen, R. G., and T. A. Griner. Electromagnetic dosimetry in a sitting rhesus model at 225 MHz. Bioelectromagnetics 3(3):385-389 (1982).

Olsen, R. G. Far-field dosimetric measurements in a full-sized man model. Bioelectromagnetics 3(4):433-441 (1982).

Olsen, R. G., and W. C. Hammer. Thermographic analysis of waveguide-irradiated insect pupae. Radio Sci 17:95-104 (1982).

Olson, S. C., and M. F. Iskander. An in-situ procedure for measuring dielectric properties of low complex permittivity materials. IEEE Trans IM-35(3) (1986).

Osepchuk, J. M. (ed.). Biological Effects of Electromagnetic Radiation. New York: IEEE Press, 1983.

Pauly, H., and H. P. Schwan. The impedance of a suspension of spherical particles surrounded by a shell. Z Naturforsch 14b:125-131 (1959).

Pauly, H., and H. P. Schwan. Dielectric properties and ion mobility in erythrocytes. Biophys J 6:621 (1966).

Pennock, B. E., and H. P. Schwan. Further observations on the electrical properties of hemoglobin-bound water. J Phys Chem 73:2600-2610 (1969).

Pennycuik, P. R. A comparison of the effects of a variety of factors on the metabolic rate of the mouse. Aust J Exp Biol Med Sci 45:331, 499-509 (1967).

Peterson, D. J., et al. An investigation of the thermal and athermal effects of microwave irradiation on erythrocytes. IEEE Trans BME-26(7):428-436 (1979).

Phillips, R. D., et al. Field measurements, absorbed dose, and biologic dosimetry of microwaves. Ann NY Acad Sci 247:499-509 (1975).

Pohl, H. A. Biophysical aspects of dielectrophoresis. J Biol Phys 1:1-16 (1973).

Pressman, A. S. Electromagnetic Fields and Life. New York: Plenum Press, 1970.

Provins, K. A., et al. Tolerance of heat of subjects engaged in sedentary work. Ergonomics 5:93-97 (1962).

Rajewski, B. The biophysical basis of ultrashort wave therapy. Radiology 31:697-706 (1938).

Rogers, J. A., et al. The dielectric properties of normal and tumor mouse tissue between 50 MHz and 10 GHz. Br J Radiol 56:335-338 (1983).

Rogers, R. J. Radiofrequency burn hazards in the MF/HF band, pp. 76-89. In J. C. Mitchell (ed.). Proceedings of a Workshop on the Protection of Personnel Against Radiofrequency Electromagnetic Radiation. USAFSAM Aeromedical Review 3-81, Sep 1981.

Rosenblum, L. A., and R. W. Cooper. The Squirrel Monkey. New York: Academic Press, 1968.

Rosskey, P. J., and M. Karplus. Solvation. A molecular dynamics study of a dipeptide in water. J Am Chem Soc 101:1913-1937 (1979).

Rowlandson, G. I., and P. W. Barber. RF-energy absorption by biological models: Calculations based on geometrical objects, p. 50. In Abstracts of Scientific Papers. URSI International Symposium on the Biological Effects of Electromagnetic Waves, Airlie, VA, 30 Oct-4 Nov 1977.

Rowlandson, G. I., and P. W. Barber. Absorption of higher frequency RF energy by biological models: Calculations based on geometrical optics. Radio Sci 14(6S):43-50 (1979).

Roy, O. Z., et al. 60 Hz ventricular fibrillation and pump failure thresholds versus electrode area. IEEE Trans BME-23:45-48 (1976).

Rozzell, T. C., et al. A nonperturbing temperature sensor for measurements in electromagnetic fields. J Microwave Power 9:241-249 (1974).

Ruch, T. C., and H. D. Patton. Physiology and Biophysics, Vol. III. Philadelphia: W. B. Saunders Co., 1973.

Rukspollmuang, S., and K. M. Chen. Heating of spherical versus realistic models of human and infrahuman heads by electromagnetic waves. Radio Sci 14(6S):51-62 (1979).

Ruppin, R. Calculation of electromagnetic energy absorption in prolate spheroids by the point-matching method. IEEE Trans MTT-26(2):87-90 (1978).

Ruppin, R. Electromagnetic power deposition in a dielectric cylinder in the presence of a reflecting surface. IEEE Trans MTT-27(11):912-914 (1979).

Rush, S., et al. Resistivity of body tissues at low frequencies. Circ Res 12:40-50 (1963).

Salati, O. M., and H. P. Schwan. A technique for relative absorption cross-section determination, pp. 107-112. In Proc Third Annual Tri-Service Conference on Biological Effects of Microwave Radiating Equipments, University of California, Berkeley, CA, 1959.

Schmitt, F. O., et al. Electronic processing of information by brain cells. Science 193:114-120 (1976).

Schrot, J., and T. D. Hawkins. Interaction of microwave frequency and polarization with animal size, pp. 184-192. In C. C. Johnson and M. L. Shore (eds.). Biological Effects of Electromagnetic Waves, Vol. II. Selected papers of the USNC/URSI annual meeting, Boulder CO., 20-23 Oct 1975. Washington: U.S. Govt Printing Office, HEW Publ (FDA)77-8011, Dec 1976.

Schwan, H. P. Temperature dependence of the dielectric constant of blood at low frequencies (in German). Naturforschung [C] 3B:361-367 (1948).

Schwan, H. P. Electrical properties of blood at ultrahigh frequencies. Am J Phys Med 32:144 (1953).

Schwan, H. P., and G. M. Piersol. Absorption of electromagnetic energy in body tissue: Review and critical analysis. Arch Phys Med 33:34 (1953).

Schwan, H. P., and K. Li. Capacity and conductivity of body tissues at ultrahigh frequencies. Proc IRE 41:1735-1740 (1953).

Schwan, H. P. The electrical characteristics of muscle tissue at low frequencies (in German). Naturforschung [C] 9B:245-251 (1954).

Schwan, H. P., and G. M. Piersol. The absorption of electromagnetic energy in body tissues, Part I. Am J Phys Med 33:371-404 (1954).

Schwan, H. P. The biophysical basis of physical medicine. J Am Med Assoc 160:191-197 (1956a).

Schwan, H. P. Electrical properties measured with alternating currents; body tissues. In W. S. Spector (ed.). Handbook of Biological Data. Philadelphia: W. B. Saunders Co., 1956b.

Schwan, H. P., and K. Li. The mechanism of absorption of ultrahigh frequency electromagnetic energy in tissues, as related to the problem of tolerance dosage. Inst Radio Eng Trans PGME-4:45-49 (1956).

Schwan, H. P. Electrical properties of tissues and cell suspensions. Adv Biol Med Phys 5:147-209 (1957).

Schwan, H. P., and K. Li. Capacity and conductivity of body tissues at ultrahigh frequencies. Proc Inst Radio Eng 41:1735-1740 (1957).

Schwan, H. P. The biophysics of diathermy, ch. 3, pp. 55-115. In S. H. Licht (ed.). Therapeutic Heat, Physical Medicine Library, Vol. 2. New Haven, CT: Licht Publisher, 1958.

Schwan, H. P. Theoretical considerations pertaining to thermal dose meters, pp. 94-106. In Proc Third Annual Tri-Service Conference on Biological Effects of Microwave Radiating Equipments, University of California, Berkeley, CA, 1959.

Schwan, H. P. Absorption and energy transfer of microwaves and ultrasound tissues: Characteristics, ch. 3, pp. 1-7. In O. Glaser (ed.). Med Physics. Chicago: Year Book Publishers, 1960.

Schwan, H. P., and H. J. Morowitz. Electrical properties of the membranes of the pleuropneumonia-like organism. Biophys J 2:395 (1962).

Schwan, H. P. Electrical characteristics of tissues: A survey. Biophysik 1:198-208 (1963a).

Schwan, H. P. Determination of biological impedances, pp. 323-407. In Physical Techniques in Biological Research, Vol. 6. New York: Academic Press, 1963b.

Schwan, H. P. Biological impedance determinations. J Cell Compar Phys 66:5-12 (1965a).

Schwan, H. P. Electrical properties of bound water. Ann NY Acad Sci 125:344-354 (1965b).

Schwan, H. P. Microwave biophysics, pp. 213-244. In E. C. Okress (ed.). Microwave Power Engineering, Vol. II. New York: Academic Press, 1968.

Schwan, H. P., and L. D. Sher. Alternating current field induced forces and their biological implications. J Electrochem Soc 116:170-174 (1969).

Schwan, H. P., et al. Electrical properties of phospholipid vesicles. Biophys J 10:1102-1119 (1970).

Schwan, H. P. Interaction of microwave and radiofrequency radiation with biological systems (invited paper). IEEE Trans MTT-19:146-152 (1971).

Schwan, H. P. Biological hazards from exposure to ELF electrical fields and potentials. NWL Tech Report, TR-2713, US Naval Weapons Lab, Dahlgren, VA, 1972.

Schwan, H. P. Dielectric properties of biological materials and interaction of microwave fields at the cellular and molecular level. In S. M. Michaelson and M. W. Miller (eds.). Fundamental and Applied Aspects of Nonionizing Radiation. New York: Plenum Publishing Co., 1975.

Schwan, H. P. Field interaction with biological matter. Ann NY Acad Sci 303:198-213 (1977a).

Schwan, H. P. Classical theory of microwave interactions with biological systems, p. 90. In L. S. Taylor and A. Y. Cheung (eds.). Proc of Workshop on the Physical Basis of Electromagnetic Interactions with Biological Systems, University of Maryland, College Park, MD, 15-17 June 1977b.

Schwan, H. P., and K. R. Foster. Microwave dielectric properties of tissues: Some comments on the rotational mobility of tissue water. Biophys J 17:193-197 (1977).

Schwan, H. P., and K. R. Foster. RF-field interactions with biological systems: Electrical properties and biophysical mechanisms. Proc IEEE 68(1): 104-113 (1980).

Schwarz, G. General equation for the mean electrical energy of a dielectric body in an alternating electrical field. J Chem Phys 39:2387-2388 (1963).

Shandala, M. G., et al. Patterns of change in behavioral reactions to low power densities of microwaves, p. 56. In Abstracts of Scientific Papers. URSI International Symposium on the Biological Effects of Electromagnetic Waves, Airlie, VA, 30 Oct-4 Nov 1977.

Shapiro, A. R, et al. Induced fields and heating within a cranial structure irradiated by an electromagnetic plane wave. IEEE Trans MTT-19:187-196 (1971).

Sher, L. D. Dielectrophoresis in lossy dielectric media. Nature 220:695-696 (1968).

Sher, L. D., et al. On the possibility of nonthermal biological effects of pulsed electromagnetic radiation. Biophys J 10:970-979 (1970).

Sher, L. L. Mechanical effects of ac fields on particles dispersed in a liquid: Biological implications. Ph.D. Thesis, University of Pennsylvania, Philadelpha, PA, 1963.

Sobotta, J., and Figge, F. H. J. Atlas of Human Anatomy, Vol. I. New York: Hafner Publishing Company, Inc., 1967.

Spiegel, R. J. High-voltage electric field coupling to humans using moment-method techniques. IEEE Trans BME-24:466-472 (1977).

Spiegel, R. T., et al. A thermal model of the human body exposed to an electromagnetic field. Bioelectromagnetics 1(3):253-270 (1980).

Spiegel, R. T. The thermal response of a human in the near-zone of a resonant thin-wire antenna. IEEE Trans MTT-30(2):177-185 (1982).

Stitt, J. T., and J. D. Hardy. Thermoregulation in the squirrel monkey (Saimiri sciureus). J Appl Physiol 31:48-54 (1971).

Stitt, J. T., et al. PGE1 fever: Its effect on thermoregulation at different low ambient temperatures. Am J Physiol 227:622-629 (1974).

Stolwijk, J. A. J., and J. D. Hardy. Temperature regulation in man--A theoretical study. Pflugers Arch ges Physiol 291:129-162 (1966).

Stolwijk, J. A. J. Mathematical models of thermal regulation. Ann NY Acad Sci 335:98-106 (1980).

Stolwijk, J. A. J. Evaluation of thermoregulatory response to microwave power deposition, pp. 297-305. In E. R. Adair (ed.). Microwaves and Thermoregulation. ISBN:0-12-044020-2. New York: Academic Press, 1983.

Stoy, R. D., et al. Dielectric properties of mammalian tissues from 0.1 to 100 MHz: A summary of recent data. Phys Med Biol 27(4):501-513 (1982).

Stuchly, M. A., et al. Dielectric properties of animal tissue in vivo at frequencies 10 MHz-1 GHz. Bioelectromagnetics 2:93-103 (1981).

Stuchly, M. A., et al. Dielectric properties of biological substances at radiofrequencies, part II: Experimental results. IEEE Trans MTT-30:87-92 (1982).

Stuchly, S. S., et al. Permittivity measurements at microwave frequencies using lumped elements. IEEE Trans IM-23:56-62 (1974).

Swicord, M., et al. A two-impedance method for wide range dielectrometry, pp. 451-461. In C. C. Johnson and M. L. Shores (eds.). Biological Effects of Electromagnetic Waves, Vol. II. Selected papers of the USNC/URSI annual meeting, Boulder, CO, 20-23 Oct 1975. Washington: U.S. Govt Printing Office, HEW Publ (FDA)77-8011, Dec 1976.

Takashima, S. Dielectric properties of proteins. I. Dielectric relaxation. In J. S. Leach (ed.). Physical Principles and Techniques of Protein Chemistry. New York: Academic Press, 1969.

Takashima, S., and H. P. Schwan. Passive electrical properties of squid axon membrane. J Membr Biol 17:51 (1974).

Takashima, S., and A. Minikata. Dielectric behavior of biological macromolecules. National Research Council, Washington, DC. Digest Dielectric Lit 37:602 (1975).

Teixeria-Pinto, A. A., et al. The behavior of unicellular organisms in an electromagnetic field. Exp Cell Res 20:548-564 (1960).

Tell, R. A., et al. Electric and magnetic field intensities and associated body currents in man in close proximity to a 50 kW AM standard broadcast station, p. 360. In Abstracts of National Radio Science Meeting, Bioelectromagnetics Symposium, University of Washington, Seattle, WA, 1979.

Toler, J., and J. Seals. RF dielectric properties measurement system: Human and animal data. DHEW (NIOSH) Publication No. 77-176, July 1977.

Transmission Line Reference Book, 345 kV and above. Published by EPRI, 3412 Hillview Avenue, Palo Alto, CA 94304, 1979.

Tyazhelov, V. V., et al. New artifact-free electrodes for recording of biological potentials in strong electromagnetic fields. Radio Sci 12:121-129 (1977).

U. S. Air Force Occupational Safety and Health (AFOSH) Standard 161-9. Exposure to Radiofrequency Radiation, Oct 1984.

Von Hippel, A. Dielectric Materials and Applications. Cambridge, MA: MIT Press, 1954.

Walker, E. P., et al. Mammals of the World. Baltimore: The Johns Hopkins Press, 1964.

Waterman, P. C. Symmetry, unitarity, and geometry in electromagnetic scattering. Phys Rev 3:825-839 (1971).

Way, W. I., et al. Thermoregulatory physiologic responses in the human body exposed to microwave radiation. Bioelectromagnetics 2:341-356 (1981).

Webb, S. J., and A. D. Booth. Microwave absorption by normal and tumor cells. Science 174:72-74 (1971).

Weil, C. M. Absorption characteristics of multilayered sphere models exposed to UHF/microwave radiation. IEEE Trans Biomed Eng BME-22:468-472 (1975).

Wenger, C. B. Circulatory and sweating responses during exercise and heat stress, pp. 251-276. In E. R. Adair (ed.). Microwaves and Thermoregulation. ISBN:0-12-044020-2. New York: Academic Press, 1983.

White, R. M. Generation of elastic waves by transient surface heating. J Appl Phys 34:3559-3567 (1963).

Whittow, G. C. Ungulates, pp. 191-281. In G. C. Whittow (ed.). Comparative Physiology of Thermoregulation, Vol. II. New York: Academic Press, 1971.

Woodcock, A. H., et al. Theory of the globe thermometer. Res Study Rpt BP-7, Quartermaster R & E Command, U.S. Army Natick Laboratories, Natick, MA, 1960.

Wu, C., and J. C. Lin. Absorption and scattering of electromagnetic waves by prolate spheroidal model of biological structures, pp. 142-145. Digest of International Symposium--Antennas and Propagation Society, Stanford University, CA, 20-22 June 1977.

Wu, T. K., and L. L. Tsai. Electromagnetic fields induced inside arbitrary cylinders of biological tissue. IEEE Trans MTT-25:61-65 (1977).

Wu, Te-Kao. Electromagnetic fields and power deposition in body-of-revolution models of man. IEEE Trans MTT-27(3):279-283 (1979).

Wu, T. T. Theory of the dipole antenna and the two-wire transmission line. J Math Phys 67(D):550-574 (1963).

Wyndham, C. H., et al. Criteria for physiological limits for work in heat. J Appl Physiol 20(1):37-45 (1965).

Yoneyama, T., et al. Electromagnetic power absorption in cylindrical tissue models excited by a loop antenna. Electron Lett 15(4):125-127 (1979).

Zimmer, R., and C. M. Gros. Numerical calculation of electromagnetic energy and temperature distribution in a microwave-irradiated breast carcinoma: Preliminary results. J Microwave Power 14(2):155-158 (1979).

Zimmerman, U., et al. Dielectric breakdown of cell membranes. Biophys J 14:881-889 (1974).